KfK 5108
NEA/CSNI/R(92)10
November 1992

Proceedings of the

Second OECD (NEA) CSNI Specialist Meeting on Molten Core Debris-Concrete Interactions

Karlsruhe, Germany, 1 – 3 April 1992

Editor: H. Alsmeyer
Institut für Angewandte Thermo- und Fluiddynamik
Projekt Nukleare Sicherheitsforschung

Kernforschungszentrum Karlsruhe

KERNFORSCHUNGSZENTRUM KARLSRUHE

Institut für Angewandte Thermo- und Fluiddynamik
Projekt Nukleare Sicherheitsforschung

KfK 5108
NEA/CSNI/R(92)10

Proceedings of the

Second OECD (NEA) CSNI Specialist Meeting on Molten Core Debris-Concrete Interactions

organized by

OECD Nuclear Energy Agency
in collaboration with
KERNFORSCHUNGSZENTRUM KARLSRUHE
Karlsruhe, Germany, 1-3 April 1992

compiled by Hans Alsmeyer

Kernforschungszentrum Karlsruhe GmbH, Karlsruhe

Als Manuskript gedruckt

Kernforschungszentrum Karlsruhe GmbH
Postfach 3640, 7500 Karlsruhe 1

ISSN 0303-4003

ABSTRACT

The Second CSNI Specialist Meeting on Molten Core Debris-Concrete Interactions was held at Kernforschungszentrum Karlsruhe, Germany on April 1-3, 1992. The status and progress in this field of severe reactor accidents were discussed from researchers around the world including participants from Russia and the Czech & Slovak Federal Republic.

The contributions concentrated on two main topics. The first topic is the "classical" core debris-concrete interaction, both experimental and theoretical. Integral effects and separate effects were addressed in thermal hydraulics and heat transfer, material interaction, and aerosol release during concrete erosion, with some applications to prototypical nuclear power plants. The second topic gaining more and more interest is the possibility of controlling and ending the erosion of the concrete by spreading of the core melt, and/or achieving coolability by the addition of water.

In the final session it was concluded that considerable progress has been made in understanding and modelling the important phenomena. For the first topic a broad and generally sufficient experimental data base is existing, allowing further improvement qualification of the theoretical models which at present give reasonable agreement with the most important experimental data. A validation matrix is recommended for final validation of the codes.
With respect to fission product release during MCCI measurements show that the releases are significantly less than previously estimated.

The relatively new topic of melt coolability deserves further investigations which are already underway at different places or international coordinated efforts.

ZUSAMMENFASSUNG

Konferenzbeiträge zum zweiten OECD(NEA) CSNI Spezialistentreffen zur Schmelze-Beton Wechselwirkung

Das zweite CSNI Spezialistentreffen zur Schmelze-Beton-Wechselwirkung fand vom 1. bis 3. April 1992 im Kernforschungszentrum Karlsruhe statt. Stand und Fortschritte in diesem Gebiet schwerer Reaktorunfälle wurden von Forschern aus der ganzen Welt diskutiert, wobei auch Teilnehmer aus Rußland und der Tschechoslowakei vertreten waren.

Die Beiträge behandelten zwei Schwerpunkthemen. Das erste Thema ist die "klassische" Schmelze-Beton-Wechselwirkung, über die aus Sicht der Experimente und der Theorie berichtet wurde. Integrale und spezielle Effekte wurden angesprochen aus dem Bereich der Thermohydraulik und des Wärmeübergangs, des Materialverhaltens und der Aerosolfreisetzung während der Betonerosion. Anwendungsrechnungen für einige prototypische Reaktoranlagen wurden vorgestellt. Das zweite Thema, das zunehmend an Interesse gewinnt, befaßt sich mit der Möglichkeit, die Erosion des Betons zu beeinflussen und nach Möglichkeit zu beenden, indem die Kernschmelze weit verteilt wird und/oder durch Fluten mit Wasser gekühlt wird.

In der Abschlußsitzung wurde festgestellt, daß bedeutende Fortschritte beim Verständnis und der Modellierung der wichtigen Phänomene gemacht worden sind. Für den ersten Themenbereich existiert eine breite und allgemein ausreichende experimentelle Datenbasis, die eine weitere Verbesserung, Qualifizierung und Überprüfung der theoretischen Modelle erlaubt. Diese Modelle zeigen heute eine angemessene Übereinstimmung mit den wichtigsten experimentellen Größen. Für die abschließende Überprüfung und Bestätigung der Rechenprogramme wird eine Validierungsmatrix empfohlen. Im Hinblick auf die Freisetzung von Spaltprodukten während der Betonzerstörung zeigen Messungen, daß die Freisetzungen wesentlich geringer sind als sie früher abgeschätzt wurden.

Das relativ neue Thema der Kühlbarkeit von Schmelzen sollte weiter untersucht werden. Arbeiten hierzu werden bereits an verschiedenen Stellen durchgeführt, zum Teil im Rahmen internationaler Zusammenarbeit.

CONTENTS

Section II: MOLTEN CORE-CONCRETE INTERACTIONS UNDER PREDOMINANTLY DRY CONDITIONS AND CODES - PART B: MODELLING
Co-Chairmen: P.N. Smith and B.D. Turland (AEA Technology, UK)

Integral Codes

Thermal-Hydraulics

Material Properties

Integral Codes

Code Comparisons

Plant Applications

Summary and Recommendations

The Second CSNI Specialist Meeting on Core Debris-Concrete Interactions was held in Karlsruhe, Germany, on April 1 to 3, 1992. It was hosted by the Kernforschungszentrum Karlsruhe (KfK) and organized in collaboration by OECD-NEA and KfK. About sixty experts attended the meeting, from 13 countries including Russia and the Czech & Slovak Federal Republic and of 2 international organisations. Thirty-seven papers were presented in five sessions on the different aspects of core concrete interaction including melt coolability aspects. The final session summarized the results and discussed the current status of knowledge and the direction of future work.

The first CSNI Specialist Meeting on Core Debris-Concrete Interactions had been held at Palo Alto, California in September 1986. Since this meeting, major experimental programs and substantial modelling work had been undertaken worldwide. The scope of the second meeting was to review the experimental and theoretical work and the predictive capabilities for severe accident evaluation. In addition to the scope of the previous meeting the issues of melt spreading and coolability were addressed as options to mitigate or end a severe accident.

The contributed papers were presented in the following sessions:

I. Experiments on molten core-concrete interactions under predominantly dry conditions

II. Modelling and codes of molten core-concrete interactions under predominently dry conditions

III. Experiments on melt spreading and coolability

IV. Modelling and codes on melt spreading and coolability

V. Code comparisons and plant applications.

Conclusions and Recommendations

The following general conclusions and recommendations were formulated after a careful evaluation of the presentations and discussions:

1. A significant integral effects data base on dry molten core debris-concrete interaction now exists which consists of independent experiments in several different facilities, so that no additional large scale experiments under dry conditions are necessary. The data base is adequate for thermal hydraulics, chemical reactions, and aerosol and fissison product release during dry MCCI.

2. The present results of the codes in modeling the experiments are promising. To make optimal use of the existing experimental data base it is recommended that a matrix of selected and consistent experiments is set up covering the different aspects of MCC. This matrix would be used to provide final validation for the codes.

3. Considerable progress has been made in the physico-chemical modelling of MCCI melts. This needs to be completed and supported by additional physical property measurements, in particular viscosities and liquidus/solidus temperatures. These should be incorporated into the MCCI codes.

4. A considerable data base has been collected on the release of fission products during MCCI which shows that the releases are significantly less than previously estimated. The modelling of chemical thermodynamics of the multicomponent melt helps develop the understanding of the reasons for fission products retention in the melt, and should be completed for the releases of the important fission products.

5. Significant experimental and theoretical efforts are underway to determine the coolability of molten corium in the containment. Presently, the coolability of the melt by a water overlayer has not been demonstrated, thus the work should be continued. Relevant physical property data should also be measured as needed for modelling and validation. Melt spreading in containments was deemed to be important for analytical and further confirmatory experimental investigations since it affects coolability and containment integrity in some designs.

6. Investigation of physical phenomena related to core catcher design should be continued by the countries interested in such designs.

7. In order to test the codes for application to prototypical accident scenarios and to compare the predictions of different codes, a set of benchmark calculations should be performed. This should include short term and long term applications as well as different reactor cavities and concrete types.

The following is a summary of the five sessions:

I. Experiments on Molten Core-Concrete Interactions under Predominantly Dry Conditions

The session consisted of six contributions which described the results recently gained in the SURC test series (Sandia), in the BETA V5 series (KfK) and the ACE Program Phase C (EPRI) which is concerned with fission product release from molten corium concrete interactions (MCCI). Out of these six, one UK paper dealt specifically with the initial interaction between a fuel melt and concrete, i.e. the behaviour of the melt during the initial jet impingement phase of a MCCI.

B. Turland reported on a scoping experiment on the interaction between a superheated uranium dioxide jet and cold concrete. The test has been carried out at the Winfrith Technology Centre using its Molten Fuel Test Facilities. 24 kg of a molten fuel simulant represented by a mixture of 81% uranium dioxide and 19% molybdenum at a temperature of 3600 K poured under gravity onto the cylindrical target of basaltic concrete. With the high superheat a vigorous interaction took place. The impingement of the molten jet caused a depression in the centre of the concrete target which was about 60 mm in diameter and 33 mm deep. In the neighbourhood of the jet impact enhanced erosion was observed which corresponds to a local heat flux of the order of 10 MW per m^2. The vigorous interactions on initial contact have been reasonably replicated by an interim version of CORCON Mod. 3.

In the discussion it was concluded that although the high superheat may not be representative for accident scenarios, melt splashout may be an important issue in this context.

E.R. Copus from Sandia presented the highlights of the SURC test series related to sustained uranium dioxide/concrete interactions. The purpose of these integral tests was to study the protracted interaction of an oxidic melt pool on various basemat materials, when liquid water is not present. The 200 kg melt mixture was composed of 63% UO_2, 27% ZrO_2 and 10% Zr; the 40 cm diameter concrete basemat was formed from limestone concrete in SURC-1 and basaltic or siliceous concrete in SURC-2, respectively. In SURC-1 the interaction was sustained for over 130 minutes and in SURC-2 for over 180 minutes, i.e. over 3 hours. The major conclusions from the experiments are that the interaction temperatures remain well (about 300 K) above the concrete melting point and that the Zr chemistry drastically affects the ablation rate and the gas composition of both types of concrete. As a baseline response 5 – 15 cm/hr has been derived for one-dimensional (downward) concrete erosion in

the absence of Zr metal which can accelerate to 15 – 30 cm/hr when Zr metal is included.

In the discussion two aspects were mentioned: The high level of the interaction temperatures has to be considered in context with the oxidic melt, because the heat transfer from the oxidic melt in comparison to a metallic melt is lower. VANESA seems to generally overpredict the fission product release from MCCI in a conservative sense.

The presentation of H. Alsmeyer specifically focused on the influence of Zirconium metal oxidation on melt/concrete interaction phenomena. He reported on the corresponding BETA test series V5 recently performed at KfK. In these experiments the initial melt mixture was composed of 300 kg (mostly) iron, 80 kg Zr and an oxidic portion of 50 kg. A cylindrical melt crucible fabricated from siliceous concrete provided information on the two-dimensional erosion process. The decay heat generation was simulated by induction heating which was varied in the three tests from 670 W/kg metal to 3300 W/kg metal. It turned out that the exothermic Zr oxidation in the melt mixture dominates the interactions in the very first minutes. This is combined with a fast cavity erosion and a high gas and aerosol release. However, the exothermic Zr oxidation has no significant influence on the melt temperature behaviour in the BETA tests. The fast decrease from 2100 K to some 1750 K indicates an effective heat transfer to the concrete structure.

In the discussion it was confirmed that the comparison of different thermocouples (KfK/ANL/Sandia) revealed a good agreement in the temperature measurements ($\Delta T = 30$ K). Due to the high heat transfer from the metallic melt the interaction temperature in the BETA test series is in the metal freezing range. Due to the two-dimensional erosion process in BETA the Zr oxidation (consumption) is faster than that observed in the SURC tests.

There were three papers related to the ACE-Program. The first presentation given by B.R. Sehgal described the Program Phase C which concentrates on fission product release from molten corium concrete interactions (MCCI). In the corresponding L-series seven experiments have been carried out with four different concrete types. The corium mixture was derived from both PWR and BWR conditions.

The second paper presented by D. Thompson provided an overview of thermal hydraulic results from the ACE MCCI tests, which comprise melt temperatures, ablation rates and off-gas compositions. In general, the thermal-hydraulic data obtained may serve as excellent benchmarks for computer models used for MCCI analysis.

In the third part, J.K. Fink focussed on the aerosols released during these experiments. The release fractions were determined for corium, the fission products and the various control materials. Without repeating all the detailed information described in the paper it might be mentioned that the release fractions of the fission products were significantly below those predicted by the present VANESA code.

In conclusion, it is expected that a summary report on the Phase C test program will be issued by September 1992.

In the discussion it was stated, that the phenomenological similarities between the Phase C tests and the SURC tests confirm the common understanding of the main MCCI phenomena. The experimental information provided by the Phase C Program extends the data base for prototypical melts.

Conclusions of Session I

From both, paper presentations and discussions, it is concluded that the dominating mechanisms and phenomena of MCCI under dry conditions are sufficiently well understood. This comprises the containment load phenomena (concrete erosion, gas production) as well as fission product release into the containment.

In this respect, the (exothermic/endothermic) Zr and Si chemistry which now is represented in the MCCI code versions plays an important role. On the other hand, foaming phenomena observed in some test cases are considered to influence the long-term MCCI consequences only to a limited extent. In case of fission product release it became obvious from comparison with experimental observations (ACE-Phase C) that the models (e.g. VANESA) tend to overpredict the release.

There is a broad experimental database for MCCI under dry conditions available from several test series which have been carried out with various concrete types. These data may stimulate further code improvements.

II. Modelling and Codes of Molten Core-Concrete Interactions under Predominantly Dry Conditions

Codes and Thermal Hydraulics

The session on integral codes contained four presentations on the status and validation of the 3 most widely used MCCI codes (CORCON, DECOMP and WECHSL). In addition there were two papers describing analysis of the ACE-L6 test, which has been the subject of a blind post-test code comparison exercise, and a paper considering the uncertainties in heat transfer correlations arising from uncertainties in thermal-physical properties.

New versions have recently been completed of the 3 most widely used MCCI codes. WECHSL-Mod3 has been used in France and Germany for more than 1 year, and an extensive validation programme has been undertaken. This was described by C. Renault (CEA). The validation matrix contains tests from the BETA, SURC and ACE programmes. Only comparisons of calculated against experimental vertical ablation were presented. Apart from the later stages of the BETA V3.2 test (limestone concrete) and the ACE-L6 and L2 tests there was good agreement overall; the tests noted above showed differences between predictions and experimental data of up to a factor of 2. In the case of the ACE tests this may be due to the omission of the endothermic reduction of SiO_2 to SiO by Zr; in the case of BETA V3.2 this may be due to the different degradation process for the limestone concrete.

The WECHSL-Mod3 code has also been assessed using the data from BETA V5.1. This was presented by J. Foit. The WECHSL-Mod3 code does include the reduction of SiO_2 by Zr to Si. The experimental data for the BETA V5.1 (a metallic melt with Zr) confirm the modelling in the code for temperatures below 2100 K. Even during the exothermic oxidation of the Zr, both the code and the experiment showed a rapid decrease in temperature, indicating good heat transfer from a metal layer. Some differences between calculation and experiment were noted, particularly the overprediction of H_2 and CO; indicating that the oxidation of Si was being overestimated by the code.

The CORCON-Mod3 code incorporates many model changes and new options. These include slag film models for heat transfer to concrete, condensed phase reactions, the ability to calculate, or force, layer mixing, the inclusion of VANESA (with feedback for aerosol generation), and improved coolant heat transfer models. The code has not been generally released yet, or a full validation programme undertaken. However, D. Bradley's paper presented a comparison with three experiments (SURC-

4, SURC-1 and ACE-L6). Good agreement on ablation, and, in general, on melt temperature was obtained for the SURC tests, but the temperature and ablation rate were underpredicted for the ACE-L6 test. The code also predicted radionuclide releases to within an order of magnitude, except for Mo and Ru which were underpredicted by several orders of magnitude.

M. Plys (FAI) described the version of DECOMP incorporated into MAAP-4. The code contains simplified models, which may be calibrated using detailed first principle methods. No validation material was presented. Plys observed that in his opinion "physical chemistry of the melt is more important than thermal-hydraulics."

As noted above the ACE-L6 test has proved difficult to match accurately with code calculations. J. Sugimoto (JAERI) presented calculations for this test with a version of CORCON Mod 2.04 in which Greene's correlation for convective heat transfer was replaced by that of Kutateladze. This provided a good match to the overall ablation in the test, although the respective times for insert and basemat ablation differed from the test data. A calculation for the aerosol release with VANESA 1.01 indicated that there was a need to obtain a better estimate of the oxygen potential by allowing for condensed phase reactions.

M. Corradini presented an energy balance of the ACE-L6 test. On the basis of Si detected in the aerosol system, it was assumed that during the ablation of the insert SiO_2 reacted endothermically with Zr producing SiO gas; during the basemat ablation it was assumed that half of the remaining Zr was oxidised by SiO_2 endothermically. These assumptions gave a good energy balance for both parts of the test.

F. Gonzalez surveyed the dependency of heat transfer correlations on uncertainties in material properties, represented by differences between values in different data bases. He demonstrated how regression analysis could be used to determine priorities for material property determinations.

Observations/Recommendations

There are no agreed criteria for what is an acceptable level of agreement between codes and experimental data. As there is now a broad range of experimental data, the ability to match erosion data to ± 30 % and melt temperatures to ± 100 K should be considered reasonable, and seems to be within the reach of the new codes. The ability to predict fission product releases to within an order of magnitude (only necessary for those species with a significant release) also seems to be close to being achievable.

So far the only code for which a systematic attempt at validation has been published is the WECHSL-MOD3 code. It is important that there is an agreed understanding of the data (and the uncertainties in data) for experiments which are used to validate codes. The type of analysis applied to ACE-L6 (and elsewhere to BETA V5.1) is welcomed. To obtain the greatest credibility for code validation it is reommended that

(1) Data that are contradicted by measurements be modified in the database of the codes (e.g. viscosity, solidus).

(2) Validators of the different codes select a common set of experiments and attempt to reach a common understanding of each experiment, including recommending appropriate boundary conditions.

(3) Care should be taken to ensure that the codes are validated for all important phases (including initial and long term behaviour) of the core-concrete interaction.

The data are now available and a good start has been made. The current models are probably already acceptable for most applications; the recommended work would give this judgement a technical underpinning, which is not yet fully developed.

Materials Properties

M. Mignanelli reported a series of calculations using the SOLGASMIX-REACTOR Code which showed that the predicted releases of some fission products during MCCI are particularly sensitive to the oxygen potential and the configuration of the melt; there were also lesser dependencies on melt temperature and gas production rate. In addition the CSNI code comparison exercise showed that the predicted releases are extremely sensitive to the thermodynamic data and to the models used for the condensed phases; at the time of the CSNI exercise the predicted releases of some species varied by many orders of magnitude between the different submissions.

In order to overcome the discrepancies resulting from the ad hoc development of pseudo-binary ideal models, two programmes have begun to assess the available thermodynamic data and develop models for the melt in a systematic manner.

The programme of D. Powers to develop non-ideal solution models was reported by E. Copus. Powers uses the Kohler equation to combine subregular models for the binary sub-systems to produce a model for the metal phase. His model for the oxide phase is based on an associate model which has proved useful in the description of

complex geological melts. These models have recently been included in the VANESA code.

The other programme is being carried out by a collaboration between CEA and AEA and was reported by M. Mignanelli and P.Y. Chevalier. By analysing new systems and using data already available from NPL and Thermodata a complete set of unary and binary data, along with data for important ternary systems, has been compiled for the UO_2-ZrO_2-SiO_2-CaO-MgO-Al_2O_3-FeO-BaO-SrO-La_2O_3 system. The model for the oxide phase indicates that it behaves as a pseudo-binary eutectic rather than the pseudo-binary ideal models previously used. The data have been used in the MTDATA-nuclear and GEMINI codes to predict the solidus and liquidus temperatures for experiments carried out at ANL. The predicted solidus temperatures are in good agreement with the measured values, but there remain unexplained discrepancies in the predicted and measured liquidus temperatures. Both the new model and the experiments indicate that the difference between the solidus and liquidus temperatures is much greater than calculated by CORCON. The new model of the oxide phase also predicts strong interactions between barium, strontium and lanthanum and the zirconia and silica in the melt, which results in activity coefficients which are much less than unity for the fission products. As a result, barium, strontium and lanthanum are retained in the melt and their releases are greatly overpredicted by ideal solution models. Databases are already available for the gaseous and metallic phases. Therefore, to complete the system a model for the interaction between the metal and oxide phases must be developed. This is particularly important as it determines the oxygen potential, to which the predicted releases have been found to be particularly sensitive. To develop such a model will take a few years.

G. Bamford reported that the BUSCA pool scrubbing code has been updated since the previous CSNI MCCI specialists meeting in Palo Alto. Models have been included for: condensation onto aerosol particles; different bubble shapes; bubble breakup; bubble clusters and swarms. However, modelling has not been included for the churn turbulent flow regime, which is the most relevant regime for water pools overlying molten corium.

III. Experiments on Melt Spreading and Coolability

This session dealt with a topic which was not a part of the previous CSNI specialist meeting on core debris concrete interaction. The session primarily addressed the phase of severe accident in which interaction of the corium melt with water takes place during the MCCI. The issue is whether water will be able to cool the corium

melt so as to halt the MCCI and stabilize and stop the accident. The session also dealt with the spreading of the melt in the PWR containment cavity or BWR drywell and considered either dry or wet conditions.

The first paper by H. Alsmeyer et al. described a test performed in the BETA facility in which the primarily metallic melt interacted violently with the water present in the annulus of the BETA crucible. The steam explosion produced ~5 bar pressure. The main conclusions derived from this test were that the water presence outside the crucible cylinder did not retard the MCCI so that failure of the concrete wall did occur. The interaction of the metallic melt with water is not representative of the prototypic conditions. A similar experiment performed a week before the meeting produced the same conclusions, and the energy generated in the steam explosion was larger and partially damaged the BETA facility. The visit to the BETA facility demonstrated the extent of the damage.

Melt spreading experimental research was the focus of the paper by B.R. Sehgal and B. Spencer. They proposed a set of large scale tests using prototypic corium melt material for spreading in containment cavity representations. These tests would use the MACE equipment and the MACE furnace with a receiver vessel having either a simple geometry (channel or a sector) or a faithful replica of an actual containment. They proposed to perform a set of tests with a one-dimensional receiver vessel for purposes of validating the code MELTSPREAD, which models the physics of spreading. That code has embodied complex physical phenomena and needs data for validating the models.

B.R. Sehgal described the status of the ACE program phase D i.e., the MACE Program. He argued that the coolability conditions for the melt do not necessarily have to be that the melt is completely quenched. Indeed the minimum coolability condition is that the melt is reduced in temperature to less than the concrete solidus temperature ($\simeq$ 1500 K) and subsequently heat removal rate by water is equal to the decay heat generation rate in the solidified melt. Sehgal briefly described the main features of MACE test M0 and M1 and in terms of the programme status told about the near term scheduling of the MACE test M1B.

B.R. Sehgal was followed by Spencer who gave more detailed descriptions of the tests M0 and M1 performance and the results obtained in the tests. The test M0 provided important observations and results which were useful in the modelling of the coolability phenomena (currently there is not enough knowledge base on coolability and many scenarios have been proposed for either coolability or lack of coolability). Spencer argued that the melt swells up periodically to contact the crust formed in the

MACE test M0 and breaks through and contacts water. This was observed in the MACE test M0 and a debris bed was formed on top of the crust. Spencer described the operation of the test M1 and pointed out that the specified initial conditions of melt-water contact were not achieved. A sintered thick layer of the initial powder separated the water from the melt; however, it allowed the gas to pass through. The data obtained from the test M1 are not applicable for coolability issue resolution.

The MACE test description was followed by the description of the WETCOR test performed at Sandia Laboratories by E. Copus. The test employed about 35 kg of oxidic high temperature simulant material interacting with concrete and surrounded by a high temperature tungsten cylinder. This test produced a thick crust which precluded the cooling of the melt. A video of the test was also shown. Copus's conclusion was that it probably is not possible to cool or quench a prototypic melt in prototypic accident scenarios.

W. Tromm described a conceptual design of a core catcher which is studied in Germany and later described the experiments currently being carried out at KfK to obtain data on the physical phenomena on which the core catcher concept is based. In particular, the experiments were directed towards the melt fragmentation that may occur when water is introduced in a melt layer from below. The experiments performed at KfK with thermite (Al_2O_3, Fe and CaO) have shown fragmentation of the melt layer when water was introduced before the melt interacting with concrete. The experiment with $\simeq$ 38 kg of melt resulted in a quenched bed. The fragmentation pieces were 5 mm or larger size. No steam explosion occurred. Experiments with a plastic melt have also been conducted to obtain visual information on the melt quenching process.

In summary, significant experimental efforts are in place to identify the feasibility of cooling and/or quenching a molten corium mass released from the RPV after a core melt down accident. Generally the conditions for melt coolability (thickness of the corium layer, power density, ways of flooding, etc.) are not yet well established. Spreading tests are being proposed to study the melt coolability during its movement in the containment. Also, alternative modes of water addition are being investigated for melt cooling/quenching, in conjunction with a design effort on core catchers.

IV. Modelling and Codes on Melt Spreading and Coolability

The need for more detailed or mechanistic modelling of melt spreading and coolability stems from consideration of a number of factors.

One postulate for ex-vessel debris-water interactions for the case in which water is added as an overlying pool has been the assumption of uniform spreading and fragmentation of the debris (or significant water ingression) such that the effective surface area for heat transfer and thus heat removal is enhanced. This postulated behaviour allowed for the development of simple surrogate models for heat transfer which predicted rapid melt quenching and coolability.

However, the integral tests performed to date, SWISS, WETCOR, BETA, and MACE have not provided confirmation of the fundamental behaviour implicit in the simplified modelling approach. All of the tests performed to date have indicated a propensity for the melt to form an impervious crust at the melt/water interface. Thus, it is seen that analysis of the tests as well as reactor analysis should include modelling to account for crust formation including those mechanisms serving to inhibit crust development (i.e. gas sparging) as well as the mechanisms which act to cause failure of a crust after one has formed (thermal stresses, gas pressure from concrete decomposition).

For reactor designs which allow for greater spreading of molten debris, thus enhancing prospects of cooling and avoiding structural damage, validated models are needed to ensure analyses of greater spreading are realistic. Earlier models have focused on the hydrodynamic aspects of melt spreading and have not rigorously treated the influence of heat transfer on the melt spreading behaviour, i.e., melt immobilization and material flowing over previously frozen material.

In the event that corium water heat transfer in the static post spread configuration is insufficient to quench core debris it may be beneficial to more accurately model heat transfer in the transient and spreading mode of the process.

Modelling approaches have been described which focus on the initial formation of the crust (ANL) by evaluating the effects of the superficial gas velocity as well as an approach which incorporates into the CORCON-UW code (University of Wisconsin) more detailed modelling of the stresses created in a floating or bonded crust which would cause eventual crust failure. Incorporation of crust formation criteria into the CORQUENCH code and analysis of the MACE scoping tests by M. Farmer (ANL) showed good agreement with observed behaviour and measured heat fluxes. It is important to note that while small scale experiments have produced continuous crusts spanning the vessel cross section (20 – 50 cm) scaling studies and stress analysis performed by R. Engelstad (U. of Wisconsin) predict that at a lateral dimension greater than 2 m thermal and bending stresses would cause crust failure. However, there is a dearth of material property data relevant to thermo-physical properties

(including fracture strength) of crustal material. This is an area which should be pursued.

An alternative approach to modelling of heat transfer to overlying water in the presence of a crust was presented by J.M. Seiler of CEA/CENG in which the focus of analysis was the entrainment of molten material by sparged gas through defects in the crust. This analysis indicated corium entrainment characterized as an entrainment coefficient of .007 cm^3 of debris per liter of sparged gas would be sufficient to quench a debris bed 30 cm deep.

All of the models for predicting crust behaviour including that for mass entrainment appear to be based on a solid crust or in the case of the CEA/IPSN model a crust which is solid except for large discrete openings which would allow entrainment of molten debris. All of the integral tests involving oxidic melts (WETCOR, MACE) have produced crusts which are porous to gas flow but non porous to water ingression or melt entrainment. The models should be examined for the applicability to porous crusts and should receive further validation against experimental data.

In order to improve the prospects for ex-vessel coolability for new reactors various design features have been considered. One such design which is intended to avoid both molten core-concrete interactions and steam explosions has been proposed by A. Turricchia of ENEL-DCO. The basic feature is a three dimensional lattice of staggered graphite beams located beneath the reactor pressure vessel. The heat capacity and thermal conductivity of the graphite provides for the initial cooling of the debris; surface area enlargement for heat transfer is accomplished by the staggered arrangement of the beams which lessens the need for altering the lateral dimensions of the reactor cavity. Long term cooling of the corium would require flooding of the reactor cavity. While transient heat conduction calculations of the graphite temperatures achieved upon initial contact with the corium indicate temperatures below those associated with chemical reactions or graphite burning, additional analysis in combination with experimental tests would be valuable to confirm this view. It was also suggested that additional analysis is needed to ensure the integrity of the design for moderate and high pressure melt ejection events in case that depressurization of the primary system could not be achieved.

V. Code Comparisons and Plant Applications

M. Firnhaber reported the results of International Standard Problem ISP 30 on BETA Test V5.1. The presentation first recalled the objectives of the test, which involved both thermal hydraulic behaviour with high Zr content and Zr chemistry in

the condensed phase, and two-dimensional erosion and aerosol release. Accordingly, two types of variables were considered: thermal-hydraulics and aerosol release.

Different results were obtained with the codes WECHSL and CORCON; WECHSL was observed to predict more accurately than CORCON the initial decrease of the temperature, while, for erosion, the axial velocity was initially too high for WECHSL and too low for CORCON; the prediction of the total eroded mass was rather good.

The gas production was underestimated, because the release from the upper part of the concrete device had not been taken into account.

For Zr chemistry, calculations performed with condensed phase chemistry models exhibit rapid elimination of metallic zirconium.

The conclusions have stressed the following points:

- importance of condensed phase chemistry modelling;
- slow temperature evolutions in CORCON;
- interest in an experimental validation matrix for future work.

Results of aerosol code comparisons with releases from ACE MCCI Tests were reported by J. Fink. The calculations presented were performed for the ACE L6 test, with 30% Zircaloy oxidation and a siliceous concrete. Different participants to the code comparison exercise have used the codes SOLGASMIX, CORCON, and VANESA.

Very large differences in aerosol release predictions were observed; differences between the codes and the experiment can be tentatively attributed to:

- the differences in oxygen potential modelling;
- the absence of modelling of chemical reaction between condensed phases;
- zirconium chemistry;
- no modelling of metal vaporization;
- influence of the different databases used.

It has to be noted that, for some fission products, the released quantity is less than the detection limit.

As a conclusion, the author recommended to continue the work on thermodynamic databases - including experiments if necessary - and to increase the efforts for condensed phase chemistry modeling.

The calculations presented by F. Müller analysed a VVER 1000 reactor with a 2.50 m thick basemat consisting of serpentine concrete. The effects of instrumenta-

tion tubes in the walls of the reactor pit and a connecting door to the other parts of the containment were considered. Results suggest that these instrumentation tubes could constitute a potential cause of early containment failure in the case of core-concrete interaction, as they are located relatively close to the inner part of the reactor pit walls.

In the subsequent discussion, it was pointed out that a satisfactory simulation of MgO chemistry to describe the serpentine concrete behaviour may be obtained by considering it as CaO in the WECHSL calculation.

Also, the possibility for corium cooling subsequent to spreading was suggested as a possibility for further studies.

Application of the WECHSL code to PWR and BWR calculations were reported by J. Foit. Two basic cases were considered in this study:

- PWR like configuration with siliceous concrete and water ingression after 0.9 m erosion;
- BWR like configuration with limestone concrete of higher decomposition temperature and a very small reactor cavity
- These calculations also differed by the thickness of the basemat and the residual power being considered.

For the PWR case, a penetration of 6 m was predicted to occur in about five days. Sump water ingression hardly changed this time. For the BWR case, time was shorter due to the absence of lower crust formation.

These figures were given for further comparison with other codes (for example CORCON).

Members of the Programme Committee and/or Session Chairmen

Dr. Hans Alsmeyer (KfK, Germany) - *Chairman*
Dr. Bernhard Kuczera (KfK, Germany)
Mrs. Catherine Lecomte (CEA/IPSN, France)
Dr. B. Raj Sehgal (EPRI, USA)
Dr. Paul N. Smith (AEA Technology/WTC, UK)
Mr. Charles Tinkler (USNRC)
Dr. Brian D. Turland (AEA Technology/SRD, UK)

Mr. Jacques Royen [OECD (NEA)] - *Secretary*

Overview Paper

EX-VESSEL MELT BEHAVIOR AND ITS ROLE IN SAFETY ASSESSMENT OF LWR

Invited paper by

J. ROHDE* and G. CENERINO**

(*) Gesellschaft für Reaktorsicherheit (GRS) mbH
Schwertnergasse 1
D-5000 Köln 1
F.R.G.

(**) Institut de Protection et de Sûreté Nucléaire
Département de Protection de l'Environnement
et des Installations
Service d'Etudes sur les Accidents
IPSN/CEA - BP N°66 - 92265 Fontenay-aux-Roses Cedex
France

1. INTRODUCTION

In the unlikely event of a severe accident in a nuclear power plant, if recovery of the safety functions cannot be obtained, the core may degrade, melt through the vessel and slump in the floor of the reactor pit.

This process is strongly dependent on the in-vessel core degradation, progression and lower head failure modes.

Depending on the reactor design and the pressure in the primary circuit at the time of the vessel failure, the corium can react with the atmosphere of the reactor (DCH: "Direct Containment Heating"), or with the available water in the reactor pit or with the floor of the cavity.

The "Direct Heating" needs an open geometry of the reactor pit : in that case, under the primary circuit pressure effect, the corium is blown and fragmented in the reactor containment and this process can, under some restricted conditions, generate a peak of pressure in the containment. Some countries have included in their accident management procedures a primary circuit depressurization, which can avoid this effect.

On actual LWR reactors, the floor is made of concrete and the hot mixture of the core material called "corium" interacts thermally with the concrete basemat. Under thermal effect, the concrete of the basemat is eroded into oxide liquid or solid compounds (SiO2, CaO, MgO,...) and gas compounds, such as CO2 and H2O. These oxides mix with the molten fuel and steel stuctures and the gas are partly reduced into CO and H2. This phenomena is called "Core-Concrete Interaction: CCI" or sometimes "Molten Core Concrete Interaction: MCCI".
When water is present in the reactor pit, there could be an energetic interaction due to the contact between the superheated liquid fuel and the coolant: this phenomena is known as "steam explosion".

These two aspects of a severe accident are presently under studies with international experimental programs (BETA at KfK/Germany, SURC and WETCOR at SNL/USA, ACE and MACE at ANL/USA, FARO at ISPRA/Italy, ...) or national programs (especially concerning the steam explosion). Up to now, there was only one scenario leading to a real case of MCCI: the TCHERNOBYL accident.

On future reactors, the bottom of the reactor pit could include some corium retention devices usually called "core-catchers".

From a safety point of view, if no mitigation actions are done to reach ex-vessel coolability of the corium, the MCCI is an important aspect of the overall severe accident, because of its possible consequences:
- release of aerosols, generation of steam and combustible gases into the containment
- possibility of basemat penetration and loss of containment leaktightness, side wall attack, hole penetration.

The relevance to containment loading was shown by a number of special national investigations (NUREG 1150, DRS-B).

If an ex-vessel steam explosion occurs, the effects on the containment structures, on the local aerosol resuspension and gas distribution, have to be evaluated.

Consequently, the accident management, either on actual LWR reactors or future ones, requires to answer some main safety questions, **if a vessel melt through occurs**, related to the coolability of the corium and the containment integrity. These two main safety questions are closely connected and cannot be separated.

2. BOUNDARY CONDITIONS FOR EX-VESSEL MELT BEHAVIOR

The main boundary conditions for the ex-vessel melt behavior are determined by the process of core degradation, mass slumping into the lower plenum, quenching of hot material by the residual water and details of the structural design of the RPV bottom.

2.1 Metal-water reaction

The extent of the exothermic reaction of steam - mainly with zircaloy - will be controlled by the temperature level of the core materials, the local availability of steam, together with the accessibility of unoxidized metallic surfaces containing zirconium. A high degree of oxidization leads to a high energy release into the core region resulting in an acceleration of the core degradation. In addition, the degree of oxidization determines the type of debris formation and the melting temperature of oxidized and metallic materials, the quantity of unoxidized metal in the melt at the time of vessel failure and the amount of pre-existing hydrogen at vessel-failure time.

2.2 Core slumping

The initial slumping of molten materials from the core region into the lower plenum of the RPV could result in high steam production rates due to the quenching of hot material in the vessel. This would lead to an acceleration of the melting process because of the increased exothermic reaction between zircaloy and steam in the core region. The mass flowrate of molten materials into the lower plenum is of major importance. A short term slump of molten materials will lead to different melt or debris conditions prior to vessel failure, than would be expected in case of an extended core slumping process.

2.3 Failure mode of the RPV

After an evaporation of residual water, solidified materials in the lower plenum will heat up again by decay heating to the melting point. It might be also that molten material penetrate water without complete break up and subsequently evaporation of only limited amount of water would occur. As a result, the RPV lower structures, being covered by solidified and/or molten materials, would be heated up. Due to system pressure and/or temperature loads, the vessel would fail.
Structural details of the RPV and connecting pipework determine the failure mode of the primary system under pressure. Penetrations in the lower part of the RPV, such as core instrumentation nozzles, are generally assumed to fail first, leading to a limited opening for the discharge. A gross head failure mode, such as a ballooning-type is more likely to occur in a design of the bottom head without penetrations. Such a failure mode could severely damage the reactor cavity and the vessel support structure, with a subsequent dispersal of debris and steam into the containment. Under low pressure conditions, one can also distinguish between local and global vessel failure. Local failure is due to local melt-through of one, or several penetrations through the lower vessel head while a global vessel failure means that the lower head fails as a whole due to weakening of the vessel wall at the height of the inner melt pool. Mode and timing of vessel-failure are very important to subsequent events.

2.4 Melt conditions

Mixing of molten materials takes place in the lower plenum prior to vessel failure. The possible incorporation of significant quantities of steel into the melt is important. This affects the amount of chemical energy available in case of a possible DCH as well as general conditions of the melt. A longer time span between core slumping and vessel-failure implies a higher temperature of the melt and a larger mass in the lower plenum. Therefore for early vessel failure there will be less molten materials on the bottom of the vessel at a lower temperature level.

To summarize, the main issues of importance for the release of molten materials from the RPV into the reactor cavity are:

* system pressure prior to vessel failure;

* mode of vessel (or system) failure;

* mass of molten material in the lower plenum;

* composition of the melt and gases in the system;

* temperature of the melt.

3. THE MOLTEN CORE CONCRETE INTERACTION (MCCI)

3.1 The MCCI phenomenology

3.1.1 Corium mass and composition

The initial composition of a corium depends on the reactor type (BWR, PWR, VVER,...). Anyway, a typical initial corium mass includes masses from the fuel (UO2, Zr, Ag, B4C,) and additional masses of metal (mainly stainless steel) coming from the core and the bottom internal structures and a part of the lower head of the vessel.

3.1.2 Internal source of heating

The decay heat is the dominating internal heat source, except at the beginning of a MCCI, as long as the metal oxidization processes takes place.

Using one percent of the normal reactor thermal power as the internal decay heat in a corium is a conservative assumption of the decay heat evolution. A more precise value depends on the accident scenario and does not take into account the volatile fission products (mainly noble gases, iodine, tellurium) released in vessel during the core degradation.
The fission products are mainly under oxidic form.

The Zr and Cr oxidization processes, especially between Zr and CO2, H2O and SiO2, are very exothermic. As a consequence, the oxidization power can exceed the residual power by a factor of 10 to 40. Meanwhile, these oxidization processes are very fast and occur during the first hour and even less of a MCCI. As a consequence, this period of time corresponds to a strong corium agitation by the gas coming from the concrete erosion process. But even during this period of a MCCI, the ACE experiments showed that the fission products release stayed neglectable in front of the in-vessel release.

3.2 Existing experiments

Since the last OECD specialist meeting on core concrete interaction (Palo Alto, USA, Sept. 1987), new MCCI experiments were done :
- the BETA II series in KfK, FRG
- the ACE tests in ANL, USA
- Some SURC tests in SNL, USA.

New tests are also under preparation such as the ALPHA tests (Japan).

Different groups of MCCI international experts were following all these tests. Two International Standart Problems (ISP 24 on SURC4 and ISP 30 on BETA V5.1) were organized by the CSNI/OECD.
The ISP 24 (1988) showed a lack of modelling in the codes concerning the condensed phase zirconium chemistry. The ACE and BETA II tests were very useful to solve the problem and, today, all codes considering the condensed phase zirconium chemistry show better agreement with the experimental results than before. This was one of the conclusion of the ISP30.

To sum up, there are today a series of MCCI tests, enough to create a validation matrix covering the different aspects of MCCI for the main types of basemat concretes: silicate, limestone/common sand, limestone/limestone and even refractory (serpentinite) type of concrete.

There exist also code validation based on some experiments, not on others, depending on the code and the version of the code.

As a consequence, and it is one of the ISP30 recommandation, it is recommended that further code assessment should use validation matrices based on different experiments and test facilities, to overcome the experimental imperfections of a single experiment.

3.3 Overview on codes and transfer to real plant conditions

There are today several MCCI codes (e.g. WECHSL, CORCON, DECOMP). As quoted precedently, there is a need for a global code comparison on a complete experimental test matrix. This could be useful to situate the state of validation of all codes in comparison with the achieved experiments.

Concerning the transfer to real plant calculation, a code User group appears to be a very efficient way to solve problems and to analyse the code user feedback.
Experiments solve only special aspects of MCCI (e.g. chemistry, concrete erosion). As codes are not attached to an experiment configuration, and due to the number of physical phenomena occuring during a MCCI, the use of code for reactor calculation must be understood only as a general tendancy of what could happen in case of a real MCCI .

There exists three main aspects in a MCCI: the basemat erosion, the hydrogen production and the fission product release from the melt.
Concerning the concrete basemat erosion, calculations show that, if the corium is not spread and cooled from its surface before starting enough concrete ablation to increase the height of the molten pool, the basemat penetration is bound to happen.
After a short peak value for the hydrogen production rate, the long term production depends on the content of metals in the molten pool of corium and concrete materials. Low release rates were calculated for the hydrogen in this long term range.
The ACE experiments showed that the presence of silicates and zirconates in the melt explains the strong fission products (FP) retention in the pool during the MCCI: the general FP release at the beginning of a MCCI is several orders of magnitude less than the FP release corresponding to the "in vessel core degradation" phase.

4. THE CORIUM COOLABILITY

4.1 General principles to avoid a concrete basemat penetration

For typical LWR of about 1000 MWe, a corium can only be stopped in a semi-infinite concrete structure if the core material mixed with the liquefied concrete fills a very large semispherical or semi-elliptical volume where the decay heat can be completely transported into the concrete structure by steady state conduction. Typical dimensions of such a cavity are more than 20 m. This means that basemat thicknesses on present reactors (from 5 to 10 m) are not sufficient to cool and to stop the corium.
To avoid the basemat penetration, another efficient cooling is needed. As the larger the exchange surface is, the more the cooling phenomena is effective, it is important, before looking at different ways of cooling, to look at the two main phenomena allowing the exchange surface to grow: the corium spreading and the corium fragmentation.

4.2 Corium spreading

One of the key issues to study the coolability of a corium deals with the capability for a corium to spread on a given surface, with and without water.

As a matter of fact, one of the main parameters controlling the corium cooling is the heat exchange surface between the melt and the coolant. To increase the heat exchange surface in a completely safe way, one possibility consists in increasing the available

spreading surface for the corium. Most of the proposed core-catcher designs are using this approach.

Of course, an accurate knowledge of the lower head vessel failure mode and kinetics (allowing to calculate the corium pour rate, melt composition...) is necessary to predict as best as possible the corium spreading, because these are initial conditions of the spreading. These initial conditions were discussed in chapter 2.
But even in the case of well defined initial conditions, uncertainties regarding melt progression and freezing phenomena remain large because only little experimental works have been done up to day on melt spreading.

4.2.1 Existing experiments

Many melt freezing experiments have been done in the frame of fast reactor studies with real material, but only limited results are of interest for our purpose because tests were performed in tubes of low hydraulic diameters (a few millimeters) at high driving pressures.

- Fauske & Associates performed tests in which alumina-iron thermite was poured in a rectangular channel, but the instrumentation was limited (1).

- Experiments with low melting temperature simulant materials have been performed by GREENE and al. (1988), with small amount of simulant (lead) and also limited instrumentation. Howewer, some spreading correlations have been derived (2).

This explains that new programs to study the corium spreading have been initiated:

- Experiments with low melting temperature simulant materials are done presently by CEA/IPSN, France. The main objective of these tests is to model hydrodynamics of melt spreading and crust behaviour of the melt on the substrate. These tests are called CORINE experiments (**COR**lum relocation a**N**alytical **E**xperiments) (3).

- More realistic tests for LWR melt spreading investigation, using about 300 Kg of real material melts, are planned to be done by EPRI at ANL (SMELTR program) (4).

Nota:
Experiments on steel spreading (SPREAD) are also performed in Japan but more informations about these tests are not yet available at the time of this publication.

4.2.2 Overview on codes and transfer to real plant conditions

There exist today only few codes to calculate the corium spreading (the MELTSPREAD code (EPRI, USA)). These codes need validation before their results can be transfered to real plant conditions.

4.2.3 Reactor protection and safety problems

For actual reactors, if some actions are decided allowing a corium spreading in the containment, it is important to check that this possibility doesn't interfere with other safety functions (e. g. : don't prevent the sump water recirculation).

For future reactors, there is no special problem except the risk of a steam explosion if the corium has the possibility to contact the water. Possible damage to the cavity design, the distribution of melt particles in the containment together with the resulting gas, and aerosols distribution, have to be analysed.

4.4 Corium fragmentation

A corium fragmentation increases of course the exchange surface for the corium coolability. This fragmentation can be the consequence of a steam explosion, or the results of the corium entrainment by the gas bubble in an overlaying water pool for example, or the required consequence of a specific design (core catcher).

4.4.1 Fragmentation in a water pool

A steam explosion could result from a drop of superheated liquid corium in a water pool, or by a quick destabilisation (trigger) of an established corium/water contact (water pool over corium for instance).
But, of course, one cannot rely on a steam explosion to get a corium coolability by creating corium fragmentation because it is not a "controlled" phenomena and it can generate an energetic interaction.

The more the corium is fragmented when falling in the water, the more efficient the steam explosion (if it happens) is.

4.4.1.1 Existing experiments

There exist today a CEC experimental program to study the pre-mixing in a closed vessel: the FARO experiments (Ispra, Italy), and some small scale national programs (KfK, CEA, UKAEA, NRC, ...), more general about steam explosion.

4.4.1.2 Overview on codes and transfer to real plant conditions

Codes on pre-mixing (IVA III (KfK), TRIO MC (CEA), CHYMES (Winfrith,AEA), IFCI (SNL), PM-ALPHA (UCSB), TEXAS-II (UW/JRC)) are today on the state of validation.

4.4.2 Fragmentation as result of gas entrainment

The corium entrainment out of the corium pool in a water pool could be, in some cases with high gas release, an efficient cooling phenomena, by creating a coolable particles debris bed.

4.4.2.1 Existing experiments

None, but some informations on the debris bed characteristics can be obtained from the MACE tests.

4.4.2.2 Overview on codes and transfer to real plant conditions

CEA/IPSN has developed the PERCOLA modelling to study this phenomena.

4.4.3 Fragmentation as result of a core catcher design

If, as derived from core-catcher goals, it is decided to create voluntarily a corium fragmentation, a thermal conduction calculation shows that fragmented corium, considered as spheres with a radius exceeding around 30 cm, cannot be cooled.

4.5 Corium cooling

A second aspect of an efficient corium cooling is the way of cooling. If water is used, it is interesting to note that the most efficient cooling is obtained when the water injection in the corium is situated at the bottom of the corium pool.

It could also be of interest to use some material whose change of state (fusion, vaporization, sublimation) is endothermic or to use endothermic chemical reactions.

Then of course, radiation or heat exchangers can participate to a corium cooling.

The energy to evacuate is an important parameter for an efficient cooling. As a consequence, it seems reasonable to wait that the main exothermic chemical reactions between the corium and the concrete are finished (Zr oxidization with SiO2, CO2 and H2O), that means some hours (1 to 3) after the beginning of the MCCI.

4.5.1 Cooling with water

There are 3 ways to introduce water in a corium pool:
- a water injection over the corium pool
- a water injection inside the corium pool,
- a water injection under a corium pool.

If the corium pool is assumed to be a thick debris bed, orders of magnitude of the drying heat flux of a fully wetted thick debris bed show that in case of a water injection over the corium pool, the extracted energy is similar to the radiated energy when the corium is dry at the beginning of the interaction (high superficial gas velocity from corium). Later (small superficial gas velocity) the extracted energy can be higher than the decay heat.

In case of a water injection under the corium, the efficiency is much more important that the one of the water injection over the corium pool (factor 3).

4.5.1.1 Existing experiments

The MACE experiments (realised by Argonne National Laboratory, USA) have started and look at the pouring of water on real materials (UO2 + concrete) interacting with concrete.

The WETCOR experiments consist in pouring water over a sustained heated melt obtained by a thermite reaction.

4.5.1.2 Overview on codes and transfer to real plant conditions

Only limited modelling at the present time.
In the usual MCCI codes such as CORCON or WECHSL, the modelling consists in a film mode or an enhanced heat transfer mode.

4.5.1.3 Reactor protection and safety problems

There are two safety problems to be aware of:

- a steam explosion:

Concerning this point, it is advised to wait several hours after the beginning of the MCCI to introduce water on the corium, whatever the way is. Doing so, the internal heat to extract is lower and the viscosity of the corium should have increased (due to concrete mixing), reducing the fragmentation process.

- the containment overpressurization of the reactor containment by the steam coming from the water vaporization.

4.5.2 Cooling with endothermic phenomena

A material could be used to absorb the energy, when in contact with the corium, either by change of state (fusion, vaporization, sublimation) or by chemical reaction.

This material should have a temperature of endothermic change of state as low as possible (less than 2400 K) and as endothermic as possible.

When comparing the latent heats of fusion of some material like water, aluminate, lead, concrete and UO2, it appears that the concrete has the greater value: around 4800 MJ/M^3 of concrete.

But it could be seen (paragraph 2.1) that melting of the available concrete is not enough to assure a corium cooling if no spreading occurs.

After the concrete, the water is one of the most efficient coolant.

4.5.3 Cooling using radiation

The radiation process, to participate efficiently at the cooling of the corium needs such a spreading surface that the thickness of the corium does not exceed some tens of centimeters.

4.5.4 Cooling using a heat exchanger

Using a heat exchanger raises the question concerning the availability of this system in all the situations: should such a system be passive or not ?

Should such a system be the main cooling system or a contributor to the cooling ?

5. ROLE OF CODES AND USE TO PRA

The understanding of the MCCI phenomenon has improved significantly as the result of the extensive experimental and theorical investigations, carried out during the last years. Computer codes have been developed and validated against large scale experiments, where prototypic and non-prototypic materials have been used. The simulation of the major sources of energy were realized by thermite reaction and inductive heating or direct electrical heating with electrodes.

By this, the direct use of experimental data and the codes, transfering the main experimental findings to real plant applications, have to be investigated carefully.

Although a concentrated effort was made to base the fundamental phenomenological modelling on the best state-of-the-art technical knowledge available, e.g. physics, chemistry and thermal hydraulics, in many cases, such knowledge is limited. Many of the physical regimes beeing modeled lie outside the range of thoroughly understood physics and chemistry. Material properties such as thermal conductivity, viscosities, specific heats and surface tensions are not well known, or perhaps not measured at all the temperatures above 2000 °C. Previously performed studies continue to provide insights from which these model uncertainties can be reduced.

Estimates of the magnitude of such model uncertainties can be made through a combination of scientific judgment and carefully planed and executed sensitivity studies.

Information required as input for codes, describing the MCCI processus, must be derived from plant specifications and output data from other accident analysis codes that treat the in-vessel phenomena.

In particular, these informations and input variables are:

* composition and material properties of the cavity concrete,

* initial geometric configuration of the reactor pit,

* composition and mass of the core debris at the time core-concrete interaction is initiated,

* initial temperature of the debris,

* mass flow rate and temperature of additional debris if deposition is continuous,

* fission product inventory present in the debris at the time of the vessel failure.

Except for the first two items, concrete composition and cavity shape, the inputs listed above must be derived from the in-vessel and melt progression codes. The first two items are plant specific data.

For PRA's, the existing and qualified codes must be able to estimate the potential risk related consequences of core-concrete interactions:

* radioactive and inert aerosols release from core debris,

* combustible gas production (H_2 and CO),

* non condensable gas generation (H_2, CO, CO_2),

* convective and radiative heat from debris pool surface,

* erosion (radial **and** axial) of concrete and other structures.

The consequences of the thermal and chemical core-concrete interactions may significantly impact containment loading and the mode of containment failure.

But it has to be stated that the loads deriving from MCCI are related to the longterm regime of a severe accident (several hours after SCRAM).

6. NEW CONCEPTS

New concepts include some corium retention devices usually called "core-catchers". A tentative list of safety recommandations for such design is listed below:

6.1 Safety Recommandations for a Core Catcher

If a core catcher concept happens to be choosen for a new reactor design, or added to an actual reactor, it should, from a safety point of view:

- be passive (?) or active (?) or a mixed option (?)

- don't disturb the normal reactor functioning

- don't interfere with other safety

- don't increase the loads to the reactor containment

- be able to manage large number of scenarii of severe accident

- have an efficient cooling

- be tight to fission products release in the ground

- have all instrumentation needed for the accident management

6.1.1 Be passive (?) or active (?) or a mixed option (?)

This is an important point, open to discussion: should a core catcher, under the safety point of view, be a non passive or passive design or a mixed option ?

6.1.2 Don't disturb the normal reactor functioning

None of the systems included in a core catcher should disturb the normal reactor functioning. This recommandation seems very important especially if a core-catcher is added to a current reactor design.

6.1.3 Don't interfere with other safety

Careful analyses must be made to check that all the safety systems are not disturbed by a core-catcher, in a future or actual reactor.

A care must be taken to avoid criticity and to assure a biological protection of the core-catcher.

6.1.4 Don't increase the loads to the reactor containment

Depending on the core-catcher principle, one must be sure not to increase loads to the reactor containment, that could result from:
- a combustible gas production
- a pressurization
- a fuel coolant interaction

6.1.5 Be able to manage large number of scenarii of severe accident

A core catcher should be designed to handle a large number of scenarii of severe accident, such as for example:

- high pressure ejection of the corium in the cavity,

- low pressure ejection

- core concrete interaction starting 1 or 2 hours after SCRAM (this means that the decay heat will be maximum)

- core concrete interaction starting 1 day after SCRAM
(this means that the containment will be already under pressure due to the vaporisation during 1 day of the water coming from the safety injection system).

List non limitated...

6.1.6 Have an efficient cooling

A core-catcher must cool a corium without any doubt.

As a consequence, it is advised to combine several passive ways of cooling. To increase the efficiency of these cooling phenomena, an increase as better as possible of the exchange surface of the corium is to be found. A good determination of the heat transfer coefficients between the corium and materials of the core-catcher needs probably a R&D program, especially if water is used as a coolant of a steel plate in contact with the corium.

6.1.7 Be tight to fission products release in the ground

A core-catcher must be tight to fission products for very long term. Depending on its situation, biologic shield must be taken into account.

6.1.8 Have all instrumentation needed for the accident managment

The instrumentation of the core-catcher is very important to manage a severe accident and control the core-catcher efficiency.
Such instrumentation should include: (not exhaustive)

- check of the corium state (temperature, pressure)

- check of the corium localization (is the spreading effective ?)

- check of the tightness

- check of the corium activity

- check of the gas release and composition

- check of the gas activity

7. OPEN QUESTIONS

Before listing some open questions, it is of interest to list some conclusions and recommandations of the first CSNI Specialist meeting on Core-Concrete Interaction which are still valid for the application to real nuclear plants:

* The effect of uncertainties in the prediction of containment loads and fission products releases must be taken into account.

* Code predictions of the temperature history of core-concrete interactions are sensitive to initial and boundary conditions.

* Containment loading was predicted to be sensitive to concrete composition and to assumptions about upwards heat transfer.

* The consequences of molten-core-concrete interaction depend on (1) initial composition of debris, (2) initial temperature, (3) amount and rate of discharge from the reactor vessel, and (4) geometric configuration of debris in the reactor cavity.

* Metallic Zircaloy can have important effects on the prediction of aerosols and radionuclides releases.

* More attention should be focused on long-term phenomena: containment temperature, pressure, aerosol loading, steam content of containment atmosphere, containment basemat penetration, stabilization of the core debris in the ground and effects of

delayed flooding on melt coolability, magnitude of melt-coolant interaction, and resuspension of radionucleides that may be present in the flooding water source.

All these past and present investigations raise some questions:

Do we know enough about the thermal-hydraulics of MCCI ? Is the present knowledge enough to calculate a basemat penetration and a radial erosion, taking the general level of uncertainties of the phenomena during a severe accident into account ?

Do we know enough about the fission product release during a MCCI, regarding the level of the in-vessel release ?

Do we have identified the key phenomena explaining the fission product retention in the corium during a MCCI ?

Are we sure that we can extrapolate the fission product release results and thermohydraulic of MCCI to reactor case ? to core catcher ?

References:

(1) FARMER M.T., SIENICKY J.J., SPENCER B.W.
"The MELTSPREAD 1 Code for the Analysis of Transient Spreading in Containments"
ANS Winter Meeting Session on Thermal Hydraulics of Severe Accidents, Washington D.C., November 11-15, 1990.

(2) GRENE G.A., FINFROCK C., KLAGES J., SCHWARZ C.E.
"Experimental studies on melt spreading, bubbling heat transfer and coolant layer boiling."
BNL NUREG 42299, 1988.

(3) VETEAU J.M., GRUSS J.A., CENERINO G.
Simulant Material Experiments in Support of the Analysis of Melt Spreading in Reactor Containments: CORINE Experiments.
IPSN, March 1992.

(4) SEGHAL B.R.
Proposed joint program of experiments on spreading of melt in reactor containments (SMELTR), EPRI, March 1992.

SECTION I

MOLTEN CORE-CONCRETE INTERACTIONS UNDER PREDOMINANTLY DRY CONDITIONS - PART A: EXPERIMENTS

Thermal-Hydraulics and Aerosols

Interaction Between a Superheated Uranium Dioxide Jet and Cold Concrete

L D Howe[1] M K Denham[2] B D Turland[1] L M G Dop[2] and R J Humphreys[1]

Abstract

A scoping experiment has been carried out at the Winfrith Technology Centre using its Molten Fuel Test Facilities to examine the initial interaction between a fuel melt and concrete. A molten fuel simulant consisting of 81% UO_2 and 19% Mo with a large superheat ($T \simeq 3600K$) was poured onto a basaltic concrete target. Thermocouple data indicate that there was an initial high rate of ablation. The test demonstrated that in the case of such high superheats, a vigorous interaction between the jet and the target takes place, with much of the impinging material ejected within the first few seconds. There was a depression eroded into the target by the jet. The experiment has subsequently been modeled at Culham Laboratory using a version of the CORCON MCCI (molten core – concrete interaction) computer code. The calculations were able to produce a representation of this effect. The results of the experiment and the calculation have been compared with jetting correlations, and reasonable agreement has been found. We conclude by advising caution when applying the results of this isolated test to more prototypic interactions.

1 Introduction

It is possible that, in the unlikely event of a severe accident in a pressurized water reactor (PWR), the pressure vessel could fail locally in such a way that a jet of molten core material would impinge on the concrete basemat of the reactor containment. Most studies of molten core-concrete interactions (MCCIs) have concentrated on the longer term part of the interaction, when a pool of molten corium and concrete decomposition products would gradually ablate the concrete in a quasi-steady manner.

Experiments with molten, metallic fuel simulants, such as the TURC-1T test [1], have shown very vigorous interactions, with substantial amounts of melt ejected out of the test crucible during the initial jet impingement phase. Conversely, tests with molten fuel oxides, such as the TURC-2 and TURC-3 tests [2], did not produce a vigorous interaction, possibly because of the low superheat in the oxide melts. This scoping test (together with the subsequent analysis) was designed to investigate the behaviour of the melt during the initial jet impingement phase of a MCCI.

The study began with an experimental scoping test which is described in section 2. The post-test analysis is described in section 3. The experiment was modelled using an interim version of the MCCI computer code CORCON Mod3, supplied by Sandia National Laboratories. The assumptions of this model are described in section 4. The results of the calculation, which are described in section 5, were compared with those of the experiment. The object of the calculation was to discover whether or not the

[1]AEA Safety and Reliability, Culham Laboratory, Abingdon, Oxon, OX14 3DB, UK.
[2]AEA Reactor Services, Winfrith Technology Centre, Dorchester, Dorset DT2 8DH, UK.

experiment could by explained purely in terms of the excess superheat of the melt, using a quasi-steady state model, or whether some other model, including the effect of the jet, is required. Section 5 therefore includes calculations using jetting models [3, 4].

2 Experimental details

The experiment was carried out in the Winfrith Large Melt Penetration Rig (LMPR). Figure 1 shows the experimental arrangement used for the test. 24 kg of molten fuel sim-

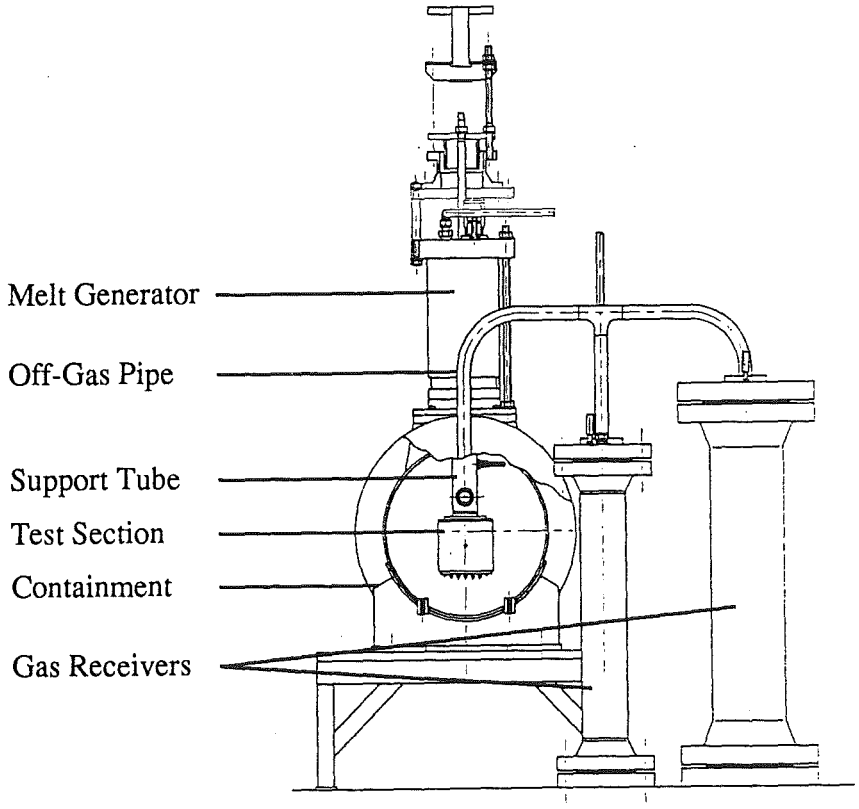

Figure 1: The Experimental Arrangement of the LMPR.

ulant was generated using a thermite mixture of powdered uranium metal and molybdenum trioxide, which when ignited in a sealed charge container by an electrically operated Pyrofuse, produces a mixture of uranium dioxide (81%) and molybdenum (19%) at a temperature of 3600K±150K.

The charge container was connected to the test section by a steel support tube of 20 mm inside diameter, which determined the initial diameter of the melt jet. The test section consisted of a cylindrical concrete target, 176 mm diameter and 76 mm thick, contained in a steel casing and mounted directly below the support tube. The concrete was of a basaltic type.

The test section was connected via 38.1 mm nominal bore steel pipework to two gas

receiver vessels. These were also connected to the charge container via its venting mechanism. The test section/support/gas vessel system was completely isolated from the main containment vessel and was provided with vacuum and argon purge facilities. The containment vessel was vented to the outer containment building to relieve any pressure generated in the event of a breach of the test section by the melt.

The pressures developed in the charge container, support tube and gas receiver vessels were monitored throughout the experiment together with the temperatures inside the gas vessels. The concrete test section was instrumented with ten type 'K' thermocouples at various depths to measure the heat transfer and concrete erosion. The thermocouples were mineral-insulated, grounded junction types, with 0.5 mm diameter stainless steel sheaths. In order to ensure that the positions of the thermocouples were maintained while the concrete was poured, the thermocouples were supported in rigid steel sheaths, leaving the hot junctions well exposed.

Initially the test assembly was evacuated, then purged with argon to atmospheric pressure. At this stage the charge container was still isolated from the rest of the system. When the argon purge was complete and the argon supply isolated, the following test sequence was initiated to provide a gravity pour of the melt onto the target:

1. The charge was ignited.
2. On completion of the burn the charge container was vented to the gas receiver vessels.
3. The pressures in the charge container, gas receiver vessels and test section were allowed to equalize and then the melt was released from the charge container via the support tube onto the concrete target.

3 Results and Post-Test Analysis

After the experiment the test section and support tube were removed from the containment vessel. There was a layer of frozen melt debris on the surface of the concrete and it was not possible to see the extent of erosion of the target. There was evidence to suggest that melt had been violently ejected back up the support tube and about 30 mm along the pipe to the gas receiver vessels. There was a substantial deposit of melt in the pipe which had formed a hole of about 5 mm diameter through the pipe wall. This hole meant that the system was no longer closed, so it was not possible to use the pressure measurements from the gas receiver vessels.

The depth of the concrete ablated was greatest near the centre where there was a saucer shaped depression about 60 mm in diameter and 33 mm deep at the centre. Outside this depression, the depth of the ablation was $\sim$22 mm.

The test section was cut with a circular saw fitted with an abrasive cutting wheel using a water based cutting fluid. A cross-section is shown in figure 2. It was possible to make a clean cut which did not disturb the constituent parts. Two regions could be seen, separated by a well defined interface. Below the interface was unablated concrete; above there were two distinct phases, (i) a continuous phase which was rather homogeneous

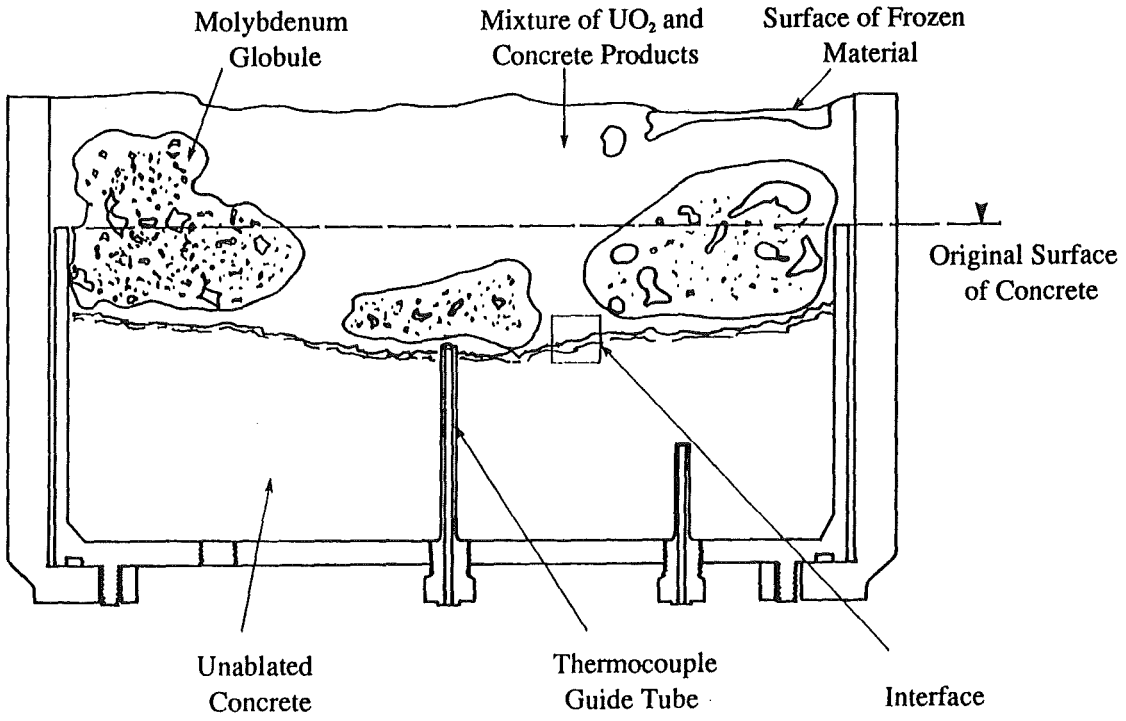

Figure 2: Features of the Test Cross-section.

in appearance and consisted mainly of UO_2 and (ii) a dispersed phase consisting of molybdenum metal in the form of large globules. The interface layer was ~10 mm thick and contained two layers which merged into their respective parent regions above and below. The lower layer looked like concrete, but was almost white, much paler in colour than the bulk of the unablated concrete beneath, which was greyish-pink. The upper layer appeared to be an inhomogeneous mixture of UO_2 and concrete. There was a crack between the two layers, along which they tended to separate when further cuts were made. Subsequent cuts confirmed the above analysis, and showed that the molybdenum was in the form of globules, rather than the torus which is a possible interpretation of figure 2. The Mo and UO_2 phases had similar densities, specific heats, latent heats and freezing points. It is believed, therefore, that the presence of Mo did not significantly influence the interaction.

A sample which included the interfacial region was cut, mounted and polished, to provide an area about 20 mm square for analysis using scanning electron microscopy (SEM). Figure 3 shows a composite micrograph of this sample. At the bottom, the inhomogeneous constitution of the concrete can be clearly seen. This gives way to a more homogeneous region, about 6 mm deep, believed to be concrete which has melted and refrozen. Towards the top of the micrograph is a further inhomogeneous region consisting of UO_2 particles surrounded by molten concrete. Some cracks and holes are visible; these became filled with resin during the preparation of the sample, and appear dark on the micrograph.

In order to determine the composition of the various regions and phases seen in the

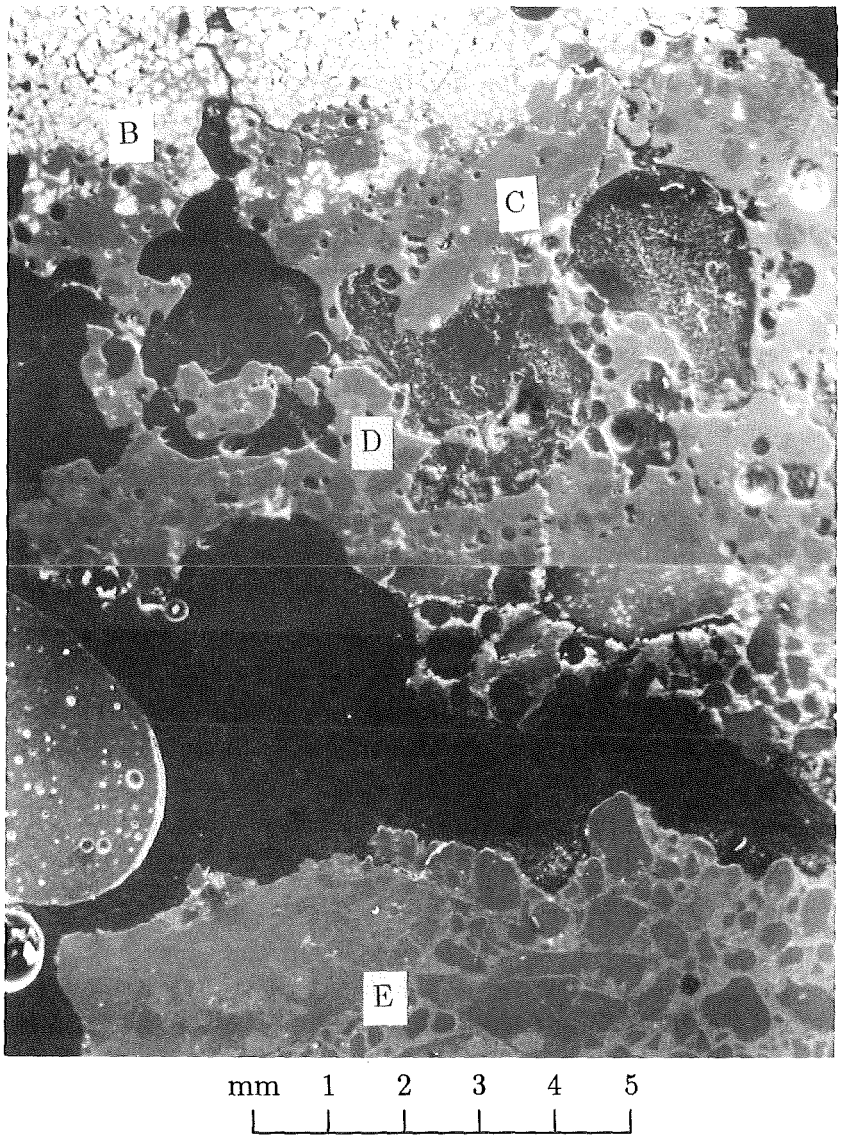

Figure 3: Micrograph of the prepared sample. Region 'A' is above the top of the micrograph.

micrograph, SEM was used to examine several regions in more detail. The proportions of elements present were determined for five regions. The regions range from region 'A' in the predominantly UO_2 region, through 'B', 'C' and 'D' to region 'E' in the undisturbed concrete. 'A' and 'E' were approximately 16 mm apart. An area of about 1 mm^2 was scanned in each case and the results were averaged over this area.

The results are shown in table I. The 'balance' column represents mainly oxygen, which is not measured specifically by SEM. In region 'E', 16.7% (*i.e.* about one quarter of the balance) may be due to pore water (based on the porosity of cement pastes, which is often as high as 40%). This figure is much higher than that usually associated with reactor grade concrete. It is not clear whether this represents unevaporated water or is simply the result of the re-adsorption of water, either during the cutting process or during the post-experimental period. In the undisturbed concrete region (E) the constituents

were mainly Si and Ca as expected. However, the proportion of Ca was much higher than expected and, together with the high possible water content, may indicate that the SEM analysis included a disproportionate amount of cement paste relative to the overall composition of the concrete. There was no uranium in this region. Even in the melted concrete (region 'D') the proportion of uranium was negligible, although closer to the UO_2/melted concrete interface ('C') there was a detectable amount (0.9%). In the UO_2 region close to the melted concrete, the proportion of uranium was much greater, while the concrete constituents represented a much smaller mass fraction than in regions 'C' to 'E'. Further away from the interface (region 'A') the proportion of UO_2 was even higher, but there was still a significant proportion of concrete constituents present. Assuming that the uranium was present as UO_2, the proportion of urania present was ~60% by mass.

A more detailed study of the interface region was performed by measuring the composition at points along a line across the interface in region 'C'. Eleven points spanned a length of 2.5 mm running from the edge of the UO_2 rich zone into the melted concrete. Concrete ablation products were predominant over the whole region.The proportion of uranium fell from ~2% to zero over a distance of 1.25 mm from the interface, and was zero below that, apart from ~0.8% found 2 mm below the interface. It is clear that there was some inhomogeneity in the melted concrete zone; the proportion of Ca, like that of UO_2, was low between 1.25 mm and 1.75 mm from the interface, probably because the material there was derived from a grain of flint, which is predominantly silica. However, it can be concluded that UO_2 did not penetrate in significant amounts more than ~1 mm into the concrete layer.

Higher magnification micrographs were produced from the three regions 'B', 'D' and 'E'. The micrograph from region 'D' is shown in figure 4. In region 'B', just above the UO_2/concrete interface, UO_2 dendrites were visible surrounded by melted concrete in which three separate phases were identified. In region 'D' (see figure 4) a number of silica grains were visible. These were surrounded by concrete products which were

Table I: Post-test SEM composition analysis (%wt). Note that the balance is mainly oxygen, although in region 'E' up to 16.7% may be due to pore water.

Area	Description	Si	Al	Ca	Cr	Fe	U	Bal
A	UO_2 away from concrete	10.8	1.7	2.9	2.4	1.8	51.6	28.8
B	UO_2 near to concrete	14.0	1.8	3.7	1.4	1.3	41.4	36.4
C	Melted concrete near to UO_2	28.4	3.0	5.5	0.0	2.6	0.9	59.6
D	Melted concrete away from UO_2	27.8	2.0	8.1	0.0	1.5	0.0	60.6
E	Undisturbed concrete	22.2	2.3	9.2	0.0	1.8	0.0	64.5

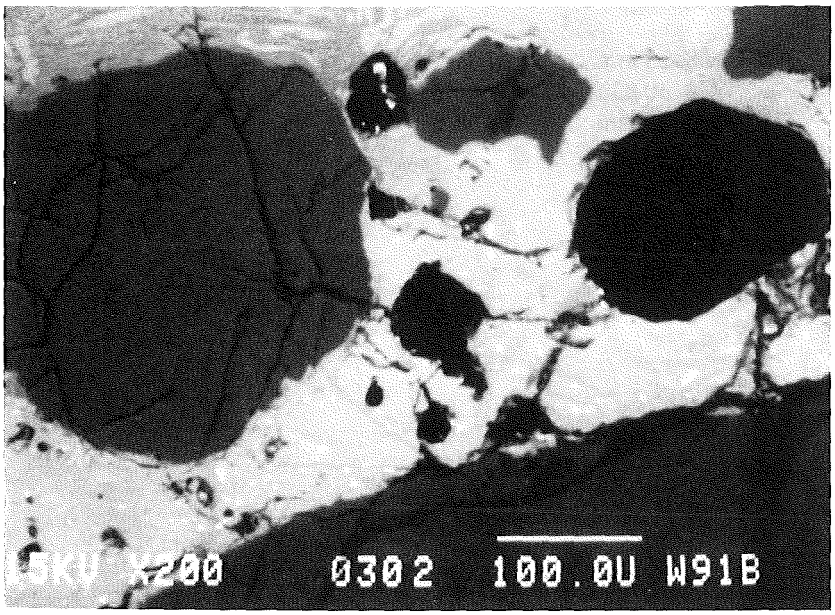

Figure 4: Micrograph of region 'D'. Grains of various sizes and areas of differing flux intensity can be seen.

rich in calcia and silica. The bright particles were mainly Fe, probably in the form of FeO. Region 'E', which was in the undisturbed concrete, showed the inhomogeneous microstructure that would be expected, with phases that were much more distinct than those found in the melted concrete region. The micrographs do not support the idea that the metals, when present in small quantities, separate out into layers. The evidence here supports a model of the melt in which, when solidified, a heterogeneous mixture of distinct phases is formed. It is probable that the phases would be miscible in the liquid state.

Figure 5 shows the response of the thermocouples in the unablated portion of the concrete target. Some thermocouples showed classical rises in temperature versus time, depending on their depths (*e.g.* T/C-6 at 30 mm). Others, notably T/C-2, showed sudden rises to about 100°C, followed by a plateau, then a gradual rise thereafter. It has been speculated that the latter thermocouples might have been surrounded by boiling water generated as the concrete decomposed. However the post-test analysis revealed nothing in the structure of the concrete near T/C-8 which would indicate the reason for this behaviour. There were no obvious cracks through which boiling water or steam might have passed. The porosity of cement pastes is typically ~40% and steam and water may have passed through the pores, but this does not explain why some thermocouples displayed this behaviour while others at similar depths did not. Nevertheless, there did not seem to be any resultant non-uniformity in the ablation. Coupled with the absence of any associated physical effects on the concrete, this suggests that the phenomenon did not seriously affect the mechanism of ablation. However, the generation of steam may have affected both the heat transfer from the molten pool to the concrete and the ejection of molten material.

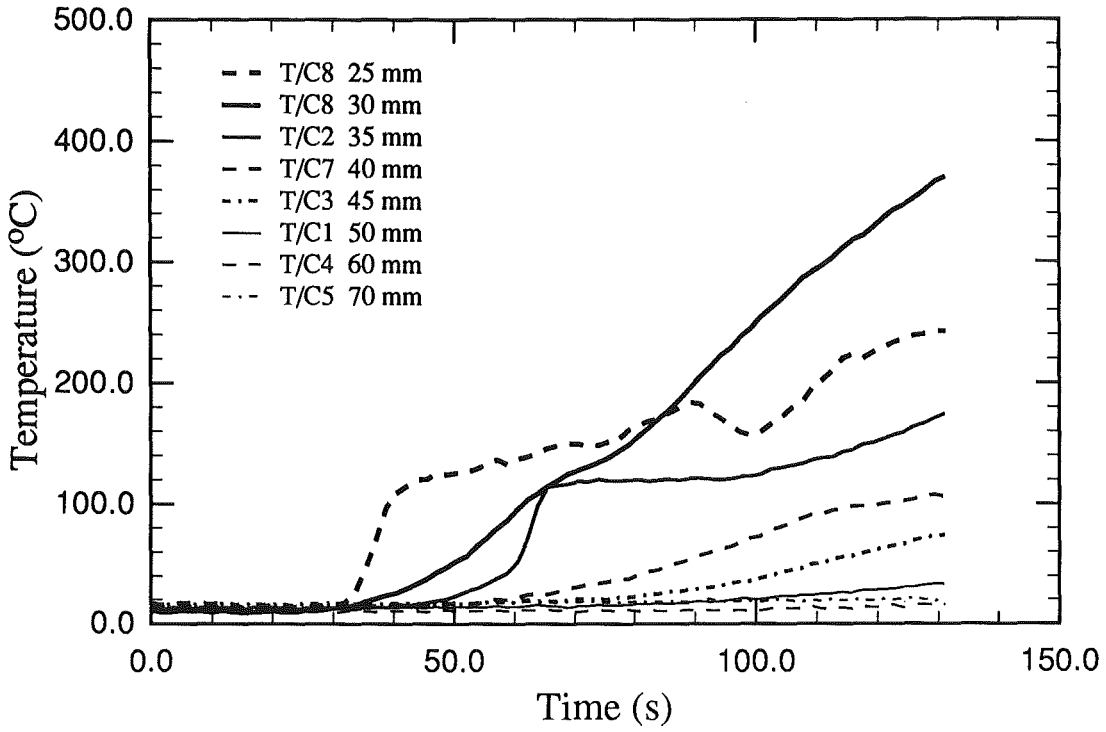

Figure 5: Response of thermocouples in the concrete target. T/C-2 and T/C-8 exhibit behaviour like that associated with boiling water.

4 Modelling Assumptions

The test has been modelled with an interim version of CORCON Mod3 supplied by Sandia National Laboratories. In the experiment the jet impinged upon the centre of the concrete target and much of the material was ejected within the first few seconds. It is estimated that the melt took a minimum of 3 s to be poured onto the basemat. Considering the interference effect of the upward, ejected material on the downward, poured material, it is likely that the duration of the impingement phase could have been considerably longer. All but about 4 kg of melt was ejected from the target area. However, some of the enthalpy of the ejected material must have been transferred to the target area. Modelling the test by pouring the corium to form a uniform layer of melt covering the target failed to give the correct final cavity shape for the ablation. Using a corium mass of 4 kg under-predicted the total ablation depth, while using a corium mass of 24 kg over-predicted it, as expected.

In order to model the experiment, the melt was constrained to form a column 50 mm in diameter for the first ten seconds. This was intended to mimic the jet impingement phase where material was poured in and ejected, without spreading significantly. To be consistent with the correlations discussed in the next section, it is assumed here that there was a significant heat transfer over an area greater than that of the original jet. The melt was then allowed to collapse, covering the entire surface area of the concrete target. Sustaining the column for 10 s gave the correct amount of ablation in the centre of the target relative to that at the edge, irrespective of the assumed mass of the poured

melt. In order to take account of the enthalpy transferred from the ejected melt, the calculation was scoped with initial melt masses of 4kg, 6kg and 8kg.

The calculations began with time steps of 0.1 s increasing over the first four minutes to 30 s. This was found to give the best results in terms of consistency and economy.

The initial melt temperature was set to 3600 K. The default CORCON basaltic concrete was used, with an initial temperature of 300 K and an ablation temperature of 1450 K. The emissivity of the concrete was set to 0.6, while those of the oxide and surroundings were set to 0.8. Molybdenum is not included in the CORCON master species list; therefore the poured melt was assumed to be entirely UO_2. This assumption was justified in section 3. The surroundings were assumed to be at 300 K for the entire calculation. In the experiment, the sides of the crucible were steel, whereas CORCON models the sides as concrete.

5 Analysis of CORCON calculations

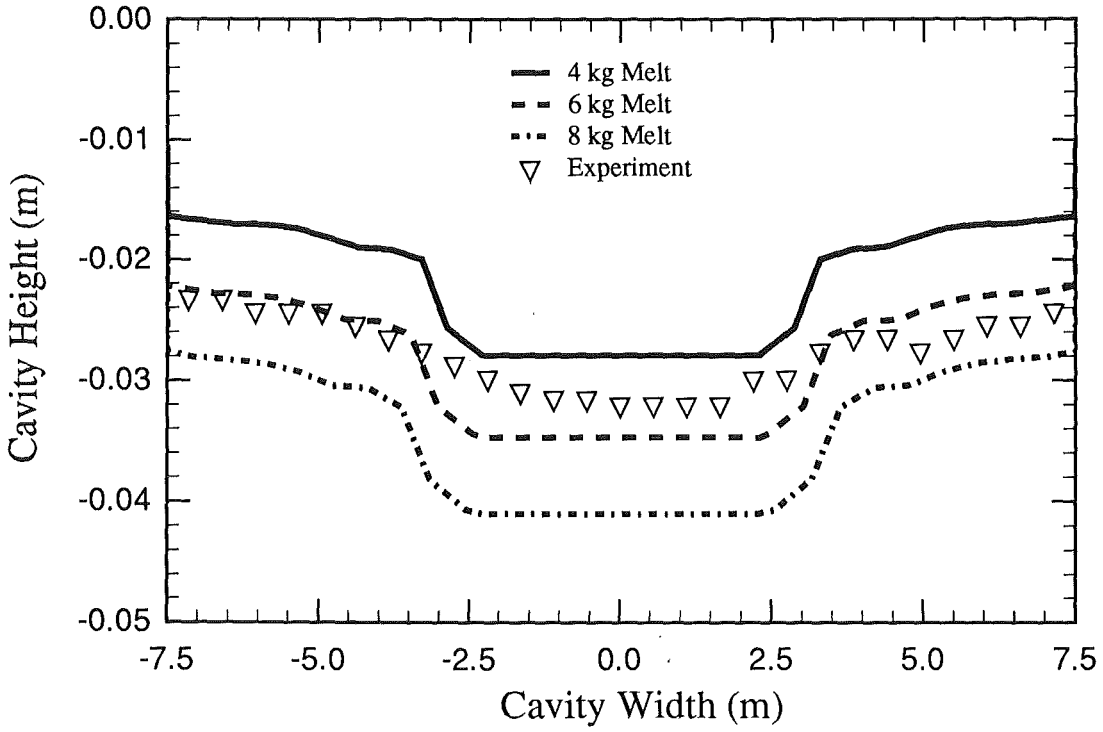

Figure 6: The profile of the melt/concrete interface after ablation. The calculation with 6 kg melt poured produced a good representation of the experimental data.

The final profile of the melt/concrete interface is shown in figure 6. The experimental points are derived from figure 2. As is to be expected, the calculation with 4 kg of melt gives too little ablation, because of the extra enthalpy which must have been transferred from the ejected material. The calculation with 8 kg of melt considerably over-predicts the ablation, giving an upper bound to the extra enthalpy. The calculation with 6 kg

of melt shows good correspondence with the experiment, indicating that the ejected material probably lost about ~7.5% of its enthalpy during the pour and interaction with the target (see below). A better appreciation of the relationship between the calculated values for ablation and the experimental points can be gained from figure 7.

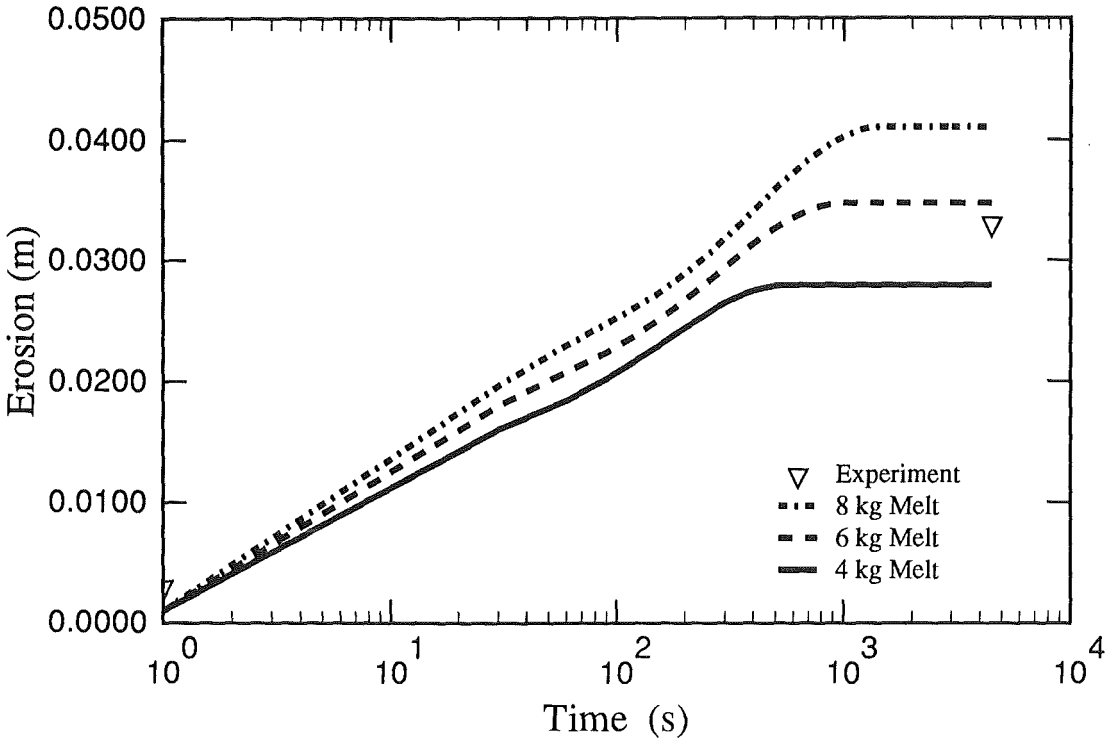

Figure 7: Calculated ablation versus time. There are only two experimental points, one from the thermocouple at a depth of 3 mm, the other from the post-test analysis. Both points lie on the axis of the concrete target.

All three calculations predict about the same amount of ablation during the first few seconds, but there is a slight difference in the rate, which is sustained throughout the calculations. The difference between the times at which ablation ceases is the main cause of the significant difference between the final depths of ablation for the three calculations. The final depth of maximum ablation for the 6 kg calculation is very close to that measured during the post-experimental analysis.

The concrete profile predicted by the calculations shows a central depression of about the correct diameter and depth, although the sides are somewhat steeper than those of the depression discovered experimentally. CORCON is able to produce this result by a simple constraint of the melt to a limited radius for a few seconds. The length of time determines the depth of the central depression relative to the surrounding depth; the assumed excess mass of the original melt has little effect. This is because there is only a small drop in the average melt temperature during the first few seconds.

It is clear from the post test analysis that the impingement of the molten jet caused a depression in the centre of the concrete target. CORCON can model this depression adequately if the melt radius is constrained to imitate the jet during the impingement

phase. If CORCON's heat flux is similar to that expected from an impinging jet (see below), then the length of time over which the melt radius needs to be constrained may give a good indication of the period of the jet impingement. Taking into account the estimated minimum time of 3 s, together with the interference effect of the melt ejection, the period of constraint used in the calculations, 10 s, is not unreasonable. If the CORCON model is valid for this type of short term phenomenon, then it is possible to estimate the enthalpy transferred to the target area by the ejected material. An extra 2 kg of UO_2 was needed in the calculation to give the correct amount of ablation. The melt was poured at 3600K and ablation is calculated to have ceased when the average melt temperature was 1311 K. Integrating down from 3600 K to 1311 K for 2 kg of UO_2 gives an increase in the enthalpy transferred to the target area of 3.21 MJ. If the enthalpy has been lost from the 20kg of ejected material, it represents ~7.5% of the total enthalpy of the ejected material; the average drop in temperature of the ejected material would have been ~320 K.

Constraining the melt radius, as has been done here, is only justified if the heat transfer modelling in CORCON gives heat fluxes similar to those anticipated for jet impingement. In order to model the heat transfer from an impinging jet two correlations have been developed. Spencer and Sienicki [3] used

$$Nu = 1.87 \times 10^{-3} Re^{0.948} Pr^{0.42} \tag{1}$$

where Nu = Nusselt number
Re = Reynolds number
Pr = Prandtl number

while the Zion Probabilistic Safety Study [4] employed

$$Nu = 0.78 Re^{0.5} Pr^{0.35} \tag{2}$$

Both of these correlations are based on the experimental data reviewed by Martin [5]. The correlations are compared with the experimental data (as reviewed by Martin) in table II. The maximum velocity of the impinging jet was calculated as 2.7 m s^{-1}. Because

Table II: Nusselt numbers from correlations based on the experimental data reviewed by Martin compared with Martin's data. The maximum experimental heat transfer was measured at a distance equal to twice the original jet diameter (2D) away from the axis.

Re (Pr=1.0)	Sienicki & Spencer	Zion	Martin's Data [5]	
			Axis	Max (2D)
1.25 $\times 10^5$	127	276	260	280
2.50 $\times 10^5$	245	390	275	420
3.75 $\times 10^5$	360	478	365	635

of the probable interference effect of the ejected material, the real velocity may have been considerably less than this. A lower bound of 1 m s^{-1} has been assumed here.

The physical properties used for the calculations are shown in table III. The heat of decomposition is the amount of latent heat necessary to allow the concrete to break up and be removed from the target. The time of failure of the thermocouple at 3 mm (0.8 s)

Table III: Physical properties used in the calculations.

	UO_2	Concrete
Density kgm^{-3}	9862.7	2340
Viscosity 10^{-3} kg m^{-1} s^{-1}	3.5365	
Jet Diameter m	0.02	
Specific Heat J kg^{-1} K^{-1}	503.25	1281
Heat of Decomposition 10^5 J kg^{-1}		2.719
Conductivity W m^{-1} K^{-1}	3.0	
$T_{solidus}/T_{ablation}$ K	3123	1450

indicates an initial ablation rate of 3.75 mm s^{-1}. However, uncertainties in the position of the thermocouple and the surface of the concrete (*e.g.* caused by shrinkage), together with the fact that cement pastes can contain voids of the order of 1 mm diameter, suggests a lower bound for the ablation rate of 1 mm s^{-1}. These properties give maximum and minimum heat fluxes of $\Phi_{max} = 15.3$ MW m^{-2} and $\Phi_{min} = 4.1$ MW m^{-2}. The downward heat flux calculated by CORCON, using its bubble induced convection model with allowance for a slag film, is 4.126 MW m^{-2}. CORCON predicts a thin ($\sim 350\mu$m) crust during the jet impingement, which is consistent with the use of the solidus temperature in the jetting correlations. The Nusselt numbers can be calculated from these heat fluxes using

$$Nu = \frac{\Phi d}{k(T_m - T_s)} \tag{3}$$

where k = Thermal Conductivity of melt
d = Jet Diameter
T_m = Pour Temperature of melt
T_s = Solidus Temperature of melt

The use of the solidus temperature here assumes that only (but all of) the melt superheat is used in the jetting correlations. The Nusselt numbers calculated from the experimental data and the CORCON calculation are compared with those for the two correlations in table IV. The Reynolds numbers and Prandtl number are $Re_{max} = 1.51 \times 10^5$, $Re_{min} = 0.56 \times 10^5$ and $Pr = 0.59$. All four calculations give reasonable agreement, although the Zion jet attack model gives values which are somewhat higher than the other calculations. The facility to constrain the melt radius in CORCON calculations enables the experimental data to be well matched. Without such a constraint it is impossible to calculate the central depression in the concrete surface. It is possible that the lower values of Nusselt number are more realistic, given the probable interference between the ejected material and the impinging jet.

Table IV: Calculated values of Nusselt number. There is reasonable agreement between all four calculations.

	Sienicki	Zion	Experiment	CORCON
Min	47	153	57	57
Max	122	252	214	

6 Discussion and Conclusions

A scoping test has been performed in which 24 kg of UO_2/Mo melt with a high superheat (~500K) was poured under gravity onto a basaltic concrete target. Because of limited instrumentation and lack of visual record, some details of the interaction are uncertain. However, a number of conclusions may be drawn from the test:

1. With a high superheat, there was a vigorous interaction, which led to ejection of ~20 kg (> 80%) of the melt.

2. There was enhanced erosion in the neighbourhood of jet impact, corresponding to a local heat flux of the order of 10 MW m^{-2}. This heat flux is of the same order as that predicted by jet impingement correlations, using the melt superheat as the appropriate temperature difference.

3. The concrete decomposition products appeared to be rather uniformly incorporated into the melt.

4. The limited amount of concrete decomposition products at the melt interface (which had not been incorporated into the melt layer) observed in the post-test analysis indicates either the presence of a slag film or some continued ablation after the bulk of the melt had effectively frozen.

5. The experimental results may be replicated reasonably by CORCON Mod3 (interim version) using the option of constraining the melt radius for the pour duration. The CORCON calculations implied that the duration of the jet impingement phase was 10 s and the amount of enthalpy transferred to the target area by the ejected material was 3.21 MJ. These values are consistent with information derived from the experiment.

Applications of these conclusions to more prototypic interactions (*i.e.* with considerably lower superheat and considerably more mass) must be tentative, but they appear to indicate that:

1. there may be a vigorous interaction on initial contact. This is particularly significant if there is a water pool through which the melt pours as it enhances the likelihood of the formation of a coolable configuration.

2. Above an undefined superheat, concrete decomposition products are readily incorporated into a UO_2 melt.

3. The model of Siernicki and Spencer for the initial interaction is consistent with the experimental data, when the heat flux is calculated using the initial superheat of the melt.

4. CORCON may be a useful tool for modelling MCCIs including the impingement phase, but a range of experimental results for different superheats and masses would be necessary in order to chose the correct values for the melt radius constraint parameters and the mass fraction to be used in the calculation.

Acknowledgements

The experiment was funded by the Department of Energy General Nuclear Safety Research Programme and the analysis was funded by the UK Health and Safety Executive as part of a programme of nuclear safety research. The authors acknowledge contributions made by the staff of the Melt Facilities and Analytical Chemistry at the Winfrith Technology Centre. We thank Sandia National Laboratories in making an early release of CORCON Mod3 available.

References

[1] J E Gronager, A J Suo-Anttila, D R Bradley and J E Brockmann
TURC1: Large Scale Metallic Melt-Concrete Interaction Experiments and Analysis
NUREG/CR-4220 SAND85-0707 (1986)

[2] J E Gronager, A J Suo-Anttila, D R Bradley and J E Brockmann
TURC2 and 3: Large Scale $OU_2/ZrO_2/Zr$ Melt-Concrete Interaction Experiments and Analysis
NUREG/CR-4521 SAND86-0318 (1986)

[3] J J Sienicki and B W Spencer
The Jet Impingement Phase of Molten Core-Concrete Interactions
Proceedings of the Committee on the Safety of Nuclear Installations (CSNI) Specialists' Meeting on Core Debris-Concrete Interactions
EPRI NP-5054-SR (1987) p 4.29 - 4.47

[4] Zion Probabilistic Safety Study
Commonwealth Edison Co.
Docket No. 50-295 (1981)

[5] H Martin
Heat and Mass Transfer between Impinging Gas Jets and Solid Surfaces
Advances in Heat Transfer Vol 13 *eds. J P Hartnett & T F Irvine Jr.*
Academic Press (New York 1977) p 1 - 60

SUSTAINED URANIUM DIOXIDE/CONCRETE INTERACTIONS TESTS: THE SURC TEST SERIES

E. R. Copus
Sandia National Laboratories
Albuquerque, NM USA

Abstract

The SURC-1 and SURC-2 tests were large-scale tests of the interactions of molten UO_2-ZrO_2-Zr mixtures with limestone and siliceous concretes. The tests were conducted to validate models of core debris interactions with concrete. The tests were done with such similar thermal histories that they provide a clear indication of the differences in behavior of limestone and siliceous concretes during interactions with high temperature melts. Each of the tests included in the melt charge a selection of fission product elements. Releases of these elements provide data for development and validation of fission product release models.

The SURC tests involved about 200 kg of UO_2-ZrO_2-Zr mixtures heated by the embedded ring-susceptor technique at rates of about 0.25 W/g. Crucibles used in the SURC tests were magnesium oxide annuli with cylindrical concrete plugs 40 cm in diameter and 40 cm deep. Once the melt was formed and ablated a 2 cm thick ZrO_2 board the melt began to attack the concrete. The ensuing interactions of the melts with concrete were found to progress in two distinct phases. In the first phase when metallic zirconium is present, concrete in the essentially one-dimensional configuration was eroded at rates of 15-30 cm/hr. Once the zirconium was consumed ablation rates slowed to 5-15 cm/hr. In the second phase, power input to the molten charge was increased to reestablish high erosion rates observed when metallic zirconium was present. Gas generation rates in the tests varied between 7-65 moles/m^2-min for siliceous concrete and 14-120 moles/m^2-min for limestone concrete. Aerosol generation rates varied over the range of 10-100 g/m^2-min.

Major conclusions can be derived from the SURC tests. The tests show that heat transfer models developed for the CORCON[10] computer code can predict the erosion of concrete by oxidic as well as metallic melts. Zirconium chemistry drastically affects the interactions of melts with concrete and must be included in the models of ex-vessel core debris interactions to

predict loads on reactor containments early in the ex-vessel phase of a severe accident. Aerosols produced during the interactions are predominantly composed of concrete constituents, but also contain significant amounts of barium, cerium, and uranium. The results of the SURC tests provide a vehicle for substantial validation of models such as CORCON and indicate that an adequate understanding now exists concerning core debris interactions with concrete when liquid water is not present.

Introduction

Core concrete interactions have been studied for over a decade[1,5]. We now have both an extensive data base and well-validated computer tools for predicting the physical responses which are likely to occur during the initial two to ten hours of these ex-vessel events for cases where there is no water present. Our data base includes experiments performed at Sandia[2,3,7,9], Argonne[18], and KFK[6]. It includes metallic and oxidic debris simulants on both limestone and basaltic basemats for a range of power input conditions. In addition there are tests in the data base which include chemistry effects due to zirconium and aerosol characterization due to a limited number of fission product simulants[13,15]. A summary of this data base is shown in Table 1.

Results from these experiments fall into three major areas of assessment:

1) Heat transfer and basemat ablation,
2) Chemical reactions and flammable gas production, and
3) Inert and fission product aerosol generation.

The SURC test series performed at Sandia National Laboratories was designed especially to evaluate core-concrete interactions in these three assessment areas. These two tests characterize the core debris-concrete interaction for oxide materials at high temperatures and for the range of concrete types typical to United States reactors.

SURC-1 and SURC-2 tests in the SURC series were integral tests using a 200 kg mixture of 63 w/o UO_2-27 w/o ZrO_2-10 w/o Zr over a 40 cm diameter concrete basemat formed from either limestone concrete (SURC-1) or basaltic concrete (SURC-2). The purpose of these tests was to study the protracted interaction of an oxidic melt pool on a range of concrete basemat materials. Before these tests were conducted, the bulk of the data

available for evaluating the ex-vessel core concrete interaction was either from tests using metallic iron as the core debris simulant or from tests which lasted only a few minutes. The SURC-1 test sustained the oxide-concrete reaction for over 130 minutes and the SURC-2 experiment was sustained for 150 minutes. During the course of these tests it was our goal to measure all of the essential aspects of the core-concrete interaction, namely; melt temperatures, erosion rates, overall heat balance, thermal conduction into the concrete, gas release rates, gas release chemistry, aerosol release rates and aerosol chemistry. The data return from both tests was excellent and provides comprehensive, redundant, and well characterized information on the oxide-concrete interaction which should be well suited for code validation efforts.

Geometry and Instrumentation

The SURC-1 experiment was conducted using the same geometry and instrumentation scheme as was used in SURC-2 and in SURC-4[9,17]. The basic geometry consisted of a 60 cm diameter interaction crucible with a 40 cm diameter limestone concrete cylinder in the base of a magnesium oxide (MgO) annulus. A 10 cm thick, circular cover of MgO was fabricated and placed on top of the crucible. The interaction crucible and induction coil were housed in a sealed, water cooled, aluminum containment vessel. A schematic of this vessel and some of the rest of the test apparatus is shown in Figure 1. The vessel was 180 cm high, 120 cm in diameter and contained feedthroughs for the induction power leads, instrumentation leads, and an exhaust gas port connected to the flow and aerosol sampling instrumentation. The interaction crucible was instrumented with over 100 thermocouples cast into the concrete cylinder, MgO annulus and MgO cover. A 280 kW induction power supply and coil were used to heat and melt the 200 kg charge within the test article and to sustain the interaction for the duration of the experiment. Additionally, 3.4 kg of fission product simulants in the form of $BaMoO_4$, CeO_2, La_2O_3, and Nb_2O_5 were added into the melt to study fission product release. Flow-rates of generated gases were measured using a sharp edge concentric orifice, a laminar flow device and two dry gas clocks. Gaseous effluents produced during the experiment were monitored and sampled using an infrared gas analyzer, a mass spectrometer, and by an integral grab sample technique. Aerosols were captured on filters, cascade impactors and a cascade cyclone. Erosion characteristics were measured using type K, S, and C thermocouples. Three tungsten thermowells containing optical pyrometers were embedded in the charge in

order to define the melt pool temperature and overall heat balance. The apparatus was sealed and purged with argon gas in order to direct the majority of the reaction gas and aerosol effluents through a 5 cm diameter flow pipe. Both tests were run at local atmospheric pressure (.83 atm) and at an ambient temperature of 25°C.

Test Materials

The charge materials for both SURC-1 and SURC-2 consisted of 200 kg of UO_2-ZrO_2 and Zr metal in the form of powder, crushed isostatic pressed cylinders and metal chips. The initial density of this mixture was calculated to be 3.6 g/cm^3. The relative weight percentages for the total unmelted charge material was calculated to be 63 w/o UO_2, 27 w/o ZrO_2, and 10 w/o Zr. In order to produce a homogenous mix, Zr metal chips were added to crushed UO_2-ZrO_2 cylinder material to produce the desired ratios. Five tungsten plates were embedded within the charge to serve as susceptors to heat and melt the charge. These plates were spaced approximately 10 cm apart within the charge and were allowed to collapse together as the melt-concrete reaction proceeded.

The concrete materials for the SURC-1 and SURC-2 tests were varied to represent the range of aggregate materials used in the United States construction industry. SURC-1 used a limestone aggregate material. This concrete melts over a range of 1635-1873 K and typically liberates 30-35 weight-percent CO_2 gas and 4 to 5 weight-percent H_2O vapor when heated to melting. The SURC-2 concrete contained a siliceous aggregate material. Siliceous concretes melt over a range of 1350-1650 K and typically liberate 1.5 weight-percent CO_2 gas and 5 weight-percent H_2O vapor when heated to melting. Both concrete types contain minor percentages of K_2O and Na_2O which will vaporize to produce aerosols at concrete melting temperatures.

Test Conduct and Summary of Results

The charge materials for both SURC-1 and SURC-2 were heated to melting in just over two hours using a 250 kW inductive power supply. Net input power to the charge for both tests are shown in Figures 2 and 3. These two power histories are nearly identical and provide excellent points of comparison for the three major operational phases observed in each test. These three phases can be identified as: 1) The initial (Zr rich) attack phase, 2) The low power (Zr depleted) quasi-steady attack phase and 3) The high power

(Zr depleted) quasi-steady attack phase. Results for each of these phases are shown for the major measured parameters of melt temperature, erosion rate, gas flow, gas composition, and aerosol density in Tables 2 and 3.

Comparison of Temperature Results

The temperature histories for SURC-1 and SURC-2 are shown in Figures 4 and 5. The temperature at the onset of concrete ablation was 2600-2700 K for both experiments. These initial temperatures dropped as concrete was ablated and temperatures at the end of both tests were 2000-2100 K. Temperatures were at all times greater than the melting range for concrete by at least 300 K. During the interval between the onset of ablation and the end of the experiment, the temperatures from the SURC-1 experiment were consistently higher than those for the SURC-2 test. The effects of lower ablation rates, higher melting temperatures, and higher temperature melt-concrete eutectics for limestone vs. siliceous concretes all contribute to this observed behavior. The enthalpy required to melt limestone aggregate concrete is 760 J/g as compared to 550 J/g for basaltic concrete and the melting points for limestone concrete and its eutectics are 1650-1850 K vs. 1350-1650 K for siliceous concrete and its eutectics[8]. This results in higher temperatures at the concrete-meltpool interface for limestone aggregate concretes which translate directly to higher meltpool temperatures. Temperatures in the meltpool for both experiments are seen to increase when power to the melt was increased late in the test. This, along with the fact that meltpool temperatures are well in excess of the concrete meltpoint, is a strong indicator of a significant thermal resistance at the melt-concrete interface.

Comparison of Ablation Results

Limestone and siliceous concretes display markedly different erosion characteristics when subjected to attack by molten oxide materials. A comparison of the erosion profiles for the SURC-1 and the SURC-2 tests is shown in Figures 6 and 7. The limestone concrete in the SURC-1 test erodes at a slower rate throughout the experiment as compared to the siliceous concrete of SURC-2. The principal factor responsible for this difference is again the enthalpy of melting which is 760 J/g for limestone material and 550 J/g for basaltic materials. Since the total erosion depth for SURC-1 was 27 cm and 35 cm for SURC-2 under nearly identical input

conditions, this implies that the average downward heat flux was nearly identical for both concrete types despite their differences in chemistry and gas release rates. Early in both experiments, however, the concrete is seen to erode at a rate which is greater than that which would be predicted from input power levels alone. This indicates that there is a link between erosion rates and concrete chemistry for the period when Zr metal is present in the melt and confirms the need for models which include exothermic reactions between SiO_2, CaO and Zr in addition to the gas reactions between H_2O, CO_2 and Zr[14].

Comparison of Gas Production and Gas Chemistry

The total gas release and gas chemistries are also very different for limestone and siliceous concretes. As seen from Tables 2 and 3, the principal components of limestone concrete decomposition are CO and CO_2 whereas H_2 and H_2O are the principal decomposition products from siliceous concretes. The basic effluent gases of CO_2 and H_2O are reduced by the metallic components present in the experiment, namely Zr metal in the meltpool and the tungsten susceptors used to sustain the debris-concrete interaction. The ratio of reduced to unreduced gas is generally high (8 or 9 to 1) for either concrete type throughout the SURC tests. A slight enhancement of the reduced gas components is seen early in both tests during the time that metallic Zr is being oxidized, thus indicating a higher oxidation potential for Zr and also the potential for oxide-metal reactions in addition to gas-metal reactions. Despite having a higher ablation rate, the siliceous concrete has 20 to 50 percent lower gas release rates than does the limestone concrete. This is a direct consequence of the fact that limestone concrete has a 40 w/o gas release potential as compared to a 7 w/o gas release potential for siliceous concretes. Total gas generation release rates vary from 7-65 moles/m^2-min for the siliceous conrete in SURC-2 to 14-120 moles/m^2-min for the limestone concrete in SURC-1.

Comparison of Aerosol Release and Composition

The aerosol release from either SURC experiment was estimated at 2-3 kg with approximately one-third of that total being accounted for by the aerosol measurement and characterization system. The range of aerosol release rates is from 1-10 g/min for both tests. Aerosol release rates are also roughly proportional to the gas release rate which acts as a driver

for the aerosol components. A comparison of the elemental composition of the SURC-1 and SURC-2 aerosols is shown in Tables 4 and 5. A qualitative assessment of the aerosol production shows that aerosols are attributable to the concrete constituents Si, Na, K, and Ca, the experiment materials of Mg and W, and the meltpool materials of U, Ba, Ce, and Zr. A quantitative appraisal shows that most of the aerosol material in either test is from the concrete constituents. Although both concrete types display the potential for continuous releases of Ba, Ce, Mo and Zr, the silicate chemistry concrete seems to reduce the amount of release of these components by a factor of 10 as compared to the limestone chemistry concrete. This suggests that silicate chemistry is an important factor in modelling potential long-term aerosol releases. Two other refractory species used as fission product simulants were Nb and La. Both concrete chemistries were able to consistently retain these materials.

Summary and Conclusions

The SURC-1 and SURC-2 experiments form a major part of the core debris-concrete interactions data base. These tests were designed to measure, model, and assess the range of responses which are most likely during the initial two to ten hours of these ex-vessel events. The range of response was measured using an oxide debris of UO_2-ZrO_2 on both limestone and siliceous concretes. Also included were a Zr metallic component and a limited number of fission product simulants. Both tests sustained the core debris-concrete interaction for over two hours using an identical power input history of .2-.3 w/g.

Data comparison for the two tests indicate a range of responses. The baseline response is 5-15 cm/hr for concrete ablation in the absence of zirconium metal which can accelerate to 15-30 cm/hr when zirconium metal is included. Gas generation response rates vary from 7-65 moles/m^2-min rich in H_2 for siliceous concrete interactions to 14-120 moles/m^2-min rich in CO for limestone concrete basemats. The total aerosol generation response from either concrete basemat ranges from 1-100 g/m^2-min and has been shown to be rich in the concrete components of potassium, sodium, silicon, and calcium with important trace amounts of uranium, barium, cerium, and molybdenum.

The major conclusions from the tests are that interaction temperatures remain well above the concrete melting point, that zirconium chemistry affects the ablation rate and the gas composition for both types of concrete, and that silicate concrete chemistry seems to retain more of the fission product simulants in the melt than does limestone concrete chemistry. The results of the SURC tests provide a substantial base for validation of the heat transfer, gas chemistry, and aerosol release models such as those found in the CORCON code and indicate that a relatively complete understanding now exists concerning the initial phases of core debris interactions with concrete when liquid water is not present. We feel that the understanding derived from the combined oxide and metal data base is reasonably adequate for current regulatory purposes. Future regulations or new reactor design efforts will be able to tap this technology base but may also suggest a new range of responses which need definition.

REFERENCES

1. U.S. Nuclear Regulatory Commission, Reactor Safety Study - An Assessment of Accident Risks in U.S. Commercial Nuclear Power Plants, NUREG-75/014, WASH-1400, 1975.

2. D. A. Powers, et al., Exploratory Study of Molten Core Material/Concrete Interactions, SAND77-2042, Sandia National Laboratories, Albuquerque, New Mexico, February 1978.

3. D. A. Powers and F. E. Arellano, Large-Scale Transient Tests of the Interactions of Molten Steel With Concrete, NUREG/CR-2282, SAND81-1753, Sandia National Laboratories, Albuquerque, New Mexico, January 1982.

4. Office of Nuclear Reactor Regulation, Liquid Pathway Generic Study, NUREG-0440, U.S. Nuclear Regulatory Commission, Washington, D.C., February 1978.

5. Gesellschaft fur Reaktorsicherheit mbH, German Nuclear Reactor Risk Study Phase B, GES-72, June 1989.

6. G. H. Alsmeyer, et al., "Beta Experimental Results on Melt/Concrete Interaction: Silicate Concrete Behavior," and "Beta Experimental Results on Melt/Concrete Interactions: Limestone Concrete Behavior," Proc. CSNI Specialists' Meeting on Core Debris-Concrete Interactions, EPRI-NP-5054-5R, pp 2-3 and 2-17, Electrical Power Research Institute, Palo Alto, California, February 1987.

7. R. E. Blose, J. E. Gronager, A. J. Suo-Antilla, and J. E. Brockmann, SWISS: Sustained Heated Metallic Melt/Concrete Interactions with Overlying Water Pools, Sandia National Laboratories, Albuquerque, New Mexico, NUREG/CR-4727, SAND85-1546.

8. D. R. Bradley, and E. R. Copus, Interaction of Hot Solid Core Debris with Concrete, Sandia National Laboratories, Albuquerque, New Mexico, NUREG/CR-4558, SAND81-1739, 1986.

9. E. R. Copus, R. E. Blose, et al., Core Concrete Interactions Using Molten Steel with Zirconium on a Basaltic Basemat: The SURC-4 Experiment, Sandia National Laboratories, Albuquerque, New Mexico, NUREG/CR-4994, SAND87-2008, 1989.

10. R. K. Cole, et al., CORCON-Mod2: A Computer Program for Analysis of Molten Core-Concrete Interactions, NUREG/CR-3920, SAND84-1246, Sandia National Laboratories, Albuquerque, New Mexico, August 1984.

11. H. Alsmeyer, et al., A Model Describing the Interactions of a Core Melt With Concrete, NUREG/TR-0039, English translation of KFK-2395, Kernforschungszentrum Karlsruhe, West Germany, September 1978.

12. E. R. Copus, et al., Core-Concrete Interactions Using Molten Aluminum on a Siliceous Basemat: The SRL-2 Experiment, Sandia National Laboratories, SAND91-2805, Draft, February 1992.

13. D. R. Bradley, "Modelling of Heat Transfer Between Core Debris and Concrete", 1988 National Heat Transfer Conference, Houston, Texas, July 1988.

14. D. A. Powers, D. R. Bradley, J. E. Brockmann, and E. R. Copus, "Validation of Core Debris - Concrete Interactions and Source Term Models," International seminar on Fission Product Transport Processes During Reactor Accidents, Dubrovnik, Yugoslavia, 1989.

15. J. E. Brockmann, "Ex-Vessel Releases: Aerosol Source Terms in Rector Accidents," Progress in Nuclear Energy, Vol. 19, p. 17-68, 1987.

16. G. A. Greene, Heat, Mass, and Momentum Transfer in a Multi-Fluid Bubbling Pool, Draft NUREG/CR and BNL-NUREG Report, Brookhaven National Laboratory, Upton, New York, 1990.

17. E. R. Copus, et al., Core-Concrete Interactions Using Molten Urania with Zirconium on a Limestone Concrete Basemat: The SURC-1 Experiment, Sandia National Laboratories, Albuquerque, New Mexico, SAND90-0087, Draft, December 1990.

18. M. F. Roche and L. Leibowitz, Liquidus-Solidus Temperatures for Core-Concrete Mixtures, Argonne National Laboratory, Argonne, Illinois, November 1990.

19. W. W. Tarbell, et al., Sustained Concrete Attack by Low-Temperature, Fragmented Core Debris, NUREG/CR-3024, SAND82-2476, Sandia National Laboratories, Albuquerque, New Mexico, July 1987.

20. D. A. Powers, J. E. Brockmann, and A. W. Shiver, VANESA: A Mechanistic Model of Radionuclide Release and Aerosol Generation During Core Debris Interactions with Concrete, NUREG/CR-4308, SAND85-1370, Sandia National Laboratories, Albuquerque, New Mexico, July 1986.

TABLE 1: SUMMARY OF CORE-CONCRETE INTERACTION TESTS

METALLIC TESTS

TESTS	POWER	CONCRETE TYPE	GEOMETRY	RESPONSE REGIME
HSS-1	SUSTAINED	LCS	1D - 15 CM	LONG TERM
FRAG 1,4	SUSTAINED	SILICEOUS	2D - 20 CM	LONG TERM
FRAG 2,3	SUSTAINED	LCS	2D - 20 CM	LONG TERM
SWISS 1,2	SUSTAINED	LCS	1D - 20 CM	QSS POOL
TURC IT, 1SS	TRANSIENT	LCS	1D - 40 CM	TRANSIENT
SURC 3, QTD	SUS + ZR	LIMESTONE	1D - 20 CM	QSS POOL
SURC 3A, QTE	SUS + ZR	LIMESTONE	2D - 20 CM	QSS POOL
BETA 1,2	SUSTAINED	SILICEOUS	2D - 40 CM	QSS POOL
BETA3 SERIES	SUSTAINED	LIMESTONE	2D - 40 CM	QSS POOL
BETA5 SERIES	SUS + ZR	SILICEOUS	2D - 40 CM	QSS POOL
SURC 4	SUS + ZR	SILICEOUS	1D - 40 CM	QSS POOL

OXIDIC TESTS

TESTS	POWER	CONCRETE TYPE	GEOMETRY	RESPONSE REGIME
HSS-3	SUSTAINED	LCS	1D - 15 CM	LONG TERM
TURC 3,3A	TRANSIENT	LCS	1D - 40 CM	TRANSIENT
SURC1.a	SUS + ZR	LIMESTONE	1D - 20 CM	QSS POOL
.b	SUSTAINED	LIMESTONE	1D - 40 CM	QSS POOL
.c	SUSTAINED	LIMESTONE	1D - 40 CM	QSS POOL
SURC2.a	SUS + ZR	SILICEOUS	1D - 40 CM	QSS POOL
.b	SUSTAINED	SILICEOUS	1D - 40 CM	QSS POOL
.c	SUSTAINED	SILICEOUS	1D - 40 CM	QSS POOL
MACE 0	SUS + ZR	LCS	2D - 30 CM	QSS POOL
ACE L SERIES	SUS + ZR	ALL TYPES	1D - 50 CM	QSS POOL

TABLE 2: SURC-1 DATA SUMMARY

	Early (with Zr)	Mid (without Zr)	Late (without Zr)
Time	130-190 min	190-220 min	220-280 min
Melt Temperature	2700-2400 K	2400-2100 K	2150-2050 K
Erosion Rate	15 cm/hr	2.5 cm/hr	12.5 cm/hr
Gas Flow	150 slpm	40 slpm	80 slpm
Gas Composition	5% H_2 - 5% H_2O	7% H_2 - 8% H_2O	5% H_2 - 5% H_2O
	85% CO - 5% CO_2	75% CO - 10% CO_2	80% CO - 10% CO_2
Aerosol Density	50 g/m^3	30 g/m^3	60 g/m^3

TABLE 3: SURC-2 DATA SUMMARY

	Early (with Zr)	Mid (without Zr)	Late (without Zr)
Time	130-160 min	160-220 min	220-280 min
Melt Temperature	2700-2100 K	2050-2100 K	2150-2050 K
Erosion Rate	30 cm/hr	5 cm/hr	15 cm/hr
Gas Flow	110 slpm	20 slpm	50 slpm
Gas Composition	75% H_2 - 5% H_2O	70% H_2 - 5% H_2O	75% H_2 - 5% H_2O
	15% CO - 5% CO_2	15% CO - 10% CO_2	15% CO - 5% CO_2
Aerosol Density	90 g/m^3	50 g/m^3	40 g/m^3

TABLE 4: ELEMENTAL ANALYSIS OF SURC-1 AEROSOL

SAMPLE	Ba	Ca	Ce	Cl	K	La	Mg	Mo	Na	Nb	Si	U	W	Zr	Moisture
Filter 2	.28	.54	.051	1.14	5.9	<.01	33.7	<.005	.68	<.05	32.9	<.1	<.05	.070	.56
Filter 5	.56	1.0	.080	1.71	12.8	<.01	29.0	.024	1.4	<.05	30.6	<.1	.06	.076	.38
Filter 8	.46	1.2	.063	1.91	22.7	<.01	19.3	.081	2.4	<.05	22.5	.2	2.2	.16	1.22
Filter 11	.07	.35	.01	3.24	25.2	<.01	8.0	.07	1.8	<.05	7.6	<.1	1.5	.05	4.27
Orifice	.34	.84	.038	.30	15.0	<.01	14.4	.11	2.2	<.05	16.9	.1	7.9	.26	---
Ball Vale	.23	.61	.072	.66	11.4	<.01	20.2	.098	1.4	<.05	21.2	.2	5.0	.23	---

TABLE 5: ELEMENTAL ANALYSIS OF SURC-2 AEROSOL
WEIGHT PERCENT OF ELEMENT IN SAMPLE

SAMPLE	Ba	Ca	Ce	Cl	K	La	Mg	Mo	Na	Nb	Si	U	W	Zr
Cyclone 1	.035	.010	.001	.88	9.00	.009	.47	.054	33.3	<.001	5.91	.18	4.88	.010
Cyclone 2	.050	<.005	.002	.96	7.60	.012	2.11	.020	31.0	<.001	23.7	.15	2.36	.011
Cyclone 3	.048	<.005	.001	.81	5.76	.001	1.58	.008	27.0	<.001	16.2	.14	.08	.007
Cyclone 4	.041	<.005	.003	.90	10.9	<.001	2.00	.004	14.	<.001	37.6	.13	.02	.004
Cyclone 5	.037	<.005	.002	.76	6.73	<.001	1.94	.004	14.5	<.001	30.7	.13	.03	<.001
Cyclone 6	.033	.033	.001	.72	5.07	<.001	1.61	.004	44.9	<.001	15.9	.09	.02	<.001
Filter 2	.058	<.005	.003	1.56	5.00	<.001	2.10	.005	25.3	<.001	23.9	.17	.058	.022
Filter 4	.057	<.005	.002	1.62	4.81	<.001	2.10	.004	25.9	<.001	24.0	.16	.046	.016
Filter 6	.045	<.005	.001	1.98	3.35	.012	1.89	.007	25.1	<.001	19.2	.10	.070	.001
Filter 9	.029	<.005	<.001	.95	4.30	.007	1.92	.021	27.2	<.001	21.8	.31	2.41	<.001
Filter 11	.009	<.005	<.001	1.60	7.24	.002	.72	.36	10.3	<.001	9.39	.26	26.3	<.001
Filter H	.016	<.005	<.001	.90	29.1	.003	1.18	.10	11.8	<.001	14.5	.22	13.5	<.001
Filter J	.002	1.35	<.001	1.74	1.25	<.001	.01	.37	6.29	<.001	21.0	.26	31.5	<.001

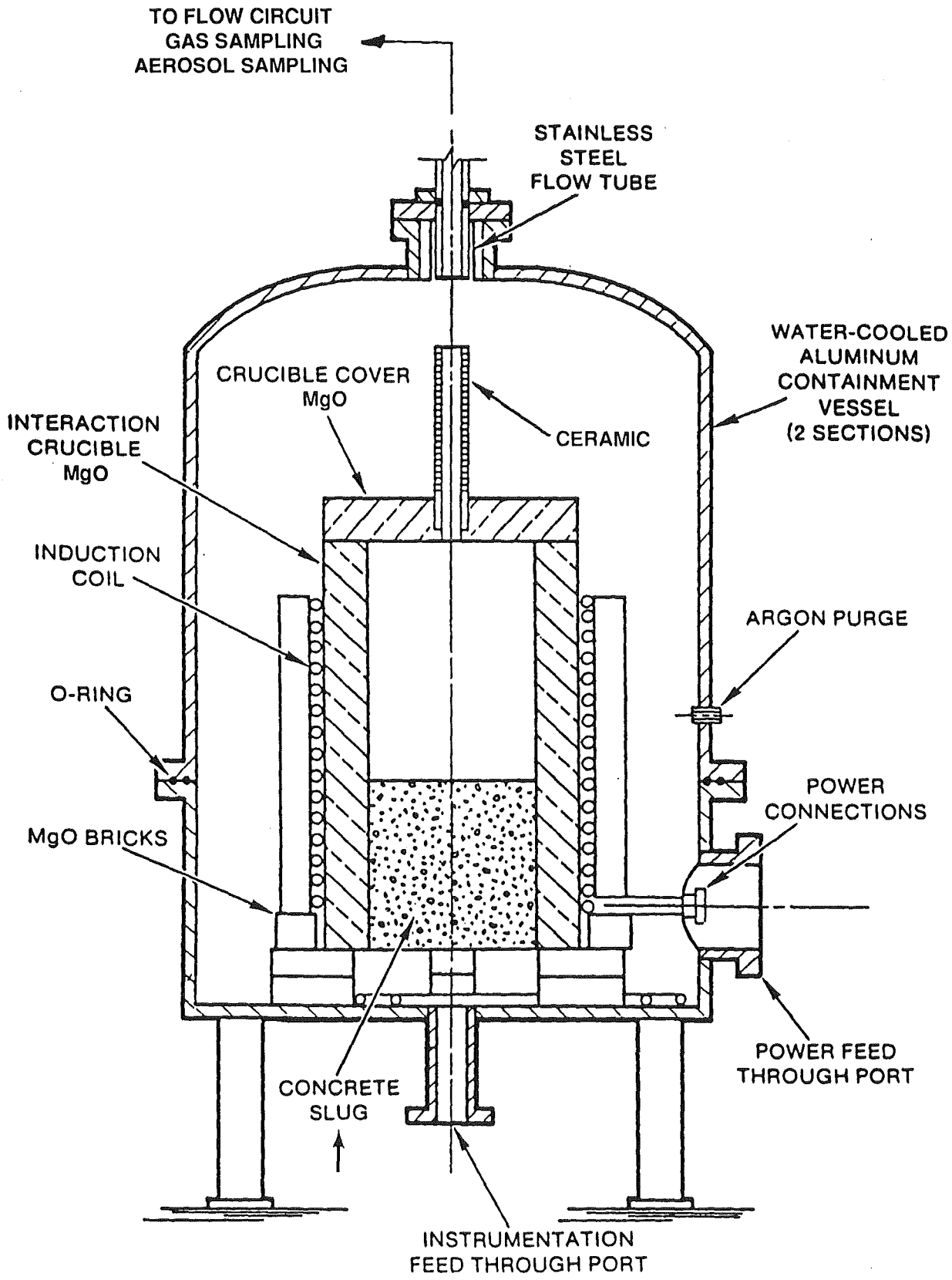

Figure 1. SURC Experimental Geometry

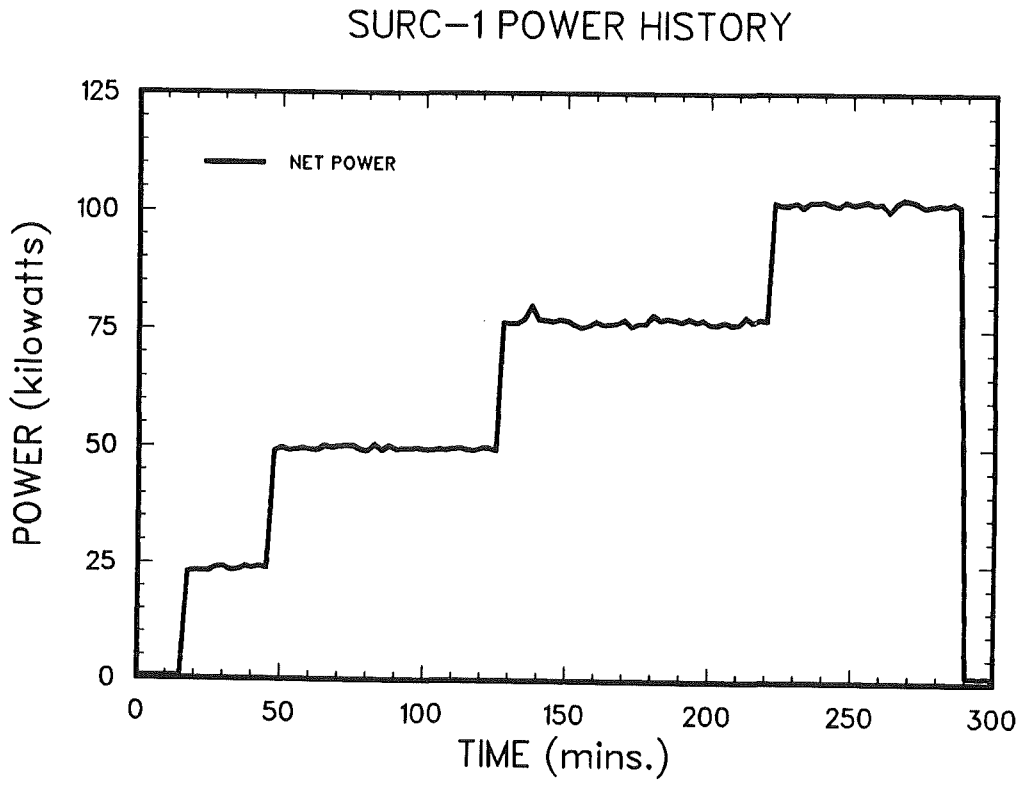

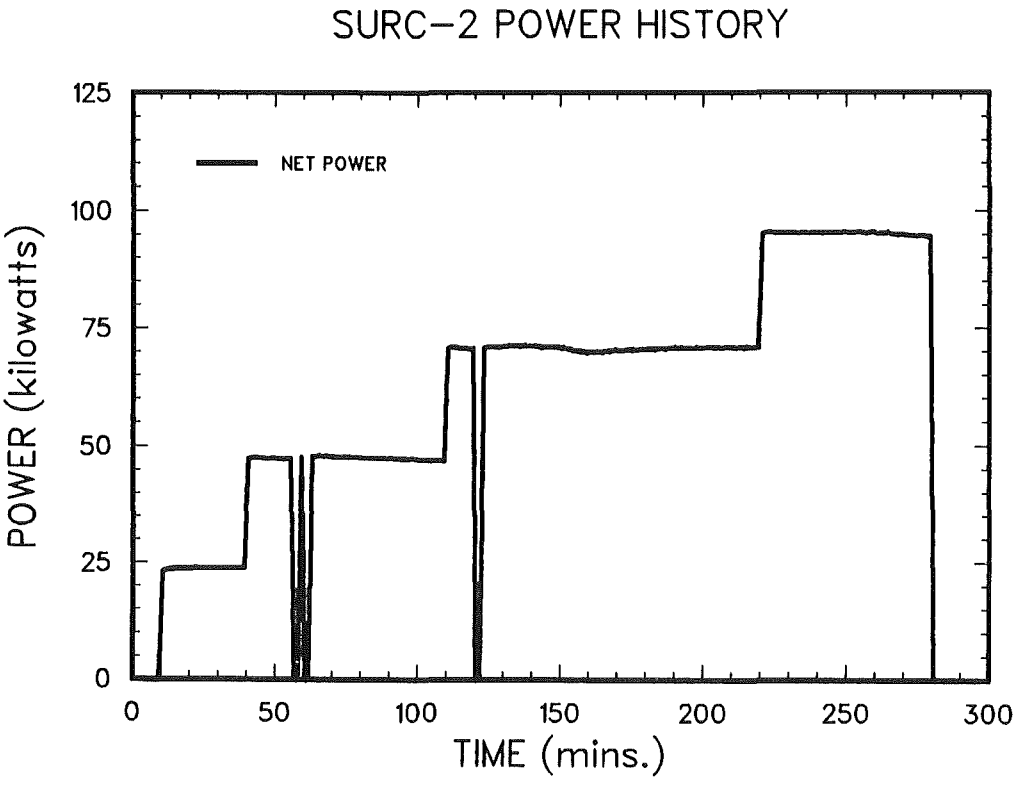

Figures 2 & 3. Comparison of SURC-1 and SURC-2 Power Histories

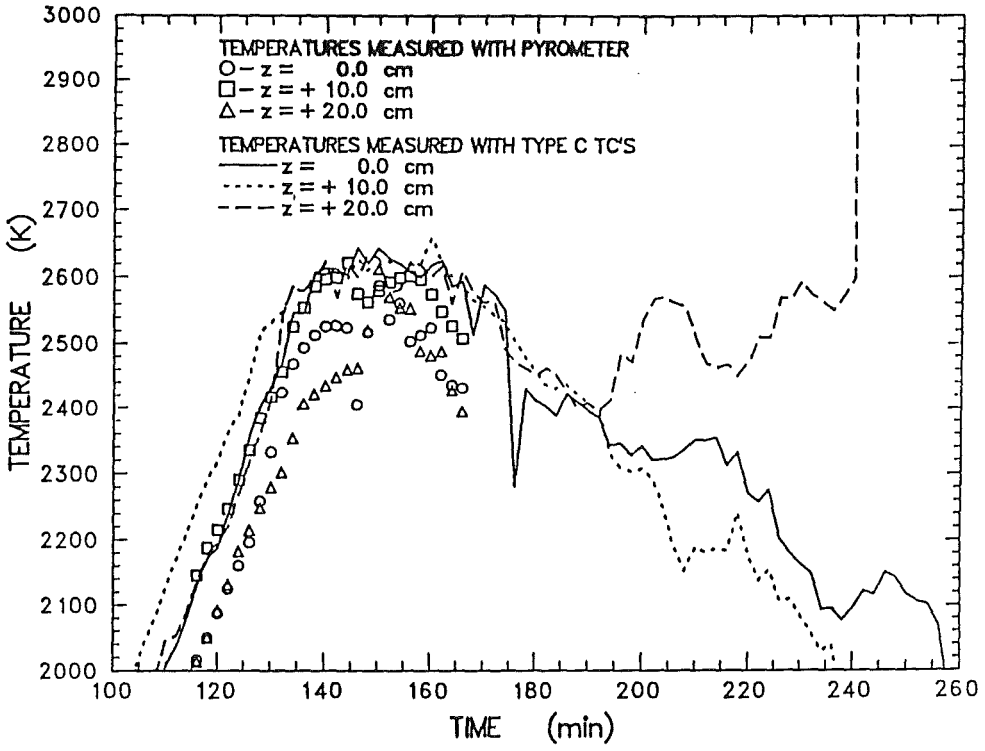

Figure 4. Meltpool Temperatures in SURC-1

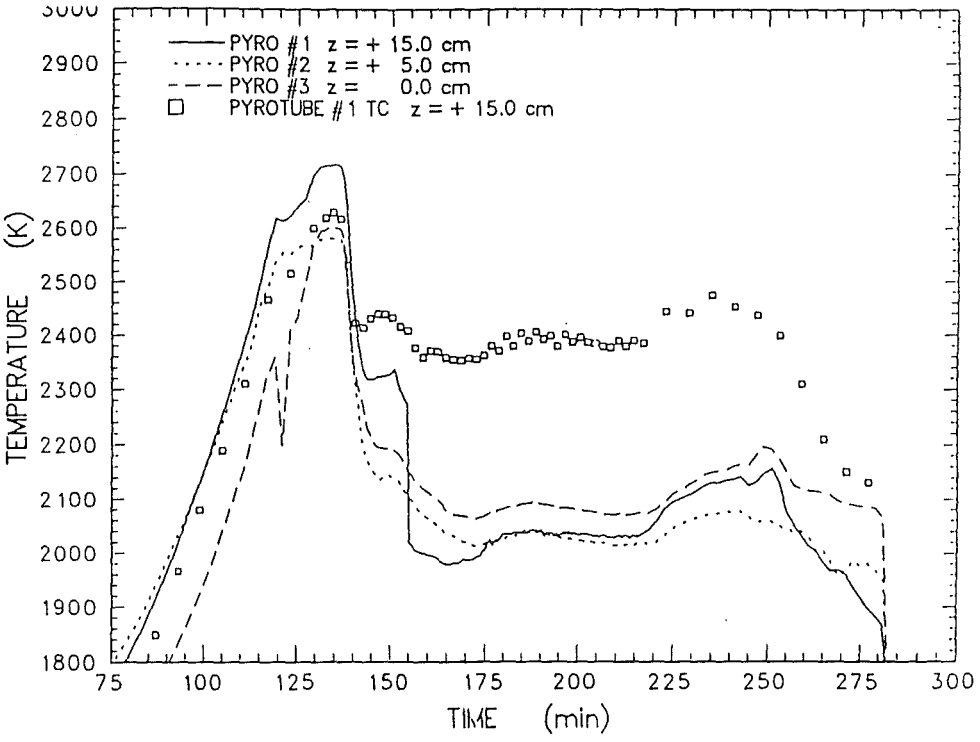

Figure 5. Meltpool Temperatures in Surc-2

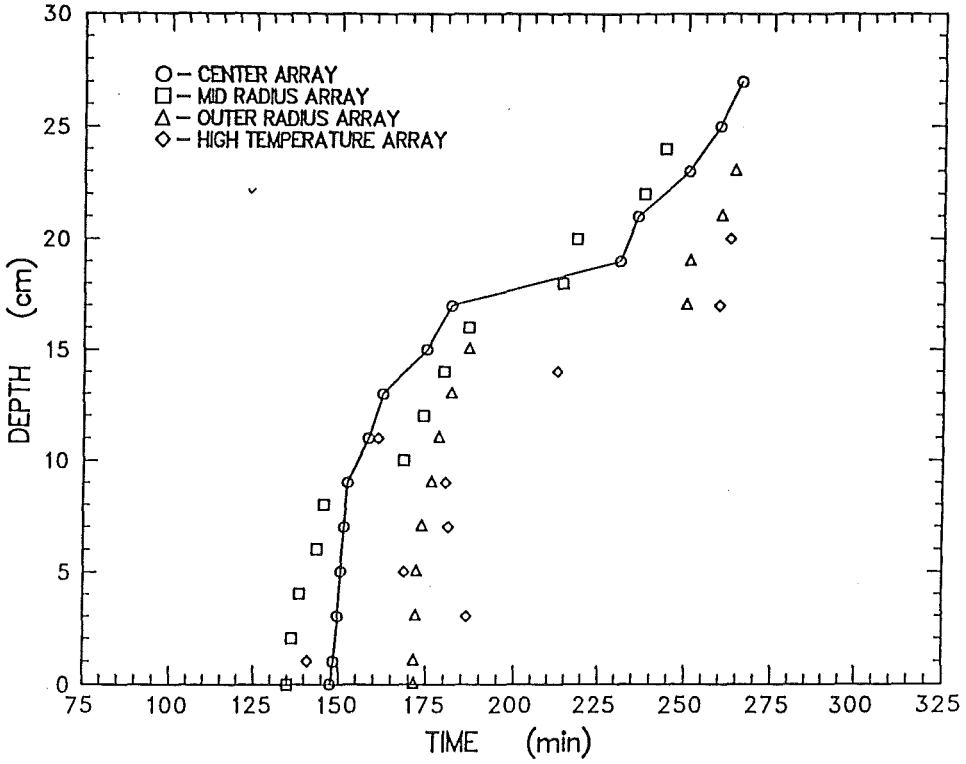

Figure 6. Location of the SURC-1 Erosion Front

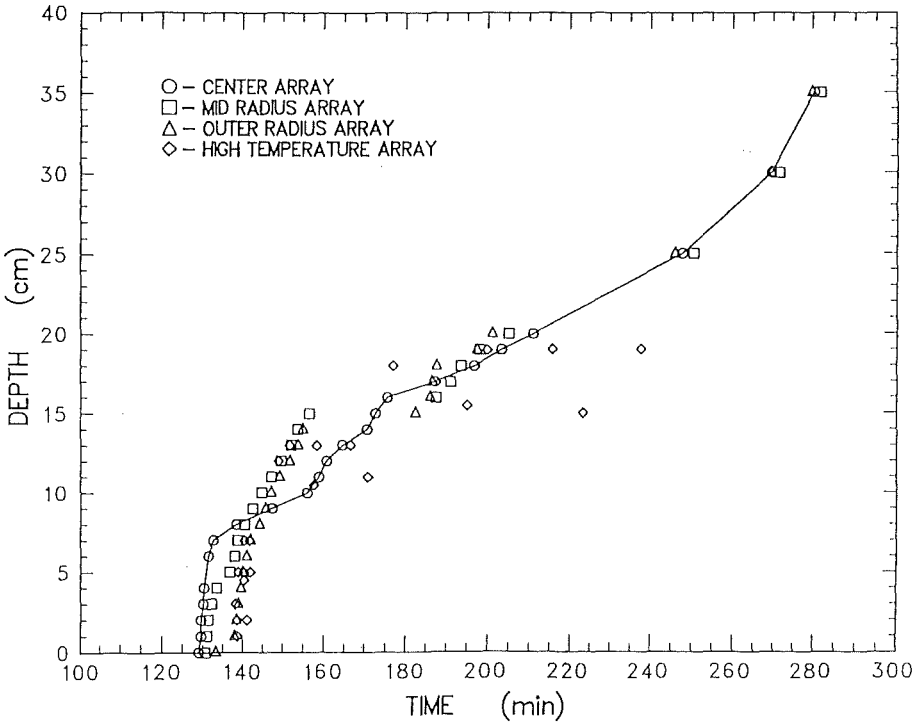

Figure 7. Location of the SURC-2 Erosion Front

BETA EXPERIMENTS ON ZIRCONIUM OXIDATION AND AEROSOL RELEASE DURING MELT-CONCRETE INTERACTION

H. Alsmeyer, C. Adelhelm, H.-G. Dillmann, M. Heinle, W. Ratajczak, G. Schumacher, W. Schöck, A. Skokan, W. Tromm

Kernforschungszentrum Karlsruhe
Postfach 3640, W-7500 Karlsruhe 1, Germany

ABSTRACT

Three experiments on melt-concrete interaction have been carried out in the BETA facility to investigate the zirconium oxidation processes during concrete attack and their influence on concrete erosion and aerosol release. The results clearly show the dominance of the condensed phase chemistry, that is the chemical reaction of Zr and SiO_2 leading to the rapid oxidation of 80 kg of Zr and the formation of Si in the metallic melt within a few minutes only. The high chemical energy release from this reaction produces fast concrete erosion and a pronounced gas spike dominated by hydrogen release. After the completion of Zr oxidation the erosion is determined by the much lower internal decay heat level with moderate interaction processes. The temperature of the melt is measured to decrease very fast to the freezing temperature which can be explained by the very effective heat removal to the melting concrete. The overall downward erosion of 40 to 50 cm of the concrete crucible produces characteristic 2-dimensional cavity shapes.
Aerosol release including simulated fission product behavior is reported with respect to aerosol rates, chemical composition, and characteristic particle size.

1. INTRODUCTION

In the sequence of uncontrolled core-melt accidents in Light-Water-Reactors, the corium melt would erode the concrete basemat. The thermal energy of this process results from the decay heat of the fuel and from the chemical energy of oxidizing components of the metallic melt. Under this aspect the chemical behavior of zirconium is of major importance as zirconium alloys are used as fuel cladding in PWR's and in considerable higher quantities in BWR's also in form of channel boxes. Therefore, the Zr oxidation - during a critical phase of the accident with respect to

containment failure - may strongly influence the release of hydrogen and fission prodcuts during concrete erosion.

Recent experiments in SNL [1] and ANL [2] led to the conclusion that besides oxidation by the gases from the decomposing concrete, i.e. by H_2O and CO_2, zirconium can be oxidized through reduction of molten silica. This condensed phase chemical reaction would dominate the early oxidation process as the amount of SiO_2 in most cases exceeds the amount of gases from the concrete, and could therefore possibly lead to a faster oxidation process and faster chemical energy release.

According to chemical equilibrium considerations, the chemical reaction of zirconium and silica below some 2200 K could follow the reaction

$$Zr + SiO_2 \rightarrow ZrO_2 + Si + 2.1\ kJ/gZr\ . \qquad (1)$$

In parallel to this reaction, Zr oxidation takes place by the gases H_2O and CO_2 released from the melting concrete. After depletion of Zr these gases could oxidize the elemental Si produced by reaction (1) which was dissolved in the metallic melt.

The processes influence on one side the chemical energy input: The faster energy release could increase melt temperature, erosion velocity, and gas rates which correspondingly increase the aerosol release from the melt. On the other side, the oxygen potential in the melt is largely determined by the chemical status of Zr and could therefore change the release rates of specific aerosol species by the formation of different chemical components. Because of these different aspects, Zr behavior has gained considerable interest.

2. EXPERIMENTAL CONDUCT

To investigate the Zr oxidation process three experiments in the BETA Test Series II were conducted in 1990 to 1991 under PWR and BWR specific conditions as well. Table 1 summarizes the main experimental parameters in the three tests.

BETA Test	Initial Melt, ~ 2200 K	Fission Product Mock-ups and Additives	Planned Heating Power	Main Objectives
V 5.1	300 kg Fe + Cr + Ni 80 kg Zry-4 50 kg Al_2O_3 + SiO_2 + CaO	none	400 kW	PWR: Zr chemistry, consequences on erosion and aerosol release
V 5.2	as V 5.1	1 kg Mo, 0.5 kg $ZrTe_2$, 1.5 kg CeO_2, 1 kg BaO, 0.5 kg La_2O_3, 0.5 kg SrO, 6 kg B_4C in steel containers	200 kW	BWR with B_4C absorber, low power: Zr chemistry and related processes
V 5.3	as V 5.1	1 kg Mo, 1 kg CeO_2, 1 kg BaO, 0.5 kg La_2O_3, 0.5 kg SrO, 6 kg B_4C in steel containers	800 kW	BWR with B_4C absorber, high power: Zr chemistry and related processes

Table 1: Main Parameters for the Zr-related BETA Experiments

The melt interacting with the concrete crucible is composed of a metallic melt, mostly iron with 5 % chromium and 5 % nickel of 300 kg in total plus 80 kg Zirconium. This corresponds to 21 % Zr in the steel melt which is a reasonably high mass and concentration compared to the accident situation. The initial 50 kg of oxidic melt, 65 % Al_2O_3, 20 % SiO_2, and 15 % CaO, will be dissoluted during the erosion process by the products from the decomposing concrete and further oxides from the metal melt.

To understand the experimental simulation, the BETA facility as used throughout the tests is depicted in figure 1. The melt is kept in a cylindrical concrete crucible fabricated from siliceous concrete. The inner cavity has an initial diameter of 38 cm and allows downward and sideward erosion by the melt so that a predominantly 2-dimensional cylinder-symmetric erosion may take place. The melt of initally some 2200 K is poured from the thermite reaction tank into the crucible at start of the interaction test. The Zr addition was accomplished by dropping 80 kg of solid zircaloy rubble into the crucible before pouring the melt. The metallic part of the melt is heated electrically by the induction coil surrounding the crucible. Gases and aerosols produced during the experiment are fed through the off-gas system and a fiber filter into the environment.

Fission products were simulated in the melt with respect to low volatile species where the release processes need more clarification. Additionally in test V 5.2, tellurium in the form of $ZrTe_2$ was added as different chemical forms of Te may exist

with specific release rates. The addition of the fission product mock-ups was accomplished by dropping a material lance from the tank for the measurement probes into the melt early in the test or by placing the mock-ups on the bottom of the crucible before pour of the melt. Similarly, the 6 kg of B_4C in the BWR specific experiments are placed on the crucible bottom enclosed in steel capsules. This should allow the initial eutectic melt formation of B_4C and steel, which is expected during the in-vessel melting of the BWR absorber rods and which determines the early B_4C speciation.

The experiment uses a variety of instrumentation to analyse the experimental processes as listed in figure 1. In order to measure the temperature of the eroding melt, three different types of thermocouples were used in parallel: Pt10Rh/Pt and W5Re/W26Re-thermocouples embedded in the lower crucible (figure 2) and protruding into the melt after some concrete ersion, as used in SNL and ANL experiments, respectively. Additionally, the standard BETA technique of dip in thermocouples (W3Re/W25Re) was used, operated from the upper probe tank. Simultaneously, these dip-in lances extract material probes from the melt during the test which are needed to clarify e.g. the Zr oxidation processes. The experiments could be conducted successfully with typically 40 to 50 cm downward concrete erosion. Besides their principal clarification of physical and chemical processes they are beeing used to validate MCCI-computer codes, e.g. the WECHSL-code [3].

3. EXPERIMENTAL RESULTS

3.1 HEATING OF THE MELT

In the BETA facility, heating of the melt in the crucible, besides the chemical reactions, is by sustained electrical induction heating. Therefore, only the metallic melt has internal heat sources while the oxidic melts receive the energy by convective heat transfer. Following the nature of induction heating, the heating efficiency depends strongly on the surface of the metal phase as "seen" by the induction coil. As the efficiency of heating can be measured in BETA, interesting conclusions on the distribution of the metal can be drawn.

The experiments V 5.1 through V 5.3 realize different power densities in the melt to quantify the power - or temperature effect on the other processes. The realized power of 200 to some 1000 kW corresponds to a power density of around 670 W/kg metal to 3300 W/kg metal. During the later part of the test, the electrical power

generated in the melt is nearly constant as in test V 5.2 (figure 3) or slightly decreasing as in the tests V 5.1 and V 5.2. Specific for all three tests however is a pronounced increase of the inductor efficiency to some 50 % immediately after pour of the melt and a subsequent drop to a reduced efficiency of some 30 % between 100 s and 200 s, resulting in the negative power slope in figure 3. As confirmed by other observations, this early phase is directly related to the oxidation of metallic Zr which is accompanied by a strong release of gases which increases the "effective" melt level seen by the induction coil. With depletion of Zr a major chemical energy source is exhausted and after some delay which is determined by the excess internal energy of the melt, the interaction of melt and concrete is less vigorous. The time span of this early oxidation phase is increasing for lower electrical power input confirming the positive feedback of concrete erosion rate and Zr oxidation rate.

3.2 CRUCIBLE EROSION

The BETA experiments allow substantial erosion of the concrete crucible into downward and radial direction as well. For the experiment V 5.2 with the lowest power input the downward erosion reached 40 cm after 2940 s at the end of heating (figure 4). The average downward erosion rate is from 0.014 mm/s in V 5.2 to 0.028 mm/s in V 5.1 and 0.057 mm/s in V 5.3, and roughly proportional to the heating power. The downward erosion rate is nearly constant in time, and it is remarkable that the effect of the early Zr oxidation process on downward erosion is not very pronounced. For the radial erosion, the three tests show similar behavior in that the radial propagation comes to an end after some 5 to 15 cm erosion in the first period of the tests.

The final cavity shapes as obtained from the sectioned crucibles are given in figure 5. Test 5.2 shows the most pronounced radial erosion in the lower crucible, whereas the other tests have a slender cavity. This is in agreement with the BETA test Series I and is attributed to different heat transfer modes at high and low heating power [4]. Low power allows a thin metal crust to form at the concrete interface strongly reducing the downward heat flux. The slightly converging shape of V 5.1 is a somewhat untypical behavior which is probably due to the strong splashout and loss of metallic melt to the upper structures in the inital phase of the test reducing the lower metal mass from 300 kg to 104 kg only. Hence, specific data on erosion are believed to be more reliable in test V 5.2 and V 5.3.

Comparing the upper cavity shapes with the results of BETA Series I which had no zirconium in the melt, the recent tests show a more pronounced upper cavity erosion by the early Zr-rich metallic melt attack. This occurs during the first 100 s or so during the Zr oxidation phase and explains on the other side the limited influence of Zr oxidation on the downward propagation. The feedback of concrete erosion, gas release, and Zr oxidation with high void in the melt causes the Zr oxidation to occur not only in the lower but also in the upper crucible. This is confirmed by video records of the tests showing a highly agitated splashing melt in the early test phase, and by the increase of efficiency of the electrical induction heating as well.

3.3 TEMPERATURES AND GAS RELEASE

The temperature of the melt is an important information needed to validate the heat transfer models and to understand aerosol releases. However, temperature measurement in the eroding melt is difficult because of the limited life-time of thermocouples in the high temperature and chemically aggressive melt. Therefore, three different thermocouple systems have been applied to cross-check the measurements. This was done also with regard to discussions on earlier BETA experiments where a relatively low temperature was measured in the melt. This seemed to be contradicting to similar experiments of other laboratories which measured higher temperatures.

Detailed comparison of the three types of temperature measurements in the experiments under consideration shows agreement within ± 25 K. Dip-in thermocouples give clear information when the melt has a low viscosity which is the case in the early test phase, but need sufficient settling time in the later period. The embedded thermocouples failed very early especially in the V 5.3 high power test, probably as they start to protrude in the melt. These thermocouples in some cases form a new thermocouple junction in later phases of the tests with a valid temperature signal. Parallel measurements of the ohmic resistance of selected thermocouples during the test indicate indeed that the new junction gives a valid information. Using all data a consistent picture of the temperature in the metal melt is obtained with a high degree of reliability.

The temperature histories of the metallic melt as measured in the three tests are given in figure 6. Common to the tests is the fast decrease of the metal temperature from some 2100 K at the beginning to the long-term value of some 1750 K

which occurs in the first 100 to 200 s of the interaction. This coincides with the period where the zirconium is being oxidized. Thereafter, the metal temperature is obviously the freezing temperature of the (Fe, Cr, Ni, Si)-melt eventually influenced by dissolved B_4C in the experiments V 5.2 and V 5.3. The long-term temperature agreement within some 30 K is remarkable, also with respect to the independence of the metal temperature from the heating power. This indeed indicates that the heat transfer to the concrete is so effective that the temperature of the melt drops until solidification processes control the heat flux. This is a confirmation of the BETA Series I results [4]. The slight depression and subsequent increase of the metal temperature between 150 s to 400 s might be caused by a change of the metal composition which simultaneously changes the freezing temperatures. It is hypothesized that this is due to some transition of boron from the metal to the oxide, which has a strong influence on the metal freezing temperature. From the dissolution process of B_4C, boron is initially expected in the metal melt as boride [5]. Because of its low oxigen potential the boron would be readily oxidized after Zr depletion to form borate in the oxidic melt.

Of course, the fast early temperature drop is the most striking observation. The Zr oxidation by eq. (1) would contribute an energy of some 1.7 MW·100 s. Comparing this chemical energy input with an earlier BETA test V 1.8 [4] without Zr but run at 1.8 MW electrical power input, the temperature behavior is very similar. In all cases, the very effective heat transfer to the melting concrete easily absorbes the chemical or electrical power input. BETA test V 1.8 only shows a slightly higher long-term metal temperature because the steel composition is different without Zr and Si which reduce the freezing temperature.

Gas rate and integrated gas release from the melt are plotted in figure 7a and b, respectively for the test V 5.2. The results of V 5.1 and V 5.3 are qualitatively similar. Gas release in V 5.2 is dominated by H_2 and a somewhat lower release of H_2O. The small amount of CO_2 and CO is due to low carbonate content in siliceous concrete. Methane is in the range of some permill, other gases are not detected. From 0 to 200 s, a pronounced peak of the dominant gases is observed (fig. 7a), corresponding to the early vigorous melt interaction during Zr oxidation. This peak exceeds the long-term quasi-steady gas release by one order of magnitude typically. Gas rates especially of H_2O and to a minor extent of CO_2 are influenced by the transient heat-up of upper surfaces without melting, which is a consequence of the early high voiding and splashing of the melt. This increases the long-term release of gases which did not react with the metal melt. Comparing the actual measure-

ments with earlier BETA tests the long-term release of H_2 and CO seems to be smaller than expected. Detailed interpretation of the gas release needs further application of the MCCI computer codes.

3.4 MATERIAL ANALYSIS FROM THE MELT

Chemical analysis of the melt composition gives information on the sequence and velocity of the oxidation reactions. Table 2 gives the composition of the main components of the metallic and oxidic melt as solidified after the test.

Table 2: Melt Composition (w%) at End of Test V5.1 and V5.2

Metallic Melt			Oxidic Melt		
Species	V5.1	V5.2	Species[1]	V5.1	V5.2
Fe	~86.8	~82.5	SiO_2	60	61
Cr	4.7	4.15	Al_2O_3	6.5	7.2
Ni	5.4	6.01	CaO	9.2	9.4
Zr	0.02	0.075	ZrO_2	18.4	12.7
Sn	n.d.	0.28	B_2O_3	0	1.6
Si	2.8	4.3	Fe_2O_3	2.5	4.3
C	0.24	~0.29[2]	Cr_2O_3	0.6	0.5
B	0	0.35	Residual	2.8	3.3

1) calculated from the content of the elemental metals
2) concentration taken from experiment V5.3

The metallic zirconium is completely oxidized and is found in the oxidic melt. As a consequence of the condensed phase reaction eq. (1), silica is found in the metal phase in a significant percentage. If Zr oxidation were to occur by gas reactions only, the initial 80 kg of Zry-4 would not have been depleted.

Chromium oxidation throughout the test was relatively small. The nickel content did practically not change, as Ni is the most stable metallic component. A small amount of 0.24% C was found in the metal of V5.1 indicating the minor role of the coking reaction (reduction of CO_2 to C). The slightly higher C-concentration in test V5.2 may be attributed to the addition of 1.5 w% B_4C to the metal melt. However, most of the boron is found in the oxidic melt at end of the tests.

The final composition of the oxidic melt is largely determined by the admixture of molten siliceous concrete and the oxidized zirconium.

The material probes from the dip-in thermocouples in experiment V 5.2 give the time dependence of the oxidation processes. Figure 8 shows the very fast oxidation of Zr and the simultaneous formation of Si in the metallic melt according to the chemical reaction equ. (1) in a time span of less than 100 s only. The succeeding oxidation of the other elements such as Si or Cr by gases from the concrete is comparably slow, resulting in a moderate release of H_2 and CO (see Section 3.3). On the whole, figure 8 gives a clear and consistent picture of the oxidation processes. The concentration of the oxidic components later in the experiment is influenced by the admixture of the molten concrete.

3.5 AEROSOL RELEASE AND FISSION PRODUCTS

The experiments also give information on aerosols and specific fission products which had been added as non-active simulants to the melts of test V5.2 and V5.3, while test V5.1 was run without fission product mock-ups. The detailed material analysis is still under evaluation but some important results are available.

The fission products mock-ups of test V5.2 as added to the melt are listed in table 1 of chapter 2. Analysis of material probes from the melt V 5.2 shows that Mo is persisting in the metallic melt in some 0.3% throughout the test corresponding to the added mass. The other mock-ups are found in the oxidic melt in the concentration of some permill or less according to their added mass but are below the detection limit in the metal phase. However, Te from the added $ZrTe_2$ could not be detected either in the metallic nor in the oxidic melt, with a typical detection limit of 0.05 to 0.07%. This refers to a fast vaporizational release of tellurium also if initially present in the form of $ZrTe_2$ as is indeed confirmed by the aerosol analysis.

All aerosol filter probes taken throughout the test show Te as the dominant element found in the 20 to 60 w% range. Up to 3 percent of Ba was found on the early filter but Ba concentrations are below the detection limit of less than 1% lateron. None of the other simulated fission products could be detected on the filters. From the other aerosols, Sn is the dominant species with up to 20%. Tin is released as one of the Zry-4 components probably in the form of SnO_2, followed by K (~5%), B (~4%), Si (~3%), and Na (~1%). BETA V5.1 test gives a similar result but without Te, Ba, and B. Consequently, the relative concentrations of the other aerosol spe-

cies are higher. The data reported above were taken at 100 s and later, that is after the early Zr oxidation.

During the very early melt interaction including the Zr oxidation phase until some 200 s after the pour, the aerosol release rate is very high as determined in figure 9 from the filter samples of test V5.1. Lateron the aerosol release decreases by 1 or 2 orders of magnitude which was confirmed also for the other tests. Electron microscopy reveals that the primary aerosol particles are spherical with a typical diameter of 0.1 to 0.5 µm forming agglomerates of some microns. Under some conditions whisker-like aerosol shapes were found.

4. CONCLUSIONS

The three tests investigated the interaction of predominantly metallic melts of high initial Zr concentration with siliceous concrete in a cylindrical crucible. They give clear and consistent data on Zr oxidation and related processes which may be summarized as follows:

- Oxidation of 80 kg Zry-4 in 300 kg metallic melt dominates the interaction during the first 2 or 3 minutes. Material investigation shows the depletion of Zr within only 1 minute and a simultaneous increase of Si concentration in the metallic melt as described by the condensed phase chemical reaction $Zr + SiO_2 \rightarrow ZrO_2 + Si$.

- In spite of the high energy deposition from Zr oxidation and from electric heating the temperature of the metal in all three BETA tests drops to its freezing temperature within some 150 s. This is combined with fast cavity erosion, high gas release, and extreme voiding and agitation of the melt.

- Gas release shows a pronounced spike during this period with important H_2 release persisting at a lower level throughout the later test.

- The cavity shape depends on the long-term power input to the melt in agreement with previous BETA experiments.

- High initial aerosol release decreases after early Zr depletion. From the fission products added to the melt substantial Te release was observed whereas the release of Ce, La, Sr, Ba, Mo is small and mostly below the detection limit.

- Some portion of B_4C which was added to the melt to represent BWR absorber material leads to the formation of borates in the oxidic melt which contribute to the aerosols.

The following topics need further considerations: (i) The chemical reaction of Zr and SiO_2 may lead to the formation of Si or SiO, depending on the reaction temperature. Si formation was observed in the present tests, while SiO was found in the ACE experiments at higher temperatures [2]. The transition temperature between the reactions needs clarification. (ii) The freezing temperature of the multicomponent metal melt including Fe, Cr, Ni, Zr, Si, B is lower than presently modeled in computer codes. (iii) The experimental H_2 rates need computer analysis to quantify the Si-steam reaction velocity in the steel melt.

5. LITERATURE

[1] E.R. Copus et al., "Core-Concrete Interactions Using Molten Steel with Zirconium on a Basaltic Basement: The SURC-4 Experiment", NUREG/CR-4994, April 1989.

[2] B.R. Sehgal, B.W. Spencer. D.H. Thompson, J.K. Fink, M.T. Farnier, "ACE Program Phase C: ACE/MCCI and MACE Coolability Experiments", Int. Topical Meeting on Safety of Thermal Reactors, Portland, Or., July 21-25, 1991.

[3] J.J. Foit, "Improved WECHSL Models Including Zirconium Oxidation and its Verification by new BETA Experiments", 2nd OECD CSNI Specialist Meeting on Core Debris - Concrete Interactions, Karlsruhe, April 1-3, 1992.

[4] H. Alsmeyer, "Melt-Concrete Interaction during Severe Light Water Reactor Accidents", Kerntechnik 53 (1988), 1, 30-38.

[5] P. Hofmann, M. Markiewicz, J. Spino, "Reaction Behaviour of B_4C Absorber Material with Stainless Steel and Zircaloy in Severe LWR Accidents", KfK 4598, July 1989.

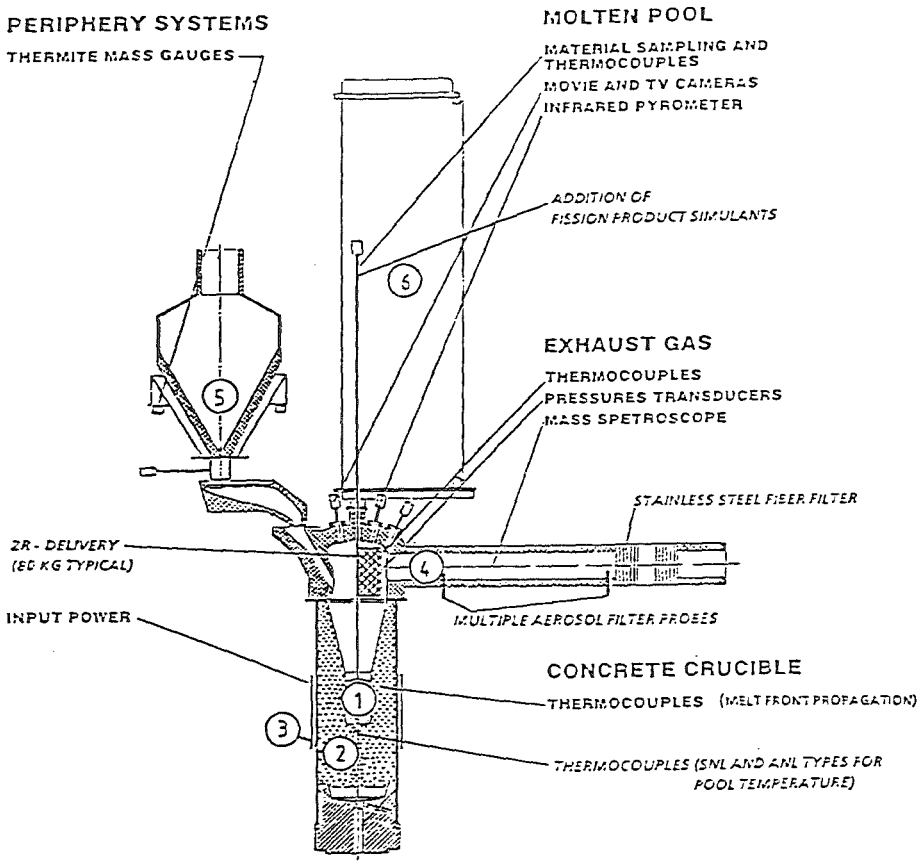

Figure 1: Schematic View of BETA Facility in Zr Related Tests

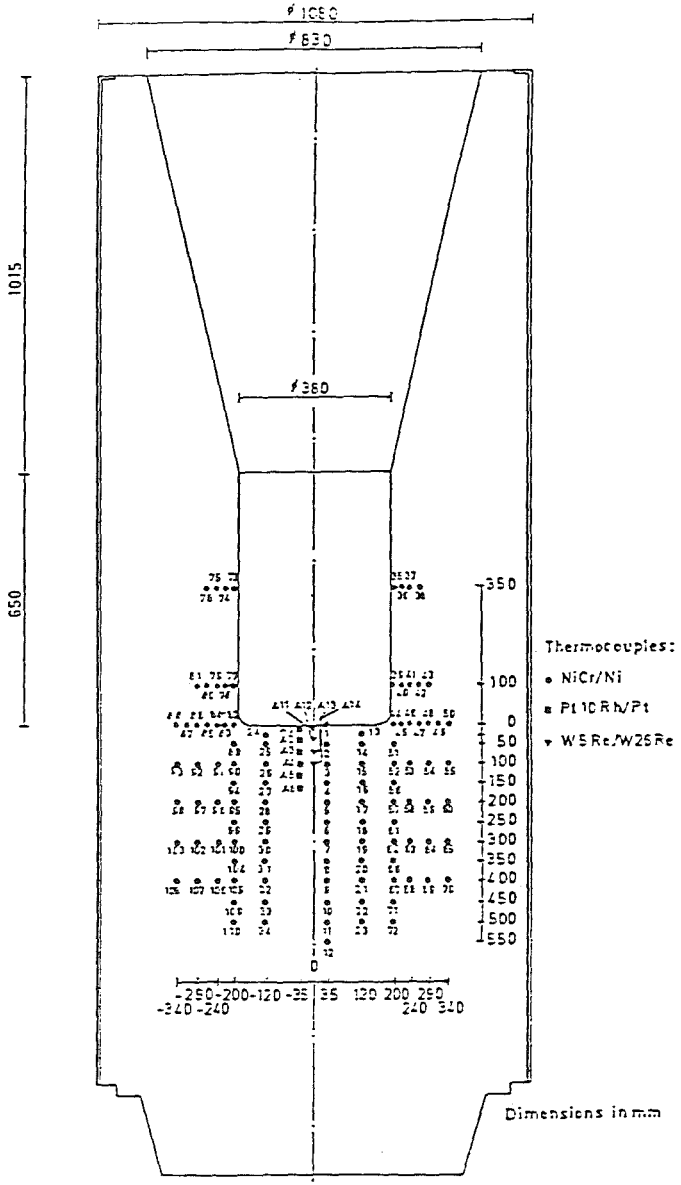

Figure 2: Crucibles Used in BETA Experiments V 5.1,V 5.2,V 5.3

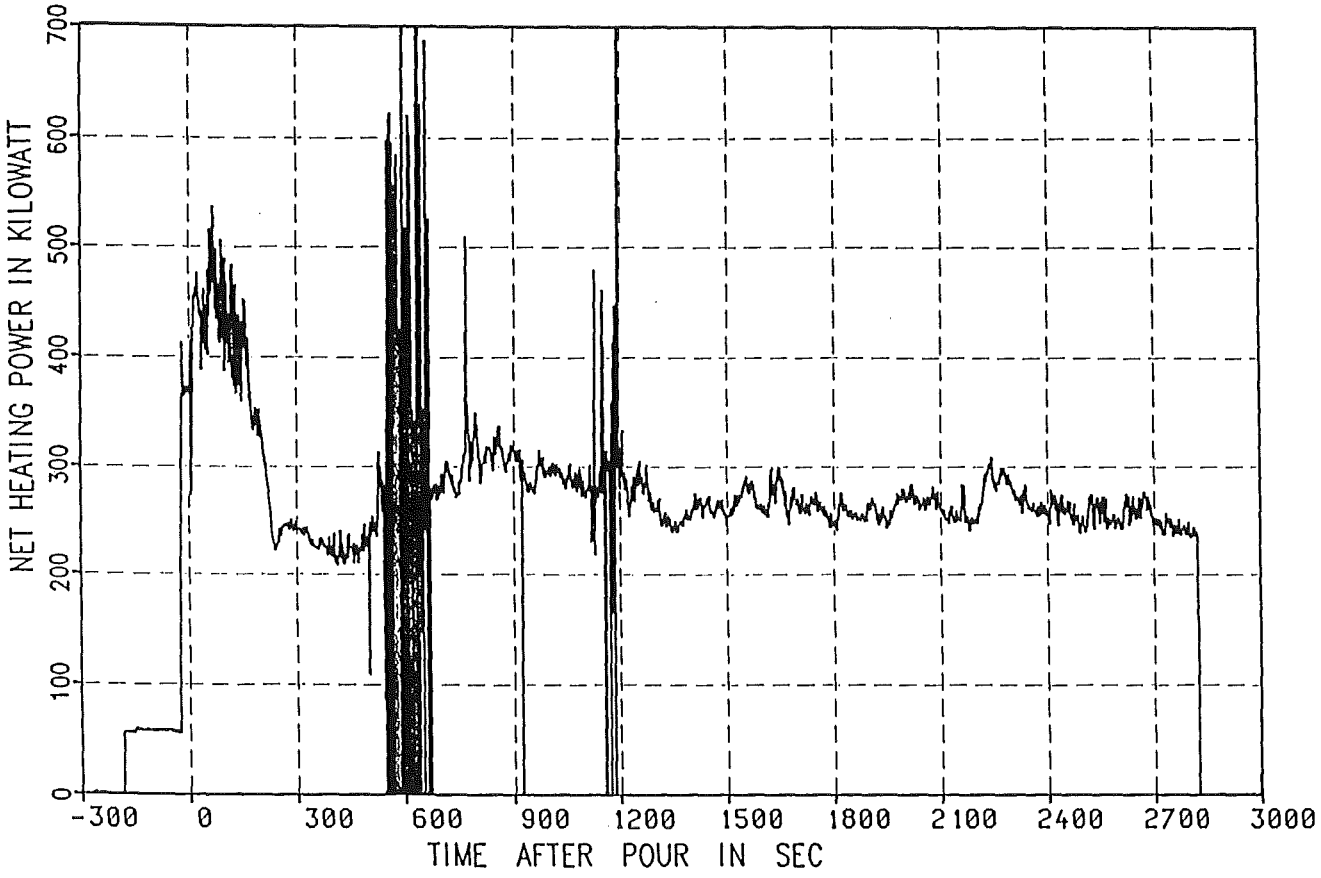

Figure 3: Net Heating Power in BETA V 5.2

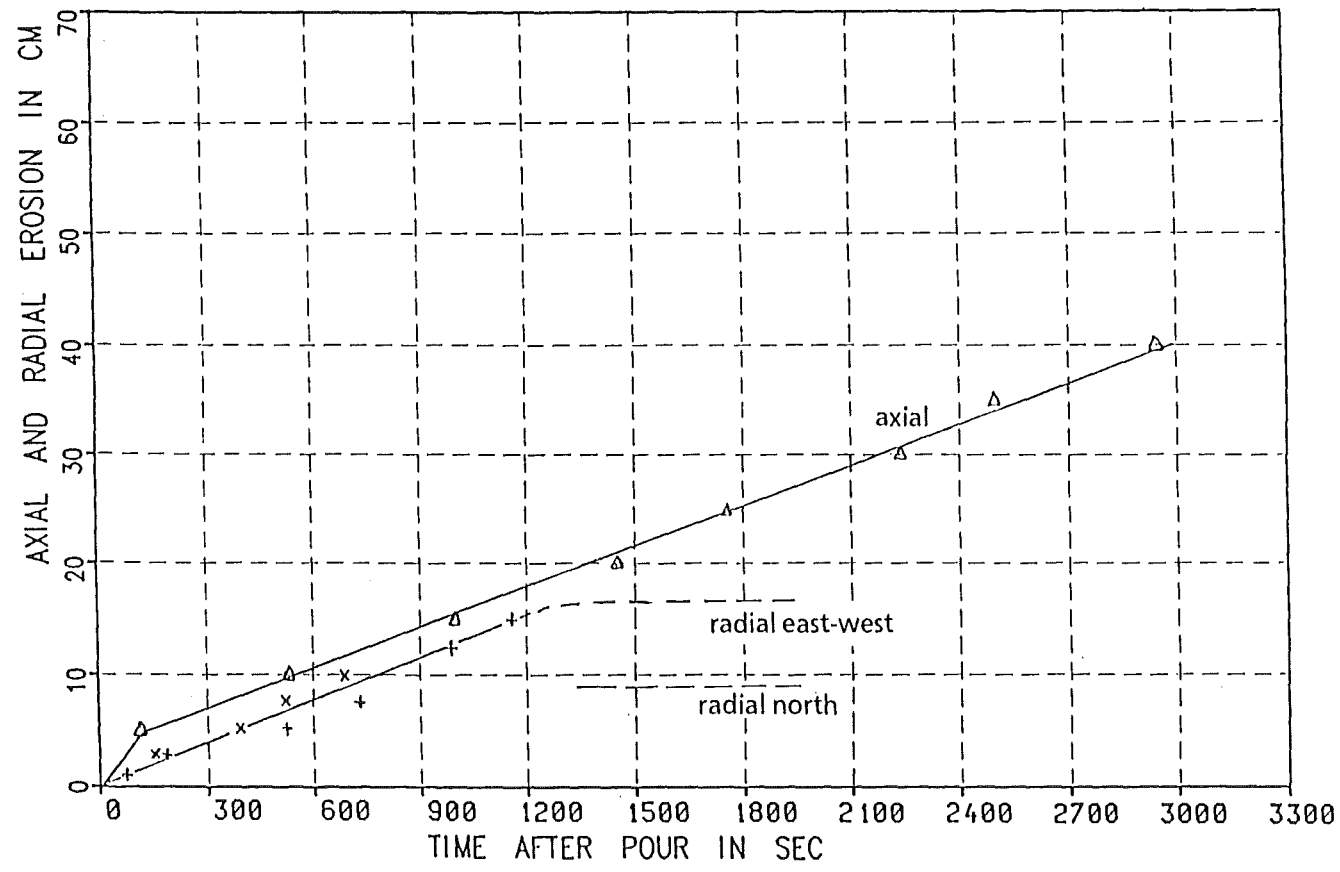

Figure 4: Concrete Erosion of BETA Crucible V 5.2

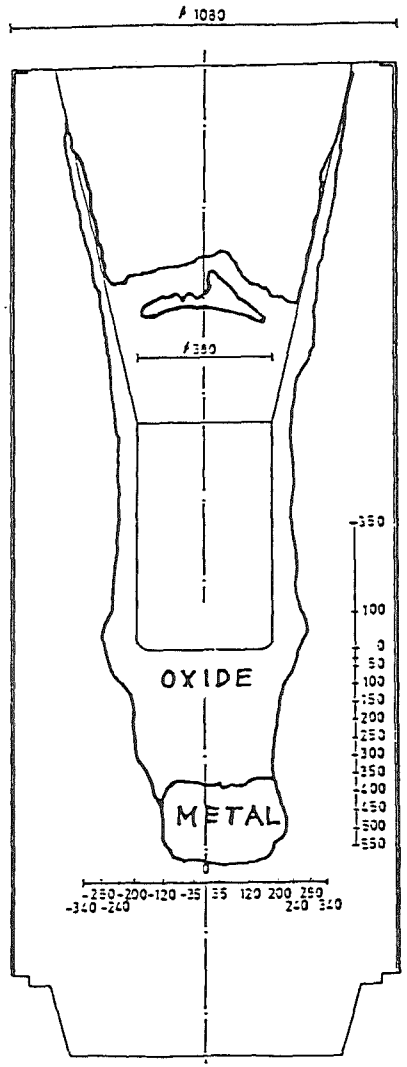

V 5.1

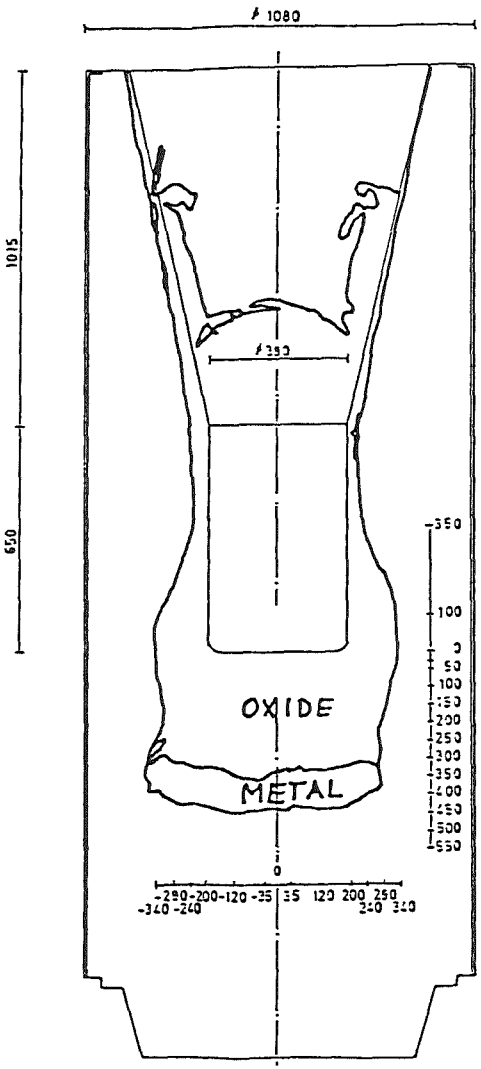

V 5.2

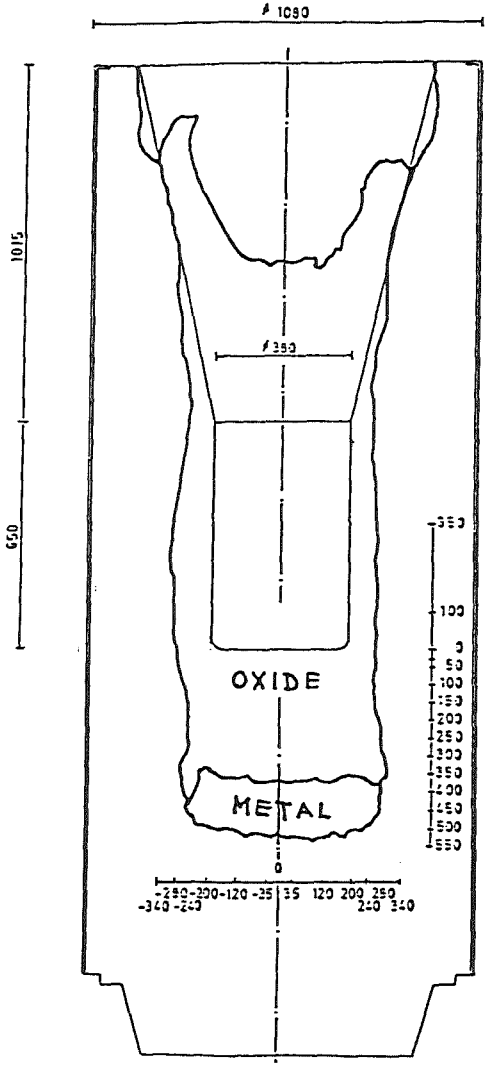

V 5.3

Figure 5: Crucibles of BETA Test V 5.1, V 5.2, and V 5.3

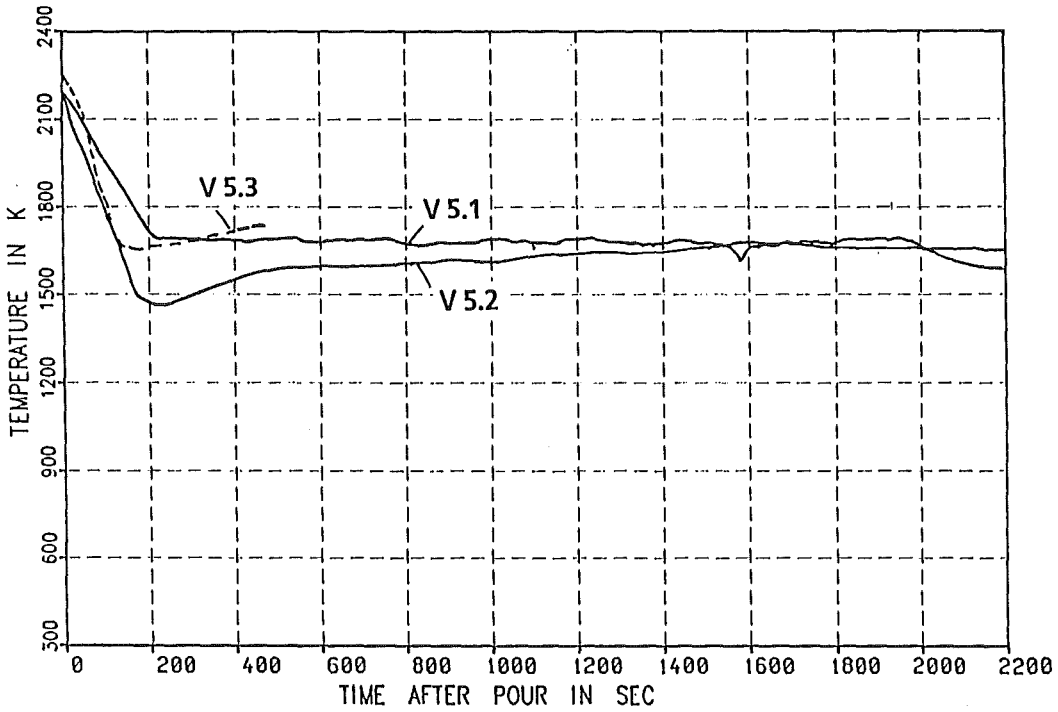

Figure 6: Temperature History of the Metallic Melt in BETA V 5.1,V 5.2,V 5.3

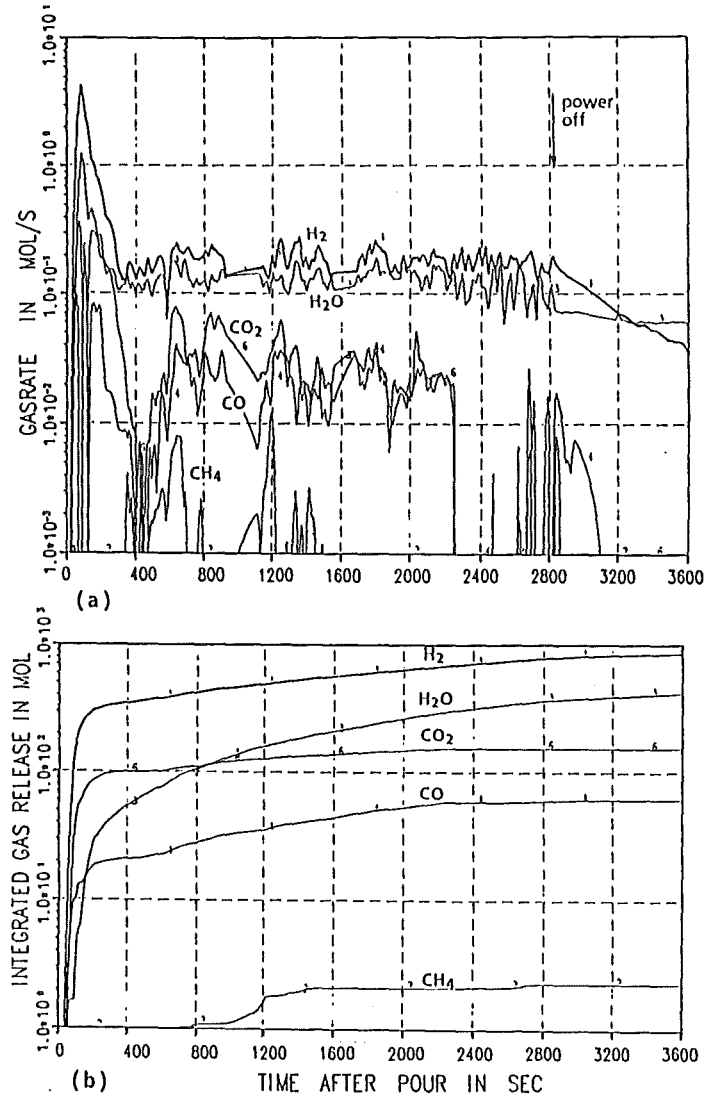

Figure 7: Gas Release in BETA V 5.2

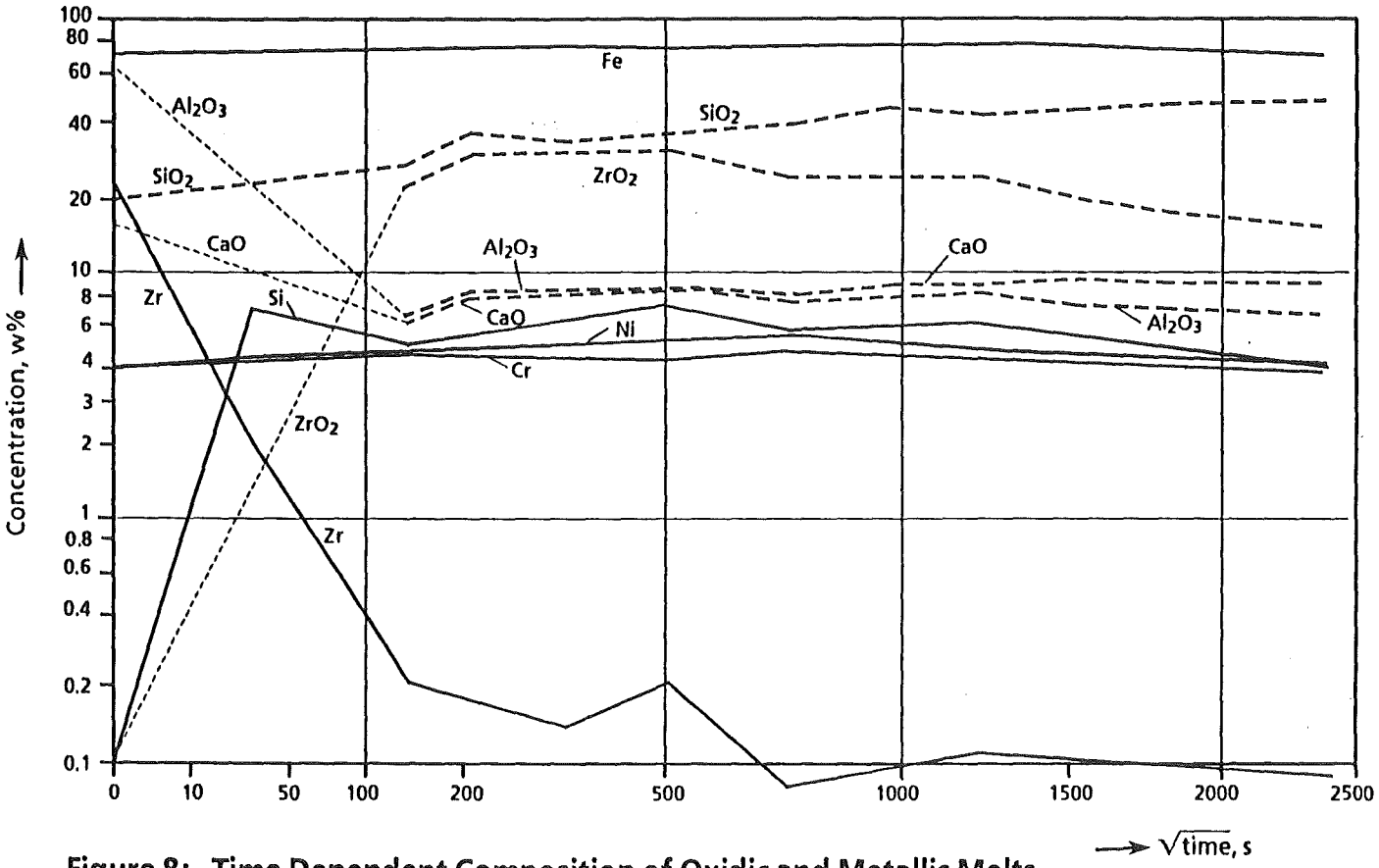

Figure 8: Time Dependent Composition of Oxidic and Metallic Melts in BETA V 5.2 as Determined from Dip-in Lances (——Metallic, – – –Oxidic)

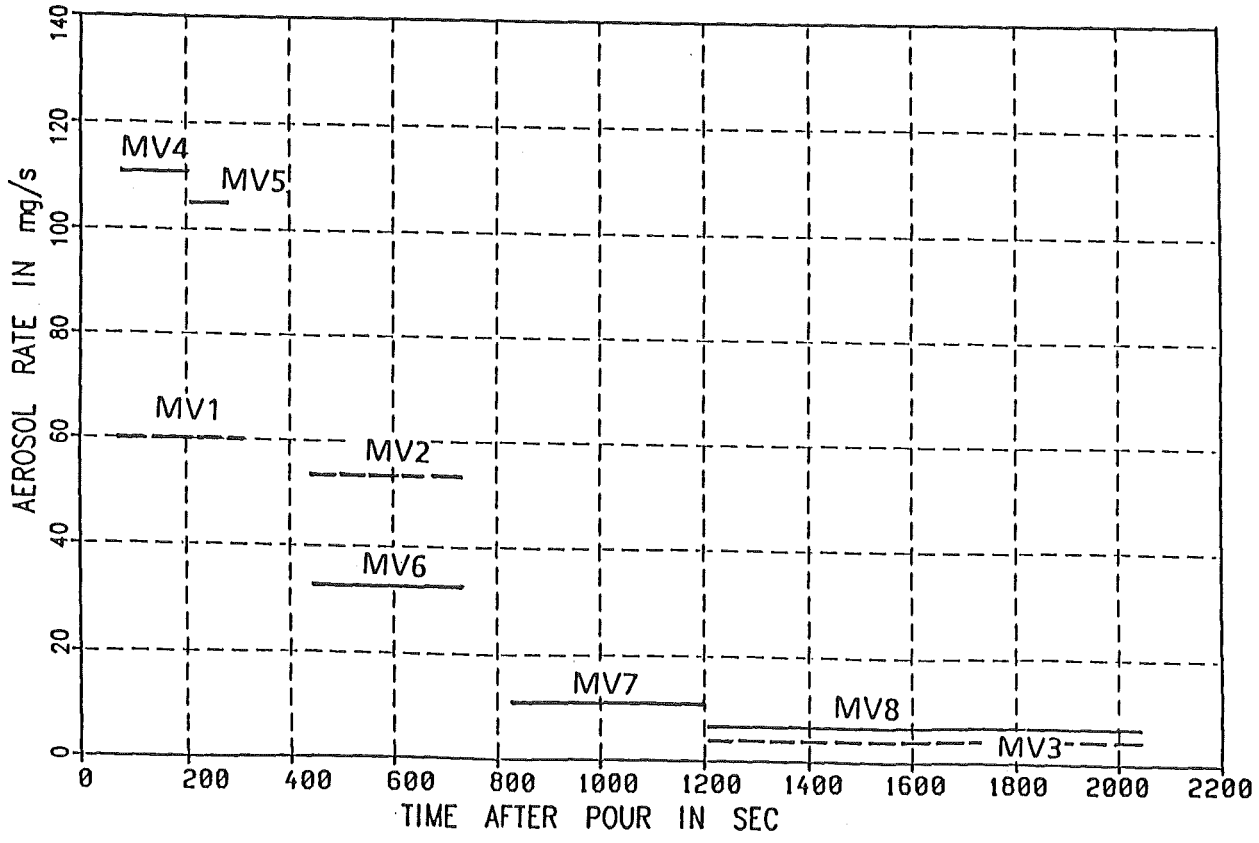

Figure 9: Aerosol Rates in BETA V 5.1

ACE Program Phase C: Fission Product Release From Molten Corium Concrete Interactions (MCCI)

by
B.R. Sehgal, Electric Power Research Institute
3412 Hillview Avenue, Palo Alto, CA 94303

and

B.W. Spencer, Argonne National Laboratory
9700 S. Cass Avenue, Argonne, IL 60439

Abstract

A program of experiments on the release of fission products during MCCI has recently been completed at Argonne National Laboratory (ANL). These experiments formed the Phase C of the advanced containment experiments (ACE) program which is sponsored by a consortium of 19 countries and managed by the Electric Power Research Institute (EPRI). The major objective was to obtain data on the release of fission products in realistic and extrapolatable simulations of accident conditions.

Data has been obtained on the release of the volatile and the less volatile refractory fission products, and the release of other aerosols during the MCCI. Thermal-hydraulic data have also been obtained.

These experiments are currently being analyzed by consortium members to validate the various MCCI models and codes, e.g., CORCON, VANESA, WECHSEL and MAAP-DECOMP.

This paper will provide an overview of the ACE MCCI experimental program.

Introduction

Nuclear power plant risk evaluation is concerned primarily with the evaluation of the frequency and the consequences of postulated severe accidents (1) in which

the core melts and fission products are released. In case the postulated severe accident proceeds to the point of vessel failure, the molten core material is discharged to the BWR pedestal region or to the PWR containment cavity. During this ex-vessel phase of the accident, molten corium interacts with concrete, resulting in release of copius quantities of concrete products as well as substantial quantities of combustible (H_2, CO) and non-condensible (CO_2, H_2O) gases which pressurize the containment. If the MCCI proceeds for a long time (tens of hours) and melt quenching (through water addition) and containment pressure reduction (e.g., through heat removal) measures are not successful, containment failure and/or basemat penetration may occur. Fission products are released to the environment if the containment fails; although the release is small if the containment integrity is maintained for several hours. The basemat penetration is of serious concern; although the environmental effects may be very much site-specific.

The gases produced during MCCI (H_2O, CO_2, SiO) sparge through the molten corium pool, undergoing chemical reactions and transporting the volatilized fission product compounds to the containment atmosphere. The metals contained in the corium, i.e., Zr, Fe, Ni, Cr are oxidized by the concrete gases creating substantial amounts of exothermic energy which supplements the decay heat and raises the melt temperature further. The vaporized materials condense to form aerosols which interact with the aerosols already present in the containment atmosphere.

The fission products released during the MCCI are extremely important in evaluating the source term (within containment) and its possible release to the environment. The magnitude of the release of the refractory fission products, i.e., La, Ba, Sr, Ce during the MCCI has been a source term issue ever since the APS study [2]; since these releases occur late in the accident scenario and the fission product compounds released are relatively long-lived and biologically toxic. There have been large differences between the predictions made for the releases of those fission products by the various MCCI codes, e.g., MELCOR [3], CORCON [4], VANESA [5], MAAP-DECOMP [6]. Since the fission product releases are a function of the thermal-hydraulic modeling (melt temperature, melt mixing, gas sparging rate, etc.) and the chemical reaction modeling, the uncertainties in the phenomenological models and the physical property data

had not allowed a discrimination between the widely-different results obtained from the various codes.

Previous Work

Extensive experimental and analytical research has been conducted to understand and model the thermal-hydraulic dynamic behavior of the MCCI. The experimental work had utilized simulant and real materials at various scales as, e.g., in the test series BETA [7], SURC [8], HS [9], TURC [10] and measured the concrete spatial ablation rates and the gas and aerosol generation rates. These tests, except for one SURC test, did not measure the fission product releases during MCCI. The analytical model development has culminated in the CORCON series of codes [4,13], developed at Sandia under NRC sponsorship, CORCON-UW [11], WECHSEL [12] and the DECOMP-METOXA [14] code. The thermal-hydraulic models employed in these codes have substantial differences between each other.

ACE Program

The ACE program [15] is a cooperative research program funded by the countries and organizations shown in Table 1 and managed by EPRI. This program consists of four phases: Phase A, already completed, obtained data on the decontamination potential of candidate filter designs, e.g., from Germany, France, Soviet Union, Sweden, etc. Phase B of the program, also completed, obtained data on iodine transport and partitioning in the containment during prolonged residence after the postulated accident, including effects of hydrogen burns and high levels of radiation. Phase C, described further in this paper, obtained data on fission product release during MCCI, and Phase D described in another paper at this meeting, will obtain data on the coolability of a molten corium pool with a water overlayer during MCCI.

ACE Phase C: MCCI Program

The guiding principal of the ACE Phase C Program has been to obtain data which could be applied directly for evaluating the consequences of prototypic accident scenarios. This necessitated the establishment of accident conditions at a relatively large scale. For the Phase C integral experiments, about 300 kg of

prototypic corium material containing representative inactive fission product compounds is heated to a molten state and to an initial temperature of about 2500K, whence it interacts with a block of prototypic concrete. In the experiment, appropriate thermal and chemical environment is achieved in a 50 cm X 50 cm X 15 cm interaction zone such that the aerosol release data is scale-independent and can be applied directly to the prototypic accident situations. Sufficient variations of the controlling parameters in the experiments resulted in data which could test the applicability of the different thermal-hydraulic and chemical models employed in the extant codes.

The objectives of the ACE Phase C program were:

1. To measure the release of the low volatility refractor fission product species.

2. To measure the physical and chemical characteristics of the aerosols generated.

3. To measure the thermal-hydraulic behavior, i.e., concrete ablation rate, gas generation rate, etc.

4. To analyze the tests to enable testing of MCCI thermal-hydraulic and chemical interaction models.

5. Support and encourage code comparison activities among ACE consortium members through pre- and blind post-test analyses.

Experimental Approach

The experimental approach was to employ powdered oxidic core materials, i.e., UO_2, ZrO_2,and add the metallics, e.g., Zr, stainless steel, control material (Ag, In for PWRs and B_4C for BWRs) as rods to obtain the corium mixture. Prototypic concretes, i.e., siliceous, limestone sand, limestone and serpentine (Russian) were employed in the basemat block. The heat generation in the corium mixture was simulated through direct electrical heating (DEH), which initiated the melting of the corium powder and then maintained the internal heat generation equal to 1% of the nominal power in the melt (decay heat rate at 2 hours after shutdown) during the MCCI. The approach on melt containment in the

experiment is the "cold-wall" technique in which the corium melt is contained in a water-cooled furnace on whose walls the sintered-crusted corium powder served as an insulating envelope. The heat transfer to the water-cooled side walls is measured and the power addition to the electrodes is programmed to compensate for the side wall heat losses on a continuous basis, during the corium heatup and the MCCI. It was decided to keep the corium-concrete interaction as one-dimensional in order to facilitate benchmarking of the MCCI models and codes.

The experimental approach on the design of the aerosol system was to collect all of the aerosol mass released, in order to establish the mass balance. At the start of the ACE Phase C Program, an aerosol working group consisting of experts from member countries was established to advise the designers. This group provided the functional requirements of aerosol system as: 1) measurement of total aerosol mass release and composition; 2) measurement of off-gas release and composition as a function of time; 3) measurement of aerosol concentration and composition as a function of time; 4) measurement of the composition and particle size distribution of respirable fraction as a function of time.

The other recommendations of the Aerosol Working Group were to employ a porous metal diluter for cooling and dilution of the off-gases. A separate line was recommended for collection of the aerosols just above the melt surface without any dilution and cooling. A vacuum pump operation system was recommended so that isokinetic sampling is possible in the constant flow system obtained without perturbations by any bursts in the off-gas release.

The Test Facility

The test facility consisted of the furnace, power supply, aerosol system, water-cooling system, ventilation and exhaust system and the data acquisition system. The furnace shown in Figure 1 was contained in a confinement cell. The aerosol collection system shown in Figure 2 was connected to the main gas line at the top of the furnace. The furnace side walls were water-cooled copper panels. Tungsten rod electrodes were fastened on two walls to provide the energy input into the corium powder. Corium heating was started through power input into a tungsten starter coil connected between the tungsten rod electrodes near the top edge of the corium mixture. The electrical conductivity of the corium powder is

increased considerably on melting and direct electric heating becomes effective. The corium melt started at the top and migrated downward towards the concrete basemat. The Zr rods were included as an insert on top of the concrete basemat and were encased in a slab of concrete material. The Zr did not oxidize prematurely with this method of addition to the corium powder. The furnace contained a view port in the lid through which video images are recorded.

The gas aerosol system design followed the advice of the international expert group. The system diluted, sampled and filtered the off-gas and aerosols released during MCCI. A helium atmosphere was maintained within the confinement surrounding the furnace. The helium flow rate to the furnace enclosure was kept larger than the peak off-gas flow rate. Mostly the helium was drawn into the aerosol system until the off-gasing from the corium started and reduced the helium in-flow.

A light extinction system was used to determine, on-line, the aerosol concentration in the off-gas flow. That is followed by a set of 10 cyclones and filters. The cyclones and filters also characterized the ratio of large to small particles and the transient variation of composition. An on-line mass spectrometer measured the concentration of CO_2, CO, H_2O, H_2 and He in the off-gas. A series of impactors were used to provide the fraction of the respirable aerosols and measure their particle size distribution. Migration of gas and water downwards into the concrete basemat-block was determined through hygrometer sampling of the gas below the concrete block. The aerosols collected at various locations are analyzed chemically.

A custom-made power supply providing several voltage and current ranges was obtained. The data acquisition system had more than 200 channels to record data every five seconds during the test. The system processed the recorded data into thermal-hydraulic parameters, e.g., the concrete ablation rate, the superficial gas velocity, etc.

Test Matrix

The ACE test matrix was approved by the ACE Technical Advisory Committee (TAC) after considerable discussions between technical representatives of the member countries. The matrix was refined mid-stream several times and the

final test matrix as completed in 1991 is shown in Table 2. The principal parameters varied were the concrete type, the zirconium content in the corium, the type of corium mixture (PWR, BWR with the corresponding control materials) and the net heat generation rate/Kg of UO_2. Each of the tests employed about 300 kg of corium atop a concrete block of 25 cm depth. The interaction area was 50 cm X 50 cm. The inactive fission products added to the corium mixture were at concentrations much higher than expected in the plants, in order to improve the detectability of the releases. The test matrix of seven tests was deemed to be sufficient for establishing the magnitude of the release fractions of refractory fission products in the postulated accident scenarios. Table 3 shows the composition of corium for each of the tests.

Test Operations

Nominally, the test operations consisted of initiating the corium powder melting process by heating up a set of tungsten coils attached between electrodes. Once the melt zone in the immediate vicinity of the coils became large enough, the conduction path through the powder was established and the melting process started in earnest. The melt front going downards reached the layer of Zr rods encased in the concrete and a vigorous oxidation reaction ensued which added a lot of energy to the melt. The melt temperature rose considerably (about 2500K), vigorous mixing took place and any powder overburden at the top of the melt mixed into the melt. The total time taken for the melting of about 300 kg of the corium powder and the metal incorporation was 2 to 3 hours. After the metal incorporation, the melt attacked the concrete. The tests were continued (unless prematurely terminated) to a total concrete ablation of about 12.7 cms, while collecting all the aerosols produced. The time elapsed during the concrete ablation phase was about 1 hour, except for test L8 when the power level was reduced.

The above description of the test operations sounds simple and straightforward. However, the test operations were much more complex and difficult; and with the very harsh conditions for the equipment, there were a few equipment failures which led to early termination of 2 tests and repeat of another. In test L2, the off-gas line plugged at the diluter due to the condensation of the Si species. In test L1, the melt foamed, filled up the plenum and burned a hole in the lid. In test L6, there was a loss of cooling failure in two of the furnace panels and the

this meeting. The tests were successful in maintaining the required MCCI conditions and obtaining definitive data on the release of fission products and other aerosols.

Experimental Results

The experimental results obtained for the thermal-hydraulic and the aerosol release behavior during MCCI for these tests are described in the accompanying papers. Briefly, the data obtained on the fission product releases, being prototypic and scale-independent, can be extrapolated easily to the accident scenarios. The results show that the releases for the refractory fission products are very low indeed and these data directly contradict the very high release values obtained from the VANESA and MELCOR codes for the reactor accident scenarios.

The thermal-hydraulic data obtained from these tests is for a one-dimensional MCCI and are not scale-dependent. These data serve as benchmarks for the MCCI thermal-hydraulic codes, e.g., CORCON, WECHSEL and DECOMP. These data are based on quite comprehensive variation of the type of concrete, type of corium, type of control rod material, zirconium content, and the decay power input rate.

Analyses and Code Comparison Activity

As part of the ACE Phase C program, an analyses and comparison activity was initiated in which several of the member countries participated. This activity, also reported at this meeting, is continuing and may develop into a more extensive and structured effort in the future. The guiding principal was to have the analysts with their respective codes and models provide the results of their analyses without previous access to the experimental results. The tests L6, L7 and L8 were designated as code comparison tests for which the data were sequestered until the analysts submitted the results of their calculations. The test L7 was only for thermal-hydraulic behavior comparison, while the tests L6 and L8 were for both thermal-hydraulic and aerosol release behavior comparison.

The code comparisons for test L6 are not as encouraging as one may have hoped on the basis that the codes have developed over a number of years while analyzing previous Sandia and the German BETA tests. From the preliminary observations, it

The code comparisons for test L6 are not as encouraging as one may have hoped on the basis that the codes have developed over a number of years while analyzing previous Sandia and the German BETA tests. From the preliminary observations, it appears that there are substantial differences in the analytical models used in the various codes and that the predictions from the codes for the rates of concrete ablation, gas generation and the aerosol release have substantial differences from the measurements.

Documentation

An extensive documentation effort has been pursued during the entire Phase C program. Each test was described through a pre- and a post-test report. After the test results are obtained (including chemical and electron microscope analyses for the aerosols), thermal-hydraulic and aerosol release data reports are issued for each test, except for the code comparison tests, whose reports are issued only after the analysts have submitted the results of their calculations. Reports have also been issued on the microstructural analysis of the aerosols performed in the AEA Laboratories in England. A summary report on the Phase C test program is planned. It is expected that all the reports will be issued by September 1992.

Summary and Conclusions

The ACE Phase C program, consisting of 7 tests, for obtaining data on the release of refractory fission products during MCCI, has been completed. The test program used prototypic materials and reproduced the actual accident environment to obtain scale-independent aerosol release data, which can be easily applied in the source term assessment of prototypic accident scenarios in LWR plants. The thermal-hydraulic data obtained should serve as excellent benchmarks for the models and codes used for MCCI analysis.

It was found that the measured releases of refractory fission products during MCCI are very much lower than the estimates obtained from the VANESA code.

References

1. B.R. Sehgal and J.J. Carey, "Degraded Core Accidents - An Overview", Proc. Int. Mtg. Light Water Reactor Severe Accident Evaluation, Cambridge, MA, August 28 - September 1, 1983, American Nuclear Society, 1983.

2. Report to the American Physical Society of the Study Group on Radionuclide Release From Severe Accidents at Nuclear Power Plants, Rev. Mod. Phys., Vol. 57, No. 3, Part II, July 1985.

3. R.M. Summers, et al., "MELCORE 1.8.0: A Computer Code for Nuclear Reactor Severe Accident Source Term and Risk Assessment Analysis", NUREG/CR-5531, SAND90-0364 (January 1991).

4. R.K. Cole, D.P. Kelley and M.A. Ellis, "CORCON-mod2: A Computer Program for Analysis of Molten-Core/Concrete Interactions", U.S. Nuclear Regulatory Report NUREG/CR-3920, SAND84-1246 (1984).

5. D.A. Powers, J.E. Brockman and A.W. Shiver, "VANESA: A Mechanistic Model of Radionuclide Release and Aerosol Generation During Core Debris Interactions With Concrete", U.S. Nuclear Regulatory Report NUREG/CR-4308, SAND85-1370 (1985).

6. R.E. Henry and M.G. Plys, "MAAP3.0B - Modular Accident Analysis Program for LWR Power Plants", Vols. 1 and 2 EPRI Report NP-7071-CCML (November 1990) and R.E. Henry, "A Model for Core-Concrete Interactions", Proc. Int. Mtg. on LWR Severe Accident Evaluation, Cambridge, MA, Paper 12.10 (August 28 - September 1, 1983).

7. H. Alsmeyer, "BETA-Experiments in Verification of the WECHSEL-Code: Experimental Results on the Melt-Concrete Interaction", Nuclear Engineering and Design 103, 115-125 (1987). Also see H. Alsmeyer, et al., "Beta Experimental Results on Melt/Concrete Interactions: Silicate Concrete Behavior", Proceedings of the Committee on the Safety of Nuclear Installations (CSNI) Specialists Meeting on Core Debris-Concrete Interactions, EPRI NP-5054-SR (February 1987).

8. D.R. Bradley and E.R. Copus, "Significant Results From SURC-3 and SURC-3A Experiments", presented at 15th Water Reactor Safety Meeting, National

Bureau of Standards, Gaithersburg (October 16-30, 1987); and E.R. Copus, et al., "Core-Concrete Interactions Using Molten Steel With Zirconium on a Basaltic Basemat: The SURC-4 Experiment", NUREG/CR-4994, SAND87-2008, R3, R5, R7 (August 1987); and M. Lee and R.A. Bari, "International Standard Problem No. 24, ISP-24, SURC-4 Experiment on Core-Concrete Interactions", Restricted CSNI Report No. 155 (December 1988).

9. E.R. Copus and D.R. Bradley, "Interaction of Hot Solid Debris With Concrete", NUREG/CR-4558, SAND85-1739 (1986).

10. J.E. Gronager, A.J. Suo-Anttila, D.R. Bradley and J.E. Brockman, "TURC1: Large-Scale Metallic Melt-Concrete Interaction Experiments and Analysis", NUREG/CR-4420, SAND85-0707 R5, R7 (January 1986); and J.E. Gronager, A.J. Suo-Anttila and J.E. Brockman, "TURC2 and TURC3: Large-Scale $UO_2/ZrO_2/Zr$ Melt-Concrete Interaction Experiments and Analysis", NUREG/CR-45231, SAND86-0318 R5, R7 (June 1986).

11. J.K. Norkus and M.L. Corradini, "Modeling of Molten-Core/Concrete Interactions: Fission Product Release", Proc. Intl. Conf. on Thermal Reactor Safety, Avignon, France, October 2-7, 1988 and EPRI NP-7495 (September 1991).

12. M. Reimann and W.A. Murfin, "The WECHSL Code: A Computer Program for the Interaction of Core Melt With Concrete", Karlsruhe Report KfK-2890 (1981).

13. D.R. Bradley, "CORCON-3" to be published by Sandia National Laboratory (1992).

14. M.G. Plys and M.A. McCartney, "A Mechanistic Model for Core-Concrete Interactions and Fission Product Release in Integrated Accident Analysis", Draft ARSAP Report (June 1988).

15. B.R. Sehgal, R.L. Ritzman, M. Merilo, F.J. Rahn and A.J. Machiels, "The Advanced Containment Experiments (ACE) Project", Proc. of the Eighth Pacific Basin Nuclear Conference, Taiwan, April 12-16, 1992.

Table 1
Current Membership of the ACE Consortium

TRACTEBELL*	Belgium
CUAEPP	Bulgaria
Ontario Hydro	Canada
JRC Ispra	Commission of the European Communities
NRI/NPPRI	Czechoslovakia
GRS	Federal Republic of Germany
VTT*	Finland
CEA	France
VEIKI	Hungary
ENEA	Italy
JAERI	Japan
ININ	Mexico
KEMA*	Netherlands
AEC*	Republic of China
SKI, SSPB, ABB	Sweden
PSI	Switzerland
Kurchatov Institute	Union of Soviet Socialists Republics
AEA*	United Kingdom
DOE, EPRI, NRC, Westinghouse	United States of America

* Lead organization

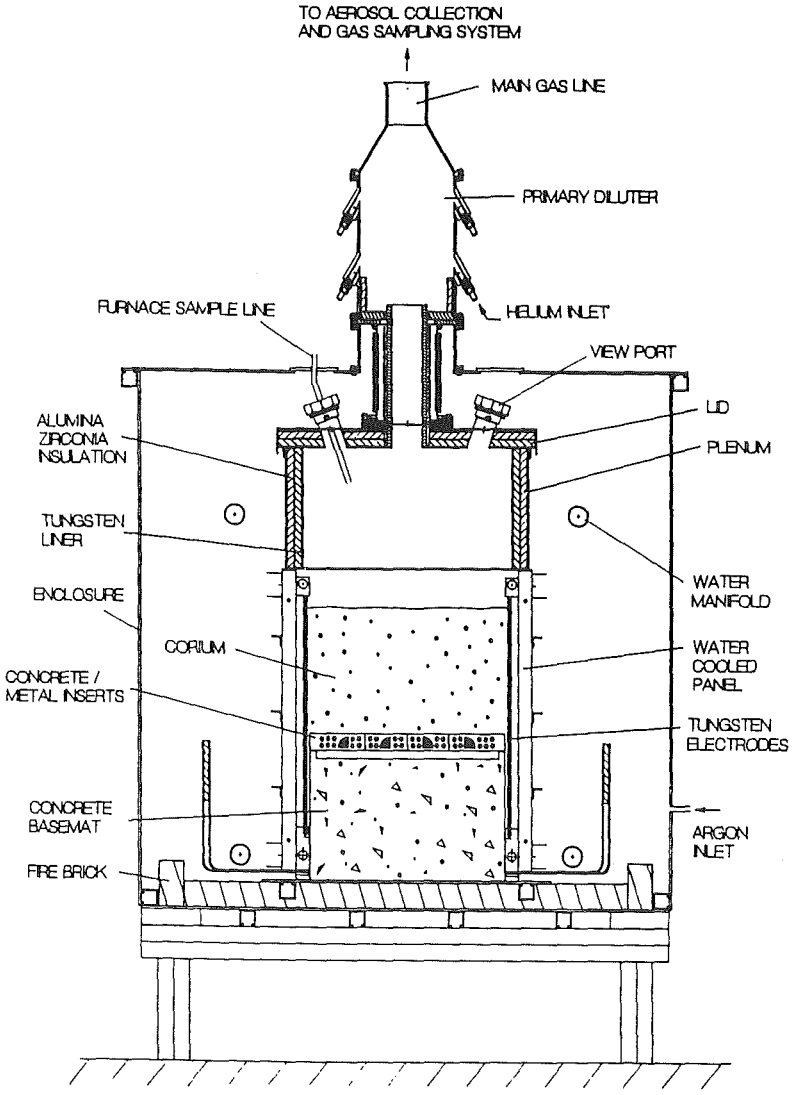

Figure 1: Diagram of the ACE MCCI Test Apparatus

Table II
Conditions for the Series of ACE MCCI Fission Product Release Tests

- Oxides from in-vessel: UO_2, ZrO_2, Fe_2O_3, Cr_2O_3, NiO
- Oxides from early ex-vessel ablation: CaO, SiO_2
- Metals: Zr or Zry, Fe, Cr, Ni, Ru-steel alloy
- Fission products: La_2O_3,, BaO, SrO, CeO_2

Test No.	Concrete Type (1)	Net Heat Generation (W/Kg UO_2)	Corium Mixtures	Initial Zr Oxidation %	Absorber Material
L5	L/S	325	PWR	100	–
L2	S	450	PWR	70	–
L1	L/S	350	PWR	70	–
L6	S	350	PWR	30	Ag, In
L4	S	250	BWR	50	B_4C
L7	L/S	250	BWR	70	B_4C
L3	L/S	350(2)	PWR	30	Ag, In
L8	L/L	350(2)	PWR	70	Ag, In

Note: (1) concrete type:

L/S: limestone/common sand concrete plus rebar
S: siliceous concrete plus rebar
L/L: limestone/limestone concrete plus rebar

Note: (2): reduced power operation after Zr is fully oxidized to represent longer term corium-concrete interaction

Table III
Corium Composition

Consti-tuent	Content in ACE MCCI Experiment (kg)						
	L5	L2	L1	L6	L4	L7	L8
UO_2	184.2	216	216	219	192	188.5	211.5
ZrO_2	34.0	42.5	42.5	18.5	43.2	59.4	41.6
Zr	–	13.4	13.4	21.1	30.3	17.7	12
Zirc-4	–	–	–	1.8	1.1	1.1	1.1
Fe_2O_3	54.1	–	–	–	–	–	–
NiO	5.2	–	–	–	–	–	–
Cr_2O_3	13.4	–	–	–	–	–	–
Type 304 SS	–	–	–	9.1	0.6	0.6	–
CaO	–	3.0	11.4	7.3	00	11.5	20.6
MgO	–	–	–	–	7.2	–	–
SiO_2	–	20.9	12.4	16.9	16.8	12.5	3.4
BaO	0.4	0.8	0.8	0.79	1.4	1.4	1.55
La_2O_3	0.4	0.6	0.6	0.6	1.1	1.14	1.23
SrO	0.4	0.5	0.5	0.5	0.96	0.96	1.04
CeO_2	1.0	1.3	1.3	1.3	2.32	2.32	2.51
MoO_2	–	0.9	0.5	0.94	1.7	1.7	1.84
SnTe	–	0.2	–	–	–	–	–
$ZrTe_2$	–	–	0.2	0.2	0.18	0.18	0.2
Ru	–	–	–	0.38	–	–	–
B_4C	–	–	–	–	1.0	1.0	–
Ag	–	–	–	1.19	–	–	1.19
In	–	–	–	0.22	–	–	0.22

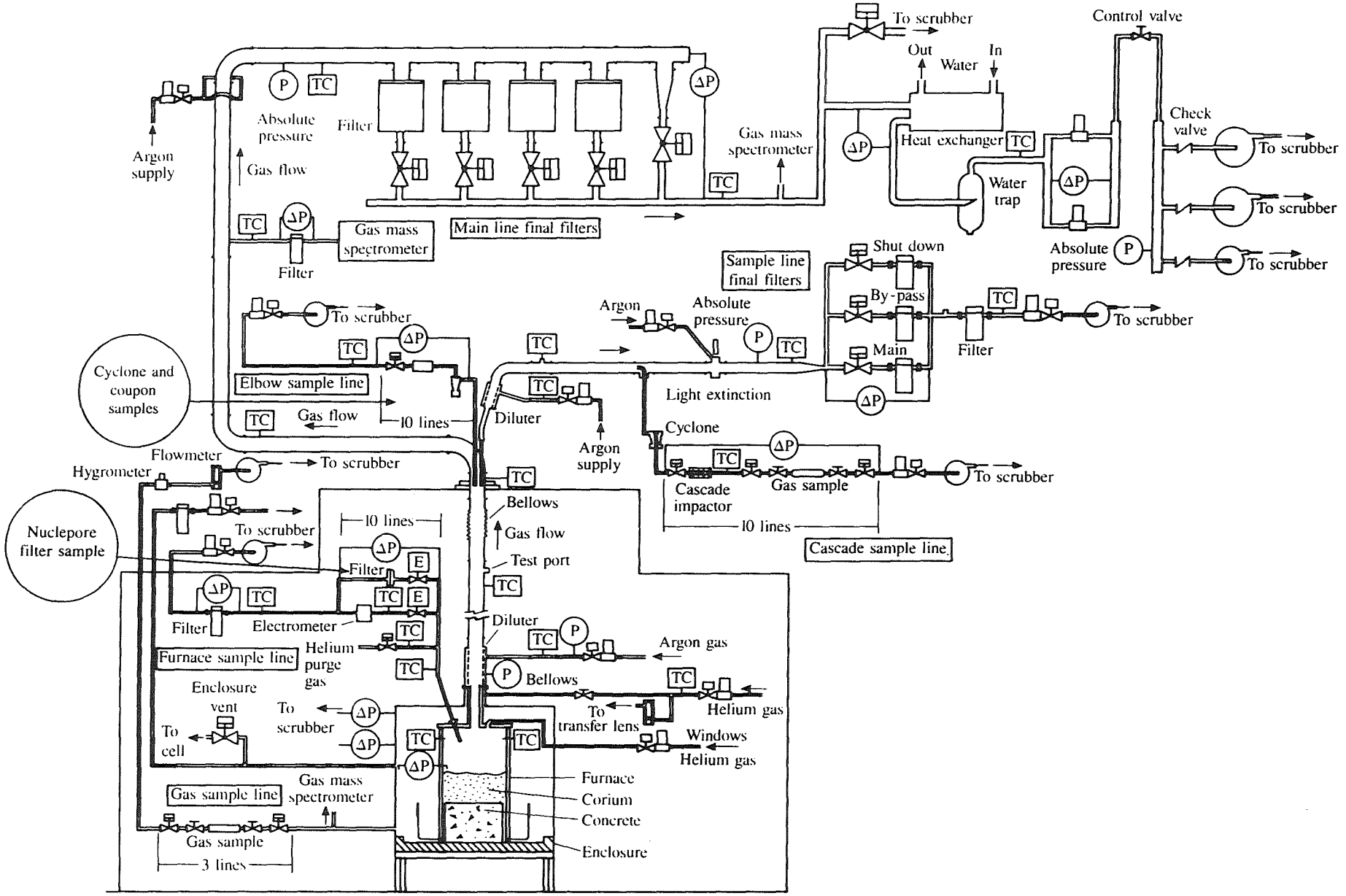

Figure 2: ACE MCCI Aerosol System

THERMAL-HYDRAULIC ASPECTS OF THE LARGE-SCALE INTEGRAL MCCI TESTS IN THE ACE PROGRAM

D. H. Thompson, J. K. Fink, D. R. Armstrong, B. W. Spencer, and B. R. Sehgal*

Argonne National Laboratory
Argonne, Illinois 60439 USA

*Electric Power Research Institute
Palo Alto, California 94303 USA

ABSTRACT

Seven large-scale molten core concrete interaction (MCCI) tests have been performed at Argonne National Laboratory as part of the internationally sponsored Advanced Containment Experiments (ACE) Program. One of the objectives of the ACE MCCI/fission product release tests was to investigate the thermal hydraulic aspects of the MCCI. The tests were performed using four types of concrete (siliceous, serpentine, limestone, and limestone/common sand) and a range of metal oxidation for both boiling water reactor and pressurized water reactor core material. Melt temperatures, ablation rates, off-gas composition, and superficial gas velocity as a function of time during each test were processed from the recorded test data. These thermal hydraulic results are described for the ACE MCCI tests.

INTRODUCTION

The fission product release occurring during a molten core-concrete interaction is one of the major contributors to the uncertainty in risk calculated for nuclear power plants. A series of large-scale integral accident simulations has been performed in the ACE Program to investigate the thermal hydraulic and chemical processes of MCCIs and to expand the database on release of low volatility refractory material fission products for further development and validation of MCCI/fission product release codes. This paper describes the thermal hydraulic results of the ACE MCCI tests. The ACE MCCI experimental program [1] and aerosol release during the ACE MCCI tests [2] are described separately.

Characteristics of the ACE MCCI tests are described in Table 1. The core debris contained UO_2, ZrO_2, stainless steel oxides or zirconium and stainless steel, plus nonradioactive fission product simulants (BaO, La_2O_3, SrO, CeO_2, MoO_2, $ZrTe_2$, Ru etc.) and control rod material. Appropriate ratios of fuel to structural materials were used for pressurized water reactor (PWR) and boiling water reactor (BWR) core material. The initial extent of oxidation of the core structure was one of the test parameters. Absorber materials were silver plus indium for PWRs, boron carbide for BWRs. Fission product simulants were included in the corium at concentrations higher than found in reactor plants to improve detectability in the aerosols. To preclude early oxidation, metal was located in concrete/metal inserts directly above the test concrete that represented the reactor basemat. Tests were performed using four types of concrete: siliceous, serpentine, limestone, and limestone (coarse aggregate)/common sand (fine aggregate). Core melt material, termed corium in this paper, and the concrete basemat were contained within a water cooled test apparatus. Direct electric heating was used to initiate the core melt and maintain internal heat generation during the sustained interaction of the melt with the basemat. Two-hour decay heat levels were maintained to achieve the target initial melt temperature of ~2500 K. A reduction in decay heat level after the completion of metal oxidation was included in the test matrix to address the longer term aspects of the MCCI.

TEST FACILITY

The facility for conducting the ACE MCCI/fission product release tests consisted of a confinement cell, test apparatus, power supply, gas/aerosol diagnostics system, water cooling system, gas cleanup/exhaust system and data acquisition system. The test apparatus, shown in Figure 1, was constructed of eight water cooled copper panels which formed the four walls enclosing the concrete basemat and the corium. Tungsten rod electrodes formed two inner walls of the apparatus and were connected near the top of the corium volume by four open spiral wound coils of tungsten wire for initial heating of the corium. An insulated, water-cooled gas plenum and lid connected the test apparatus to the gas/aerosol diagnostics system. The gas plenum contained thermocouples for measuring gas temperatures above the melt; the lid contained ports for viewing the melt surface by an optical pyrometer and video cameras.

Table 1. ACE MCCI/Fission Product Release Test Conditions

Test	Concrete Type*	Net Heat Generation, W/kg UO_2	Reactor Type	Initial Zr Oxidation, %	Control Rod Material
L5	L/S	325	PWR	100	
L2	S	450	PWR	70	
L1	L/S	350	PWR	70	
L6	S	350	PWR	30	Ag, In
L4	Soviet	250	BWR	50	B_4C
L7	L/S	250	BWR	70	B_4C
L8	L	350/150	PWR	70	Ag, In

*L/S = limestone/common sand
S = siliceous
Soviet = serpentine layer over siliceous
L = limestone

The test apparatus, concrete basemat, and gas/aerosol diagnostic system were heavily instrumented. Over 200 channels of data were logged on a five-s period during a test. Data were logged by personal computers; key information was processed on line and displayed to monitor and guide experimental operations.

INTERACTING MATERIALS

Each ACE MCCI test was performed with 300 kg of corium and a 200 kg concrete basemat having a surface area of 2500 cm^2. The corium was predominately fuel and core structure plus 8% by weight of the major concrete constituents. It also included oxide forms of nonvolatile fission product simulants Ba, La, Sr, Ce, and Mo; Te was present as SnTe or $ZrTe_2$. The fuel was natural and depleted UO_2, present as powder or crushed pellets. Presence of the concrete constituents represented erosion of the basemat during the jet impingement phase of the accident that would precede the early aggressive interaction and longer term

erosion phases of the MCCI simulated in the ACE tests. Fission product simulants were present in twice the concentration typical in a reactor. This was later increased to four times the reactor concentration to improve the detectability of the fission products in the aerosols. Control rod materials, Ag plus In for PWRs and B_4C for BWRs, were included in some tests. Based on prior experience, Ag and In were limited to a concentration 25% that of a PWR to reduce the possibility that aerosols containing Ag and In would obscure detection of other elements having a greater radiological consequence. The corium compositions for Test L6 (PWR, 30% initial oxidation) and Test L7 (BWR, 70% initial oxidation) are shown in Table 2.

Metal in the corium was located in concrete/metal inserts directly above the basemat to preclude early oxidation. Ru was alloyed with Type 304 stainless steel to produce a 10 w/o solution in stainless steel for Test L6. $ZrTe_2$ was located in zircaloy-4 sleeves. Ag and In were alloyed together. The remaining Type 304 stainless steel and the zirconium were present in rod form. In BWR accident simulations, B_4C was located within the concrete/metal inserts in thin walled stainless steel tubing.

Concrete basemats were 30.5 cm high and about 50 cm on a side. Each included one or more arrays of Type K thermocouples to determine depth of erosion and ~15 W5Re/W26Re thermocouples to measure the melt temperature. W5Re/W26Re thermocouples used in the ACE MCCI tests were purchased with design characteristics as per recommendations of the High Temperature Instrumentation Working Group. Concrete mix designs for specific U.S. reactors or provided by ACE consortium members were used in concrete preparation. Reinforcing rod was contained in most basemats, located at two elevations within the volume of the basemat to be eroded. Reinforcing rod was eliminated in Tests L7 and L8 so that iron oxidation would not mask or delay the attainment of a fully oxidized melt and the planned reduction in power level. Compositions of the various types of concrete used in the ACE MCCI tests, determined by chemical analysis, are shown in Table 3. Solidus and liquidus temperatures, determined by differential thermal analysis [3], are shown in Table 4.

Table 2. Corium Composition

Constituent	Test L6	Test L7
	PWR, 30% Oxidation	BWR, 70% Oxidation
	Mass, kg	
UO_2	219	188.5
ZrO_2	18.5	59.4
Zr	21.1	17.7
Zirc-4	1.8	1.1
Type 304 SS	9.1	0.6
CaO	7.3	11.5
SiO_2	16.9	12.5
BaO	0.8	1.4
La_2O_3	0.6	1.1
SrO	0.5	1.0
CeO_2	1.3	2.3
MoO_2	0.9	1.7
$ZrTe_2$	0.2	0.2
Ru	0.4	---
Ag	1.2	---
In	0.2	---
B_4C	---	1.0

Table 3. Concrete Composition

Constituent	Limestone/ Common Sand	Siliceous	Soviet		Limestone
			Serpentine	Siliceous	
	Mass %				
SiO_2	28.3	69.0	34.3	69.1	6.2
CaO	26.0	13.5	9.8	10.8	45.9
Al_2O_3	3.5	4.0	1.8	8.8	1.7
MgO	9.6	0.7	30.7	0.7	3.6
Fe_2O_3	1.6	1.0	6.4	1.7	0.9
K_2O	0.6	1.4	0.1	1.6	0.6
TiO_2	0.14	0.8	0.0	0.15	0.09
Na_2O	1.1	0.7	0.06	2.7	0.4
SrO	0.03	0.02	0.013	0.036	0.05
BaO	0.03	0.02	0.01	0.1	0.03
Cr_2O_3	0.009	0.007	0.19	0.006	0.007
MnO	0.05	0.03	0.13	0.05	0.03
V_2O_5	0.01	0.0	0.0	0.0	<0.009
CuO	0.005	0.0	0.007	0.004	0.004
ZnO	0.007	0.0	0.009	0.007	0.009
ZrO_2	0.02	0.0	0.0	0.009	0.008
NiO	0.005	0.0	0.2	0.004	0.004
CoO	0.003	0.0	0.0	0.0	<0.003
H_2O - bound - free	6.1	3.68	11.3 3.1	1.1 0.8	3.74 2.36
CO_2	21.4	4.23	0.9	1.2	33.3
SO_3	0.58	0.51	0.52	0.58	0.44
Cl^-	0.045				0.02

Table 4. Solidus and Liquidus Temperatures of Concrete

Type of Concrete	Temperature, K	
	Solidus	Liquidus
Limestone/common sand	1393	1568
Siliceous	1403	1523
Limestone	1495	2577

TEST OPERATION

Test operation began after gas lines in the aerosol system reached a 400 K operating temperature and the pretest calibration of the gas mass spectrometer was completed. During initial low power operation, all current flowed through four coils of tungsten wire that connected the two sets of electrodes. The temperature of the corium in and around the coils increased until the corium became electrically conducting. Power was increased gradually in each ACE MCCI test until the planned net power level was reached. Net power was calculated on line as the difference between the total electric power input and the sidewall power losses to the test apparatus cooling water. About two hours was required to reach the operating power level (~1% equivalent decay heat). Overburden collapse exposed the melt surface, which grew laterally as the melt front progressed down through the corium toward the inserts and the basemat.

A helium atmosphere was maintained around the test apparatus. Helium was drawn through the gas plenum of the test apparatus and into the aerosol system at a flow rate exceeding the maximum off-gas release rate expected in each test. Argon was injected into the primary diluter to cool and dilute the gas stream. The helium fraction of the gas stream decreased as helium was displaced by off gas. Volumetric flow rate in the aerosol system remained nearly constant to facilitate isokinetic sampling. Each of the three sampling modules in the aerosol system sampled for the entire duration of a test. The first sample was drawn from startup until off gassing and significant aerosol release began. This occurred as the surface temperature of the concrete/metal inserts approached 373 K. The remaining aerosol samples (10 per module) collected by parallel operation

of each sampling module were taken in sequence until the test ended.

The erosion of the basemat was monitored. A 1673 K temperature indication by Type K thermocouples in the basemat was used to define the location of the melt front. A reduction in power level was made if the test called for operation at ~0.5% equivalent decay heat power level to address longer term corium-concrete interactions. When the target ablation depth was reached (12.7 cm in most tests), the power was turned off and aerosol sampling was stopped. After test operations ended, the gas mass spectrometer was taken off line for posttest calibration. The cooling water system operated until the interacting materials had been cooled to near room temperature.

MODIFICATIONS AND UPGRADES

Both the test apparatus and aerosol system required modifications during the ACE MCCI Program to match capacities to test conditions. The off-gas flow rate/temperature capacity of the aerosol system was exceeded during the rapid initial ablation of the basemat in Test L1. Foaming of the melt to completely fill the gas plenum imposed a heat load on the lid that burned a hole through the lid structure between external cooling water coils. The aerosol system was modified and capacities expanded as per recommendations of the ACE Technical Advisory Committee Aerosol System Work Group [2].

Early in Test L6, the test apparatus suffered a loss-of-cooling failure in two adjacent cooling panels. An ACE MCCI Design Review was held to investigate the loss-of-cooling incident and review the proposed redesign of the cooling panels and cooling water system. Cooling panel failure was attributed to boiling in a cooling channel, which vapor locked the water cooled panel from further cooling water flow before the heat load could be dissipated. Possible causes of the loss of cooling included failure of solder joints in the fabricated plate brass cooling panels, air/vapor accumulation in the cooling panels, and melt contact with the cooling panels. The inside of the test apparatus had been lined with zirconia felt prior to loading corium for each test. For Test L6, zirconia insulating board (1.27 cm thick) was located adjacent to the inner faces of the cooling panels as added protection against possible damaging effects from the

increased inventory of unoxidized metal. The exact cause or sequence of events leading to local failure of the two cooling panels was not established. Instead, the consensus was that the failure involved a number of factors including the presence of the zirconia insulation board.

The proposed modification to the test apparatus cooling panels and water cooling system included fabrication of new cooling panels from 5.1-cm thick copper billets and increasing the number of cooling water supply lines and pumps, and the flow capacity, in the cooling water system. Each of the new cooling panels would be built with two separate cooling circuits. Water flow velocity would be at a level high enough to sweep out any gas or vapor. The diagnostics and panel displays would be upgraded to improve operator control and provide additional information on system status. The proposed modifications were judged to be more than adequate to address the suspected causes of the cooling panel failure in Test L6. New cooling panels were built. The cooling water system was modified as proposed and tested extensively. This system performed flawlessly throughout the remainder of the ACE MCCI Program.

EXPERIMENTAL RESULTS

Thermal hydraulic results from six of the seven ACE MCCI tests are summarized in Table 5. Results from Test L8 are being sequestered until the blind posttest code comparisons for Test L8, currently in progress, are completed.

Melt Temperature

The target melt temperature for the ACE MCCI tests was 2500 K, which was above the melting point of all the fission product simulants. Below ~2400 K, the vapor pressure over La_2O_3 is too low to produce a detectable La release. Melt temperatures exceeding 2400 K were measured in all but two tests - L5 and L4. The temperature reached by the melt is dependent on the solidus/liquidus temperatures of the corium, and possibly influenced by the level of chemical reaction power. In Test L5, the corium was fully oxidized; there was no reduction of H_2O and CO_2 off gases. In tests with partially oxidized corium, CaO and SiO_2 were the major concrete constituents present in the initial corium

Table 5. Thermal Hydraulic Results from ACE MCCI Tests

	L5	L2	L1	L6	L4	L7	L8
Concrete type	L/S	S	L/S	S	Soviet	L/S	L
Mass of reinforcing rod, kg	2.8	2.8	2.9	2.9	2.6	0	0
Insert depth, cm	---	---	---	7	7.9	5.7	4.3
Metal, kg	0	13.6	13.6	34	32.2	19.6	14.7
Net electric power, kW	60	100	75	75	50	50	75/35
Peak chemical reaction power, kW	0	7	60	7	60	37	150
Max. melt temperature, K	2200	2420	2625	2425	2300	2515	2480
Max. ablation rate, mm/min	1.6	3.9	8.1	9	4.6	1.7	5.3
Ablation depth, cm	11	12.7	~4	16	14.2	3	13
Max. off gas flow rate, sLpm	61	49	300	40	260	81[a]	720[b]
Max. superficial gas velocity, cm/s	4.2	2.9	24.6	2.6	17	5.7[a]	48.8[b]

[a]Higher values during insert ablation (156 sLpm, 11 cm/s)

[b]Higher values during insert ablation (780 sLpm, 53.4 cm/s)

inventory of all tests but L4. Major concrete constituents in the Soviet serpentine concrete were MgO and SiO_2. In Test L4, the initial melt temperature was 2150 K and increased to reach 2300 K after erosion into the siliceous concrete and uptake of CaO and SiO_2 into the melt.

Ablation Depth

The rate at which a reactor basemat is ablated influences the mass flow rate of concrete constituents entering the melt and the volumetric flow rate of decomposition gases, which stir the melt and supplement the decay heat when reduced by unoxidized metal. In the ACE Program, it was expected that Test L5, with fully oxidized corium, would yield the lowest ablation rates. Test L5 ablation rates were low, decreasing from 1.5 mm/min at the start of basemat ablation to 0.6 mm/min when the test ended. The ablation depth vs time in six of the seven ACE MCCI tests is shown in Figure 2. Although the test operating conditions varied significantly in reactor type, in fraction of core structure oxidized, and in gas content of the concrete, the resulting ablation rates cluster about ~4 mm/min or more or about ~1 mm/min. Ablation rates of ~4 mm/min

or more were observed early in Tests L2, L1, L4 and late in Test L6. Ablation rates of ~1 mm/min were observed in Tests L5 and L7, also early in Test L6 and during the initial ablation of the siliceous concrete in Test L4.

Most tests exhibited a decrease in ablation rate with time as the corium concrete interaction proceeded. Departures from this response were observed in Tests L4 and L6. In Test L4, ablation of the upper 5.1 cm of serpentine concrete occurred rapidly, even though the melt temperature was only 2150 K. The downward progress of the melt front seemed to halt when the siliceous concrete was reached. Thereafter, the ablation rate increased gradually as the melt temperature increased to reach a maximum of ~3 mm/min when the test ended. An increasing ablation rate with time was also observed in Test L6. Both Test L4 and Test L6 had high metal content in the corium and high silica concrete (L4 when the Soviet siliceous concrete was reached). The endothermic reaction of zirconium with silica in these two tests is thought to have been a major factor in depressing the ablation rate while metal was present. This reaction produces SiO(gas), which forms silica chains when cooled rapidly. In Tests L2 and L6, both with siliceous concrete, the silica chain formation in the primary diluter of the aerosol system forced early termination of aerosol sampling; test operation continued until the reference ablation depth was reached. In Test L4, also containing siliceous concrete, the zirconia tube connecting the test apparatus lid to the primary diluter was nearly plugged by aerosols which consisted primarily of Si species [2]. In Tests L1 and L7, both with limestone/sand concrete, the combination of unoxidized metal, appreciable silica content of the concrete and a higher off-gas release than in siliceous concrete caused foaming of the melt. The melt filled the test apparatus in each test and caused test termination before the target ablation depth was reached.

Gas Release

The composition and flow rate of off gases were a function of the type of concrete, ablation rate, and presence or absence of metal. Only 50 to 75% of the concrete decomposition gases was observed in the aerosol system. H_2, H_2O, CO, and CO_2 also migrated downward into and through the concrete.

The composition of the gas flowing through the main line of the aerosol system was determined by a gas mass spectrometer. Gas and water migration downward

through the concrete was determined by a hygrometer and from samples of gas drawn from beneath the basemat. In Test L8, a second gas mass spectrometer monitored the gas composition of the volume below the basemat. Changes in the gas composition of the volume below the basemat were coincident with changes in off-gas composition in the aerosol system.

Peak superficial gas velocities, based on the measured upward release of off gas, were between 25 cm/s and 3 cm/s. Presence of vapor species such as SiO(gas) was not included.

Melt Behavior

From visual observation of the melt surface, the melt appeared to be thoroughly mixed by gas sparging in each test. No crust development was observed on the melt surface; a thin film developed, then disappeared, in a periodic manner. Foamed melt material was discovered in the test apparatus during disassembly of all tests performed with siliceous and limestone/common sand concrete that contained metal.

ACKNOWLEDGEMENTS

Work sponsored by the Electric Power Research Institute under Contract RP 2802-12.

REFERENCES

1. B. R. Sehgal and B. W. Spencer, "ACE Program Phase C: Fission Product Release from Molten Corium Concrete Interactions (MCCI)," paper presented at the OECD CSNI Specialist Meeting on Core Debris Concrete Interactions, Karlsruhe, Germany, April 1-3, 1992.

2. J. K. Fink, D. H. Thompson, B. W. Spencer, and B. R. Sehgal, "Aerosols Released During Large-Scale Integral MCCI Tests in the ACE Program," paper presented at the OECD CSNI Specialist Meeting on Core Debris Concrete Interactions, Karlsruhe, Germany, April 1-3, 1992.

3. M. F. Roche, Argonne National Laboratory, private communication, November 1990.

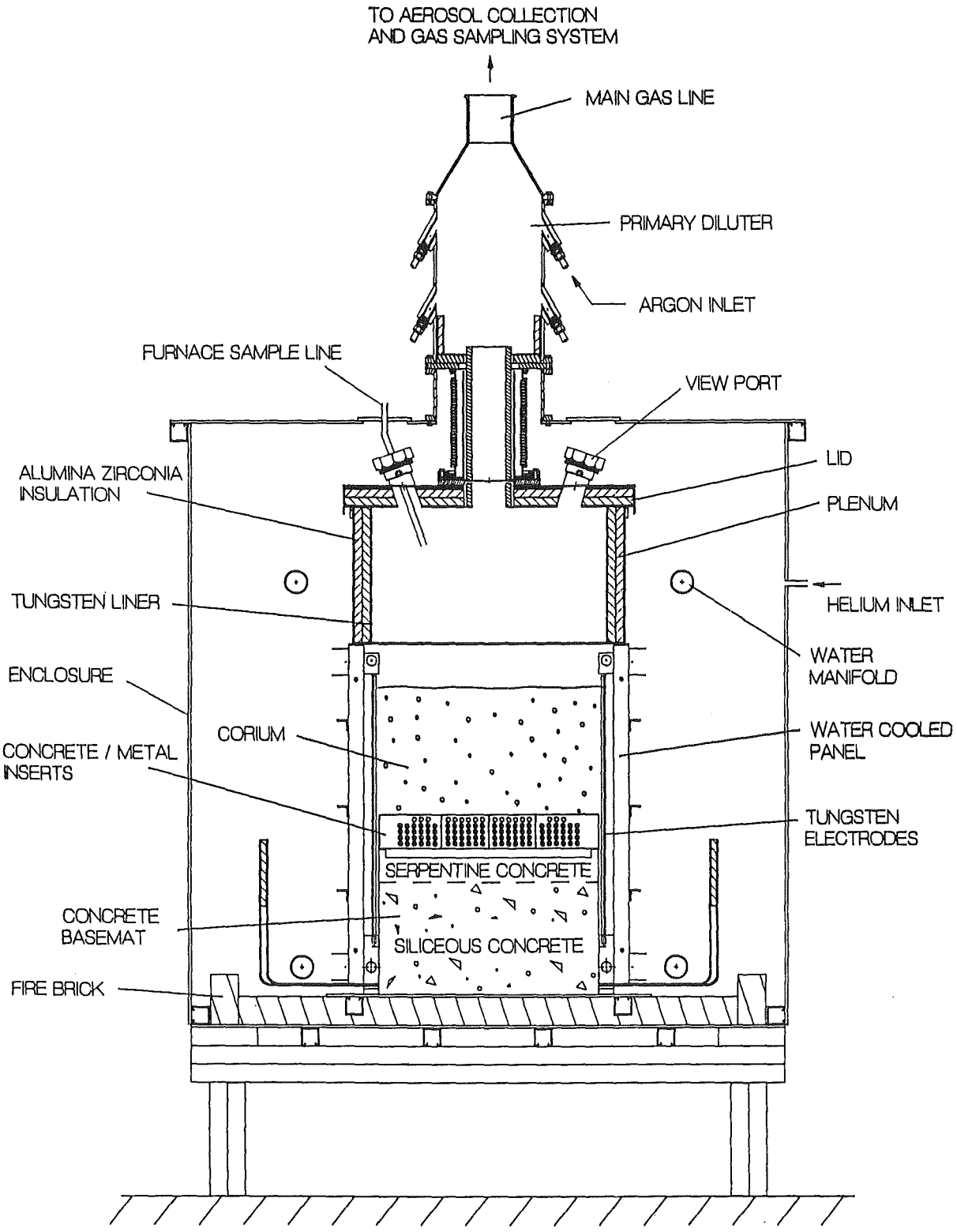

Figure 1. ACE MCCI Test Apparatus

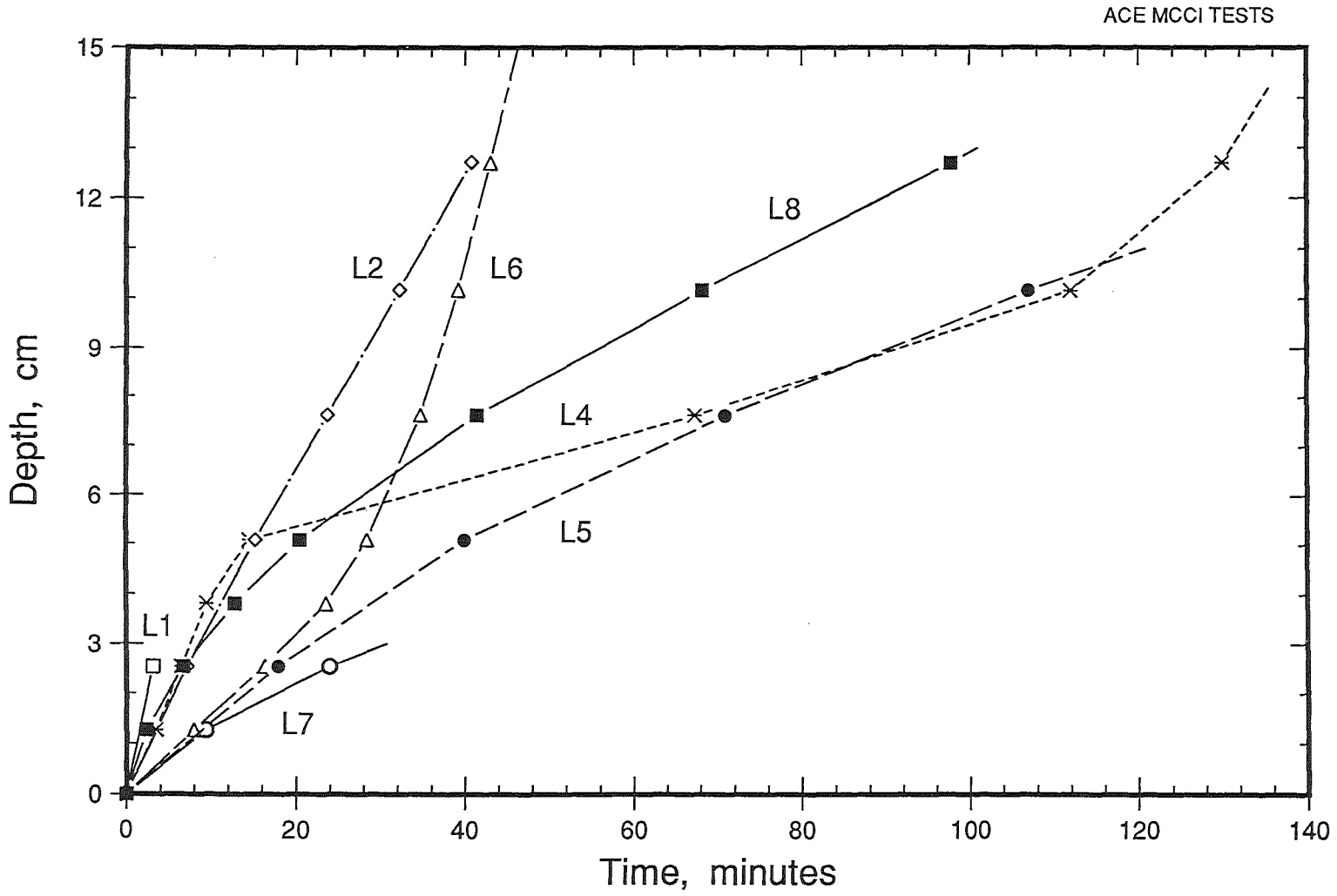

Figure 2. Ablation Depth

AEROSOLS RELEASED DURING LARGE-SCALE INTEGRAL MCCI TESTS IN THE ACE PROGRAM

J. K. Fink, D. H. Thompson, B. W. Spencer, and B. R. Sehgal*

Argonne National Laboratory
Argonne, Illinois 60439 USA

*Electric Power Research Institute
Palo Alto, CA 94303 USA

ABSTRACT

As part of the internationally sponsored Advanced Containment Experiments (ACE) program, seven large-scale experiments on molten core concrete interactions (MCCIs) have been performed at Argonne National Laboratory. One of the objectives of these experiments is to collect and characterize all the aerosols released from the MCCIs. Aerosols released from experiments using four types of concrete (siliceous, limestone/common sand, serpentine, and limestone) and a range of metal oxidation for both boiling water reactor and pressurized water reactor core material have been collected and characterized. Release fractions were determined for UO_2, Zr, the fission-products: BaO, SrO, La_2O_3, CeO_2, MoO_2, Te, Ru, and control materials: Ag, In, and B_4C. Release fractions of UO_2 and the fission products other than Te were small in all tests. However, release of control materials was significant.

INTRODUCTION

The test matrix for the ACE MCCI experiments is shown in Table 1. The ACE MCCI experiments and the thermal hydraulic results have been described in two other papers [1,2]. The focus of this paper is the aerosols released during these experiments. Therefore, only a short description of the experiments is given below followed by a section describing the aerosol system. The aerosol results are given in the third section. Release fractions of fission product elements and control materials are discussed in the last section.

The reactor core debris designated as corium contained UO_2, ZrO_2, oxides of fission-product elements and a small amount of the concrete constituents SiO_2 and CaO (MgO for serpentine concrete) to represent the concrete incorporated during

Table 1. ACE MCCI/Fission Product Release Test Conditions

Test	Concrete Type*	Net Heat Generation W/kg UO_2	Reactor Type	Initial Zr Oxidation, %	Control Rod Material
L5	L/S	325	PWR	100	
L2	S	450	PWR	70	
L1	L/S	350	PWR	70	
L6	S	350	PWR	30	Ag, In
L4	Soviet	250	BWR	50	B_4C
L7	L/S	250	BWR	70	B_4C
L8	L	350/150	PWR	70	Ag, In

*L/S = limestone/common sand
S = siliceous
Soviet = serpentine layer over siliceous
L = limestone

the jet impingement phase. Appropriate ratios of fuel to structural materials were used for pressurized water reactor (PWR) and boiling water reactor (BWR) core material. The initial extent of oxidation of the core structure was one of the test parameters. Oxides of fission-product elements Ba, Sr, La, Ce, and Mo were included in the corium at twice the typical reactor concentration in all early tests and at four times the concentration in tests L4, L7, and L8 to improve detectability in the aerosols. Tellurium was added as zirconium telluride. Ruthenium was alloyed with stainless steel. The Ag and In were alloyed. These metal alloys, Zr metal, B_4C, and stainless steel were included in concrete/metal inserts, which sat on top of the concrete, as shown in Figure 1. Tests were performed using four types of concrete: siliceous, serpentine, limestone, and limestone (coarse aggregate)/common sand (fine aggregate).

The aerosol compositions and release fractions have been determined for the seven experiments. Because Test L8 is an aerosol code comparison test, results from that test are being sequestered until calculations are complete. Thus, results

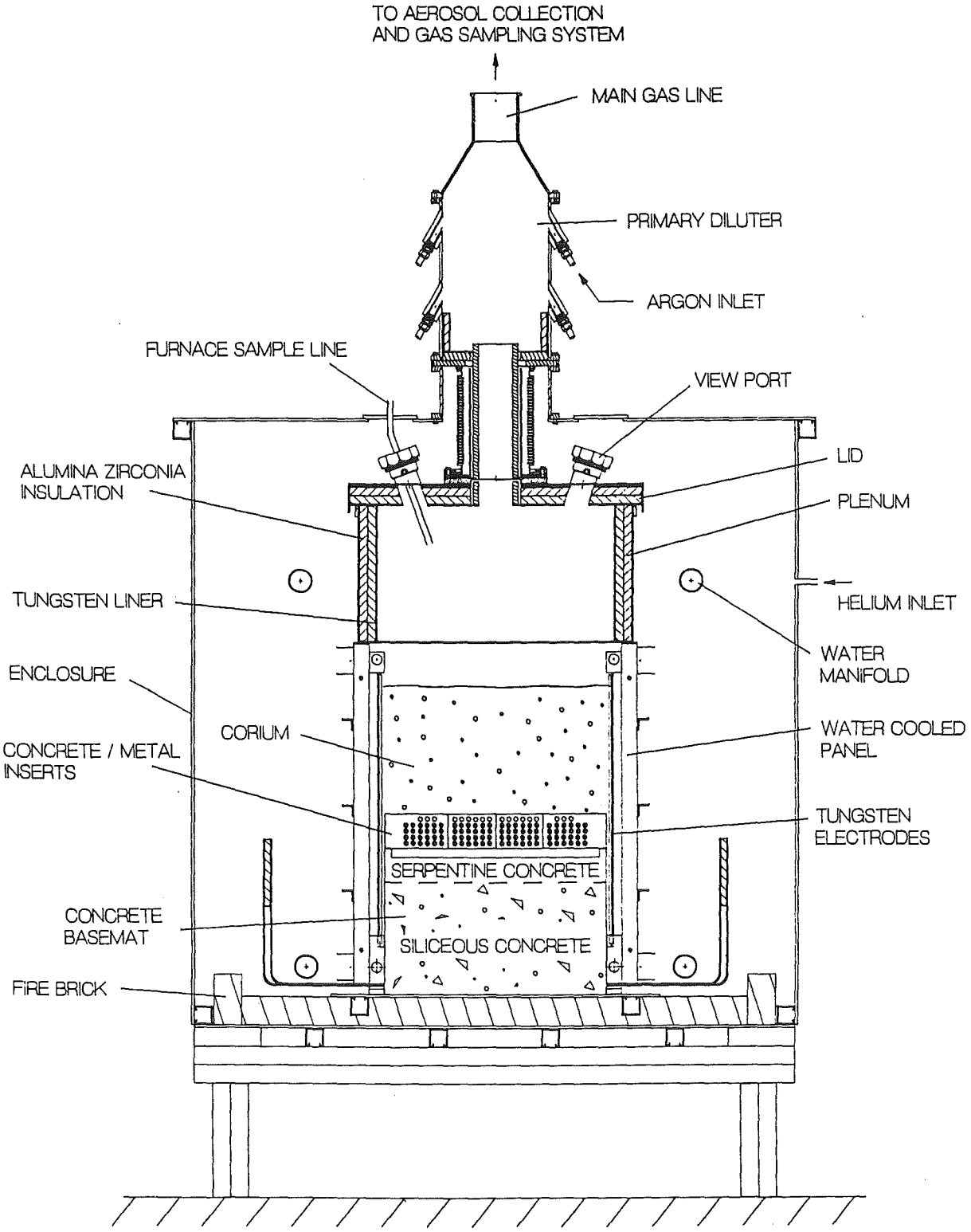

Figure 1. ACE MCCI Test Apparatus for Test L4

from Test L8 are not included in this paper.

All the aerosols released from these integral tests were collected by the aerosol system so that the total aerosol mass released was measured. The aerosol compositions were determined from chemical analysis of representative samples of the aerosols released and the mass collected at each sampling location. A statistical analysis of the posttest sampling procedure was performed for Test L6 to ensure that reliable aerosol compositions and release data were obtained. The sampling error was less than the 10% uncertainty in the chemical analysis.

AEROSOL SYSTEM

The ACE MCCI aerosol system underwent a number of modifications and upgrades during the ACE program to alleviatte plugging by Si aerosols and to accommodate various test conditions. The aerosol system used in Tests L5, L2, and L1 was based on design recommendations of the Aerosol Working Group of the ACE MCCI Technical Advisory Committee (TAC) at a meeting October 14-15, 1987. In Test L2, the porous metal diluter became plugged with aerosols formed from quenching the SiO gas. In Test L1, the off-gas flow rate/temperature capacity of the aerosol system was exceeded during rapid initial basemat ablation and foaming of the melt to completely fill the gas plenum. The foaming created a lid heat load that burned a hole through the lid structure between the cooling coils.

On June 1, 1991, the Aerosol Working Group met to review a proposed redesign of the aerosol system to alleviate diluter plugging, to increase flow and temperature capacity, and to include instrumentation to distinguish between mechanically sparged and condensed vapor aerosols. Features of the redesign included: (1) a 10 cm diameter stainless steel main line with a control system to maintain constant flow volume, (2) a larger diameter primary diluter with a metal screen insert and uniform distribution of dilution gas, (3) a zirconia sleeve lining the off-gas channel from the lid of the test apparatus to the diluter, (4) retention of the original 7.6 cm main line as a sample line downstream of a secondary diluter, (5) a secondary diluter to reduce aerosol concentrations in the sample line, and (6) a taller plenum in the apparatus to provide additional clearance for the melt, (7) addition of cyclones ahead of each of ten filters in the elbow sample line to provide separation of large and small particles, and (8) additional vacuum pumps and flow controllers. During the

discussion of the redesign by the Aerosol Working Group, consideration was given to changing from a vacuum pumped mode to a positive pressure mode of operation. However, the change in mode of operation was not implemented because it would compromise the isokinetic sampling.

This revised aerosol system was used first in Test L6. Because plugging occurred in the diluter in Test L6, the design of the diluter was modified further. The metal screen was eliminated. The new design, shown in Figure 1, had an abrupt expansion at the zirconia inlet and two sets of four gas nozzles to direct the cold dilution gas upward away from the inlet. This diluter operated well in Tests L4, L7, and L8.

Additional changes following Test L6 included a switch in media from a Gortex fabric to metal cartridges as final filters to accommodate higher gas temperatures and from a pleated metal to a cylindrical design to alleviate high pressure drops with low aerosol loading of pleated metal filters. Twelve backup filters were added to the sixteen metal filters in four filter housing to provide additional capacity. Cooling water lines were included on the horizontal sections of the main line in Tests L4, L7, and L8. Additonal vacuum pumps and flow controllers were added for increased flow capacity.

The off-gas flow expected for Test L8 (1200 sLpm) exceeded the system capacity if operated in a vacuum pumped mode like Test L7. Because operation in a positive pressure mode would reduce the quality of aerosol data, additional modifications were made to continue operation in a vacuum pumped mode. A low pressure regulator was added to maintain a constant pressure within the test enclosure and a low pressure drop exhaust flow controller was added in series with existing flow measuring instruments.

A schematic of the aerosol system used in the ACE MCCI Test L7 is shown in Figure 2. This system consisted of a main gas line, sample gas line, primary and secondary diluters, and three aerosol sampling modules (furnace sample line, elbow sample line, and cascade impactor sample line) plus vacuum pumps, filters, gas mass spectrometer, and pressure and temperature instrumentation. The furnace sample line rested on top of the enclosure; the remainder of the aerosol system was located on the aerosol deck above the test cell.

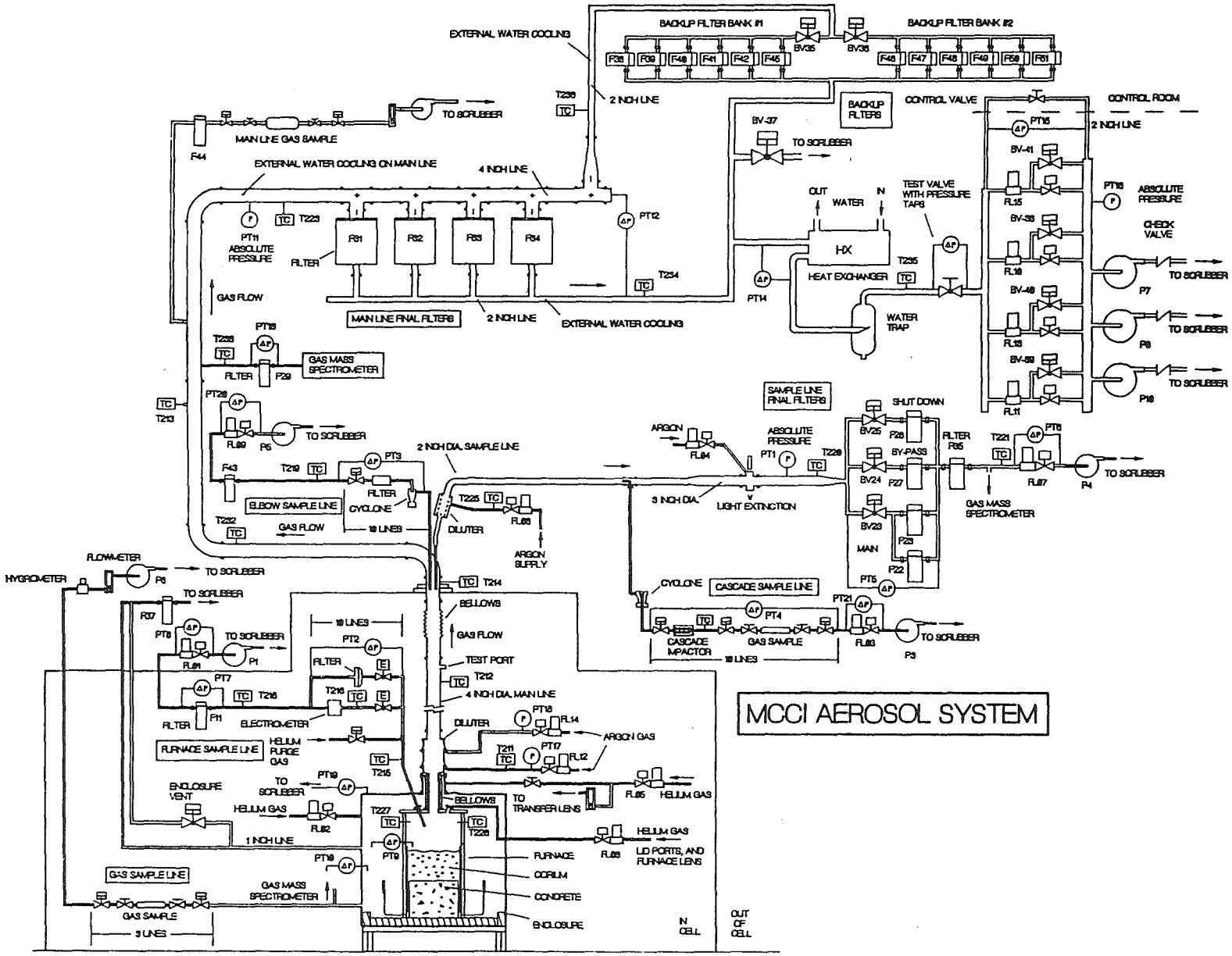

Figure 2. ACE MCCI Aerosol System for Test L7

The released gas and aerosols were cooled and diluted in the primary diluter directly above the test apparatus. From the vertical gas line above the primary diluter, two continuous isokinetic gas sample streams were drawn - one into the elbow sample line module, the other into the sample line. The elbow sample line module contained ten cyclones followed by filters. Aerosol concentrations and compositions, and the ratio of large (mechanically generated aerosols) to small particles (vapor condensation aerosols) were determined as a function of time throughout the tests from the elbow line cyclone and filter data. Thus, variations in aerosol concentration and composition with changes during the tests such as change in concrete type, decrease in metal inventory, foaming, and change of input power were studied.

The sample line aerosols were further diluted in a secondary diluter located ahead of the extinction system and sampling nozzle for the impactors. Variation in aerosol concentration with time was provided on line by the extinction system located on the sample line. Isokinetic samples by ten cascade impactors served to characterize the respirable fraction of the aerosols both in terms of particle size distribution and variation in composition with size.

The first elbow in the main line changed the direction of flow from vertical to horizontal downstream of the sampling nozzles. The remainder of the main line was horizontal. An on-line mass spectrometer off the horizontal main line provided gas compositions throughout each test. Flows were obtained from computer evaluation of the mass spectrometer data and the calibrated argon flow to the primary diluter. A gas sample was taken from the main line for posttest analysis using a different mass spectrometer to confirm the pre and posttest calibrations of the on-line mass spectrometer.

The furnace sample line module collected a small fraction of the gas and aerosols directly from the test enclosure without any dilution or cooling. The alumina sampling tube to this module was located low in the plenum, directly above the melt. The electrometer in the furnace sample line indicated the charge distribution on the aerosols.

The aerosol system was designed to collect the total aerosol mass released. Most of the aerosol mass was collected by large final filters and backup filters located at the end of the main line. Significant mass was also deposited in the main line. Samples for chemical analysis were selected from these filters, from deposits throughout the main line, and from sampling modules to completely characterize the aerosols. The aerosol mass distribution throughout the entire aerosol system was determined during aerosol system disassembly.

TEST OPERATION

The gas/aerosol system was started and filters for collection of aerosols were on line when power was turned on to heat the corium. Direct electrical heating was used to initiate the core melt and to maintain internal heat generation in the melt. The molten pool started at the top of the corium and expanded horizontally and vertically until it reached the concrete/metal inserts. Little aerosol mass was released during corium heating. Because corium is an excellent insulator, the temperature of the concrete/metal inserts did not increase significantly above room temperature until shortly before insert ablation began. Significant aerosol release began when the concrete/metal inserts reached 373 K and free water was released from the concrete in the inserts. Sequential aerosol sampling was initiated at the start of significant aerosol release. Prior to sequential sampling, flow in the sequential sampling modules was directed to bypass filters. Main line and sample line filters were on line and collected aerosols throughout the entire test.

Collection of aerosols by the aerosol system was terminated before the end of tests in Tests L2 and L6 because the aerosol system became plugged by aerosols. In Test L7, foaming attenuated the release of aerosols near the end of ablation of the concrete/metal inserts. Although sampling was continued throughout the entire test, no significant aerosol mass was collected after 3 min prior to basemat ablation.

GAS RELEASE

The composition of off gases flowing upward through the melt were determined by an on-line gas mass spectrometer on the aerosol system. The composition and flow rate of off gases were a function of metal content, ablation rate, and concrete type. In all tests, only 50 to 75% of the moles of concrete decomposition gases

were detected in the off gas. Migration of H_2, H_2O, CO_2 and CO downward through the concrete was confirmed by a hygrometer and gas samples drawn from the area beneath the basemat. In Test L8, a gas mass spectrometer monitored the gas composition of the volume beneath the basemat. Changes in the gas composition of the volume below the basemat coincided with changes in the upward off gas.

Because aerosol release tracks the off-gas release, detection of off gas that is less than the gas theoretically available from concrete decomposition impacts aerosol release and the aerosol release calculations. Downward migration of water and gas also decreases the moles of these species available for metal oxidation which impacts the melt chemistry and the chemical energy from oxidation reactions.

AEROSOLS RELEASED

Results of these experiments indicate that except for Te, the release of fission-product elements was small (less than 1% of the aerosol mass) in all tests. Aerosols were composed primarily of concrete decomposition products. Consequently, the aerosols released varied in concentration, composition, and form for tests with different concretes. The major constituents in the five concretes used in these tests are given in Table 2.

Aerosol Mass Released and Concentration

A summary of the total aerosol mass and off gas concentrations for all tests is given in Table 3. The time of aerosol release (collection), ablation depth during aerosol collection, and concrete mass incorporated in the melt during aerosol collection have been included in Table 3 as an aid in interpreting the results. Aerosol collection time is the time from the start of significant aerosol release (at the start of concrete off gassing) to the end of the test, the time the aerosol system plugged (Tests L2 and L6), or the time foaming attenuated aerosol release (Test L7). Maximum aerosol concentrations in the noncondensable off gas from the MCCIs ranged from 30 g/m^3 to 4400 g/m^3. Average aerosol concentrations in the off gas ranged from 18 to 3300 g/m^3. The lowest aerosol concentrations were from Test L5 which was a fully oxidized test with limestone/common sand concrete. The highest concentrations were from MCCIs

Table 2. Major Constituents in Concrete

Constituent	Limestone/ Common Sand	Siliceous	Soviet Serpentine Siliceous		Limestone
	Mass %	Mass %	Mass %		Mass %
SiO_2	28.3	69.0	34.3	69.1	6.2
CaO	26.0	13.5	9.8	10.8	45.9
Al_2O_3	3.5	4.0	1.8	8.8	1.7
MgO	9.6	0.7	30.7	0.7	3.6
Fe_2O_3	1.6	1.0	6.4	1.7	0.9
K_2O	0.6	1.4	0.1	1.6	0.6
Na_2O	1.1	0.7	0.06	2.7	0.4
H_2O	6.1	3.68	14.4	1.9	6.1
CO_2	21.4	4.23	0.9	1.2	33.3

Table 3. Aerosol Mass Released in ACE MCCI Tests

Test	L5	L2	L1	L6	L4	L7
Aerosol Mass, g	153	455	1213	6546	4760	1077
Average Aerosol Concentration, g/m^3[a]	18	442	435	3300	395	324
Maximum Aerosol Concentration, g/m^3[a]	30	----	820	4400	1440	440
Maximum Off Gas Flow, sLpm	61	49	300	40	260	160
Metal, kg	0	13.6	13.6	34	32.2	19.6
Ablation Depth, cm[b]	11	3.8	4	8.8	14.2	----
Insert Depth, cm	----	2.5	2.5	7	7.9	5.7
Insert Concrete, kg	0	4.6	3.9	22.4	24.3	15.7
Basemat Concrete, kg	66	22.7	23.9	49.6	75.6	0
Total Concrete Mass, kg	66	27	28	72	100	16
Aerosol Release/Collection Time, min	121	52	7	85	180	50
Concrete Type	L/S	S	L/S	S	Sov	L/S

[a]In off gas

[b]Depth ablated for aerosol collection

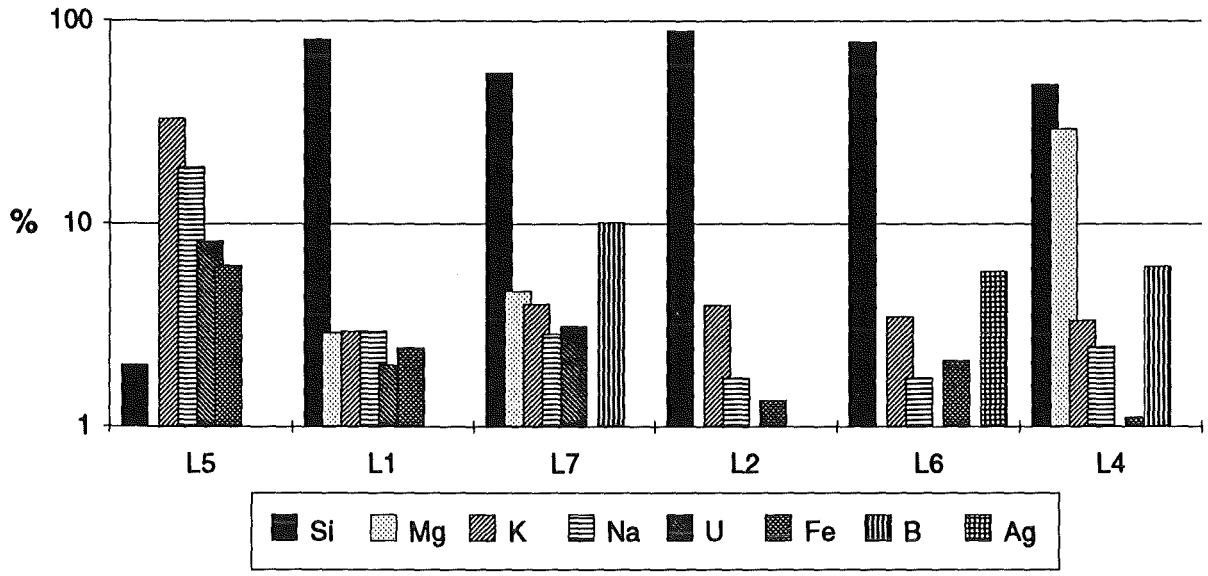

Figure 3. Mass Percent of Species of Major Elements in Aerosols in ACE MCCI Tests

with siliceous concrete. Siliceous concrete had the lowest gas content of all the concretes. The highest mass released and highest aerosol concentrations in the off gas were from Test L6, the siliceous test with the highest metal inventory. The effect of increased metal in the inventory on aerosol concentration and mass released is evident from comparison of results from Tests L2 and L6. Test L6 contained 34 kg of metal, 23 kg of which was Zr.

Aerosol Composition

The mass percent of the species of the major elements in the aerosols from each test are given in Figure 3. Most elements, other than Ag, were in oxide form. However, K and Na were also found as chlorides. Si species included SiO_2, SiC, and Si. Variations in aerosol composition with the presence of Zr in the melt were evident for all types of concrete. Variation in composition with the presence of Zr was most pronounced for limestone/common sand concrete. When Zr was present (L1 and L7), the aerosol compositions were high in Si; with no metal in the inventory (L5), the aerosol composition contained mainly Na and K species. In Test L5, K and Na species comprised 33 and 19%, respectively, of the aerosol mass. For Test L1, the aerosols were dominated by Si species, which comprised 81% of the aerosol

mass. K and Na species each attributed only 3%.

In both limestone/common sand concrete and siliceous concrete tests with metal in the inventory, Si species dominated the aerosols. SiO_2 in the melt reacted with Zr to form SiO gas which condensed to form Si and SiO_2 or reacted with other off gases, vapors, and/or aerosols to form SiC and silicates. SiO_2, SiC, and Si have been identified in deposits from the ACE MCCI tests. In Test L4, which contained serpentine concrete, $MgSiO_3$ and $MgSiO_4$ were identified in deposits. Silicon speciation for all ACE MCCI tests is in progress. In tests with siliceous concrete, the high concentration of SiO in the off gas and its rapid condensation in the aerosol system led to the formation of fibers or chains which then trapped other aerosols causing plugging in the primary diluter.

Effect of Concrete on Composition

The effects of concrete composition on the aerosols released is most clearly illustrated by the variation in aerosol composition as a function of time in Test L4. Test L4 employed two types of Soviet concrete in a layered basemat. A 5.1 cm layer of serpentine concrete rested on siliceous concrete. Serpentine concrete was used in the insert in this test. Figure 4 shows the main constituents of the aerosols released in Test L4 for 4 time periods: insert ablation, ablation of the serpentine concrete, beginning of ablation of the siliceous concrete, and end of ablation of the siliceous concrete. Although SiO_2 dominates the release at all times, SiO_2 release is highest during insert ablation, when the metal concentration is the highest. It decreases during ablation of the high magnesia serpentine concrete and then increases during ablation of siliceous concrete. The MgO fraction is the highest during ablation of the high magnesia serpentine concrete and at the start of ablation of the siliceous concrete.

Importance of Control Rod Materials

Inclusion of control rod materials Ag and In or B_4C also effected the aerosol composition because the release of Ag, In and B species was significant. Figure 3 shows that when Ag or B were present in the inventory, Ag or B species comprised significant fractions of the aerosol mass. Boron species (assumed to be B_2O_3) comprised 10% of the aerosol mass in Test L7; 6% in Test L4. Silver and indium were included in Tests L6 and L8. In both tests, Ag was a major constituent of the aerosols. Indium release was significant although it did not comprise as large a

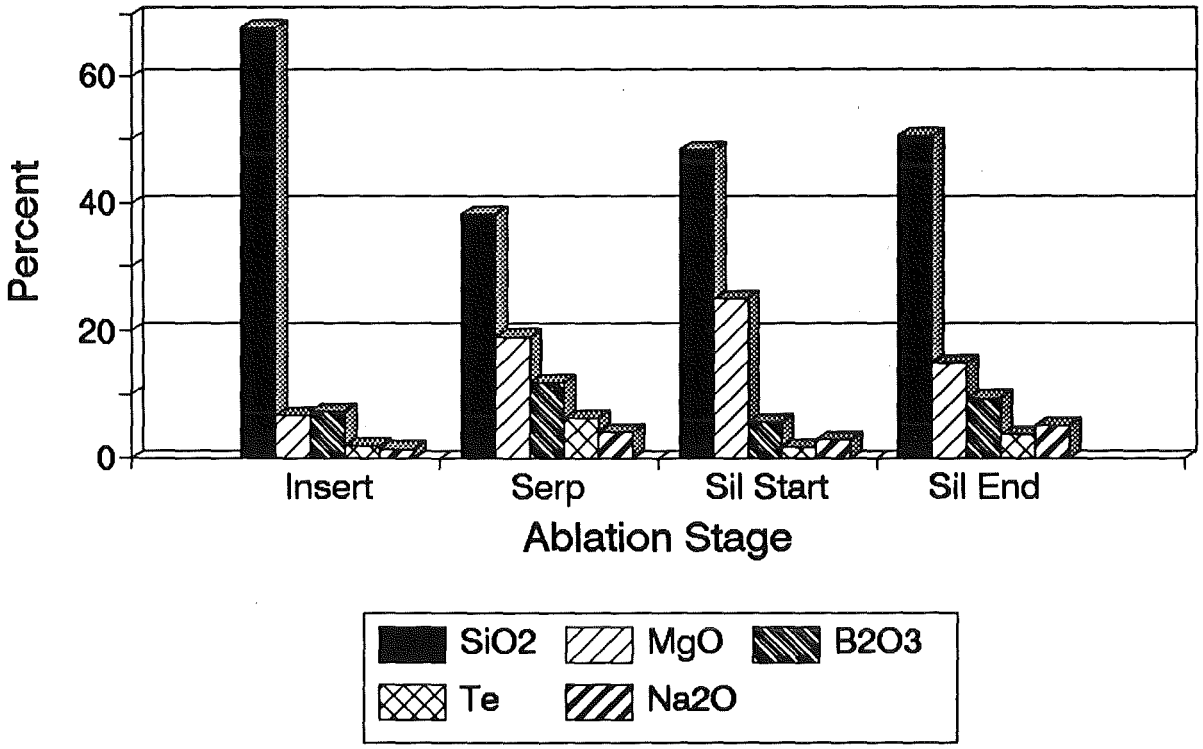

Figure 4. Mass Percent of Major Species in Aerosols Released at Four Time Intervals in Test L4

fraction of the aerosols.

RELEASE FRACTIONS

Aerosol releases from constituents in the core-concrete melt may be characterized by the release fraction which has been defined in the ACE MCCI program as: moles (gram-atoms) of element in the aerosols divided by moles (gram-atoms) of the element in the melt. In all tests except Test L5, the entire corium and metal inventories entered the melt and participated in the core-concrete interactions.

Although the release fractions of U and fission-product elements other than Te were small, release fractions of control materials were significant. The release fraction for boron was 0.12 in Test L4; 0.045 in Test L7. Release fractions for Ag and In in Test L6 were respectively 0.32 and 0.41.

The tellurium release fraction was close to 0.5 in most tests. Tellurium was detected in the aerosols primarily as a metal or metal telluride. The high Si release in all tests except L5 caused difficulty in detection of Ce and La. For

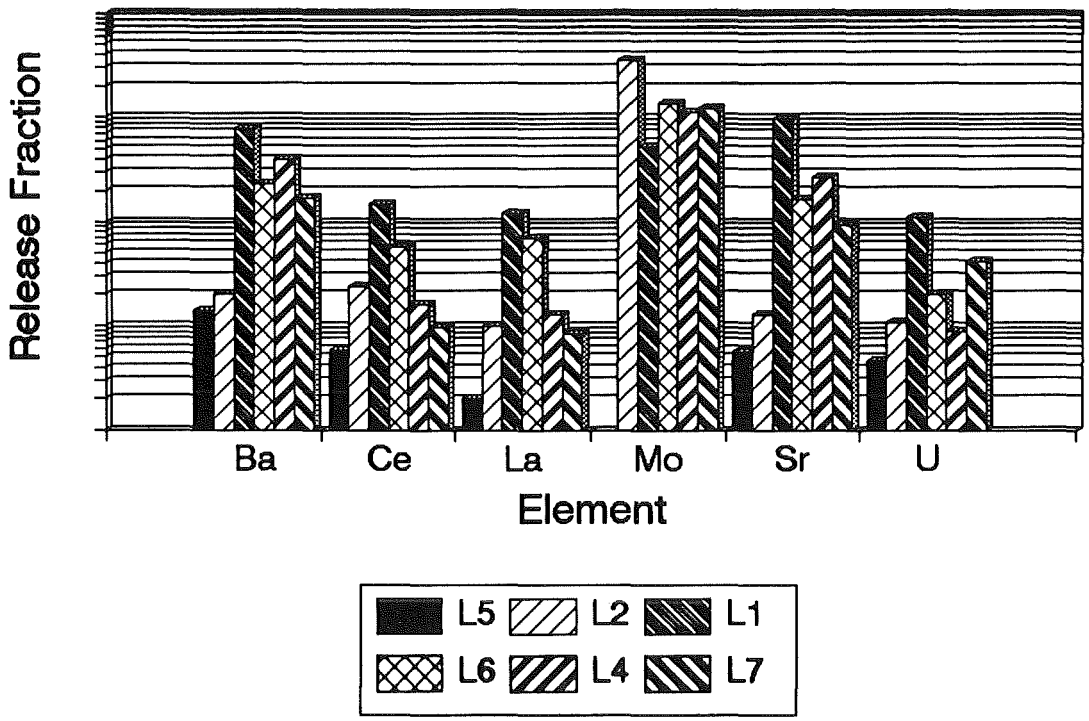

Figure 5. Relative Releases of Fission Product Elements and U for the First 7 Minutes of Each Test

tests L2, L1, L6, and L4, the Ce and La values were below the limit of detectability in most aerosol samples. Consequently, release fractions of Ce and La for these tests are calculated from maximum releases based on the limit of detectability in the chemical analysis. Neutron activation analysis for Ce and La is underway so that definitive releases may be determined. Because aerosol release in each test lasted a different length of time, and a different mass of concrete entered the melt during aerosol release and collection, comparison of total release fractions from one test to another provides little information. Consequently, in Figure 5, release fractions of the low volatility fission products and U for the first seven minutes of basemat ablation in each test are shown. Seven minutes was chosen for comparison because that was the duration of aerosol release and collection in Test L1. For Test L7, the release fractions are for 7 min of insert ablation because foam attenuated aerosol release during basemat ablation. Comparison of releases from the tests with limestone/common sand concrete (Tests L5, L1, and L7) shows that inclusion of metal in the inventory in Tests L1 and L7 increased the releases at the start of the tests. The higher release fractions for L1 compared to L7 may be due to partial aerosol attenuation by foam and the lower ablation rate in L7. During L7 insert ablation, concrete was

incorporated in the melt at the rate of 0.8 kg/min; the rate for Test L1 was 3.3 kg/min. The release fractions of Ba and Sr were significantly higher for Test L6 than Test L2. Test L6 had a higher metal content than Test L2. The release fractions of Ba, Ce, La, and Sr were significantly below those predicted by the NRC code VANESA 1.01 [3,4].

ACKNOWLEDGMENTS

Work sponsored by the Electric Power Research Institute under Contract RP 2802-12.

REFERENCES

1. B. R. Sehgal and B. W. Spencer, "ACE Program Phase C: Fission Product Release from Molten Corium Concrete Interactions (MCCI)," paper presented at the OECD CSNI Specialist Meeting on Core Debris Concrete Interactions, Karlsruhe, Germany, April 1-3, 1992.

2. D. H. Thompson, J. K. Fink, D. R. Armstrong, B. W. Spencer, and B. R. Sehgal, "Thermal-Hydraulic Aspects of the Large-Scale Integral MCCI Tests in the ACE Program," paper presented at the OECD CSNI Specialist Meeting on Core Debris Concrete Interactions, Karlsruhe, Germany, April 1-3, 1992.

3. D. A. Powers, J. E. Brockmann, A. W. Shiver, "VANESA: A Mechanistic Model of Radionuclide Release and Aerosol Generation During Core Debris Interactions with Concrete," NUREG/Cr-4308, SAND85-1370, July 1986.

4. J. K. Fink, M. Corradini, A. Hidaka, E. Hontañón, M. A. Mignanelli, E. Schrödl, and V. Strizhov, "Results of Aerosol Code Comparisons with Releases from ACE MCCI Tests," paper presented at the OECD CSNI Specialist Meeting on Core Debris Concrete Interactions, Karlsruhe, Germany, April 1-3, 1992.

SECTION II

MOLTEN CORE-CONCRETE INTERACTIONS UNDER PREDOMINANTLY DRY CONDITIONS AND CODES - PART B: MODELLING

Integral Codes

Thermal-Hydraulics

Material Properties

MODELING AND VALIDATION PROGRESS WITH MAAP 4 DECOMP

Martin G. Plys
Zhe Wang
Fauske and Associates, Inc.
16W070 W. 83rd St.
Burr Ridge, IL 60521 USA

K. Bing Cady
Ward Laboratory
Cornell University
Ithaca, NY 14853 USA

1.0 ABSTRACT

Improvements to the MAAP 3.0B model for core-concrete interactions, DECOMP, are in progress to create a new version for the accident management code MAAP 4. This paper describes the first version for MAAP 4, its validation, and future plans. Since DECOMP must fit into an integral code, it contains simplified representations of many phenomena. Significant new features are independent sideward and downward erosion, capacity to incorporate complex pseudo-binary phase diagrams, and benchmark capability using the integral code itself. Code performance for the BETA, SURC, and ACE experiments is promising, but indicates that oxide systems are difficult to model because of the paucity of phase diagram data and the coupling of solidification behavior, viscosity, and heat transfer.

2.0 INTRODUCTION AND PHILOSOPHY

Interactions between core debris, concrete, coolant, and a region atmosphere are considered in the integrated severe accident codes MAAP 3.0B [1] and MAAP 4 through subroutine DECOMP and several associated routines. Models for these interactions will be referred to here as the DECOMP model. DECOMP has been improved for MAAP 4 in order to consider

recent research such as the ACE program [2,3,4], new BETA tests [5], and the SURC tests [6,7]. The main difference between MAAP 3.0B and MAAP 4 is that the scope of MAAP 4 covers severe accident management applications. DECOMP improvement will continue in MAAP 4 as experimental and analytical progress is made in such applications as ex-vessel debris coolability and in particular to quantify phenomena observed during the MACE tests [8].

Since DECOMP must fit into an integrated accident analysis that considers a plethora of other phenomena, the challenge is to create a model that represents pertinent phenomena with an appropriate level of detail. There must be a provision to consider uncertainty in the phenomena that are modeled. The appropriate level of detail then must achieve acceptable agreement for experiments and allow reasonable extrapolation to reactor systems considering realistic uncertainties. In practical terms, this has led to the use of parametric approaches for certain processes considered by DECOMP which are described below.

DECOMP validation is made using MAAP 4 "off the shelf" as described later in this paper so that benchmarks may be repeated or extended by any code user.

3.0 CONSIDERATION OF PHENOMENA

Past experience and recent experimental results are discussed here to motivate choices made in DECOMP models.

3.1 Sideward Versus Downward Erosion

Erosion rates are by observation not equal sideward and downward, though the majority of our data for this judgement come from the BETA tests. In these tests, the underlying steel layer can transfer heat efficiently downward because the immiscible concrete slag boundary layer

is hydrodynamically unstable and the melt-concrete contact surface is frequently renewed. Sideward, the interfacial surface tension may allow a thicker slag boundary layer which adds an extra heat transfer resistance.

In reactor applications where the concrete slag will be miscible in either an underlying oxide layer or a well-mixed pool, the relative resistance to heat transfer in each direction may be more similar. In the oxidic MACE scoping test [8], sideward erosion was allowed and the ratio of downward to sideward erosion was about 2 to 1, though at one location peak sideward erosion equalled downward erosion.

The point of the preceding discussion is that uncertainty in the relative extent of sideward and downward erosion must be considered when structural failures are possible. Given the difference between BETA and MACE results, is difficult to extrapolate to reactor systems without some uncertainty. Therefore, provision is made for parametric variation of the sideward versus downward erosion in DECOMP.

It is noteworthy that except for rapid transient cases the total amount of erosion is fairly insensitive to variation in the relative amounts of sideward and downward erosion. This is because decay power must either go into upward losses or erosion, and upward losses are only weakly affected by differences in the amount of sideward erosion. Consequently, the heat load to the containment and the production of offgas is also insensitive to relative erosion directions. Ultimately, variations in the pool internal heat transfer model affect only the debris temperature to first order, which therefore impacts upon fission product release.

3.2 Debris Temperature

The primary mission of DECOMP is to handle oxidic pools and comments here are pertinent to such cases. Heat transfer in metallic

systems is much more efficient than in oxidic systems, the solidus and liquidus values are much better known for metallic systems than oxidic systems, and the difference between solidus and liquidus values is much lower for metallic systems than oxidic systems. For all these reasons, it is much more difficult to predict temperature for an oxidic system than for a metallic system.

Debris temperature is governed by a balance that includes many factors: First, a quasi-steady temperature above the debris solidus temperature is governed by the value of the heat transfer coefficient. Second, the heat transfer coefficient is influenced by viscosity. Third, viscosity increases rapidly with increasing debris solid fraction (equivalently, decreasing temperature for a two-phase mixture) [9]. Last, the solid fraction depends upon the debris temperature above the solidus temperature. Putting these facts together, for any given debris composition, there is a temperature at which viscosity is low enough to allow convective heat transfer at a rate equal to the sum of decay plus chemical power.

The debris temperature can thus only be quantified when both the debris solidus temperature and the internal heat transfer process can be accurately quantified. Put another way, a heat transfer coefficient model cannot quantify debris temperature accurately alone because the solidus temperature must be known. More generally, first-order uncertainty in debris temperature exists because of uncertainty in the solidification behavior of debris, especially with regard to the solid fraction and its variation in the two phase range. This problem is being solved analytically by the GEMINI-OXY5 effort [10,11].

Debris temperature is important because it governs the rate of fission product release. Its value is most uncertain when zirconium is present. This is precisely the time when many fission products are most prone to release by chemical reactions.

Concluding this discussion, a reliable oxide phase diagram is necessary for prediction of debris temperature and fission product release.

4.0 MODEL CONTENT

4.1 Content Summary

Major model features are represented in Figure 1. Debris in a region physically contacts a floor and a sidewall, radiates to one or two upper walls, and experiences convection to an atmosphere. The heat sinks are all one-dimensional, they may erode, and they contain up to 15 temperatures distributed in fine outer nodes and coarse inner nodes. If they erode, their slag enters the pool, while only the gas from the lower floor enters the pool. All walls communicate with the debris independently and therefore may erode independently. Provision is made for sidewalls to be made of a non-eroding material. Cavity geometry may be either cylindrical or parallelepiped.

The pool itself has a single lumped energy and a mass balance for up to 50 condensed phase compounds from the standard MAAP list. Three independent crusts, the lower, side, and upper crust, are assumed to have parabolic temperature profiles (due to internal heating). The pool-crust interface temperature is the debris solidus and is thus the same for all crusts, while the crust-concrete interface temperature of the lower and side crusts is set equal to the wall surface temperature and the upper crust-atmosphere interface temperature is set by continuity of heat flux. Independent metal and oxide layers are not considered because the Zr will dissolve with the core oxides and the amount of steel is generally small.

Mass (for each compound), pool energy, and crust thicknesses are state variables whose rate of change is the essential model output.

Heat sink temperatures and eroded distance are also state variables. Rates of change are integrated by the central MAAP integrator to yield new state variable values. The auxiliary variables debris temperature, solidus, liquidus, and liquid fraction are then derived from the new mass and energy via the constitutive relationships for each compound and the phase diagram. Given the auxiliary variables, individual process rates of change are found and summed for the total state variable rates of change.

Heat transfer from the debris to crust is at present given as the sum of a convective and conduction term using a user-input nominal heat transfer coefficient multiplied by the liquid fraction raised to a user-input power. Experimental validation is used to provide good nominal values for the heat transfer coefficient, though results are relatively insensitive for reactor cases. Chemical equilibrium calculations with the METOXA [12] subroutine include condensed phase reactions and user-input activity coefficients to simulate compound formation and non-ideal behavior of key fission products such as strontium and barium.

4.2 Oxide Pseudo-Binary Phase Diagram

The oxide debris is treated as a pseudo-binary system of core oxide (UO_2, ZrO_2) and concrete oxide (SiO_2, CaO, MgO, Al_2O_3, etc.) as shown in Figure 2. It is inspired by the recent work in France and Britain [10,11]. The concrete solidus and liquidus are user-input while the core values are calculated as described later. The solidus curve is bilinear featuring a quick slope to a broad plateau; the connecting point is user-input. The liquids curve consists of four segments (based on three user-input points) so that either the smooth shape shown in Figure 2, a third order shape with an inflection point, or a pseudo-eutectic minimum may be specified.

A table of liquid fraction as a function of average composition and temperature is specified by the user because the lever law cannot be

used on a pseudo-binary diagram; corresponding lines of constant liquid fraction are shown in Figure 2. Thus, the solidus and liquidus lines do not necessarily represent continuous transitions between pure solid or liquid to two-phase states, but may include a discontinuity in liquid fraction.

At present, specification of the phase diagram is tedious and stymied by a paucity of data. It is intended that programs produced during current research [10,11] would be used to provide this input for various concrete types and for various U-Zr-O mixtures.

4.3 Dissolved Zr Treatment

In the reactor vessel, metallic Zr dissolves with UO_2 to form a U-Zr-O mixture. This mixture is assumed to be in equilibrium for the ex-vessel phase and approximations to the ternary phase diagram are contained in subroutines PSOL and PLIQ based upon the MATPRO routines and data sources [13]. A far lower solidus is obtained using this method compared to that of UO_2-ZrO_2 mixtures typically assumed in ex-vessel analyses. For example, a value of about 2173 K is expected for most reactor cases, versus a minimum of 2800 K possible for the oxides alone. Given the strong impact of the concrete oxides on depression of the overall mixture solidus, this effect is not noticeable in oxidic experiments used for model validation. (It should be noted that dissolved Zr and Si do cause a noticeable reduction in the solidus for metallic tests like the BETA and SURC series). In reactor cases, the chief impact of Zr dissolution will be to provide a potential for lower overall debris temperatures and consequently lower releases of fission products.

4.4 Lumped Versus Distributed Parameter Approach

The lumped approach means that an explicit temperature profile is not calculated in the crusts or within the pool. Its major drawback is

that the solid debris heatup rate cannot be accurately calculated. The transition from all solid to part liquid is less accurate using a lumped parameter model which is better suited to long-term quasi-steady behavior.

Of course, solid debris is often encountered in reactor cases, such as when debris is quenched ex-vessel, then boils off the overlying water, reheats, and begins eroding concrete (which may occur before or after debris begins to melt). For reactor cases, some error in the solid debris heatup rate is acceptable because the debris heatup period prior to ablation is generally short compared to either the time the debris may be water-covered or later causing concrete attack, and other factors such as the assumed area over which debris is spread may be more important contributors to uncertainty. For experimental validation, such as with ACE or SURC, the heatup rate error is annoying and instead the conditions at the start of ablation are used to initialize a calculation.

Overall, this is believed to be an area in which the model detail necessary for experimental simulation exceeds that which is necessary for reactor applications. However, since MAAP 4 is intended to be a tool for accident management, and water addition to debris is an important aspect of this scope, a simplified distributed parameter model is being pursued at this time for a future DECOMP revision. In this approach, each crust would have a calculated temperature distribution.

4.5 Validation Technique

Validation of DECOMP in MAAP 4 is accomplished using the whole MAAP 4 code rather than by using an experiment-specific driver code. This capability was devised in order to eliminate the need to maintain such experiment-specific drivers, to demonstrate the true function of the integral MAAP 4 code models in the MAAP 4 environment, and ultimately to

allow any MAAP 4 user to repeat a past benchmark or perform a new benchmark.

Validation is accomplished by specification of a simple containment, with one node representing the crucible and the other representing an expansion volume. Initial conditions are specified in a standard input file or in a special interface subroutine called BENCH. This interface subroutine allows free initialization of wall temperature distributions, debris and concrete composition, etc., as well as time-dependent inputs. A good example of time-dependent input is the zirconium insert used in several ACE tests: the concrete composition is changed to include or exclude zirconium depending upon the ablation depth.

5.0 VALIDATION

5.1 Approach

Validation of the DECOMP model includes testing of important model parameters and selection of appropriate values for reactor cases. The oxidic ACE and SURC experiments are of primary interest for reactor cases, and the four ACE tests will be considered here - L2, L5, L6, and L7. The BETA tests and metallic SURC tests also provide valuable data, and one test of each series will be considered here, BETA V5.1 and SURC-4. Erosion and debris temperature are the primary parameters of interest; fission product validation will be neglected here. The validation matrix will be expanded as the model evolves and better phase diagrams and activity data are available too for temperature and fission product comparisons.

The primary parameters to be considered form the heat transfer law: h = a*f**n where h is the heat transfer coefficient, a is its nominal value, f is the liquid fraction, and n is an exponent. The nominal

value is expected to be lower for oxidic experiments than metallic experiments, and be on the order of 1,000 to 10,000 W/m**2/K, while the exponent is expected to be lower for metallic experiments than oxidic experiments and range from 1 to 3.

5.2 Results and Discussion

Figures 3, 4, and 5 display predicted erosion and temperatures for the six experiments. These results were obtained with one pair of parameters for the oxide experiments, a = 5000 and n = 2.75, and another for the metal experiments, a = 7000 and n = 1. Table 1 compares the erosion results for one experiment, ACE L7, for a number of parameter pairs to illustrate the sensitivity of results to their selection. Note that excellent agreement for any single test may be obtained by varying the model parameters; the point of this exercise is that a consistent set can be found for all tests.

Erosion is fairly well-predicted by the model in all cases. This indicates a good relative balance between upward losses and heat transfer to the walls and floors contacting the debris. This is consistent with Table 1, which shows that variation in the heat transfer parameters does not dramatically change the predicted erosion. For the ACE and SURC simulations, upward losses are sensitive to the imposed temperature boundary conditions because the debris is heated in place and the calculation is initialized when ablation starts. Errors in debris temperature can account for several centimeters error in erosion for any of these tests. The relative erosion error due to temperature error of course decreases for tests of longer duration.

The temperature predictions for L2 and L5 are considered good, while those for L6 and L7 appear to be low. The temperature prediction for SURC-4 does not follow the increase upon Zr addition but is otherwise good, and the temperature prediction for BETA V5.1 is presumed to be too high because condensed phase Zr and Si does not affect the metal

solidus in DECOMP. Temperature predictions may also suffer from the lumping of oxide and metal in DECOMP for the metallic tests.

Considering the oxide tests, the error appears late in time, after substantial concrete addition. This indicates that the assumed phase diagram is inaccurate, but such inaccuracy was expected because experiment-specific calculations with advanced codes were not used. Part of the temperature error is also due to the heuristic heat transfer law.

6.0 SUMMARY

The core-concrete interaction model within MAAP 3.0B, called DECOMP, is being upgraded for MAAP 4. It contains simplified models to account for phenomena observed during current experiments and yet run fast within an integrated accident analysis. It allows independent sideward and downward erosion and can account for uncertainty in their relative magnitudes. Debris temperature for oxide systems is strongly influenced by solidification behavior which is the most important uncertainty for dry interaction cases. DECOMP contains general pseudo-binary phase diagram capabilities to account for this behavior, and input for this diagram must come from advanced codes.

Validation of the model shows acceptable performance and provides guidance to the parametric heat transfer coefficient which heuristically accounts for viscosity increase with solid fraction. It is expected that better phase diagram data for the oxides will yield better overall results. Future work will consider better data when available, a distributed parameter approach to the debris crusts, and consideration of results obtained in the MACE program.

7.0 REFERENCES

[1] MAAP 3.0B - Modular Accident Analysis Program for LWR Power Plants, EPRI NP-7071-CCML, November, 1990.

[2] D.H. Thompson and J.K. Fink, ACE MCCI Test L5 Test Data Report, ACE-TR-C7, Argonne National Laboratory, March 1989.

[3] D.H. Thompson and J.K. Fink, ACE MCCI Test L2 Test Data Report, Volume I - Thermal Hydraulics, ACE-TR-C10 Vol. 1, Argonne National Laboratory, April 1989.

[4] D.H. Thompson and J.K. Fink, ACE MCCI Test L6 Test Data Report, Volume 1 - Thermal Hydraulics, ACE-TR-C26 Vol. 1, Argonne National Laboratory, August 1991.

[5] H. Alsmeyer, Report on Recent BETA Experiments V5.1, V5.2, and V6.1, CSARP Meeting, Bethesda, MD, May 6-10, 1991.

[6] E.R. Copus et al, Core-Concrete Interactions Using Molten Steel with Zirconium on a Basaltic Basemat: The SURC-4 Experiment, NUREG/CR-4994, April 1989.

[7] E.R. Copus et al, Core-Concrete Interactions Using Molten Steel with Zirconium on a Basaltic Basemat: The SURC-1 Experiment, draft for comment.

[8] B.W. Spencer, M. Fischer, M.T. Farmer, and D.R. Armstrong, MACE Scoping Test Data Report, MACE-TR-D03, Argonne National Laboratory, June, 1991.

[9] M. Roche, D. Steidl, L. Leibowitz, J. Fink, and R. Seghal, Viscosity of Core-Concrete Mixtures, ACE TAC Meeting, Argonne National Laboratory, June 13, 1991.

[10] P.Y. Chevalier, Presentation of the OXY5-GEMINI Code to the ACE-TAC Meeting at Palo Alto, November 4-8, 1991.

[11] M.A. Mignanelli, Calculation of Phase Diagrams: Determination of Solidus-Liquidus Temperatures, ACE TAC Meeting, Argonne National Laboratory, June 11-14, 1991.

[12] M.G. Plys, M.A. Kenton, and R.E. Henry, Ex-Vessel Fission Product Release Modelling Within Integrated Accident Analysis, Proc. CSNI Specialists' Meeting on Core Debris-Concrete Interactions, EPRI NP-5054-SR, February, 1987.

[13] J.K. Hohorst, Editor, SCDAP/RELAP5/MOD2 Code Manual Volume 4: MATPRO - A Library of Materials Properties for Light Water Reactor Accident Analysis, NUREG1CR-5273, EGG-20555, Vol. 4, Rev. 3, February, 1990.

TABLE 1: Selected sensitivity of ACE L7 erosion (nominally 10 cm including the zirconium inserts) for various heat transfer law parameters.

PARAMETER		RESULT
a	n	X (cm)
3600	1.4	10.2
3700	1.5	9.8
4300	1.5	10.8
4300	2.0	8.0
5000	1.5	11.7

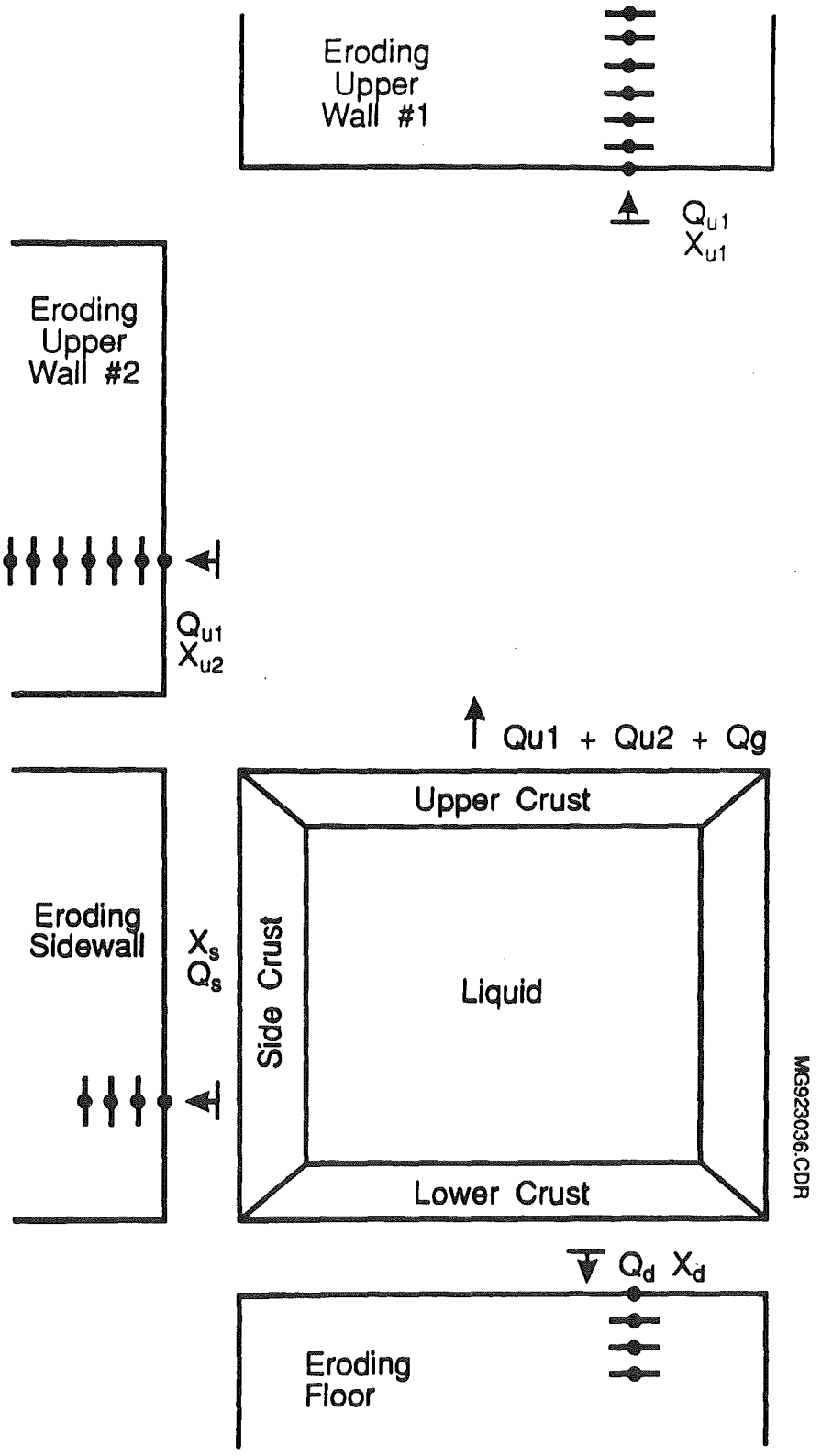

FIGURE 1: DECOMP representation of debris and region heat sinks; Q = power and X = eroded distance.

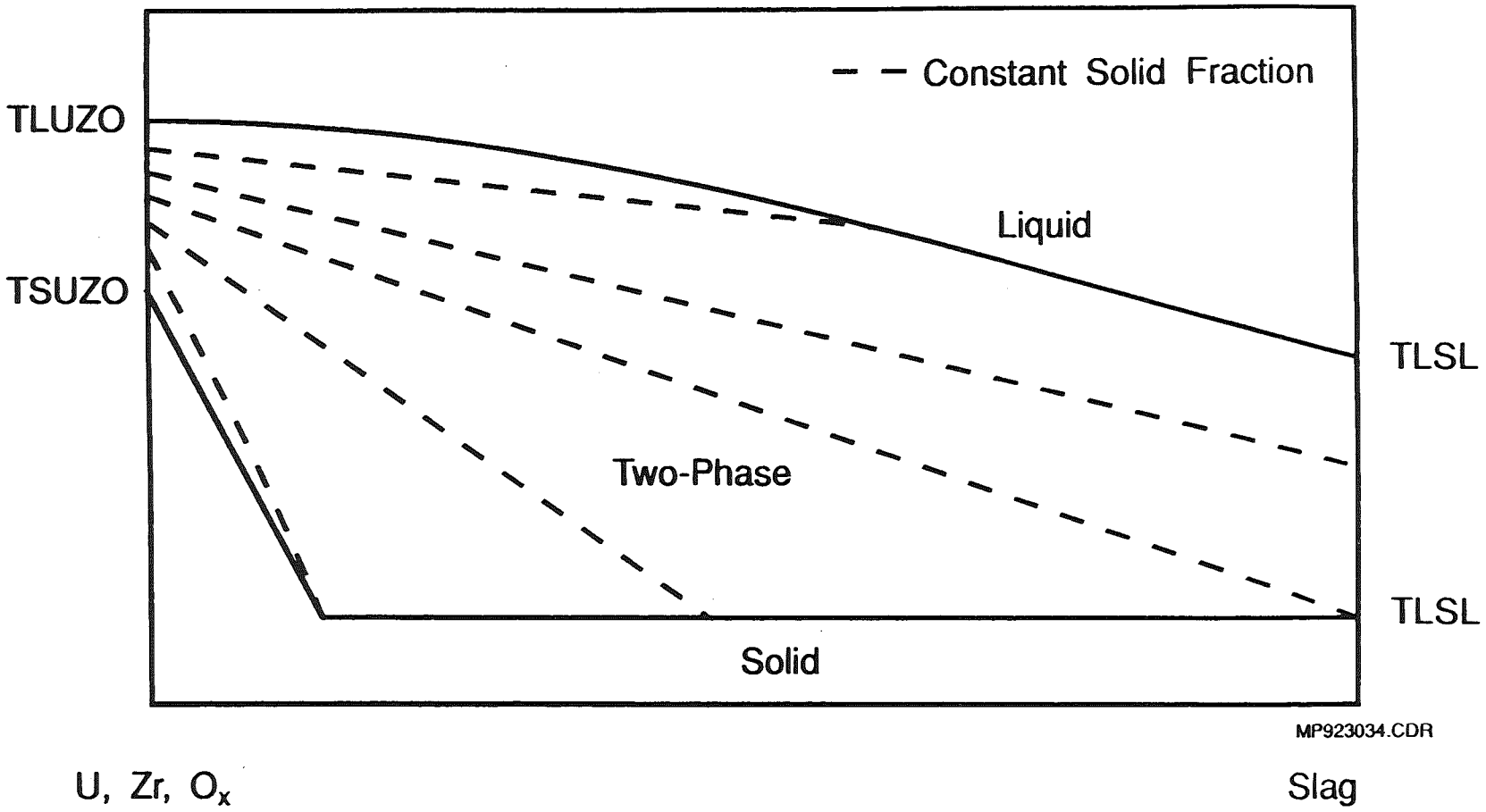

FIGURE 2: Pseudo-binary phase diagram considered by DECOMP showing the solidus and liquidus as solid lines and using dashed lines for constant solid fraction.

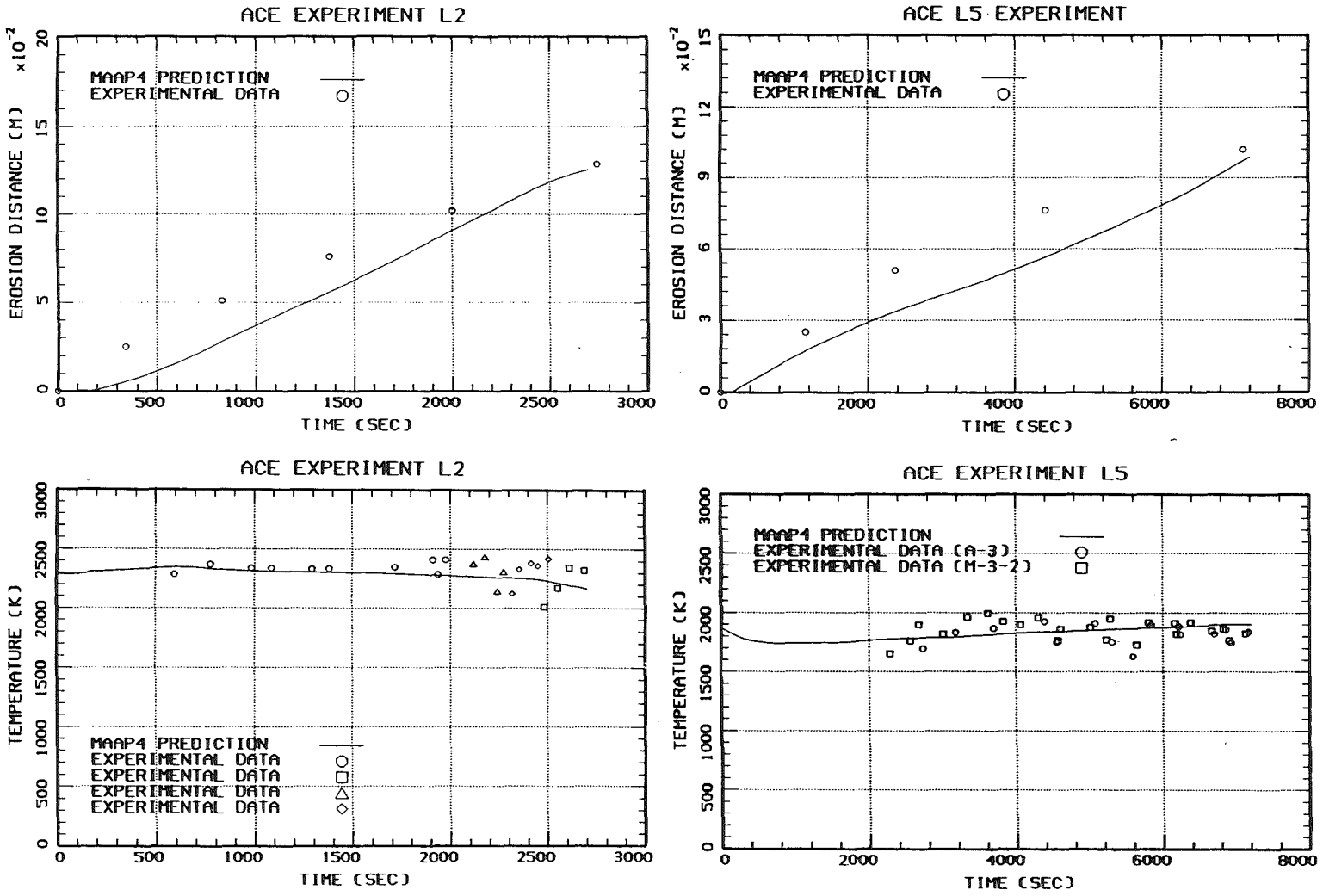

FIGURE 3: ACE L2 and L5 erosion distance and average melt temperature predictions.

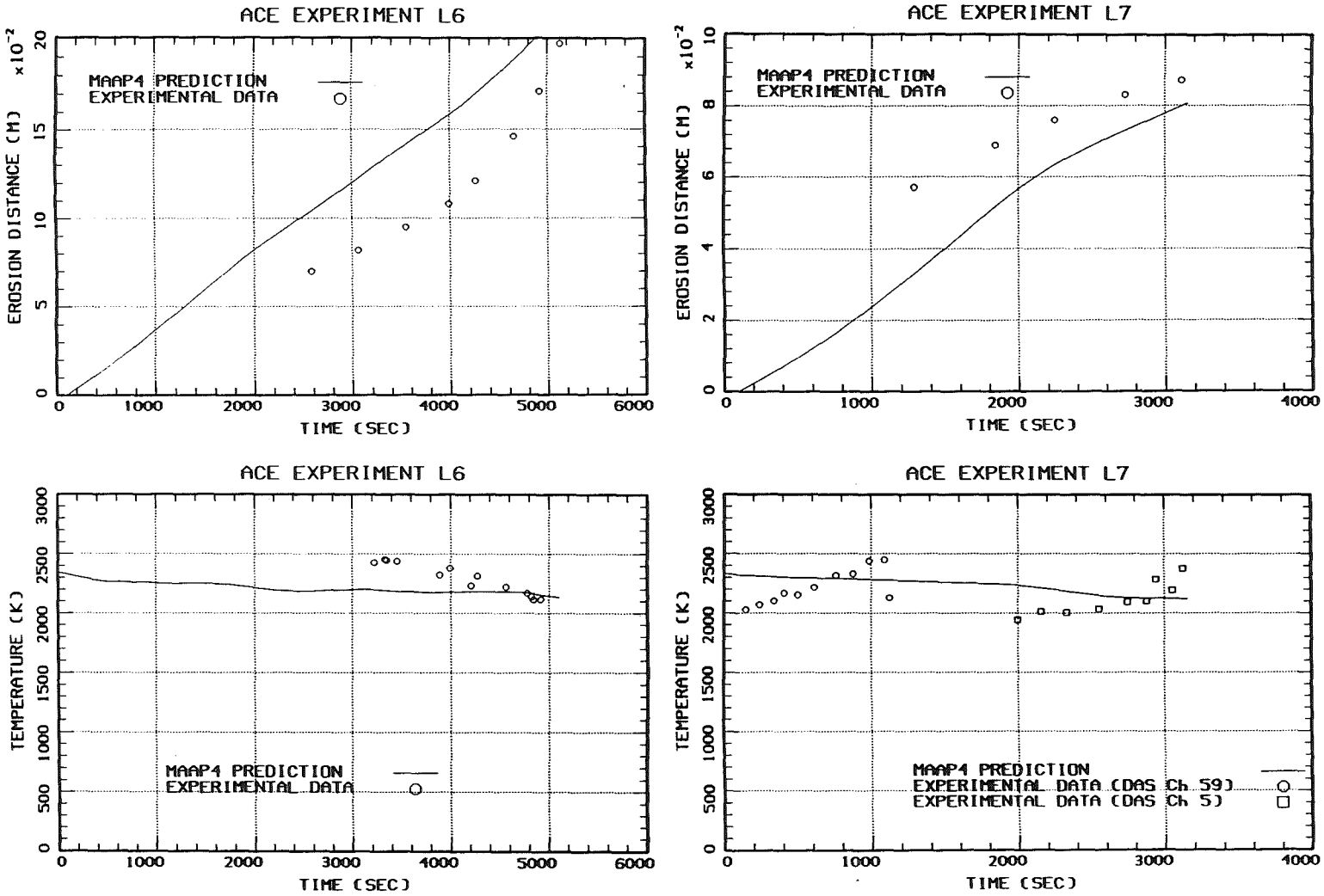

FIGURE 4: ACE L6 and L7 erosion distance and average melt temperature predictions.

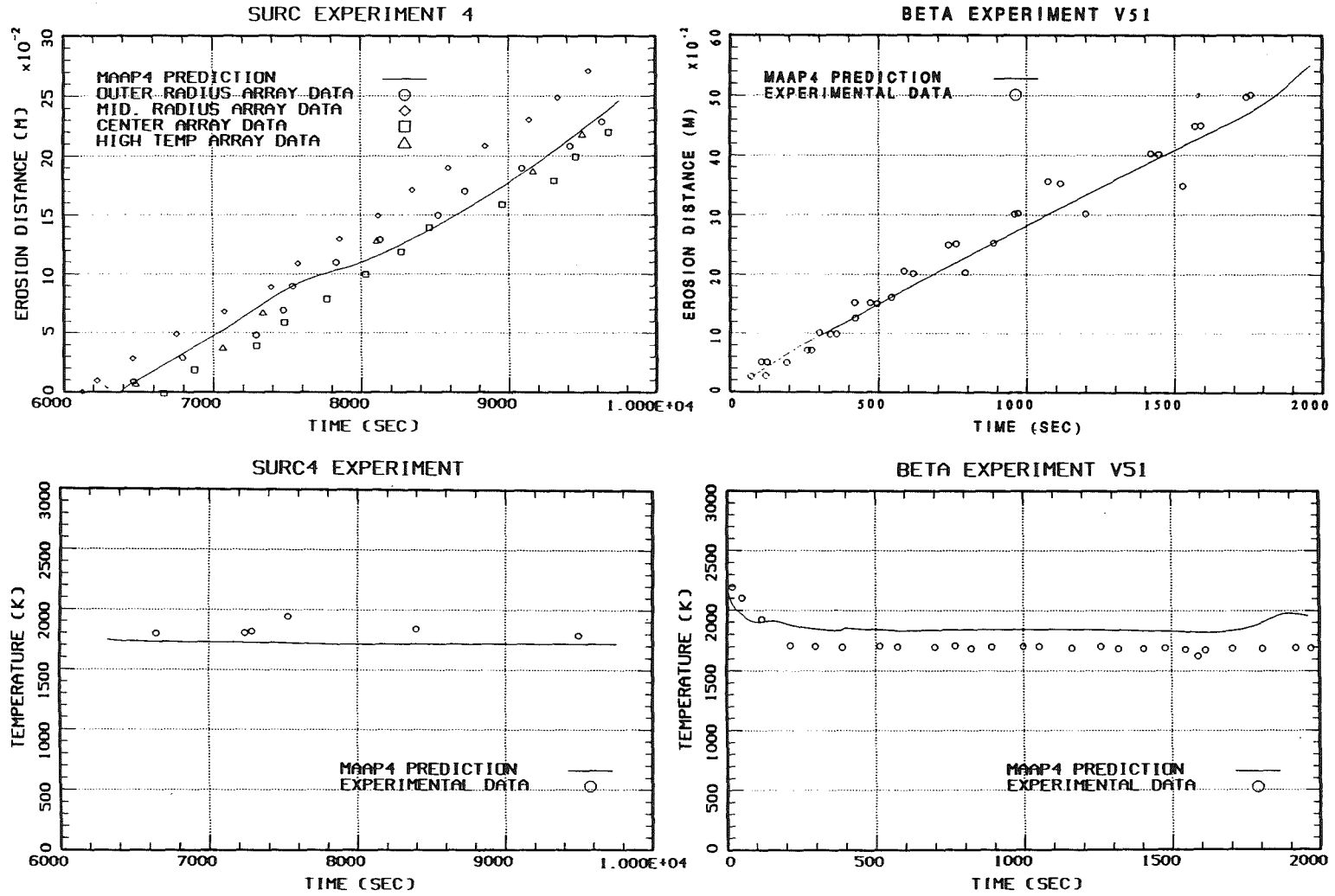

FIGURE 5: SURC4 and BETA V5.1 erosion distance and average melt temperature predictions.

IMPROVED WECHSL MODELS INCLUDING ZIRCONIUM OXIDATION AND ITS VERIFICATION BY NEW BETA EXPERIMENTS

J. J. Foit

Kernforschungszentrum Karlsruhe GmbH
Institut für Angewandte Thermo- und Fluiddynamik
Postfach 36 40
W-7500 Karlsruhe 1
Federal Republic of Germany

ABSTRACT

Recently the experimental programs SURC at SNL (USA), ACE at ANL (USA) and BETA at KfK (Germany) have been carried out in order to investigate the phenomena which are likely to occur during the ex-vessel phase of a core-melt accident, predominantly in the high temperature phase of concrete erosion with high zirconium content of the melt. During this phase of interaction the condensed phase reaction between zirconium and SiO_2 is considered to play an important role. On the base of this BETA test series the improved WECHSL code is validated.

I. INTRODUCTION

The BETA V5.1 test has been carried out in order to investigate the Zr/SiO_2 condensed phase chemistry during the interaction of a metallic melt with a siliceous concrete crucible. The Mod3 version of the WECHSL code is used to evaluate this experiment.

The WECHSL code [1] aims at modelling the physical phenomena governing the molten core/concrete interaction. WECHSL models one-dimensional as well as two-dimensional melt/concrete interactions. It is assumed that an underlaying metallic layer consisting of Zr, Cr, Fe, Ni and Si exists covered by an oxidic layer composed of UO_2, ZrO_2, CaO, SiO_2, Al_2O_3, Cr_2O_3 and FeO or that only one oxidic layer is present which can contain a homogeneously dispersed metallic phase.

Internal energy can be produced either by decay heat or by exothermic reactions. The concrete decomposition velocity is assumed to be quasi-stationary. For the heat transfer from melt to concrete a film model, a discrete bubble model or a transition boiling model is used depending on the existing gas flow and on the inclination of the interface. Since the melt is intensively stirred by the gases released during the concrete ablation process, the bulk of each layer of the melt is assumed to be isothermal with the boundary layers of the interfaces. The heat transfer between the metallic and the oxidic layers is also modelled. During the cool-down of the melt crust formation is modelled starting from the metal/concrete interface and from the upper melt surface which eventually leads to a fully frozen layer. Crusts are assumed to be permeable to gases.

The solidus and liquidus temperatures of the metallic phase in WECHSL are calculated by a simple fit to a chromium-nickel-iron ternary phase diagram. The influence of the Zr and Si on the liquidus and the solidus temperatures is not taken into account. It is known that they lower the solidus temperature. For the oxidic phase the solidus and liquidus temperatures are determined either by a binary phase diagram which is used in the present calculation or by a user input table. Liquid decomposition products of the concrete dilute the oxide layer. This effect changes the properties of the oxidic melt continuously. Above all the solidification temperature is reduced. The gases and the SiO_2 released from the decomposed concrete oxidize the constituents of the metallic phase. The metal oxidation reactions take place in the order Zr, Si, Cr and Fe.

II. ANALYSIS OF THE WECHSL RESULTS

II.1 Oxidation Reactions

The performed BETA V5.1 experiment shows the dominant effect of the Zr/SiO_2 condensed phase chemistry, i.e. the reduction of the SiO_2 by the metallic zirconium. In the temperature range below about 2200 K the SiO_2 is reduced mainly to metallic Si in an exothermic reaction. The oxidation reactions of Si proceed also in an exothermic way. The chemical reactions under consideration with their reaction enthalpies are given by

$$Zr + SiO_2 \rightarrow ZrO_2 + Si + r_{Zr,SiO_2}, \qquad (1)$$

$$r_{Zr,SiO_2} = 2.1 \cdot 10^3 \, [J/gZr], \quad (2)$$

$$Si + 2H_2O \rightarrow SiO_2 + 2H_2 + r_{Si,H_2O}, \quad (3)$$

$$r_{Si,H_2O} = 17.9 \cdot 10^3 \, [J/gSi], \quad (4)$$

$$Si + 2\,CO_2 \rightarrow SiO_2 + 2\,CO + r_{Si,CO_2}, \quad (5)$$

$$r_{Si,CO_2} = 12.3 \; 10^3 \, [J/gSi]. \quad (6)$$

A complete reduction of SiO_2, H_2O and CO_2 is assumed.

Analyses of metal probes taken before 180 s show that the Zr-content is diminishing and Si is formed (5 %). The content of Zr and Si in the solidified metallic regulus, i.e. at the end of the experiment is equal to 0.02 % and 2.8 %, respectively. The WECHSL results indicate an end of the Zr-oxidation at t = 78 s and a formation of 6 % Si in the melt. In the final state at 2000 s only 1.6 % Si are contained in the metallic melt.

II.2 Melt Front Propagation and Cavity Shape

During the early phase of the experiment a substantial part of the melt, mainly the metallic phase, was splashed against the upper hood. This effect is responsible for the loss of metal during the first 180 s of melt/concrete interaction. The metal regulus at the end of the experiment was estimated to be 104 kg compared to the initial mass of 300 kg. The reduced metal mass may cause many uncertainties, among others an irregular cavity shape (Fig. 1). Hence the eroded volume is a quantity which should be compared to the results of the calculations. The eroded mass of concrete was estimated from the section of the crucible to be about 397 kg $\pm$ 49 kg compared to 379 kg calculated by WECHSL.

Even though the volumes agree quite well with other, the calculated value of the axial erosion speed is higher than the measured one during the first 200 s (Fig. 2).

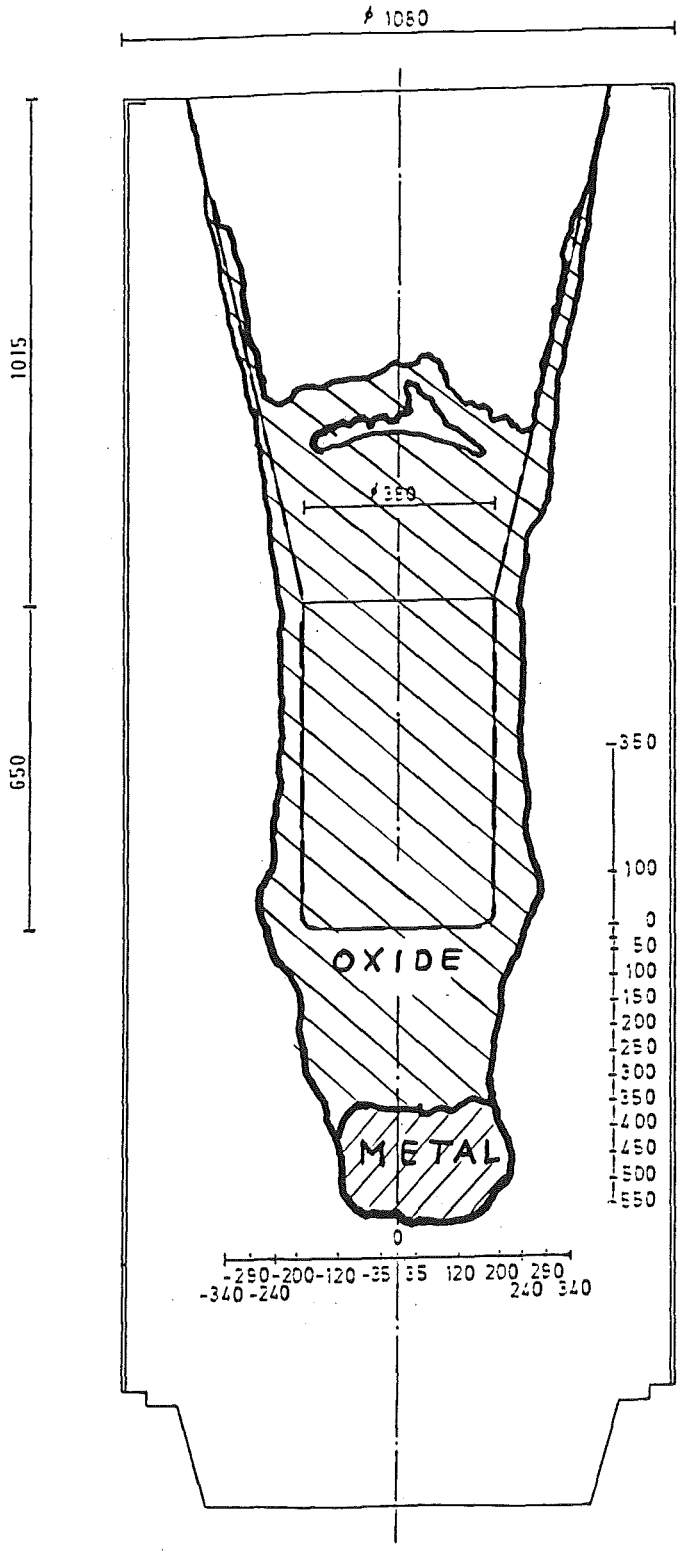

Fig. 1: BETA V5.1 cavity shape

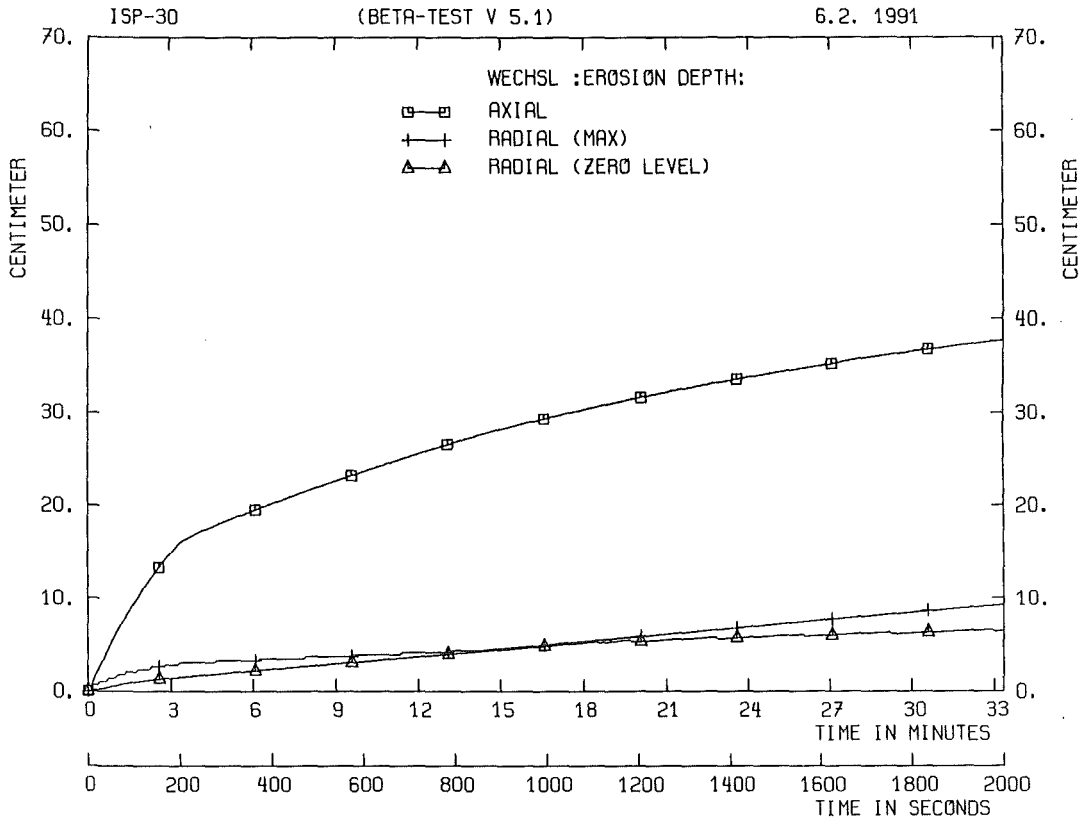

Fig. 2: Concrete erosion

II.3 Gas Release

II.3.1 Gas Release Rates

During the Zr oxidation phase high gas release rates dominated by H_2O and H_2 were observed. The measured H_2 and CO release rates show a high peak with a maximum value of 5.5 mole /s and 0.7 mole/s, respectively at t = 100 s. The duration of this release peak is about 300 s. The WECHSL results provide a maximum value of 4.0 mole/s for H_2 and 0.5 mole/s for CO at earlier time of 20 s. The width of these peaks is 200 s. In the time period t > 200 s, the duration of the Si oxidation phase, the release rates of H_2 and CO are higher and consequently, the CO_2 release rate is lower than the measured data (Fig. 3). This may indicate different Si oxidation reaction kinetics than modelled in WECHSL.

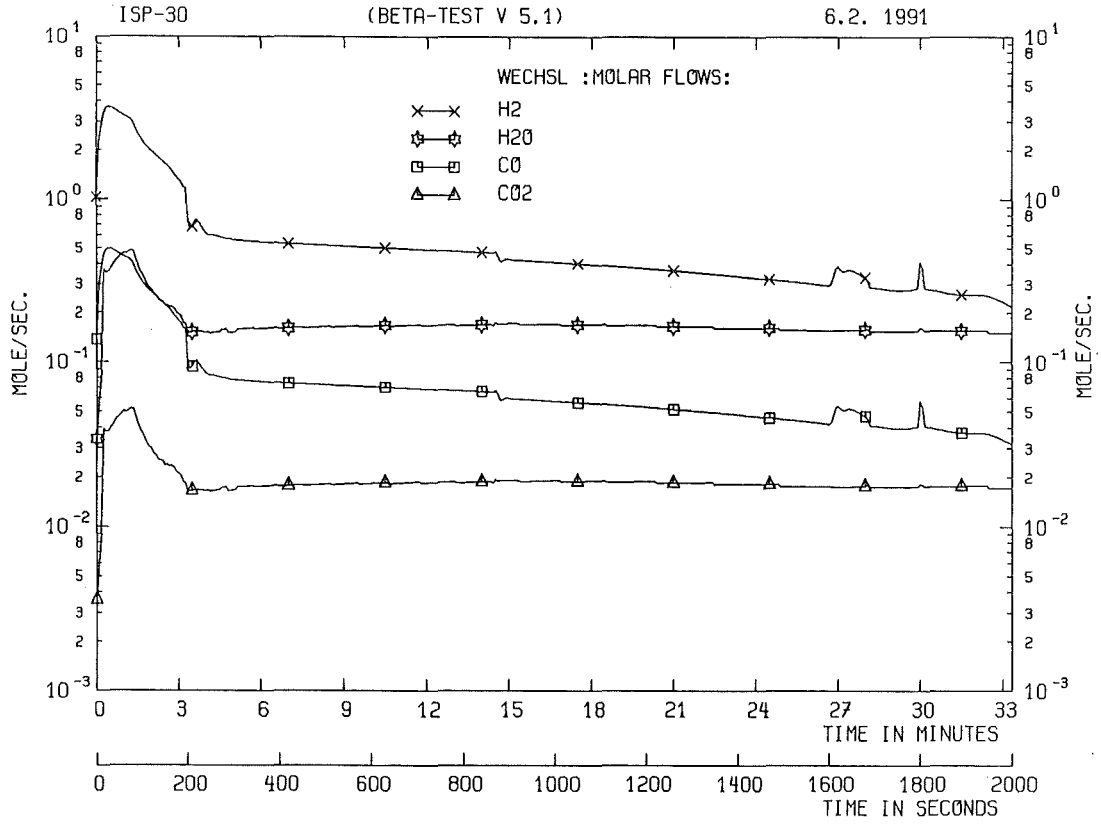

Fig. 3: Gas release rates

II.3.2 Integrated Gas Release

The integrated values of released gases are depicted in Fig. 4.

The ratio of the measured moles to the calculated values of released gases at the end of the experiment (t = 2000 s) are given in the following table, Tab. 1.

Moles	Measurement	WECHSL	Ratio
H_2O	1295	353.1	3.7
H_2	649	1208	0.54
CO_2	83	39.07	2.1
CO	88	167.7	0.52

Tab. 1: Comparison of measurement and WECHSL results

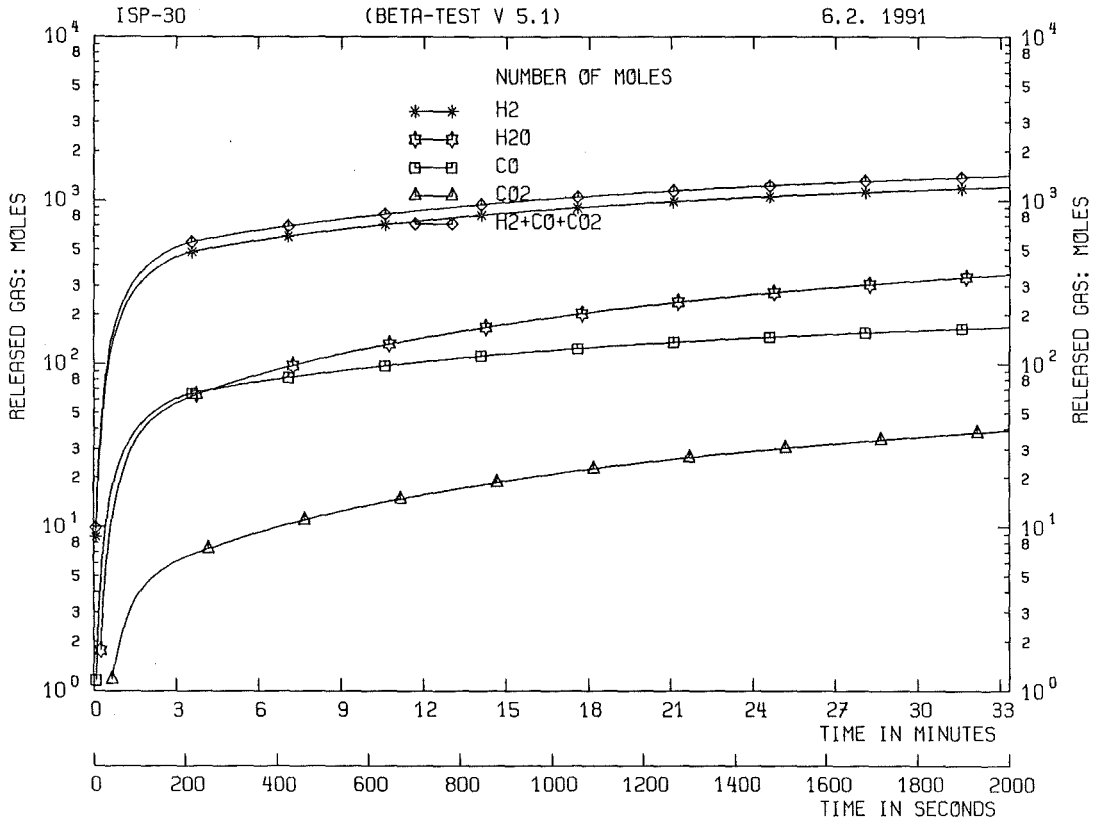

Fig. 4: Released gases

The much higher release of H_2O in the experiment compared to the calculated value can be explained by the release of H_2O from the upper part of the crucible. The sum of all measured moles of C including the Carbon contained in the melt gives 200 moles, whereas the value calculated by WECHSL is 207 moles. The discrepancy in the ratios of H_2 and CO is probably caused by a different Si oxidation reaction kinetics. Calculations with a reduced mass of the melt lead to a better agreement of the released H_2 and CO compared to the experiment but they are still out of the range of the measurement errors.

II.4 Temperature of Melt

Experimental melt temperature data are available only for the metallic phase. The measured temperature of the metallic melt starts at 2200 K and decreases rapidly during the first 200 s to a stationary level of 1690 K. The calculated melt temperatures as a function of time are shown in Fig. 5.

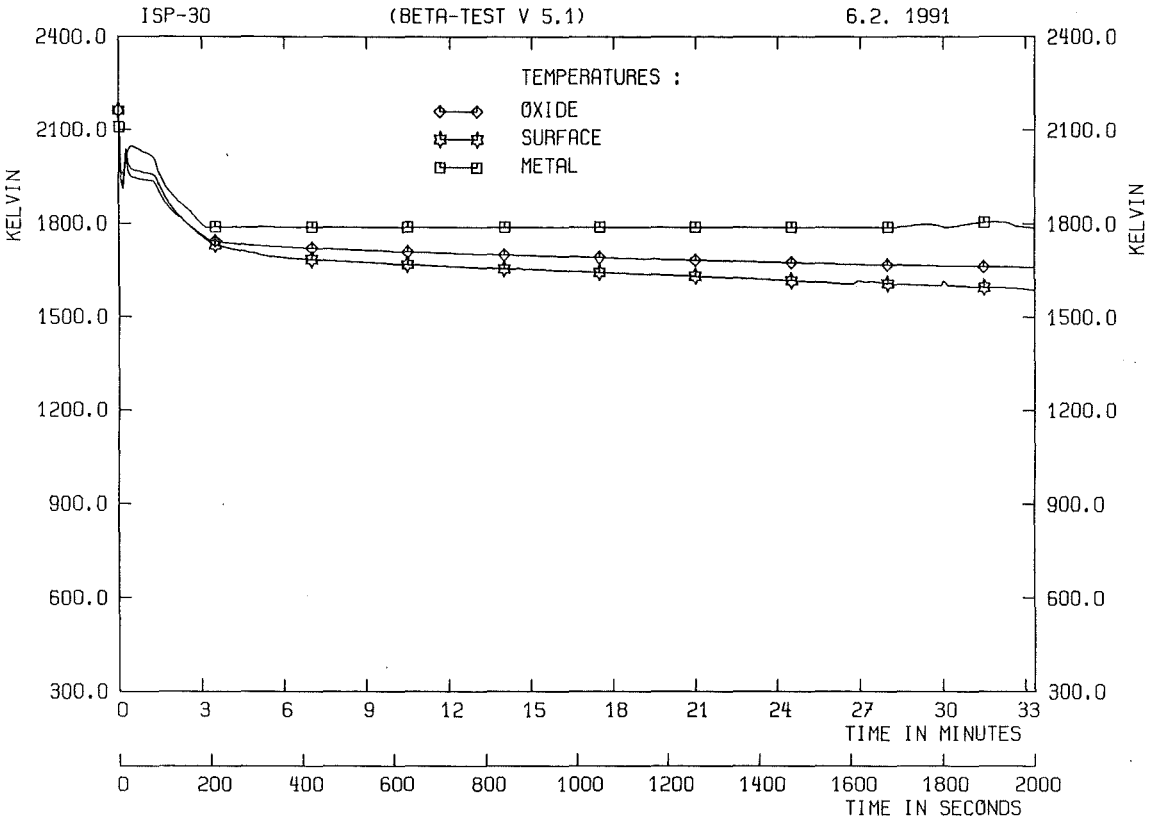

Fig. 5: Melt temperatures

The results of the WECHSL analysis also show a rapid decrease of the temperature within the first 200 s, but the stationary level in the calculations is about 100 K higher than in the experiments. This is because the modelling of solidus temperatures in WECHSL doesn't account for the presence of Si and Zr in the melt which is known to lower the freezing temperature.

III. CONCLUSIONS

The performed BETA V5.1 experiment shows the dominant effect of the Zr/SiO_2 condensed phase chemistry. The high energy release of the exothermic Zr oxidation reactions which are completed within 180 s leads to high gas release rates. In spite of the high amount of chemical energy released in the melt the temperature decreases to a stationary level. The results obtained using the WECHSL code are in quite good agreement with the findings of the experiment. The calculated metal

temperature also shows a rapid decrease but the stationary level attained in the calculations is higher than that in the experiments with Zr contained in the melt.

Even though the calculated integral value of the released gases are in good agreement with the measured data, WECHSL overpredicts the gas rates of H_2 and CO after the zirconium has been burned out. This indicates different Si oxidation kinetics than that considered in WECHSL.

REFERENCES

[1] M. Reimann et al., "The WECHSL-Mod2 Code: A Computer Program for the Interaction of a Core Melt with Concrete including the Long Term Behavior", KfK 4477 (1989).

ASSESSMENT STATUS OF THE WECHSL-MOD3 CODE

C. Renault
Institut de Protection et de Sûreté Nucléaire
CEN Cadarache
F-13108 St Paul lez Durance

J.J. Foit
Kernforschungszentrum Karlsruhe
Postfach 3640
D-7500 Karlsruhe 1

ABSTRACT

The predictive capability of the WECHSL-Mod3 code is evaluated on the basis of a significant set of experiments selected from the BETA I, SURC and ACE test matrices. The prediction of concrete erosion is generally in close agreement with data for all corium compositions and concrete types. The modeling of condensed phase chemistry appears as a major contribution to the proper calculation of the tests where Zr oxidation played a role. Some discrepancies observed for the prediction of concrete ablation and melt temperature for the case of oxidic melts are discussed with respect to the modeling of liquidus/solidus temperatures, of melt-concrete heat transfer and of Zr chemistry at very high temperature.

1. INTRODUCTION

The WECHSL code is a mechanistic code aiming at the description of phenomena occurring during MCCI (molten corium concrete interaction). The code is capable of treating both simulation experiments and full scale reactor meltdown accidents. Recently, substantial developments have been implemented, particularly for the modeling of oxidic melt behaviour. These developments in addition to a complete rewriting of the code have led to the Mod3 version.

This paper is a review of the assessment status of the WECHSL-Mod3 code. The goal was to make an evaluation of the code predictive capability on the basis of a set of tests covering as well as possible the range of parameters relevant to reactor application. It is worth pointing out that all calculations have been performed with the standard Mod3 version of the code without any modifications except for sensitivity studies. Due to limited space, this paper concentrates on the analysis of concrete erosion. A more detailed study including melt temperature and gas release analysis is available in the WECHSL-Mod3 assessment report [1].

2. MAIN FEATURES OF WECHSL-MOD3

A detailed description of the modeling in WECHSL is given in [2]. Here it is only intended to point out the main developments realized in version Mod3 and to recall the logic of melt-concrete heat transfer in the code.

Heat transfer logic

Although no significant modification was done on this subject for Mod3, the logic of the melt-concrete heat transfer model in WECHSL is recalled here (figure 1) for a better understanding of the analysis presented in the next sections. The heat transfer regime is assumed to be controlled by gas superficial velocity (represented by the gas Reynolds number) and by crust thickness. In the film mode, a continuous gas film prevents direct contact between the melt and the concrete; this regime is typical of high gas release conditions or thick crust situations. The bubble mode is similar to nucleate boiling in two-phase flow; it is based on experiments with gas flowing through a porous medium into a liquid pool. The mixed mode is a transition region where the melt may contact concrete intermittently. The original Berenson criterion was modified in order to expand the range of this transition region. This modification was supported by the idea of an early gas film destabilization likely to occur in the case of melt attack in contrast to typical boiling [3]. The critical values of crust thickness and Reynolds number controlling the transitions between regimes were adjusted according to BETA tests.

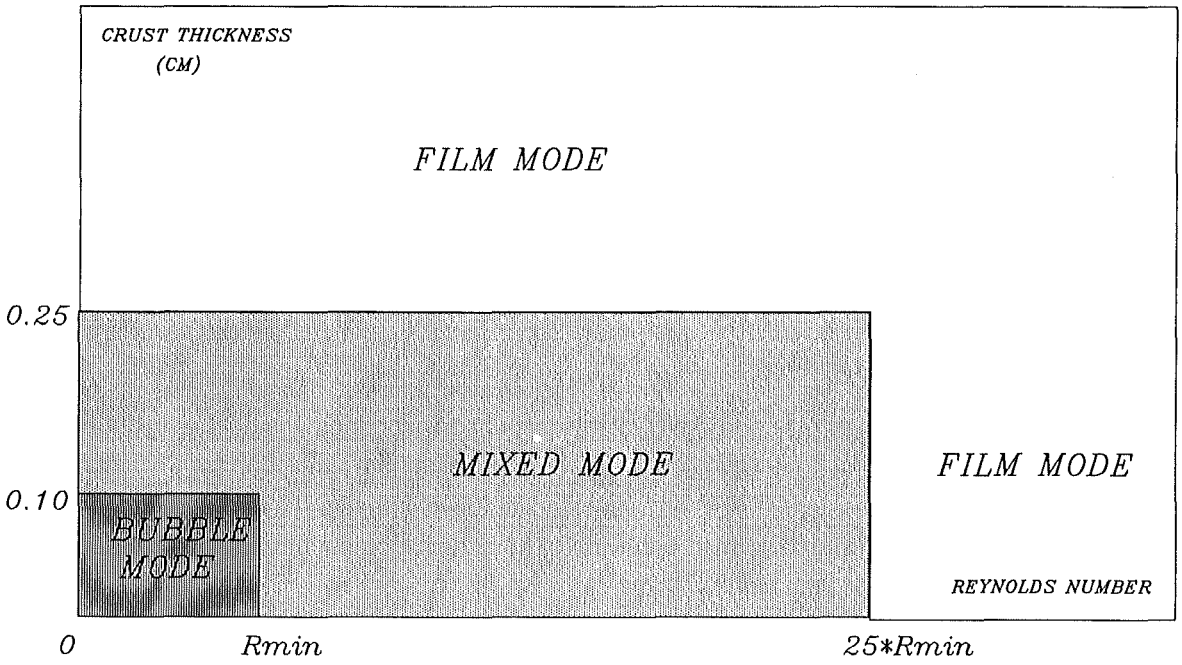

Figure 1

Mixing option

In version Mod2, WECHSL considered the separation of the melt into a metal and an oxide layers, with the heavier metal at the bottom. This conceptual model may be appropriate for particular situations. However, when a high gas release occurs (early stage of interaction) or when the melt is greatly oxidized, this picture is not relevant and must be replaced by a concept of layer mixing.

In version Mod3, the option of an oxidic melt with dispersed metal is available ("mixing " option). In that case, the melt is considered as a homogeneous mixture and physical properties are calculated as follows :

- heat capacity is averaged over the set of oxidic and metallic components,

- kinematic viscosity and surface tension of the mixture are assumed to be those of the oxide phase,

- heat conductivity is calculated assuming that metal is in the form of spherical balls dispersed in oxide [4].

Condensed phase chemistry option

In Mod2, the only chemical reactions taken into account were the reactions of metal oxidation by gases. In Mod3, the oxidation of Zr by SiO_2 has been included (optional). This option assumes a complete reduction of SiO_2(c), H_2O(g), CO_2(g) (where c denotes the condensed phase and g the gas phase). The reactions proceed in the order Zr, Si, Cr, Fe. The set of reactions considered in the new option is :

$$Zr + SiO_2 \rightarrow ZrO_2 + Si + 2.1\ kJ/gZr,$$

$$Si + 2H_2O \rightarrow SiO_2 + 2H_2 + 17.9\ kJ/gSi,$$

$$Si + 2CO_2 \rightarrow SiO_2 + 2CO + 12.3\ kJ/gSi.$$

The possible endothermic oxidation of Zr at very high temperature (> 2200 K) is not accounted for.

3. ASSESSMENT MATRIX

A number of experimental programmes have been dedicated to the study of corium-concrete interaction particularly in KfK (FRG), SNL and ANL (USA). The main parameters investigated in these integral experiments were the geometry of the crucible, the corium composition and physical state (molten, solid), the concrete composition, and the presence of water at the top of the corium.

These experiments form all together a rather comprehensive database that can be used for code validation. A limited subset of tests has been selected from this database for the assessment of WECHSL-Mod3 (table 1). In order to explain the rationale of this assessment matrix, it is convenient to split these tests into two groups according to corium composition.

EXPERIMENT	*BETA*				*SURC*		*ACE*		
TEST	*V1.8*	*V2.3*	*V3.3*	*V3.2*	*SURC4*	*SURC2*	*L5*	*L2*	*L6*
CAVITY	*38 cm D*				*40 cm D*		*50 * 50 cm*		
CONCRETE	*S*		*LCS*	*L*	*S*		*LCS*	*S*	
MELT	*METAL*				*METAL*	*OXIDE*	*OXIDE*		
ZR	*NO*				*ADDED*	*YES*	*NO*	*YES*	*YES*

Table 1

Metallic melt experiments

The initial melt was mainly composed of metals. The BETA test series V2.3, V3.3, V3.2 was selected to study the effect of concrete composition (siliceous, limestone/common sand, limestone). V1.8 was included because power input was very high. SURC4 was added in order to assess the influence of Zr oxidation.

Oxidic melt experiments

The melt was almost entirely oxidic possibly with small amounts of metal, under the form of Zr essentially. In the selected ACE tests, Zr fraction is variable, representing different degrees of oxidation in a LWR (30, 70, 100% oxidized). The test conditions of SURC2 were similar to ACE L2 and L6 but the physical behavior appeared to be different.

4. ANALYSIS OF BETA EXPERIMENTS

General remarks

The BETA test facility was designed to represent melt-concrete attack under accident conditions. A melt of typical 300 kg steel and 150 kg oxide, initial temperature of 2000°C, was poured into a 2D concrete crucible of 38 cm inner diameter and heated electrically by induction up to 1900 kW [5,6]. A series of 19 experiments was carried out from 1984 to 1986 (BETA I program). It must be pointed out that the initial melt composition was not representative of the conditions of concrete attack in a reactor core melt accident where the oxide content is dominant.

BETA Test V1.8

V1.8 was an experiment with a high power input corresponding to short term interaction in a reactor core melt accident. The propagation of the melt was predominantly downward with a very limited sidewall erosion. The axial erosion velocity was very large and power was switched off after only 8 mn of interaction.

The axial and radial erosion depths calculated by WECHSL are presented and compared to data on figure 2. The predicted heat transfer regime was the mixed mode (transition regime) with no crust or a very thin one until power cut-off. This prediction is probably consistent with the experiment because crust growing was unlikely to occur due to the large power generated in the melt. After power cut-off, concrete erosion still proceeded but the calculated ablation rate was much smaller because a thick crust (> 2.5 mm) formed and switched heat transfer to the film mode. The agreement between the calculation and the experiment is very satisfactory with respect to concrete ablation. The axial erosion depth was only slightly underestimated at the end of the heating phase.

In both the experiment and the calculation, the corium temperature decreased continuously at a high rate during the interaction because the heat transfer between molten corium and concrete was very effective. However, the temperatures for both the metal phase and the oxide phase were overpredicted. Therefore the heat transfer coefficient seems to have been underpredicted in the mixed mode. This conclusion is consistent with the small underprediction of erosion depth observed at the end of the heating period.

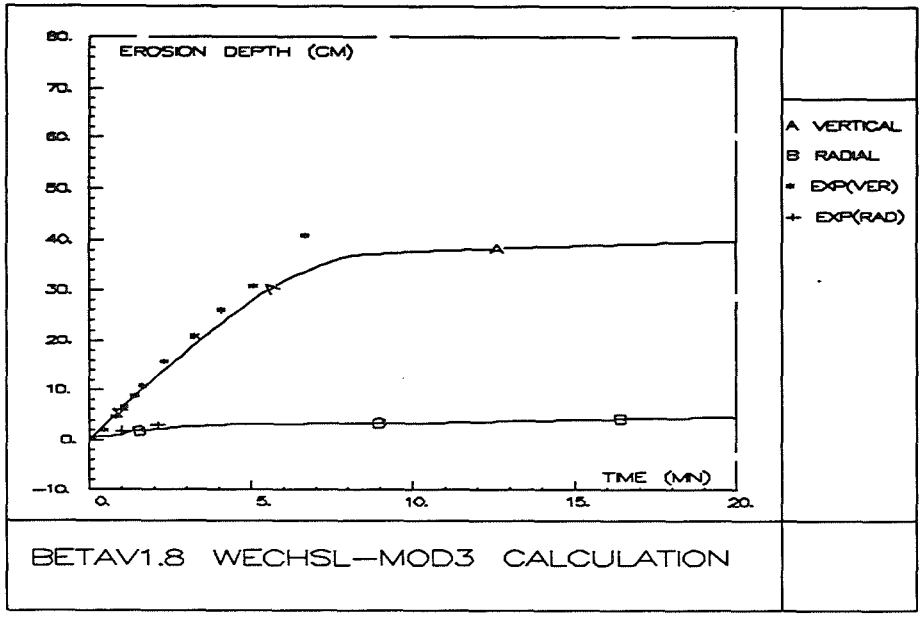

Figure 2

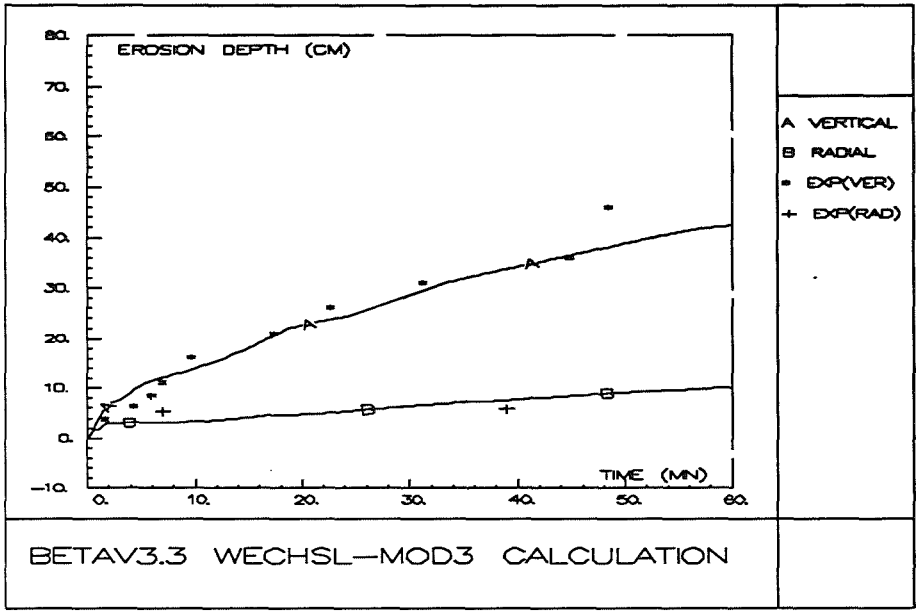

Figure 4

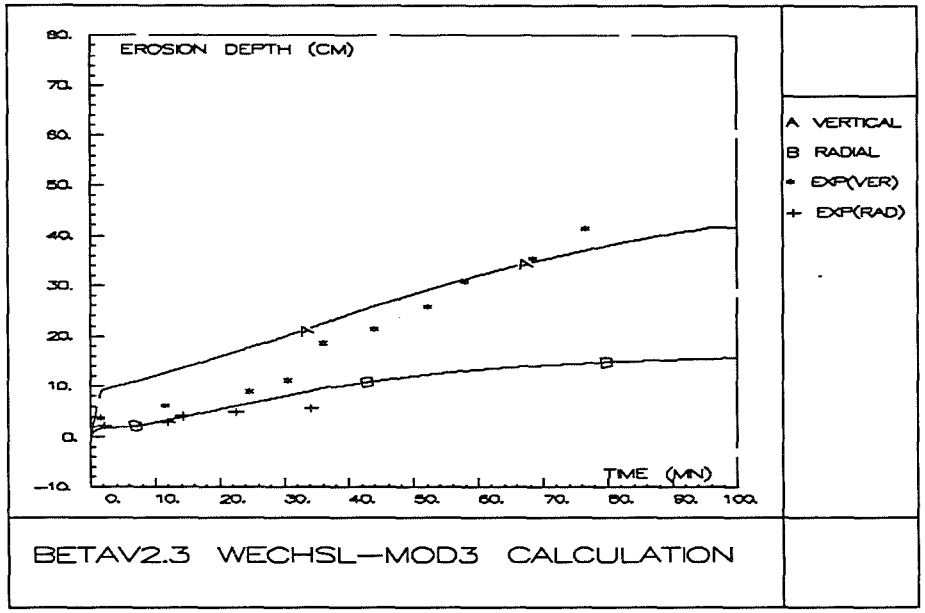

Figure 3

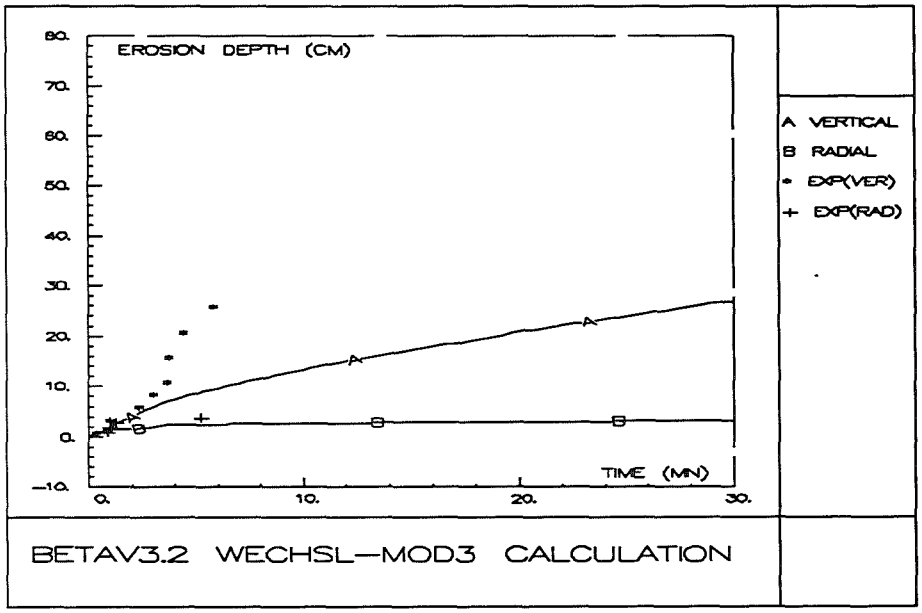

Figure 5

BETA Tests V2.3, V3.3, V3.2

In tests V2.3, V3.3, V3.2, power input was much smaller than in V1.8. Consequently the erosion rate was much smaller and the heating period could be extended considerably (up to 1 h 30 min in V2.3). In contrast to V1.8 where concrete erosion was clearly governed by liquid metal/concrete heat transfer, it may be expected that erosion was widely controlled by crust formation at the metal-concrete interface. The sideward and downward melt propagations were much more balanced compared to V1.8.

For V2.3 (siliceous concrete), the calculation showed a very early and rapid crust growth. After 108 s, the crust thickness was calculated to be larger than 2.5 mm and the heat transfer regime was then the film mode (cf § 2). The ablation rate was almost constant equal to 20 cm/h. The axial erosion was well predicted at the end of the heating phase (figure 3). However it was significantly overestimated in the initial phase; this may indicate an earlier transition to the gas film heat transfer regime than predicted by the code.

In V3.3 (limestone-common sand concrete), input power was about 65% higher than in V2.3. In contrast to V1.8 and V2.3 experiments with siliceous concrete, the shape of the eroded cavity was very asymmetrical. During most of the time, the predicted heat transfer regime was the mixed mode because crust thickness never reached the critical value of 2.5 mm. Although the gas superficial velocity was rather large, it was not sufficient to turn to the film mode. The film mode regime was predicted to occur only after power cut-off when the crust could develop. The prediction of axial and radial erosion depths is in very good agreement with measured values (figure 4.).

In V3.2 experiment, concrete was pure limestone (80% of $CaCO_3$ in weight) and the heating power was double of V3.3. The calculation predicted no crust formation for these test conditions. In the first 10 s, the predicted heat transfer regime was the film mode because the gas superficial velocity was very large (high gas release associated to limestone concrete). As gas release was decreasing, the heat transfer regime remained in the mixed mode (with no crust) until power cut-off where it turned to the bubble mode. The mixed mode and the bubble mode corresponded to erosion velocities of 45 cm/h and 20 cm/h respectively. The erosion depth was well calculated at the beginning of the interaction but was significantly underpredicted later (figure 5). Actually the data about erosion cannot be considered as reliable after 3 min. Indeed it is likely that thermocouples failed due to mechanical crack of the concrete before they were reached by the melting front. It has been mentioned that concrete decomposition was influenced by lime burning (reduction of concrete into CaO which is a material of very small mechanical strength) [7]. This process of concrete decomposition is not taken into account in the WECHSL code.

5. ANALYSIS OF SURC EXPERIMENTS

General remarks

The SURC experimental facility was operated in Sandia National Laboratories (USA) from 1986 to 1988. The crucible was of cylindrical geometry with a concrete basemat (20 or 40 cm diameter) and refractory magnesia (MgO) side walls. Therefore, the melt propagation was limited to the downward (axial) direction. The initial melt was composed of either metals (Fe, Cr, Ni) or oxides (UO_2, ZrO_2) for a typical 200 kg material inventory.

In the frame of WECHSL assessment, two experiments have been selected in the SURC test matrix : SURC4 and SURC2. Both tests were conducted with basaltic (siliceous) concrete. In SURC4, the melt was initially purely metallic and some Zr was added after the beginning of corium-concrete interaction. In SURC2, the initial corium was a mixture of UO_2, ZrO_2 and Zr. SURC4 and SURC2 were chosen for their contribution to the study of Zr effect on corium-concrete interaction.

SURC4 Test

In SURC4 experiment, the initial corium was a mixture of Fe, Cr and Ni (about 200 kg). 20 kg of Zr were added to the melt 13 min after the initiation of corium-concrete interaction. The net input power was 60 kW except during a 7 min time interval where the power was cut. The ablation rate was seen to increase shortly after Zr addition. This was interpreted as a real effect of Zr oxidation because input power had just been stopped at this moment.

For the WECHSL calculation, the mixing option (cf § 2) was not used because the initial melt was purely metallic. But the chemistry of condensed phase was taken into account (Zr oxidation by SiO_2, cf § 2).

The calculated erosion depth is compared to data in figure 6. Except during a very short initial period, the predicted heat transfer regime was the film mode because a thick crust formed early at the bottom of the melt (low initial temperature). The calculated erosion rate was almost constant in the average (20 cm/h) with the exception of a spike at 30 min corresponding to the reset of power. Although an increase of erosion rate was predicted after Zr addition, this effect was much less than in the experiment. This behavior is related to crust history (figure 7) : after Zr was added, the crust thickness started to decrease due to additional energy to the melt (chemical energy coming from exothermic oxidation) but not enough to modify the heat transfer mode because in the same time input power was cut. On the overall, the calculation of erosion agreed properly with the measured data on the centerline of the basemat.

It is interesting to discuss the effect of chemistry in more details for this test. Figures 8 and 9 show the results of two calculations performed with different assumptions, one with the condensed chemistry option (oxidation of Zr by SiO_2) and the other without this option (oxidation of Zr by gases). Although the activation of condensed phase chemistry significantly increased the chemical power input to the melt, the impact on the calculation of erosion depth was surprisingly relatively small. The calculations showed that higher chemical power resulted in higher melt temperature and larger upward heat losses. The rate of Zr burning was very different in the two calculations (figure 9). Zr was depleted very slowly under the assumption of Zr oxidation by gases because oxidation was strongly limited by the availability of gases released (gas production is sparse for siliceous concrete). The second assumption led to a much faster Zr burning because SiO_2 availability was more favourable to complete the oxidation of Zr. In both cases, the impact of Zr oxidation on erosion velocity was mitigated by the presence of a thick crust at the time of Zr addition. The improvement brought by the implementation of the condensed phase chemistry option into the code was more clear in the prediction of gas release [1] and this was confirmed by the analysis of BETA V5.1 test [8].

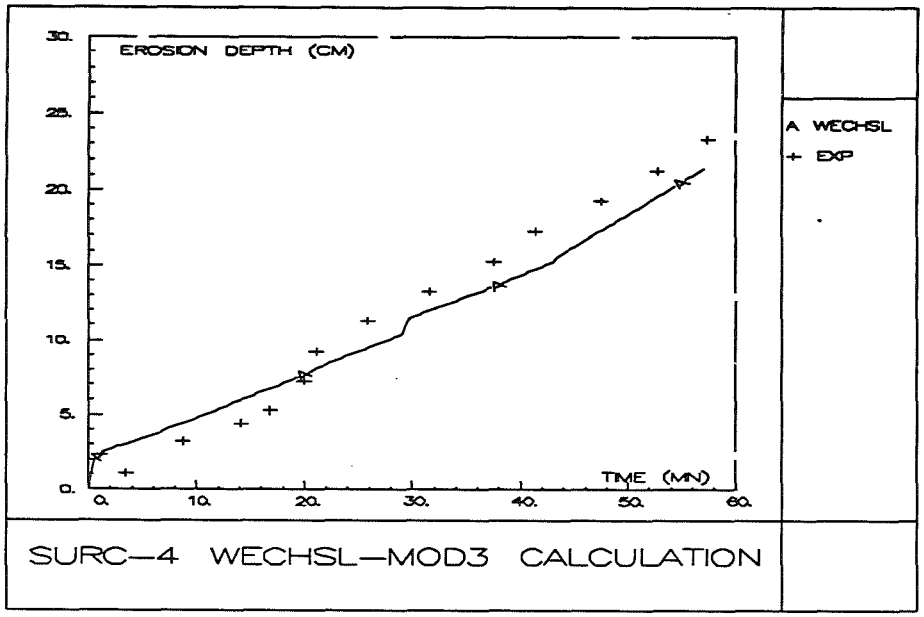

Figure 6

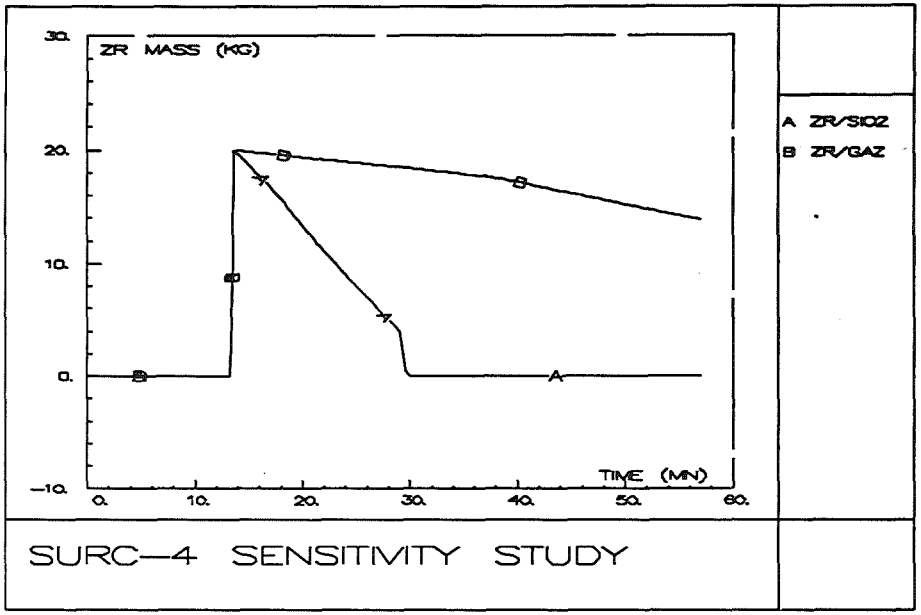

Figure 9

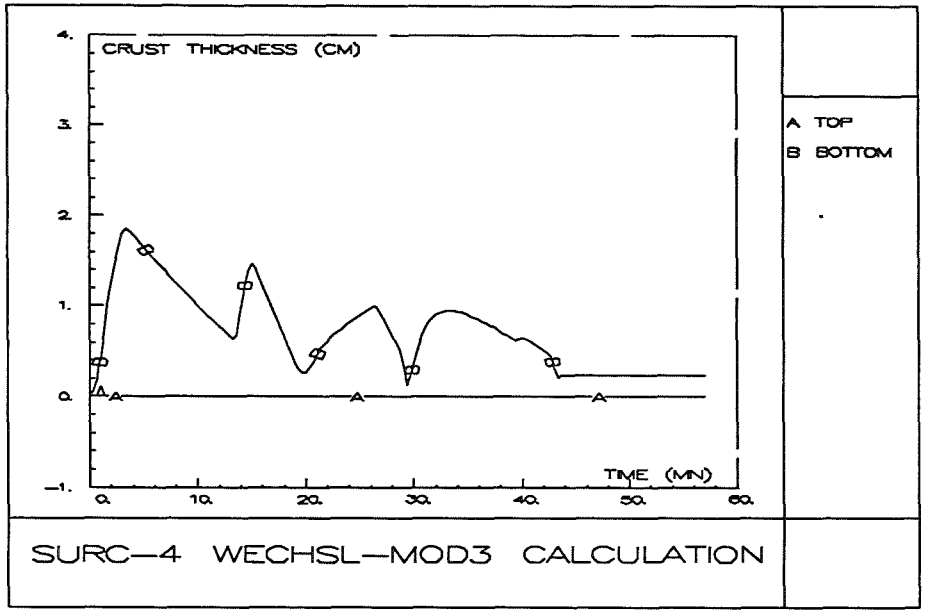

Figure 7

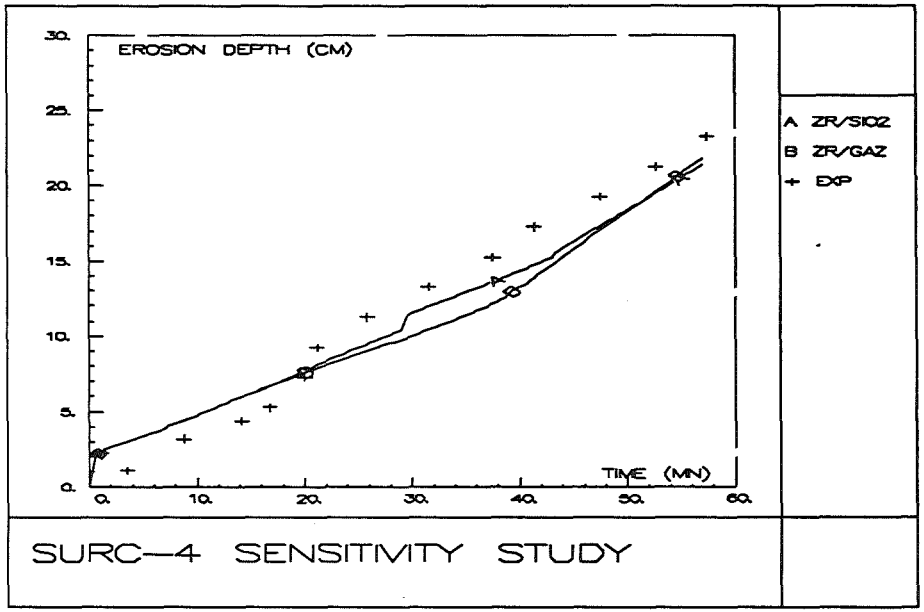

Figure 8

SURC2 Test

In SURC2 experiment, the corium was initially composed of oxides (UO_2, ZrO_2) with approximately 8% of Zr incorporated. The induction power was kept constant to 142 kW during 89 min and was then increased to 190 kW.

The WECHSL calculation was performed with both options of mixing (because the melt was essentially oxidic) and of condensed phase chemistry (since Zr was present in the melt).

The calculation showed a very large erosion rate (figure 10) during an initial period of 1 min (the heat transfer regime was the mixed mode). After this short period, the regime was calculated to be the film mode (crust thickness > 2.5 mm) and the ablation rate was then 10 cm/h. Due to power increase (89 min after the beginning of concrete erosion), the crust thickness decreased and the heat transfer regime turned to the more efficient mixed mode again (ablation rate of 15 cm/h). These results are in fairly good agreement with the experiment qualitatively and quantitatively.

In the calculation, crust growth lasted until 15 min (figure 11). After that, the crust thickness started to decrease continuously because the incorporation of concrete components into the melt lowered the solidus temperature. Crust remelting speeded up after the power was increased.

The calculation predicted that Zr was depleted very quickly during the initial stage of interaction. During this period, the ablation velocity was very large and the amount of concrete SiO_2 incorporated into the melt was sufficient to oxidize Zr entirely within 3 mn.

6. ANALYSIS OF ACE EXPERIMENTS

General remarks

The ACE program was funded by a large consortium of contributing organizations involving most countries having concern with nuclear energy and safety. The ACE Phase C experiments, devoted to corium-concrete interaction, were performed in ANL. Although the ACE Program was particularly oriented towards the study of the source term aspect of MCCI (aerosol and FP release), only the thermal-hydraulic aspects will be dealt with in this paper on purpose of WECHSL assessment.

The ACE test apparatus consisted of water panels (forming water-cooled refractory sidewalls) which enclosed the concrete basemat (50 cm * 50 cm) and the corium. This configuration only allowed the one-dimensional (vertical) melt propagation like SURC. Internal heat generation was supplied by direct electrical heating (tungsten electrodes). In contrast to BETA I, the molten pool (mixture of UO_2, ZrO_2 and small amounts of metals for an overall inventory of 300 kg typically) was representative of the corium in a postulated reactor meltdown accident.

For the assessment of the WECHSL code, 3 tests were selected in the ACE matrix : L5 with a fully oxidized corium, L2 with 70% of Zr initially oxidized, and L6 with only 30% of Zr oxidized. This subset of experiments was thought to be particularly relevant for the parametric study of Zr content influence.

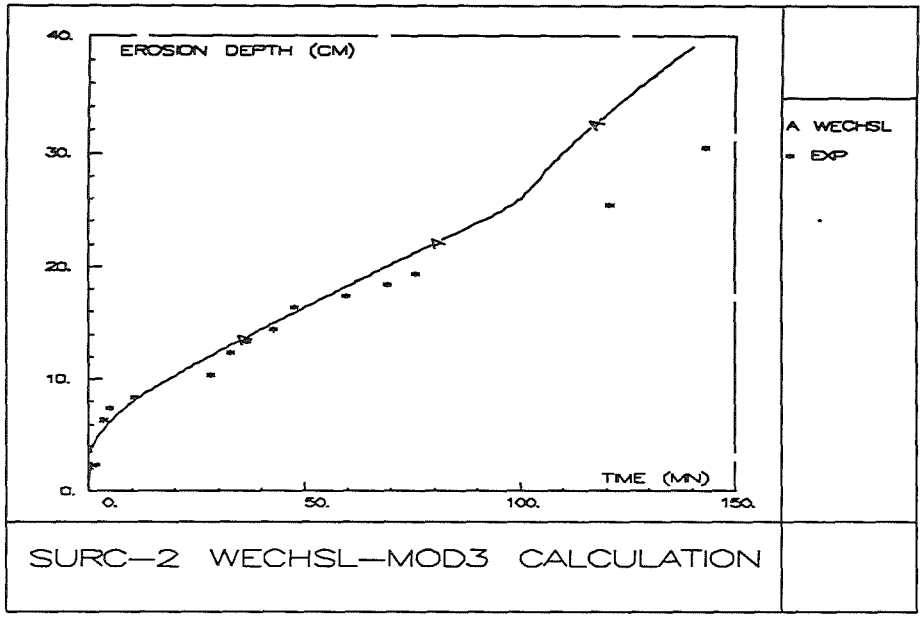

Figure 10

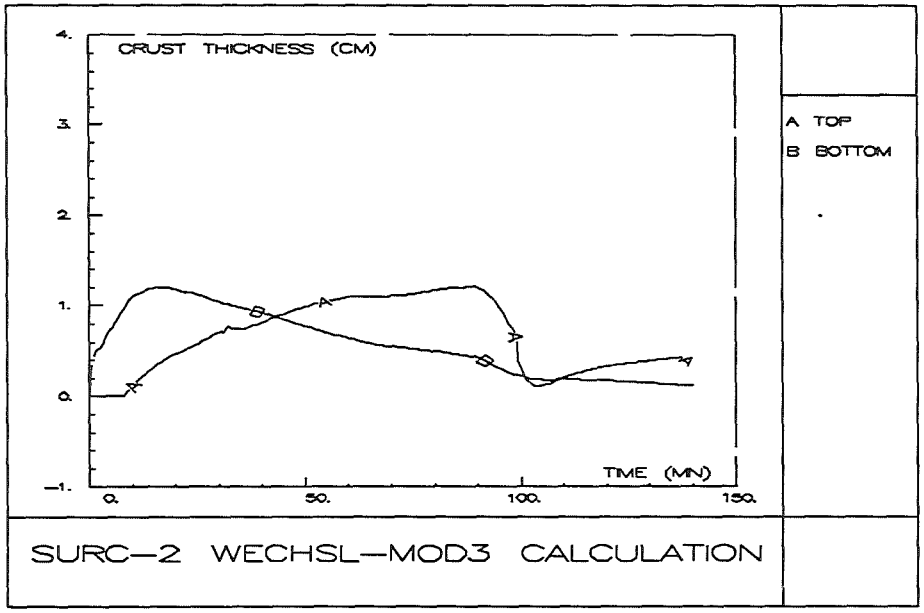

Figure 11

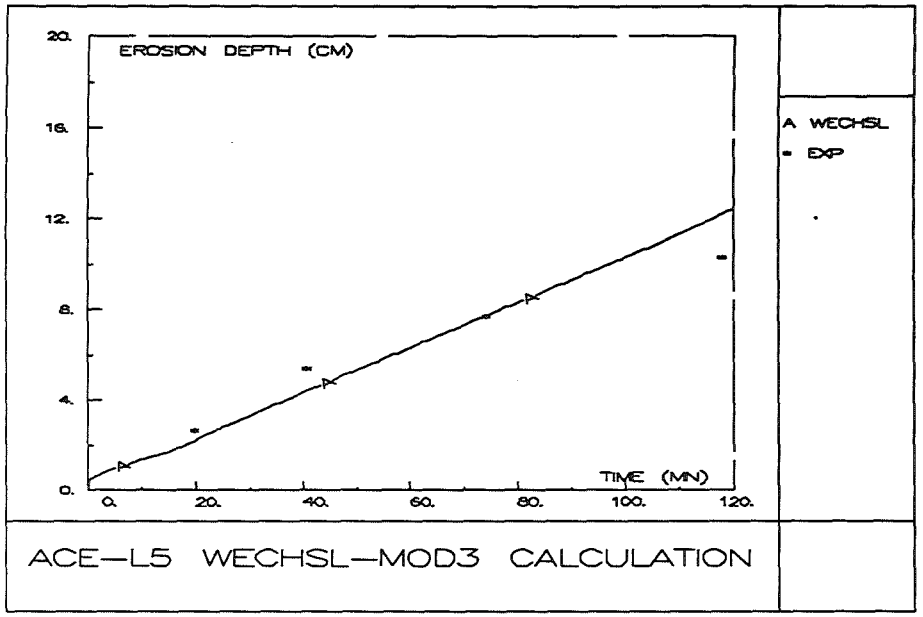

Figure 12

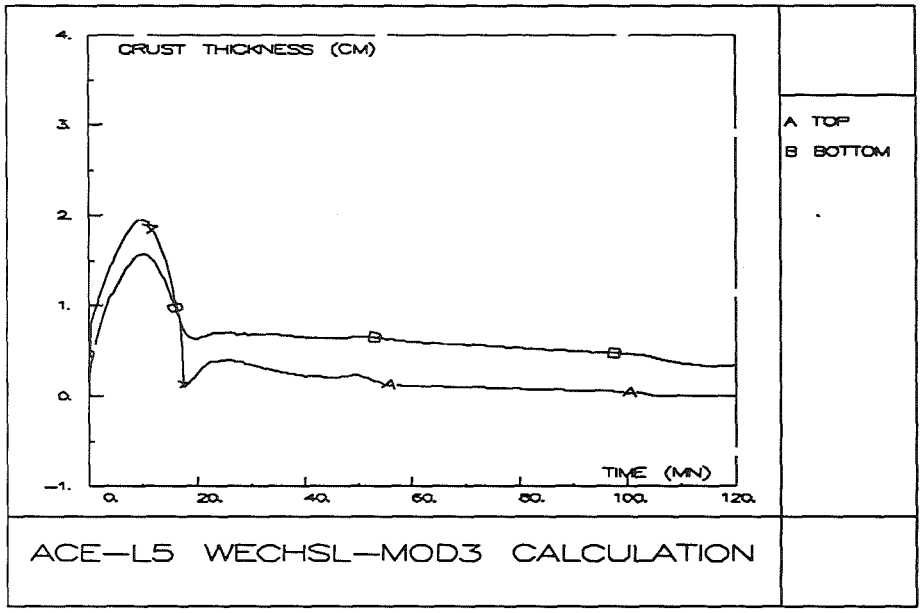

Figure 13

ACE Test L5

In L5 the basemat was made of limestone/common sand concrete. The net power to the melt (gross power minus side heat losses) was rather constant at 55 kW. L5 can be considered as a reference test because the melt was fully oxidic and chemistry did not play any significant role.

The calculation was performed using the standard options (no mixing, no condensed phase chemistry) since there was no metal in the melt.

The code predicted the formation of a thick crust at the bottom of the corium from the very beginning of the melt-concrete interaction (figure 13). This was because the initial temperature was relatively low (2000 K), only slightly above the solidus temperature determined by the code. Due to power increase (from initial 40 kW to 60 kW at 15 min), crust thickness began to decrease and finally stabilized. The calculated ablation rate kept then constant at a value of 6 cm/h. The predicted erosion depth was in close agreement with the data (figure 12).

ACE Tests L2 and L6

It is interesting to analyze the two tests L2 and L6 simultaneously because they were performed with similar conditions but with a different Zr metal inventory. In both tests the basemat was made of siliceous concrete and Zr was included in a so-called metal insert forming the top of the basmat (2 cm in L2 and 7 cm in L6). The average internal power was 102 kW for L2 and only 55 kW for L6. Two stages could be considered in L2 and L6 experiments : first the incorporation of the metal included in the insert and second the actual concrete ablation.

The same assumptions were made for the calculation of both tests L2 and L6 with the WECHSL code. Both mixing and condensed phase chemistry options were activated.

For L2 the code predicted that a crust formed from the beginning of ablation. This crust grew very rapidly and the the heat transfer regime was the film mode. The calculated ablation velocity was rather large equal to 22 cm/h due to the high power input. Later on the crust started to remelt and the mixed mode heat transfer regime was predicted to occur after 1700 s. Therefore concrete ablation speeded up. The final erosion was significantly overpredicted (22 cm at 40 min instead of 12 cm in the experiment, figure 14).

For L6 the calculated results showed a similar behavior as in L2 but the heat transfer regime was always the film mode because the input power was smaller and the crust thickness remained always greater than 2.5 mm (except during a very short initial period). In both calculations, the initial ablation rate was very large; in the experiment, it seems to have been rather small in contrast to SURC2. The Zr oxidation was predicted to be complete at the end of the metal insert ablation stage. Afterwards Si was oxidized by the gases (H_2O, CO_2) released by concrete decomposition. As in L6, the final erosion was overpredicted (25 cm at 80 min instead of 19 cm in the test, figure 15) but this overprediction appeared to be due to the calculation of the metal insert ablation stage. The duration of this phase was 2580 s in the experiment and only 610 s in the calculation. But the predicted erosion during the stage of concrete ablation was in good agreement with data.

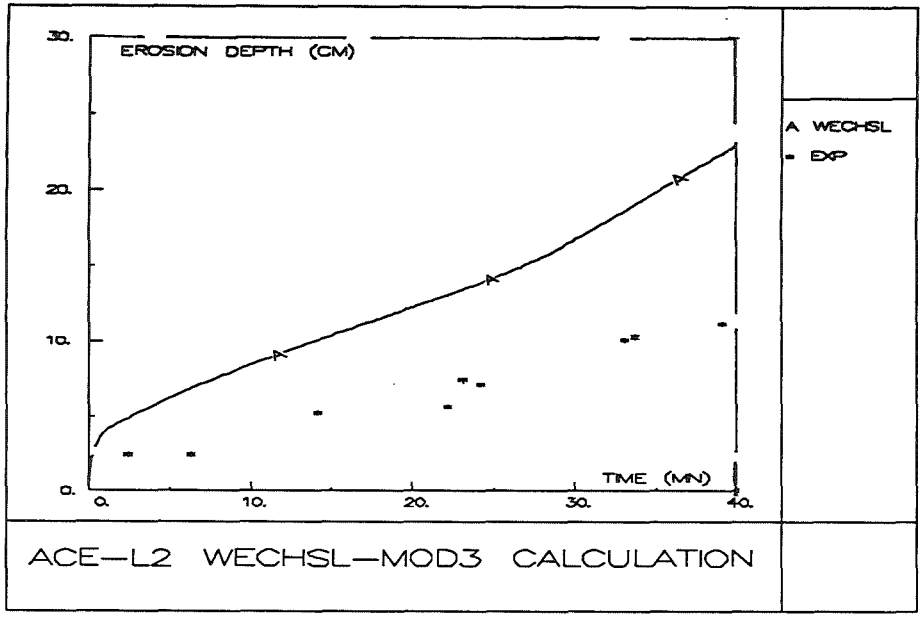

Figure 14

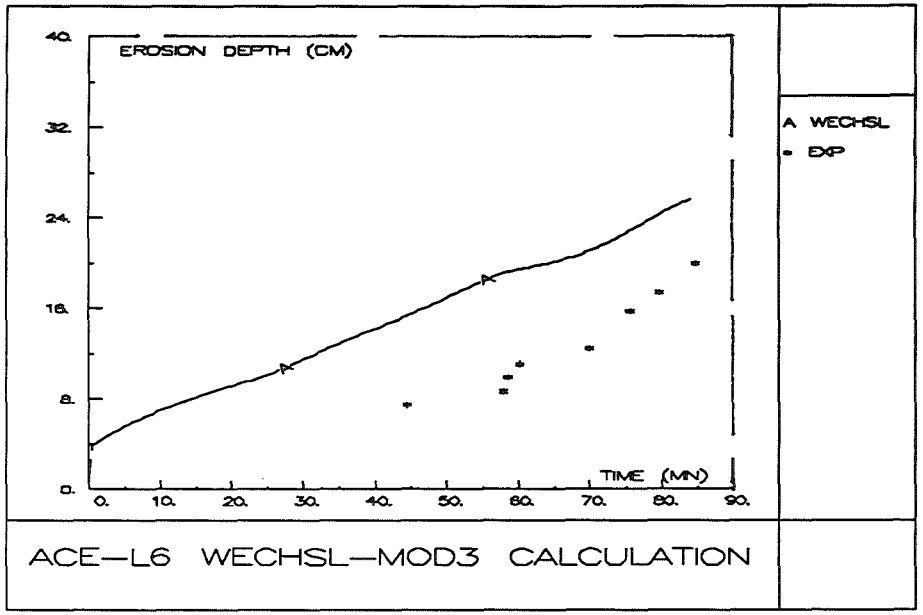

Figure 15

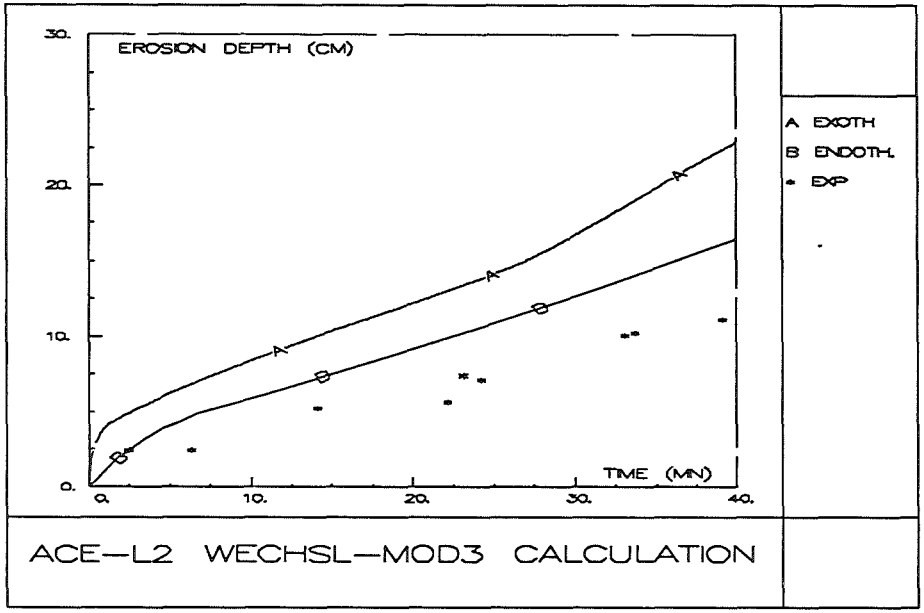

Figure 17

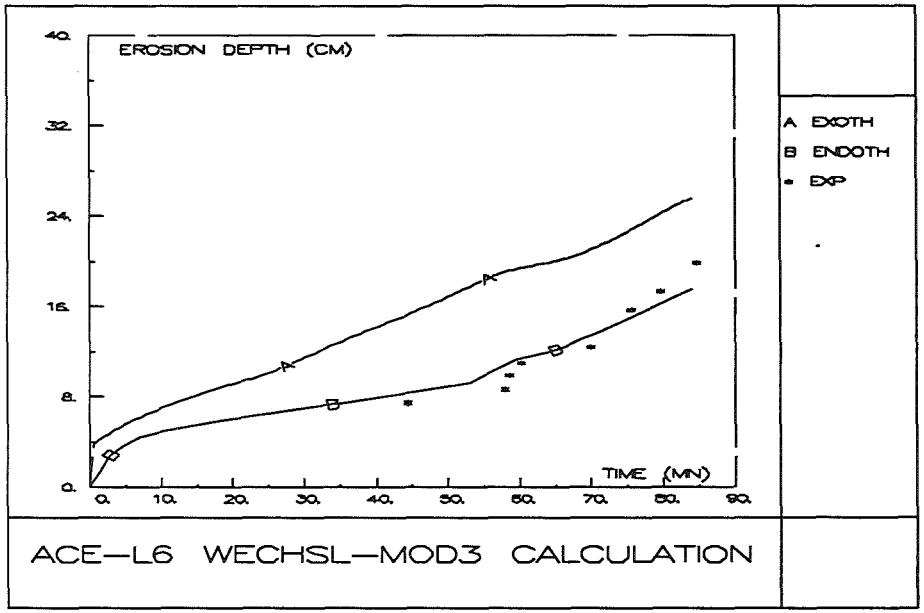

Figure 16

General discussion on L2 and L6

In order to explain the observed discrepancies between the calculations and the data for L2 and L6, the following possible causes have been raised :

- the calculation of liquidus/solidus temperatures,

- the modeling of Zr chemistry,

- the heat transfer models.

The calculations also showed a significant underprediction of melt temperature. Sensitivity calculations performed with increased solidus temperature produced a much smaller erosion for L6 in good agreement with the data. However there is no real physical basis for a high solidus temperature according to recent ANL liquidus/solidus data and to predictions with the GEMINI code.

In the range of measured melt temperatures in L2 and L6 (over 2100 K), the oxidation of Zr by SiO_2 must have been at least partially endothermic as mentioned in §2. The ablation depth calculated under the assumption of a complete endothermic oxidation of Zr is shown on figure 16 for L6. The agreement with data is then very satisfactory. Unfortunately the same assumption did not result in such a large improvement for L2 (figure 17).

The modeling of heat transfer between melt and concrete may also be questionable. Because of the low conductivity and high viscosity of oxides, a large temperature gradient is expected to exist between the melt bulk and the melt surface. This behavior should be properly taken into account and some more investigations are needed.

All these uncertainties on the modeling of the interaction of oxidic melts with concrete suggested to undertake a simple calculation of energy balance in L2 and L6 on the basis of experimental data on energy distribution. This analysis showed that energy balance could be closed for L6 but not for L2 using the same assumptions. Experimental uncertainties must be accounted for, but it seems that there could be some unconsistencies between L2 and L6 data. Particularly, the initial melt temperature and the starting time of interaction may not be fully reliable.

7. CONCLUSIONS

The code WECHSL-Mod3 has been assessed against a comprehensive set of experiments selected in the BETA, SURC and ACE test matrices. This assessment has shown that the code has a wide range of applicability in terms of corium composition, concrete type and internal power.

For high power conditions, it was confirmed that the code calculated BETA experiments quite well. Particularly, the rationale of heat transfer modeling in WECHSL according to gas superficial velocity and crust formation was found to be adequate to represent a large variety of physical conditions from liquid metal attack to crust dominated ablation. However corium composition was not realistic in BETA experiments (no UO_2, no ZrO_2) and extrapolation to reactor case could not be considered as reliable.

For lower power conditions and greatly oxidized coriums, the agreement between predictions and data was found generally satisfactory, especially for SURC tests and ACE test L5. However some discrepancies were noticed in the calculation of ACE L2 and L6 experiments. In a preliminary analysis, it was suggested that some unconsistency may have affected the data.

The modeling of the condensed phase chemistry appeared as a major contribution to the proper calculation of the tests where Zr oxidation took place. However, as mentioned earlier, there are still large uncertainties on the analysis of such experiments (ACE L2 and L6 especially). It will be fruitful to assess the WECHSL code against the recent BETA II experiments for which the initial content of Zr metal was large (V5.1, V5.2, V5.3).

It must be pointed out that the liquidus/solidus temperatures were estimated very roughly by the code and are probably questionable especially for the case of an oxide-concrete mixture. Up to now there was no clear evidence in the calculations that it was responsible for the observed discrepancies. However it will be interesting to recalculate the SURC2 and ACE experiments with more reliable data on the liquidus/solidus temperatures (cf the GEMINI-OXY5 code developed by THERMODATA).

8. REFERENCES

[1] C. RENAULT, J.J. FOIT
WECHSL-Mod3 Assessment Report.
To be published as a joint KfK-CEA report.

[2] M. REIMANN, S. STIEFEL
The WECHSL-Mod2 Code : A Computer Program for the Interaction of a Core Melt with Concrete including the Long Term Behavior. Model Description and User's Manual.
KfK Report, KfK 4477.

[3] M. REIMANN
Verification of the WECHSL Code on Melt-Concrete Interaction and Application to the Core Melt Accident.
Nucl. Eng. Des., 103, pp 127-137, 1987.

[4] B. SCHULZ
Thermal Conductivity of Composites.
Proceedings of the 1975 International Conference on Composite Materials, 2, pp 578-601, 1975.

[5] H. ALSMEYER
Containment Loadings from Melt-Concrete Interaction.
Nucl. Eng. Des., 117, pp 45-50, 1989.

[6] H. ALSMEYER
Recent Results from BETA/WECHSL Melt-Concrete Interaction.
International ENS/ANS Conference on Thermal Reactor Safety, Avignon, France, 1988.

[7] H. ALSMEYER and al
BETA Experimental Results on Melt/Concrete Interaction : Limestone Concrete Behavior.
Proceedings of the Committee on the Safety of Nuclear Installations (CSNI). Specialists' Meeting on Core Debris Concrete Interactions, February 1987.

[8] J.J. FOIT
Improved WECHSL Models including Zr Oxidation and its Verification by New BETA Experiments.
To be published in the same conference.

DEVELOPMENT AND VALIDATION OF CORCON-MOD3

David R. Bradley

Science Applications International Corporation
2109 Air Park Rd.
Albuquerque, NM 87106

ABSTRACT

CORCON-Mod3 is the next major version of the CORCON computer code. This version, which will be released in the near future, contains many model improvements over the previous version of the code, CORCON-Mod2. This paper briefly describes some of the most significant new features of the code, and then presents comparisons of CORCON-Mod3 predictions to the results of three experiments: the SURC-4 and SURC-1 experiments at SNL, and the ACE L6 experiment at ANL.

1. INTRODUCTION

The CORCON-Mod1 [1] and CORCON-Mod2 [2] computer codes were developed at Sandia National Laboratories (SNL) during the early to mid 1980's. At that time, there was little experimental data available upon which to base the phenomenological models in the codes. It should not be surprising then that CORCON-Mod1 and CORCON-Mod2 do not predict well the results from integral core-concrete interaction experiments performed at SNL, at Argonne National Laboratory (ANL), and at Kerfornschungszentrum Karlsruhe (KfK).

The vast body of experimental data now available from these integral experiments has allowed us to develop improved models for CORCON, and has led to the completion of a new version of the code, CORCON-Mod3 [3]. CORCON-Mod3 includes model improvements in many areas and includes several new models that were not present in the earlier versions of CORCON. In addition to these modeling improvements, CORCON-Mod3 provides the user with the capability to modify important models in the code through input.

This paper describes briefly some of the more important modeling improvements in CORCON-Mod3. This description is followed by comparisons of code predictions to the

results of three experiments: the SURC-4 [5] and SURC-1 [6] experiments performed at SNL, and the ACE L6 test [7] performed at ANL.

2. MODEL IMPROVEMENTS INCLUDED IN CORCON-MOD3

CORCON-Mod3 includes many significant improvements over the models available in CORCON-Mod2. Some of the more significant code improvements and model additions include:

- improved models for axial and radial heat transfer to concrete,
- addition of a model for condensed phase chemical reactions between the metallic and oxidic phases, and expansion of the chemical species list to include the products of such reactions,
- addition of models for interlayer mixing due to entrainment, and stratification due to settling of entrained droplets,
- inclusion of the VANESA model as a subroutine of CORCON,
- improved coolant heat transfer models, and
- addition of models for the activity coefficients of metal and oxide phase constituents.

These code modifications are discussed in greater detail below.

2.1 Modification of Melt-Concrete Heat Transfer Models

When CORCON was originally developed, a stable gas film was thought to exist at the core debris-concrete interface. Thus, heat transfer to the concrete was believed to be by a process analogous to film boiling. In the film boiling analog, heat transfer across the gas film is by a combination of radiation and convection. When CORCON calculations were subsequently applied to some of the early melt-concrete experiments, the code was found to significantly overestimate concrete ablation in some cases and significantly underestimate ablation in others. This discrepancy between the code predictions and experiment results was believed to be due to the heat transfer models in the code. Subsequent examination of the models and the available heat transfer literature resulted in major revisions to the code.

Our current concept of the processes controlling heat transfer is significantly different from what was originally believed. We now believe that there is no stable gas film at

the debris-concrete interface. Instead, there is intermittent direct contact between the core debris and the concrete surface. Gas is released from the concrete coincident with melting of the concrete surface. A layer of molten concrete grows and is periodically removed from the surface as gas bubbles depart. Depending on the temperature of the molten core material, thin crust layers may also form adjacent to the melting concrete. This layer of solidified core material also may be displaced from the surface and entrained by the rising bubbles. A model for these processes has been incorporated into CORCON-Mod3 [3,11]. In addition, our literature review yielded a better understanding of bubble-driven convection within the molten core debris. As a result, the convective heat transfer correlations in the code have also been revised.

The gas film model has been retained in the code as an alternative representation. The user may choose to use the gas film model at either the radial or axial melt-concrete interface.

2.2 Addition of Condensed Phase Chemistry

In the CORCON-Mod2, chemical reactions were assumed to occur only between the metallic phase of the core debris and gases released from the concrete. The SURC-4 experiment [5] and recent experiments with aluminum [8] have shown that metal-oxide reactions in the condensed phase are also important. This is particularly true when the core debris contains a reactive metal such as zirconium or aluminum, and the concrete has a relatively low gas content and a high silica content. In the SURC-4 experiment, the following chemical reaction was found to be important:

$$Zr + SiO_2 \rightarrow ZrO_2 + Si + 2.1 \text{ MJ/kg Zr}$$

If the user so desires, CORCON-Mod3 will calculate condensed phase chemical reactions between the metal phase of the core debris and oxides from concrete ablation. The code will also calculate condensed phase reactions between resident oxides and metals in a mixture layer.

2.3 Implementation of Interlayer Mixing Models

We have developed an interlayer mixing model for CORCON-Mod3 based on the mechanistic models developed by Greene at BNL [9]. The model calculates mixing due to entrainment of a layer into the less dense layer above it, and then calculates deentrainment (i.e., settling) of the suspended droplets in the mixture.

The code first determines whether entrainment is possible. Based on the mixing work by Greene, two entrainment criteria were selected: the ratio of the densities of the two layers must be less than 3, and the bubble volume must exceed a critical value for entrainment. If both conditions are met, the entrained droplet volume per bubble is calculated using an entrainment correlation developed by Greene. Given the superficial gas velocity through the surface and the bubble volume, the number of bubbles per unit area per unit time (i.e., the bubble flux) is determined. Since each bubble has associated with it an entrained droplet of a known volume, the entrainment mass flux can be calculated. Multiplying the entrainment mass flux by the interfacial area and time step gives the mass entrained during the time step. This mass and its associated enthalpy are transferred into the mixture layer.

CORCON-Mod3 also calculates deentrainment due to droplet settling. The droplet settling velocity is calculated using the droplet drag coefficient correlations proposed by Greene. These correlations follow the drag curve for spherical droplets until a critical value for the settling velocity is reached. At this critical settling velocity, droplet oscillations were observed by Greene and the drag coefficient was observed to increase dramatically. The code iterates to determine a consistent droplet settling velocity and drag coefficient. Given this settling velocity, the droplet size, and the volume fraction of droplets in the mixture layer, the mass flux of settling droplets is easily calculated.

Two mixture layers are possible: a mixture of "light" oxide with suspended metal droplets, or a mixture of metal with suspended "heavy" oxide droplets. Mixture layers are created in two ways. First, mixture layers can be created by entrainment of one layer (the denser of the two) into the other. Mixture layers are also created when an overlying layer becomes more dense than the layer below it. In this case mixing is assumed to occur instantaneously (i.e., during a single calculation timestep). In CORCON-Mod2 the latter situation was handled by assuming that a "layer flip"

occurred; in other words, the denser oxide layer was assumed to migrate through the metal layer and combine with the overlying oxide layer.

In CORCON-Mod3, the user may choose to begin the calculation with a stratified melt configuration or with a fully mixed pool. The user can also select whether or not the code will perform the mixing calculation. Hence, the user can begin the calculation in a fully mixed configuration and then allow the code to calculate deentrainment and re-entrainment, or the user can force the melt to remain mixed. Similarly the user can select to begin the calculation with a stratified melt, and then allow the code to calculate entrainment and deentrainment, or he can force the melt to remain stratified.

2.4 Inclusion of VANESA as a Subroutine of CORCON-Mod3

The VANESA computer code [4] was developed to model radionuclide release during core debris interactions with concrete. In the past, coupled CORCON/VANESA calculations have been performed by running CORCON and VANESA in series. First, CORCON would be run, and the results needed by VANESA would be written to a file. Next, VANESA would be run using the results from the CORCON calculation. This approach neglected much of the feedback inherent in the phenomena modeled by the two codes.

VANESA is now included as a subroutine of CORCON-Mod3, and is called during every timestep. From CORCON, VANESA obtains the current melt composition, composition of gas exiting the melt, bubble properties, and the thermophysical properties of the melt. VANESA then calculates aerosol generation due to vaporization/condensation and due to mechanical processes. In CORCON, energy associated with the released aerosols is then subtracted from the total energy of the melt. If radionuclides are released, the decay power generation in the melt is reduced appropriately.

2.5 Coolant Heat Transfer Modifications

CORCON-Mod2 models the full boiling curve. The code includes the effects of pressure and coolant subcooling on nucleate boiling heat transfer. It also includes the effects of pressure on film boiling heat transfer. In most applications, CORCON-Mod2 predicts heat transfer by film boiling since the surface temperature of the core debris remains

well above the film collapse temperature (i.e., Leidenfrost point).

CORCON-Mod2 neglects two potentially important effects on film boiling heat transfer: the effects of coolant subcooling, and the effects of noncondensable gas injection. Both effects can lead to a significant increase in the film boiling heat flux, and can also lead to film collapse (i.e., transition to nucleate boiling) at higher surface temperatures. The effects of coolant subcooling and noncondensable gas injection have been included in CORCON-Mod3.

2.6 Addition of Non-Ideal Chemistry Models

For the sake of computation time, CORCON-Mod3 uses a relatively simple representation of the chemistry of the core debris. This is probably adequate if the only concern is flammable gas generation or chemical energy addition. However, for the evaluation of aerosol generation and radionuclide release, a more detailed representation is needed.

In order to treat the complex chemical reactions that occur in real core melts, we have implemented activity coefficient models for the metallic and oxidic phases. A subregular solution model has been adopted for the metallic phase, while an associated solution model has been adopted for the oxidic phase. The calculated activity coefficients are used in the VANESA subroutine to adjust the chemical activity of the condensed phase species.

The chemical interactions between species are modeled using binary interaction parameters that are determined from the relevant binary phase diagrams. CORCON-Mod3 contains a complete set of binary interaction parameters for the metallic phase. Work is now underway to determine the interaction parameters for the oxide phase. This work should be completed by the time CORCON-Mod3 is released later this year. (A more detailed discussion of the activity coefficient models is provided in a companion paper by Powers [10].)

2.7 Other Model Improvements

The chemistry equilibrium solver in CORCON-Mod2 predicts formation of condensed carbon during reactions between carbon dioxide and reactive metals such as zirconium. This reaction is referred to as carburization or coking in the metallurgical industry. Though predicted by the code, carburization has not been observed to a significant extent in any of the melt-concrete experiments to date. Therefore, in CORCON-Mod3 we have provided the user with the option of disabling carburization through specification of an input flag.

With the implementation of interlayer mixing models and the inclusion of VANESA as a subroutine of CORCON, it became necessary to improve the bubble behavior models in the code. Improved models have been implemented for the bubble size, bubble rise velocity, and void fraction of the melt.

CORCON-Mod3 provides the user with the capability to modify many of the important models and parameters in the code through input. The user may, for example, specify alternate heat transfer models for convective heat transfer within the bulk melt. The user also may modify the boiling curve or change the film collapse temperature. Currently, twenty-six different models and parameters can be modified by the user.

3. VALIDATION OF CORCON-MOD3 BY COMPARISON TO EXPERIMENTS

This section describes validation of CORCON-Mod3 through comparisons to three experiments: the SURC-4 and SURC-1 experiment at SNL, and the ACE L6 experiment at ANL. These comparisons focus primarily on the thermal-hydraulic models in the code. Comparisons for aerosol generation and radionuclide release are provided when reliable aerosol generation and radionuclide release data are available.

3.1 Comparisons to the Results of the SURC-4 Experiment

The SURC-4 experiment [5] was designed to investigate the effect of zirconium metal on the interaction of molten stainless steel with a siliceous concrete. The charge in SURC-4 consisted of 200 kg of stainless steel along with 6 kg of fission product simulants. Twenty kilograms of zirconium was added to the melt after concrete

ablation had begun. The 40 centimeter diameter crucible used in the SURC-4 experiment had refractory oxide (MgO) sidewalls and a basaltic concrete basemat. This type of concrete releases very little gas when heated (approximately 6 w/o H_2O and 2 w/o CO_2), and has a high silica content (approximately 55 w/o).

The crucible was enclosed within a water-cooled aluminum containment vessel that was purged with argon during the test. Gases and aerosol exited the crucible through a flow tube flanged to the top of the containment vessel. The test was instrumented to measure concrete ablation, melt temperature, gas generation, gas composition, aerosol concentration, and sidewall and upward heat losses.

During the experiment, the steel charge was melted in place within the interaction crucible. Concrete ablation was first detected after approximately 105 minutes of induction heating. After 119 minutes and approximately 5 centimeters of concrete ablation, 20 kg of zirconium metal was added to the molten steel. Approximately 5 minutes later, a cooling line failed and the power supply tripped off line. The line was quickly repaired and induction heating was resumed. The power was held constant for the remainder of the test. The average net power to the steel during the test is estimated to be 64 kW. Average heat losses through the sidewalls of the crucible are estimated to be 29 kW.

Examination of the crucible following the test showed that the oxidic layer of the melt had foamed at some time during the test. Based on experience with an earlier scoping test, foaming is believed to have occurred soon after zirconium addition to the melt. The foam insulated the upper surface of the metallic melt and efficiently trapped aerosols released from the melt.

To simulate the one-dimensional melt-concrete interaction in SURC-4 using the inherently two-dimensional CORCON code, it was necessary to minimize the effect of radial interactions. This was accomplished by artificially increasing the radial dimension of the crucible to 10 meters. By doing this, the area of concrete sidewall exposed to the melt became small relative to the basemat concrete surface. To compensate for the expansion in the radial dimension, all masses and input powers were scaled by the area (or volume) ratio. The scale factor for the SURC-4 test is 314.16 m^2/0.1257 m^2 or 2500.

The input power used in the CORCON simulation was determined by subtracting sidewall heat losses from the net induction power supplied to the steel. Sidewall heat losses were determined by multiplying the sidewall heat flux (reported in Reference 5) by the estimated sidewall surface area exposed to the melt. The net induction power was determined by multiplying the gross power to the induction coil by the measured induction heating efficiency. These values are also reported in Reference 5.

The temperature of the steel melt was assumed to be 1760 K at the onset of the melt-concrete. This is approximately the temperature measured by the thermocouples embedded in the concrete soon after the onset of ablation. Zirconium was assumed to be added to the melt over a period of 90 seconds and at an initial temperature of 2000 K. The assumed zirconium addition period accounts for the time required to dissolve the solid Zr slugs in the steel melt. The assumed initial temperature accounts for the exothermic heat of solution of zirconium in iron. The temperature of the surfaces above the melt was determined from the thermocouples in the MgO wall. To account for the insulating effect of the overlying foam, the emissivity of the surroundings was reduced to 0.01 following zirconium addition.

The calculation was performed using the new melt-concrete heat transfer models, and with the condensed phase chemical reactions enabled. Since foaming of the oxide phase prevented significant interlayer mixing, the mixing models in the code were not activated.

Figures 1 and 2 show a comparison of the calculated and experimental results for concrete ablation distance and melt temperature. As the figures illustrate, CORCON-Mod3 accurately predicts (i.e., within the error of the experiment measurements) both the ablation distance and the melt temperature. Particularly significant is the close comparison between the calculated and experimental melt temperature following zirconium addition. We feel that this demonstrates quite clearly that the heat transfer models in the code are accurate for metallic melts, and that the treatment of condensed phase chemistry is correct.

The aerosol and flow system became plugged by the foam soon after zirconium addition. For that reason, aerosol results are available only for the period prior to Zr addition. During this period, CORCON-Mod3 appears to overpredict the aerosol

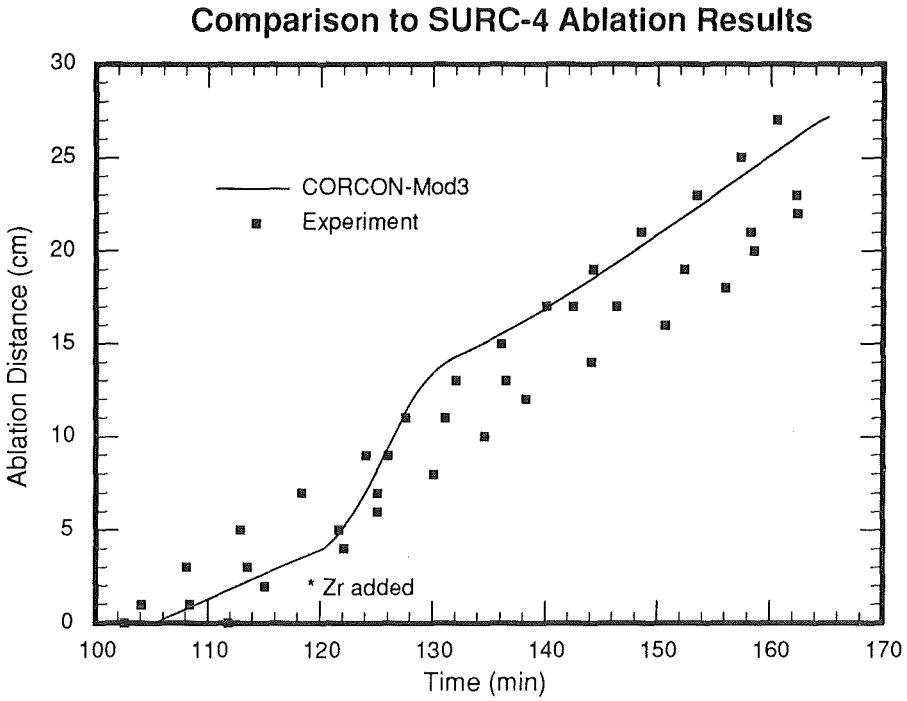

Figure 1. CORCON-Mod3 Comparison to SURC-4 Ablation Results

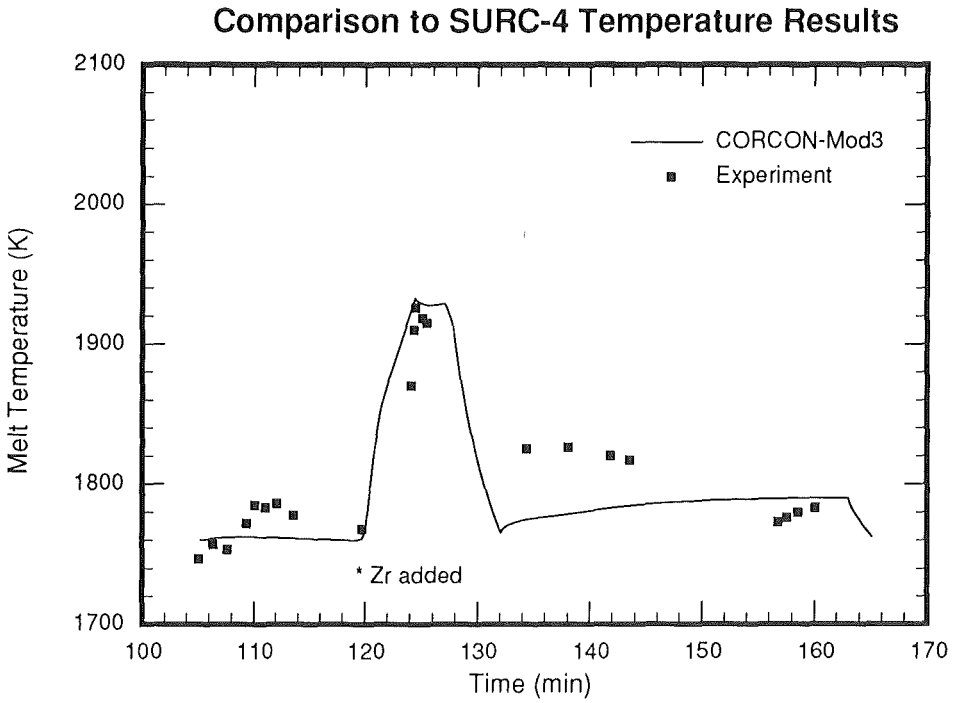

Figure 2. CORCON-Mod3 Comparison to SURC-4 Melt Temperature Results

concentration by a factor of 2 to 6. However, the experiment measurements are likely to be less than the actual aerosol concentration since not all of the aerosol is transported to the aerosol sampling location. Some aerosol is trapped within the containment vessel, while other aerosol is deposited in the piping upstream of the sampling location. Hence, the actual differences between the code predictions and the experiment results are probably much smaller.

Aerosols sampled during the initial interaction period were found to be rich in tellurium (50 to 70 w/o), with significant concentrations of potassium, sodium, and silicon from the concrete (3 to 10 w/o). Cerium and molybdenum were found at concentrations of between 0.1 and 0.02 w/o. Barium and lanthanum concentrations were below detectable limits (< 0.02 w/o). CORCON-Mod3 underpredicted the tellurium content of the aerosols by a factor of 2, while it overpredicted the concentrations of the concrete oxides by a factor of 2 to 4. The cerium content of the aerosols was underpredicted by a factor of 4, while the molybdenum content was underpredicted by 5 to 6 orders of magnitude. The barium content of the aerosol was overpredicted by a factor of 10 or more. The predicted lanthanum content of the aerosols was always less than 0.02 w/o. The errors in molybdenum and barium release are significant, and point to deficiencies in the code. The higher molybdenum release in the experiment is believed to be due to the formation of volatile compounds that are not currently treated in the VANESA model. When these compounds are identified they will be added to the code. The lower release of barium in the experiment is believed to be due to formation of stable (non-volatile) silicate and zirconate compounds. These compounds will be accounted for when the activity coefficient models for the oxide phase are fully implemented.

3.2 Comparisons to the Results of the SURC-1 Experiment

The SURC-1 experiment [6] used basically the same design as the SURC-4 experiment with a few notable exceptions. First, the charge in the SURC-1 test was composed of a mixture of UO_2 (63 w/o), ZrO_2 (27 w/o), and Zr (10 w/o). The charge included also 3.36 kg of oxidic fission product simulants. Because the oxide charge does not couple efficiently to the induction power supply, five tungsten rings were embedded within the charge. The tungsten rings are heated by the induction power supply, and then transfer heat to the oxide. The SURC-1 experiment used a concrete with a limestone

coarse and fine aggregate. Because this type of concrete has a high carbonate content, it releases a substantial amount of carbon dioxide when heated.

The charge was heated in place within the interaction crucible. After 130 to 140 minutes of heating, concrete ablation was detected. Initially, the ablation rate was quite rapid as the zirconium metal in the charge was oxidized. After the zirconium was completely oxidized, the ablation rate decreased significantly. After about 40 minutes of this rather benign interaction, the induction power was increased by about 30%, and a more vigorous interaction ensued.

Examination of the interaction crucible after the tests showed that not all of the 200 kilograms of the charge had participated in the interaction with the concrete. A significant portion of the charge had either not melted or had collected above two tungsten rings that had become pinned to the sidewalls by solidified oxidic material. It is estimated that only 110 kg of the initial charge had interacted with the concrete during the tests.

As in the SURC-4 simulation, the SURC-1 simulation used a crucible radius that was artificially set to 10 meters in order to reduce the effect of radial melt-concrete interactions. All masses and input powers were then scaled up by a factor of 2500. The charge mass was reduced to account for the material that did not participate in the interaction. The masses of the fission product simulants were not reduced since the fission products were placed at the bottom of the charge and would have been completely incorporated into the melt.

In the SURC-1 simulation, it was assumed that 110 kg of the original oxide charge participated in the interaction. The input power to the melt was calculated assuming that 60 percent of the available power (i.e., 3 out of 5 rings) was supplied to the melt interacting with the concrete. Sidewall heat losses were determined by multiplying the sidewall heat flux reported in Reference 6 by the estimated sidewall area exposed to the melt. The net power input used in the calculation was then determined by subtracting the sidewall losses from the power to the melt. The upper surface of the melt was treated as an adiabatic boundary since heat losses were blocked by the presence of a heated overlying crust. There may, in fact, have been some heating of the melt by the overlying crust since the temperature of the melt decreased during the

test, while the upper solid material remained hot.

The calculation was performed using the new melt-concrete heat transfer models. The melt was assumed to remain fully mixed, with the metallic zirconium dispersed in the oxide. Since chemical reactions between the core debris and the gases from the concrete are dominant for interactions with limestone concrete, condensed phase chemical reactions were disabled. The coking reaction was also disabled in the SURC-1 simulation.

Figures 3 and 4 show a comparison of the calculated and experimental results for concrete ablation distance and melt temperature. In general, concrete ablation is predicted well by the code. The most significant differences are during the early ablation phase when zirconium oxidation controls the interaction. In the calculation, we assumed that 45% of the available zirconium metal was held up within the unmelted oxide layer in the upper portion of the crucible. It is possible that this material melted and migrated downward into the molten oxide. If so it would have greatly increased concrete ablation during the initial interaction phase. The temperature of the oxide melt is predicted fairly well by the code. Early in the calculation, the melt temperature is underpredicted by 100 K or less, while late in the calculation, the melt temperature is overpredicted by approximately the same amount. (It should be noted that the temperatures plotted in the figure were from thermocouples that may have been above the melt surface at the end of the test. The measured values are probably not representative of the temperature of the melt.)

During the initial interaction phase, the code predicts an aerosol concentration of between 400 and 700 g/m^3 (STP), while the measured aerosol concentration during this period was 120 to 200 g/m^3. The actual aerosol concentration during the test is likely to have been higher than the measured values since not all of the aerosol was transported to the sampling location. A significant fraction of the aerosol was trapped within the containment vessel or became deposited upstream of the sampling point. We feel that the code predictions are probably within a factor of two of the actual concentration in the experiment. Late in the experiment, the aerosol concentration was measured to be approximately 40 g/m^3. This compares well with the calculated concentration of 33 g/m^3 (STP).

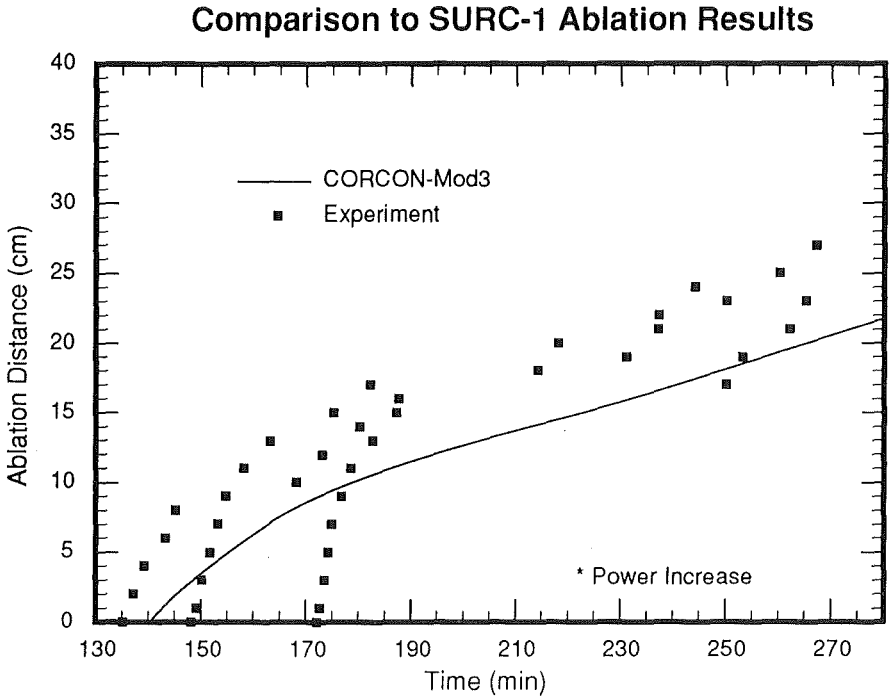

Figure 3. CORCON-Mod3 Comparison to SURC-1 Ablation Results

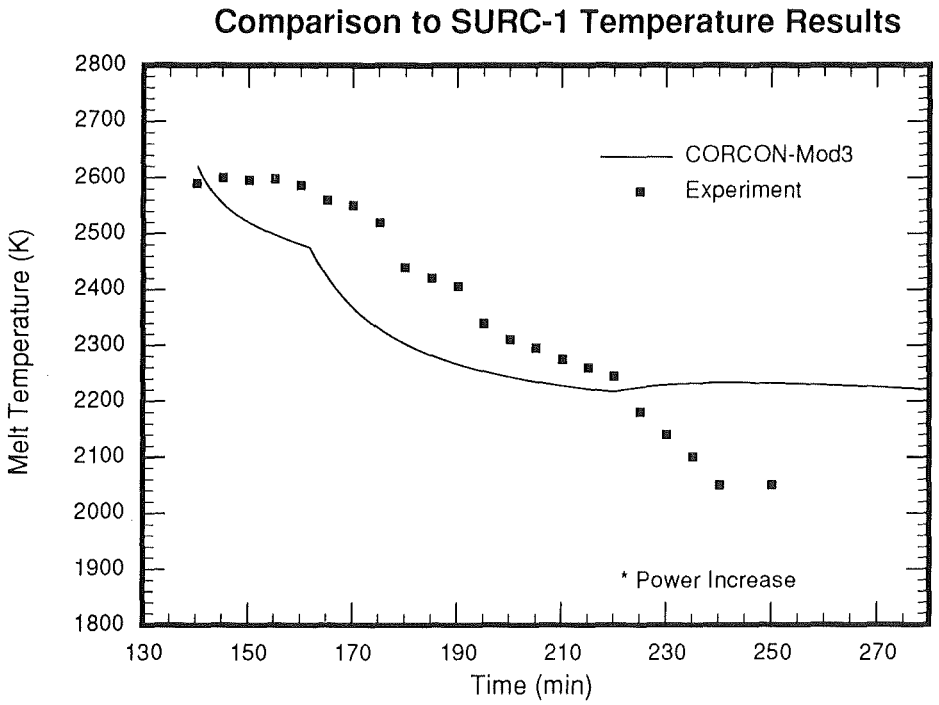

Figure 4. CORCON-Mod3 Comparison to SURC-1 Melt Temperature Results

The aerosols collected in the experiment were found to contain mostly magnesium, potassium and silicon from the concrete. This was true also of the CORCON simulation. In general, the composition of these three constituents was well predicted by the code. Barium, cerium, and lanthanum release were overpredicted by approximately a factor of 5. Again, this is likely to be due to the formation of stable compounds (in this case, zirconates) that are not considered in VANESA. This deficiency should be corrected when the oxide phase activity coefficient models are fully implemented in the code. As in the SURC-4 comparison, molybdenum release was underpredicted by several orders of magnitude.

3.3 Comparisons to the Results of the ACE L6 Experiment

The ACE L6 experiment [7] was designed primarily to study radionuclide release during melt-concrete interactions, though measurements of concrete ablation, melt temperature, and gas release were also made. The ACE L6 experiment used a predominantly oxidic mixture containing UO_2, ZrO_2, and siliceous concrete. The charge also contained approximately 5 kg of fission product simulants. Metallic zirconium and stainless steel were incorporated into the siliceous concrete basemat, and entered the melt gradually as the concrete ablated. The zirconium was included in the first layer of concrete (referred to as the concrete/metal insert). This layer included 24 kg of Zr, 9.1 kg of stainless steel, and 22.4 kg of siliceous concrete. Below the concrete/metal insert was the siliceous concrete basemat. The basemat contained 2.85 kg of reinforcing rod placed at 5.1 cm and 10.2 cm below the surface.

The interaction crucible used in the ACE tests had an internal cavity with a nearly square cross-section measuring 50.2 cm by 49.2 cm. Two walls of the crucible were water cooled tungsten cooling panels. The other two walls of the crucible were water cooled tungsten electrodes. The tungsten electrodes were used to melt and sustain the oxidic charge by direct electrical heating. Because the walls are water cooled, wall heat losses are easily determined from the increase in the temperature between the water inlet and outlet. The power supply voltage was controlled during the tests to maintain an approximately constant net power to the charge. (Here, net power is defined as total input power minus sidewall losses). During the experiment, the voltage was adjusted to maintain the net power to the charge at approximately 75 kW.

The ACE L6 charge design complicates the CORCON simulation of the experiment since the initial interaction is with an atypical "concrete" composed of 60 w/o metal. To account for this it was necessary to perform the calculation in two phases. In the first phase, the interaction is with the concrete/metal insert. To model this phase, we modified the code so that the user could specify the composition of the "rebar". (Previously, CORCON assumed that the rebar was composed entirely of iron.) The concrete/metal insert was assumed to ablate at a temperature of 2000K. The insert ablation phase was assumed to continue for 43 minutes, which was the duration observed in the experiment. The melt composition and temperature at the completion of the first calculation were then used as input to the calculation of the basemat ablation phase. The basemat ablation phase was assumed to continue for 40 minutes.

As in the two SURC simulations, the one-dimensional concrete ablation in the ACE L6 experiment was simulated in CORCON-Mod3 by expanding the radial dimension of the concrete cavity to 10 meters. All masses and input powers were scaled by the ratio of the assumed cavity area (314.15 m^2) to the actual cavity area (0.247 m^2). (Note that the cavity area was not reduced by the oxide crust lining the tungsten walls. A uniform 1.5 cm crust would reduce the cavity area to 0.218 m^2, and increase the net power in the calculation by 13%.)

Figures 5 and 6 compare the calculated and experimental concrete ablation distance and melt temperature for the ACE L6 experiment. As shown in Figure 5, ablation during the insert ablation phase is underpredicted by approximately 30 % (4.7 cm vs. 7 cm), while ablation during the basemat ablation phase is underpredicted by 25 % (9.7 cm vs. 12.5 cm). These differences can be explained, in part, by noting that the actual interaction area in the experiment was less than was assumed in the calculation. Hence, the net power in the calculation should have been greater. With this effect considered, the calculated ablation is likely to be 20 to 25 % less than the measured value. This difference is within the uncertainty attached to the melt-concrete heat transfer models [11].

The calculated melt temperature is significantly less than the measured values during most of the calculation. During the insert ablation phase, the differences are as large as 200 K. Part of this difference is attributed to uncertainty in the modeling of insert ablation. The calculation assumed an ablation temperature of 2000 K during the insert

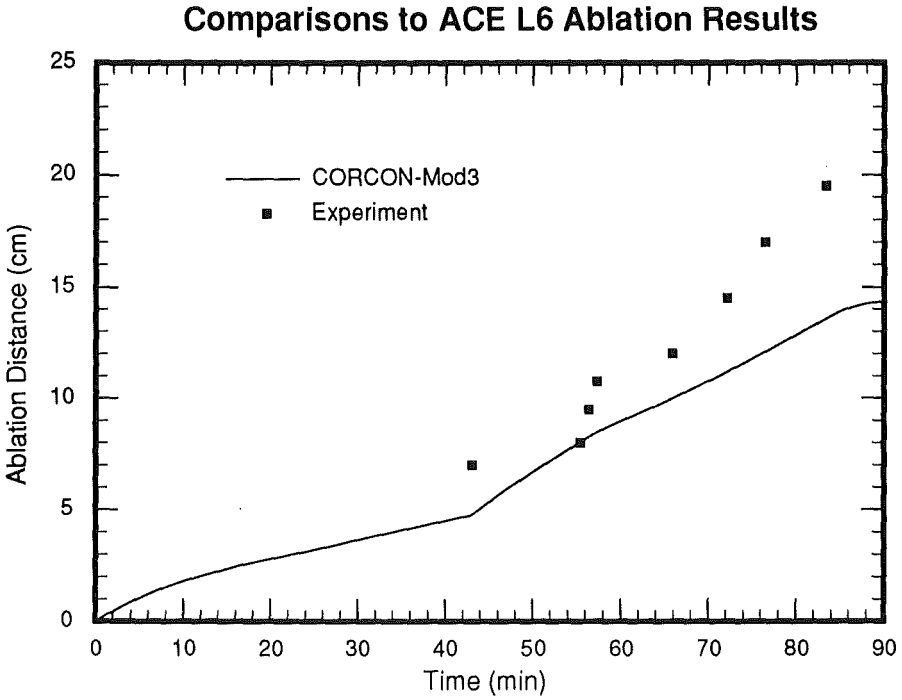

Figure 5. CORCON-Mod3 Comparison to ACE L6 Ablation Results

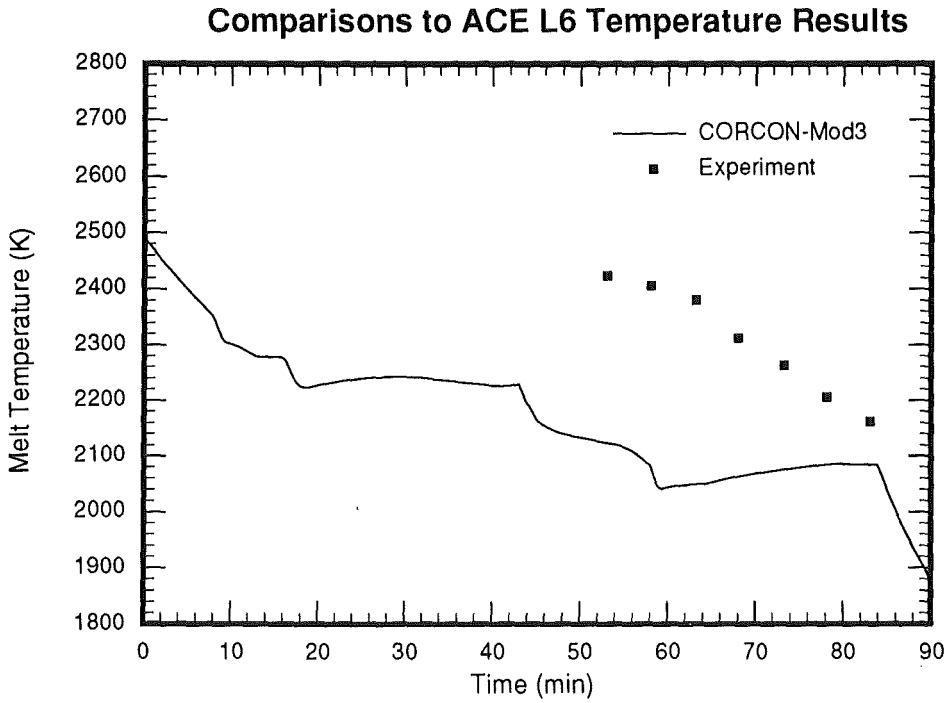

Figure 6. CORCON-Mod3 Comparison to ACE L6 Melt Temperature Results

ablation phase. Perhaps a higher ablation temperature would have been more realistic. A higher ablation temperature would lead to higher melt temperatures during the insert ablation phase. The differences between the calculated and experimentally measured melt temperatures are even greater during the basemat ablation phase, with differences as large as 350 K soon after the start of basemat ablation. The magnitude of this difference and the general consistency of this result with the SURC-1 comparison points toward a possible error in the modeling of heat transfer from oxidic melts. Another explanation is that the viscosity of the oxide mixture may be significantly greater than is currently predicted by the code. (Convective heat transfer is much less efficient when the melt viscosity is high.) Support for this hypothesis is provided by the results from recent experiments at ANL [12]. Other explanations are, of course, possible. As CORCON-Mod3 is applied to an increasing number of experiments with oxide melts, the need for model improvement should become clearer.

The ANL experimenters have reported radionuclide release results in terms of the fractional release from the melt [13]. Table 1 compares the calculated and experimental release fractions for several of the more important fission product simulants. As the table shows, the release fractions are, for the most part, predicted to within a factor of 6. The exceptions to this are the releases of molybdenum and ruthenium which are significantly underpredicted by the code. The predictions of barium, strontium, cerium, and lanthanum release should improve when implementation of the oxide phase activity coefficient model is completed.

Table 1.

Comparison of Calculated and Experimentally Determined Release Fractions

Radionuclide	Experiment Release Fraction	Calculated Release Fraction
Te	0.63	0.999
Mo	0.0053	3.0×10^{-7}
Ru	0.002 (max) 6.0×10^{-6} (min)	1.3×10^{-6}
Sr	0.002	0.012
Ba	0.0017	0.0063
Ce	0.0005 (max) 5.6×10^{-6} (min)	0.00115
La	6.0×10^{-4} (max) 1.6×10^{-5} (min)	1.56×10^{-4}

4. SUMMARY AND CONCLUSIONS

The CORCON-Mod3 computer code contains many significant improvements over the previous version of CORCON, CORCON-Mod2. This paper has provided a brief description of the major model improvements included in the code, and has presented comparisons of CORCON-Mod3 predictions to the results of the SURC-4, SURC-1, and ACE L6 experiments. Based on these comparisons we conclude that the code accurately models heat transfer from metallic melts. The comparisons for oxidic melts were not as good, and may point toward the need for further model improvement. We will be better able to judge the need for code improvement following additional comparisons to the results of experiments with oxidic melts. Such comparisons are planned as part of the ongoing CORCON-Mod3 validation effort.

In general, the code was found to predict radionuclide release within an order of magnitude of the measured values. This was not true, however, of molybdenum and ruthenium release, which were underpredicted by several orders of magnitude. This discrepancy is attributed to neglect of volatile, and as yet unidentified, molybdenum and ruthenium compounds. The releases of barium, strontium, cerium, and lanthanum

were consistently overpredicted by the code. We attribute this to formation of stable silicate and zirconate compounds in the melt. CORCON-Mod3 will implicitly treat these compounds when the activity coefficient model for the oxide phase is fully implemented.

REFERENCES

1. J. F. Muir, et al., CORCON-MOD1: An Improved Model for Molten-Core/Concrete Interactions, SAND80-2415, Sandia National Laboratories, Albuquerque, NM, 1981.

2. R. K. Cole, et al., CORCON-Mod2: A Computer Program for Analysis of Molten-Core Concrete Interactions, SAND84-1246, NUREG/CR-3920, Sandia National Laboratories, Albuquerque, NM, 1981.

3. D. R. Bradley, and D. R. Gardner, CORCON-Mod3: An Integrated Computer Model for Analysis of Molten Core-Concrete Interactions - Users' Manual, NUREG/CR-5843, SAND92-0167, Sandia National Laboratories, Albuquerque, NM, March 1992 (draft for comment).

4. D. A. Powers, J. E. Brockmann, and A. W. Shiver, VANESA: A Mechanistic Model of Radionuclide Release and Aerosol Generation During Core Debris Interactions with Concrete, NUREG/CR-4308, SAND85-1370, Sandia National Laboratories, Albuquerque, NM, July 1986.

5. E. R. Copus, et al., Core-Concrete Interactions Using Molten Steel with Zirconium on a Basaltic Basemat: The SURC-4 Experiment, NUREG/CR-4994, SAND87-2008, Sandia National Laboratories, Albuquerque, NM, April, 1989.

6. E. R. Copus, et al., Core-Concrete Interactions Using Molten Urania with Zirconium on a Limestone Concrete Basemat: The SURC-1 Experiment, NUREG/CR-5443, SAND90-0087, Sandia National Laboratories, Albuquerque, NM, April, December 1990 (draft for comment).

7. B. W. Spencer, D. H. Thompson, and J. K. Fink, ACE MCCI Test L6 Test Data Report: Vols. 1 and 2, Argonne National Laboratory, Argonne, IL, 1992 (to be published). (See also: several papers presented at the Second OECD-CSNI Specialist Meeting on Core Debris-Concrete Interaction, April 1-3, 1992, Karlsruhe, Germany.)

8. E. R. Copus, et al., Core-Concrete Interactions Using Molten Aluminum on a Siliceous Basemat: The SRL-1 Experiment, SAND89-2166, Sandia National Laboratories, Albuquerque, NM, 1991.

9. G. A. Greene, "Heat, Mass, and Momentum Transfer in a Multi-Fluid Bubbling Pool," Advances in Heat Transfer, Vol. 21, 1991.

10. D. A. Powers and D. R. Bradley, "Non-Ideal Solution Modeling for Predicting Chemical Phenomena During Core Debris Interactions with Concrete," OECD-CSNI Specialist Meeting on Core Debris-Concrete Interaction, April 1-3, 1992, Kernforschungszentrum Karlsruhe, Germany, 1992.

11. D. R. Bradley, "Modelling of Heat Transfer Between Core Debris and Concrete," Proc. 25th National Heat Transfer Conference, Houston, TX, July 24-27, 1988.

12. M. Roche, presentation at the ACE Technical Advisory Committee meeting, Argonne National Laboratory, June 1991.

13. J. K. Fink, presentation at the ACE Technical Advisory Committee meeting, Argonne National Laboratory, June 1991.

ENERGY MODELLING OF THE ACE MCCI EXPERIMENT L6

Valerii Strizhov*
John Ptacek
Michael Corradini

January 1992

Nuclear Engineering and Engineering Physics
University of Wisconsin
Madison, WI 53706

*Visiting Scientist from
Institute of Nuclear Safety
Academy of Sciences
Moscow, Russia

ABSTRACT

The current focus of MCCI experimentation is to determine if the release of fission products during the interaction is low and the reasons for such results. To accomplish this independent of sophisticated computer modelling requires detailed examination of data. A first principles analysis of the ACE experiment L6 was performed to identify the uncertainties in the test data. Such an analysis is only possible if one makes some assumptions about the chemical reaction scenario occurring during the experiment. Based on the experimental evidence and our associated analysis, the test data seems consistent with an uncertainty of less than 10%.

INTRODUCTION

Fission product release during a molten core concrete interaction (MCCI) is one of the more important phenomena during the progression of a severe accident due to its radiological impact if the containment is breached. Many experiments have been carried out to understand this process under dry cavity conditions (e.g., SURC, BETA [1,2]). A more recent series of MCCI experiments has also been performed in the framework of the international Advanced Containment Experiments (ACE) program to provide additional data on fission product releases from the MCCI. The current focus of these ACE tests and associated analysis [3] (Phase C) is to determine if fission product releases are low and the possible reasons for this result.

Unfortunately computer models used for simulation of these tests do not follow precisely the experimental conditions and cannot be applied directly without some assumptions. That is why different benchmark exercises provide experience and information for model validation and improvements. The ACE L6 test [4] was chosen as one of the benchmark tests for model predictions and comparisons as well as to demonstrate consistency of the experimental data.

The preliminary results of the blind post-test modelling calculations are detailed in Reference 5, along with the MCCI computer model calculations.

The internal consistency of these experimental results is very important to understand the MCCI behavior and to explain the differences between computer calculations and experimental data. In this paper experimental data are considered with a first principles modelling approach and an experimental energy balance is calculated.

TEST DESCRIPTION

The detailed test description is provided in the ACE L6 report [4-5] and we only mention those features of the experimental facilities which may influence the experimental modelling for heat input and heat losses.

EXPERIMENTAL FACILITY

The main geometrical data used for calculations are presented in Table 1. The heating of the corium was provided by direct electric power input causing Ohmic resistance heating and was initiated by a tungsten wire connected between two electrodes. The net electrical power was determined to be the gross electric power input less the side heat loss to the cooling panels. Power was maintained at approximately 70 kw throughout the test during ablation except immediately prior to and during a range change in the power supply. Thermocouples were installed on the concrete basemat and also extended through the walls to measure the pool temperature history. In order to measure the upward heat loss the upper lid was cooled behind refractory insulation and a tungsten heat shield layer. In addition thermocouples were installed on either side of this upper lid to estimate the heat loss and provide an upper temperature boundary condition for MCCI code calculations.

The decomposition gas generated by downward heat loss and concrete oblation passes through the melt pool and then is carried by an argon cover gas into the aerosol collection system. The cold argon gas serves two purposes; first to quench the decomposition gas as it exits the melt pool and second to carry any aerosols away into the collection system. After the conduct of the test it was found that some of the decomposition gases leaked downward through the concrete (and installed thermocouples) and evidently did not pass through the melt pool. This gas flow and composition is then measured downstream.

Table 1. GEOMETRY CHARACTERISTICS OF L6 TEST

TEST	L6
Dimensions (cm)	50.2*49.2
Area (cm**2)	2470
Volume of basemat (cm**3)	75330
Mass of Basemat Concrete (kg)	173.3
Mass of insert (kg) including	56.4
Metal inserts (kg)	34.0
Concrete (kg)	22.4
Thickness of insert (cm)	7.0

The nominal ACE geometry for these tests included the metal-concrete inserts above the basemat concrete. This insert allowed for inclusion of metals and metallic fission product simulants, as the corium pool eroded the metal-concrete insert and before the concrete basemat ablation began. Once the molten corium pool was formed by resistance heating, it grows in size to the sidewalls and downward to the metal-concrete insert basemat; a quasi-steady condition is reached. The test is considered to begin when thermocouples register near ablation temperatures at the initial concrete surface for the insert. Table 2 and 3 presents the composition of the concrete and the metal-concrete inserts.

Table 2. COMPOSITIONS OF SILICEOUS CONCRETE

SiO2		0.69
CAO		0.135
A1203		0.04
K2O		0.014
Fe2O3		0.01
TiO2		0.08
MgO		0.07
Na2O		0.07
CO2		0.042
H2O		0.037
	free	0.017
	bound	0.02

Table 3. COMPOSITIONS OF METAL/CONCRETE INSERTS

Zr	21.1
Zry	1.8
Type 304 SS	9.1
FP simulants	1.8
Concrete	22.4

ANALYSIS OF TEST L6

ENERGY BALANCE

One of the most important features of this experimental facility in comparison to past work is the possibility to measure the overall heat gains and losses from the molten corium. The experimental data provides information about power input, side and upward losses, as well as downward erosion depth. But some energy processes cannot be measured directly; e.g., the heat produced due to chemical reactions and downward energy losses, which are calculated from other experimental data. The chemical power data reported [4] is derived from measurements of the hydrogen gas produced and assumes metallic zirconium being oxidized by the water vapor and carbon dioxide to produce this measured hydrogen. The downward power data reported [4] is derived from the difference of the input power and the sideward and upward losses, which assumes that the temperature of the melt remains unchanged.

It seems due to these reasons that it is necessary to check the consistency of the experimental data to understand any discrepancies that may be identified in the code comparison results [5].

The overall energy balance is calculated to understand the main features of experiments. Energy balance calculations are based on the following assumptions:

(a) There is no uncertainty about total power input and sideward losses as well as upward heat losses and the erosion data. Experimental data were integrated over time and then time-averaged to obtain average power values.

(b) All other information should be calculated from these data. All parameters necessary for estimations were calculated using the CORCON models for the thermophysical properties [6,7].

(c) Two phases of the interaction are considered separately; i.e., first metal insert ablation then secondly, the concrete ablation phase.

(d) The uncertainties in downward losses and chemistry are accommodated by:
   - Downward heat losses were calculated from the erosion depth;
   - Chemical heat input was calculated using content of gaseous components in inserts and basemat concrete. Some oxidation scenario must be assumed to complete the analysis, and this is discussed below.

First phase: Metal Inserts Ablation. A general energy balance of the first phase is summarized in Table 4 and graphically illustrated in Figures 1-4. During the first phase of the interaction the erosion depth was 7 cm and the total mass of decomposed material is known (Table 3). Figure 1 indicates the experimental erosion history and the predictions from the CORCON computer model analysis. The metal insert was ablated after seven cm of erosion and this is estimated to have occurred after about 40 minutes based on thermocouple data [4]. At the same time the melt pool (Figure 2) decreased in temperature only 50K to 2450K. Figure 3 indicates what the average power downward into the concrete would have to be consistent with this erosion (27-30kW). This average downward power is usually lower than that calculated by the power differences from the measure input and side losses by about 10-25%; although it falls below the average at power range changes. The experimental information presented [4] indicates that the average power input was about 70kW (accounting for side losses) and the upward energy losses (Figure 4) were nearly 25-27kW. Integration of upward losses gives total losses almost 70 MJ during the first phase. Erosion data suggests an energy loss into the concrete of 61 MJ compared to the inferred value of 69 MJ from input/side power differences. The energy needed for heating up of inserts decomposition products to the pool temperature gives a value of about 37 MJ. In addition the energy change due to cooling of the melt by 50K is about 7MJ. Assuming the measured chemical power is appropriate (10 MJ for this phase), the energy balance indicates a surplus of about 25 MJ; this corresponds to a power error of 10 kW or 15% of the net power input. Considering a different chemical power scenario the result can be quite different.

Second phase: Concrete Ablation. During the second phase of interaction of molten corium with basemat concrete the total erosion depth was 12.7 cm which accounts for about 40% of the concrete inventory. Taking into account changes in the interaction area (90% of the total geometric area) the estimated concrete erosion is less than 65 kg; consider the value to be 65 kg. All other estimates are arrived at similar to the first phase. The erosion rate increases (Figure 1) in the concrete basemat material from 10 cm/hr to a rate as large as 25 cm/hr as the melt pool temperature decreased 300K to 2150K (Figure 2). If the erosion rate is again used to calculate the average power downward one finds it is larger than that derived from simply power differences by 10-50% (Figure 3). This is consistent with the observation that the melt pool temperature decreased with an energy loss

Table 4. ENERGY BALANCE FOR FIRST PHASE OF INTERACTION

	Experiment		Estimation	
	Integral (MJ)	Power (kW)	Integral (MJ)	Power (kW)
Power input	181	70	Experimental	
Erosion power	-69	-27	-61	-24
Upward losses	-68	-28	Experimental	
Chemical power	10	4	-19	-8
Energy change due to melt temperature change	Calculated		7	3
Energy for heating of inserts and gas from 1500 to 2500 K	Calculated		-39	-14
Balance	24	8	1	1

Mass of melt (kg)	262
Temperature change (K)	50
Time of interaction (sec)	<2500
Average melt heat capacity (J/kg°K)	530

Metal inserts decomposition enthalpy (MJ/kg of concrete)	2.74
Mass of eroded concrete (Kg)	22.4

Table 5. ENERGY BALANCE FOR SECOND PHASE OF INTERACTION

	Experiment		Estimation	
	Integral	Power	Integral	Power
Power input	172	70	Experimental	
Erosion power	-92	-37	-102	-41
Upward losses	-69	-28	Experimental	
Chemical power	18	7.3	15	6
Energy change due to melt temperature change	Calculated		56	21
Energy for heating of concrete and gas from 1500 to 2160 K	Calculated		-52 (-45 to -62)	-24
Balance	40	16	20	8

Mass of melt (kg)	315
Temperature change (K)	290
Time of interaction (sec)	2460
Average melt heat capacity (J/kg°K)	640

Concrete decomposition enthalpy (MJ/kg of concrete)	1.85
Mass of eroded concrete (Kg)	55-65

of over 50 MJ. Table 5 summarizes the experimental and calculated values. During this phase of the interaction the energy deficit is approximately the same as in the first phase or about 23 - 25% of net power input.

In these calculations we have not considered the change in the amount of solids in the melt pool due to solidification or melting. During the first phase this would be reasonable since the pool temperature was large and relatively steady, and the pool compositional dilution would have been small. However, during the second phase this assumption may not be valid because the pool temperature decreased markedly along with a dilution of the pool by concrete decomposition products. If the pool cooled off substantially compared to its solidus temperature then more solids would have been present and this would have the energy deficit. There is no way to directly estimate this effect, although one would consider the theoretical change in the liquidus and solidus temperatures to compute the net heat loss or gain. The calculation also considered energy loss by gas outflow; however, this is a small loss (5-10MJ) and would counter the solids effect.

CHEMICAL REACTIONS

It was recognized even before the SURC-4 experiment that the reactions in the condensed phase may play a very important role [2]. SURC-4 dramatically demonstrated that this chemistry can influence the temperature behavior and energy distribution. Modelling of the L6 experiment also shows that this reaction can contribute to the overall energy balance. So it is interesting to consider this problem in more detail. The initial inventory of gases and possible products which may define the reactions in the condensed phase for L6 experiment is presented in Table 6.

Table 6. INITIAL INVENTORY OF REAGENTS (gmoles)

Component	Corium	Inserts	Concrete	Concrete Eroded
Zr		250		
SiO2	280	258	1990	600 - 800
H2O		46	356	125 - 150
CO2		21	165	55 - 70

From these estimates a total gas release for H_2 and H_2O of about 125-150 moles and 50-70 moles for CO and CO_2 is expected. The observed gas release is presented in Table 7 and in Figures 5-and 6. This measured gas release was much less than expected. The reason for this has been mentioned previously and is discussed in the L6 data report [4]; i.e., gas leakage out the bottom of the basemat crucible and the hood. In a manner similar to the downward power measurements we used the measured erosion data to compute the gas superficial velocity and the cumulative H_2/H_2O and CO/CO_2 history for this test, if all the gas exited through the melt and was measurable. These calculated cumulative amounts would be in better agreement with MCCI calculations (although qualitative inconsistencies for CO/CO_2 are not fully understood). So for the first phase the H_2/H_20 release was 55 moles or a little larger than expected, while the CO/CO_2 release was about 12 moles or half of the expected value. The second phase shows a much lower release than expected; i.e., 3-5 times less than actually observed (Table 8).

For our calculations we considered only zirconium and silicon chemistry because it seems to be the most important reactions for this particular benchmark case. The possible list of condensed phase chemical reactions are as follows:

$$Zr + 2H2O = ZrO2 + 2H2 + 701 \text{ kJ/mole Zr} \quad (1)$$
$$Zr + 2CO2 = ZrO2 + 2CO + 535 \text{ kJ/mole Zr} \quad (2)$$
$$Zr + SiO2 = ZrO2 + Si + 190 \text{ kJ/mole Zr} \quad (3)$$
$$Si + 2H2O = SiO2 + 2H2 + 500 \text{ kJ/mole Si} \quad (4)$$
$$Si + 2CO2 = SiO2 + 2CO + 424 \text{ kJ/mole Si} \quad (5)$$
$$2Si02 + Zr = 2SiO(gas) + Zr02 - 410 \text{ kJ/mol Zr} \quad (6)$$

The chemical reactions with silica (3 and 6) represents the zirconium chemistry in the condensed phase. These estimates are shown in Table 9.

Table 7. EXPERIMENTAL GAS RELEASES

	Time		
	-43 min	0	41
H_2	14.8 moles	40.3	70.4
H_2O	13.6	15.6	17.6
CO	0	7.0	20.0
CO_2	3.7	4.7	9.6

Table 8. COMPARISON OF OBSERVED AND EXPECTED GAS RELEASES

	Phase 1		Phase 2	
	Observed	Expected	Observed	Expected
	(mole)		(mole)	
$H_2 + H_2O$	27	46	32	105-140
$CO + CO_2$	12	21	18	50-65

We consider the following scenario of oxidation (Tables 4 and 5). During Phase I the quantity of reagents is enough to oxidize most of the Zr. So we propose that the oxidation of Zr was due to the available masses of steam and carbon dioxide and the remaining Zr is oxidized by SiO_2 in some chemical reaction. The reason for this choice is the fact that the experimental ratio of H_2/H_2O is about 10-15 for both phases and CO/CO_2 near 7, indicating almost complete gas reduction. Now one must recognize that silicone and more probably silicone-oxide gas can be vaporized during this time (CORCON predicts this early in the transient [7]). During the first phase of the interaction we assume that the zirconium not reacting with the decomposition gases can undergo the endothermic reaction of producing SiO gas. This is consistent with the observed aerosols collected and with pre-test and post-test calculations [8]. Of the 220 moles of Zr remaining after the metal-gas oxidation we assumed about one-half is consumed in this endothermic reaction. The remainder (~120 moles) is left to be oxidized by gases and SiO_2 in the second phase. In this final phase we arbitrarily assumed a 50/50 split of the zirconium oxidation between the gases and silicone dioxide. Because we do not know the actual partition this can only be confirmed by more detailed MCCI calculations. Comparison to CORCON.UW seems to bear out this simple assumption.

Table 9. ESTIMATED CHEMICAL HEAT RELEASE FOR PHASE I

	Experiment		Estimation	
Component	Release (mole)	Heat (MJ)	Release (mole)	Heat (MJ)
H_2O	25	9	46	16
CO_2	7	2	22	6
SiO(gas)	>62*	-25	200	-41
Total	>94	-14	268	-19

Due to this oxidation scenario the estimated chemical heat is presented in Table 9. Experimental oxidation was calculated taking into account the zirconium reactions with only

---

*Total Si detected in the aerosol system was 85.4 moles. This is considered a lower bound because SiO_2 and SiC deposits were detected in the test enclosure. The fraction released during the first phase is estimated from an elbow sample line (J. Fink, Private Communication, December, 1991).

gases. For our calculated values the heat release is actually endothermic and different than the experimental values and the total inventory of SiO(gas) is about 200 moles. The total oxidation during the second phase seems to be about 240 moles. So the initial metal inventory is sufficient to burn throughout Phase 2. Table 10 presents the estimated heat releases during this second phase.

Table 10. ESTIMATED CHEMICAL HEAT FOR PHASE 2

	Experiment		Estimation	
	Release (mole)	Heat (MJ)	Release (mole)	Heat (MJ)
H_2	32	11	100	35
CO	15	4	20	5
SiO(gas)	>24	-10	120	-25
Total	>71	5	240	15

Let us now return to the Tables 5 and 6 to consider the calculated energy balance with chemical heat included from this scenario. The estimates for the first phase give a positive deficit of 3 MJ and the second phase a positive value of about 27 MJ. So the combined energy balance for both phases seems to be quite good; i.e., within 10%. Changes in this possible scenario (for instance the reasonable proposal that zirconium oxidation may take longer than the first phase) can redistribute chemical heat between these two phases, but the combined results are valid. Also any solidification of the melt pool as the temperature falls, particularly in second phase, will cause an energy change that brings the total energy balance even into better agreement (remember phase change was neglected).

Table 11 presents the summary of the energy accounting. During the first phase the input power provide about 85% of needed energy and 11% is due to chemical reactions. About 23% of input energy provided the heating of decomposition products up to melt temperatures. Remaining power is distributed between upward and downward losses in about equal proportion. During the second phase the internal heat of melt provides about 6% of energy needed, the role of electrical heating drops to 71%. The heating of concrete decomposition products absorb about 21% of total energy. The relative role of upward and downward losses changes a little due to an increase of the downward power. Finally Table 12 presents the calculations of superficial gas velocity and heat transfer coefficients to concrete based on the data.

Table 11. OVERALL ENERGY BALANCE SUMMARY in MJ

	Phase 1	Phase 2
Input power	180 (85%)	172 (71%)
Cooling of melt	7 (4%)	56 (23%)
Chemical heat	-19 (11%)	15 (6%)
Total input	168	243
Downward losses	61 (36%)	102 (47%)
Upward losses	68 (41%)	69 (32%)
Heating up	37 (23%)	44 (21%)
Total losses	165	215

Table 12. ESTIMATED AVERAGE HEAT TRANSFER COEFFICIENTS

	Superficial gas velocity cm/s		Heat transfer coefficient W/m**2K	
	Exp.	Calculated*	Exp.	Calculated*
Phase 1	0.6	2.5		200
Phase 2	1-2	4-10		150-500

*Based on concrete erosion depths.

CONCLUSIONS

The experimental heat balance is quite good taking into account the chemical reaction in the condensed phase for the first and second stages of the experiment. The expected gas release rate for the second stage of the experiment is quite low compared to measurements. This difference by at most a factor of three would have a large effect on the computed heat transfer coefficients for the ablation of concrete in more detailed MCCI computer analyses. This should be considered in any further analyses for ACE tests.

The authors would like to acknowledge the financial support of the Electric Power Research Institute and the Department of State for Dr. Strizkov's visit. Thanks also to Drs. B.R. Sehgal and J. Fink for their comments and help.

REFERENCES

1. J.E. Gronager, et al., SURC 1: Large Scale Metallic Melt-Concrete Interaction Experiments and Analysis. NUREG/CR-3920, SAND-84-1246 (1984).

2. H. Alsmeyer, et al., "BETA Experimental Results on Melt-Concrete Interactions: Silicate Concrete Behavior," OECD-CSN1 Specialist Meeting on Core Debris/Concrete Interactions, Palo Alto, CA (Sept, 1986).

3. J.C. Casas, et al., "Analysis of Argonne Core-Concrete Experiment (ACE) Using a Modified CORCON Model," NURETH-4, Karlsruhe, FRG (October, 1989).

4. D. H. Thompson, J. Fink, "ACE MCCI Test L6 Test Data Report: Volume 1 Thermal-Hydraulics," ACE-TR-C26 (August 1991)

5. J. Ptacek, M. L. Corradini, "Post-Test Blind Benchmark Exercise: ACE L6 Experiments," ACE-TR-C27 (October 1991)

6. R.K. Cole, et al., CORCON-MOD2: A Computer Program for Analysis of Molten Core Concrete Interactions, NUREG/CR-3920, SAND 84-1246 (August 1984).

7. J. Norkus, Modelling of Molten Core Concrete Interaction and Fission Product Release, PhD Thesis, University of Wisconsin (August 1988).

8. J. Fink, Argonne National Lab, Private Communication (December 1991).

Figure 1: ACE-L6 LCS-Concrete

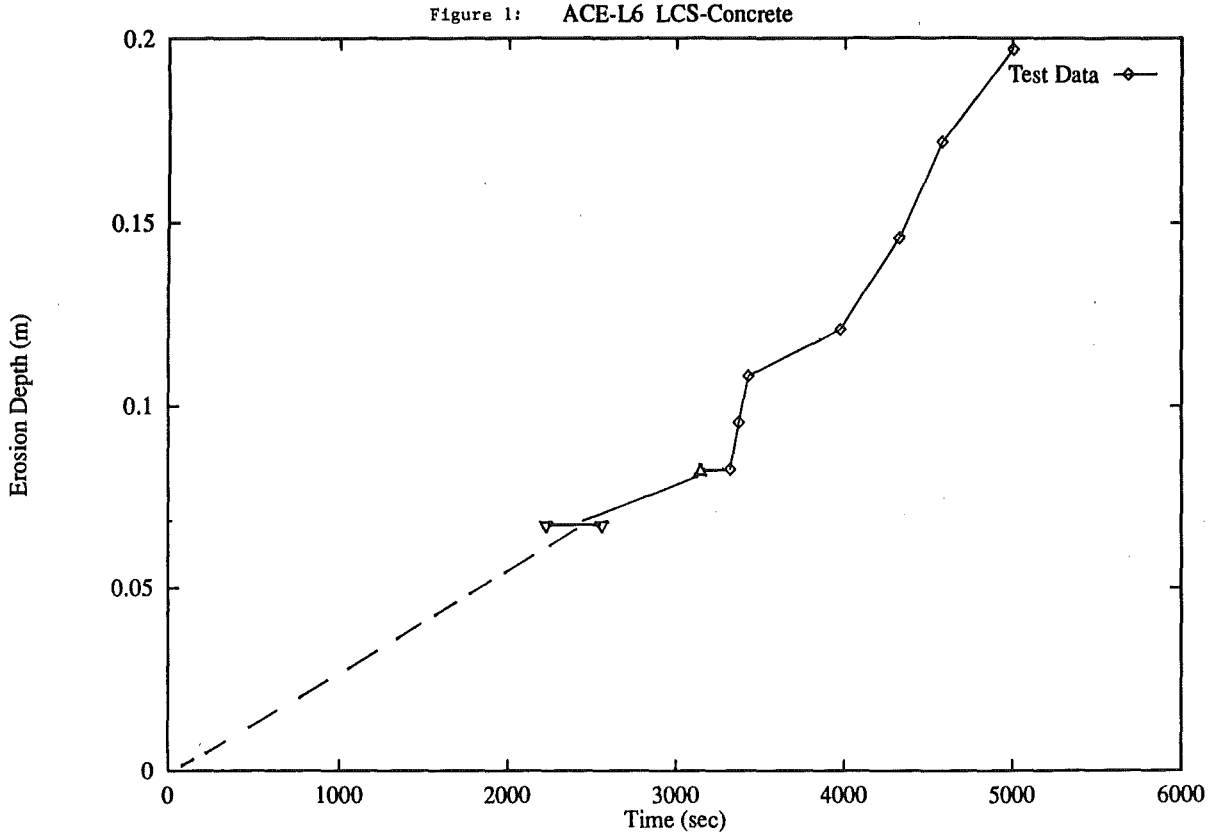

Figure 2: ACE-L6 LCS-Concrete

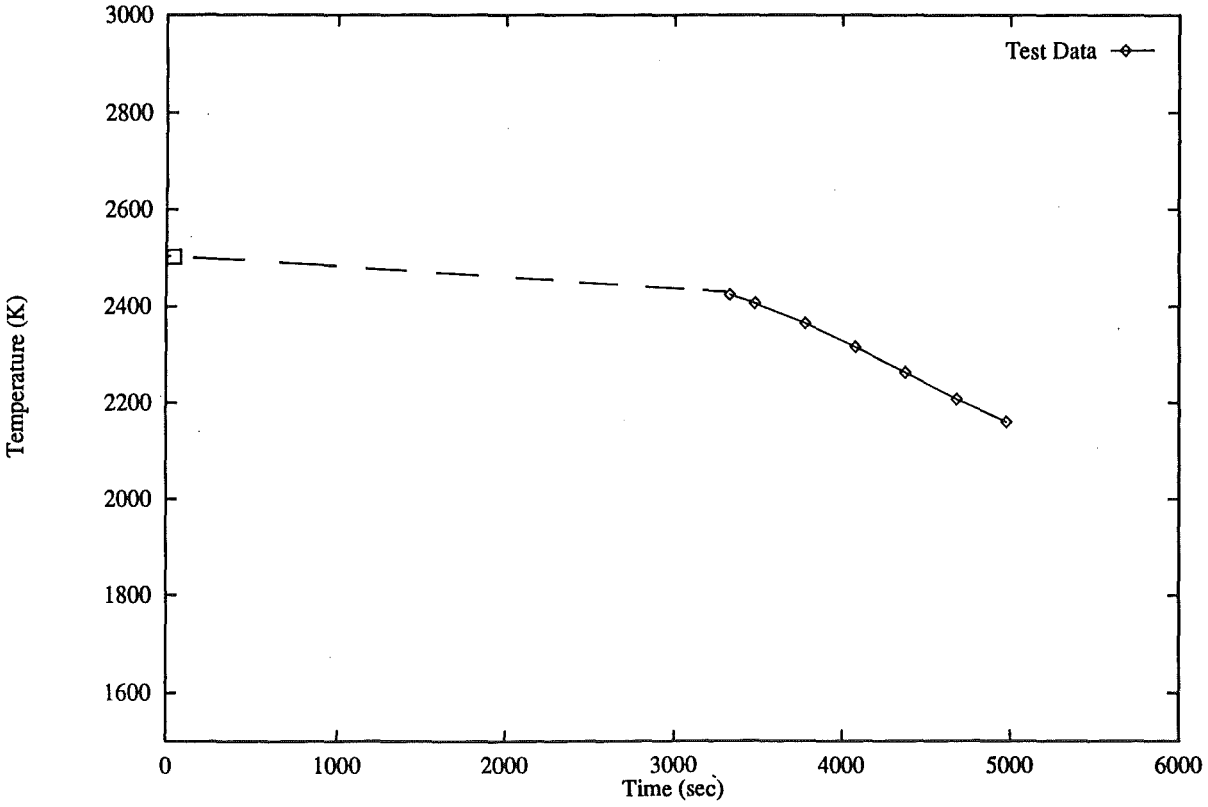

Figure 3: ACE-L6 LCS-Concrete

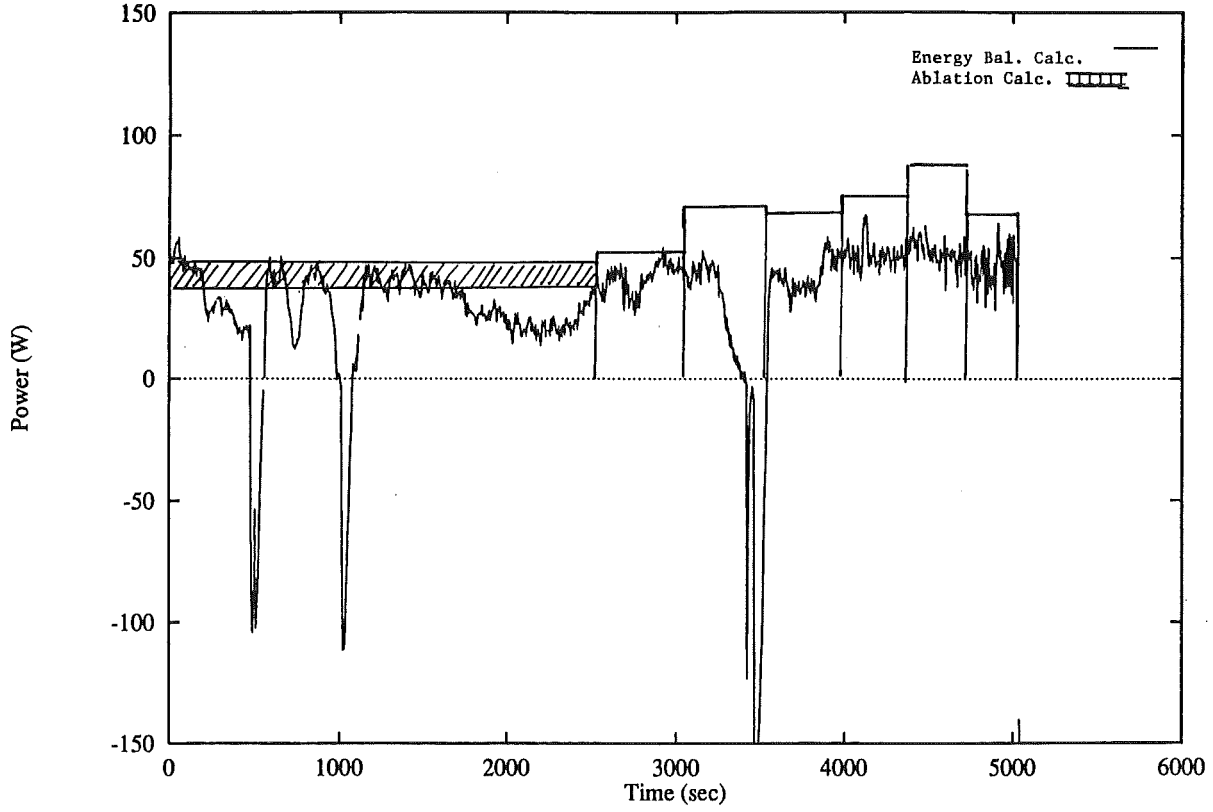

Figure 4: ACE-L6 LCS-Concrete

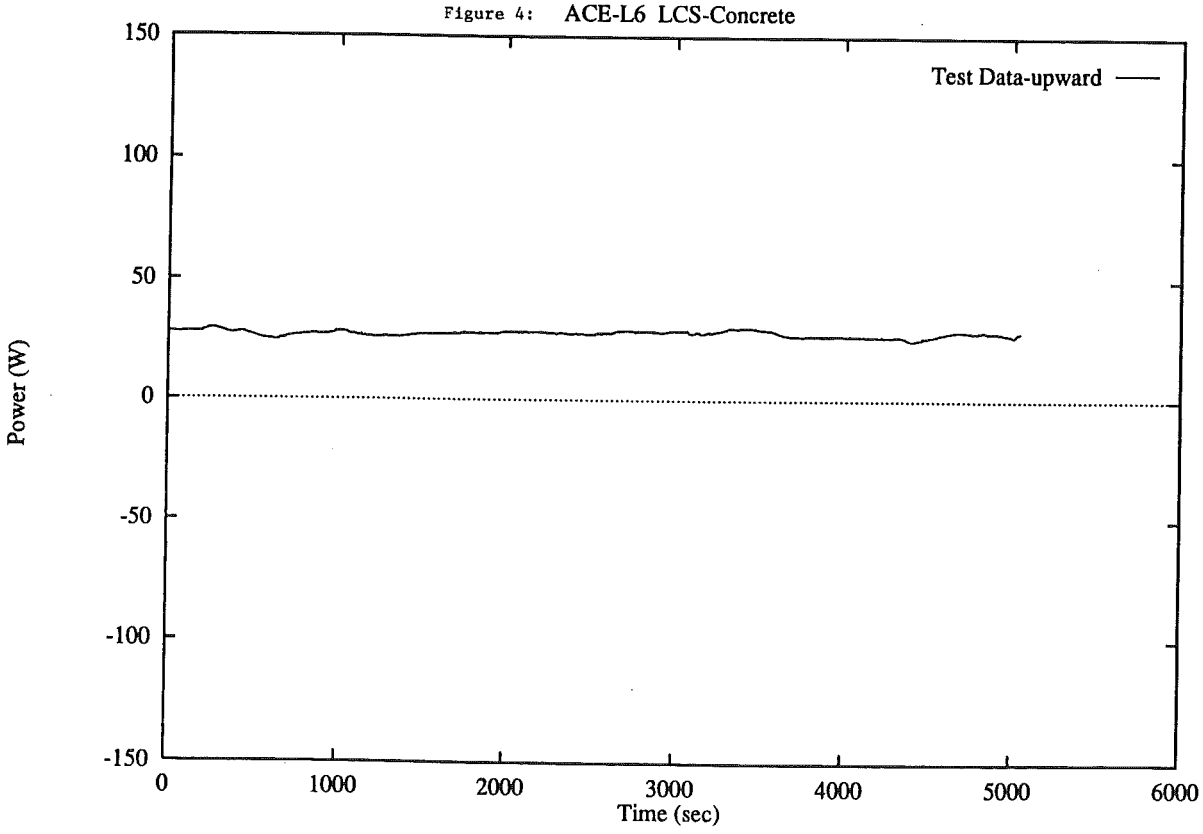

Figure 5: ACE-L6 LCS-Concrete

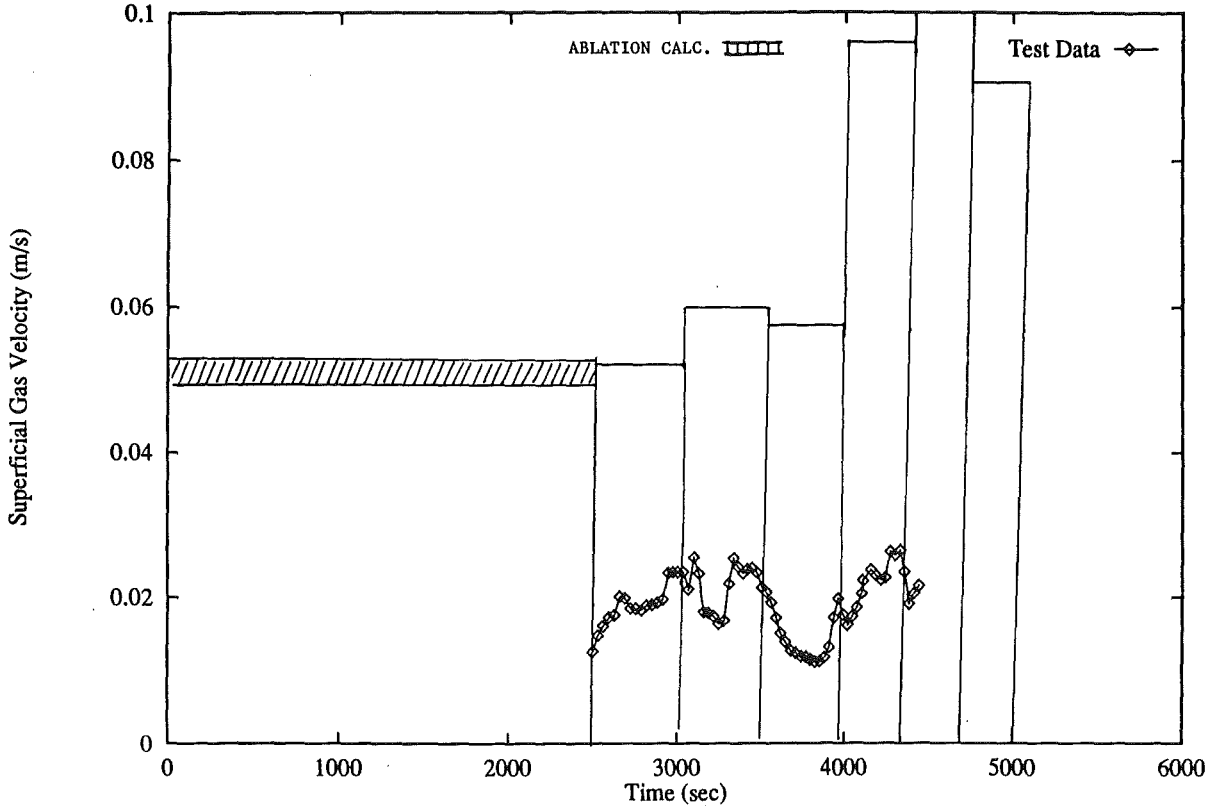

ANALYSES OF ACE MCCI TEST L6 WITH THE CORCON/VANESA CODE

A.Hidaka, K.Soda, J.Sugimoto, N.Yamano and Y.Maruyama

Japan Atomic Energy Research Institute
Tokai-mura, Naka-gun, Ibaraki-ken, 319-11 Japan

ABSTRACT

Analyses of ACE MCCI Test L6 were performed at JAERI to evaluate the quantity of FP(fission products) release and the behavior of concrete erosion during an MCCI. The CORCON/Mod2.04 code was used for the thermal-hydraulic analysis and the estimations of concrete erosion and gas generation during an MCCI. The VANESA1.01 code was used for the prediction of species and quantity of released FP aerosols during an MCCI. The convective heat transfer model for horizontal surfaces in the CORCON code was modified from the Greene's to the Kutateladze's in the present analysis to better predict concrete ablation rate. Furthermore the VANESA1.01 code was modified such that the upper limitation of the partial pressure for each species was set at 0.001 MPa as in the VANESA1.00 code to eliminate overestimation of the partial pressure. It was found in the present analysis that the following models and assumptions were found to influence an overall calculation of MCCI; the heat transfer for horizontal surfaces, chemical equilibrium, coking reaction and oxygen potential.

1. INTRODUCTION

Release of fission products (FP) during a molten core-concrete interaction (MCCI) is one of major contributors to the source term uncertainties of a severe accident at a nuclear power plant[1]. Therefore one of the test series of Phase C of the Advanced Containment Experiment (ACE) program organized by Electric power Research Institute (EPRI) of U.S.A. focused its attention to quantify and evaluate FP release and concrete erosion behavior by MCCI. Eight MCCI tests[2] have been performed as the ACE MCCI tests to investigate the thermal-hydraulic and chemical processes of MCCI and to provide data on the release of low-volatile FP in a severe accident of LWR.

One of the ACE MCCI Tests, L6, was selected as a benchmark exercise among the participants of the ACE program. JAERI participated in the exercise and performed "posttest blind" analyses of Test L6 using the CORCON/Mod2.04[3] and VANESA1.01[4] codes. The purposes of the analyses were to assess capabilities of the two codes and to identify areas of uncertainties which might have caused differences between the analyses and the

experiment.

2. OUTLINES OF TEST L6

Test L6, the fourth large-scale MCCI/fission product release test, was performed to investigate an interaction of 30% oxidized PWR corium melt with siliceous concrete in the test apparatus shown in **Fig. 1.** The apparatus consisted of the water cooled furnace which enclosed the concrete basemat and the corium inventory. The decay heat was simulated by the electric power supply to the tungsten electrodes.

Test L6 was initiated by turning on the electric power to the metal layer at -190 min before ablation of basemat concrete. Aerosol sampling began at -53.7 min and ablation of the concrete/metal inserts was initiated at -43 min. At 31 min after the start of basemat ablation, aerosol plugging was detected in the primary diluter and the electric power was turned off at 41 min to end the test.

3. ANALYTICAL METHOD

3.1 Computer Code

The CORCON/Mod2.04 code was used for the present analyses to describe the thermal-hydraulic behavior of MCCI and to predict concrete erosion and gas generation. The CORCON/Mod2.04 code was updated by implementing the fourth correction set supplied by the Sandia National Laboratories (SNL). For the convective heat transfer for horizontal surfaces in the melt pool, the Kutateladze's correlation[5] was used instead of the Greene's correlation[6] used in the original CORCON/Mod2.04. For the radial convective heat transfer in the melt pool, the Blottner's model[7] was used.

The VANESA1.01 code was used for prediction of the species and quantities of FP released during an MCCI. In the preliminary calculation with the original VANESA1.01 code, aerosol generations of several materials, i.e. SiO and Si_2, were overestimated since equilibrium partial pressures of the materials became extremely high. In order to avoid the overestimation of partial pressure of several species and to make the summation of partial pressures equal to the atmospheric pressure, in the present calculation, the VANESA1.01 code was modified such that the upper limitation of the partial pressure for each species was set at 0.001 MPa as in the original VANESA1.00 code.

3.2 Input Data

Input data for the CORCON/Mod2.04 code in the present calculation was prepared based on the selected data for Test L6. ACE MCCI Test L6 was the one dimensional concrete attack experiment and no sideward ablation occurred. In order to apply the two dimensional ablation model used in the CORCON/Mod2.04 to the one dimensional concrete ablation, the cavity floor area, the quantity of melt and the electric power were multiplied arbitrarily by 100 so that the effect of sideward concrete ablation could be ignored as compared to downward ablation. The electric power used in CORCON calculation was multiplied by 100 to account for the increase of the area of cavity floor. Quantity of each component of the corium melt was also multiplied by 100 to conserve the depth of the melt.

Input data of the VANESA code for the melt temperature and the basemat concrete ablation were taken from the experimental data. The VANESA code calculates the chemical equilibrium between the metal and gases in the melt using the quantity of H_2O and CO_2 which were generated by the concrete ablation. The experimental data were used for the addition of H_2 and H_2O generations as the total available H_2O in the VANESA calculations. For the available CO_2 in the calculation, the quantity of CO_2 predicted from the concrete ablation data and the constituent of CO_2 in the concrete was input rather than the CO and CO_2 generation data from the Test L6 on-line mass spectrometer in order to take the coking reaction into account in the VANESA calculations.

4. RESULTS OF ANALYSIS

4.1 Thermal-Hydraulics

The analysis of thermal hydraulics with the CORCON/Mod2.04 code was performed from the initiation of concrete/metal inserts ablation at -43 min to the cut off time of the electric power at 41 min.

(1) Energy Source

The electric power, chemical heat by oxidation and the heat transfers from molten pool to concrete and from the pool to atmosphere are compared in Fig. 2. The time of concrete-ablation initiation detected in the experiment was set at 0 min in the present analysis. All of the electric power was assumed to be given to the oxide layers.

In the CORCON model, chemical reaction of metal with gases occurs only in the metal layer and the reaction is calculated using the method of minimization of the Gibbs free energy. According to the method, metal Zr is to be oxidized first among the metals in the melt pool because the oxide of

Zr, namely, ZrO_2 is the most stable material in stoichiometry among the melt constituents. Therefore most of the calculated chemical heat at an early phase of the experiment was generated by the following reactions.

$$2H_2O + Zr = 2H_2 + ZrO_2 + 220 \text{ kcal/mol}, \quad (4.1)$$

$$CO_2 + Zr = C + ZrO_2 + 178 \text{ kcal/mol}. \quad (4.2)$$

The experiments with the siliceous concrete[8] suggested the importance of $Zr-SiO_2$ reactions in the melt pool. However, the current version of CORCON code does not model the chemical reactions between Zr and SiO_2, and between Si and H_2O or CO_2.

The reactions of equations (4.1) and (4.2) proceed to produce the reaction heat when H_2O and CO_2 are supplied to the melt. In the present analysis, the concrete basemat began to be ablated at -8 min and large quantity of gases was generated at that time. Furthermore, it was predicted that the inversion of melt pool layer occurred at 1.6 min and the temperature of the melt close to the concrete increased. Therefore, supplies of H_2O and CO_2 were increased at -8 min and 1.6 min and it resulted in the increase of the chemical heat shown in Fig. 2.

The rate of heat transfer from the melt pool to the concrete was increased at -8 min and 1.6 min. This is because large chemical heat was generated in the metal layer by the reaction described in the above and the generated chemical heat was transferred from the melt pool to the concrete.

(2) Melt Pool Model

The melt pool model of the CORCON/Mod2.04 code is shown in Fig. 3. The melt pool is assumed to consist of a light oxide layer, a metal layer and a heavy oxide layer. The light oxide layer is defined as an oxide layer of which average density is lighter than that of the metal layer. The heavy oxide layer is defined as an oxide layer of which average density is heavier than that of the metal layer. At the initial state, the melt pool is assumed to consist of a metal layer and an oxide layer.

In the present analysis, a heavy oxide layer was assigned to the oxide layer at the calculation initiation at -43 min because its main constituent was UO_2 (10.96 g/cm^3) and the density of the oxide layer was heavier than that of metal layer. It was assumed that there was no light oxide layer at -43 min. However a light oxide layer began to be formed after that because ZrO_2 generated by the oxidation in the metal layer became the constituent of the light oxide layer. In the heavy oxide layer, the density decreased gradually because of the inflow of concrete-dissolved materials. The heavy oxide layer became the light oxide layer when the density of the heavy oxide layer de-

creased less than that of the metal layer at 1.6 min by the inflow of concrete-dissolved materials such as SiO_2 which are much lighter than UO_2.

(3) Temperature of Melt Pool

Calculated melt pool temperature of each layer is shown in Fig. 4. The initial average temperature of the whole melt pool was assumed 2500 K in the present analysis. Initial temperature of the metal layer located on the heavy oxide layer was estimated 2021 K taking into account the heat transfer from the melt surface to the atmosphere. Temperature of the metal layer became highest at 2370 K at -15.5 min and began to decrease after that. The reason is that the crust at the top of the heavy oxide layer disappeared at -15.5 min due to the temperature increase to the melting point of the crust. Then the rate of heat transfer from the metal layer to the oxide layer was dominated by the effective convective heat transfer in the melt pool after the disappearance of the crust. A flow of the concrete-dissolved materials such as SiO_2 into the heavy oxide layer resulted in the change of the heavy oxide layer to the light oxide layer. Zero temperature at 1.6 min indicates the completion of the change. After 1.6 min, temperature of the metal layer became lower than that of the light oxide layer because the rate of heat transfer from the metal layer to the concrete became large due to direct contact of the metal layer with concrete.

(4) Mass of Melt Pool

The masses of the heavy oxide layer, the light oxide layer and the metal layer are shown in Fig. 5. Mass of the metal layer decreased slowly because the metal was changed to the oxide due to the chemical reactions as shown in equations (4.1) and (4.2). On the other hand, mass of the light oxide layer increased gradually because oxide such as ZrO_2 was generated by the oxidation reaction of the metal with gases. Mass of the heavy oxide layer also increased gradually since oxide such as SiO_2 was generated by dissolution of the concrete and the mass was added to the heavy oxide layer.

(5) Composition of the Metal Layer

Composition of the metal layer is shown in Fig. 6. CORCON code calculates the oxidation of the metal by the method of minimization of the Gibbs function. According to this method, Zr was oxidized first then carbon followed by Cr. The source of carbon was that trapped in the melt by the coking reaction. Calculated quantity of Zr in the metal layer increased after the initiation of concrete/metal inserts ablation at -43 min and began to decrease after the completion of the inserts ablation at -8 min. It should be

mentioned that Zr was not completely depleted yet at the end of the calculation at 43 min. It is also noted that the current version of CORCON code does not model Zr-SiO_2 reactions. Therefore if this reaction was taken into account, the timing of Zr depletion in the metal layer would have been earlier and H_2 generation at an early stage would have been larger compared with the present calculation.

(6) Crust Formation

While crust is present, the governing heat transfer to the concrete or the atmosphere is heat conduction through the crust, not by convection. Therefore the crust formation at the surface of the melt plays an important role on the rate of heat transfer from the melt pool to the concrete or to the atmosphere above the melt. The crust thickness at the top of each layer is shown in Fig. 7. The crust thickness at the top of the light oxide layer becomes zero temporarily at 1.6 min because the temperature of the light oxide layer increased due to the inversion of the melt pool layers. After that, the crust thickness at the top of the light oxide layer increased gradually because the temperature of whole pool dropped due to the heat transfer from the melt to the concrete.

The crust thickness at the bottom of each layer is shown in Fig. 8. Overall trend is almost the same as the top crust thickness shown in Fig. 7. It can be seen that the crust thickness at the bottom of the heavy oxide layer became thin at -8 min because the solidus temperature of the heavy oxide decreased due to the flow of concrete-dissolved materials into the light oxide layer and it became lower than the average temperature of the heavy oxide at -8 min. The disappearance of the crusts in the light and heavy oxide layers at 1.6 min corresponds to the inversion of the melt pool layer. The crust began to be formed at the bottom of the metal layer after that because the rate of heat transfer from the metal to concrete became large due to the contact of the metal layer with concrete and the temperature of metal layer decreased.

(7) Concrete Erosion

The calculated erosion depth is shown in Fig. 9 for the case in which the Kutateladze's model was used for the heat transfer calculation for horizontal surfaces. Figure 10 shows the downward erosion depth calculated by using the Greene's model. The use of the Kutateladze's model resulted in about two thirds slower downward concrete ablation rate because the rate of heat transfer calculated by using the Kutateladze's model is about one tenth of the rate calculated by the Greene's model. The concrete ablation rate was

larger in the period between -8 min and 12 min than that before -8 min or that after 12 min since the thickness of crust close to the concrete became thin during this period and the rate of heat transfer from the melt to the concrete increased.

(8) Gas Generation

The comparison of calculated amounts of H_2 and H_2O generations with the experiment is shown in Fig. 11. Since it was reported that the plugging by aerosol occurred in the primary diluter at 31 min after which measured data were not reliable, the comparison was performed only for the period until 31 min. Calculated amount of H_2 generation was overestimated by a factor of 4.5. The reason for the overestimation of H_2 generation is that the CORCON code assumes the instantaneous chemical equilibrium between the metal and steam, and therefore the metal in the melt reacted instantaneously with steam in the calculation. On the other hand, the instantaneous chemical equilibrium could not be established in actual situation since a bubble containing steam passes through the metal layer in a limited time, for example about 1 sec.

Calculated H_2O was generated at 2 min because the inversion of melt pool layer occurred at this time and the vertical surface of the sidewall concrete was ablated by the light oxide layer even though the experiment did not show the sideward ablation. The sideward concrete ablation was caused by the two dimensional model used in the CORCON code as mentioned in chapter 3.2. However the amount of H_2O generation calculated by the sideward concrete ablation was small and it can be ignored.

The comparison of calculated amounts of CO and CO_2 generations with the experiment is shown in Fig. 12. Calculated CO generation was underestimated by a factor of 5 because the coking reaction proceeded too much in the calculation and CO_2 generated by the concrete ablation was reduced in the metal layer to the elemental carbon. The elemental carbon was then trapped in the metal layer. Calculated amount of CO_2 generation was estimated large at a later phase since the inversion of melt pool layers occurred at 2 min and after that, CO_2 generated by the ablation of sideward concrete was released through the light oxide layer. Therefore it is not meaningful to compare calculated amount of CO_2 generation with the experiment data.

4.2 Aerosol Generation

The VANESA1.01 code was used for the analysis of aerosol generation between the initiation of aerosol sampling at -53.7 min to the occurrence of

aerosol plugging in the primary diluter at 31 min.

(1) Oxygen Potential

The oxygen potential in the metal layer plays an important role in determining the rate of chemical reactions. The oxidation reaction between the metal and the gases proceeds faster when the oxygen potential is higher. Therefore oxygen potential has an effect on the mass fractions of oxide and metal in the melt pool and consequently on partial pressure of each species in the melt which affects the quantity of aerosol generation by vaporization process. The oxygen potential is defined as:

$$J = RT \ln P(O_2) \qquad (4.3)$$

where J ; oxygen potential (J/mol),

R ; gas constant (J/mol/K)),

T ; temperature (K), and

$P(O_2)$; partial pressure of oxygen (atm).

Calculated oxygen potential is shown in **Fig. 13.** It is noted in the present calculation that metal Zr was remained in the metal layer until the end of the calculation and therefore the result indicated the oxygen potential for the condition that the Zr-water reaction was dominant chemical reaction in the melt pool. The oxygen potential began to decrease after 0 min because the partial pressure of oxygen decreased after that in addition to the decrease in melt temperature due to the initiation of concrete basemat ablation. The reason for the decrease in partial pressure of oxygen after 0 min is that the following reaction proceeded as the temperature decreased.

$$H_2 + 1/2O_2 \text{ --> } H_2O \qquad (4.4)$$

It is expected that the oxygen potential would increase after Zr was depleted by the chemical reactions because Zr depletion causes the decrease in partial pressure of H_2 and the relative increase in partial pressure of O_2. Therefore if Zr-SiO_2 reactions was taken into account, Zr would have been depleted at an earlier stage than the present calculation and calculated oxygen potential would have increased after Zr depletion.

(2) Cumulative Amount of Generated Aerosol

Cumulative amount of generated aerosol was calculated by the VANESA1.01 code and the results are shown in **Fig. 14.** The largest amount of generated aerosol was SiO_2. The released mass was 223g (3.7 mol) at 31 min after the concrete ablation initiation. Tellurium was the aerosol which was generated the most among the materials existed in the corium from the beginning. The released mass was 95g (0.75 mol) at 31 min. The reason for the large amount of generated aerosol of SiO_2 and tellurium was that their

equilibrium partial pressure in the melt pool was estimated to be 0.001 MPa, which was the maximum partial pressure in the present analysis.

(3) Release Fraction of Aerosol

Calculated release fractions of aerosols are shown in **Fig. 15.** The results were compared with the experimental data as shown in **Table 1.** The largest fractional release of aerosol at 31 min was tellurium which has relatively volatile characteristics and the calculated release fraction to the initial inventory was 64%. This result showed a good agreement with the measured data of 63%. The good agreement is attributed to use of the upper limitation of the partial pressure for each species at 0.001 MPa in the present calculation. In the sensitivity calculation without this limitation, the release fraction of tellurium was overestimated to be about 100%.

Calculated release fraction of Si was underestimated by 4 % of the measurement data. This indicates that the limitation of partial pressure at 0.001 MPa used in the present calculation was too small or inappropriate for the calculation of Si release while this convenient method was appropriate for the tellurium release calculation.

The release fractions of Ce, La, Ba and Sr were overestimated and those of Ru, U and Zr were underestimated compared with the measured data. However, these differences were scattered within two orders of magnitude. These discrepancies are considered to have been caused by the underestimation of oxygen potential which was caused by lack of the model of Zr-SiO_2 reactions in the present calculation, and the treatment of the melt as an ideal solution in the current version of the VANESA1.01 model.

5. CONCLUSIONS

The analyses of the ACE MCCI Test L6 was performed by using the CORCON/Mod2.04 and VANESA1.01 codes. The convective heat transfer model for horizontal surfaces in the CORCON code was modified from the Greene's model to the Kutateladze's model to better describe the heat transfer in the melt pool governed by bubble-driven convection, and the VANESA1.01 code was modified such that the upper limitation of the partial pressure for each species was set to be 0.001 MPa to avoid the overestimation of each partial pressure and to make the summation of partial pressures equal to the atmospheric pressure.

The following findings were made.

(1) Use of the Kutateladze's model resulted in good agreement with the experiment data.

(2) Use of the instantaneous chemical equilibrium model between the metal and H_2O or CO_2 resulted in overestimation of H_2 generation.

(3) The active coking reaction was the cause of underestimation of CO generation.

(4) Calculated tellurium release showed a good agreement with the experiment while the releases of Ce, La, Ba and Sr were overestimated and those of Ru, U, Zr and Si were underestimated. Possible reason for the discrepancies was due to the underestimation of oxygen potential by the current version of the VANESA1.01 code which does not model the $Zr-SiO_2$ reactions.

(5) The models and assumptions of heat transfer for horizontal surfaces, chemical equilibrium, coking reaction and oxygen potential influence MCCI calculation.

ACKNOWLEDGMENTS

Authors thank Dr. A.J. Machiels, the Chairman of the ACE Project Board, to permit us to present the result to the CSNI workshop. Authors also wish to express their appreciation to Dr. D.A.Powers of SNL for his technical comments relating to the aerosol release model of the VANESA code.

REFERENCES

1) USNRC, "Severe Accident Risks : An Assessment for Five U.S.Nuclear Power Plants," NUREG-1150 (1990).

2) B.R.Sehgal et al., "ACE Program Phase C: Fission Product Release from Molten Corium Concrete Interactions (MCCI)," Proc. of the OECD CSNI Specialist Meeting on Core Debris Concrete Interactions, Karlsruhe, Germany (1992).

3) R.K.Cole et al., "CORCON/Mod2: A Computer Program for Analysis of Molten-Core Concrete Interactions," NUREG/CR-3920 (1984).

4) D.A.Powers et al., "VANESA: Mechanistic Model of Radionuclide Release and aerosol Generation During Core Debris Interactions with Concrete, NUREG/CR-4308 (1986).

5) S.S.Kutateladze and I.G.Malenkov, "Boiling and Bubbling Heat Transfer under the Conditions of Free and Forced Convection," Proc. of 6th Int. Heat Transfer Conf., Toronto, 1, 281 (1978).

6) T.Ginsberg and G.A.Greene, "BNL Program in Support of LWR Degraded Core Accident Analysis," Proc. of the U.S. Nuclear Regulatory Commission Tenth Water Reactor Safety Research Information Meeting, NUREG/CP-0041,

2, 364 (1983).

7) F.G.Blottner, "Hydrodynamics and Heat Transfer Characteristics of Liquid Pools with Bubble Agitation," NUREG/CR-0944 (1979).

8) E.R.Copus et al., "Core-Concrete Interactions Using Molten Steel with Zirconium on a Basaltic Basemat: The SURC-4 Experiment," NUREG/CR-4994 (1989).

Table 1 Composition of Calculated Aerosol Release Fraction with the Measured Data

Species	Calculated	Measured	Error	
Te	0.64	0.63	0.0159	
Ag	$7.2X10^{-2}$	0.32	-0.775	
Ce	$5.3X10^{-2}$	$5.1X10^{-4}$	103	(max)
		$6.3X10^{-6}$	8410	(min)
La	$3.3X10^{-3}$	$6.2X10^{-4}$	4.32	(max)
		$1.6X10^{-5}$	205	(min)
Ru	$4.7X10^{-7}$	$2.1X10^{-3}$	-0.999	(max)
		$6.4X10^{-6}$	-0.927	(min)
Ba	$1.1X10^{-1}$	$1.7X10^{-3}$	63.7	
Sr	$1.4X10^{-1}$	$2.2X10^{-3}$	62.6	
U	$6.8X10^{-5}$	$1.9X10^{-4}$	-0.642	
Zr	$4.6X10^{-6}$	$9.7X10^{-5}$	-0.953	
Mo		$7.0X10^{-3}$		
Si	$3.4X10^{-3}$	$8.4X10^{-2}$	-0.960	

$$\text{Error} = \frac{\text{Calculated} - \text{Measured}}{\text{Measured}}$$

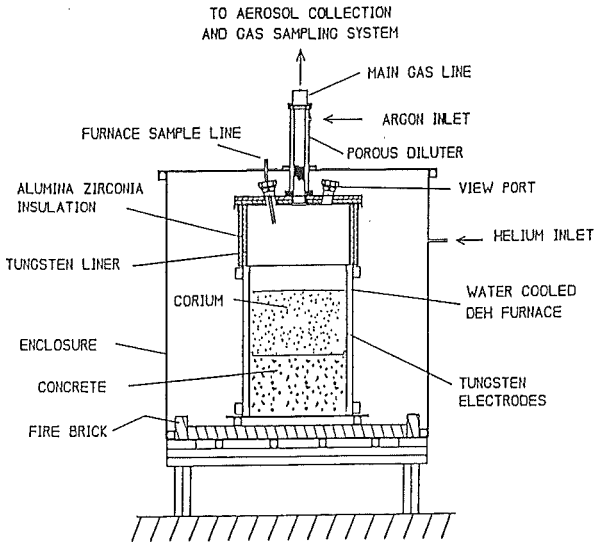

Fig. 1 ACE MCCI Test Apparatus

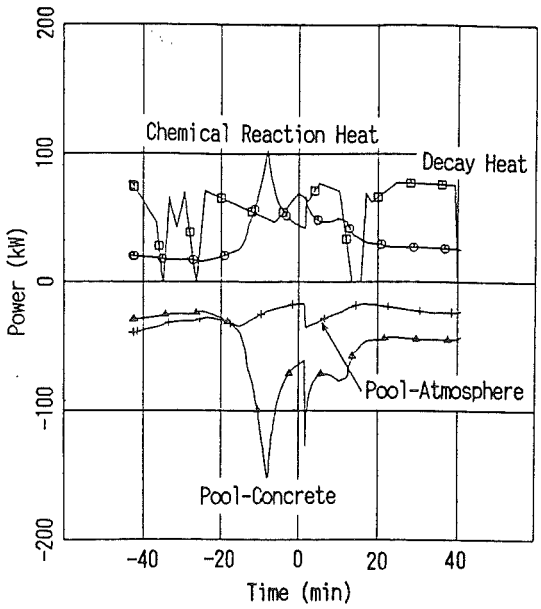

Fig. 2 Energy Balance

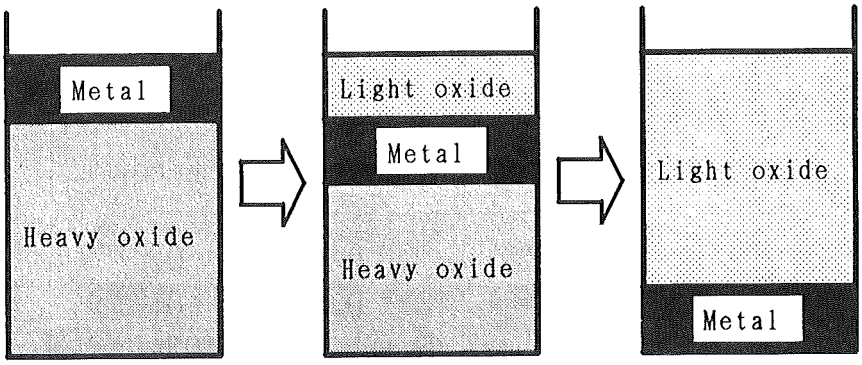

Fig. 3 Melt Pool Model of CORCON Code

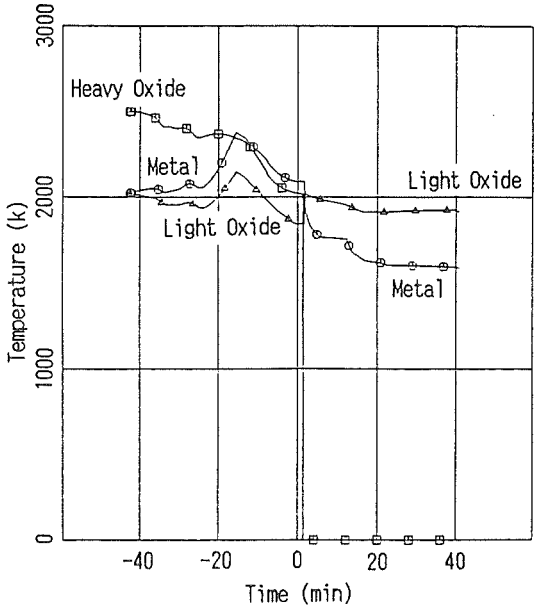

Fig. 4 Temperature of Melt Pool

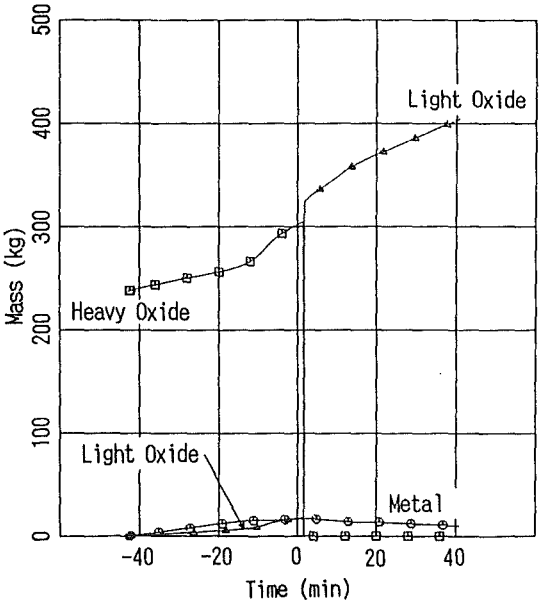

Fig. 5 Mass of Melt Pool

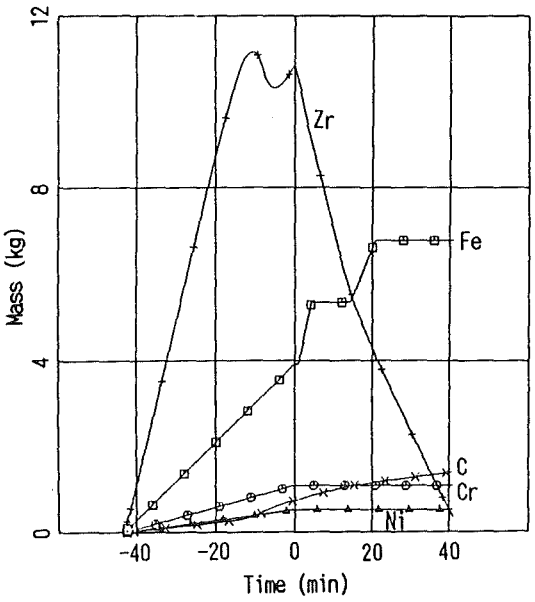

Fig. 6 Composition of the Metal Layer

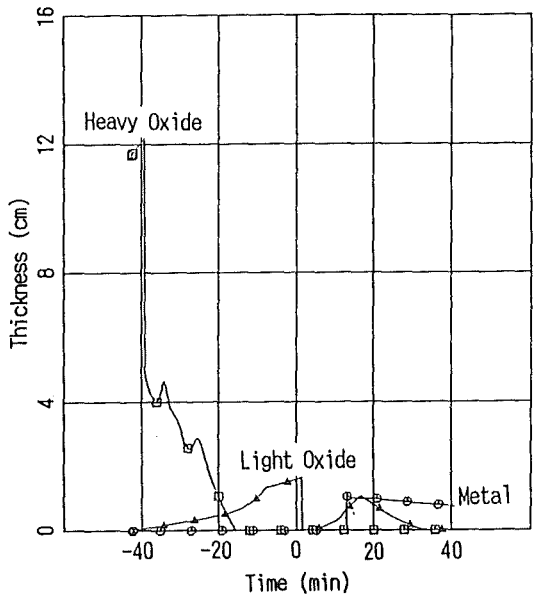

Fig. 7 Crust Thickness at the Top of Each Layer

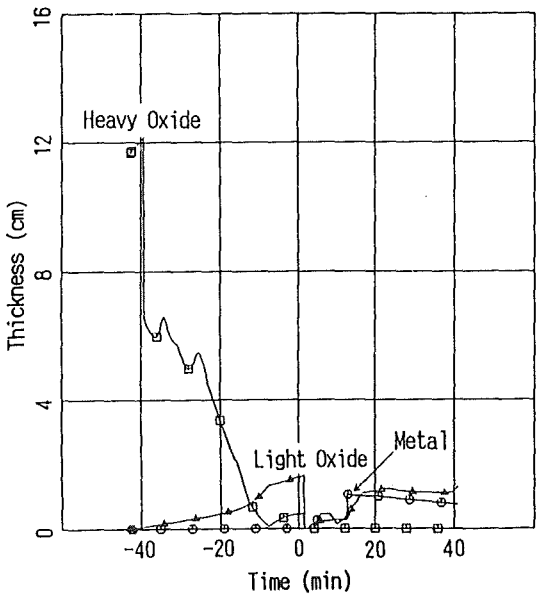

Fig. 8 Crust Thickness at the Bottom of Each Layer

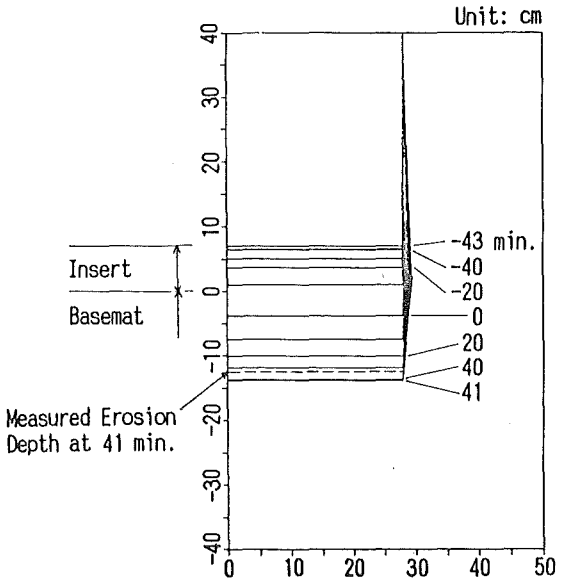

Fig. 9 Erosion Depth (Kutateladze's)

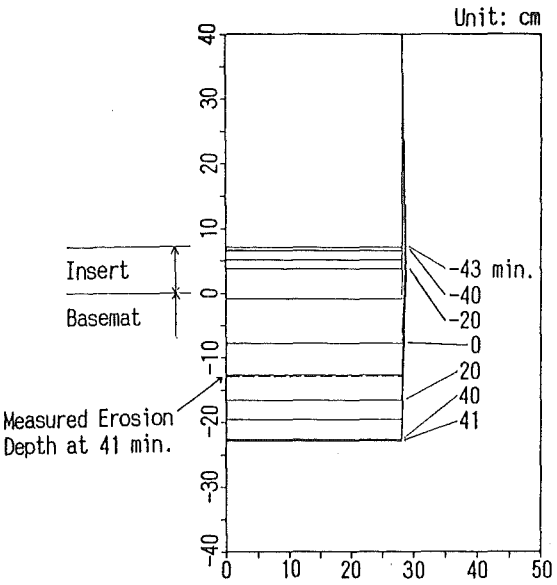

Fig. 10 Erosion Depth (Greene's)

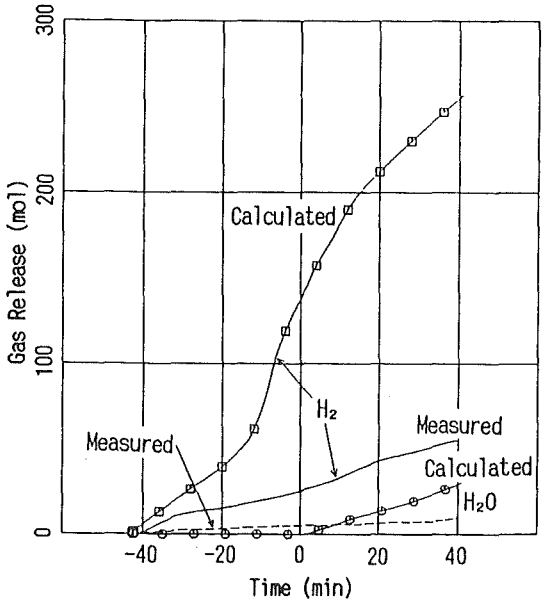

Fig. 11 Amount of Generated H_2 and H_2O

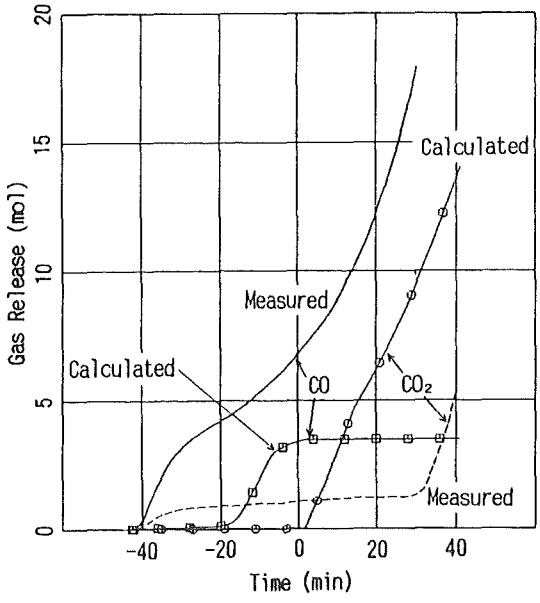

Fig. 12 Amount of Generated CO and CO_2

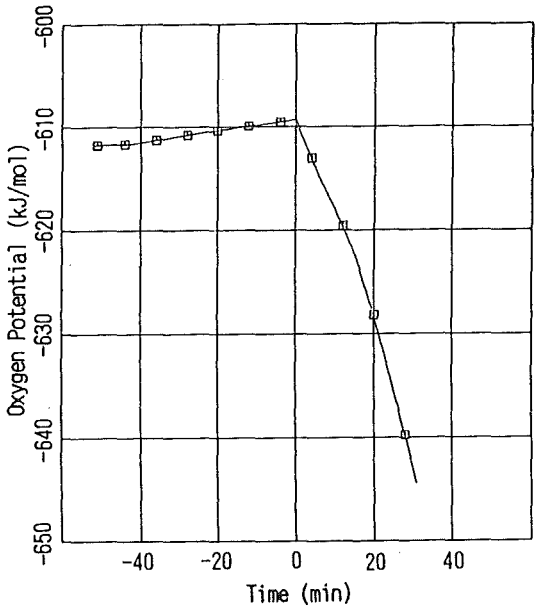

Fig. 13 Oxygen Potential in Melt Pool

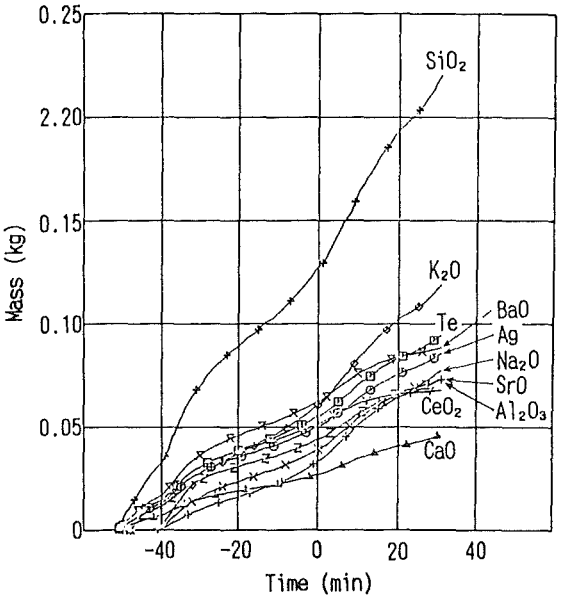

Fig. 14 Amount of Generated Aerosol (1)

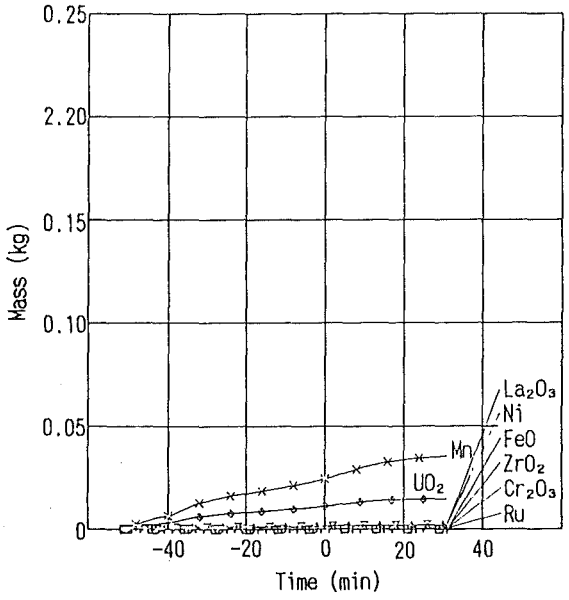

Fig. 14 Amount of Generated Aerosol (2)

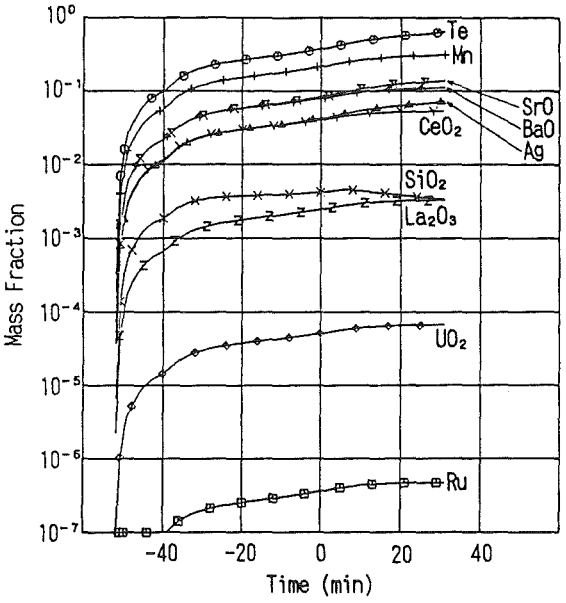

Fig. 15 Release Fractions of Generated Aerosol

UNCERTAINTY OF CORIUM-CONCRETE HEAT TRANSFER CORRELATIONS DUE TO UNCERTAINTY OF MELT TRANSPORT PROPERTIES

F.J. González Pindado

Cátedra de Tecnología Nuclear
E.T.S. Ingenieros Industriales
Universidad Politécnica de Madrid
C/ José Gutiérrez Abascal, 2
28006 MADRID, (SPAIN)

ABSTRACT

It has been largely recognized that many uncertainties remain in the prediction of corium-concrete interactions. One of these uncertainties, and not the smallest one, is the spread of values offered by different data bases on melt transport properties. An uncertainty and sensitivity analysis of the corium-concrete heat transfer correlations is presented. The uncertainty of heat transfer coefficients due to uncertainty of properties has been quantified; the relative importance of each property has also been obtained.

The results of the analysis may be used to decide where to put experimental efforts to reduce more effectively the present uncertainties. Analysis techniques based on Latin Hypercube Sampling, LHS /13/, and linear regression analysis, PCCSRC /14/, were used to study the behaviour of heat transfer coefficients in forty-two cases, representative of almost all possible situations in LWR's.

INTRODUCTION

A limited number of models and correlations have been proposed to predict corium-concrete axial heat transfer. CORCON 2 /1/ has a gas film model coupled to the Greene's correlation for melt-interface-gas film-concrete surface heat transfer, Greene's correlation is also used to predict interlayer heat transfer. WECHSL /2/ has a logic based on the Reynolds number to discriminate between discrete bubble, transition or gas film regimes, described by

different correlations; the one used for the discrete bubble regime is the Reinecke's correlation. As there is evidence that the superficial velocities for reactor cases are not high enough to maintain a gas film, CORCON 3 /3/ has incorporated a slag film model developed by D.R. Bradley coupled with the Kutateladze's correlation. The scope of this work is limited to the study of Greene's, Reinecke's and Kutateladze's correlations which are collected in table I.

Other models which can affect corium-concrete heat transfer are the prediction of detachment bubble size from the corium-concrete interface, and the bubble population density limiting value. Among the three correlations cited, only the Greene's one has an explicit dependency of bubble radius, whereas the Reinecke's one is the only that has a limiting value on heat transfer coefficient due to bubble population density considerations. The models proposed to predict the bubble radius are similar, this is a constant times the Laplace constant, varying in the way to choose or the value chosen for the leading constant, which in almost all cases are related to the contact angle or simulant experiment observations. The values range from a minimum offered by the Fritz equation /4/ near 0.5, and a maximum implemented in CORCON 2, which is 3.97, another references /2/,/5/,/6/ give values between those above.

About the melt transport properties, i.e. density, dynamic viscosity, thermal conductivity and surface tension, there are many discrepancies between different data bases for single species, and also between models predicting mixture properties /7/. The problem arises not only because of the difficulties to obtain reliable high temperature data, but also when extrapolating them to mixture temperatures below the fusion temperature of single species but above the *solidus* temperature of the mixture. From a collection of different data bases and models for mixtures (/1/,/2/, /3/,/4/,/8/,/9/,/10/,/11/,/12/) one can obtain, for a given temperature and composition, the uncertainty range of each property as the interval between the maximum and minimum values calculated using those data bases and the models mentioned above.

The aim of this work can be formulated in the following way: (a) obtain the uncertainty range of heat transfer coefficients calculated with the Greene's, Kutateladze's, and Reinecke's correlations, plus bubble radius (4 output variables), due to uncertainties in density, viscosity, thermal conductivity,

and surface tension of the melt, plus gas density and bubble radius constant (6 input variables), and (b) obtain the relative importance of the input variables on the uncertainty of the output variables.

To obtain a complete description of the uncertainty ranges, 42 different cases have been analyzed trying to cover all the possible reactor situations, as it can be seen in table II. Variations of melt character (metal or oxide), temperature, type of corium (BWR or PWR), type of concrete (limestone/common sand, limestone/limestone, or siliceous), and weigth percent of concrete in the corium were combined. Finally the analysis was completed varying the superficial velocity to take into account the former and later stages of the core-concrete interactions.

The statistical description of input variables has been based on *uniform* distributions, with maximum and minimum values given by the different data bases and models for mixtures. *For each of the 42 cases* an input sample matrix of size 100*6 (100 is the sample size) was generated using LHS. After this, the input sample was fed to the heat transfer models obtaining an output sample matrix of size 100*4, which was used to describe the uncertainty range of output variables through the mean, the standard deviation and the 95 and 5 percentile. These output and input matrixes were then fed to PCCSRC, which makes a linear regression analysis. A ranking of variable importance was based on an ordering of the absolute value of standardized regression coefficients (SRC), and a measure of the successfulness of the regression model was made by the closeness of the determination coefficient (R^2) to 1.

RESULTS

Uncertainty of Input Variables

The uncertainty range for the input variables has been calculated by the procedure explained above. The results for the 42 cases are given in figs. 1 to 5.

For DENL (melt density), fig. 1, an overlapping between Zr rich metal melt cases and oxide melt cases can be observed; a mixture of metal and oxide without segregation could be anticipated even with low gas superficial

velocities. On the other hand, for Si rich metal melts, differences between the oxide and metal densities would preclude mixing, except in the case of higher gas superficial velocities.

For VISL (melt viscosity), fig. 2, oxide cases 4,7,11,16,19 and 23 include recent experimental data /11/,/12/, along with code models /1/,/2/, this is the reason for the broad uncertainty range in these cases, since experimental values are generally very much greater than those calculated from code models. For the metal phase, CORCON and WECHSL employ the viscosity of pure Fe; other models tested were molar and mass averages of a mixture of only Fe, Ni and Zr /4/, because of lack of data for Cr and Si.

For CONL (melt conductivity), fig. 3, CORCON and WECHSL have constant values for single species, without temperature dependence, and that for Zr shows a great discrepancy.

For SURL (melt surface tension), fig. 4, the greater the SiO_2 content the broader the uncertainty ranges for the oxide phases, mainly due to the particular correlation implemented in the WECHSL code. For the metal phase, lack of data gives artifical narrow uncertainty ranges.

For DENG (gas density), fig. 5, the minimum value is given by the CORCON code and the maximum by the ideal gas law for a mixture of CO_2 and H_2O.

For BRCT (bubble radius constant), the influence of superficial velocity was not taken into account, giving only the fixed maximum and minimum limits cited previously.

Uncertainty of Output Variables

The uncertainty calculated for the output variables due to the uncertainty of the input variables, is summarized in fig. 6, which shows a normalized measure of uncertainty (100*standard deviation/mean) for all the 42 cases and 4 output variables. This allows to make a comparison between them avoiding units and absolute values dependencies. On the other hand, figs. 7 to 13 show the mean value and the 95 and 5 percentile for each of the 42 cases, and also for high and low superficial velocities, which in turn give an idea of the absolute value of uncertainty.

Comparing the results shown in fig. 6, abnormal cases can be observed corresponding to those cited when speaking about VISL, due mainly to VISL being the most important input variable affecting HKUT (Kutateladze), as shown in fig. 16. This gives a high degree of relative uncertainty (near 70%) for these cases, in spite of the lower absolute value showed in figs. 8 and 12.

Returning to fig. 6, BUBR (bubble radius) has the higher relative uncertainty (near 50%). Due to the fact that BUBR is the most important variable, through BRCT, affecting HGRE (Greene) as one can see in figs. 14 and 15; so, it is also coherent to obtain a high relative uncertainty (near 40%) for HGRE.

The relative uncertainty of HREI (Reinecke) and HKUT is (except the special cases cited above) within a band limited by 10% and 30%, not changing very much from case to case. It has to be noted that, for high superficial velocity cases, sometimes there are crossed the limits for transitions within the formulation of HKUT and HREI, giving the differences observed in fig. 6; in turn, for cases not crossing those limits the relative uncertainty must be the same whichever the value of Vs may be, but differences can be appreciated looking at the absolute values shown in figs. 7 to 13.

Another evident observation that could be made is that HGRE gives values some orders of magnitude higher than those from HREI and HKUT, already shown in a paper by D.R. Bradley /15/. In that paper the inadequacy of HGRE to predict corium-concrete heat transfer was demonstrated, but it could be still valid to simulate interlayer heat transfer by only modifying its experimentally determined coefficients to match prototypic corium situations /3/. Comparing HREI and HKUT, it can be seen that HREI approximately doubles the values given by HKUT; these differences should be solved taking into account that when applied to corium-concrete heat transfer /3/, HKUT is accompanied by a slag film resistance, whereas HREI is applied without heat transfer limitations /2/.

Relative Importance

The main result from the linear regression analysis is a ranking in order of relative importance, it gives a qualitative measure of the sensitivity of the output variables to changes, within their uncertainty ranges, in the input variables. The value of SRC's is shown in figs. 14 to 21, distinguishing

between oxide and metal cases because of their marked differences. Within each figure, SRC values from the linear regression of one output variable with all the input ones are shown for each case.

Variable HGRE, fig. 14, is mainly influenced by BRCT, which is the same to say by the bubble radius. This fact is truth for all the cases, with a large margin relative to other input variables. The second place could be assigned to SURL, but sometimes VISL competes for it. For metal cases, fig. 15, DENL is near BRCT for cases with higher Si content; for cases with higher Zr content, DENL, CONL, and VISL compete for the second place. Another observation is that for all the cases the relative importance of DENG is negligible.

For HKUT, fig. 16, in almost all cases VISL is the most important input variable, except for cases with 25%w of L/L concrete, for which CONL competes with VISL. For all the other oxide cases, CONL and DENL compete for the second place in the ranking. Looking to the metal cases, fig. 17, it is difficult to draw out conclusions because of the competition between DENL, CONL and VISL. In any case one can extract the following general observations. The relative importance of DENL increases with the Si content and the opposite occurs with CONL and VISL; also the relative importance of VISL increases strongly with the temperature, the opposite occurs with CONL and DENL; as in HGRE, DENG has the lowest order of importance.

For HREI, looking only to the oxide cases, fig. 18, there is a clear competition between SURL and CONL for the first place of the ranking, having VISL only a minor importance, but not negligible; for these cases, the lower the concrete content the higher the importance of CONL and the lower the importance of SURL. For the metal phase, fig. 19, one can observe a similar behaviour than that explained above for HKUT, with the only difference that VISL never reaches the first place of the ranking. As for previous output variables, DENG has the smallest importance.

For BUBR, figs. 20 and 21, it is clear that for all cases BRCT is the most important parameter, far from the other ones. For the oxide cases BRCT is followed in the ranking by SURL, and then by DENL, occurring the opposite for the metal cases. Finally DENG has again the smallest importance.

To finish the analysis of results it is important to turn one's eyes towards the determination coefficient to see how successful the regression model has been in representing the relation between the input and output variables; this has been represented in fig. 22. One can see in that figure that, except for those special cases already cited, the R^2 are all above 0.8, which indicates the success of the regression model.

CONCLUSIONS

Great differences have been evidenced between the heat transfer correlations in absolute values, HGRE (Greene) is some orders of magnitude higher than HKUT (Kutateladze) and HREI (Reinecke), and HREI nearly doubles HKUT. It was also evidenced that the property or properties having the highest relative importance are not the same from one correlation to another, indicating that in describing the same phenomena different approaches were taken. Within each correlation similarities were found between oxide and metal cases respectively, with remarkable differences from each other.

It could be noted that if there were a explicit inclusion of bubble radius within the heat transfer correlations, the bubble radius leading constant could be the most important parameter affecting the results. So it could be recommended to make this relation explicit, and to construct models to predict this constant, based on superficial velocity and contact angle, which in fact depends on composition of the three media and temperature.

The results of this analysis could be used to fix priorities in any experimental program devoted to reduce the uncertainty introduced in heat transfer correlations, of the type studied, by melt transport properties. This could be achieved by assigning the highest priority to the properties with the highest relative importance and so on.

REFERENCES

/1/ R.K. Cole, D.P. Kelly, M.A. Ellis. CORCON-Mod 2: A Computer Program for Analysis of Molten-Core Concrete Interactions. August 1984. NUREG/CR-3920, SAND84-1246.

/2/ M. Reimann, S. Stiefel. The WECHSL-Mod 2 Code: A Computer Program for the Interaction of a Core Melt with Concrete including the Long Term Behavior. June 1989. KfK-4477.

/3/ D.R. Bradley. Integration of Accumulated Code Modifications to Create the Interim Version of CORCON-Mod 3. November 1991. Sandia National Laboratories.

/4/ D.A. Powers, J.E. Brockmann, A.W. Shiver. VANESA: A Mechanistic Model of Radionuclide Release and Aerosol Generation During Core Debris Interaction with Concrete. July 1986. NUREG/CR-4308, SAND85-1370.

/5/ M. Lee, M.S. Kazimi, G. Brown. A Heat Transfer Model for the corium/concrete interface. International Meeting on LWR Severe Accident Evaluation. Cambridge, Massachusetts. 1988. TS-12.6.

/6/ V.K. Dlir, J.N. Castle, I. Catton. Role of Taylor Instability on Sublimation of a Horizontal Slab of Dry Ice. Journal of Heat Transfer. August 1977. Vol 99.

/7/ J. González. Some Physical Properties of the Melt. Presented at the ACE-TAC Meeting, Palo Alto, California, November 1991.

/8/ D.L. Hagrman, G.A. Reymann, R.E. Mason. MATPRO-V11(rev.1): A Handbook of Materials Properties for use in the Analysis of Light Water Reactor Fuel Rod Behavior. February 1980. NUREG/CR-0497.

/9/ TRAC-PF1/MOD1: An advanced Best-Estimate Computer Program for PWR Thermal-Hydraulic Analysis. NUREG/CR-3858. LA-10157-MS.

/10/ D.R. Olander. Fundamental Aspects of Nuclear Fuel Elements. 1976. USDOE, TID-26711-P1.

/11/ M. Roche, D. Steidl, L. Leibowitz, J. Fink, R. Sehgal. Viscosity of Core-Concrete Mixtures. June 1991, ACE-TAC, Argonne, Illinois.

/12/ M. Roche, D. Steidl, L. Leibowitz, J. Fink, R. Sehgal. Viscosity of Core-Concrete Mixtures. November 1991, ACE-TAC, Palo Alto, California.

/13/ Iman R.L., et al., "A Fortran 77 Program and User's Guide for the Generation of Latin Hypercube and Random Samples for the Use with Computer Models", NUREG/CR-3624, SAND83-2365, March 1984.

/14/ Iman R.L., et al., "A Fortran 77 Program and User's Guide for the Calculation of Partial Correlation and Standarized Regression Coefficients". NUREG/CR-4122, SAND85-0644, June 1985.

/15/ D.R. Bradley, "Modelling Heat Transfer Between Core Debris and Concrete Proc. 25th National Heat Transfer Conference, ANS Trans. Houston, TX, 1988, pp. 37-49.

Symbols

A,	Laplace constant = $(\sigma_l/g(\rho_l-\rho_g))^{1/2}$
C_p,	Specific heat
g,	Gravity constant
h,	Heat transfer coefficient
k,	Thermal conductivity
Ku,	Kutateladze number $(Pr_l.p.Vs)/(g.\mu_l)$
p,	Pressure
Pr,	Prandtl number ($\mu cp/k$)
Vs,	Superficial velocity
V_{tr},	Transition velocity
ρ,	Density
μ,	Dynamic viscosity
σ,	Surface tension

Abbreviations

DENL,	Melt Density
VISL,	Melt Viscosity
CONL,	Melt Thermal Conductivity
SURL,	Melt Surface Tension
DENG,	Gas Density
BRCT,	Bubble Radius Leading Constant
HGRE,	Greene heat transfer coefficient
HKUT,	Kutateladze heat transfer coefficient
HREI,	Reinecke heat transfer coefficient
BUBR,	Bubble Radius
L/S,	Limestone/Common Sand Concrete
L/L,	Limestone/Limestone Concrete
S,	Siliceous Concrete.

Underscripts

l,	Melt
g,	Gas

Greene:

$$h = 5.05 \frac{k_l}{r_b} \left(\frac{\rho_l V_s r_b}{\mu_l}\right)^{0.5} \left(\frac{\mu_l Cp_l}{k_l}\right)^{0.8}$$

Reinecke:

$$h_1 = \sqrt{\frac{k_l}{A} \frac{(1.65)^2}{\sqrt{6}} Pr_l^{0.84} \frac{k_l \rho_g V_s}{\mu_l}}$$

$$h = \min\left(h_1,\ 4.63.(k_l/A).Pr_l^{0.38}\right)$$

Kutateladze:

$$h_1 = 1.5\ 10^{-3}\ (k_l/A)\ ku^{2/3} \qquad V_s < V_{tr}$$

$$h_2 = h_1\ (V_s/V_{tr})^{-1/2} \qquad V_s > V_{tr}$$

$$V_{tr} = 4.3x10^{-4}\ (\sigma_l/\mu_l)$$

Table I. Heat Transfer Correlations Studied.

CASE	OX/MET	TEMP(K)	CORIUM	CONCRETE	%CONCRETE	
1	OXIDE	1800	BWR	L/S	25	BWR = 70%w UO2, 30%w ZrO2
2					50	
3				L/L	25	
4					50	
5				S	25	
6					50	
7			PWR	L/S	25	PWR = 80%w UO2, 20%w ZrO2
8					50	
9				L/L	25	
10					50	
11				S	25	
12					50	
13		2500	BWR	L/S	25	
14					50	
15				L/L	25	
16					50	
17				S	25	
18					50	
19			PWR	L/S	25	
20					50	
21				L/L	25	
22					50	
23				S	25	
24					50	
25	METAL	1800	COMP1	L/S	--	COMP1 = 90%w Zr, 5%w SS, 5%w Si
26				L/L	--	
27				S	--	
28			COMP2	L/S	--	COMP2 = 50%w Zr, 5%w SS, 45%w Si
29				L/L	--	
30				S	--	
31			COMP3	L/S	--	COMP3 = 5%w Zr, 25%w SS, 70%w Si
32				L/L	--	
33				S	--	
34		2500	COMP1	L/S	--	
35				L/L	--	
36				S	--	
37			COMP2	L/S	--	
38				L/L	--	
39				S	--	
40			COMP3	L/S	--	
41				L/L	--	
42				S	--	

CASE A : HIGH SUPERFICIAL VELOCITY
OXIDE = 0.2 M/S
METAL = 0.7 M/S

CASE B : LOW SUPERFICIAL VELOCITY
OXIDE = 0.01 M/S
METAL = 0.3 M/S

L/S = 30%w SiO2, 27%w CaO, 5%w Al2O3, 10%w MgO, 22%w CO2, 6%w H2O
L/L = 7%w SiO2, 47%w CaO, 2%w Al2O3, 4%w MgO, 34%w CO2, 6%w H2O
S = 71%w SiO2, 14%w CaO, 5%w Al2O3, 1%w MgO, 5%w CO2, 4%w H2O

Table II. Cases Analysed.

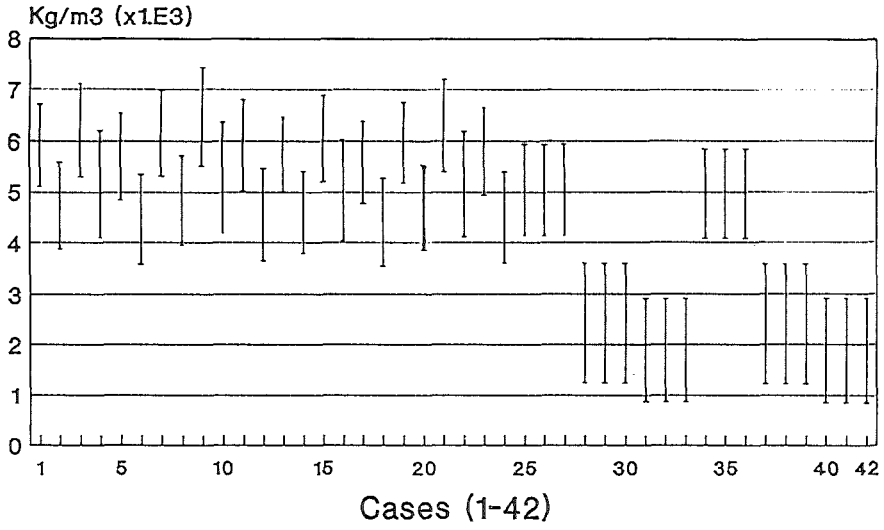

Figure 1.- Uncertainty Range. DENL.

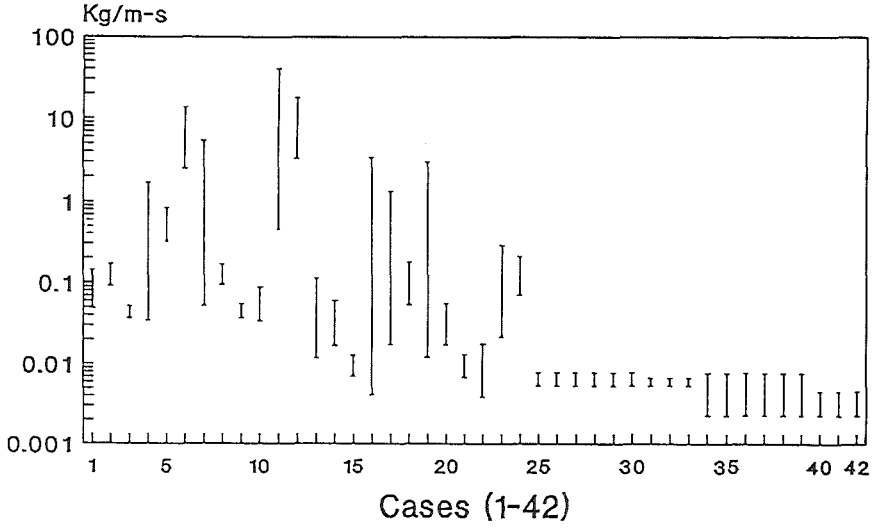

Figure 2.- Uncertainty Range. VISL.

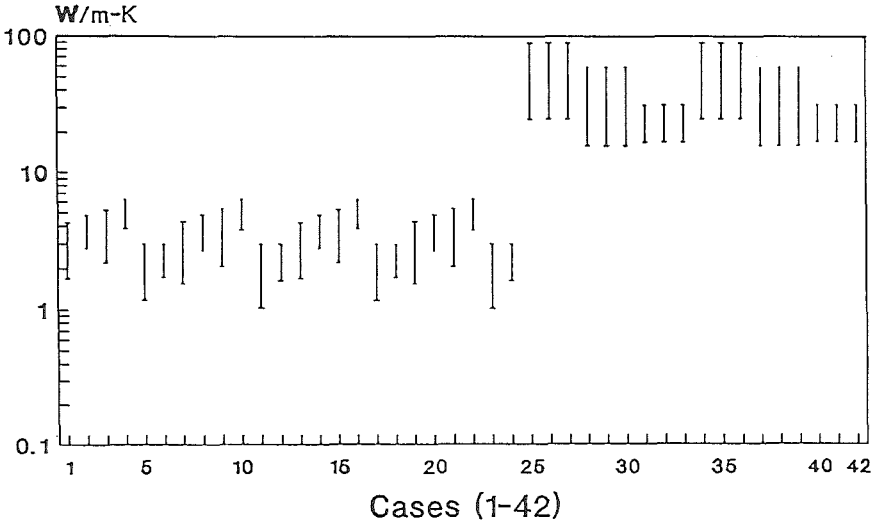

Figure 3.- Uncertainty Range. CONL.

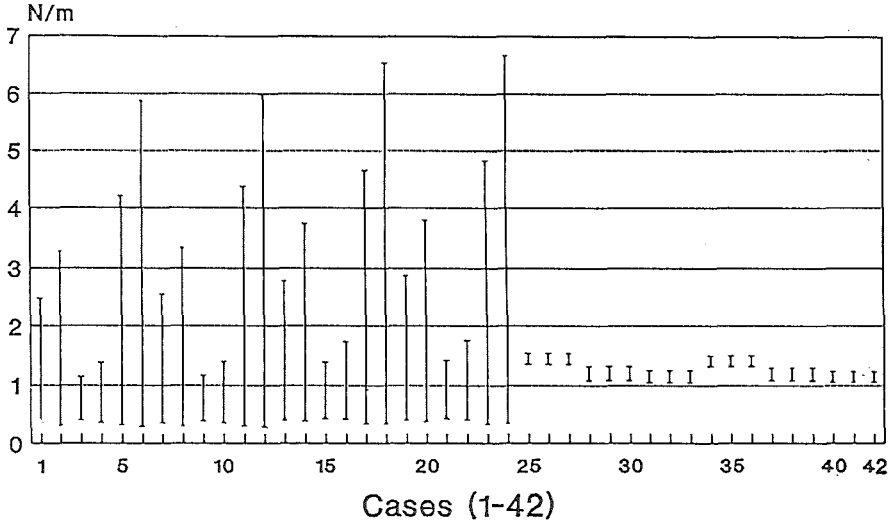

Figure 4.- Uncertainty Range. SURL.

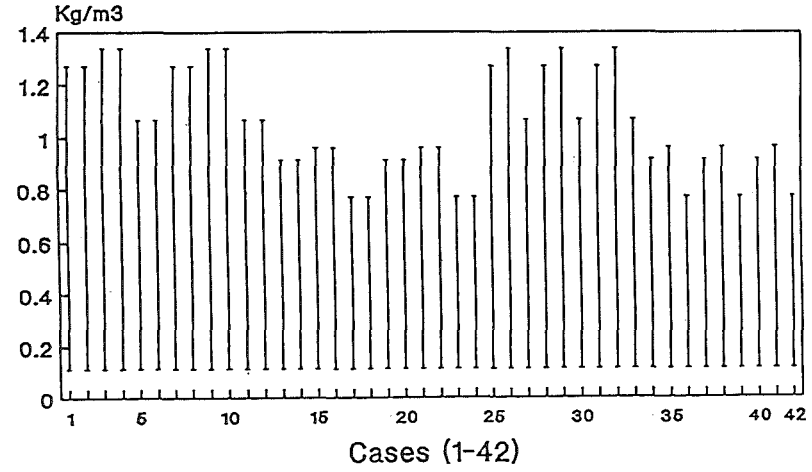

Figure 5.- Uncertainty Range. DENG.

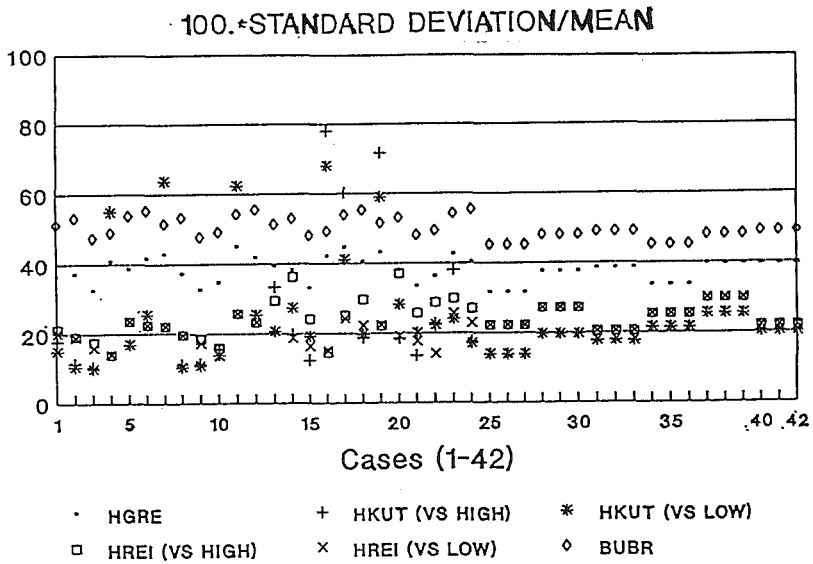

Figure 6.- Relative Measure of Uncertainty.

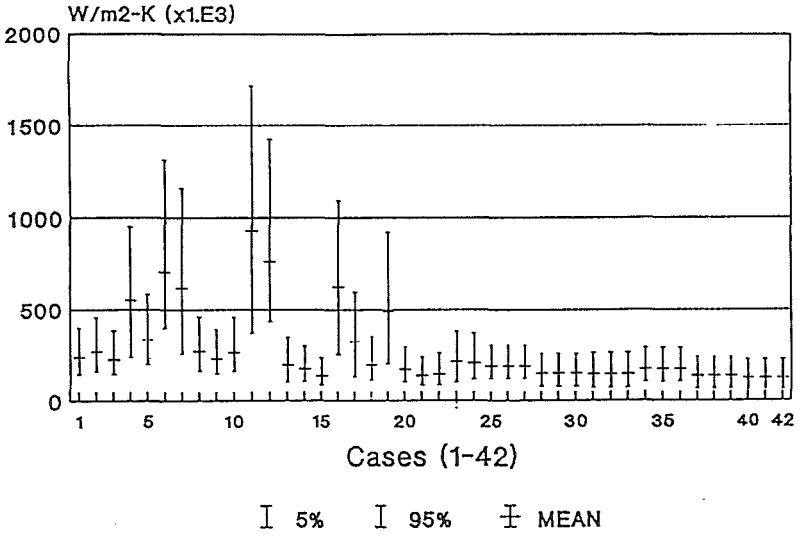

Figure 7.- Uncertainty Range. HGRE (Vs High).

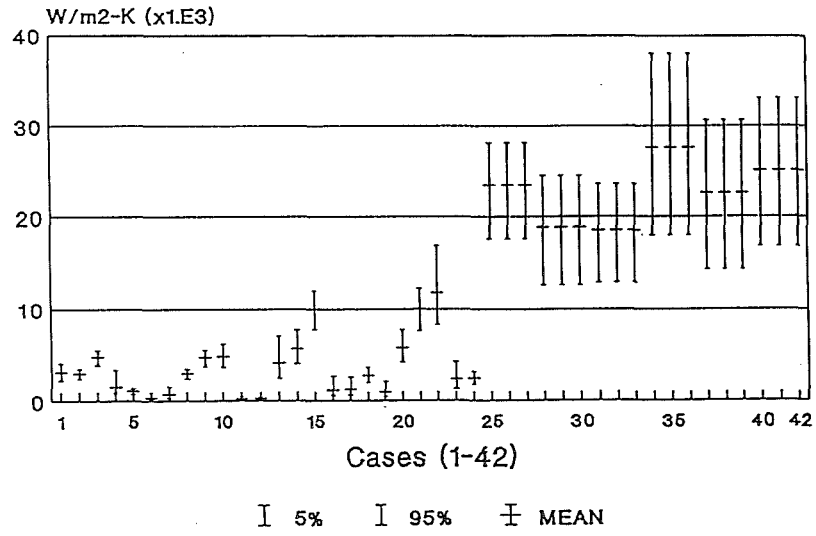

Figure 8.- Uncertainty Range. HKUT (Vs High).

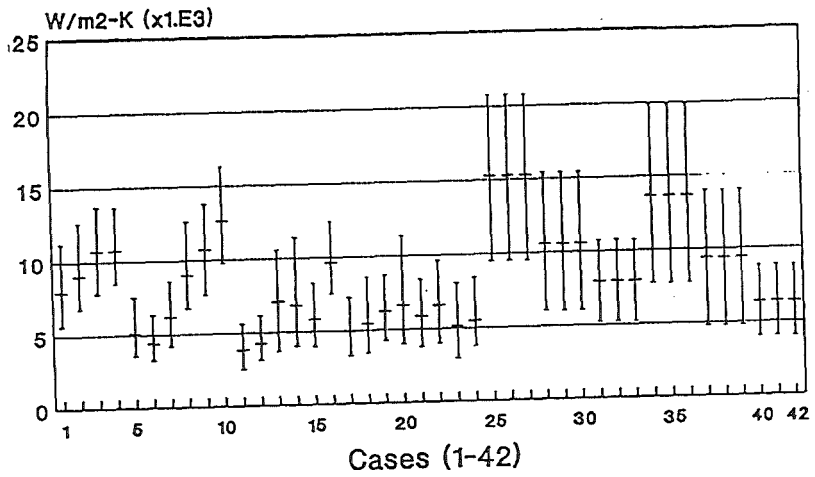

Figure 9.- Uncertainty Range. HREI (Vs High).

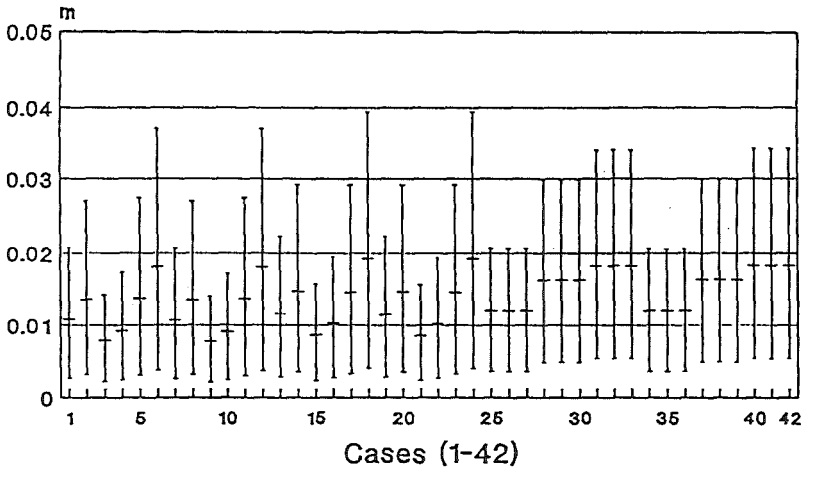

Figure 10.- Uncertainty Range. BUBR.

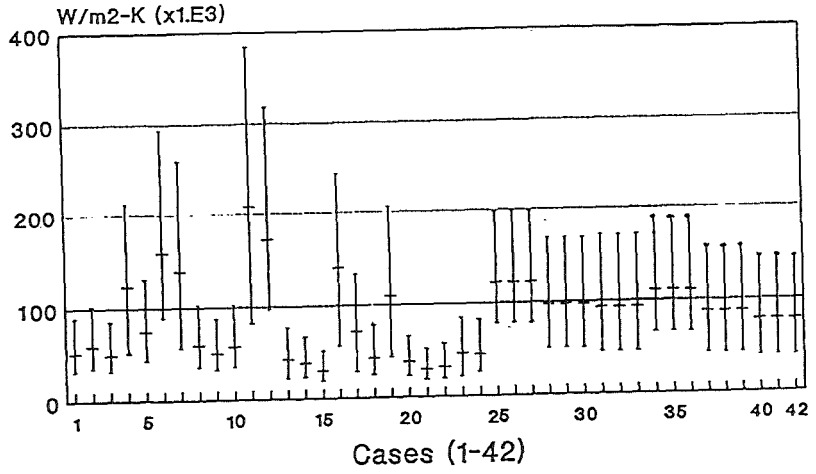

Figure 11.- Uncertainty Range. HGRE (Vs Low).

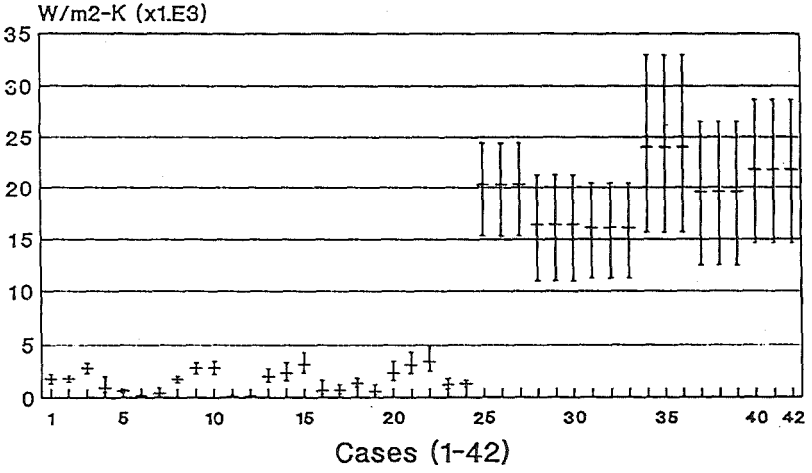

Figure 12.- Uncertainty Range. HKUT (Vs Low).

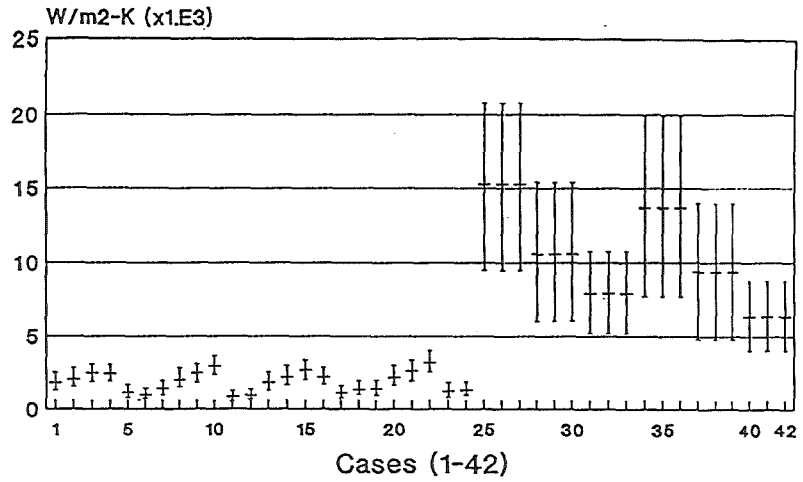

Figure 13.- Uncertainty Range. HREI (Vs Low).

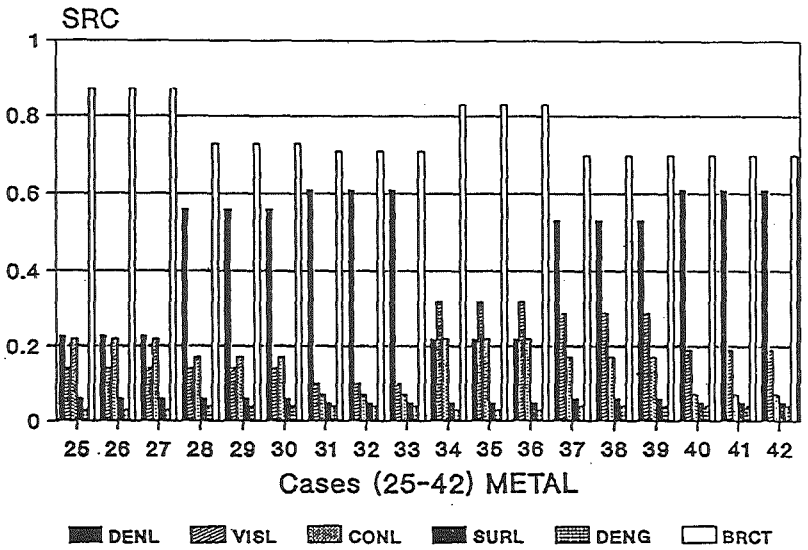

Figure 15.- Relative Importance on HGRE (Metal).

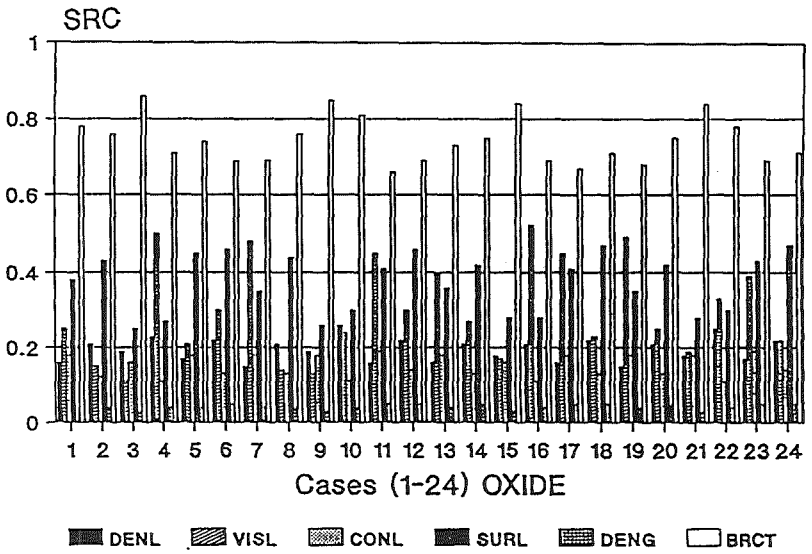

Figure 14.- Relative Importance on HGRE (Oxide).

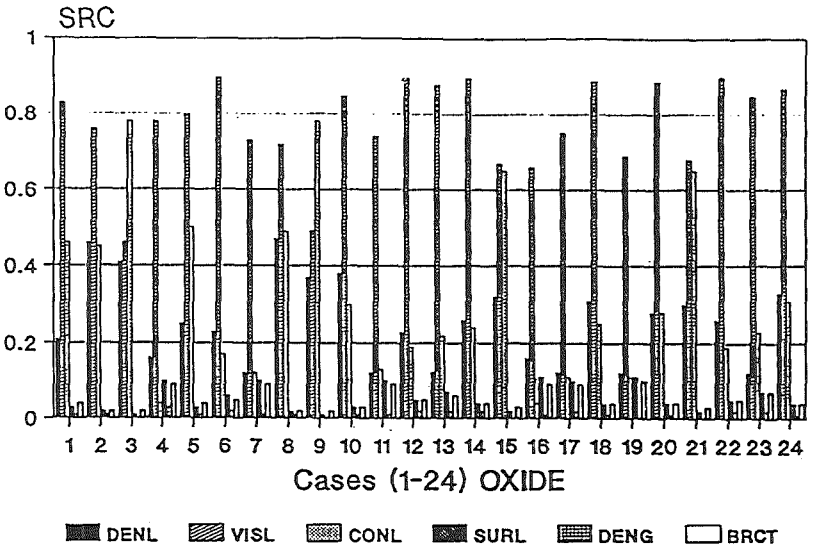

Figure 16.- Relative Importance on HKUT (Oxide).

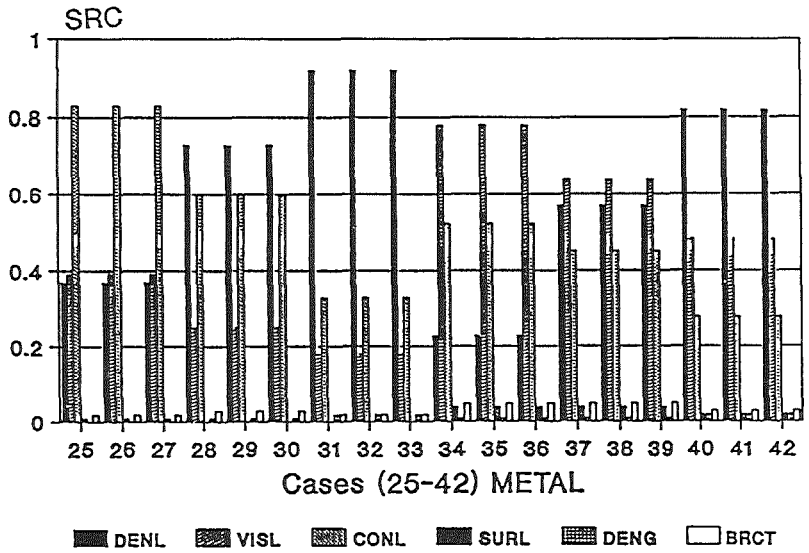

Figure 17.- Relative Importance on HKUT (Metal).

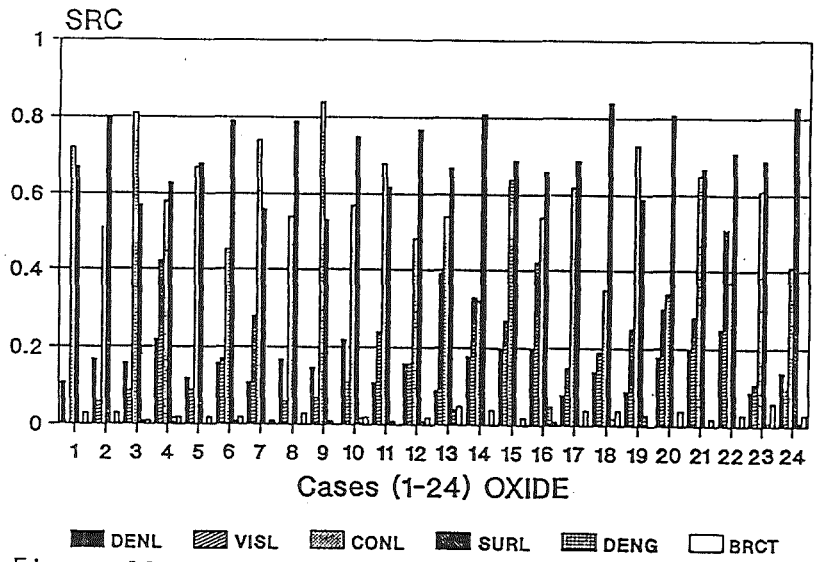

Figure 18.- Relative Importance on HREI (Oxide).

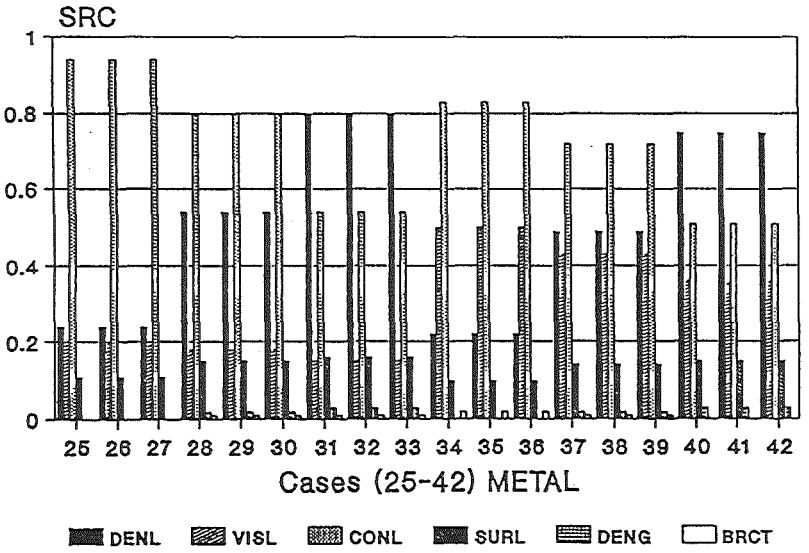

Figure 19.- Relative Importance on HREI (Metal).

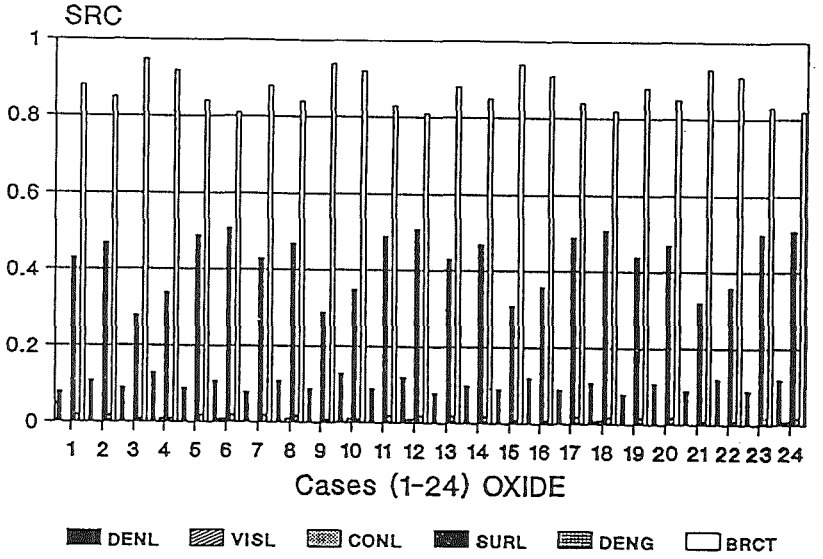

Figure 20.- Relative Importance on BUBR (Oxide).

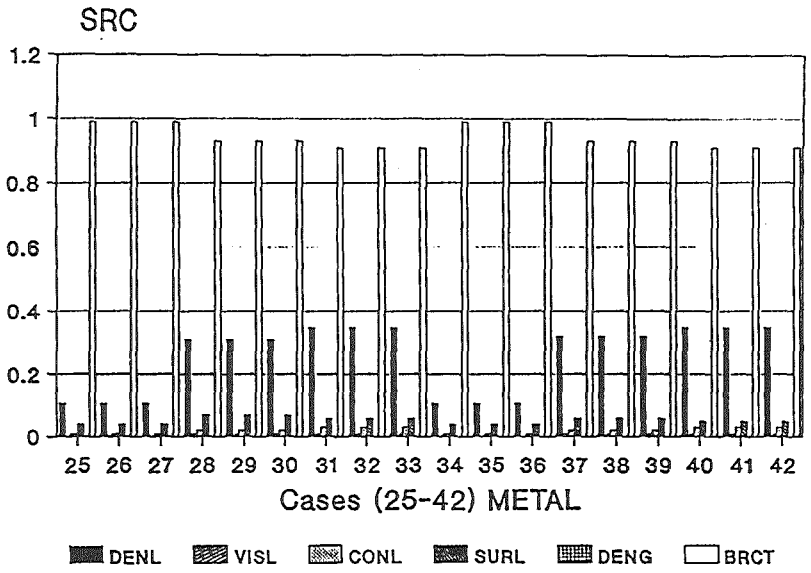

Figure 21.- Relative Importance on BUBR (Metal).

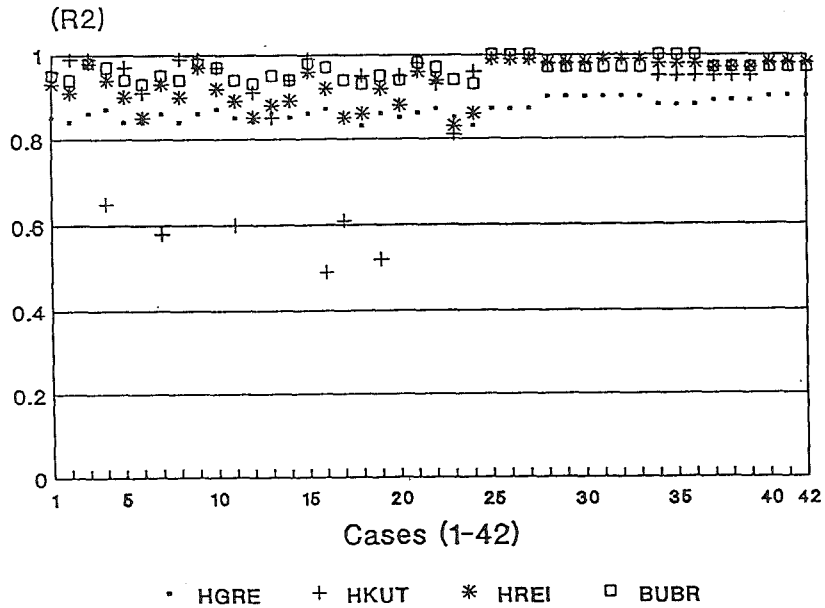

Figure 22.- Determination Coefficient (R^2).

NON-IDEAL SOLUTION MODELING FOR PREDICTING CHEMICAL PHENOMENA DURING CORE DEBRIS INTERACTIONS WITH CONCRETE

D.A. Powers
Sandia National Laboratories
Albuquerque, NM

ABSTRACT

Non-ideal solution models for the metallic and oxide phases of molten reactor core debris are developed to improve predictions of fission product behavior during core debris/concrete interactions. The non-ideal solution model of the metal phase of core debris is based on use of the Kohler equation to extrapolate the available data and models for binary combinations of melt constituents to predict properties of the multicomponent mixture. Subregular models are used for the constituent binary alloys. Parameters for the models have been taken from the literature or estimated. The non-ideal solution model for the oxide phase is based on an associated solution model that has proved of use in the description of complex geological melts. The excess free energy of mixing in the oxide phase is expanded in terms of the properties of hypothesized, stoichiometric species. Parameters for the model are determined from data for binary combinations of constituents and from comparisons of model predictions to known phase diagrams.

I. INTRODUCTION

The uninterrupted progression of a severe nuclear reactor accident will result in the deposition of molten reactor core debris onto concrete in the reactor containment. The interactions of core debris have been the subject of extensive experimental and analytic studies. The heat and pressure loads placed on containments by core debris/concrete interactions as well as combustible gases expelled into the containment atmosphere are features

of the interactions that have been extensively studied. The interactions of core debris with concrete have also been found to be important sources of aerosol generation and radionuclide release during severe accidents.[1]

Vaporization is the predominant mechanism of aerosol generation and radionuclide release during core debris/concrete interactions. The earliest attempts to mechanistically model the vaporization processes leading to aerosol generation and radionuclide release treated the molten core debris as two ideal solutions -- an oxidic melt and a metallic melt.[1] The ideal solution approximation becomes of questionable validity at temperatures below about 2200K and especially when siliceous material is incorporated into the melt. Therefore, an effort has been undertaken to devise a better approximation for the chemical activities of melt constituents during core debris interactions with concrete. In this paper, non-ideal solution models for the metal and oxide phases of core debris to be used in the VANESA model of aerosol generation and radionuclide release are described. Approximate models are satisfactory for this application since uncertainties in the data for high temperature thermodynamic properties of vapor species constitute an important limit on the accuracy to which these vaporization processes can be predicted.

II. ACTIVITY COEFFICIENTS FOR THE METALLIC PHASE

In the original, ideal solution, formulations of both the CORCON code and the VANESA model, it was hoped that an adequate approximation could be made by ignoring condensed phase chemical reactions. That is, oxidation-reduction reactions of primary importance would be those that involve gas species -- the classic reactions that produce hydrogen and carbon monoxide from reactions of steam and carbon dioxide with metals in the core debris. Certainly this approximate treatment is adequate for the analysis of molten steel interactions with concrete which constituted much of the early data base available for the validation of models of core debris interactions with concrete. Consistent with this first approximation, fission products and other melt constituents were segregated into either the oxide or the metal phase exclusively according to empirical data obtained by melting UO_2 with iron.[2]

The first indication that this simple partitioning of fission products might not be an adequate treatment came from the analyses of the relative

densities of the phases of core debris.[3] Zirconium was found to be capable of reducing uranium dioxide to the hypostoichiometric state and uranium metal could partition into the metal phase, raising the density of this phase. A clear indication of the inadequacy of the approximation has come from the SURC-4 test[4] and the recent BETA5.1 test. In both of these tests, it was evident that zirconium was reacting exothermically with more than just gases evolved from the concrete. These test results have been interpreted to indicate that zirconium reacts with silicon dioxide in the concrete to form silicon metal in the metallic phase of core debris though this hypothesis has not been proved.

A first step at improving the chemistry models in CORCON and the VANESA subroutine has been to permit elements to equilibrate as both oxides and metals according to the ambient chemical conditions rather than by prescription. This has made a large increase in the number of condensed-phase chemical species recognized by the code. While these changes were being made, it was also convenient to develop thermodynamic data bases for other elements that heretofore have been treated in the model by analogy. Thermodynamic data bases are now available for the 37 elements listed in Table 1.

A key factor in determining the partitioning of an element between the oxide and metallic phase is, of course, the chemical activity of an element in the metal phase. Chemical activities are also important in the analysis of vaporization of fission products such as tellurium from the metallic phase of core debris. It has been necessary then to develop a non-ideal solution model for the metallic phase of core debris to replace the original ideal solution model. First attempts to formulate such a model were based on Darken's approach for steel melts.[5] The metallic phase of core debris is, however, more chemically complex than steel melts. An empirical data base of sufficient completeness does not exist to support an empirical model such as Darken's. A model based on the excess free energy of mixing in the metallic phase has been devised. The free energy of the metal phase is taken to be:

$$G(\text{metal}) = \sum_{i=1}^{N} X(i)G^{o}(i) + RT\sum_{i=1}^{N} X(i)\ln(X(i)) + G^{xs}$$

$$RT\ln\gamma(i) = G^{xs} + \frac{\partial G^{xs}}{\partial X(i)} - \sum_{k=1}^{N} X(k)\frac{\partial G^{xs}}{\partial X(k)}$$

where

$X(i)$ = mole fraction of element i in the alloy

$G^o(i)$ = free-energy of pure, molten element i

G^{xs} = excess free energy

N = number of elements in the alloy

$\gamma(i)$ = activity coefficient of element i in the alloy

Experimentally validated models of the excess free energy of so complex a mixture as the metallic phase of core debris do not exist. What does exist are models of the excess free-energy of binary mixtures of many of the constituents of the metal phase of core debris. A variety of formulations of these excess free-energies are available. Each of the many candidate models is well suited for particular binary combinations of metals. Indeed, for metals that are sufficiently similar, simple regular solution models have been quite useful for estimating properties of binary alloys. In recent years the subregular solution model[6] has been widely used to describe binary alloys:

$$G^{xs}(A,B) = X(A)X(B)\left[W_{AB}(T)X(A) + h_{AB}(T)X(B) \right]$$

where

$G^{xs}(A,B)$ = excess free-energy of mixing of an alloy of mole fraction X(A) of element A and mole fraction X(B) of element B

$$W_{AB}(T) = W_{AB}^{o} + W_{AB}^{1}\, T = h_{BA}(T)$$

$$h_{AB}(T) = h_{AB}^{o} + h_{AB}^{1}\, T = W_{BA}(T)$$

$$RT\ln\gamma(A) = X(B)^2\left[2W_{AB}(T)X(A) + (1-2X(A)h_{AB}(T) \right]$$

$$RT\ln\gamma(B) = X(A)^2\left[W_{AB}(T)(2X(A)-1) + 2h_{AB}(T)X(B) \right]$$

For the system of elements shown in Table 1 about 666 pairs of parametric values, $W_{AB}(T)$ and $h_{AB}(T)$, are required to describe the possible binary combinations of elements in the metallic phase of core debris. For about 100 of these binary combinations, data have been reported using the subregular solution model. The data available to parameterize the models are measured activities of molten alloy constituents in these cases. In many of the cases, a subregular solution model for the liquid phase has been hypothesized as part of a study to predict phase relations in the binary alloy system. The parameters for the subregular solution models had to be derived for about 124 binary systems based on known properties of the alloys such as solubility limits or immiscibility limits.

Some binary systems that involve very strong interactions, such as binary alloys involving tellurium, simply do not conform well to the subregular solution model. Systems with very strong liquid phase interactions can usually be described in terms of an associated solution model.[7] In these cases, as well as in cases where more complex solution models have been derived for binary alloys, activity coefficients were calculated for a range of compositions and temperatures. The parameters for a subregular model were then derived from least-squares fits to the calculated activity coefficients.

For many of the possible binary alloys, there are neither phase diagram data nor thermodynamic data that can be conveniently used to parameterize a subregular solution model. In these cases, the partial molar enthalpies of mixing were estimated using a procedure developed by Miedema and co-workers.[8] Partial molar excess entropies of mixing were estimated based on suggestions by Lupis[9] and by Kubaschewski[10] that these quantities are correlated with the partial molar enthalpies of mixing. The actual correlations used were:

$$\overline{\Delta H}_i = 3000(\overline{\Delta S}_i^{xs} + 0.67) \text{ cal/mole for } \overline{\Delta H}_i > -10000 \text{ cal/mole}$$

$$\overline{\Delta H} = 625(\overline{\Delta S}_i^{xs} - 12) \text{ for } \overline{\Delta H}_i < -10000 \text{ cal/mole}$$

where

$\overline{\Delta H}_i$ = partial molar enthalpy of mixing of element i

$\overline{\Delta S}_i^{xs}$ = partial molar excess entropy of mixing of element i

To utilize models of binary alloys to predict activity coefficients in multicomponent alloys, the Kohler model[11] was used:

$$G^{xs} = \sum_{i=1}^{N-1} \sum_{j=1+1}^{N} X(i)X(j) \left[\frac{W_{ij}(T)X(i)}{X(i) + X(j)} + \frac{h_{ij}(T)X(j)}{X(i) + X(i)} \right]$$

Use of the Kohler equation to predict properties of multi-component alloys is not without controversy[12,13]. The Kohler equation as it has been adopted for this work cannot be used without some precautions to extrapolate properties of an alloy constituent to infinite dilution. There are, of course, many alternatives to the Kohler equation. Some of these alternatives have been found better suited for the prediction of phase relations in particular ternary systems. For the less demanding uses of metal activity coefficients in the CORCON code and VANESA model the Kohler equation seems to be sufficiently accurate. Because of the uncertainties in the thermodynamic properties of high temperature vapor species accuracies in $RT\ln\gamma(i)$ of ±5000 cal/mole are thought to be sufficient for calculation of vaporization.

III. ACTIVITY COEFFICIENTS FOR THE OXIDE PHASE

The state-of-the-art in modeling the solution properties of molten oxides is not as well-developed as is the modeling of metallic melts. The difficulties in modeling the oxide phase of core debris are formidable. The oxide phase of core debris is initially composed predominantly of UO_2 and ZrO_2. These classic ionic oxides can be described in terms of a two sublattice model. That is, the oxygen ions constitute a lattice which penetrates a metal ion lattice with sites occupied by zirconium and uranium ions. But, as interactions of core debris with concrete progress, network-forming oxide -- notably silicon dioxide and to some extent aluminum oxide -- are incorporated into the oxide phase of core debris. These species do not conform well to the two sublattice concepts of liquids. In fact, simply modeling melts containing silicon dioxide is itself a rather challenging undertaking. It is certainly an area of on-going research[14,15].

TABLE 1: Element and Oxide Components Considered in the Model

Element	Oxide	Element	Oxide
Ag	$AgO_{0.5}$	Nd	$NdO_{1.5}$
Al	$AlO_{1.5}$	Ni	NiO
As	$AsO_{2.5}$	Np	NpO_2
Ba	BaO	Pd	PdO
Ca	CaO	Pr	$PrO_{1.5}$
Cd	CdO	Pu	PuO_2
Ce	$CeO_{1.5}$, CeO_2	Rh	$RhO_{1.5}$
Cr	$CrO_{1.5}$	Ru	RuO_2, RuO_3
Cs	$CsO_{0.5}$	Sb	$SbO_{2.5}$
Eu	EuO	Si	SiO_2
Fe	FeO, $FeO_{1.5}$	Sm	$SmO_{1.5}$
K	$KO_{0.5}$	Sn	SnO, SnO_2
La	$LaO_{1.5}$	Sr	SrO
Li	$LiO_{0.5}$	Tc	TcO_2
Mg	MgO	Te	TeO_2
Mn	MnO	U	UO_2, UO_3
Mo	MoO_2, MoO_3	Y	$YO_{1.5}$
Na	$NaO_{0.5}$	Zr	ZrO_2
Nb	NbO, NbO_2		

TABLE 2: PARAMETERS FOR SOME BINARY CONSTITUENT MODELS

$W_{AB}(T)$ AND $h_{AB}(T)$ [cal/mole]

ELEMENT A	ELEMENT B					
	Cr	Fe	Ni	Si	U	Zr
Ag	25100-8.086T*	17276	12428-3.5T	3648-1.22T	-116-7.16T	-289070 + 34T
	25100-8.086T**	21485	15774-4.6T	10514-3.5T	-116-7.16T	-26769 + 31T
Ce	20696-6.9T	15580-9T	(a)	-60328	22210-7.4T	(a)
	43790-14.6T	49270-28T	(a)	-68723	21280-7.1T	(a)
Cr	---	3422-2.73T	340-1.29T	-10803 + 6.4T	3330	-1460 + 0.49T
		7992-4.85T	-950-1.29T	-94674 + 6.9T	1510	-19784 + 6.6T
Fe	---	---	-2000-0.24T	-41500 + 3.2T	19145 + 8.4T	-17236 + 5.7T
	---	---	-7700 + 2.7T	-25900 + 4.2T	-206.5-5.4T	-14996 + 5.0T
Ni	---	---	---	-16220 + 0.5T	-29398 + 35T	-68850 + 31T
				-25253 + 7.7T	-20076 + 20T	-47826 + 22T
Si	---	---	---	---	-47323 + 64T	-72897 + 105T
					-37285 + 48T	-58556 + 82T
U	---	---	---	---	---	9271-5.25T
						8393-5.25T

* $W_{AB}(T)$

** $h_{AB}(T)$

(a) insufficient data for parameterization

For this work, an empirical approach has been adopted. First, lattice statistics methods have been abandoned in favor of volume fraction statistics. This has been done because of the great disparities in the sizes of the various polymeric and polyatomic ions that are hypothesized to exist in the liquid phase. Second, the excess free-energy of binary combinations of oxides have been expanded mathematically in terms of the properties of hypothetical, stoichiometric liquid phase species. Thus, as an example, the properties of the binary system MgO-SiO_2 have been expressed as though the liquid phase were composed of the species MgO, SiO_2, $MgSiO_3$ and Mg_2SiO_4. Activity coefficients in this associated solution model are given by:

$$\mu_k = \mu_k^o(T) + RT\ln X(k) + RT\ln\gamma(k)$$

$$= \mu_k^o(T) + RT\left[\ln \Phi_k + \sum_{j=i}^{M} \Phi_j\left(1 - \frac{V_k}{V_j}\right)\right]$$

$$+ V_k \sum_{i=1}^{M} \sum_{j=1}^{M} \left[A(i,k) - 0.5\, A(i,j)\right] \Phi_i \Phi_j$$

where

μ_k = chemical potential of species k in the melt

$\mu^o_k(T)$ = chemical potential of the pure molten species k

R = gas constant

X(k) = mole fraction of species k in the melt

$\gamma(k)$ = chemical activity coefficient of species k in the melt

Φ_j = volume fraction of species k in the melt

$$= X(k)V_k \Big/ \sum_{j=i}^{M} X(j)V_j$$

V_k = molar volume of species k in the melt

A(i,j) = regular solution interaction coefficient between melt species i and j

(A(i,j) = A(j,i) and A(i,i) = A(j,j) =0)

This model has been used successfully to describe complex geologic melts that bear remarkable similarity to molten concrete.[16]

Two sets of parameters are being developed for this model. A very approximate set is based on considering only the melt components listed in Table 1 as melt species. A complete set of interaction constants has been developed for the major oxide constituents of core debris and molten concrete:

$AlO_{1.5}$, CaO, $CrO_{1.5}$, FeO, $FeO_{1.5}$, $KO_{0.5}$

MgO, MnO, $NaO_{0.5}$, NiO, SiO_2, UO_2, ZrO_2

These interaction coefficients have been, for the most part, based on activity data and phase diagram data. In some cases, such as for interaction coefficients between $KO_{0.5}$ and other ionic oxides, it has been necessary to estimate the interaction coefficients based on an electrostatic model of the binary melt.[17]

Coefficients for the interactions of other, low concentration, oxide, constituents with the major constituents of the melt have been determined where data have been found. Coefficients for the interactions between low concentration species have been assumed to be zero. Inspection of the expression for the activity coefficients of low concentration species shows that interaction coefficients between two very dilute species to be unimportant in determining the activity coefficient of the dilute species.

The parameters found considering only melt components as melt species yield results that are not highly accurate for broad ranges of melt composition when compared to available data for binary and ternary systems. An augmented set of coefficients has been developed by considering additional speciation of the melt. The most extensive speciation occurs when SiO_2 is an important constituent of the melt. It has been found useful to consider not only binary species but also ternary species especially when molten

TABLE 3: Some Non-Component Species Hypothesized to Form in the Liquid Phase

$3(AlO_{1.5}) \cdot 2(SiO_2)$	$2NaO_{0.5} \cdot 2SiO_2$
$2(AlO_{1.5}) \cdot CaO$	$2NiO \cdot SiO_2$
$2(AlO_{1.5}) \cdot FeO$	$SiO_2 \cdot ZrO_2$
$2(AlO_{1.5}) \cdot MgO$	$2KO_{0.5} \cdot MgO \cdot 5SiO_2$
$AlO_{1.5} \cdot KO_{0.5}$	$KO_{0.5} \cdot AlO_{1.5} \cdot SiO_2$
$AlO_{1.5} \cdot NaO_{0.5}$	$NaO_{0.5} \cdot AlO_{1.5} \cdot SiO_2$
$2CaO \cdot 2SiO_2$	$NaO_{0.5} \cdot AlO_{1.5} \cdot 3SiO_2$
$2CaO \cdot SiO_2$	$KO_{0.5} \cdot AlO_{1.5} \cdot 2SiO_2$
$FeO \cdot SiO_2$	$CaO \cdot 2AlO_{1.5} \cdot SiO_2$
$2FeO \cdot SiO_2$	$2CaO \cdot 2AlO_{1.5} \cdot 2SiO_2$
$2KO_{0.5} \cdot SiO_2$	$CaO \cdot FeO \cdot SiO_2$
$MgO \cdot SiO_2$	$CaO \cdot MgO \cdot 2SiO_2$
$2MgO \cdot SiO_2$	$NaO_{0.5} \cdot AlO_{1.5} \cdot SiO_2$
$MnO \cdot SiO_2$	$NaO_{0.5} \cdot AlO_{1.5} \cdot 3SiO_2$
$2NaO_{0.5} \cdot SiO_2$	$UO_2 \cdot SiO_2$

siliceous concrete is a major constituent of the melt. Some of the more complex species that are hypothesized to be in the melt are shown in Table 3. Use of this more refined parameter set does require an additional, iterative, solution of the melt composition in terms of the hypothesized species. This can slow execution of the model sufficiently that the additional accuracy may not be of interest to all users of the model.

IV. DISCUSSION

The introduction of non-ideal solution models has begun to provide more insight into the diversity of chemistry that can take place during core debris interactions with concrete. Only a very limited exploration of the chemical consequences of including non-ideal solution models has been possible up to now. The most profound finding has, of course, been the reduction of SiO_2 by zirconium to form Si metal in the metal phase. Chemical activities of silicon can, in some cases, get high-enough that an additional reaction becomes possible:

$$CO_2 + [Si] + [Zr] \Longleftrightarrow SiC(s) + ZrO_2.$$

Activities of zirconium are, apparently, kept low-enough, at least for the cases investigated so far, that zirconium carbide cannot form.

A second important finding is that zirconium can reduce uranium dioxide so that some uranium metal forms in the metal phase of core debris. Even a few mole percent of uranium in the metal phase is sufficient to make the metallic melt more dense than the oxide phase of core debris even before any concrete has been incorporated in the core debris.

The chemical activities of BaO and SiO are complicated. Preliminary investigations show that the activities can be low when core debris first contacts concrete because of the formation of barium and strontium zirconates in the melt. During melt interactions with calcium oxide-rich, silicon dioxide-poor concretes, the activity coefficients of BaO and SrO increase as a result of interactions of the type:

$$BaZrO_3(l) + CaO(l) \Longleftrightarrow CaZrO_3(l) + BaO(l)$$

During interactions with silicon dioxide-rich concretes the activity coefficients BaO and SrO actually decrease as a result of equilibria of the type:

$$BaZrO_3(l) + SiO_2(l) \Longleftrightarrow ZrO_2(l) + BaSiO_3(l).$$

A great deal of additional information on melt chemistry can, in principle, be derived from the non-ideal solution models. A most interesting issue that is now being addressed is whether additional melt phases can be formed. It certainly appears that a second metallic phase composed of mainly silver can separate under some conditions. Oxide phase immiscibility is more difficult to determine, but it certainly appears possible when core debris interacts with silicon dioxide-rich concretes. There are, of course, no provisions for these additional phases in existing melt/concrete interaction models.

V. REFERENCES

1. D.A. Powers, J.E. Brockmann and A.W. Shiver, VANESA: A Mechanistic Model of Radionuclide Release and Aerosol Generation During Core Debris Interactions with Concrete, NUREG/CR-4308, SAND85-1370, Sandia National Laboratories, Albuquerque, NM, July, 1986.

2. J. Fischer, J.D. Schilb, and M.G. Chasanov, J. Nucl. Materials 48 (1973)233.

3. D.A. Powers, "Chemical Phenomena and Fission Product Behavior During Core Debris/Concrete Interactions," Proceedings of the Committee on the Safety of Nuclear Installations (CSNI) Specialists' Meeting on Core Debris-Concrete Interactions, EPRI-NP-4=5054-SR, Electric Power Research Institute, Palo Alto, CA., February 1987.

4. E.R. Copus, R.E. Blose, J.E. Brockmann, R.D. Gomez and D.A. Lucero, Core-Concrete Interactions Using Molten Steel with Zirconium on a Basaltic Basemat: The SURC-4 Experiment, NUREG/CR-4994, SAND87-2008, Sandia National Laboratories, Albuquerque, NM, April, 1989.

REFERENCES (Contd)

5. L.S. Darken, Trans. AIME 239(1967)80.

6. H.K. Hardy, Acta Metallurgica 1(1953)202.

7. A.S. Jordan, Metall. Trans. 1(1970)239.

8. A.R. Miedema, F.R. de Boer, and R. Boom, CALPHAD 1(1977)341.

9. C.H.P. Lupis, Chemical Thermodynamics of Materials, North-Holland, 1983.

10. O. Kubaschewski, High Temperatures-High Pressures 13(1981)435.

11. F. Kohler, Monatsh. Chem. 91(1960)738.

12. L. Kaufman, CALPHAD 5(1981)225.

13. J. Brynested, CALPHAD 5(1981)103.

14. M. Hillert and X. Wang, CALPHAD 13(1989)253.

15. R.L. Hervig and A. Navrotsky, J. Amer. Cerom. Soc. 68(1985)314.

16. Y. Bottinga, D.F. Weill and R. Richet, "Thermodynamic Modeling of Silicate Melts," in Thermodynamics of Minerals and Melts, R.C. Newton, A. Navrotsky and B.J. Wood, editors, Springer-Verlag, 1981.

17. J. Lumsden, Disc. Faraday Society 32(1961)138.

The Calculation of Phase Equilibria of Oxide Core-Concrete Systems

R G J Ball and M A Mignanelli #

AEA Reactor Services, AEA Technology,
Harwell Laboratory, Oxfordshire OX11 0RA, UK

ABSTRACT

Thermodynamic models have been developed to describe the phase equilibria of the oxide system, UO_2-ZrO_2-SiO_2-CaO-MgO-Al_2O_3, formed during core-concrete interactions. The model has been used to estimate the solidus-liquidus surfaces for oxide compositions of the full system that describe different extents of oxidation of the zirconium in the core debris and various concrete types. The results show that the full oxide system should be treated as a pseudo-eutectic, in contrast to that used in the CORCON code, where the system is treated as a pseudo-ideal liquid and solid solution. A comparison of the calculated values of the solidus and liquidus temperatures with the available experimental data has also been performed for this system. In addition, the model has been used to follow the evolution of the different phases in the system with temperature for the ACE Phase C Test L6. In particular the relative amounts and compositions of the liquid and solid phases have been calculated. Further calculations have been performed to compare the extent of release of the components of the system by vaporization using the model and an ideal solution model.

INTRODUCTION

In order to model the thermophysical and chemical phenomena which occur during the progression of molten core debris-concrete interactions (MCCIs), it is necessary to have a good understanding of the phase equilibria in the multi-component oxide and metal solutions. The models used to describe these phases are important in the estimation of both the extent of concrete penetration and the release of species by vaporization. In the former case, the melt solidus and liquidus temperatures that are determined for a specific composition influence the heat transfer calculations and hence the predictions of the melt

This work has been carried out under contract for the Health and Safety Executive, UK, and forms part of a programme on nuclear safety research.

temperature and the onset of solidification. The amounts of the solidus and liquidus phases and the respective compositions would determine the viscosity of the melt, which is another important parameter used in the modelling of the thermal-hydraulics of the interaction. The models of the phase equilibria of the system could also be used to predict the composition of the crust formed following the addition of water to quench the interaction. The extent of release of species during MCCI are determined by the predicted temperature of the melt and the activity of the components in the oxide and metal phases. The latter thermodynamic quantity is also derived from the assessment of the phase equilibria of the system.

The development of such models requires the optimization of the available thermodynamic data and phase diagram information and the calculation of multi-component, multi-phase equilibria. In this paper, a model for the six component system, UO_2-ZrO_2-SiO_2-CaO-MgO-Al_2O_3, is described. The model has been used to estimate the solidus-liquidus surfaces for oxide compositions of the full system that describe different extents of oxidation of the zirconium in the core debris and various concrete types. A comparison of the calculated values of the solidus and liquidus temperatures with the available experimental data has also been performed for this system. Finally, the model has been used to calculate the changes in the composition of the melt formed during the progression of MCCI and the influence of the model on the composition of the gas phase.

THERMODYNAMIC MODELLING OF SOLUTION PHASES

The central problem in the calculation of thermodynamic equilibria is to obtain a representation of the Gibbs free energy of the total system as a function of temperature, pressure and composition. The equilibrium state is then obtained by minimizing the total Gibbs free energy with respect to the composition under various conditions.

The total Gibbs free energy of the system is simply given by the weighted sum of the Gibbs free energies of the individual phases present at equilibrium. If the phase is a pure substance then the Gibbs free energy can usually be obtained from standard sources of thermochemical data [1-3]. In the case of the silicates and zirconates of certain fission product species, for example Ba, Sr, La and Ce, further experimental studies and assessments are needed.

The Gibbs free energies for solution phases are more complicated to express. An important parameter for a solution phase is the Gibbs free energy of mixing, ΔG^{mix}, which is the change in Gibbs free energy accompanying the formation of the solution from its

constituents. For an ideal solution, ΔG^{mix}, is given by the configurational entropy change on forming the solution. In a non-ideal solution, however, ΔG^{mix}, will be given by the ideal configurational entropy change plus an excess Gibbs free energy term, G^{xs}. The modelling of multi-component systems is mainly concerned with deriving suitable representations of G^{xs} which reproduce the experimental phase relationships of a particular system. In some cases, this can be achieved using a Redlich-Kister polynomial. However, for some solution phases, in which there are strong interactions between atoms or molecules of the different components of the solution and hence a pronounced minima in the Gibbs free energy, a different representation is needed. The representation used in this study is an associated solution model in which an associate, A_pB_q, is allowed in the description of the solution between species A and B. To assist in the modelling of solution phases, much use is made of optimization programs which fit the available phase diagram and thermodynamic data to obtain the various parameters for the chosen representation of G^{xs}. Although, in general, only binary and ternary data are available, a multi-component solution phase can be adequately modelled using the representations for the lower order systems. Having derived representations for the Gibbs free energies of all the phases in a system, the equilibrium state can then be determined by minimizing the total Gibbs free energy.

MODEL FOR THE UO_2-ZrO_2-SiO_2-CaO-MgO-Al_2O_3 SYSTEM

The data needed for the solution model of the UO_2-ZrO_2-SiO_2-CaO-MgO-Al_2O_3 system were obtained from a collaborative programme between the CEA/THERMODATA and AEA Technology/National Physical Laboratory. Other oxide components for which data have also been provided by the collaboration are FeO, SrO, BaO and La_2O_3. Hence, data for 45 binary systems have been assessed in total for the ten component system. In addition a number of ternary sub-systems have been evaluated. The results from the critical assessment of the binary and ternary sub-systems are described in separate papers [4,5].

In this work, calculations based on the model for the six component system have been carried out using the program MTDATA-*Nuclear* [6]. In addition to the oxide solution database, a pure substance database for species appropriate to nuclear applications is also part of the program. The main functions performed by the code include the management of the thermodynamic data, the calculation of the equilibrium state for a given set of input parameters and the provision of both tabular and graphical output of the results.

PHASE DIAGRAM CALCULATIONS FOR CORE-CONCRETE COMPOSITIONS

The assessed data for the six component system have been used to estimate the solidus-liquidus surfaces for compositions appropriate to core-concrete interactions. The parameters that have been studied are the influence of the extent of oxidation of the zirconium in the core debris and different concrete types.

The phase equilibria for the six systems shown in Table 1, for compositions ranging from "pure" corium (i.e. urania and zirconia) to "pure" concrete were calculated over the temperature range 1000 to 3200K. The diagram for the 30% oxidation/siliceous concrete system, calculated by MTDATA-*Nuclear* for 40 isopleths across the system, is shown in Figure 1. The temperature at which solid begins to form from the liquid solution and the temperature at which the solid solution just begins to liquefy are obtained from an analysis of the data. Other phase changes that occur in the system as the temperature is increased are also shown in the figure.

The liquidus and solidus temperatures for the six systems in Table 1, calculated in the manner described above, are shown as a pseudo binary phase diagram in Figure 2 (a)-(c). The legend in the figure refers to the extent of oxidation of zirconium in percent (30 or 60), the concrete type (siliceous S, limestone L or limestone/sand G) and the solidus or liquidus point (S or L) respectively. It can be seen that the solidus temperatures for the siliceous and limestone/sand concrete systems do not change significantly across the composition range of the diagram. Variations of the solidus temperature of up to 300K have been determined for the limestone concrete systems. The liquidus temperatures for the core-concrete systems are similar for the corium-rich region of the diagram but show more variation for the concrete-rich compositions.

The code CORCON-MOD2 is used to predict the development of the melt temperature and concrete ablation during MCCIs [7]. In the modelling, solidus and liquidus temperatures are used in the evaluation of the heat transfer processes. The models for the phase diagram of the oxide material in CORCON are simplistic. The core-concrete system is treated as a pseudo-binary ideal liquid and solid solution, with the solidus and liquidus curves drawn between the corresponding points of the "pure" corium and concrete components. The calculations in this study indicate that the system should be treated as a pseudo-binary eutectic which results in a greater temperature difference between the solidus and liquidus curves.

COMPARISONS WITH EXPERIMENTAL DATA

The calculated values of solidus-liquidus temperatures using the model have also been compared with the available experimental data for specific core-concrete compositions. Measurements of the solidus and liquidus temperatures of core-concrete mixtures have been carried out at the Argonne National Laboratory using differential thermal analysis DTA (8). The preliminary results from the experimental study and the results from the calculations are shown in Table 2, together with the values derived from the CORCON code.

The results show that there is good agreement between the experimental and calculated values for the solidus temperatures but that the liquidus temperatures, in particular for the limestone based concretes, differ by up to 300K. This discrepancy could be due to inadequacies in the liquid solution model or to difficulties in the determination of the experimental points at such high temperatures for these complex systems. Although the CORCON values for the liquidus are in reasonable agreement with the calculated values, the solidus temperatures are significantly higher. Additional data from the DTA experimental study should provide important information for the assessment of the model predictions.

CALCULATIONS OF ACE PHASE C TEST L6

In addition to providing solidus and liquidus temperatures, the model can also be used to follow the evolution of the different phases in the corium-concrete system during the progression of the MCCI. In particular, the relative amounts and compositions of the liquid and solid phases can be calculated at a given temperature which could be used to estimate the viscosity of the core-concrete melt. Another application is the evaluation of the likely composition of the crust formed following the addition of water onto the melt.

The changes in composition of the melt during the ACE Phase C Test L6 have been assessed by performing a series of calculations using the oxide model and experimental data for the temperature of the melt and concrete ablation. It is assumed that the inventory of the zirconium metal present in this test is rapidly oxidized to zirconium dioxide during the early stage of the interaction. The results from these calculations are shown in Figure 3 (a)-(c). The model predicts that during the course of the MCCI, as the temperature falls over the range 2480K to 2250K, the ratio of the amounts of liquid to solid is reduced from 3.9 to 1.9. The liquid phase is comprised predominantly of SiO_2 and UO_2, with the amount of

urania decreasing as the temperature is reduced. The composition of the solid solution is comprised of the cubic UO_2-ZrO_2 phase and remains constant during the test.

CALCULATIONS OF THE VAPOUR PHASE OVER THE OXIDE SYSTEM

Using MTDATA-*Nuclear*, the model has also been extended to include the gas phase species of the seven element system. Similar calculations to those described above have been performed to determine the extent of release of the components of the system by vaporization. The results have then been compared with those using a model in which the associates in the liquid solution were removed and assuming all the solution phases are ideal. A comparison with a model comprised of a mixture of the stoichiometric compounds of the system has also been performed.

The results from calculations for the 30% oxidation/limestone concrete system, for compositions involving 20 and 80 mol.% concrete, are shown in Figure 4. The figure shows the variation of the partial pressures of the dominant gas phase species with temperature for the non-ideal and ideal cases. The results indicate that there are differences in the predicted partial pressures of the gaseous species SiO, UO_3, UO_2 and Mg in applying the two solution models. In the corium-rich system (early stages of MCCI), the pressures of SiO, UO_3 and Mg are increased by a factor of ~2 using the non-ideal model. Although a similar increase in the Mg pressure was determined for the concrete-rich compositions (later stages of MCCI) using the non-ideal model, the pressures of SiO, UO_3 and UO_2 decreased by factors of ~6, ~2 and ~3 respectively. Differences of up to an order of magnitude were noted for the dominant gaseous species between the results for the solution models and the mixture model. The results indicate that the interactions in the melt due to the formation of associates can have an influence on the total amount of the species in the vapour phase.

CONCLUSIONS

Thermodynamic models have been developed to describe the phase equilibria of the oxide system, UO_2-ZrO_2-SiO_2-CaO-MgO-Al_2O_3, formed during core-concrete interactions. The model has been developed from an assessment of the phase diagram data for the binary and ternary sub-systems in which the excess Gibbs free energy of each of the solution phases are described either by means of a Redlich-Kister polynomial or by an associate model. The data for the solution model were obtained from a collaborative programme between the CEA/THERMODATA and AEA Technology/National Physical Laboratory. The

calculations of the phase constitution of a system as a function of composition and temperature have been carried out using the code MTDATA-*Nuclear*. Reasonable agreement between the calculated and experimental data for the phase diagrams of the sub-systems was achieved.

The model for the sub-systems has been used to estimate the solidus-liquidus surfaces for oxide compositions of the full system that describe different extents of oxidation of the zirconium in the core debris and various concrete types. The results show that the full oxide system should be treated as a pseudo-eutectic. The phase diagram model for the system is significantly different to that used in the CORCON code, where the system is treated as a pseudo-ideal liquid and solid solution. The calculated values of the solidus-liquidus temperatures using the model have also been compared with the available experimental data for specific core-concrete compositions. The results show that there is good agreement for the solidus temperatures but that the liquidus temperatures differ by up to 300K. These discrepancies should be resolved when further experimental data become available. In addition to providing these temperatures, the model has been used to follow the evolution of the different phases in the system with temperature for ACE Phase C Test L6. In particular, the relative amounts and compositions of the liquid and solid phases in the melt have been calculated during the course of the test.

The model has also been extended to include the gas phase species of the seven element system and calculations have been performed to determine the extent of release of the components of the system by vaporization. The calculations have been compared with those from a model assuming the oxide solutions are treated as ideal and the results indicate that the interactions in the melt due to the formation of associates can influence the total amount of the species in the vapour phase.

REFERENCES

(1) JANAF Thermochemical Tables, Third Edition, J Phys. Chem. Ref. Data Volume 14, 1985. Supplement No. 1.

(2) I Barin, "Thermochemical Data of Pure Substances: Part I and II", VCH Verlagsgesellschaft mbH, Weinheim Germany, (1989).

(3) E H P Cordfunke, R J M Konings, G Prins, P E Potter, M H Rand, "Thermochemical Data for Reactor Materials and Fission Products", Elsevier Science Publishers, Amsterdam, 1990.

(4) P Y Chevalier, G Cenerino, "Thermodynamic data and calculation code adapted to the molten core concrete interaction, developed by THERMODATA and CEA", Paper presented at the OECD CSNI Specialist Meeting on Core Debris-Concrete Interactions, Karlsruhe, Germany, April 1-3, 1992.

(5) G Cenerino, P Y Chevalier, E Fischer, "Thermodynamic calculations of phase equilibria in oxide complex systems: Prediction of fission product (BaO, SrO, La_2O_3) release", Paper presented at the OECD CSNI Specialist Meeting on Core Debris-Concrete Interactions, Karlsruhe, Germany, April 1-3, 1992.

(6) T I Barry, R H Davies, A T Dinsdale, M Lacey, "MTDATA Handbook: NPL Databank for Metallurgical Thermochemistry", National Physical Laboratory, January 1989.

(7) R K Cole, D P Kelley, M A Ellis, "CORCON-MOD2: A computer program for analysis of molten core-concrete interactions", NUREG/CR-3920, SAND84-1246, 1984.

(8) M F Roche, ANL, Private communication.

Table 1 Compositions used for the core-concrete calculations

Core-concrete system	Core composition (mol.%)		Concrete composition (mol.%)			
	UO_2	ZrO_2	SiO_2	CaO	MgO	Al_2O_3
30% oxidation+siliceous	84.5	15.5	79.4	16.6	1.2	2.7
60% oxidation+siliceous	73.0	27.0	79.4	16.6	1.2	2.7
30% oxidation+limestone	84.5	15.5	10.9	70.4	17.0	1.7
60% oxidation+limestone	73.0	27.0	10.9	70.4	17.0	1.7
30% oxidation+limestone/sand	84.5	15.5	39.0	38.4	19.8	2.8
60% oxidation+limestone/sand	73.0	27.0	39.0	38.4	19.8	2.8

Table 2 Comparison of calculated, experimental and CORCON values for solidus and liquidus temperatures

Corium-concrete system	Solidus temperature (K)			Liquidus temperature (K)		
	Calc.	Expt.	Corcon	Calc.	Expt.	Corcon
Core + Siliceous	1434	1400	1723	2395	2549	2473
Core + Limestone	1550	1520	1873	2320	>2723	2373
Core + Limestone/sand	1450	1360	1673	2490	>2638	2400

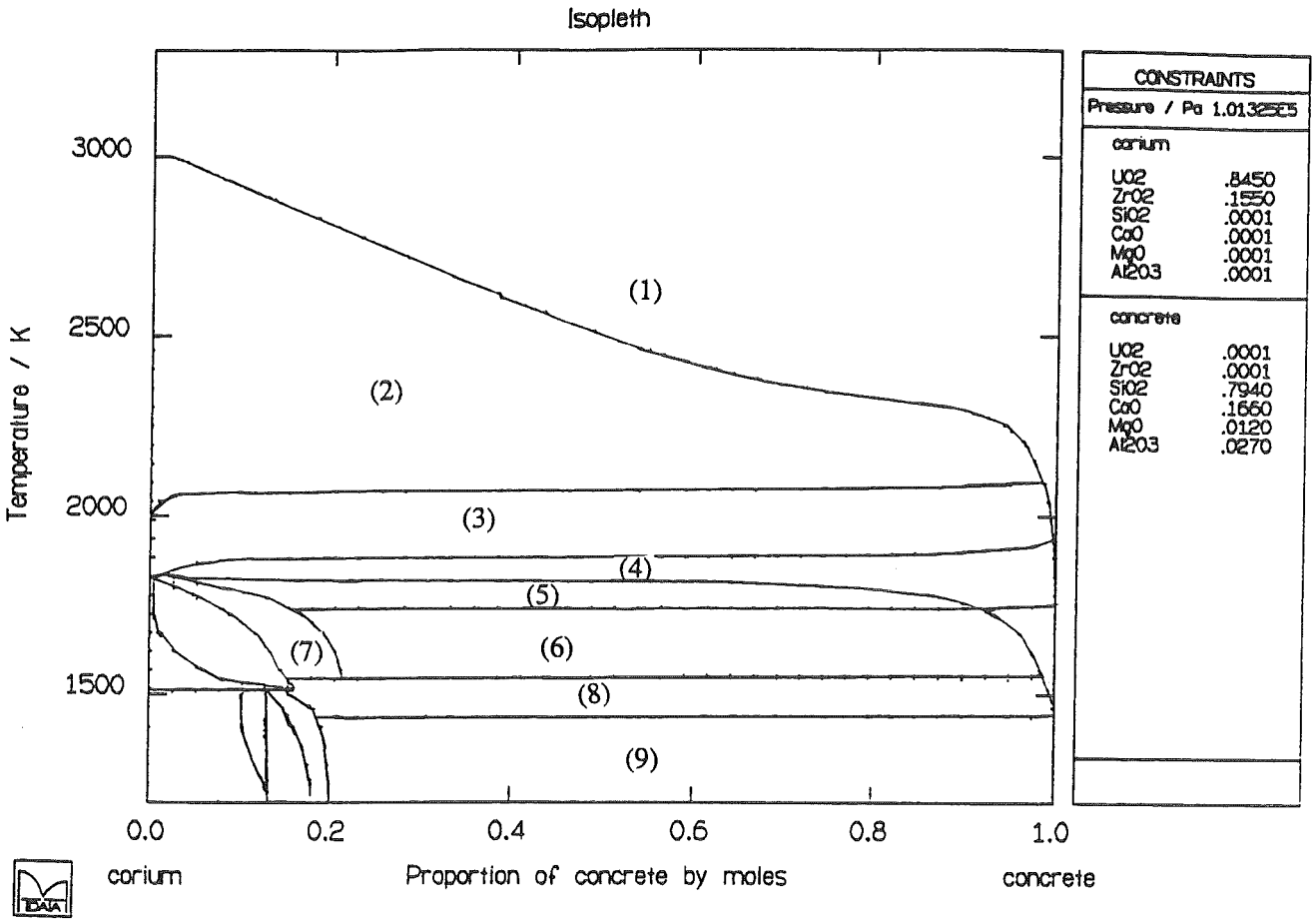

1. Liquid
2. Liquid + cubic
3. Liquid + liquid + cubic
4. Liquid + cubic + cristobalite
5. Liquid + cubic + cristobalite + zircon
6. Liquid + cubic + tridymite + zircon
7. Liquid + cubic + zircon
8. Liquid + cubic + $CaMgSi_2O_6$ + wollas + wollastonite
9. Anorthite + cubic + $CaMgSi_2O_6$ + wollas + wollastonite

Figure 1 Isopleth diagram for the 30% oxidation/siliceous concrete system

Figure 2 (a)

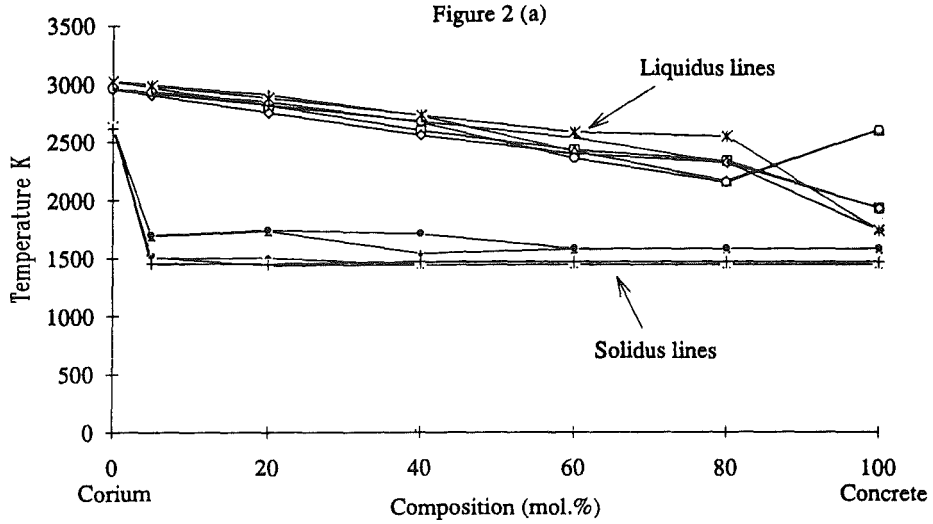

Figure 2 (b) Solidus lines

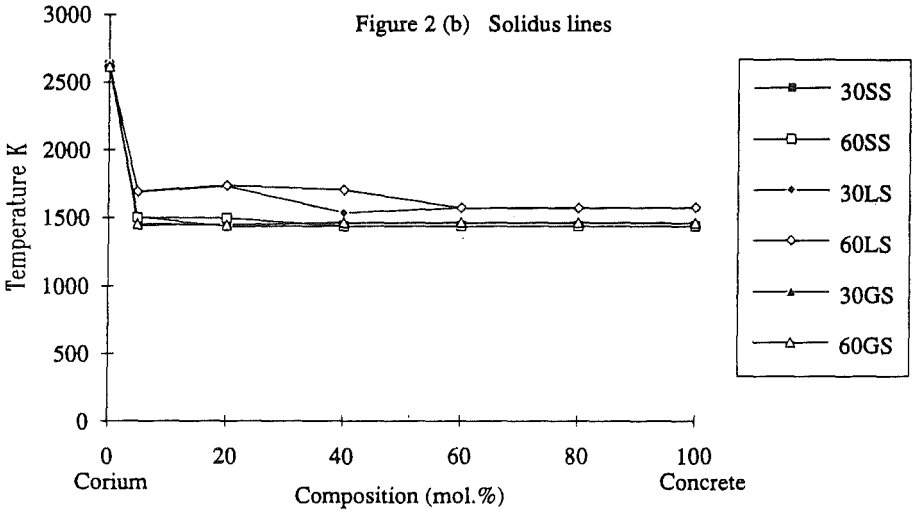

Figure 2 (c) Liquidus lines

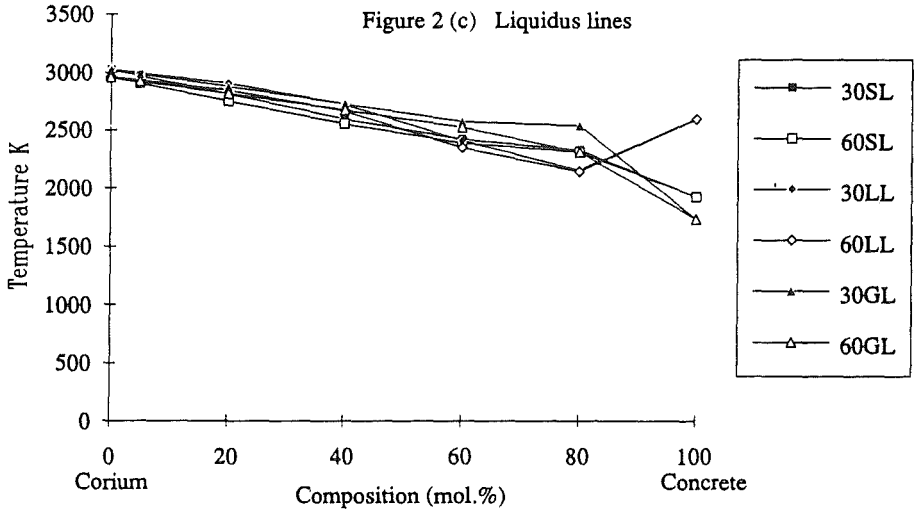

Figure 2 Variation in solidus-liquidus curves with core-concrete composition

Figure 3 (a) Amount of solid and liquid phases

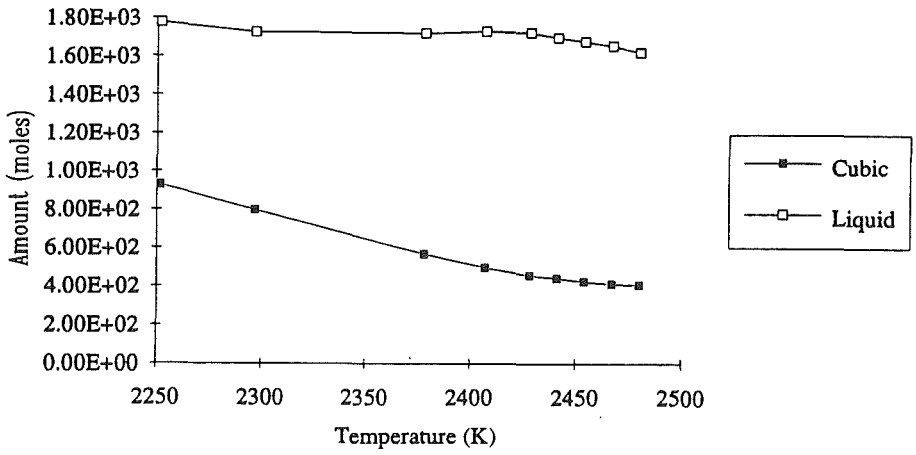

Figure 3 (b) Components of the solid phase

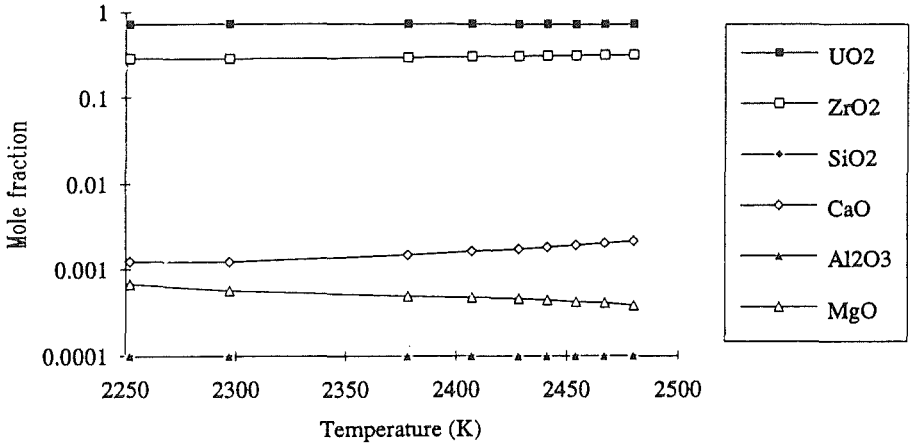

Figure 3 (c) Components of the liquid phase

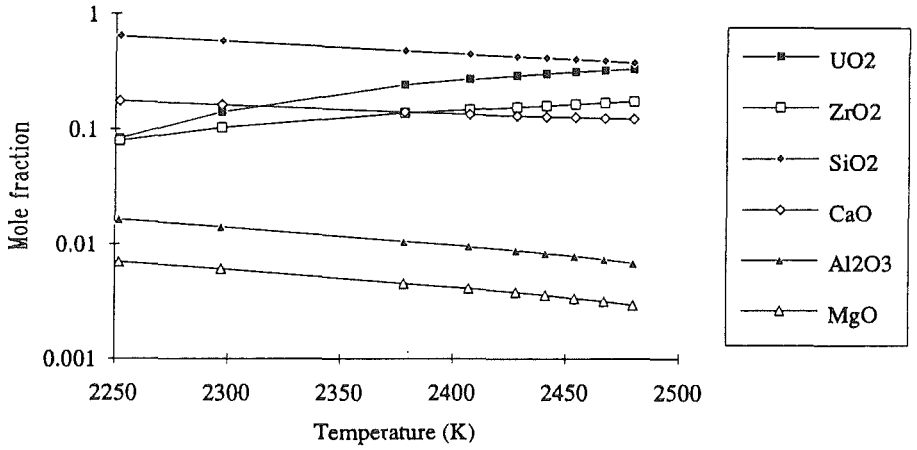

Figure 3 Composition of the solid and liquid phases for ACE Phase C Test L6

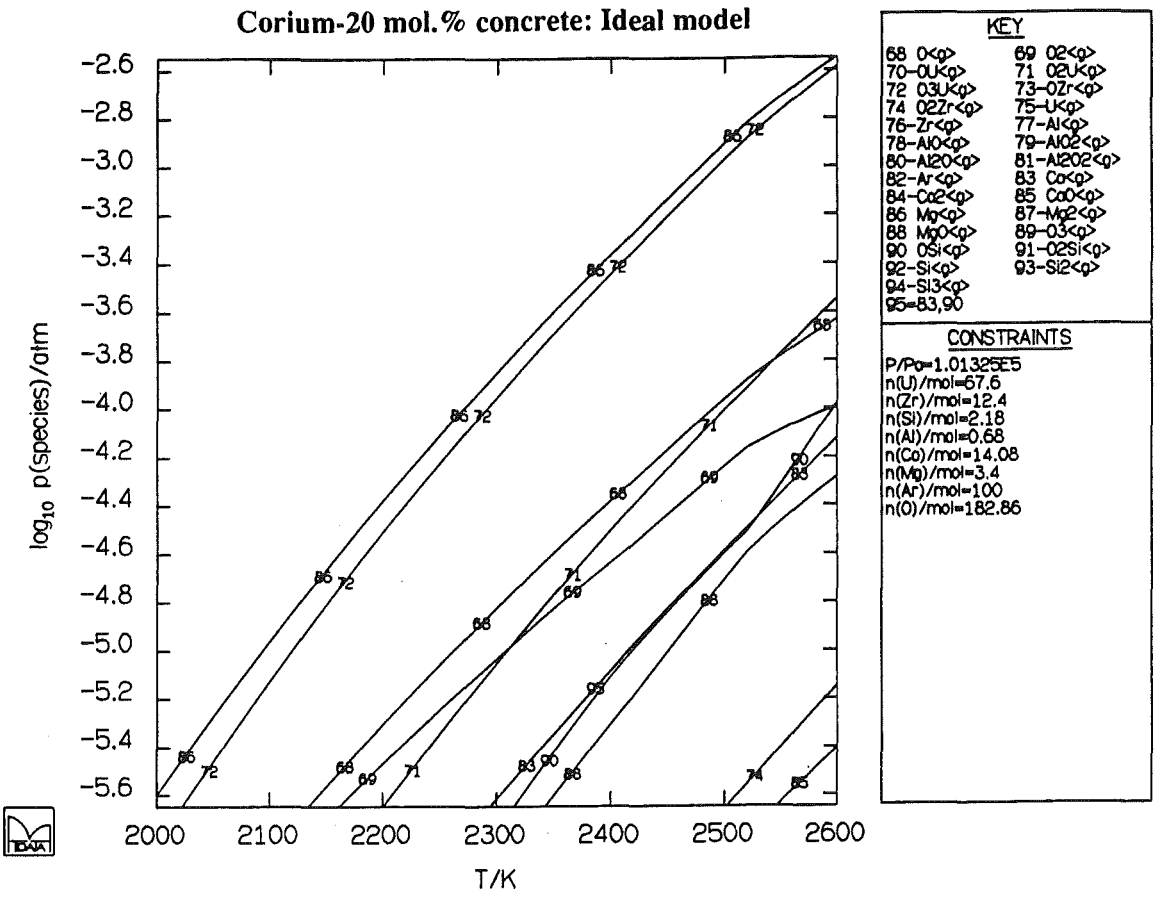

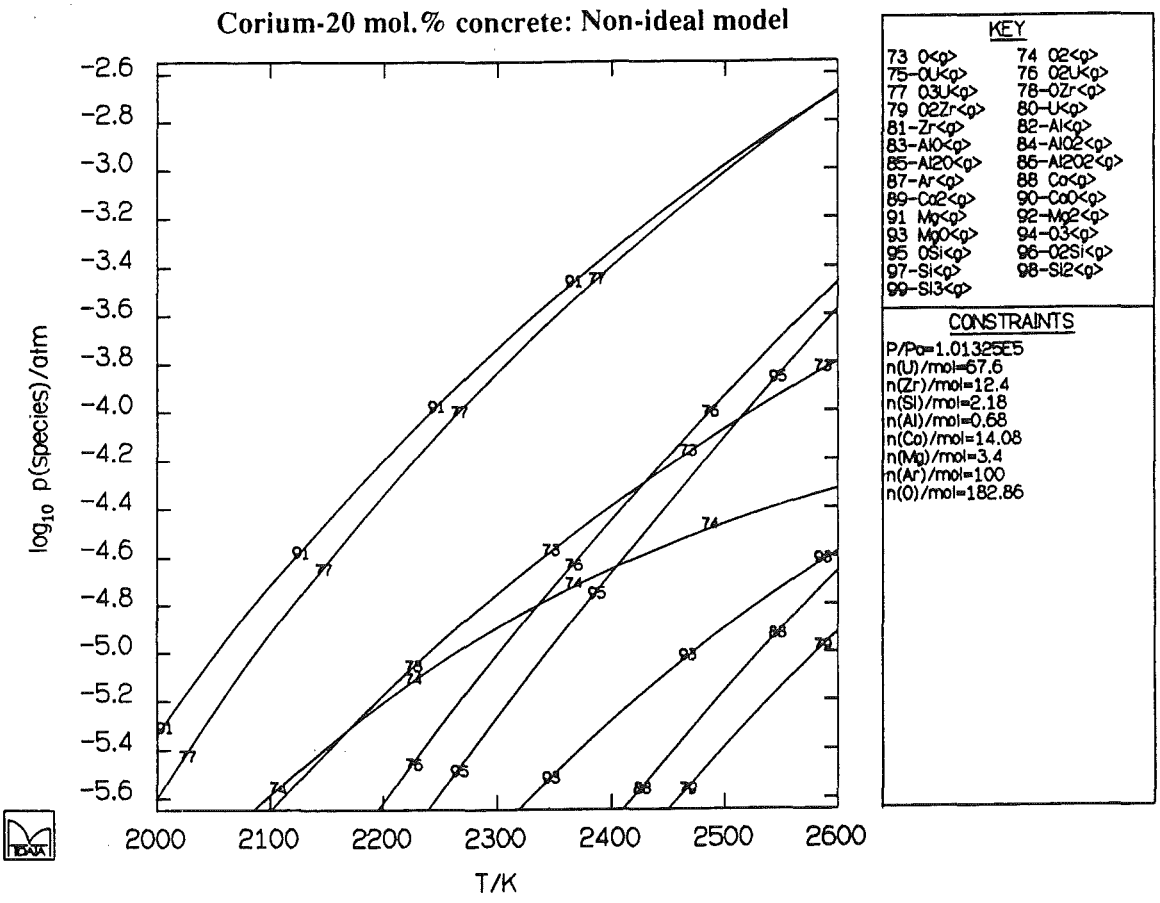

Figure 4 The variation of the partial pressures of the dominant gas phase species with temperature for 30% oxidation/limestone concrete systems

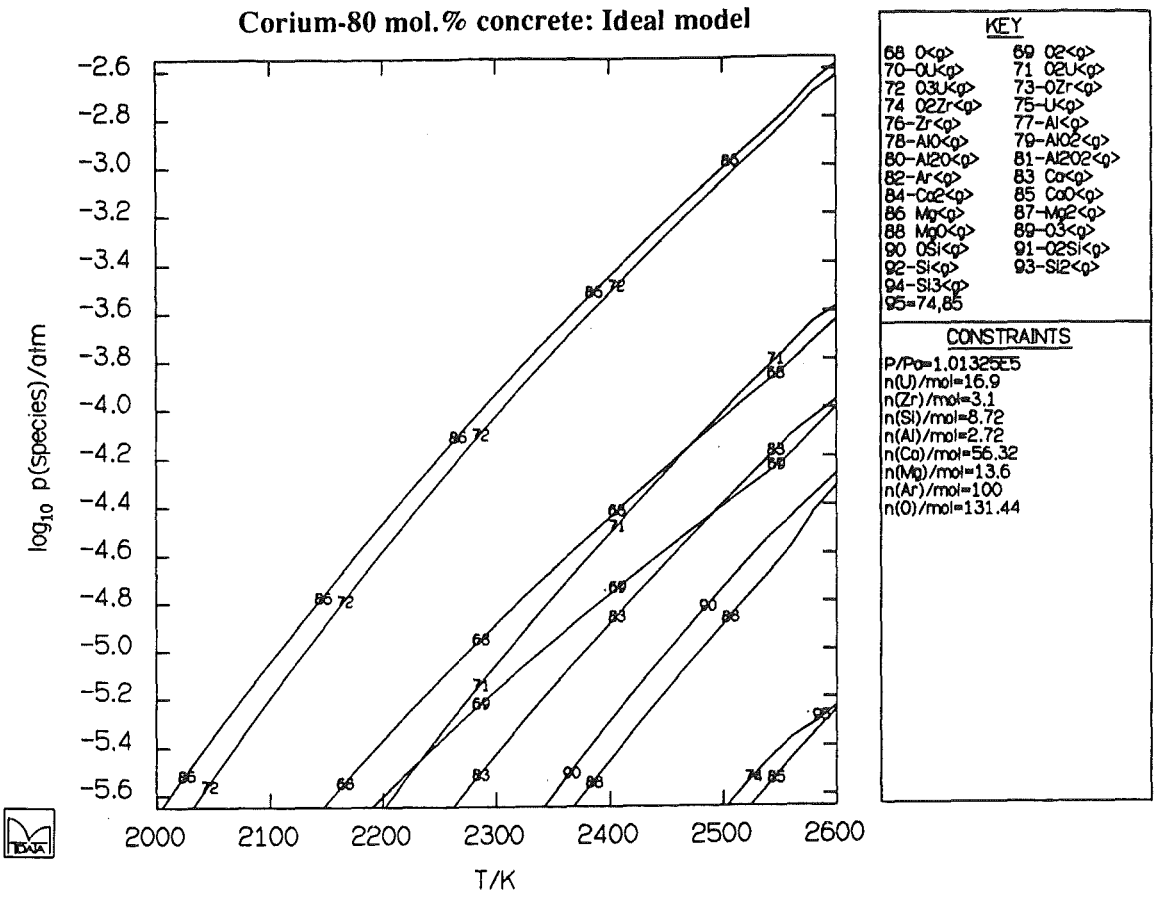

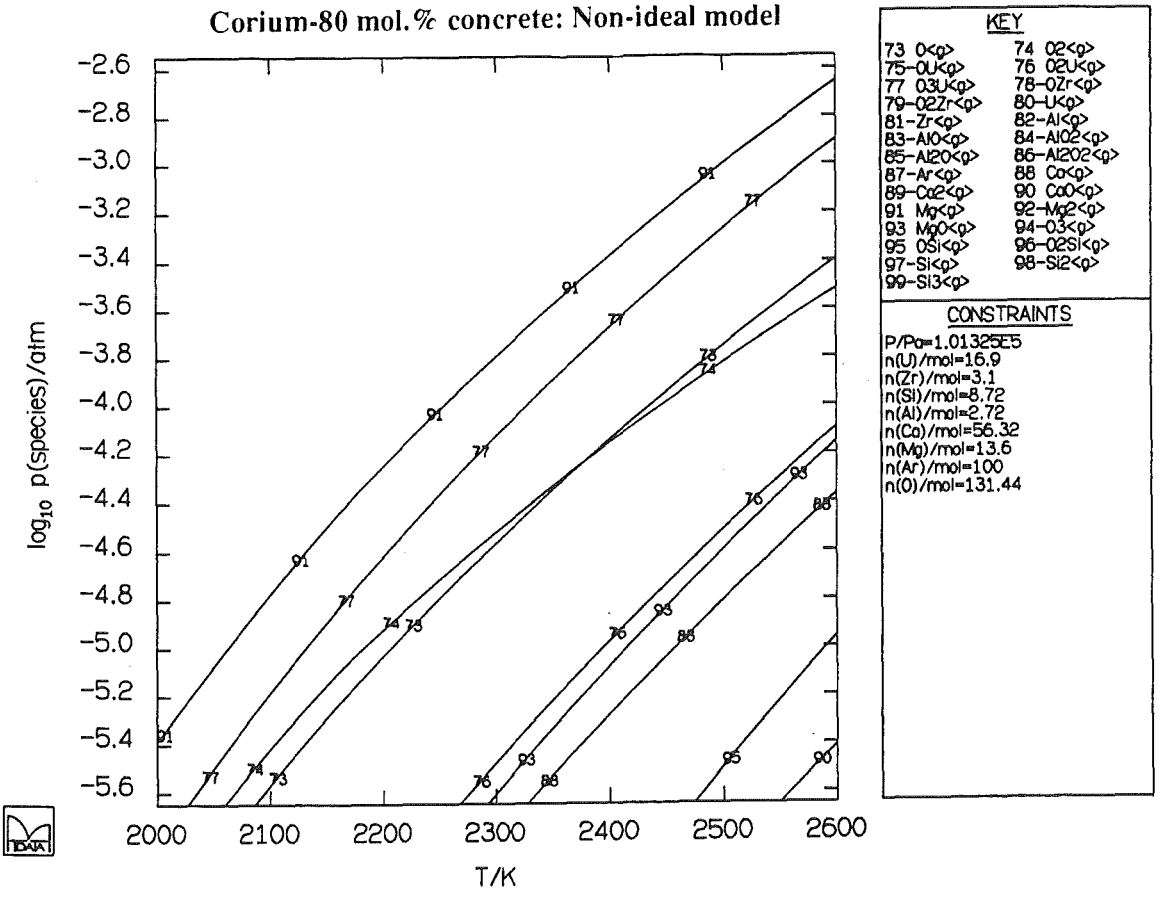

Figure 4 (Continued)

THERMODYNAMIC CALCULATION OF PHASE EQUILIBRIA IN OXIDE COMPLEX SYSTEMS :

PREDICTION OF SOME SELECTED FISSION PRODUCTS (BaO, SrO, La_2O_3) RELEASES

KfK, Karlsruhe, Germany

1st-3rd April 1992.

G. Cenerino (*)
P.Y. Chevalier, E. Fischer (**)

(*)Institut de Protection et de Sûreté Nucléaire
Département de Protection de l'Environnement et des Installations
Laboratoire de Physique des Accidents
IPSN/CEA - B.P. n° 68 - 92265 Fontenay-aux-Roses Cédex (France)

(**)THERMODATA, Domaine Universitaire de Grenoble
1001 Avenue Centrale
B.P. n° 66, 38402 Saint Martin d'Hères Cédex (France)

I. INTRODUCTION

In a previous paper [1], we have established the status of the art reached jointly by THERMODATA and IPSN from 1988 up today on the subject of thermodynamic data bases and equilibrium calculation code adapted to the molten core concrete interaction (M.C.C.I.).

This paper deals about the extension of the data base of 5 oxides (UO_2, ZrO_2, SiO_2, CaO, Al_2O_3) to 3 selected other oxides (BaO, SrO, La_2O_3), including condensed and gas phases together, in order to predict the fission products release with a good reliability, taking into account the non-ideal behaviour of the oxides in the condensed phase.

The necessity of a realistic thermodynamic modelling of condensed solution phases has been demonstrated in the first paper, and the three oxides BaO, SrO and La_2O_3 have been chosen to represent the non-volatile fission products and because thermodynamic data exist in the literature for these species.

II. THERMODYNAMIC DATA ASSESSMENT

II.1 Phase Diagrams and Thermodynamic Activity of Binary Systems Including BaO, SrO and La_2O_3.

In a first step, thermodynamic properties and phase diagrams of the limiting binary subsystems obtained between BaO, SrO and La_2O_3 and the five oxides UO_2, ZrO_2, CaO, SiO_2 and Al_2O_3 have been critically assessed by using the Lukas et al.'s program [2], which allows to obtain the optimized parameters of the Gibbs energy of all condensed solution phases and stoichiometric compounds.

The following systems have been critically assessed :

Al_2O_3-BaO,	BaO-ZrO_2,	SrO-ZrO_2,
BaO-CaO,	Al_2O_3-SrO,	Al_2O_3-La_2O_3,
BaO-La_2O_3,	SrO-La_2O_3,	CaO-La_2O_3,
BaO-SiO_2,	CaO-SrO,	La_2O_3-SiO_2,
BaO-SrO,	SiO_2-SrO,	La_2O_3-UO_2,
BaO-UO_2,	SrO-UO_2,	La_2O_3-ZrO_2.

The following phases have been identified in these systems :

- the liquid phase

- the solid solutions :

(La_2O_3-BaO),	(BaO, SrO),	(ZrO_2, BaO),
(CaO, SrO),	(ZrO_2-SrO),	(La_2O_3-CaO),
(La_2O_3-SrO),	(UO_2, La_2O_3),	(La_2O_3, ZrO_2).

- the binary stoichiometric compounds :

$Al_{12}Ba_1O_{19}$,	$Al_2Ba_1O_4$,	$Al_2Ba_3O_6$,
$Ba_1La_2O_4$,	$Ba_2Si_1O_4$,	$Ba_1Si_1O_3$,
$Ba_2Si_3O_8$,	$Ba_5Si_8O_{21}$,	$Ba_3Si_5O_{13}$,
$Ba_1Si_2O_5$,	$Ba_1U_1O_3$,	$Ba_1Zr_1O_3$,
$Al_2Sr_1O_4$LT,	$Al_2Sr_1O_4$HT,	$Al_{12}Sr_1O_{19}$,
$Al_4Sr_1O_7$,	$Al_2Sr_3O_6$,	$Al_{32}Sr_{84}O_{132}$,
$Si_1Sr_1O_3$,	$Si_1Sr_2O_4$,	$Si_1Sr_3O_7$,
$Sr_2Zr_1O_4$,	$Sr_3Zr_2O_7$,	$Sr_1Zr_1O_3$,
$Al_{22}La_2O_{36}$,	$Al_2La_2O_6$,	$La_2Si_1O_5$,
$La_4Si_3O_{12}$,	$La_2Si_2O_7$,	$La_4Sr_1O_7$,
$La_4Sr_3O_9$,	$La_2Zr_2O_7$.	

For all solution phases, no thermodynamical experimental information (enthalpy of mixing or activity) is available. For most of stoichiometric compounds, thermochemical values (heat capacity, enthalpy of formation and entropy) have been taken from classical compilations [3, 4, 5, 6] and from a more recent one [7].

The calculated phase diagrams BaO-SiO_2, BaO-ZrO_2, SiO_2-SrO and SrO-ZrO_2 are shown as examples on Figures 1 to 4. The existence of very stable stoichiometric compounds in all systems containing the three selected fission product BaO, SrO or La_2O_3 and two important oxides of the melt SiO_2 or ZrO_2, gives evidence about the strong interactions in both liquid and solid phases in these systems.

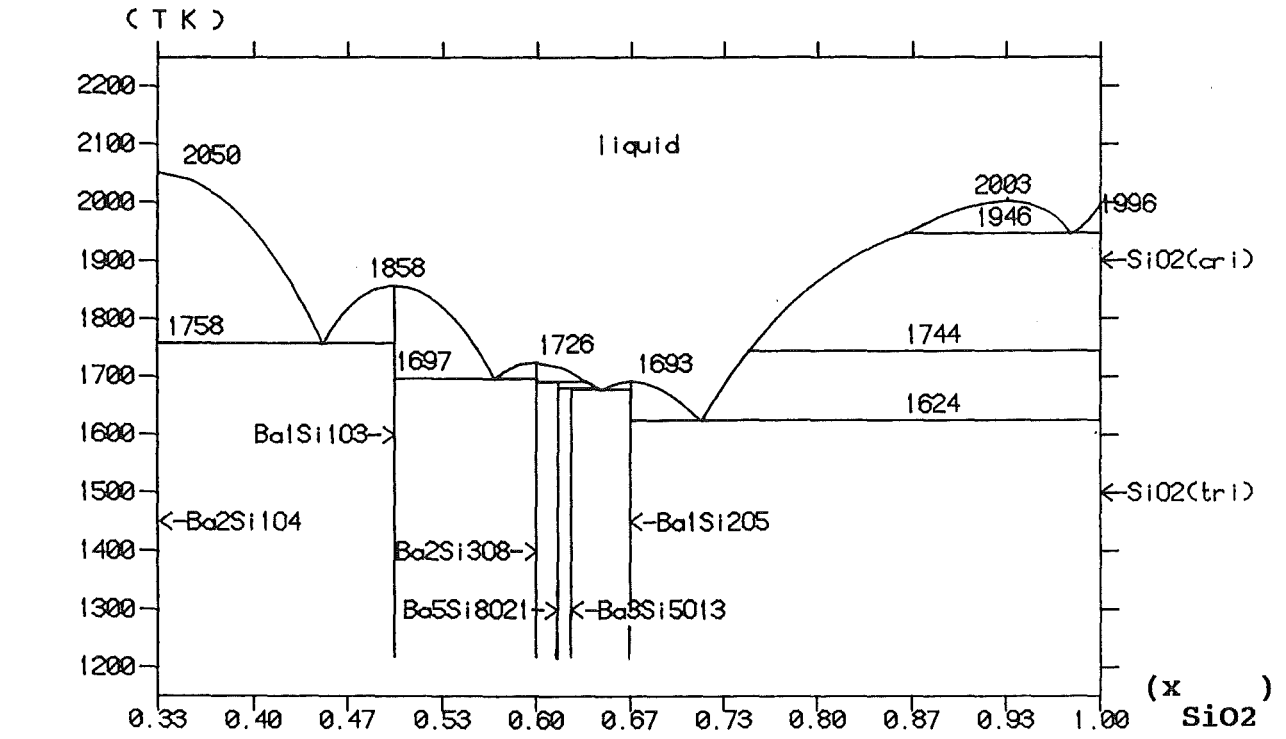

Figure 1 : calculated $BaO-SiO_2$ phase diagram.

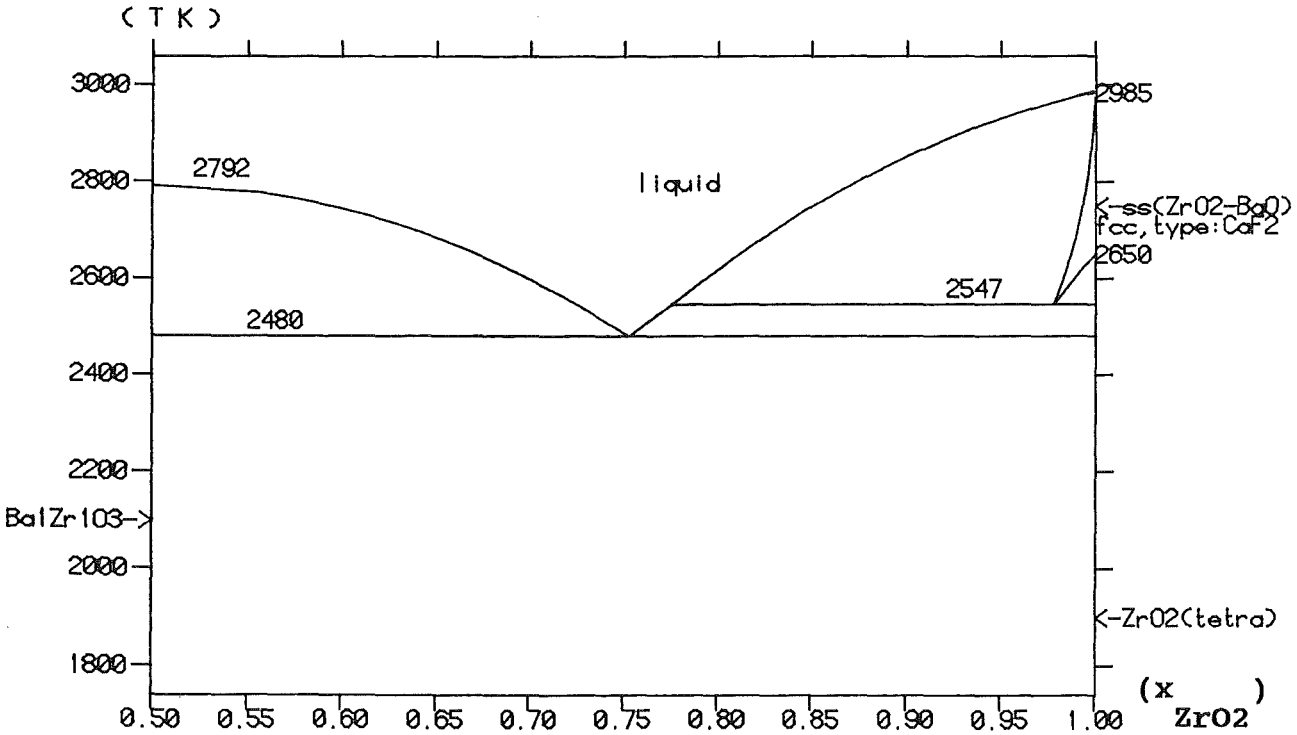

Figure 2 : calculated $BaO-ZrO_2$ phase diagram.

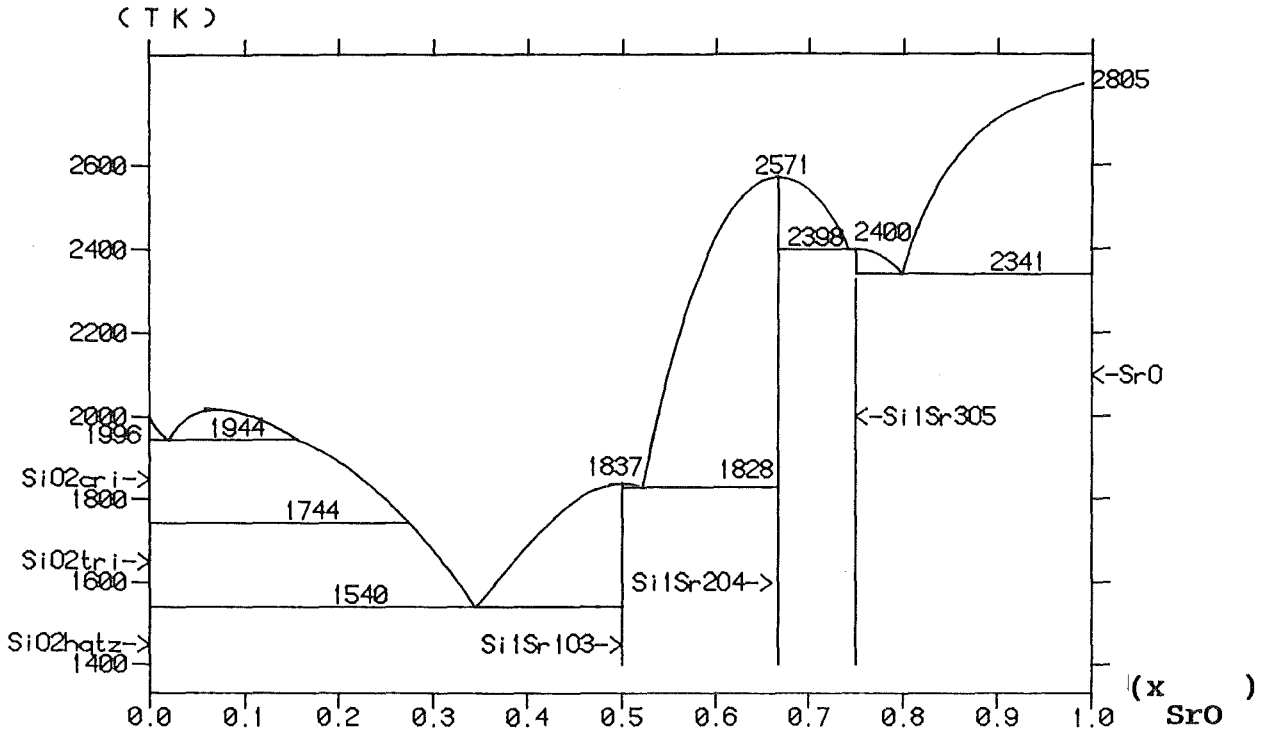

Figure 3 : calculated SiO_2-SrO phase diagram.

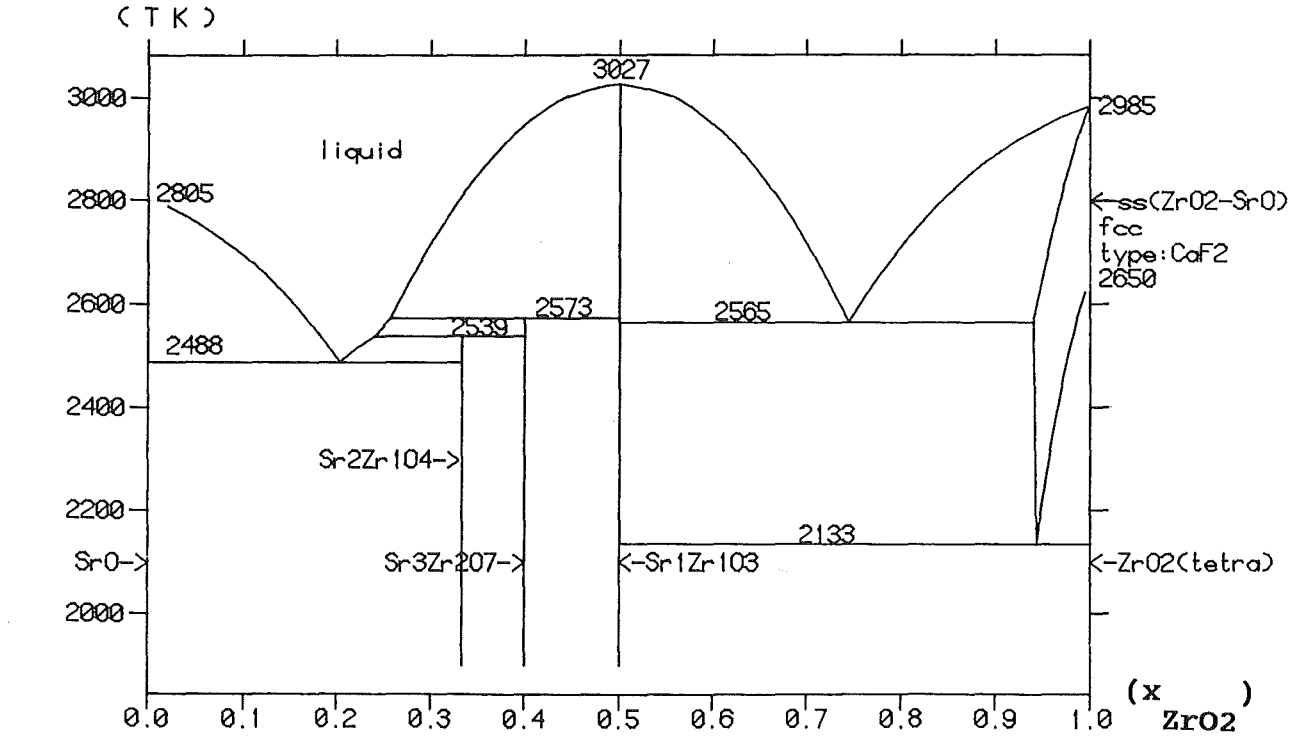

Figure 4 : calculated SrO-ZrO_2 phase diagram.

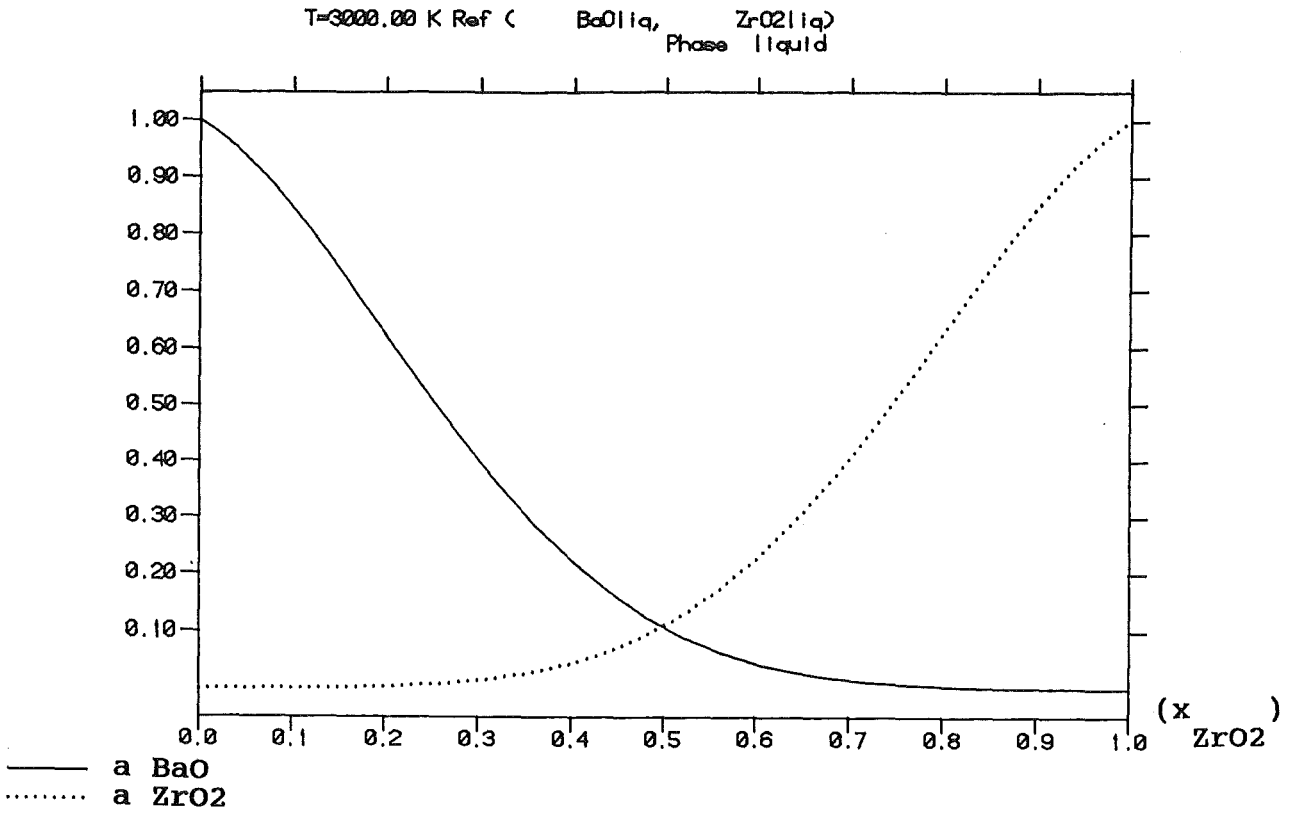

Figure 5 : estimated activity of BaO in the BaO-ZrO_2 system at 3000 K.

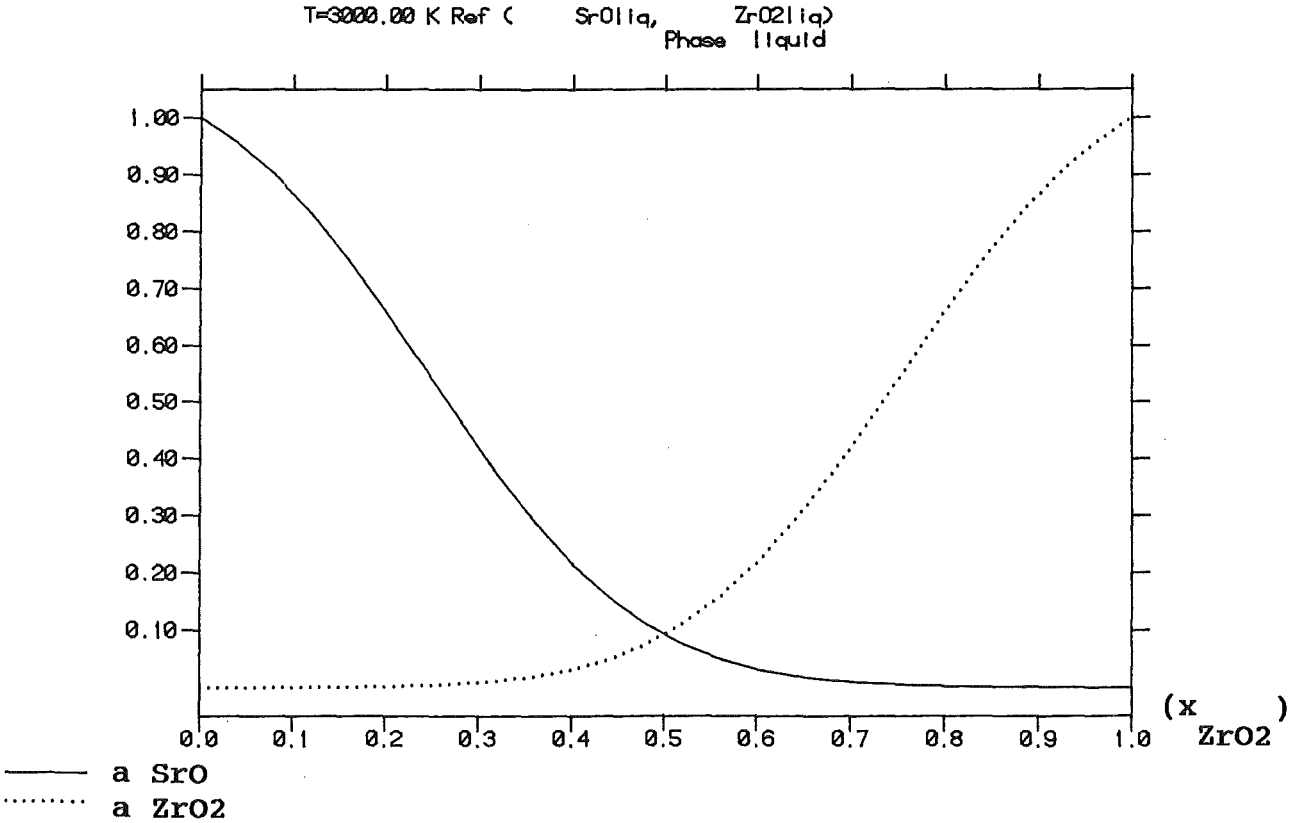

Figure 6 : estimated activity of SrO in the SrO-ZrO_2 system at 3000 K.

The predicted activity of BaO, SrO and ZrO_2 has been tabulated at 3000 K in the BaO-ZrO_2 and SrO-ZrO_2 liquid phase (figures 5 and 6). Both curves show a very important deviation from ideality. Similar behaviour has been observed for all binary systems between the three selected fission products and two main oxides of the corium, SiO_2 and ZrO_2.

II.2. Gas-Oxide data base.

In a second step, a complete data base was constructed, including the condensed phases of the quinary oxide system extended to the three selected fission products (UO_2, ZrO_2, SiO_2, CaO, Al_2O_3, BaO, SrO, La_2O_3) and all the gaseous species retrieved from the THERMODATA substance data base in the 9 constituents system (Al, Ba, Ca, La, Si, Sr, U, Zr, O).

This data base contains thermodynamic description (structure and Gibbs energy parameters) for 7 complex condensed solution phases (including liquid or solid phases), 100 solid stoichiometric compounds and 32 gaseous species.

III. CALCULATION CODE RESULTS

By using the previous data base connected to the GEMINI2 calculation code, calculations of fission products release by vaporization from the corium can be simulated in selected conditions of core concrete interactions experiments.

As an example, the equilibrium state of different core (UO_2, ZrO_2, BaO, SrO, La_2O_3) - concrete (Al_2O_3, CaO, SiO_2, BaO, SrO) mixtures has been calculated at temperatures of 2000 K and 2500 K.

The composition by mass of the core is : 83.96% UO_2, 15.50% ZrO_2, 0.18% BaO, 0.18% SrO, 0.18% La_2O_3 and the composition by mass of the calcined siliceous concrete is : 4.668% Al_2O_3, 15.564% CaO, 79.718% SiO_2, 0.024% BaO, 0.026% SrO.

Results of the code give the nature, composition and proportion of liquid, solid and gas phases at equilibrium, and also the partial pressure of each gaseous species. Some particular results are summarized in table 1, that gives the partial pressure of U, Ba, Sr and La gaseous species. Moreover, a comparison has been made with other values obtained by assuming that all condensed phases are ideal and without taking into account stoichiometric compounds including fission products. We have observed a significant overpredicting of fission products release with the ideal model, reaching 4 orders of magnitude for Ba and Sr.

IV. CONCLUSION

An important conclusion of this study is that two oxides in significant amount during the molten core concrete interaction, SiO_2 and ZrO_2, present strong interactions with the fission products, BaO, SrO and La_2O_3. As a consequence, the fission products are retained in the partially melted corium,

both in the liquid and solid phases, and are very little vaporized. A realistic thermodynamic modelling of this behaviour has been needed for a quantitative prediction of fission products release.

We must keep in mind that these results only show a tendency because three compounds have been chosen to represent the whole fission products compounds.

Moreover, in real experiments, other important elements have to be added (C, H), which bring a lot of other species in the chemical system. In real cases, the oxygen potential has a great importance and specific informations as gas volume or gas flow have to be known.

This data base and calculation code may be used to simulate any available experiment. Activity measurements in binary sub systems would be useful to be compared with the predicted values.

Table 1 : Estimated partial pressures (atm) of gaseous species with U, Ba, Sr and La over different core (83.96 wt % UO_2, 15.5 wt % ZrO_2, 0.18 wt % BaO, 0.18 wt % SrO, 0.18 wt % La_2O_3) - concrete (4.668 wt % Al_2O_3, 15.564 wt % CaO, 79.718 wt % SiO_2, 0.024 wt % BaO, 0.026 wt % SrO) mixtures at T = 2000 K and 2500 K.

wt%	concrete	0	20	40	60	80	100
	T(K)						
Ba	2000	$3.7e^{-7}$	$3.4e^{-10}$	$1.2e^{-10}$	$6.2e^{-11}$	$4.5e^{-11}$	$2.1e^{-11}$
	2500	$6.3e^{-5}$	$1.5e^{-8}$	$6.9e^{-9}$	$4.6e^{-9}$	$3.2e^{-9}$	$1.7e^{-9}$
La	2000	$3.9e^{-11}$	$4.4e^{-12}$	$3.1e^{-12}$	$2.1e^{-12}$	$1.3e^{-12}$	-
	2500	$7.1e^{-8}$	$6.2e^{-9}$	$3.4e^{-9}$	$2.3e^{-9}$	$1.3e^{-9}$	-
Sr	2000	$1.9e^{-8}$	$1.0e^{-12}$	$4.1e^{-13}$	$2.1e^{-13}$	$1.6e^{-13}$	$8.0e^{-14}$
	2500	$1.4e^{-5}$	$1.6e^{-9}$	$1.9e^{-10}$	$5.6e^{-11}$	$2.3e^{-11}$	$8.7e^{-12}$
U	2000	$0.7e^{-6}$	$6.9e^{-7}$	$7.0e^{-7}$	$7.0e^{-7}$	$7.4e^{-7}$	-
	2500	$4.0e^{-4}$	$3.9e^{-4}$	$2.6e^{-4}$	$2.0e^{-4}$	$1.4e^{-4}$	-

V. ACKNOLEDGEMENTS

The present work was financially supported by the "Institut de Protection et de Sureté Nucléaire (IPSN) of the "Commissariat à l'Energie Atomique -CEA-", France, Contract n° BC-5596.

VI. BIBLIOGRAPHY

[1] P.Y.Chevalier and G.Cenerino,
"Thermodynamic data bases and calculation code adapted to the modelling of molten core concrete interaction (MCCI) phenomena, developed jointly by Thermodata and the Institut de Protection et de Sureté Nucléaire (CEA), France",
KFK, Karlsruhe, Germany, 1-3 April 1992.

[2] H.L. Lukas, E.Th. Henig and B. Zimmermann,
Calphad 1 (3), (1977), 225.

[3] I. Barin, O. Knacke,
"Thermochemical Properties of Inorganic Substances",
Springer Verlag (1973).

[4] M.W. Chase, Jr., C.A.Davies, J.R.Downey, Jr., D.J.Frurip, R.A.McDonald and A.N. Syverud,
Janaf Thermochemical Tables,
"J. Phys. Chem. Ref. Data, Vol. 14, Sup. 1, (1985).

[5] V.P. Glushko (Ed.), L.V. Gurvich, G.A.Bergman, G.A.Khachkuruzov, V.A. Medvedved, I.V. Veyts, V.S.Yungman and C.B.Alcock,
"Thermodynamic Properties of Individual Substances",
Fourth Edition, Vol. 1, Hemisphere Pub. Corp., (1989).

[6] I. Barin,
"Thermochemical Data for Substances", VCH, (1989)

[7] E.H.P. Cordfunke, R.J.M. Konings, G. Prins, P.E. Potter and M.H. Rand,
"Thermochemical Data for Reactor Materials and Fission Products", Eur.-Contract n°.ETSN-0005-NL.

THERMODYNAMIC DATA BASES AND CALCULATION CODE ADAPTED TO THE MODELLING OF MOLTEN CORE CONCRETE INTERACTION (M.C.C.I.) PHENOMENA, DEVELOPED JOINTLY BY THERMODATA AND THE "INSTITUT DE PROTECTION ET DE SURETE NUCLEAIRE" (FRANCE)

KfK, Karlsruhe, Germany

1st-3rd April 1992.

P.Y. Chevalier (*)
G. Cenerino (**)

(*)THERMODATA, Domaine Universitaire de Grenoble
1001 Avenue Centrale
B.P. n° 66, 38402 Saint Martin d'Hères Cédex (France)

(**)Institut de Protection et de Sûreté Nucléaire
Département de Protection de l'Environnement et des Installations
Laboratoire de Physique des Accidents
IPSN/CEA - B.P. n° 68 - 92265 Fontenay-aux-Roses Cédex (France)

I. HISTORY

Since 1988, on request from the Institut de Protection et de Sureté Nucléaire (IPSN), THERMODATA has been working on the thermodynamical modelling of very complex chemical systems involved in the Molten Core-Concrete Interaction (MCCI).

This work was initiated by a "Benchmark Exercise on the Chemical Modelling of the Release of Radionuclides due to Core-Concrete Interactions" [1], proposed by the OECD/NEA/CSNI. IPSN and THERMODATA were participating to this Benchmark Exercise.

The aim of this Benchmark was to calibrate capabilities to calculate thermochemical equilibrium in simplified systems arising during the interaction of core debris with structural concrete. The first part of this work (Part A) was a simplified standard problem intended to test the numerical solution techniques involved in defining chemical equilibrium in the various codes. In this part, all thermochemical data and modelling were set as input data. The second part of this work (Part B) was intended to examine the sensitivity of results to various modelling of thermochemical equilibrium fixed by the user.

The results from part A have shown good agreement between almost all calculation codes usually employed to determine the equilibrium state composition of multicomponent systems.

On the opposite, the choice of different assumptions in the modelling of condensed solution phases (Part B) has shown large differences in the results concerning the gas phase composition.

The restrictions and disadvantages of the classical approach for thermodynamical modelling based on ideality concept and use of limited activity coefficients are very important :

As a matter of fact, with this approach, it is neither possible to calculate the partition of species between the oxide and metallic phases - *miscibility gap for example* -, nor to determine the equilibria between the solid and liquid condensed phases - *liquidus, solidus* -.

Moreover, the assumptions made on the activity coefficients can lead to calculated activities which are very different from those expected. One of the troublesome consequences is the uncertainty on the concentration of the released products in the gaseous phase, which is directly connected to the activity in the condensed phase.

At the time of the benchmark, the conclusion was that, if theoretical tools were indeed available, a strong limiting factor for the results reliability was the lack of self-consistent data for multicomponent condensed solution phases, concerning as well oxide, metal as metal-oxide systems.

For that reason, the need to improve the thermodynamic modelling of specific MCCI chemical systems was evident. As a consequence, THERMODATA and IPSN started in 1988 a work on the subject of both thermodynamical equilibrium calculation code and thermodynamic data (thanks to an European collaboration) adapted to the molten core concrete interaction.

II. CALCULATION CODE

The calculation code **GEMINI2**, developed by THERMODATA/INPG (Institut National Polytechnique de Grenoble)/CNRS (Centre National de la Recherche Scientifique) is the last stage of successive works performed in Grenoble (France) since 1972.

GEMINI2 is a code that calculates complex multiphase multicomponent chemical equilibria (ideal gas phase, stoichiometric condensed compounds and multicomponent solution phases) by minimization of the total Gibbs Energy of the system under either constant pressure or volume conditions.

The total Gibbs Energy is minimized by means of a general optimization technique, with regard to the independent variables after having taken into account the constraints of the problem, i.e. the mass balance conservation conditions.

This code has been already applied to many chemical equilibria problems, and successfully tested in the Benchmark Exercise (Part A), [1]. It includes the general multi-sublattice model (particularly the non ideal associate model and the classical substitution model) for solution phases, and its main limitations are only due to the hardware capabilities.

The practical applications of the code are calculation of phase equilibria (determination of liquidus, solidus or phase transition, proportion of equilibrium phases), cristallization paths, thermodynamic properties (Gibbs Energy, Enthalpy, Entropy, Heat Capacity), activity of pure components or partial pressure

of gas, and also heat balance for all equilibrium phases.

III. THERMODYNAMIC DATA BASES

At first, we have undertaken to work on the Al_2O_3-CaO-SiO_2-UO_2-ZrO_2 quinary system, which contains five main oxides of a "corium" obtained in the unlikely event of a severe accident in a PWR nuclear power plant, if the reactor core melts through the vessel and slumps into the concrete reactor cavity. A preliminary work on the assessment of the limiting binary systems has been made by Relave et al.[2].

Following the conclusions drawn by a specialist meeting on fission product chemistry in severe nuclear reactor accident, organized by the Commission of European Communities [3], a list of different data bases needed to solve most of problems linked to the molten core concrete interaction was drawn up.

Considering the importance of the work to be done, two European state organizations, the Institut de Protection et de Sureté Nucléaire (IPSN), France, and the United Kingdom Atomic Agency (UKAEA), United Kingdom, decided to collaborate to share the effort for producing common thermodynamical data for these selected chemical systems. National laboratories involved in this collaboration are THERMODATA for IPSN and National Physical Laboratory (NPL) for UKAEA.

Thus, an oxide data base has to be developed jointly. This data base contains as major constituents UO_2, ZrO_2, SiO_2, CaO, Al_2O_3, MgO, FeO, BaO, SrO, La_2O_3. The data base for gaseous species has been developed for many years in THERMODATA and is continuously updated.

At first, a common set of thermodynamical data has been developed in collaboration by THERMODATA (France) and NPL (United Kingdom) for the quinary oxide system Al_2O_3-CaO-SiO_2-UO_2-ZrO_2. These new data take into account a physically realistic thermodynamical modelling of all the possible equilibrium phases (stoichiometric compounds and multicomponent condensed solution phases) of the system.

The oxide quinary system has been recently extended by THERMODATA to three selected fission products, BaO, SrO and La_2O_3. In a next futur, MgO and FeO will be added to the oxide data base in collaboration with NPL and UKAEA.

IV DATA ASSESSMENT

The principle of the thermodynamic approach needs to know the Gibbs Energy of all possible phases in the chemical system. As this function is not well experimentally determined for very complex multicomponent phases, that one is modelled from the limiting binary and sometimes higher order (ternary, ...) sub-systems. Substitution, associate and multisublattice model are commonly used.

The model parameters have to be evaluated by using sophisticated optimization procedures, that allow to take into account simultaneously all the available experimental

information, as well calorimetric, electromotive force or pressure vapour measurements, as phase diagrams experimental points and also to introduce experimental uncertainties.

Thus, data assessment work needs first to evaluate self-consistent data for 10 pure unary and 45 binary oxide systems for the oxide data base.

The evaluation of the 120 ternary subsystems is not realistic in a short time, and only the most important ones are studied.

In connection with this work concerning the oxide solution data base, many pure stoichiometric condensed or gazeous components have to be updated.

V. PRACTICAL APPLICATIONS

a. Equilibrium state in the Al_2O_3-CaO-SiO_2-UO_2-ZrO_2 system, phase diagrams, liquidus and solidus, cristallization history, proportion of phases.

GEMINI2 code allows to calculate the thermochemical equilibrium state for any temperature and composition specified by the user, and gives as results the name, number of moles of all phases, the mole fraction for solution phases, and the thermodynamic activities. It offers automatic iteration capabilities either in temperature or composition. Results of the code are given numerically, and stored in files for any further exploitation.

The first important practical application has been the determination of liquidus and solidus temperatures of some selected mixtures in the quinary oxide system Al_2O_3-CaO-SiO_2-UO_2-ZrO_2 [4]. In this work, different core (UO_2-ZrO_2) - concrete (Al_2O_3-CaO-SiO_2) mixtures were studied, by varying the mass proportion. A lattice of curves (Temperature versus wt % concrete is plotted (see figure 1) for different concrete compositions (pure SiO_2, siliceous concrete, limestone common sand concrete, limestone limestone concrete, pure CaO). Concerning the liquidus curves, there exists a trend to immiscibility for the siliceous concrete and in opposite an evolution towards an eutectic behaviour when the CaO content in the concrete increases. The solidus temperatures are mainly controlled by the concrete composition. A preliminary comparison with experimental results give very satisfactory agreement for both liquidus and solidus temperatures for the siliceous case. The figure 2 presents the curves corresponding to a given proportion of liquid at equilibrium (100 % = liquidus, 0 % = solidus) for different core-siliceous concrete mixtures, which are of interest for viscosity interpretation.

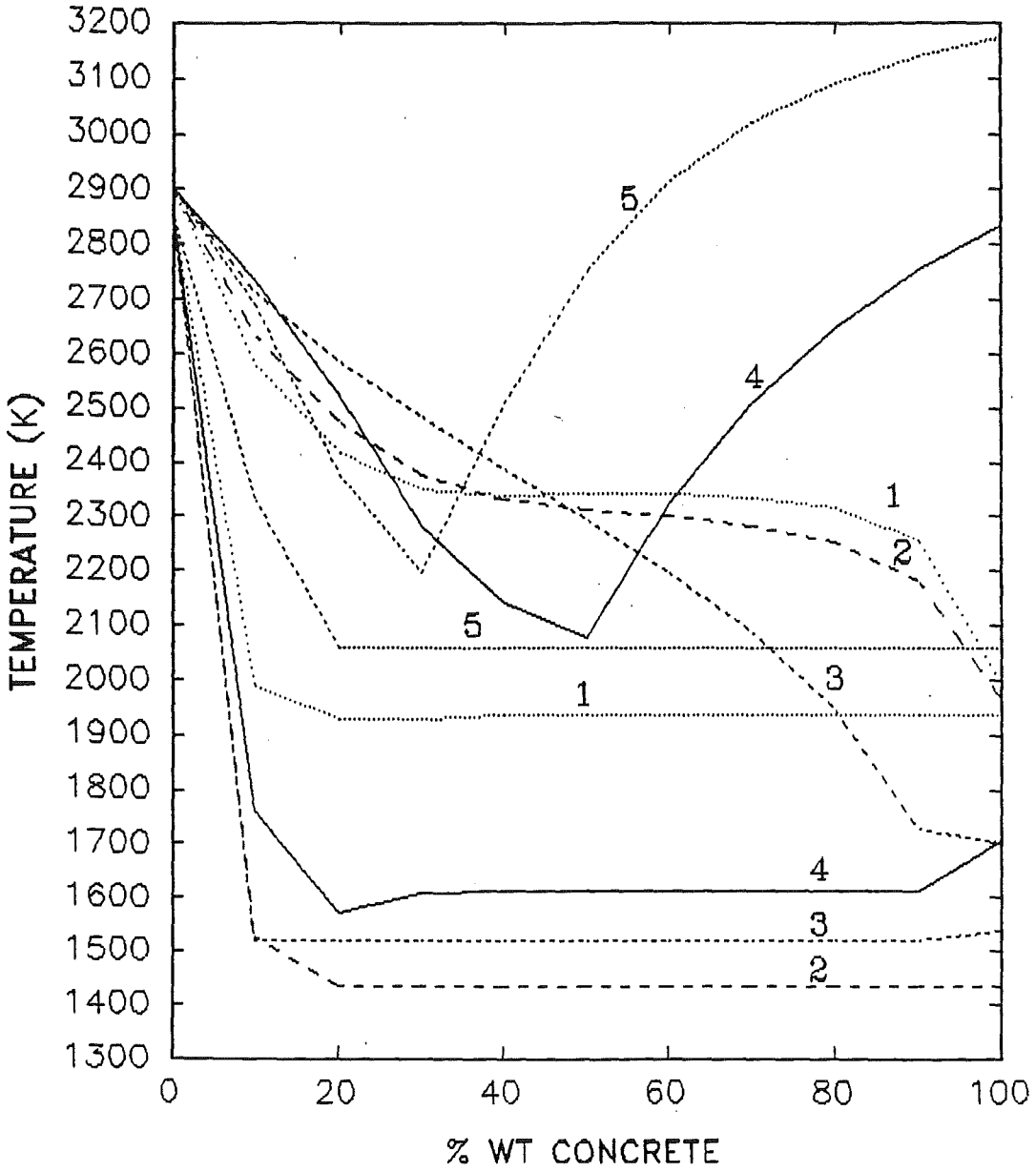

Figure 1 : calculated lattice of liquidus and solidus curves for different core (UO_2-ZrO_2) - concrete (Al_2O_3-CaO-SiO_2) mixtures) : 1 = silica, 2 = siliceous, 3 = limestone sand, 4 = limestone, 5 = lime.

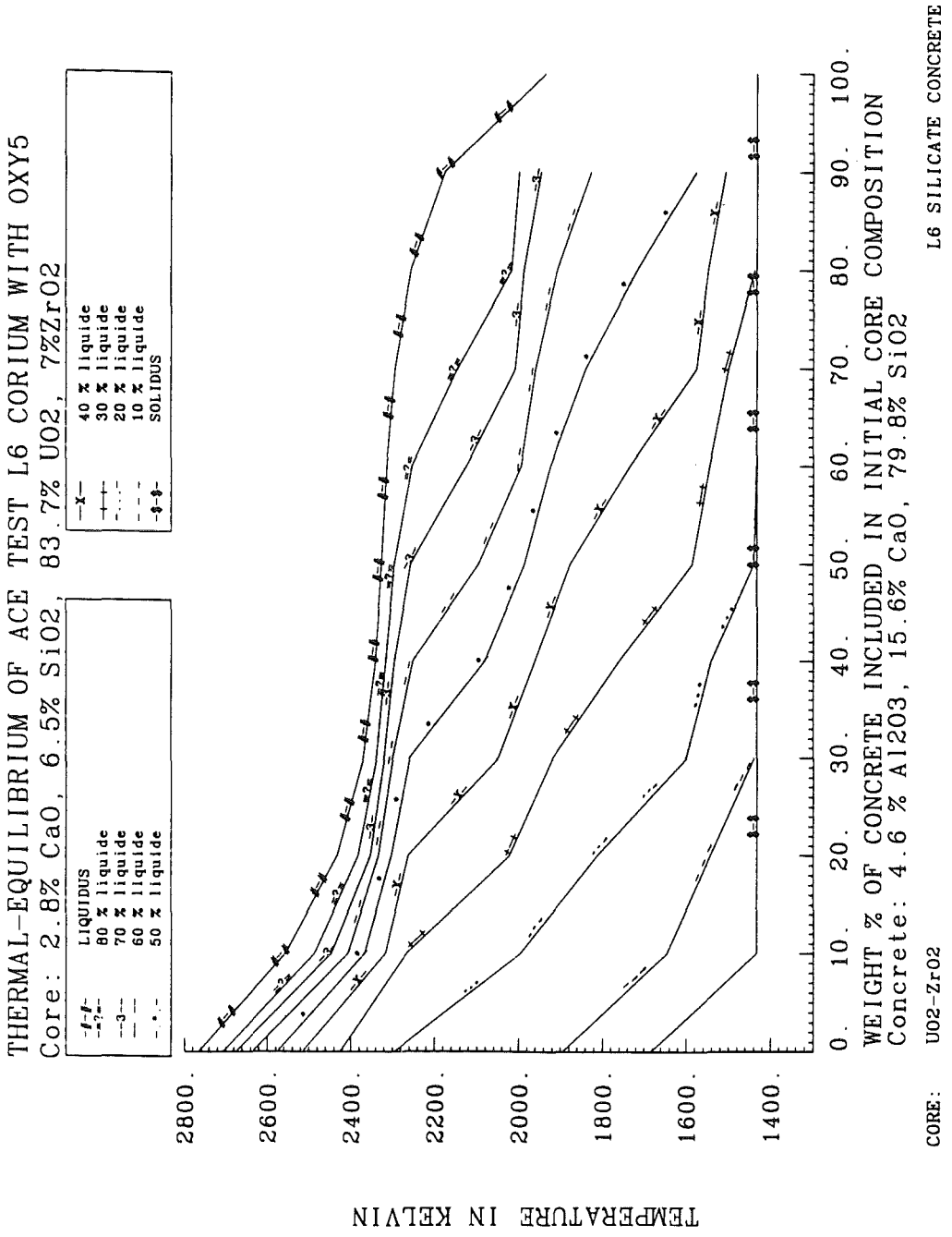

Figure 2 : liquidus, iso-liquid proportion and solidus curves for core (78% UO_2, 22% ZrO_2) - siliceous concrete (77% SiO_2, 15% CaO, 8% Al_2O_3) mixtures.

b. Modelling of the activity in condensed solution phases, fission products release from the corium.

A second practical application of great interest is a better modelling of the fission products release by vaporization from the corium needed by the Benchmark conclusions [1].

It is easier to explain the influence of the model for solution phases in the case of a simple binary system. In this case, the partial pressure of one constituent above a liquid phase, p_i is directly linked to the thermodynamic activity, a_i of that constituent at equilibrium, and to the partial pressure p°_i above the pure constituent at that temperature.

$$p_i = a_i * p^\circ_i$$

The activity a_i is linked to the atomic composition of the phase, x_i, by the activity coefficient, Γ_i.

$$a_i = \Gamma_i * x_i$$

In the ideal model, $\Gamma_i = 1$ and $a_i = x_i$. In a real case, if the components of the phase present strong attraction, $\Gamma_i < 1$ and if they present a repulsion, $\Gamma_i > 1$. Thus, the uncertainty on the partial pressure p_i can easily reach several orders of magnitude for systems with strong deviations from ideality.

Without any thermodynamic modelling of solution phases, the assumption $\Gamma_i = 1$ has no sense, because the real value of Γ_i may vary from 0 to $+\infty$, giving very few chance to the reliability of any thermodynamic prediction. A more realistic value could be given to Γ_i only if experimental results were known in advance.

In opposite, a realistic thermodynamic modelling of the Gibbs Energy of solution phase, self consistent with the phase diagram and all available thermodynamic information, allows to estimate the activity at different temperatures or compositions in all binary subsystems, and consequently to estimate the activity in the multicomponent system.

Thus, a second paper [5] deals about the thermodynamic modelling of the eight oxides system obtained by the extension of the quinary system (UO_2-ZrO_2-CaO-SiO_2-Al_2O_3) to the three selected fission products (BaO, SrO, La_2O_3) including condensed and gas phases together.

VI. FURTHER WORK

A further work will be the use of such a thermodynamical approach including both a very general calculation code and appropriate data base in order to model the extensively large experimental program parts performed in the MCCI field.

It is hoped that the use of self-consistent thermodynamic data based on phase diagram assessment and taking into account experimental results obtained elsewhere will reduce the uncertainties in the MCCI phenomena modelling.

VII. ACKNOWLEDGEMENTS

The present work was financially supported by the "Institut de Protection et de Sureté Nucléaire (IPSN) of the "Commissariat à l'Energie Atomique -CEA-", France. Contracts n° BC-4983, BC-5596. National Physical Laboratory (NPL) and Harwell Laboratory (UKAEA) are specially acknowledged for their contribution to data bases development.

VIII. BIBLIOGRAPHY

[1] M.A. Mignanelli and P.N. Smith,
"CSNI/PWG4/TGFPC Benchmark Exercise on the Chemical Modelling of the Release of Radionucleide due to Core-Concrete Interactions : Results of Part A and B"
CSNI Report 164, 15 feb. 1990.

[2] O. Relave, P.Y. Chevalier, B. Cheynet and G. Cenerino "Thermodynamical Calculation of Phase Equilibria in a Quinary Oxide System of First Interest In Nuclear Energy Field", Reprinted from User Aspects of Phase Diagrams, Proceedings of a Symposium organised by the Institute of Metals and the Commission of the European Communities, Joint Research Centre, Institute of Advanced Materials, held at Petten (N.H.), 25-27th June 1990, The Netherlands, Ed. F.H.Hayes, The Institute of Metals, 1991.

[3] A.L. Nichols,
"Fission Product Chemistry in Severe Nuclear Reactor Accidents", Report of a specialist meeting organized by the Commission of the European Communities in the frame of the Reactor Safety Programme 1988-1991 (Shared Cost Action), held at JRC-ISPRA, September 1990, EUR 12989 EN.

[4] P.Y. Chevalier,
"Thermodynamical calculation of phase equilibria in a quinary oxide system Al_2O_3-CaO-SiO_2-UO_2-ZrO_2 : determination of liquidus and solidus temperatures",
Journal of Nuclear Materials, 186 (1992) 212-215.

[5] G.Cenerino, P.Y.Chevalier and E.Fischer,
"Thermodynamic calculation of phase equilibria in oxide complex systems : Prediction of some selected fission products (BaO, SrO, La_2O_3) releases", OECD/NEA/CSNI meeting, KFK, Karlsruhe, Germany, 1-3 April 1992.

A Study of the Parameters Influencing the Release of Species by Vaporization During Core-Concrete Interactions

M A Mignanelli #

AEA Reactor Services, AEA Technology,
Harwell Laboratory, Oxfordshire OX11 0RA, UK

ABSTRACT

A sensitivity study has been performed to establish the parameters that are important in the modelling of the releases of species during molten core-concrete interactions. The factors that have been considered include the calculational method used to determine the equilibrium, the thermodynamic data and model that describes the chemical system, temperature, ablation rate, oxygen potential of the system and the configuration of the melt. The assessment of these parameters indicate that the chemical description of the melt, in particular the solution models and the configuration of the melt layers have a significant influence on the releases.

INTRODUCTION

The determination of the release of species, both radionuclides and non-radionuclides, by vaporization during molten core-concrete interactions requires information concerning the thermal-hydraulic behaviour of the melt and the variation in the chemical composition of the liquid, solid and gas phases. The method of calculating the releases, therefore, involves the estimation of the chemical equilibria of the system, in particular the composition of the gas phase, for a series of timesteps that define the progression of the interaction. The input parameters are temperature, ablation rate, the model that describes the chemical system, the appropriate thermodynamic data, the oxygen potential of the system and the configuration of the melt. Using these data, the calculation of the equilibrium composition is carried out using codes based on the minimization of the total Gibbs free energy of the system or the solution of simultaneous non-linear equations formed from the mass action and mass balance expressions, for example, the Brinkley method.

This work has been carried out under contract for the Health and Safety Executive, UK, and forms part of a programme on nuclear safety research.

The sensitivity of the calculated releases to the input parameters and the method of determining the chemical equilibria is the subject of this assessment study. The purpose of the work is to determine the uncertainty in the releases associated with the methods and data used at present. The results from the CSNI benchmark exercise on the chemical modelling of the release of radionuclides due to core-concrete interactions [1,2] provide information on some of the factors. Further sensitivity calculations have also been performed, using as a model the data obtained from Phase C of the Advanced Containment Experiments (ACE) carried out at Argonne National Laboratory [3]. The kinetic effects, including mass transfer in the melt and in the gas bubbles passing through the melt, are not considered here but have been assessed in a previous study of the initial phase of the interaction [4].

METHOD OF CALCULATING THE EQUILIBRIUM COMPOSITION

The objective of Part A of the CSNI benchmark exercise on the chemical modelling of the release of radionuclides due to core-concrete interactions [1], was to establish whether the method of calculation of the chemical equilibria in itself introduces discrepancies in the results. A simplified standard problem was devised to test the numerical methods of the codes used by various organizations. The speciation, thermodynamic data and a description of the system was provided and the participants were requested to calculate the equilibrium composition using a code of their choice.

The compositions were determined by 11 organizations using different codes and 15 results were submitted. The details of the participants and the codes used are shown in Table 1. The results from this simplified problem have shown that, with the exception of the VANESA code, there is good agreement between the results using different codes and different versions of the same code used to determine the equilibrium composition of multi-component systems. In particular, the extremely small releases of some of the species were accurately predicted. These codes determined the equilibria either by the direct minimization of the total Gibbs free energy of the system or by the Brinkley method. The latter method involves the solution of a number of simultaneous equations expressed in terms of the equilibrium constant. The assessment of the results from the VANESA calculations showed that the equilibrium solver in the code, which is based on the Brinkley method, is also capable of predicting extremely small releases of species. The VANESA 1.01 code, which has been developed specifically to model the release of radionuclides and the generation of aerosols during core-concrete interactions, was not designed to treat the highly simplfied problem in Part A. Modifications to the code and to the set problem were

required in order to produce a fair comparison. The differences in the results between the VANESA calculations and the others arises due to the specific assumptions used in VANESA to model dynamic core-concrete interactions. These assumptions will be discussed in the following sections.

THERMODYNAMIC TREATMENT OF THE MELT

The objective of Part B of the CSNI benchmark exercise [2] was to investigate the uncertainties resulting from differences in the chemical thermodynamic treatment of core-concrete melts. The problem involved the calculation of the equilibrium compositions for three cases representing typical core-concrete melts. Although the input amounts of certain species were specified in the problem, the method of treatment of the liquid and solid phases and the selection of the thermodynamic data were chosen by the participants, for example, the components of the phases, the representation of solutions as ideal or non-ideal and the consideration of the configuration of the melt.

Six sets of solutions to the problems were submitted from groups using different codes. A list of the participants and the organizations represented is shown in Table 2 together with the name of the code employed. In order to determine the origin of the discrepancies between the results from each participant for all the cases, the differences in the releases of the elements, expressed in orders of magnitude, are shown in Table 3. For each case, the maximum differences between all of the submissions (termed All) and between the submissions of Mignanelli, Dufresne and Powers (termed Sel) are presented. The particular submissions in the latter comparison were selected as comprehensive solution models and, in general, sound thermodynamic data had been used in the calculations. It can be seen that there are considerable differences between the results. It should be noted that, at present, it is not known which of the calculations, if any, are close to the ***correct*** solutions to the problems as different models for the melt have been employed based on various assumptions. The factors that have been raised during the assessment of the data that contribute to the uncertainty in the releases are, in order of decreasing importance:

1. The representation of the oxide solution as either a simple or complex phase - the use of associate models or interaction parameters to describe non-ideal behaviour.

2. The representation of the metal solution as either a simple or complex phase - the use of parameters to describe metal-metal and metal-carbon interactions.

3. The thermodynamic expressions estimated for the components of the liquid oxide phase in the ideal solution models where data are limited or unavailable, for example, the zirconates of lanthanum, barium and strontium.

4. The thermodynamic expressions estimated for species in the gas phase where data are limited or unavailable.

5. The estimation of high temperature thermodynamic data from measurements made at low temperature.

6. The uncertainties in the assessed thermodynamic expressions for the species in the gas phase.

Calculations based on the ACE Phase C Test L6 have also been performed to illustrate how the description of the oxide solution can influence the releases. Test L6 involved the interaction of a partially oxidized PWR corium melt with siliceous concrete. In the test, the corium was segregated into the oxide and metal components. All of the metal was contained in a siliceous concrete matrix placed directly on the top of the main concrete basemat. The initial temperature of the corium melt prior to concrete ablation was ~2500K. Two thermodynamic databases were used, one with and one without estimated data for the silicates and zirconates of lanthanum and using ideal solution models. The calculated release of lanthanum was reduced by a factor of 30 by the inclusion of the zirconate phase.

Some of the uncertainties in the modelling of core-concrete melts are being addressed at present by the thorough assessment of the thermodynamic data and the available phase diagrams for both oxide and metal systems [5-7]. The modification of the models to account for the results from experimental programmes is also an important part of the code development. The results from the ACE Phase C experiments are providing important information that will help to resolve some of the uncertainties [8].

THE TEMPERATURE OF THE MELT

The influence of the thermal history of the interaction on the release by vaporization have been estimated by comparing the results from calculations involving three different sets of temperature data and using the experimental configuration for ACE Phase C Test L6. The base calculation used the experimental thermal data from the test (Base Case). For the other

two calculations, the temperatures for each time interval were reduced by 50K (Case T1) and 100K (Case T2) respectively, using the same ablation rate as the Base Case.

The calculations have been performed using the SOLGASMIX REACTOR code [9] and involve the determination of the composition at nine time intervals during the test; the duration of the intervals is such that the temperature difference is not greater than 50K. In the first time interval, the interaction of the corium with the metal/concrete insert is modelled. The other intervals model the ablation of the concrete basemat. In the modelling, the system is described by 25 components, 128 species in the gas phase, 55 species in an ideal oxide liquid solution, 24 species in an ideal metal liquid solution and no stoichiometric compounds. Although the oxide solution is treated as ideal, both simple and complex constituents are included in the database. No layering of the melt was considered in the modelling of the concrete ablation; the gas, oxide and metal solution phases were assumed to be in equilibrium for each time interval. Included in the thermodynamic database are the silicates and zirconates of barium, strontium and lanthanum. During the early high temperature phase of the interaction, the oxygen potential of the system is low due to the presence of zirconium metal, -500 $kJ.mol^{-1}$. As the metal components of the corium are oxidized so the oxygen potential of the system is increased, -375 $kJ.mol^{-1}$.

The results from the three sets of calculations are shown in Table 4. These show that the effect of temperature is dependent on the volatility of the species of the element for the test conditions. For the more volatile species, for example Te, Mg, Si, K, Ag, In, Mn and Na, the total amount released by vaporization is only slightly reduced. However, for the less volatile species, for example U, Ca, Ru, Mo, La and Ce, the amount released is reduced by approximately a half for each reduction in temperature of 50K. In all three cases, the releases for Ru and Mo were the lowest, compared to the other fission product simulants, due to the very reducing conditions during the initial stages of the interaction.

THE CONCRETE ABLATION RATE

Two further calculations have been carried out to determine the effect of different rates of concrete attack on the release. The thermal conditions used were the same as for the Base Case of Test L6 but the amount of concrete subsumed in each time interval was reduced by a half (Case A1) and a quarter (Case A2). The results are also shown in Table 4.

The reduction of the ablation rate results in opposing effects on the release. As the volume of gas sparging through the melt is reduced so the amount of the species in the gas phase is

reduced. Conversely, as less oxide decomposition products are being added to the melt, the activity of the melt components are greater (as ideal solution models are used, the activity is equal to the mole fraction) for each time interval, relative to the Base Case. As can be seen from the results, in general, the release by vaporization is decreased by a reduction in the ablation rate; the release is reduced by less than an order of magnitude for the test conditions. For some species, notably barium and strontium, the release increases for Case A1 and then decreases for Case A2: the maximum increase was less than a factor of two.

Calculation carried out previously to determine the effect of concrete type on the releases (10) showed that similar releases were derived for basaltic and limestone concretes. Although approximately three times the amount of steam and carbon dioxide are produced for limestone concretes, the basaltic concrete, which contains a greater proportion of silica, releases a large amount of SiO vapour at high temperatures.

THE OXYGEN POTENTIAL OF THE SYSTEM

The final calculation using Test L6 data, involved an assessment of the influence of the oxygen potential of the system on the release. In this calculation (Case G1), the temperature history and ablation rate for the Base Case were adopted but the amount of zirconium metal was reduced to zero. The oxygen potential of the system during the early phase of the interaction was -335 $kJ.mol^{-1}$ compared to -500 $kJ.mol^{-1}$ for the situation with zirconium metal. The results of the Case G1 calculations are shown in Table 4. The absence of zirconium has a considerable effect on the release of some of the important species. The releases of barium and strontium are reduced by a factor of 40 and 70 respectively. Conversely, the releases of molybdenum and ruthenium are increased by a factor of 100 and 6500 respectively, reflecting the high volatility of the oxide species.

Some of the differences in the results between the VANESA calculations and the others described in the section on the CSNI benchmark exercise, are due to the specific assumptions used in VANESA concerning the setting of the oxygen potential of the system to model dynamic core-concrete interactions. In the versions of the code used in the exercise, the melt was considered to be layered with the metal layer initially in contact with the concrete. The oxygen potential over the oxide phase was then set equal to the value determined over the metal phase.

THE CONFIGURATION OF THE MELT

Another important parameter is the description assumed in the model for the configuration of the melt. The melt could be comprised of immiscible oxide and metal liquids and hence it might be appropriate to consider the melt as layered. However, during the early stages of the interaction, considerable amounts of gaseous decomposition products are released from the concrete which then sparge through the melt. The effect of the sparging gases is to mix the layers such that it could be conceived that the gas, oxide and metal phases are in equilibrium. Layering could then be assumed to occur during the later stages when the ablation rate is reduced and the temperatures are lower.

The study of the effect of the configuration of the melt on the releases were carried out using the code CORSOL (coupled CORCON and SOLGASMIX code). In the code, the SOLGASMIX chemistry calculations can be carried out for each of the layers in turn determined by CORCON and the gas phase passed on to the next layer. Alternatively, the compositions of all the layers can be considered in a single equilibrium calculation. Two calculations were performed, using data from ACE Phase C Test L2, in which the releases estimated using the layered structure predicted by CORCON were compared with the releases from an homogenous melt. In CORCON, the oxide layer is considered to be in contact with the concrete during the initial stage of the interaction. The results, shown in Table 5, indicate that there is a significant reduction, up to three orders of magnitude, in the releases for the layered case. The results from the ACE Phase C programme should provide information concerning the likely geometry of the melt.

CONCLUSIONS

A number of sensitivity calculations have been performed to establish the parameters that are important in modelling the releases of species, both radionuclides and non-radionuclides, during molten core-concrete interactions. The results from Part A of the CSNI benchmark exercise show that the different methods and codes that are available to perform chemical equilibrium calculations are capable of predicting accurately the releases of the species. The results from Part B of the exercise indicate that the main contributors to the uncertainty are the solution models used to describe the melt and the lack of thermodynamic data for the zirconate and silicate phases of the important radionuclides. The results from additional calculations also indicate that differences in the release for certain species up to three orders of magnitude are possible depending on the configuration

assumed for the melt structure and the oxygen potential of the system. The influence of the thermal history of the interaction and the rate of concrete ablation on the release by vaporization have shown that the differences in the releases of the less volatile species are not greater than an order of magnitude. An assessment of the release results from the ACE Phase C programme and other integral core-concrete tests, together with data from separate effect tests and thermodynamic measurements, should provide the information to resolve some of the main uncertainties.

REFERENCES

(1) M A Mignanelli, P N Smith, "Benchmark exercise on the chemical modelling of the release of radionuclides due to core-concrete interactions: Results of Part A", CSNI Report No 164 Volume A.

(2) M A Mignanelli, "Benchmark exercise on the chemical modelling of the release of radionuclides due to core-concrete interactions: Results of Part B", CSNI Report No 164 Volume B.

(3) B R Sehgal, B W Spencer, "ACE programme Phase C: Fission product release from molten corium-concrete interactions (MCCI)", Paper presented at the OECD CSNI Specialist Meeting on Core Debris-Concrete Interactions, Karlsruhe, Germany, April 1-3, 1992.

(4) P N Smith, A T D Butland, P E Potter, M A Mignanelli, G J Roberts, "The importance of core/concrete aerosol production and some containment heat sources to the source term", Proc. Symp. on Source Term Evaluation for Accident Conditions, Columbus, Ohio, 1985, IAEA-SM-281/32, 1986.

(5) R G J Ball, M A Mignanelli, "The calculation of phase equilibria of oxide core-concrete systems", Paper presented at the OECD CSNI Specialist Meeting on Core Debris-Concrete Interactions, Karlsruhe, Germany, April 1-3, 1992.

(6) P Y Chevalier, G Cenerino, "Thermodynamic data and calculation code adapted to the molten core concrete interaction, developed by THERMODATA and CEA", Paper presented at the OECD CSNI Specialist Meeting on Core Debris-Concrete Interactions, Karlsruhe, Germany, April 1-3, 1992.

(7) G Cenerino, P Y Chevalier, E Fischer, "Thermodynamic calculations of phase equilibria in oxide complex systems: Prediction of fission product (BaO, SrO, La_2O_3) release", Paper presented at the OECD CSNI Specialist Meeting on Core Debris-Concrete Interactions, Karlsruhe, Germany, April 1-3, 1992.

(8) J K Fink, M Corradini, A Hidaka, E Hontañón, M A Mignanelli, E Schrödl, V Strizhov, "Results of aerosol code comparisons with releases from ACE MCCI tests", Paper presented at the OECD CSNI Specialist Meeting on Core Debris-Concrete Interactions, Karlsruhe, Germany, April 1-3, 1992.

(9) G Eriksson, "Thermodynamic studies of high temperature equilibria ", Chem. Scr. 8, 1975, 100.

(10) A T D Butland, M A Mignanelli, P E Potter, P N Smith, "The vaporization of chemical species and the production of aerosols during a core debris-concrete interaction", Proc. CSNI Specialist Meeting on Core Debris-Concrete Interactions, Palo Alto, USA, Sept. 1986.

Table 1 Participants in the Part A exercise

Participant	Organization	Code *
M A Mignanelli	AEA Technology, Harwell, UK	SGMX
F Garisto	Atomic Energy of Canada	CHEMEQ
E Borioli	ENEL, Thermal and Nuclear Research Centre, Milan, Italy	SGMX-PV VANESA 1.01
R Sairanen	Technical Research Centre of Finland	SGMX-PV
J J de Wolff	KEMA, Arnhem, Netherlands	SGMX-PV
D A Powers	Sandia National Laboratory, USA	BRINKLEY
J Dufresne	CEA, Fontenay aux Roses, France	GEMINI-88 SGMX-88 MELANGE-88
E H P Cordfunke	ECN Petten, Netherlands	SGMX-PV
K Muramatsu	JAERI, Japan	MPEC2
G Capponi E Manilia	ENEA, Rome, Italy	VANESA 1.01
P N Smith	AEA Technology, Winfrith, UK	VANESA

* SGMX refers to the SOLGASMIX code developed by G Eriksson
SGMX-PV refers to the adaptation of the SOLGASMIX code by T Besmann, ORNL
BRINKLEY refers to code based on the Brinkley method (used in VANESA)

Table 2 Participants in the Part B exercise

Participant	Organization	Code
M A Mignanelli	AEA Technology, Harwell, UK	SGMX
J Dufresne	CEA, Fontenay aux Roses, France	GEMINI
K Muramatsu	JAERI, Japan	MPEC2
J J de Wolff	KEMA, Arnhem, Netherlands	SGMX-PV
D A Powers	Sandia National Laboratory, USA	BRINKLEY
G Capponi	ENEA, Rome, Italy	VANESA 1.01

Table 3 Differences, in orders of magnitude, in the releases of the elements between the various submissions #

	Case A 2000K		Case A 2500K		Case B 2000K		Case B 2500K		Case C 2000K		Case C 2500K	
Element	All*	Sel*	All	Sel	All	Sel	All	Sel	All	Sel	All	Sel
O	6.0	1.0	4.0	0.5	4.5	1.5	2.0	1.5	5	2.5	3	1
H	0.0	0.0	0.0	0.0	0.0	0.0	0.0	0.0	0.0	0.0	0.0	0.0
C	6.0	1.5	3.5	1.0	4.5	2.0	2.5	1	4.5	3	2.5	1.5
U	4.0	1.5	3.0	0.5	4.0	2.0	4.0	2.5	3.5	2	3.5	0.5
Zr	4.5	0.5	4.5	0.5	10.0	9.0	6.5	4.5	9	8.5	5.5	4
Fe	5.5	0.5	6.0	0.5	6.0	0.0	7.0	2	5.5	0	6.5	0
Si	10.0	4.5	7.0	3.0	5.0	1.0	2.5	2	5	1.5	3	0.5
Ca	4.5	2.0	3.0	1.0	5.5	2.0	2.5	2	6	3.5	4.5	2.5
Ce	4.5	2.0	4.0	2.0	4.0	0.0	2.5	1.5	4	1	3.5	1
La	4.0	1.0	4.5	1.5	5.0	3.5	4.5	2	4	2.5	5	3
Sr	5.5	5.5	4.5	4.0	7.0	2.0	2.5	0.5	5	2	3.5	1.5
Mo	2.0	1.0	2.0	1.0	2.5	1.0	3.5	1.5	2	1	2.5	1

Difference = max.($\Delta \log_{10} r_i$) where r_i is the amount in moles of element i released.

* All - Differences between all the submissions;

Sel - Differences between Mignanelli, Dufresne and Powers.

Table 4 Calculated amount (moles) in the gas phase of the elements at the end of the ACE Phase C Test L6

Element	Base Case	Case T1	Case T2	Case A1	Case A2	Case G1
Ba	2.49E-03	1.49E-03	7.91E-04	4.17E-03	2.45E-03	6.49E-05
O	4.52E+02	4.34E+02	4.09E+02	3.40E+02	1.37E+02	1.46E+02
U	2.24E-02	1.18E-02	5.77E-03	1.97E-02	1.00E-02	3.00E-02
Te	1.15E+00	1.15E+00	1.15E+00	1.15E+00	1.15E+00	1.15E+00
Sr	4.96E-03	3.18E-03	1.82E-03	8.28E-03	4.84E-03	7.44E-05
Mg	3.20E+00	3.04E+00	2.68E+00	2.70E+00	1.36E+00	1.57E-02
Al	8.39E-01	5.38E-01	2.95E-01	1.20E+00	3.80E-01	3.20E-03
H	3.06E+02	3.06E+02	3.06E+02	1.53E+02	7.66E+01	3.06E+02
Zr	1.45E-03	7.60E-04	3.53E-04	2.33E-03	1.34E-03	1.10E-05
Cr	6.55E+00	4.22E+00	2.56E+00	3.15E+00	1.10E+00	1.88E+00
La	8.15E-04	3.89E-04	1.71E-04	8.12E-04	4.03E-04	7.02E-05
Si	3.77E+02	3.60E+02	3.36E+02	3.07E+02	1.26E+02	2.36E+01
Ca	2.17E+00	1.14E+00	4.87E-01	6.10E+00	4.07E+00	1.47E-03
Fe	1.08E+01	6.61E+00	3.85E+00	4.94E+00	1.66E+00	2.43E+00
Ni	1.07E+00	6.13E-01	3.37E-01	4.45E-01	1.51E-01	1.17E+00
Ce	1.72E-02	9.64E-03	5.06E-03	1.49E-02	7.32E-03	9.89E-03
K	1.54E+01	1.50E+01	1.48E+01	9.90E+00	4.86E+00	9.32E+00
C	7.12E+01	7.12E+01	7.11E+01	3.39E+01	1.19E+01	7.12E+01
Mo	6.14E-05	1.97E-05	6.23E-06	6.85E-06	2.19E-06	6.46E-03
Sn	1.27E-01	9.28E-02	6.61E-02	6.45E-02	2.97E-02	1.82E-01
Ru	3.24E-05	1.42E-05	5.92E-06	1.27E-05	4.28E-06	2.09E-01
Ag	1.06E+01	1.01E+01	9.13E+00	9.24E+00	5.53E+00	1.10E+01
In	1.89E+00	1.85E+00	1.76E+00	1.76E+00	1.19E+00	1.92E+00
Mn	9.07E-02	8.92E-02	8.59E-02	6.57E-02	1.91E-02	4.97E-03
Na	1.24E+01	1.21E+01	1.18E+01	7.42E+00	3.65E+00	8.33E+00

Case T1 - Reduction in the Base Case temperature profile by 50K

Case T2 - Reduction in the Base Case temperature profile by 100K

Case A1 - Reduction in the Base Case concrete ablation rate by a half

Case A2 - Reduction in the Base Case concrete ablation rate by a quarter

Case G1 - Exclusion of zirconium metal from the corium

Table 5 Calculated release fractions for ACE Phase C Test L2 using the CORSOL code

Element	Input[a] (Moles)	Release fractions CORSOL[b]	CORSOL[c]
U	8.00E+02	1.26E-03	5.89E-05
Ba	5.22E+00	1.16E-04	7.70E-07
Sr	4.83E+00	2.45E-4	2.57E-07
La	3.68E+00	1.00E-04	2.62E-07
Ce	7.55E+00	1.65E-03	2.57E-04
Mo	7.03E+00	2.13E-02	1.01E-03
Te	8.12E-01	1.00	1.00

(a) Initial corium inventory.

(b) Calculations for single layer case.

(c) Calculations for multilayer case.

AEROSOL REMOVAL FROM GAS BUBBLES RESULTING FROM MOLTEN CORE-CONCRETE INTERACTIONS

G.J. BAMFORD and S.A. RAMSDALE

SRD Culcheth, AEA Technology
Wigshaw Lane, Culcheth
CHESHIRE WA3 4NE

ABSTRACT

Pool scrubbing, the removal of aerosol particles by bubbling contaminated gases though a water pool, could be a significant mechanism in limiting the severity of certain nuclear reactor accidents. BUSCA is a computer code designed to model bubble thermal-hydraulics and associated pool scrubbing removal processes. This paper describes the enhancements made to the code since the Palo Alto CSNI conference in 1986. BUSCA now has the ability to model effects of different bubble shapes, bulk condensation, bubble breakup, and bubble cluster and plume rise conditions. A series of sensitivity tests have been included to assess the significance of these additions on decontamination factor calculations.

1. INTRODUCTION

In the unlikely event of a severe Pressurised Water Reactor (PWR) accident the purpose of the safety system is to limit the release of radioactive material into the environment. Pool scrubbing, i.e. the cleaning of gases by bubbling through a pool of water, may provide a means of filtering out fission products released during such a core degradation. Consider the situation where a degraded core is submerged in a water pool. Here, the molten core will be reacting vigorously with the surrounding water and concrete and releasing reaction products along with various gases and steam into the boiling pool. Given this scenario can a significant amount of retention occur in the pool? If so, the pool scrubbing process can help reduce the amount of material released into the containment building and thus ease the task of other safety systems. This paper describes the work performed on the pool scrubbing code BUSCA (BUbble SCrubbing Algorithm) since the last CSNI conference in Palo Alto.

BUSCA has been designed to model the thermal-hydraulics and aerosol removal processes of hot gas bubbles as they rise through a pool of water. The code was originally developed at SRD (part of the UK Atomic Energy Authority) during the mid 1980's and since then has been further enhanced by collaboration within the European Pool Scrubbing Group. A description of an early version of the code was presented at the last CSNI conference[1]. Since then, the infant code has been developed and additional mechanisms included in its calculations. In particular, PSI (Paul Scherrer Institute, Wurenlingen) has converted the original FACSIMILE code into FORTRAN and added jet impaction modelling along with different bubble geometry and bubble rise speed options, UPM (Universidad Politecnica de

Madrid) has added the bubble breakup modelling and SRD has added the bulk condensation modelling and the cluster and plume features. Here, we describe these additions and illustrate the effects they have on Decontamination Factor (DF = aerosol mass input/aerosol mass output) calculation.

It must be stressed that the development of BUSCA is an on-going project. As the code has been developed, processes have been added on a priority basis. In relation to Molten Core-Concrete Interactions (MCCI) the code is still in its early stages. It has been important to make the code work under relatively simple conditions before attempting to model the more complicated MCCI case. MCCI reactions take place under extreme conditions in a churn-turbulent bubble regime. At present the code has a limited capability for modelling bubble cluster and plume configurations together with the bubbly flow regime. We are currently active in modelling churn-turbulent situations.

2. REVIEW OF BUSCA OPERATION

As well as modelling aerosol removal from gas bubbles, BUSCA can also model the removal of soluble gases. However, in this paper we are going to concentrate solely on aerosol removal processes.

BUSCA calculates DFs by following, in detail, a single bubble from introduction into the pool to it breaking the pool surface. A typical bubble atmosphere consists of aerosol particles together with one or more gases and steam. As the bubble rises, there is strong coupling between the thermal-hydraulic and aerosol transport processes. For example, the temperature gradient at the bubble surface affects the thermophoretic removal rate while steam condensation onto the aerosol particles enhances removal due to sedimentation and inertial impaction. In addition, the bubble atmosphere is continually changing composition as steam condenses or evaporates from the bubble-pool interface, a mechanism that also controls the diffusiophoretic removal rate. BUSCA models all these processes, resulting in a code that can predict bubble system conditions at any point during its rise time. Keeping track of all aerosol components allows the code to evaluate DFs under various bubble conditions.

The basic thermal-hydraulic modelling and the various removal mechanisms have been described in reference [1]. The additions described in this paper have been included to model bulk condensation and bubble breakup processes. Also, of importance to this conference, is the extension to modelling different bubble flow regimes. BUSCA now includes options to simulate bubble cluster and plume type flows. A cluster is defined as a collection of bubbles formed after breakup of a large gas globule. A plume is formed when the gas injection rate into the pool is continuous. The latter situation is somewhat akin to conditions found in MCCI.

As mentioned above there are still some limitations with the code. For example, it does not account for decay heating of the bubble system or for the enhancement of aerosol removal by agglomeration. These processes are assumed to have only a small effect on DF calculations, however, they may be included at a later date. Also, the modelling at present only concerns itself with the rising bubble system. Effects at the pool surface are not included in the calculations.

3. BUBBLE BREAKUP MODELLING

BUSCA now contains an option for selecting bubble breakup. This model automatically breaks up large globules into smaller bubbles depending upon certain stability criteria[2]. A final bubble size is determined from an expression for the bubble size distribution developed by Paul et al[3]. Firstly, the code determines whether the input gas globule is unstable by applying two stability criteria. The first stability level is based on the bubble's Weber number.

$$We_b = U_b^2\left[\frac{\rho_w D_b}{\sigma}\right]$$

where, U_b is the bubble terminal velocity,
D_b is the bubble diameter,
ρ_w is the density of the surrounding water,
σ is the bubble surface tension.

A critical bubble Weber number is specified and bubble breakup continues until individual bubble Weber numbers are below this value. In addition to this, the bubble radius is monitored and breakup initiated to ensure the radius stays below a level defined by Levich[4]. This level is defined as,

$$r = \frac{\sigma}{U_b^2}\left[\frac{12}{\rho_g \rho_w^2}\right]^{\frac{1}{3}}$$

where, ρ_g is the gas density. At breakup the arithmetic mean diameter (mm) of the small bubble distribution is calculated from,

$$AMBD = 10^{\left(<Log_{10}D_b> + 1.151(Log_{10}w)^2\right)}$$

where, $<Log_{10}D_b>$ is the average bubble diameter and $Log_{10}w$ is the standard deviation of the log-normal bubble size distribution. At present $<Log_{10}D_b>$ is set to 0.75 and $Log_{10}w$ is set to 0.173, in accordance with experimental results[3]. This breaks each globule into bubbles of diameter 5.6mm. All bubble parameters relating to bubble size are then scaled down to the new bubble size. BUSCA then continues to track this smaller bubble to the surface. Any further breakup is dealt with in a similar manner if the bubble is within a zone near the inlet orifice. Breakup modelling should not be confused with the cluster modelling described later in this paper.

4. BULK CONDENSATION MODELLING

Bulk condensation is the process by which steam condenses onto aerosol particles within the bubble atmosphere. This mechanism can significantly affect the removal rate of aerosols by increasing their size. An increase in size leads to an enhancement in sedimentation and inertial deposition rates. The equation that determines how the aerosol particles grow as steam condenses onto them is the Mason equation. For a given set of conditions a particle of mass μ will grow at a rate given by,

$$\frac{\partial \mu}{\partial t} = 4\pi r D_G \rho_s(p_{sat}(T_B), T_B)[S_B - S_p]\frac{Cn}{Cn + S_p}$$

This formulation of the Mason equation has been fully documented in the ITHACA physics reference manual[5], each parameter is described in detail below.

During its calculation phase BUSCA breaks the aerosol mass axis into a number of characteristic mass points. The code then performs its mass related calculations at these points. In order to determine actual aerosol quantities, an integration over these characteristic points must be performed. In addition, BUSCA can model situations with more than one aerosol component in the atmosphere. In these cases the components are assumed to be non-interacting, and each component is given its own set of mass characteristics. Therefore, for a given component q and a characteristic size i, the characteristic point (or collocation point) has a radius r_i^q, mass μ_i^q and density ρ_i^q.

EVALUATION OF THE MASON EQUATION

Determination of the Mason equation requires calculation of the following.

a). Density of steam at the saturation pressure $\rho_s(p_{sat}, T)$.
b). Collocation point radii r_i^q.
c). Bulk saturation ratio S_B.
d). Saturation ratio at the particle surface S_p.
e). Condensation number Cn.
f). Diffusivity of steam in the bubble gas D_G.
g). Thermal conductivity of the bubble gas K_G.
h). Specific latent heat of steam condensation on a particle L(T).

Steam Density Calculation

In all its calculations involving steam, BUSCA assumes that steam behaves as an ideal gas. This enables us to express the steam density as,

$$\rho_s(p_{sat}(T_B), T_B) = \frac{p_{sat}(T_B) M_{ws}}{R_G T_B}$$

where, p_{sat} is the saturated vapour pressure calculated at the bubble temperature T_B using the formula in the UK steam tables[6].
M_{ws} is the molecular mass of steam.
R_G is the universal gas constant.
T_B is the bubble temperature.

Collocation Point Calculation

The collocation point radii (r_i^q) can be calculated from the following,

$$r_i^q = \left(\frac{3}{4\pi} \frac{\mu_i^q}{\rho_i^q} \right)^{\frac{1}{3}}$$

where ρ_i^q is the collocation point density given by,

$$\rho_i^q = \frac{MASS}{VOLUME} = \frac{Y_i^q + W_i^q}{\frac{Y_i^q}{\rho^q} + \frac{W_i^q}{\rho^w}}$$

where ρ^q is the density of the component we are considering and Y_i^q and W_i^q are the aerosol component and condensed water masses, per unit volume, at collocation point i. W_i^q is related to μ_i^q, C_i^q and Y_i^q by;

$$\mu_i^q \; C_i^q = Y_i^q + W_i^q$$

with C_i^q as the number distribution per unit volume of particles at collocation point μ_i^q.

Saturation Ratio Calculations

Let us first consider the bulk saturation ratio S_B. This is given by,

$$S_B = \frac{p_s}{p_{sat}(T_B)}$$

where p_s is the bulk steam pressure at a given time, and p_{sat} is the saturation pressure at bubble temperature T_B as determined in the UK steam tables[6].

The saturation ratio at the particle surface S_p is given by,

$$S_p = \gamma^k \gamma^A$$

where γ^k is the Kelvin correction factor calculated from,

$$\gamma^k = \exp\left[\frac{2\,\sigma\,M_{ws}}{r_i^q\;\rho_i^q\;R_G\;T_B}\right]$$

and σ is the surface tension of liquid water, R_G is the universal gas constant, M_{ws} is the molecular mass of steam, and T_B is the bubble temperature. The Kelvin effect slows down and can reverse condensation onto particles depending on their size.

γ^A is the activity of soluble aerosols calculated from,

$$\gamma^A = \frac{1}{1 + M_{ws} H^q \beta^q}$$

where H^q is the Van't Hoff coefficient of the q'th component and is a measure of the number of ions produced by the component in solution. β^q is the molality of the q'th component.

Condensation Number Calculation

The dimensionless condensation number is determined from the expression,

$$Cn = \frac{K_G}{L(T_B)\ D_G\ \frac{d\rho}{dT}}$$

where K_G and D_G are the thermal conductivity and diffusivity of steam in the bubble gas. L(T) is the specific latent heat of steam condensing onto a particle,

$$L(T) = h_s(T_B) - h_w(T_B)$$

where h_s and h_w are the specific enthalpies of steam and water at temperature T. $d\rho/dT$ is given by,

$$\frac{d\rho}{dT} = \frac{d}{dT}\left(\rho_s(p_{sat}(T_B), T_B)\right)$$

with dp_{sat}/dT being determined from the expression in the UK steam tables[6].

THE THERMAL HYDRAULIC MODEL

Steam condensation onto different hygroscopic and non-hygroscopic particles also requires the solution of the rate equations for mass and heat transfer.

Steam Mass Transfer Rate

In BUSCA, condensation and evaporation can take place onto/from the aerosol particles as well as at the bubble surface. This results in an overall steam mass transfer rate of,

$$\frac{dm_s}{dt} = -\frac{dm_s}{dt}\Big|_{g \to sf} - \frac{dm_w}{dt}\Big|_{g \to a}$$

$$\frac{dm_s}{dt} = -k_m{}^* A\ Ln\left(\frac{1 - X_{si}}{1 - X_s}\right) - \frac{dm_w}{dt}\Big|_{g \to a}$$

where dm_s/dt is the rate at which the mass of steam in the bubble changes due to condensation-evaporation. The first term is the condensation rate onto the bubble surface ($dm_s/dt\,|_{g \to sf}$), and the second term ($dm_w/dt\,|_{g \to a}$) is the rate at which steam condenses onto the aerosol particles and is determined from the MASON equation. A fuller description of the first term is given in reference [1].

Heat Transfer Rate Equation

The total bubble enthalpy changes because of conduction of heat out of or into the bubble and condensation-evaporation at the bubble surface. Bulk condensation does not affect the total bubble enthalpy. The enthalpy rate of change is thus,

$$\frac{dH}{dt} = -k_H A(T_B - T_P) - h_s \frac{dm_s}{dt}\Big|_{g \to sf}$$

where $dm_s/dt\,|_{g \to sf}$ is the steam mass transfer rate onto the bubble surface. The first term is the heat transfer rate across the bubble surface and the second term determines the enthalpy change due to condensation-evaporation at the bubble surface. A full description of this rate is given in reference [1].

Bubble Temperature Equation

The rate of change of bubble temperature is derived by differentiating the expression for the total bubble enthalpy. The total bubble enthalpy is defined as,

$$H(m_s, m_w, m_N, T_B) = m_s h_s(T_B) + m_w h_w(T_B) + m_N h_N(T_B)$$

where terms that correspond to the aerosol enthalpies other than condensed steam have been neglected. The bulk condensation adds a term $m_w h_w$ which determines the contribution to the total enthalpy from the condensed steam residing on the aerosol particles. Differentiating this equation results in an expression for the rate of change of bubble temperature given by,

$$\frac{dT_B}{dt} = \frac{1}{\langle mc_p \rangle}\left[\frac{dH}{dt} - h_s(T_B)\frac{dm_s}{dt} - h_w(T_B)\frac{dm_w}{dt}\Big|_{g \to a}\right]$$

where $\langle mc_p \rangle$ is an expression for the total heat capacity of the bubble system.

5. CLUSTER AND PLUME MODELLING

Two cluster models, the GEC and Colder's cluster models, and one plume model, the Sjoen plume model, have been incorporated into BUSCA. In all three models, the main aim of the calculations is to determine an enhanced bubble rise velocity. The algorithms described in this paper concern themselves with calculation of average rise velocities for the cluster or plume. This in turn is then taken to be the average bubble rise velocity. The rise velocity is an important parameter in determining DFs. A faster bubble rise leads to a shorter gas residence time in the pool which in turn lowers the overall DF. In the present implementation, the relative bubble-liquid velocity remains unaltered so that the circulation rate in the bubble and the aerosol removal processes remain unaffected.

CLUSTER MODELS

A cluster is defined as a collection of bubbles formed when a large globule of gas breaks up.

GEC cluster model

In this model bubbles formed from the breakup of a larger gas globule rise through the surrounding liquid as an approximately spherical cluster. Internal circulation in the cluster is upward near the vertical centre axis and downward near the boundaries. This flow pattern is similar to the Hills vortex[7]. Assuming that all the energy imparted in the globule breakup is transferred to the Hills vortex the cluster rise velocity is calculated as,

$$v_c^2 = \frac{28}{30} gY \frac{\alpha}{1-\alpha}$$

where, g is the acceleration due to gravity and α is the void fraction. Y is the bubble breakup distance. The bubble rise velocity v_b is then taken to be equal to the cluster rise velocity v_c. In order to determine the cluster velocity we need only to know the void fraction α and the initial bubble breakup distance Y. Studies of bubble behaviour made during GEC's fission product scrubbing program indicate that typical void fractions are of the order 0.5 to 0.66. At present BUSCA assumes α=0.5. Y is taken to be one half the detachment diameter[7] d_d given by,

$$Y = \frac{d_d}{2} = 1.3 \frac{d_o}{2} \left[\frac{Q}{\sqrt{g d_o^5}} \right]^{0.4}$$

where, d_o is the orifice diameter,
Q is the gas injection rate into the globule.

Colder's cluster model

In this cluster model both the cluster and the bubbles are assumed to be spherical with the bubbles arranged to form a cubic lattice within the cluster. Bubble spacing in the lattice is twice the bubble diameter d_b. Bubble rise velocity is calculated from the following expression,

$$v_b = 2.221 \sqrt{d_b} \left[(1-\alpha) + \frac{\alpha^{\frac{1}{3}}}{\sqrt{d_b}} \left[\frac{Q}{0.5812} \right]^{\frac{1}{5}} \right]$$

This allows a determination of the bubble rise velocity by simply specifying the volumetric flow rate Q, the void fraction α and the bubble diameter d_b.

PLUME MODELLING

A plume of bubbles is formed when the gas injection rate into the pool is continuous, resulting in large releases of gas.

Sjoen plume model

This plume model has resulted from a study of uncontrolled releases of oil and gas from the seabed and drilling platforms[8]. Hydrodynamic models have been developed to simulate these release mechanisms and comparisons with experimental data have helped establish the mathematical model. Good agreement between the model and data is seen over a wide range of gas flow rates and pool depths. The report by Sjoen[8] has included in it a full listing of the FORTRAN program used to simulate these release conditions. This code has been included in BUSCA without modification and thus forms the basis of the BUSCA plume velocity calculations.

The model is based on two-phase flow. In general, mass momentum and energy conservation equations for each phase are expressed in terms of sets of partial differential equations. The mass and momentum transfer rates between the two phases are then defined,

leading to a closure of the plume wide equation set. A number of simplifying assumptions are made to ease the solution of this equation set. Firstly, all conservation equations are time averaged to remove turbulent features. Secondly, phase transfer rates are expressed in terms of a mixture model.

In this paper it would serve little purpose to go into the details of the equation set. Their formulation is more than adequately covered in the report by Sjoen[8]. However, it is instructive to show the form of these equations as specified in BUSCA. This will provide the interested reader with a link between the Sjoen paper and BUSCA.

Solution of the equation set is determined by three parameters, namely the relative velocity between the two phases (W_r), the rate of plume spread (entrainment coefficient β) and a scaling factor relating the velocity and void fraction profiles (λ). In addition, the volumetric flow rate and pool depth are required as input. The plume width and velocity and a measure of the void fraction are then calculated as the plume rises. The actual equation set that is solved is,

$$\alpha_c = \frac{M_2}{B^2(W+K_6W_r)(1-Z)}$$

$$\frac{d}{dZ}\left(WB^2(1-K_7\alpha_c)\right) = WB$$

$$\frac{d}{dZ}\left(W^2B^2(1-K_8\alpha_c)\right) = \frac{1}{(W+K_6W_r)(1-Z)}$$

where,

$\alpha_c(z)$ is the void fraction,
K_1-K_8 are a set of scaling constants,
Z is a non-dimensional axial cylindrical coordinate,
W is a non-dimensional axial velocity component from which the cluster rise velocity is calculated,
B is a non-dimensional plume width,
M_2 is a void fraction parameter,
W_r is the non-dimensional axial velocity component for the relative velocity between the two phases.

Here we simply note that simultaneous solution of this equation set allows the determination of the plume rise velocity v_p from the W parameter,

$$v_p = WM_1$$

where M_1 is a scaling parameter. The bubble rise velocity v_b is then taken to be equal to the plume rise velocity v_p. At present, solution of these equations is carried out in BUSCA by the IMSL[9] Runge Kutta integration package DIVRK.

CALCULATION OF THE GAS INJECTION RATE

The cluster and plume models discussed above require the gas injection rate Q to be specified. In BUSCA the injection rate Q is calculated by taking the total gas flow rate into the injection system F_T and dividing it by the number of holes through which the gas passes N_H. All the models so far described assume non-condensible flow in thermal equilibrium with the surrounding water. In BUSCA a further correction is made to the flow rate to take into account condensation-evaporation and cooling at the injection orifice. The volumetric flow rate is then given by the following expression,

$$Q = \frac{F_T}{N_H} \frac{T_p}{T_B} \frac{(1-X_s)}{(1-X_{so})}$$

where, T_p is the pool temperature,
T_B is the bubble temperature,
X_s is the mole fraction of steam in the bubble,
X_{so} is the mole fraction of steam at the bubble pool interface.

The term T_p/T_B takes account of the bubble volume change arising from bubble cooling to the pool temperature. The second term, $(1-X_s)/(1-X_{so})$, takes care of the volume changes due to condensation-evaporation during injection.

6. BUSCA MCCI CALCULATIONS

A previous set of calculations[1] were performed five years ago for assessing aerosol decontamination by water pools overlying core-concrete interactions. These simulations were based on MARCH calculations for an S_2D accident sequence. Sensitivity tests were carried out to illustrate the effects of using,

i) two different bubble gas compositions corresponding to total or zero reduction of steam by the melt.
ii) two initial bubble temperatures, corresponding to either the surface temperature of the melt or the pool saturation temperature.
iii) two pool temperatures, corresponding to either a saturated or sub-cooled pool.

This work resulted in the DF matrix shown in Table 1. The present set of calculations repeats these simulations and extends the testing to illustrate the effects of the additional bubble mechanisms described in this paper. In particular, the previous calculations were performed with spherical cap bubbles, this being the only shape modelled by BUSCA at the time. A spherical cap geometry is only appropriate for large bubbles, typical sizes being around $5cm^3$. Bubble hydrodynamic tests conducted by EPRI[10] have indicated that the volume mean bubble size is more likely to be around $0.09cm^3$ over a wide range of conditions. At this bubble size a spherical bubble shape is more appropriate. The ability to model spherical bubbles has been included in BUSCA and a simulation designed to show the effect of bubble shape on DF calculation has been included. Simulations of bulk condensation onto both soluble and insoluble aerosols have also been included. Finally, the effect of treating the rising bubbles as a plume rather than a single bubble is illustrated using the Sjoen plume model. This plume model has been used with a volumetric flow rate of $0.01m^3/s$ for a pool depth of 2m. At this input rate the flow rate was at the limit of applicability for this model.

		100% H_2	2% CO_2,98% H_2O
Pool Temp=383 K	Bub. Temp=1600K	1.04	9.42
	Bub. Temp=383K	1.02	5.50
Pool Temp=360 K	Bub. Temp=1600K	1.41	95.6
	Bub. Temp=383K	1.21	46.5

Table 1. Final DFs predicted by Original BUSCA calculation [1].

The input parameters used in these simulations are as follows,

Pool depth	2m,4m
Above pool pressure	140 000 Pa
Particle material density	2500 kg/m^3
MMR	0.5 μm
GSD	2.3
Gas composition (mol %)	100% H_2 and 98% H_2O:2% CO_2
Bubble size	5cm^3 and 0.09cm^3
Pool temperature	383K and 360K
Bubble temperature	1600K and 383K

		100% H_2	2% CO_2,98% H_2O
Pool Temp=383 K	Bub. Temp=1600K	1.05	13.97
	Bub. Temp=383K	1.02	7.86
Pool Temp=360 K	Bub. Temp=1600K	1.38	106.2
	Bub. Temp=383K	1.19	46.22

Table 2. DFs predicted by present version of BUSCA. Pool depth 2m bubble volume 5cm^3.

Varied parameter	Decontamination Factor
Soluble aerosol	154.6
Spherical bubble (bubble vol. 0.09cm^3)	7546
Pool depth 4m	31.42
Plume model	10.17

Table 3. Variation in operating conditions for the case pool temp.=383K, bubble temp.=1600K, and atmospheric composition 2%CO_2,98%H_2O.

Table 2 shows the results of the recalculation of the original BUSCA data sets, which are to be compared with Table 1 values. These calculations were performed assuming an insoluble aerosol. Although bulk condensation was switched on, close inspection showed that the bubble conditions were such that no condensation took place. The difference between the Table 1 and Table 2 values are due to enhancements and corrections made to the code during the intervening period.

The effect of making the aerosol particles soluble is shown in Table 3. In this case the particles can absorb vast amounts of water and thus dramatically increase their mass. This results in a further large increase in the removal rate through sedimentation and inertial deposition. The effect of reducing the bubble size is also shown in Table 3. The smaller spherical bubble has a larger surface to volume ratio than the spherical cap bubbles. This tends to increase the rate by which aerosol leaves the bubble. Another parameter that has a significant effect on DF calculation is the pool depth. Table 3 shows the enhancement in DF by increasing the pool depth to 4m. Finally, Table 3 shows a measure of the DF reduction expected when the bubbles are taken to rise as a plume rather than as individual bubbles.

The above variations are summarized in Figure 1 which illustrates the relative effects of the new BUSCA processes.

7. CONCLUSIONS

A number of mechanisms have been successfully introduced into the BUSCA pool scrubbing code. These include modelling of bulk condensation, bubble breakup and cluster and plume rise conditions. This paper has illustrated the effects of these changes on DF calculation.

In general, decontamination factors are seen to increase with,

i) Increasing initial mole fraction of steam in bubble,
ii) Reduction of the initial bubble size,
iii) Reduction of the pool temperature,
iv) Increasing the initial temperature difference between the pool and the bubble,
v) Increasing the pool depth,
vi) Increasing the solubility of the aerosol particles.

while a reduction in decontamination factors can be brought about by assuming the bubbles rise as a plume rather than as individual bubbles.

ACKNOWLEDGEMENTS

The authors are grateful to members of the European Pool Scrubbing Group for their contribution to the development and testing of the BUSCA code. This work was jointly funded by the U.K. Department of Energy as part of the General Nuclear Safety Research Programme and the Commission of the European Communities.

REFERENCES

[1] Clough, P.N., Ramsdale, S.A., Smith, P.N., "Aerosol Decontamination Factors in Pools Overlying Molten Core-Concrete - Code Modelling.", CSNI Specialist Meeting on Core Debri - Concrete Interactions, Palo Alto, Sept. 1986.

[2] Calvo, M., "Breakup Bubble Model. Implementation in BUSCA JUN-90", Catedra de Tecnologia Nuclear, CTN-17/91, Universidad Politecnica de Madrid, 1991.

[3] Paul, D.D., Flanigan, L.J., Cunnane, J.C., Cudnik, R.A., Collier, R.P. and Oehlberg, R.N., "Radionuclide scrubbing in water pools -Gas-Liquid Hydrodynamics", A.N.S. Meeting on Fission Product and Source Term Research, Snowbird, Jun. 1985.

[4] Levich, V.G., "Physicochemical Hydrodynamics", Prentice-Hall 1962.

[5] Wheatley C.J., Dunbar, I.H. and Ketchell, N., "ITHACA - a model of aerosol behaviour in wet atmosphere: the physics reference manual", AEA Technology, AEA TRS 5086, 1991.

[6] "UK steam tables in SI units 1970", published by Edward Arnold (London, 1970). ISBN 0 7131 3239 6.

[7] Moody, F.J., "Dynamics and Thermal Behaviour of Hot Gas Bubbles Discharged into Water", Nucl. Eng. and Design 95(1986)47-54.

[8] Sjoen, K., "Modelling of Bubble Plumes from Sub-sea Blowouts", STF15A23829, The foundation for Scientific and Industrial Research at the Norwegian Institute of Technology 1982.

[9] "IMSL Math/Library V1.1, Problem Solving Software Systems, Houston, Texas 77042-3020, Dec. 1989.

[10] Paul, D.D., Flanigan, L.J., Cudnik, R.A., Cunnane, J.C. and Collier, R.P., "Radionuclide scrubbing in water pools - Vol. 1: Gas-Liquid Hydrodynamics", EPRI NP-4154, 1985.

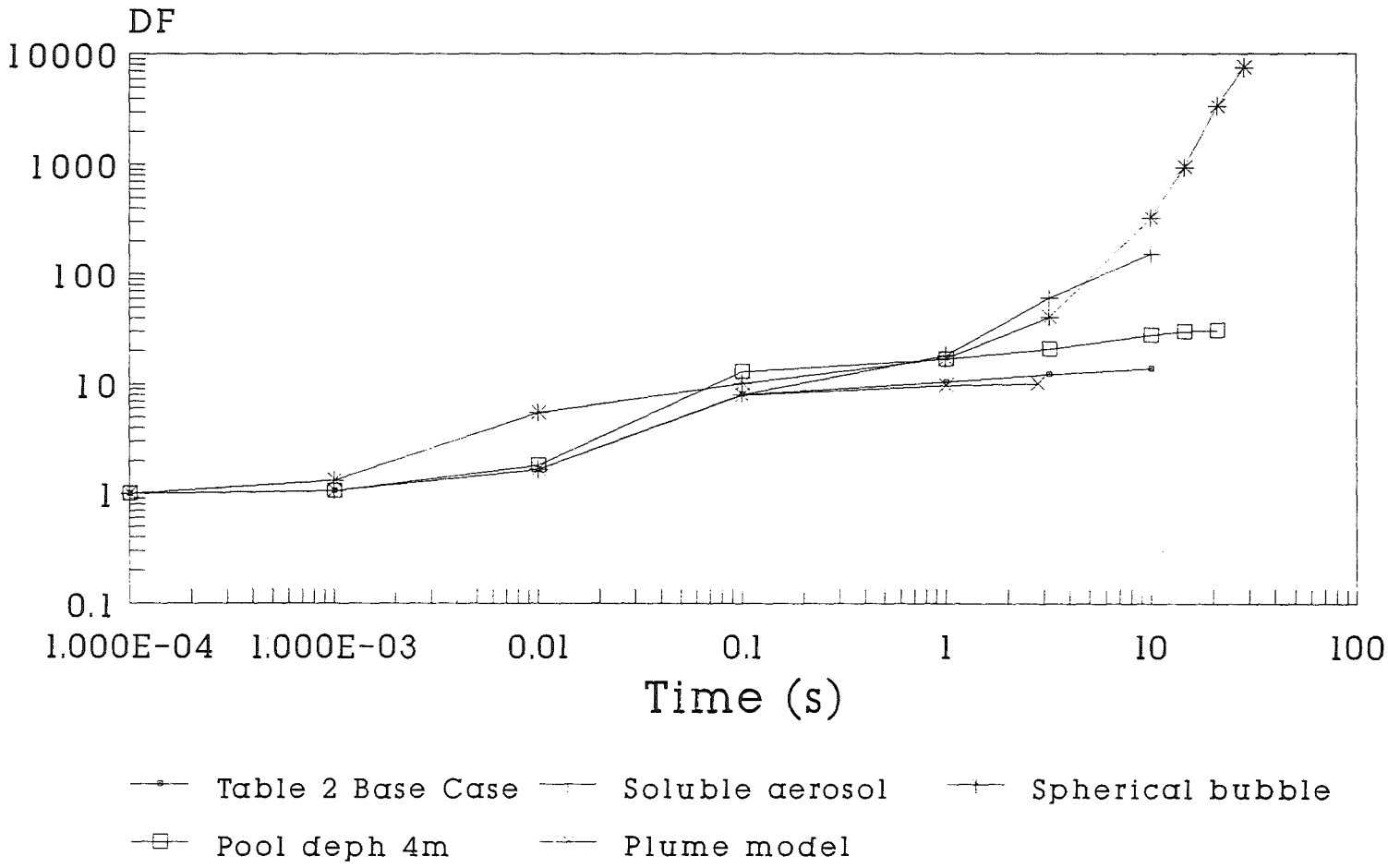

Figure 1. DF values for Table 3 runs.

SECTION III

MELT SPREADING AND COOLABILITY - Part A: EXPERIMENTS

Integral Tests

FAILURE MODE OF A CONCRETE CYLINDER DUE TO ATTACK BY AN ERODING MELT WHILE COOLED BY OUTSIDE WATER

H. Alsmeyer, C. Adelhelm, H.-G. Dillmann, M. Heinle, W. Ratajzcak, G. Schumacher, W. Schöck, S. Stiefel, A. Skokan, W. Tromm

Kernforschungszentrum Karlsruhe
W-7500 Karlsruhe 1, Germany

SUMMARY

In the BETA facility an experiment was conducted on the failure of a cylindrical concrete wall which is eroded on the inner side by a heated melt while being cooled outside by stagnant water. No decrease of the radial erosion velocity is observed when the melt front approaches the outer concrete surface and wall failure occurs after the residual wall thickness is reduced to less than one centimeter. The melt relocates into the water annulus and fast evaporation of the water and pressure increase occur. Applicability of the experimental results for LWR severe accidents is discussed.

INTRODUCTION

During the late phase of coremelt accidents the situation may arise that during the melt attack of the basemat, a vertical concrete wall is eroded from the inner side while the outer side of the wall is in contact with stagnant water. Such a condition may occur in a German standard PWR where the melt is eroding the inner biological shield which on the outside is cooled by the stagnant sumpwater on the containment floor. Therefore, the concrete erosion is a "dry" interaction from the beginning as long as the 85 cm thick concrete shield separates melt and water. Calculations as reported in the German Risk Study Phase 2 [1] predict that the erosion of the cylinder wall after some 8 hours has proceeded so far that failure of the wall might occur. The question arising from this situation is, whether the wall due to cooling by the outside water could form a self stabilizing crucible able to separate effectively melt and water or if, by failure of the wall, a contact of melt and water would occur.

The consequences for the further accident progression would be a continuation of the dry MCCI with a remarkable hydrogen concentration in the gases released from the eroding melt if no water contact should occur. Otherwise, an increase in

steam production would accelerate the pressure build-up in the containment. The late contact of melt and water would, however, not lead to a coolable melt and subsequent stop of concrete erosion as, based on experiments with simulant materials [2], fragmentation of the highly viscous and relatively cold oxidic melt can not be expected. For the planning of accident management, the possibility of water contact is important for the time of containment venting and the amount of gases to be released, and for the hydrogen problem as well.

SETUP IN THE BETA FACILITY

The BETA facility allows simulation of prototypic corium melts in concrete structures which are large enough to allow extrapolation to real reactor geometry with the aid of qualified computer codes. To address the problem of the failure mode of the concrete cylinder, a double crucible of siliceous concrete was used in the BETA facility (figure 1). Inner and outer crucible form an annulus which is filled with water to a level corresponding to 350 mm above the initial bottom of the inner crucible. The inner crucible with a wall thickness of 100 mm towards the water annulus, has 380 mm inner diameter and is filled with the metallic and oxidic melt, eroding the concrete. The outer crucible has a wall thickness of 150 mm, outer diameter 1080 mm.

The crucible was constructed in such a way that no mechanical force is acting on the inner crucible, because the weight of the upper crucible is supported by the outer crucible. This simulates a suspended "stress-free" biological shield in contrast to a wall which is loaded by its own weight or additional static forces. Consequently, the realized "stress-free" situation gives the optimum condition for stabilization of the crucible. Any other situation would lead to earlier failure of the cylinder.

The objective of the experiment is the simulation of the wall attack in a real accident after some 8 hours of melt-concrete interaction in the period where failure of the biological shield might occur. Therefore, the 10 cm wall thickness of the inner crucible simulates that portion of the shield which has not yet been eroded and is in contact with the stagnant sumpwater. Consequently, the melt composition and the simulated heat transfer condition imposed by the internal heat generated in the melt must correspond as far as possible, to the accident condition.

The simulated melt in BETA consists of 300 kg of steel, initially 93.3 % Fe, 5 % Ni, and 1.7 % Cr, and 50 kg oxide with 70 % Al_2O_3, 15 % SiO_2, and 15 % CaO. The melt is generated externally by a thermite reaction and poured into the crucible where it is mixed up with 25 kg of ZrO_2 deposited on the bottom of the inner crucible. The small amount of chromium in the metal will oxidize in the first minutes of the interaction and will be transferred to the oxidic melt. For the investigation of fission product release it was considered important, to have a representative concentration of Cr- and Zr-oxides in the oxidic melt, as these oxides may influence the fission product release by the formation of chemical compounds with some of the fission products. However, no metallic Zr is added to the melt as any metallic Zr would be completely oxidized at this stage of the simulated accident.

In the BETA facility decay heat simulation is by sustained electrical induction heating. As this method heats the metallic melt only, it is somewhat different from the accident situation where the major part of decay heat is released in the oxidic phase. Indeed, the radial attack of the biological shield in the real accident would be dominated by the oxidic melt progression. Therefore, to allow a representative experimental simulation, the internal heat generation in the BETA test is adjusted to give the same radial heat flux from the melt to the cylinder as in reality 8 hours into the accident situation. With this condition fulfilled, the metallic melt can be used for simulation. The necessary heating rate of 120 kW was determined by WECHSL calculations comparing BETA and accident conditions.

Figure 1 also shows the instrumentation of the inner crucible with 101 thermocouples, which allow the detection of the erosion front in the concrete. This is especially important in the cylinder wall to detect the possible influence of the outside water cooling on melt front progression.

The water in the annulus is introduced through a tube from the lower side of the crucible and is continuously connected to a pressure transducer to register pressure variations when boiling or melt contact would occur. The vapour, which would be produced can escape through 3 parallel plastic tubes, 25 mm inner diameter. The water temperature in the annulus is measured by three thermocouples in different heights.

In the early phase, without the influence of water, the experiment is a good simulation of a low temperature melt-concrete interaction. Therefore, it was additionally used to study "late" fission product release by adding to the melt a mock-up of

fission product simulants consisting of Mo, CeO_2, BaO, La_2O_3, and SrO. Samples of the aerosols are collected on filters.

On-line and off-line gas analysis systems are used to identify the rate and composition of gases released from the inner crucible. All gases are fed through the 300 mm inner diameter off-gas line to the environment via a large metal fiber filter.

CONDUCT OF THE EXPERIMENT

Precalculations with the WECHSL code have been conducted assuming the planned heating rate of 120 kW in the melt. The calculated cavity shapes are given in Figure 2 for time steps of 240 s. The calculation does not take into account the - unknown - influence of the water jacket, but assumes an adiabatic outer cylinder wall. The calculations predict that radial penetration of the cylinder might occur slightly below the bottom level of the initial inner cavity after some 60 minutes of erosion, caused by the metal phase. However, the simplified assumptions of the calculations do not allow a judgement if radial melt-through would really occur.

The experimental conditions could be maintained throughout the test as planned. The induction heating rate was nearly constant (figure 3), but slightly increased as the radial melt propagation improves the coupling to the induction coil. The time averaged power of 131.5 kW is 9.5 % higher than the planned 120 kW until power-off at 2352 s. The initial peak characterizes the early vigorous melt interaction during cool-down in the first 150 s before achieving the steady low temperature of the melt which corresponds to the freezing temperature of steel. Hence, the long term erosion is characterized by the steel melt close to its freezing temperature, probably forming a thin instable crust towards the bottom concrete interface. The upper oxidic melt has a temperature several 100 K lower and forms a stable and relatively cold surface crust which can not be penetrated by the dip-in thermocouple lances.

Axial and radial erosion of the concrete are slowly proceeding after slow-down of the early faster erosion during the first 150 s (figure 4). Then, axial and radial erosion velocity are very similar with 0.027 mm/s erosion rates in the average. For the behavior of the cylinder, the radial erosion is important. The thermocouples

detecting the radial erosion front have a distance of 20 mm. Within the scattering of the TC signals no influence of the outer coolant water can be observed, and it is evident that the coolant does effectively not slow down the erosion velocity even when the remaining concrete wall thickness is 10 mm only. At 2352 s (39 min) the melt penetrates into the water, as stabilization of the concrete wall by the coolant water did not occur. It is evident from figure 4, that the local wall thickness at time of cylinder failure did not exceed 8 mm. The first failure by melting evidently did occur in the neighbourhood of the thermocouple in the left part of the crucible whereas due to some asymmetry of the erosion the remaining wall thickness on the opposite side may still have some 2 cm.

During crucible erosion, the water temperature in the annulus increased with a constant rate of 0.043 K/s from 15 °C at 300 s to 90 °C at 2050 s, and then subcooled boiling of the water did occur. The constant rate of temperature rise and of steam production throughout the experiment until failure of the cylinder wall shows that the radial heat flux is only little affected when the metal melt approaches the cylinder surface, and confirms the observation of constant radial erosion rates. The heat transferred into the water is 28 kW, corresponding to 21 % of the induction heating rate.

Failure of the cylinder wall causes direct contact of the steel melt and water, leading to a characteristic pressure history. Figure 5 gives the pressure in the gas room of the inner crucible (HP-solid line) and in the water annulus (WH-broken line) at the time of cylinder failure. The latter pressure is referred to the initial bottom of the inner cavity as zero level. This pressure starts to increase at 2348 s by faster evaporation. 4 seconds later, relocation of the metallic melt starts as can be seen from the increase of electrical coupling of the induction heating system in figure 3, with the consequence of a stronger increase of the pressure in the annulus. The 3 steam tubes in the annulus are insufficient to release the steam pressure to the atmosphere and the fast pressure increase continues. At 2355 s, there is a strong interaction of melt and water accompanied by a flash to be seen in the crucible. Simultaneously, a gross circumferential failure of the inner cylinder occurs as can be seen from the sectioned crucible in figure 6. It is believed that the circumferential failure of the concrete cylinder is promoted by the higher pressure in the annulus.

The massive contact of melt and water leads to an extremely fast pressure increase to more than 1 bar overpressure for 3 seconds, exceeding the detection lim-

its of the pressure transducers. The 150 kg of water in the annulus are evaporated and ejected through the off-gas line within some 15 s only, leading to a massive steam release to the environment. 200 kg of the 300 kg metal melt relocated into the annulus where it solidified in the form of a compact ring with very little void. No damage occurred to the outer crucible, while the plastic tubes in the annulus were destroyed and some melt was ejected downwards through the tubes. Additionally, an upper sealing of the crucible failed and some minor part of the melt was blown into the experimental hall during the blow-down period.

With the high steam flux from the inner crucible a substantial transport of mostly oxidic melt material and some metallic particles took place downstream through the off-gas system. This caused a damage of the fiber filter where an oxidic "particle" of 1 kg was found. 8.3 kg of finely fragmented metallic particles were collected from the upper part of the facility and the hall. This metallic material evidently has undergone a strong interaction of melt and water while all oxidic particles have greater dimensions typically on the order of some centimeters or more. It may therefore be concluded that the fast pressure built-up is mainly due to the metallic melt fraction while the oxidic particles because of their high viscosity and consequently greater dimensions contribute very little to the fast evaporation.

Sieve analysis of the metallic particles from different locations in the facility are given in figure 7. Comparison with typical size distributions of steam explosion experiments shows that this material underwent a low effectivity steam explosion. From the upward displacement of some of the particles it is concluded that the peak gas pressure exceeded 4.3 bar.

An additional information gained from the experiment is the aerosol release from the melt before water contact, representing a typical situation of a melt some hours after start of melt/concrete interaction. The aerosol mass collected on sample filters is very low, typically 2 orders of magnitude smaller than in BETA experiments simulating the early melt interaction process. The small amount of material on the filters, from 0.4 to 0.1 mg or smaller does not allow a quantitative chemical analysis. Qualitative analysis gives some concrete elements (Si, K, Na) and of Fe from the melt. Remarkably, no elements have been detected in the aerosol which had been added to the melt as fission product simulants. Electron microscopy shows fine spherical particles of 0.3 µm diameter typical and some agglomerates up to 1 µm.

CONCLUSIONS FROM THE EXPERIMENT

The experiment clearly shows that for the conditions realized in the test the water cooling is insufficient to stabilize the melt in the inner crucible. The concrete erosion is not slowing down when the melt front approaches the water annulus because of the poor thermal conductivity of the decomposing concrete. Finally, a stable concrete layer or melt crust is not formed, and melt water contact and relocation of the materials does occur.

For the stability of the concrete cylinder the radial heat flux from the melt to the concrete wall is important. If the same heat flux is realized, the type of melt, oxidic or metallic, is of no more importance. Calculations with the WECHSL code for the experiment and the accident are given in Table. 1. The comparison shows that the heat flux in the experiment and the freezing temperature of the melt meet reasonably well the conditions of the oxidic melt in the accident under consideration. Similarly, the measured erosion velocity in this test with 0.027 mm/s = 9.7 cm/h meets the desired conditions. Therefore, the result of wall failure is transferable to the accident condition, although in the accident under consideration, because of geometrical reasons, only the oxidic melt would penetrate the cylinder.

Quantitity	BETA V 6.1 metal/concrete	Core Melt Accident after 8 hours oxide/concrete	metal/concrete
radial heat flux, kW/m^2	112	96	45
radial erosion veloc.*), cm/h	8.6	7.05	3.33
liquidus temperature of melt, K	1788	1849	1768
solidus temperature of melt, K	1778	1512	1758

*) influence of outside water not taken into account

Table 1: Comparison of Characteristic Quantities for the Erosion as Calculated with the WECHSL Code

The failure of the concrete can be understood from heat conduction estimates. To conduct the radial heat flux to the water without melting, the residual concrete layer must have a thickness s not exceeding

$$s = k\,\Delta T/\dot{q} \tag{1}$$

with k the thermal conductivity of the concrete, ΔT the temperature difference over the concrete layer (some 1300 K) and $\dot{q}$ the heat flux imposed by the melt. With the poor heat conductivity of standard concrete about 1 W/mK, eq. (1) yields a layer thickness on the order of 1 cm. However, the heat conductivity of the concrete layer is still smaller than assumed above, because the high temperature of some 1600 K at the inner side of the wall causes dehydration of the concrete and increasing porosity with negative effects on conductivity. Consequently, the thermodynamically stable wall thickness may be still lower than 1 cm, a thickness which is mechanically unstable especially under the influence of the extreme temperature gradient. Of course, any mechanical prestress would enhance the failure.

The small influence of heat extraction by the outside water before wall failure is the reason for the relatively good agreement in cavity shape and failure time comparing experiment and WECHSL pretest calculations. Calculated melt-through is at 60 minutes while the observed failure is at 40 minutes. The final cavity shapes just before failure agree resonably well.

Special consideration must be given to the melt relocation process. In the test, the low viscosity metallic melt very quickly relocated into the water annulus with the described consequences on fast steam generation and pressure spike. If the melt is oxidic with high silicate content and low temperature as in the considered accident, melt relocation and water contact are less vigorous because of the high viscosity and the smaller melt conductivity, and would be similar to volcanic lava flowing into the sea. Under this condition, a steam explosion is not expected, and the extraction of the thermal energy is delayed.

On the other side, the oxidic melt properties prevent the achievement of major coolability of the melt by direct water contact, as melt fragmentation by water contact is a minor effect. Consequently, for the accident studied in the German Risk Study, the downward erosion of the basemat is effected only little and will continue as from geometrical conditions only a minor part of the total melt is able to relocate into the outer basement area. However, due to the water contact the upward heat flux from the melt which was by radiation before, is now transferred to steam. This scenario has been studied as the reference case in the risk study. The encreased steam release into the containment leads to a faster pressure built up which would reach the failure pressure of the containment after some 5 days if no venting were taken into consideration. Simultaneously, the hydrogen concen-

tration in the containment atmosphere is decreasing, so that the hydrogen problem becomes less important.

LITERATURE

[1] Deutsche Risikostudie Kernkraftwerke, Phase, B., Verlag TÜV Rheinland, 1990.

[2] "Modellentwicklung zur analytischen Beschreibung von Kernschmelzunfällen", H. Alsmeyer, K. Dres, M. Reimann, S. Stiefel, in: Sicherheitsorientierte LWR-Forschung, Jahresbericht 1987, KfK 4450, p. 113-128.

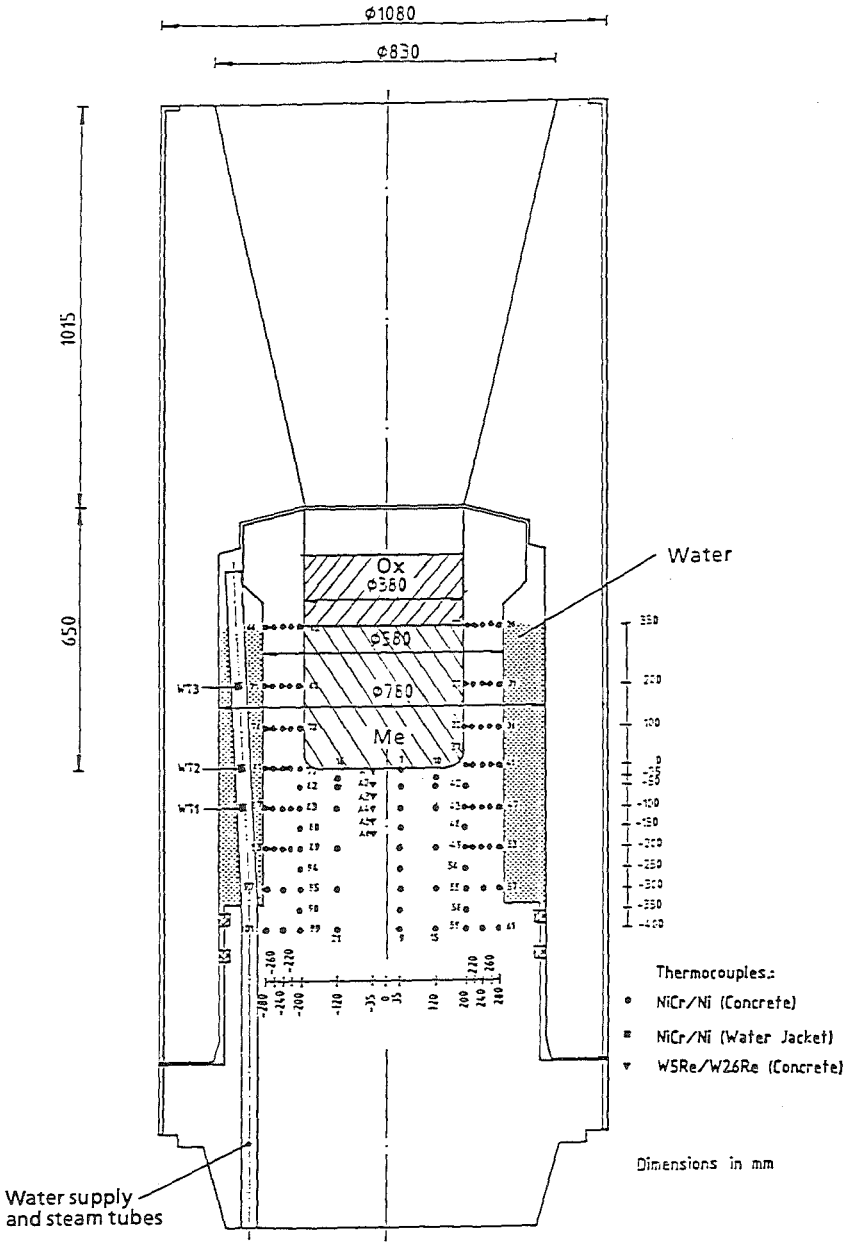

Fig. 1 CRUCIBLE OF BETA-TEST V6.1

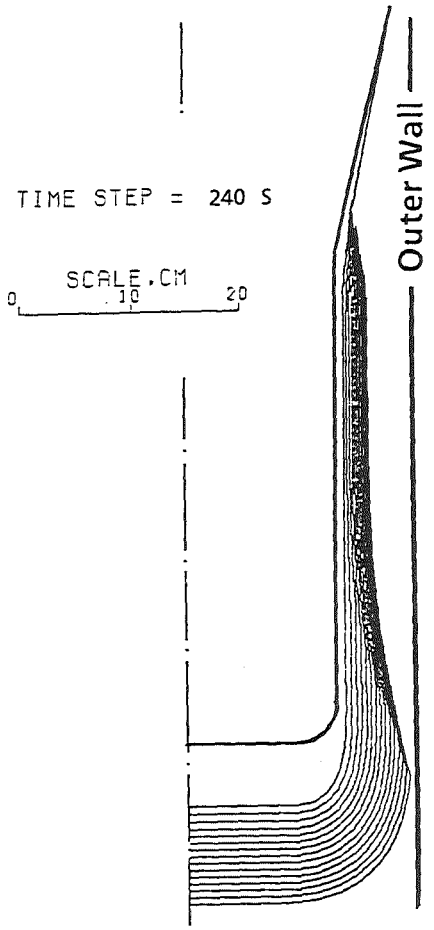

Fig. 2 BETA V 6.1: WECHSL Pretest Calculation

Calculated Crucible Erosion

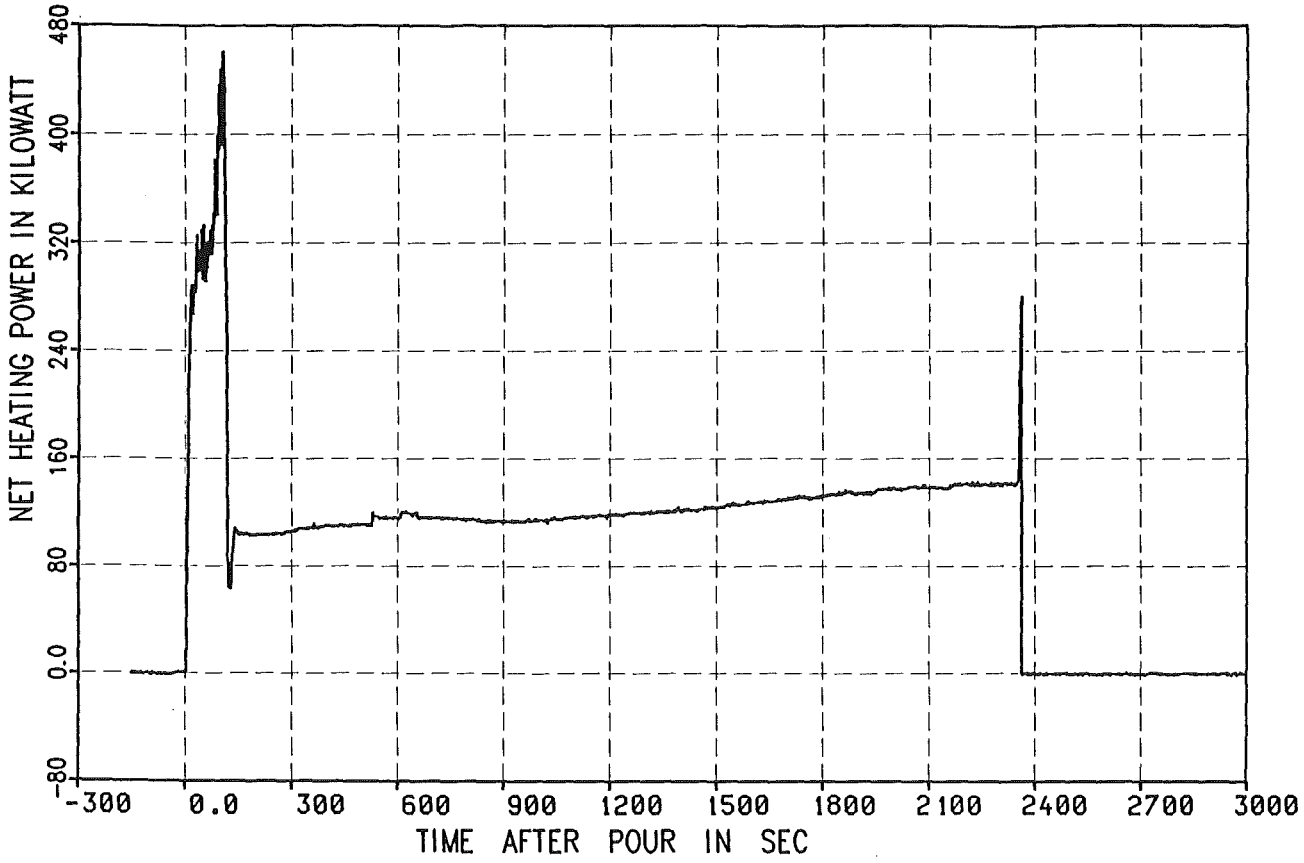

Fig. 3 Net Heating Power in BETA V 6.1

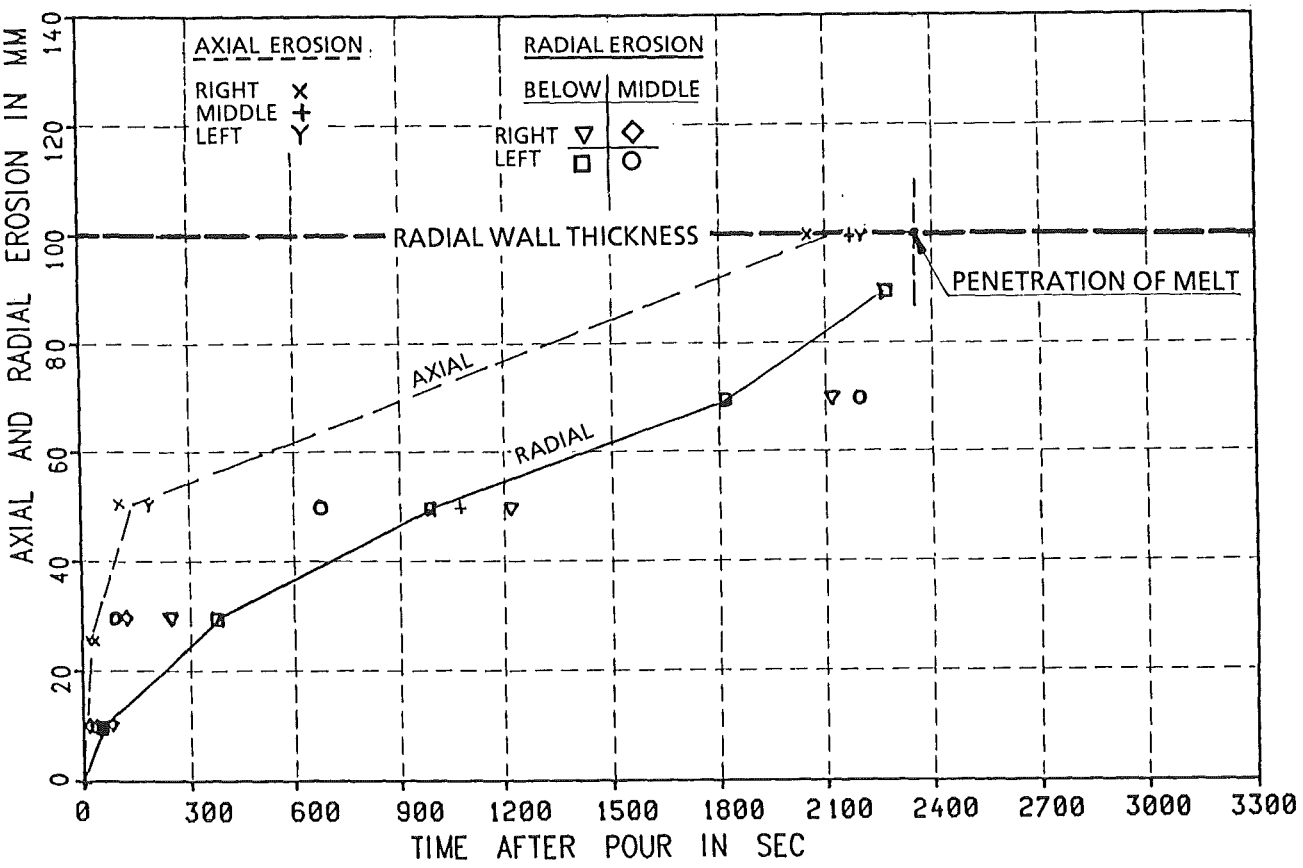

Fig. 4 Concrete Erosion of BETA Crucible V 6.1

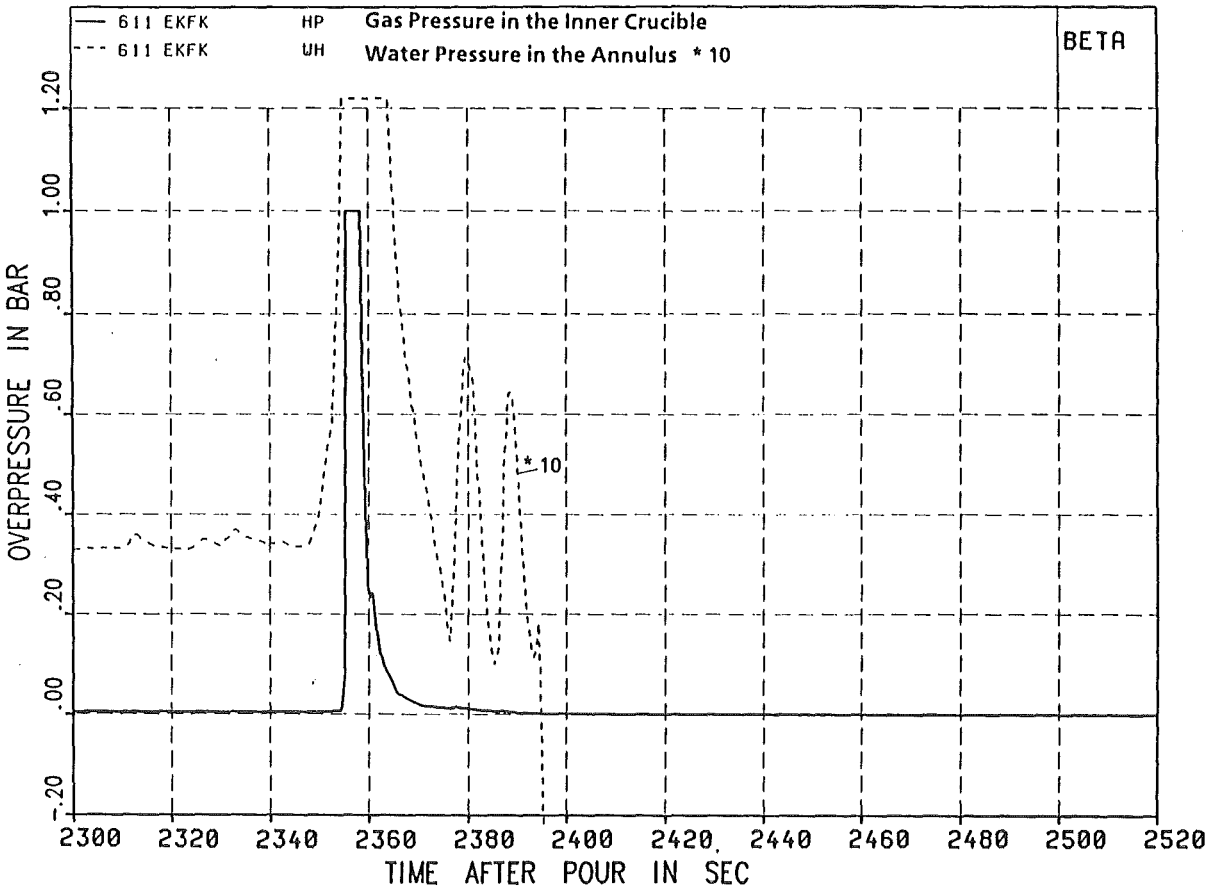

Fig. 5 Pressure History of BETA V6.1 at Time of Crucible Penetration

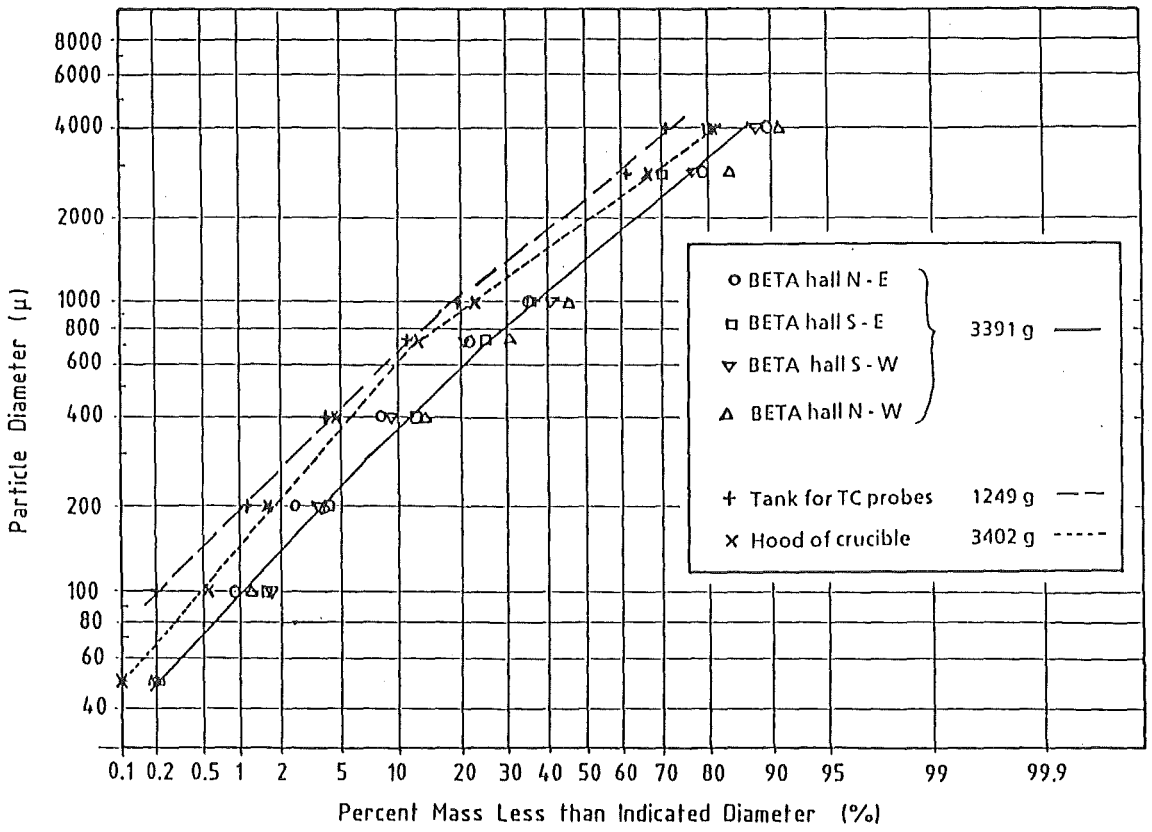

Fig. 7 Particle size distribution of metal fragments in BETA V6.1

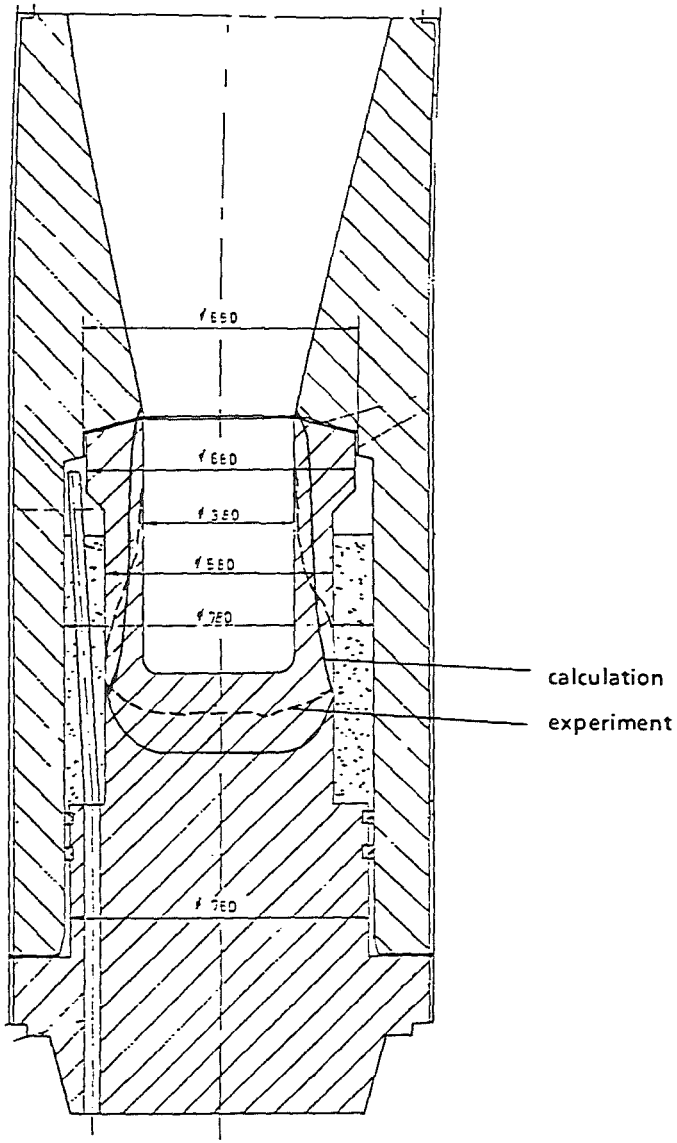

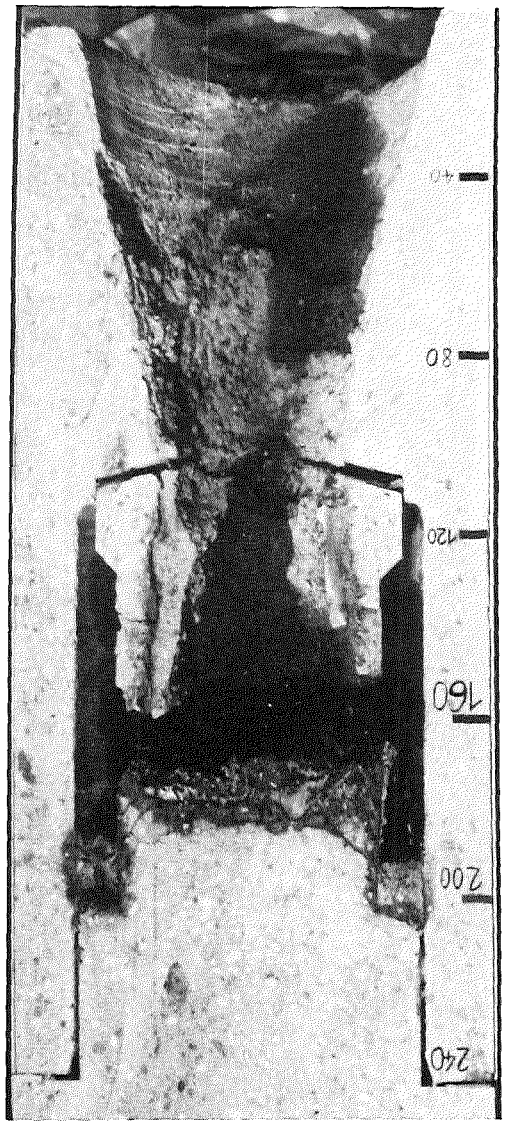

Fig. 6 CRUCIBLE OF BETA-TEST V6.1

Spreading of Melt in Reactor Containments (SMELTR)

by

B.R. Sehgal
Electric Power Research Institute
3412 Hillview Avenue
Palo Alto, California 94303 USA

and

B.W. Spencer
Argonne National Laboratory
9700 South Cass Avenue
Argonne, Illinois 60439 USA

Abstract

A cooperative program of experiments on the spreading behavior of core melts in reactor containments (SMELTR) is proposed. In this program, experiments will be performed with prototypic corium melts in a facility incorporating a melt generator and a receiving vessel (representing a containment). Experiments will be performed with and without the presence of water in the receiving vessel.

The main objectives of the SMELTR program are to: 1) obtain data on melt-spreading and heat removal for validation of the MELTSPREAD code; 2) perform confirmatory tests in properly-scaled representations of current and advanced light water reactor (ALWR) containments to obtain data for direct application. This paper will describe the essential elements of the SMELTR program.

1. Introduction and Background

If a severe accident scenario is postulated to proceed to vessel failure in a LWR, the molten material accumulated in either the core region or the lower head region is discharged into the containment. For many PWR scenarios, most current generation BWR scenario and for practically all advanced light water

reactors (ALWR) scenarios, the vessel pressure at failure is not much higher than the containment pressure. In these accident scenarios, the melt is discharged in the form of a low velocity pour stream, which impacts the containment concrete basemat and spreads laterally by gravity head.

In general, it is beneficial to spread the melt as far as possible to reduce the thickness of the melt layer. Spreading is a concern, however, if a critical safety system lies in the melt pathway and is liable to fail due to the thermal loading imposed by the melt. An important example is the BWR Mark I containment shell, which could fail[1] if the melt advance is not mitigated by water addition[2] to the BWR drywell.

Lack of spreading can result in a relatively deep melt layer which if uncoolable will keep interacting with concrete, resulting in either containment failure through steady pressurization or the penetration of the basemat. Thus, the spreading behavior is directly related to the melt coolability issue currently under intense investigation through tests and model development in the MACE program[3]. Although it is not yet clearly established, preliminary modeling and measurements point to greater difficulty of cooling or quenching melt layers of greater depth than of smaller depth.

The ALWR containment philosophy has focused on assurance of melt coolability and eventual stabilization. This has resulted in the utility requirement[4] of providing 0.02 m^2/MWt as the containment basemat floor area for both the AP-600 and the SBWR designs. This requirement was derived on the assumption of uniform spreading of the melt discharged from the breached vessel and a heat flux from melt to water of 300-500 KW/m^2. The AP-600 procedures assume a deep pool of water in the containment cavity when the melt is discharged, while the SBWR procedures, currently require water addition in the containment only after the melt has been discharged into a dry containment.

Another perspective on the melt-spreading and eventual coolability and stabilization is the efficacy of heat removal from the melt. It has been found that extremely high heat removal rates from melt to water may be achieved[5] during the melt-spreading phase. Melt and water movement and concrete gas sparging may all result in much greater heat transfer rates from melt to water than those

obtained when water comes in contact with a stationary melt. It is also conceivable that the crusts formed during the melt-spreading phase will be less stable than those observed in the stationary melt situation. Except for the data reported in Reference 5, there are no other measurements on the heat transfer rates from the melt to the containment environment (in the presence or absence of water) during the spreading phase.

There are several initial conditions which affect the melt-spreading process, whose specification is quite uncertain. These are primarily the melt discharge conditions such as: 1) the mass of the molten corium; 2) the pour rate, which may depend on the vessel failure location and the hole size variation with the melt discharged; 3) the melt temperature (superheat); and 4) melt composition; viz: fraction of metallic vs. oxidic material. In addition to the initial conditions, the presence of water in the containment prior to the melt discharge and its depth affect the melt-spreading process.

The corium-spreading process involves complex and inter-related physical phenomena, such as:

1. gravity-driven flow of a multi-phase mixture of liquids, solids and gases.

2. interaction with the concrete substrate leading to sparging gas flows in the melt which tend to mix the constituents and promote additional heat transfer from melt to concrete and to an overlying water layer.

3. chemical oxidation reactions in the metallic constituents of the melt resulting in substantial energy release and possibly promoting spreading.

4. concrete melting and ablation, resulting in introduction of slag constituents in the melt and alteration of the melt physical properties, e.g., solidus, liquidus temperatures, viscosity, conductivity surface tension, etc., which in turn modify the upwards and downwards heat transfer from the melt.

5. melt-water heat transfer as well as melt leading edge freezing and immobilization with subsequent melt-spreading over frozen material.

6. melt crust formation and crust stability.

All of the above physical phenomena have been modeled and incorporated in the MELTSPREAD code developed at ANL under EPRI sponsorship. The code can treat most spreading scenarios and the interaction of the melt with the below-vessel structures (e.g., under a BWR vessel, for example). It does not treat the interaction of a gravity-driven melt jet with a deep pool of water. The MELTSPREAD code has been employed for assessing the melt-spreading behavior for the Mark I containment and is described in a companion paper at this meeting[6].

2. Previous Work

A limited number of experimental research studies related to melt-spreading have been reported in the literature. Greene[7] conducted experiments in which molten lead jets were impinged upon plywood, marble and steel surfaces with and without the presence of an initial water layer on the surface. Based on his experiments, Greene classified melt-spreading in terms of 5 different regimes, according to the depth of water layer relative to the depth of the spread melt layer. A correlation was developed for the mean spread-melt thickness in terms of the melt volume, depth of water and the sensible and latent heats of the corium and water. The data was correlated in terms of a dimensionless spreading number and the spreading regimes and the melt thickness were correlated to the spreading number. For dry surface spreading, the melt thickness was such that the surface tension at the leading edge matched the gravity head corresponding to the melt thickness.

Greene did not employ a concrete base in his experiments, therefore the gas sparging effects on spreading and heat removal were not represented. The melt did not contain any constituents which could provide oxidation heat.

Malinovic et al[5] performed a set of experiments with molten iron-alumina thermite spreading in a 1 m long channel representing the Mark I geometry. The channel was lined with limestone-sand or siliceous concrete and except for one test contained water to a certain depth. The thermitic material had very high superheat and in every test the material spread to the end of the channel. Heat transfer from the melt to the water was measured through the increase in water temperature and the steam generation rate.

Theofanous[2] conducted water-spreading experiments in a 1/10th linear scale model of the Mark I containment in which he conserved the Froude number ($Fr = u/\sqrt{gh}$ with u the spreading velocity and h the depth of the melt layer) between the prototypic and the experiment systems. It was found that the hydraulic conditions for spreading can be made similar in the two systems by relating the volume pour rates by the scale factor raised to the power of 5/2. The water-spreading experiments did not simulate the effects of: 1) the gas sparging; 2) the melt-freezing; and 3) the heat transfer from melt to concrete and water, on the melt-spreading behavior.

In addition to the experimental studies, a limited number of analytical studies on corium spreading in Mark I containment have been performed and useful scaling laws derived. These include those of Corradini[8], Kazimi[9], Moody[10] and Farmer[11].

3. Scaling Relationships

Theofanous[2] derived a scaling relationship for purely hydrodynamic spreading of a melt in a containment. This relationship, however, is not adequate for spreading of a melt delivering heat to its environment, changing composition (through incorporation of concrete) and changing phase. Moody[10] and Farmer[11] have both considered heat transfer and melt-freezing aspects. Farmer has included, in his analysis, the effects of melt superheat, heat of fusion and heat transfer to underlying concrete, which were neglected in Moody's analysis. Farmer has derived the following non-dimensional group for the spreading distance in a sector flow:

$$r_*^2 = \frac{\Delta T_{vs}\,(h_{top} + h_{bot})\,\Theta\pi r^2}{\rho \dot{Q}\,\Delta h_f} \qquad (1)$$

where

r_*^2 = dimensionless spreading radius

ΔT_{vs} = $T_{vs} - T_{sol}$

T_{vs} = melt discharge temperature from the vessel

T_{sol} = melt solidus temperature, which changes as the melt composition changes.

Θ = dimensionless flow angle = $\phi^{o}/360$

h_{top} = heat transfer coefficient between melt and overlying medium

h_{bot} = heat transfer coefficient between melt and bottom substrate

r = radius of the melt-spread from the point of discharge

$\dot{Q}$ = melt volumetric pour rate

Δh_f = $h_{l\,s,m} + C_p \Delta T_{sup,\,m}$

$h_{l,s,m}$ = enthalpy difference between the liquidus and solidus temperature of melt, as a function of melt composition

$\Delta T_{sup,m}$ = melt superheat above the melt liquidus temperature

C_P = melt heat capacity

ρ = melt density

The dimensionless group in Eq. (1) is supplemented by others to account for metal oxidation, the relative importance of exothermic energy versus the off-setting downwards heat transfer, etc. These come into play when melt simulants are used in experiments.

4. The MELTSPREAD Code

The development of a computational ability to address corium-spreading and freezing processes was initiated by Sienicki et al[12] in the form of the MELTSPREAD code. The original version (MELTSPREAD-0) treated gravity-

driven spreading flow in Mark I configuration including the effects of melt to concrete heat transfer, melt to water film boiling heat transfer and concrete ablation and entrainment in melt. The code was used to analyze the melt-spreading tests of Malinovic and Henry[5].

The MELTSPREAD-0 code was extensively modified by Farmer et al.[13] to account for chemical oxidation of metallic melt constituents, transient concrete heatup, decomposition and gas release, corium freezing and immobilization, corium flow over previously-solidified material, etc. This new version, named MELTSPREAD-1, described in a companion paper at this meeting[6], has been used for scoping calculations[13] of melt-spreading in Mark I containments with water initially present in the drywell. These calculations have indicated the importance of considering: 1) the heat transfer processes occurring; 2) the material property (solidus, liquidus temperature, viscosity, surface tension) changes as concrete products are entrained in the melt; and 3) the freezing melt-accumulation; in the models for melt-spreading. Another effect which has been modeled in the MELTSPREAD code is the break up of the melt jet by the control rod guide structures underneath the BWR vessel.

5. Research Objectives

The principal research objective is to obtain information about and model the spreading behavior of prototypic reactor melts in LWR containment geometries. From the discussions presented in previous sections, it is perhaps clear that the inherent phenomenological complexity cannot be unravelled through analysis alone. Evaluation of the spreading scenarios can be performed through the MELTSPREAD code, however, reliability of predictions can only be assured after important models are validated.

Code model validation or information about the spreading behavior in reactor accident scenarios can be obtained through separate and integral-effect experiments. The serious issue is that of scaling of the experiments. If it can be shown that parity can be achieved for the values of the appropriate scaling group between the prototypic and the experimental scale, then the data and the spreading behavior observed can be directly applied to the reactor accident scenarios. The other alternative is to validate a code against observations from several experiments and then apply the code to make predictions for prototypic situation. In this case, it is imperative that the experiments, whose data is being used for code validation be realistic and within the range of validity of the physical models that are employed in the code.

The research objectives appropriate for resolving the technical issues pertinent to spreading behavior of melts in reactor containment have been chosen as:

1. Validate the MELTSPREAD code with reactor-material spreading data.

2. Obtain confirmatory data in properly-scaled containment mockups for possible direct application in resolving the melt-spreading technical issues.

3. Obtain confirmatory data in properly-scaled experiments on the extent of corium-spreading and the depth of the spread-corium in the ALWR containment geometries.

6. SMELTR Research Program

The SMELTR research program will consist of an experimental program together with an integrated analysis and code validation effort. The major elements are: 1) develop SMELTR test facility; 2) perform MELTSPREAD validation tests; 3) perform MELTSPREAD analysis; and 4) perform confirmatory scale model tests. These are described briefly in the following paragraphs.

A. SMELTR Test Facility

Most of the elements of the current MACE facility will be adopted for the SMELTR experimental program. The facility will be located in the same reactor containment building at Argonne National Laboratory (ANL) where the MACE facility is located so that molten corium (slightly radioactive) and water can be used in the test program. A schematic illustration of the apparatus configured for the validation tests (employing a long channel) is shown in Figure 1. The system is designed for 4 atmospheres operating pressure. The melt generator shown in Figure 2 is very similar to the MACE furnace (MgO walls), except for a release plug at bottom through which corium melt is discharged into the receiving vessel. The furnace will melt up to 300 kg mixture of UO_2, ZrO_2 by direct electric heating and Zirconium metal will be incorporated in the melt through concrete/metal inserts located at the bottom of the charge. The melt volumetric pour rate will be controlled by sizing the hole appropriately for gravity drainage given the initial melt depth. A large number of thermocouples will be located at strategic locations both in the furnace and the receiving vessel.

A. MELTSPREAD Code Validation Tests

It is proposed that the MELTSPREAD code validation tests should employ prototyic materials but simpler containment geometries. An example of the receiving vessel is shown in Figure 3, which employs a 1-D spreading channel up to 10 meters long. The channel would have a concrete basemat for spreading and thick inert Mgo walls to minimize lateral heat losses. Tests of corium-spreading in this channel will provide benchmark 1-D data for validation of MELTSPREAD models of freezing/immobilization-controlled spreading. Additionally, the channel will contain a steam chamber to collect steam and an off-gas pipe to take it to the quench tank for time-dependent measurements of the heat transfer from corium to water initially present or added later. The test section housing will be designed for 4 atmosphere pressure operation and will include thermocouples embedded in concrete to measure the spreading distance and the concrete ablation. Additional code validation experiments will be performed in a two-dimensional containment geometry vessel (not shown) which will include a confined region, wherein the melt may collect and then spread into an open region.

The code validation test will include at least two pour rates, since it was found[2] that the corium pour rates could vary a lot and that the extent of spreading depends strongly on the pour rate. Similarly, in order to delineate the dependence of spreading on the corium superheat at least two superheat values will be employed for the melt.

C. MELTSPREAD Analysis

The MELTSPREAD code will be the vehicle for the integrated analysis program which will include pre-test as well as post-test blind predictions. The comparisons with data will indicate the suitability of the various phenomenological models and the possible improvements that may be needed. It is hoped that increased understanding of the spreading process will result and its connection to the corium coolability issue clarified.

D. Confirmatory Scale Model Tests

It is anticipated that a few confirmatory scale model tests will also be included in the SMELTR research program. The objectives would be to obtain information about the prototypic containment configurations. Scale models of these will be built as receiving vessels. The current candidate containment configurations are those of Mark I BWR and the advanced PWR and BWR. These data will test the integral predictive capability of the MELTSPREAD code and they could be employed for direct application to the prototypic accident scenarios with the scaling laws previously tested in the code validation experiments.

7. Test Matrix

A preliminary MELTSPREAD code validation test matrix is being proposed for discussion purposes. Since prototypic material tests are expensive, only 6 tests have been defined, as shown in Table 1. The receiving vessel in the first part of this test series could be the one-dimensional channel shown in Figure 3. The corium loading has been chosen as 300 kg and the base corium superheat as 50K with one test using slurry material with no superheat. The base pour rate chosen is 20 kg/sec with one test proposed at pour rate of 2 kg/sec. The base substrate is chosen as limestone-common sand concrete (LCS) with one test using siliceous concrete and another using a steel plate to observe the difference in heat removal

and spreading when no gases are liberated from the substrate. Five of the six tests will use water already present in the receiving vessel. In one test with LCS concrete, water will not be added to the receiving vessel in order to observe the differences in spreading behavior and the heat removal by concrete without presence of water.

8. Summary and Conclusions

An integrated cooperative program of experiments and analysis on the spreading behavior of core melts in reactor containments (SMELTR) has been described. The experiments will be performed with prototypic corium melts in a facility incorporating a melt generator and a receiving vessel (representing a containment configuration). Water will be employed to observe its effect on melt heat removal and melt-spreading.

The MELTSPREAD code will be the vehicle for analysis of the experiments. A set of code validation experiments will be performed first to be followed by properly-scaled confirmatory tests representing prototypic containments. The validated MELTSPREAD code can then be used for design and analysis of existing and advanced containments.

9. References

1. G.A. Greene, K.R. Perkins and S.A. Hodge, "Mark I Containment Drywell Impact of Core/Concrete Interactions on a Containment Integrity and Failure of the Drywell Liner", Source Term Evaluations for Accident Conditions-Proceedings of an International Symposium on Source Term Evaluation for Accident Conditions, Columbus, OH, October 28 - November 1, 1985, pp. 429, International Atomic Energy Agency, Vienna (1986).

2. T.G. Theofanous, W.H. Amarasooriya, H. Yan and V. Ratnam, "The Probability of Liner Failure in a Mark I Containment", NUREG/CR-5423 (1990).

3. B.R. Sehgal and B.W. Spencer, "ACE Program Phase D: Melt Attack and Coolability Experiments (MACE), Proc. CSNI Meeting on Core Debris Concrete Interactions, Karlsruhe, Germany (April 1-3, 1992).

4. Advanced Light Water Reactor Utility Requirements Document, Vol. 1, ALWR Policy and Summary of Top-Tier Requirements, Electric Power Research Institute, March 1990.

5. B. Malinovic, R.E. Henry and B.R. Sehgal, "Experiments Relating to BWR Mark I Shell-Core Debris Interaction", ANS Proceedings 1989 National Heat Transfer Conference, Philadelphia, PA, August 26-30, 1989 and B. Malinovic and R.E. Henry, "Experiments Relating to Drywell Shell-Core Debris Interaction", EPRI NP-7196L (February 1991).

6. M.T. Farmer, J.J. Sienicki and B.W. Spencer, "Status of MELTSPREAD-1 Computer Code for the Analysis of Transient Spreading of Core Debris Melts", Proc. CSNI Meeting on Core Debris Concrete Interactions, Karlsruhe, Germany (April 1-3, 1992).

7. G.A. Greene, T. Ginsberg and N. Tutu, "BNL Severe Accident Sequence Experiments and Analysis Program", Trans. 12th Water Reactor Safety Research Information Mtg., NUREG/CR-0057 (1984).

8. M.L. Corradini, "Current Status of LWR Containment Loads Due to Severe Reactor Accidents", Third International Topical Meeting on Nuclear Power Plant Hydraulics and Operations, Seoul, Korea, November 14-18, 1988.

9. M.S. Kazimi, "Recent Developments in Thermal-Hydraulics of Severe Accidents", Third International Meeting on Nuclear Power Plant Thermal Hydraulics and Operations, Seoul, Korea, November 14-18, 1988.

10. F.J. Moody, "First Order Analyses of Molten Corium Heat Transfer", Proceedings 1989 National Heat Transfer Conference, Philadelphia, PA, August 6-9, 1989.

11. M.T. Farmer, J.J. Sienicki and B.W. Spencer, "On a Scaling Rationale for Corium Spreading", EPRI report in preparation.

12. J.J. Sienicki, M.T. Farmer and B.W. Spencer, "Spreading of Molten Corium in Mark I Geometry Following Vessel Melt-Through", Fourth Proceedings Nuclear Thermal Hydraulics, Washington, DC, October 30 - November 4, 1988.

13. M.T. Farmer, J.J. Sienicki and B.W. Spencer, "The MELTSPREAD-1 Code for the Analysis of Transient Spreading in Containments", ANS Winter Meeting Session on Thermal Hydraulics of Severe Accidents", Washington, DC, November 11-15, 1990.

TABLE 1: PRELIMINARY MELTSPREAD VALIDATION TEST MATRIX

Test	Corium[1] Loading, kg	Melt[2] Superheat, K	Melt Release Rate, kg/s	Substrate[4]	Water	Pressure, atm
S1	300	50	20	L/CS	Yes	1
S2	300	50	20	L/CS	No	1
S3	300	50	20	Steel	Yes	1
S4	300	50	2	L/CS	Yes	1
S5	300	50	20	S	Yes	1
S6	300	Slurry[3]	20	L/CS	Yes	1

Notes:
1. Nominal composition = 72% UO_2, 13% ZrO_2, 10% Zr, 5% concrete decomposition products.
2. Relative to liquidus temperature of ~2700K.
3. Slurry temperature is between solidus and liquidus temperature.
4. L/CS = Limestone/common sand concrete; S = Siliceous concrete.

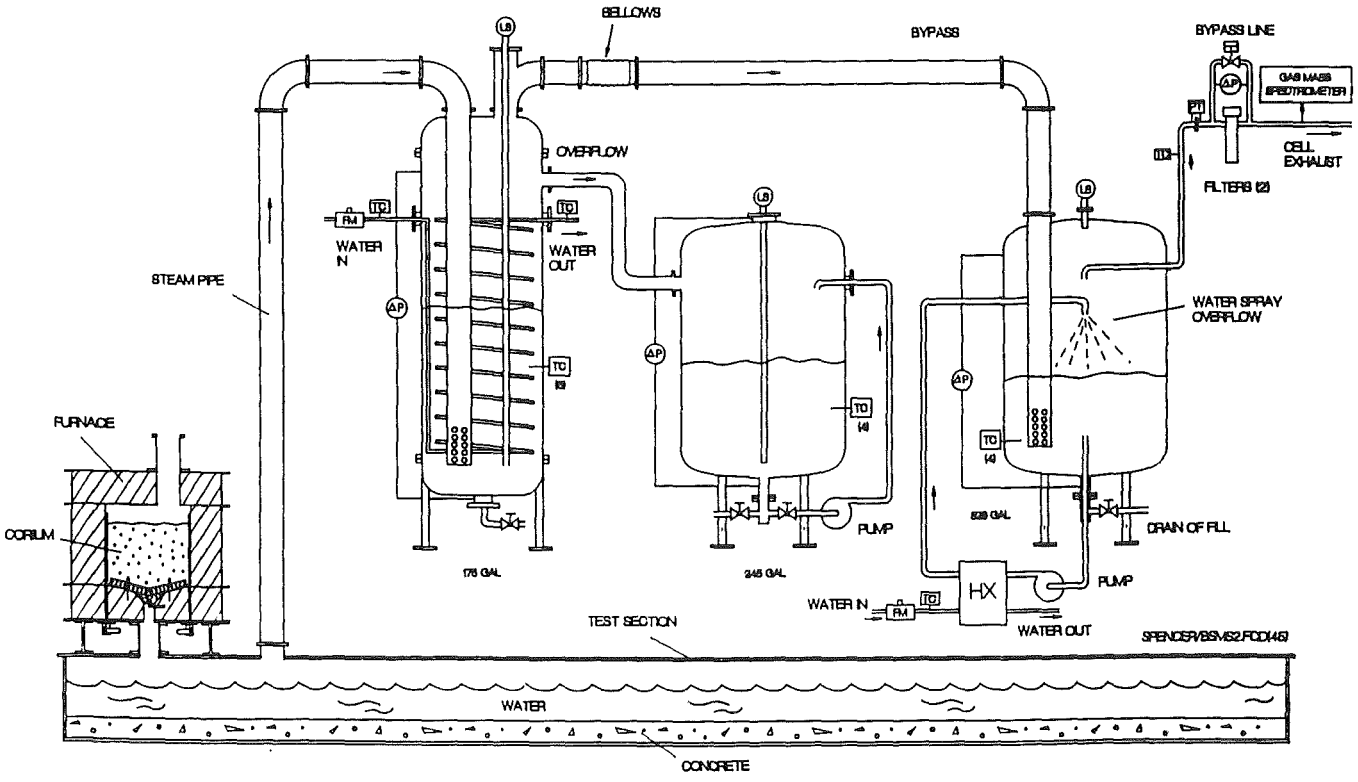

Figure 1: SMELTR Test Facility

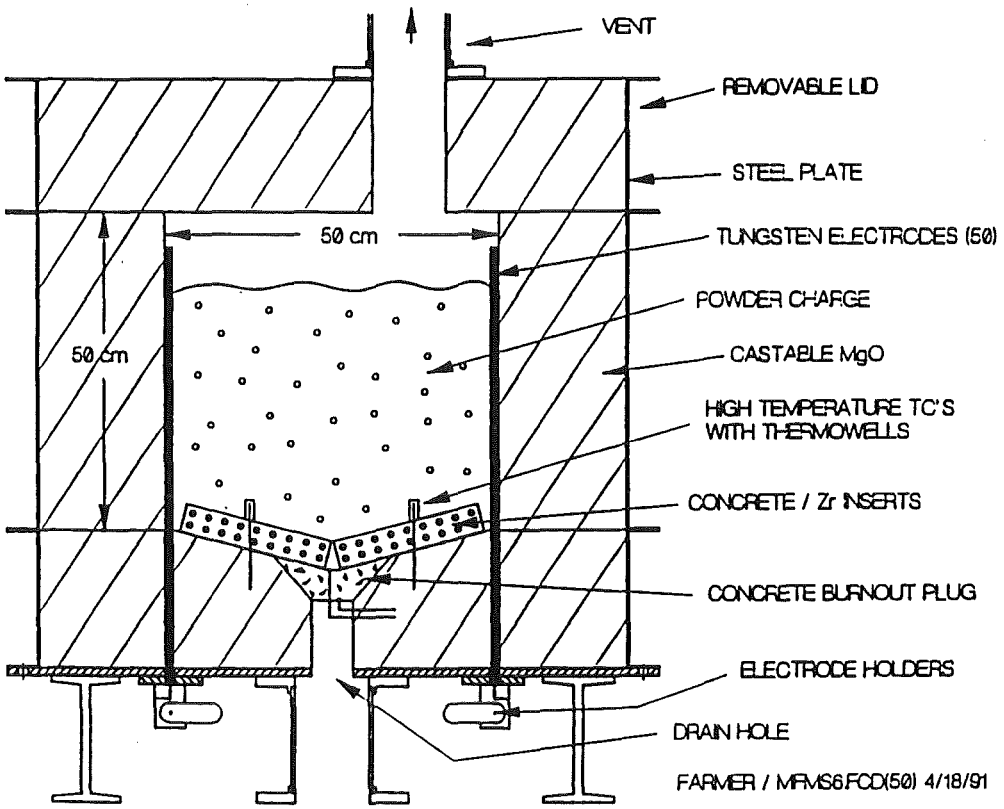

Figure 2: Illustration of Melt Generator

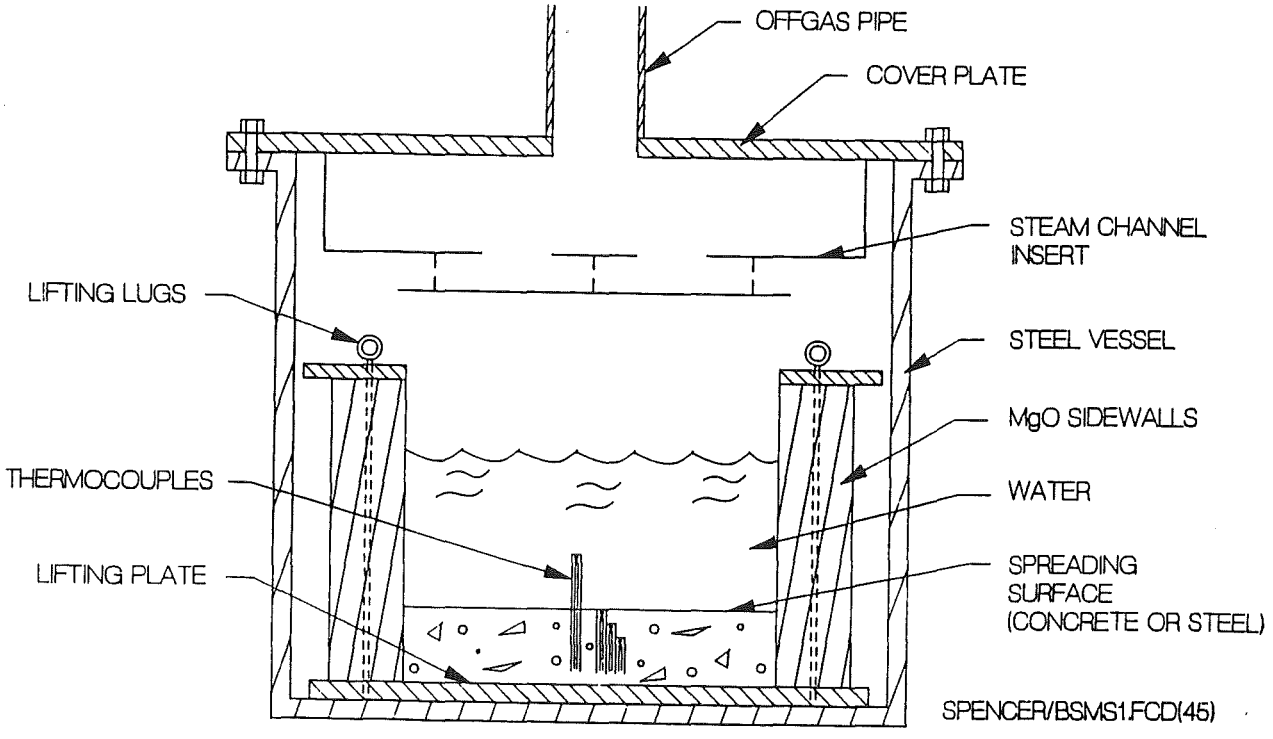

Figure 3: One-Dimensional Channel Receiving Vessel

ACE Program Phase D:
Melt Attack and Coolability Experiments (MACE) Program

by

B.R. Sehgal
Electric Power Research Institute
3412 Hillview Avenue
Palo Alto, California 94303 USA

and

B.W. Spencer
Argonne National Laboratory
9700 South Cass Avenue
Argonne, Illinois 60439 USA

Abstract

A series of large-scale experiments are being performed at Argonne National Laboratory (ANL) investigating the coolability of molten-corium by water during its interaction with concrete. The principal objectives of the MACE Program are to: 1) obtain data on heat transfer from corium melt to the overlying water and underlying concrete; and 2) develop models describing the coolability process for insertion in the U.S. and international codes on molten corium concrete interaction (MCCI).

This paper will provide an overview of the melt coolability issue, describe the MACE program and the capabilities of the experimental facility constructed. The MACE Program is managed by the Electric Power Research Institute (EPRI) and supported by U.S. NRC, U.S. DOE, EPRI and an international consortium.

Introduction

The evaluations of risks of U.S. nuclear power plants have focused attention on postulated beyond-design-basis accidents in which core melting occurs and

fission products are released. In certain low probability scenarios the molten core material (corium) causes a failure of the reactor pressure vessel (RPV) lower head and substantial quantities of corium are discharged into the BWR pedestal region or the PWR containment cavity; and pose a threat to the integrity of the last barrier to fission products, i.e., the reactor containment.

The failure of the containment by the loadings imposed by the corium discharge may be early or late, depending upon the rate of energy transfer from corium to the containment environment. The postulated early failure of containment due to high rates of heat transfer in scenarios such as the high-pressure melt ejection (HPME) for PWRs or the containment shell melt-through for the Mark I BWRs is being addressed in the programs sponsored by the U.S. NRC. Clearly, if the corium energy transfer occurs to agents which can cope with the high heat transfer rates and reduce the pressure and thermal loads on the containment, the early failure of containment may be precluded. Specific examples of these agents are water and containment structures, which have been found to be very effective in the HPME [1] and the BWR Mark I shell melt-through scenarios [2].

The longer-term threat to containment integrity is due to the decay energy generated by the corium melt resident in the containment. The containment basemats, commonly constructed of concrete, are attacked by the molten corium to generate combustible and non-combustible gases. If a heat transport cycle cannot be established, the containment temperature and pressure can reach failure threshold levels after a certain length of time. Additionally if the concrete basemat thickness is relatively small, there is a possibility of basemat melt-through and the attack of the corium melt on the subsoil. The prevention of late containment failure or basemat melt-through is again related to the potential of heat removal from the corium melt and the establishment of a heat transport cycle in the containment. It should be recognized that the environmental fission product release hazard of a late containment failure is orders of magnitude smaller than that of an early containment failure.

Perhaps the most commonly available and a very efficient agent for absorbing the corium-melt energy in the containment is water. It has a relatively large specific heat capacity and latent heat and has the ability to serve as a heat transport medium through boiling at one location and condensing at another location (e.g., structures, fan coolers, suppression pools). In addition, water is

excellent for retaining the volatile fission products, e.g., CsI and CsOH released by the reactor core during heatup and meltdown process. Also, containments, in general, have engineered safeguard systems for delivery of water through sprays or otherwise, into the various containment regions.

The current emphasis in the U.S. is on accident management, i.e., to manage the course of events, in case an accident occurs, such that the plant can be brought to a safe stable state and the fission product release is minimized. The U.S. NRC's "Integration Plan for Closure of Severe Accident Issues", SECY 88-147 (5) states that a key element to severe accident closure for each plant will be the implementation of a severe accident management program, while the NRC staff examine the Individual Plant Examination (IPE) submittals. SECY 88-147 further recognizes the beneficial effects of water addition to the containments in order to extract heat from the molten corium.

The advanced light water reactor (ALWR) designs have provided for water addition to both the BWR and PWR containments. The passive designs have specified a containment flow area based on a certain heat removal rate from the corium melt when a water overlayer is established on a melt layer, through water addition either before or after melt discharge to the containment. The adequacy of that design decision has not been established yet.

Melt Coolability Issue

Simply stated, the melt coolability issue asks the question, "Can the corium melt pool be cooled by a water overlayer such that: 1) corium interaction with concrete is halted; 2) basemat melt-through is prevented; 3) continued containment pressurization is halted; and 4) the accident is managed, stabilized and terminated? The scenario under consideration is that of a jet of molten corium being discharged from the location of vessel failure to the containment. If the containment has water present, the corium jet may suffer some fragmentation; however, the fragmentation fraction is assumed to be small and the jet spreads into a layer of certain area on the containment floor. There may be water added on top after corium has spread. The final configuration is that of a water layer on top of a molten corium pool interacting with the concrete basemat.

It is perhaps instructive to state the minimum conditions for melt coolability. Since our primary objective is that the concrete ablation is halted, the minimum condition for coolability is that the corium pool temperature falls and remains below the solidus temperature of the particular concrete* employed. Since the concrete liquidus temperature will generally be less than the corium solidus temperature, the final configuration is thus of a hot solid block of corium material confined in concrete and in contact with water. The heat transfer rate from the melt to the overlying water has to be sufficient to: 1) extract the corium sensible and decay heats on a transient basis; and 2) the decay heat being generated in the corium block on a continuous (steady-state) basis.

It is also instructive to state the maximum conditions for melt coolability. These obviously are that melt is completely quenched and attains the water saturation temperature (about 150°C) and remains at that temperature. Achieving quenchability would require, either the fragmentation of the melt into millimeter size particles and thorough mixing with water, or, if the melt does not fragment, that water ingression occurs through interconnected cracks in the surface crust and a quench front traverses the melt pool. The quenchability configurations and the time to quench depend upon the morphology of corium melt-cooling. Thus, if there is substantial fragmentation, melt water contact will occur and time to quench the melt pool could be short. On the other hand, if there are small interconnected cracks, the water ingress will be opposed by the flow of the concrete ablation gases out of the surface of the corium pool (or solidified block) and the time to quench could be quite long.

The above minimum or maximum conditions for coolability are functions of the heat transfer rate and the morphology of the corium cooling process. Clearly, the material properties are very important in terms of its conductivity and its fracture behavior as it goes from the liquid (melt) to solid-state and reduces in temperature. If the corium material has high fracture strength, it may form an impervious stable low conductivity crust on contact with water, which afterwards physically and thermally-isolates the melt from the water. The crust grows in thickness such that the heat transfer rate from the melt to water is less

---

* CORCON-MOD1 values for solidus temperatures of basaltic, limestone-sand and limestone-concrete, respectively, are 1350K, 1420K and 1690K.

than the decay heat generation in the melt. In this configuration the melt pool will not be cooled and will continue to attack the concrete.

The minimum conditions for melt coolability described above may be achieved for the physical situation of water addition to an ongoing MCCI. It is very probable that the initial melt-water contact leads to some fragmentation of the melt and mixing with water such that a substantial amount of the stored heat is transferred to water. The resultant drop in melt temperature leads to less vigorous attack on concrete and reduction in gas generation. A floating crust could form which degrades the heat transfer between the melt and the water overlayer. The heat transfer rate from melt to water could be sufficient to remove the decay heat if the crust is thin or it cracks to allow water ingress into melt or alternatively, melt ingress into the water overlayer (as observed in the MACE scoping test Mo described in a companion paper at this meeting). The melt-water contact may be continuous or periodic, depending upon the forces on the crust and the fracture strength of the crust. Thus an initial transient heat removal process in concert with either a slow continuous heat removal or a periodic large heat removal process could assure coolability and stabilization of the melt pool. There may, however, still be a highly viscous corium slurry which may periodically erode concrete at a very, very slow rate.

Experimental demonstrations of melt coolability are pursued in the MACE program described in this paper and in the WETCOR Program at Sandia National Laboratories. A primary concern in the experiments is that of prototypicality of the physical configuration of the crust formed in the experimental simulation. An anchored crust which is the likely situation in a small-scale experimental simulation may create a different thermal barrier between the melt and the water versus that for a floating crust, which is the likely configuration in the prototypical situation. In the experiment, the melt pool keeps attacking the concrete basemat and recedes from the anchored crust and the heat transfer from the pool to the crust, therefore, partially determines the heat transfer from the melt pool to the water overlayer.

The above description of melt coolability issue and scenario is indicative of the complexity involved and the difficulty of the resolution of this issue. In the following sections we will describe the MACE Program, which is wrestling with this very problem.

Previous Work

The melt coolability experimentation has not been as extensive as that for MCCI. Sandia Laboratories performed the FRAG [3] series of tests employing about 46 kg mass of 3 mm diameter steel balls heated to 1200°C to 1400°C in a 22.8 cm diameter crucible with a base of either basalt or limestone-sand concrete. The results of tests showed that the liquid concrete products mixed with steel balls and formed an impervious crust when water was added. The hot debris continued to erode concrete and was not cooled.

Sandia Laboratories also performed the series of SWISS tests [4] in which water was added to a stainless steel melt of 22.8 cm diameter and 18 cm depth interacting with a concrete basemat. In the SWISS-1 test, water was added after 12 cm of concrete was eroded, while in the SWISS-2 test, water was added to the melt only one minute after the steel-concrete interaction started. In both of these tests, an impervious anchored crust was formed, isolating the water from the melt, which kept attacking the concrete. In the SWISS-2 test, the heat flux from melt to water, after a large initial value, stabilized to about 800 kw/m^2, which is considerably less than the flat plate critical heat flux but is several times the value of the film boiling heat flux. This value is also quite sufficient to extract decay heat from a 25 cm corium melt layer. The power input into the SWISS-2 stainless steel melt was larger and led to the continued concrete ablation by the steel melt, in spite of the heat removal by water.

Several simulant material tests have been done to understand melt coolability behavior. Theofanous and Saito [5] employed liquid nitrogen/water and liquid nitrogen/Freon 11 fluid pairs with air injection at different superficial velocities. They found that the crusts formed at very low gas velocities were unstable at higher gas velocities and that there was an order of magnitude increase in heat transfer as the gas velocities increased to levels expected in MCCI. Greene [6] performed tests with liquid metals and water/freon with gas injection in the melt. He observed increase in heat transfer from melt to water with increase in gas velocity up to approximately 6 times the classical Berenson correlation [7]. The melt layers in Greene's experiments became a bubbling slurry and ultimately cooled as a solidified porous mass allowing gas to flow through and coolant to

ingress. Kazimi [8] observed similar slurry mode of freezing and crust formation in a bubbling simulant material pool.

Recently, a coolability test has been performed in the WETCOR facility at Sandia using simulant high melting temperature oxidic material with heated walls interacting with concrete at the bottom and cooled by water at the top. It was found that a crust was formed, which again isolated the melt from the water, and melt coolability could not be achieved in the time span of the experiment.

The above information has led to the considerable divergence of opinion on the feasibility of cooling or quenching a large deep molten corium pool. The lack of understanding of the coolability mechanisms for different materials has also hampered the development of models describing melt coolability.

The MACE Program

The MACE Program forms the Phase D of the ACE Program, a cooperative research program funded by the ACE international consortium. The program is managed by EPRI and the MACE tests are being performed at ANL and address the ex-vessel melt coolability issue central to the severe accident management and advanced LWR containment design. The principal objectives of the MACE Program are to: 1) obtain data on heat transfer from the corium melt to the overlying water layer and underlying concrete; and 2) develop models describing the coolability process for insertion in the U.S. and the international codes.

The emphasis of the MACE Program is to examine the thermal-hydraulic processes of melt-water interaction in stratified geometry, which ultimately determines whether sufficient energy is extracted from the melt so that the concrete attack is stopped and a coolable debris configuration is achieved. A MACE test will terminate either when a quench is achieved or when it is established that the melt cannot be cooled. The post-test examination will form an important part of the data. In the case of melt quench, the debris bed formed will be characterized in terms of particle size and composition. While in the case of non-coolability the impervious crust layer will be characterized in terms of its composition, its fracture strength and its attachment to the walls.

MACE Experimental Approach

The MACE experimental approach is similar to that of the ACE Phase MCCI tests in that a conscious effort was made to reduce scaling distortions, such that the data obtained can be easily extrapolated to the prototypic situation. The materials used for the MACE tests are corium with mixture (UO_2, ZrO_2, Zr) compositions representative of a LWR, the basemats are also of prototypic concrete mixtures and the power input is specified to be equal to the decay heat after two hours of shutdown. Water is added to the melt after it starts attacking concrete to simulate the prototypic condition obtained after the melt discharge from the vessel is completed.

Perhaps the most significant scaling distortion that can occur in a small-scale experiment of melt coolability is the interaction of the crust formed with the walls of the experimental apparatus. Since the experiment size is small, the surface crust, if it anchors or binds with the walls, may be able to support the loadings imposed on it of the water pool on top or the gas pressure from below. Thus, the crust could be detached from the melt surface, since the melt layer interacting with concrete will recede from its original level. In the prototypic situation, however, the crust span is several meters and it most probably will not attach to the walls and will float on the surface of melt layer. There could be significant differences in the heat extracted from the melt by the water in the two cases. The possibility of having this particular scaling distortion was recognized in the formulation of the MACE program and an attempt has been made to make the lateral size of the test vehicle as large as physically feasible. The nominal size chosen was 50 cm X 50 cm with the design capable of having a test size of 75 cm x 75 cm. In addition, the differences in the heat transfer resistance posed by the anchored crust versus the floating crust will be examined experimentally and analytically.

MACE Test Matrix

It was recognized from the very start of the MACE Program that the test matrix specification could not be comprehensive due to uncertainties about the success of experiments. The factors were: 1) complexity and difficulty of the tests; 2) possible energetic interaction (steam explosion); 3) lateral size of test vehicle (50 cm X 50 cm); and 4) the crust behavior in the test vehicle. A three-test matrix

shown in Table 1 was approved by the ACE Technical Advisory Committee (TAC) and Board. The test Mo is of smaller size than tests M1 and M2. The amount of corium used for test Mo is about 100 kg, while it is about 400 kg for tests M1 and M2. The MACE facility can accommodate a test vehicle of 75 X 75 cm cross-section, which will require about 1000 kg of corium for 25 cm deep melt layer. In general, the test matrix is reviewed after each test by the TAC.

Table 1: Current MACE Test Matrix

Test #	Concrete Type	Corium Composition	Melt Depth	Size (cm)	Water Addition	Pressure (Bar)	Parameter Investigated
0	L/S	Oxidic + 30% Zr	15	30x30	Immedi-ately after MCCI	1	Scoping test
1	L/S	Oxidic + 30% Zr	25	50x50	Immedi-ately after MCCI	1	Scaling
2	Siliceous	Oxidic + 30% Zr	25	50x50	Immedi-ately after MCCI	1	Different concrete

MACE Test Facility

The MACE test facility is located in a containment building of a decommissioned fast reactor critical assembly, at the ANL site, to safeguard against the risk of a steam explosion. The facility is shown schematically in Figure 1, with its components. The test vehicle is a furnace similar to that employed for the ACE Phase C tests except that instead of using cold walls to contain the melt, a parallelopiped of Mgo is employed with the concrete basemat forming the bottom. The corium powder located on top of the concrete basemat is melted by direct electric heating (DEH) applied through electrodes on two (opposing) sides of the Mgo vessel. The placement of the Zr metal rods is at the bottom of the corium powder bed so that Zr oxidation does not occur prematurely during the corium powder heatup phase. Water is added to the corium after the powder is completely molten and has started interacting with the concrete basemat. The water flow is initiated through two weirs along the tops of two walls adjacent to the electrode walls.

MACE TEST APPARATUS

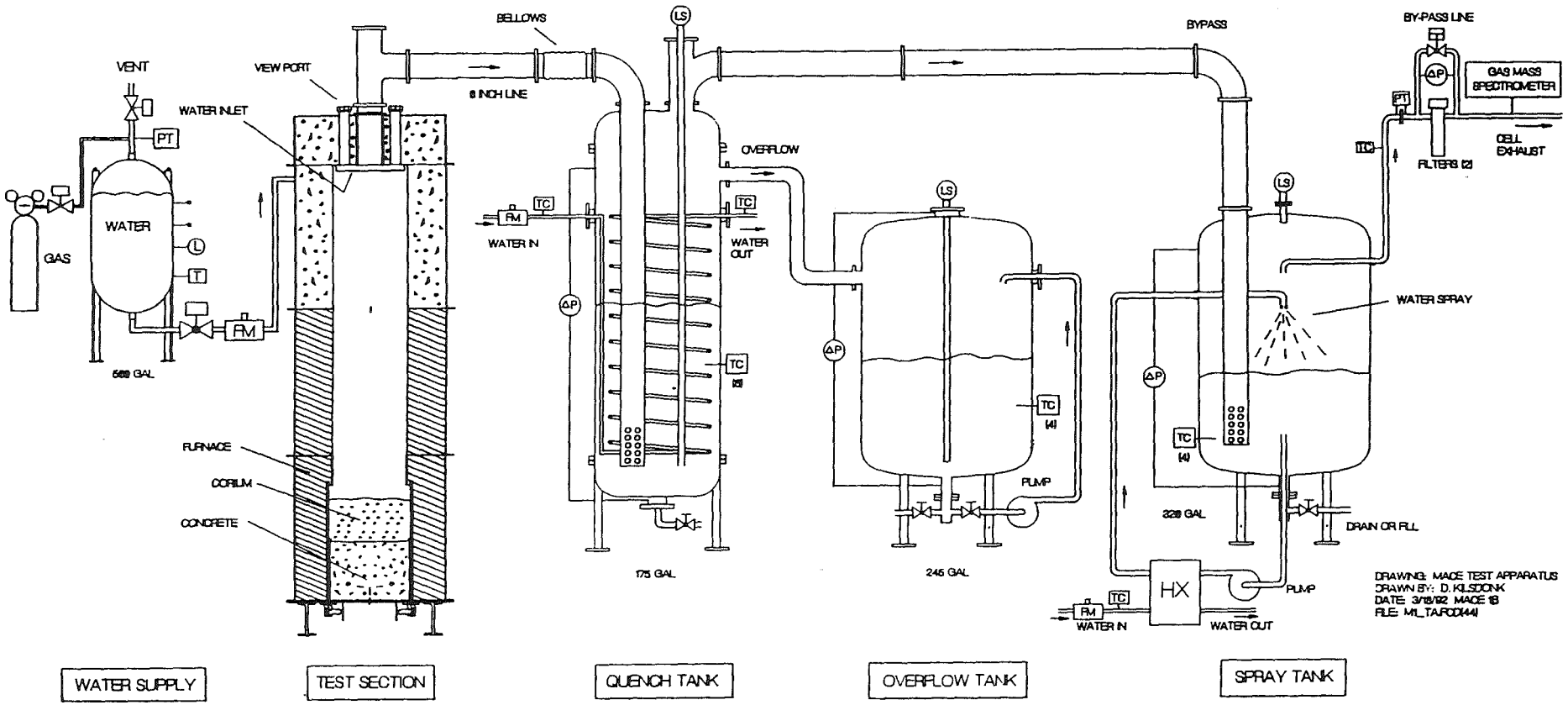

Figure No. 1

The steam and non-condensible gases produced are routed in a large pipe at the top of the test vehicle to a small heat exchanger and then to a large quench tank, in order to obtain high resolution measurements of the heat transport rate as well as accommodate very large heat transfer rates if they occur. The non-condensible gases leaving the heat exchangers are routed to a mass spectrometer to measure their time-dependent composition on line.

The instrumentation provided includes thermocouples embedded in the concrete basemat to measure the rate of ablation. Melt temperature is measured through a chain of thermocouples protruding from the concrete into the melt zone embedded in tungsten thermowells. Thermocouples are also included in the Mgo vessel sidewalls. The viewports at the top of the Mgo vessel are used for videocameras.

The MACE test vehicle is also equipped with 4 lances which are driven like control rods from above into the melt zone. They are equipped with thermocouples at the bottom end and their functions are to: 1) measure the temperature of the melt as a function of its depth; and 2) detect the location of crust if it is formed.

Further details about the facility are given in the MACE project reports.

MACE Program Status

The MACE Program was started in 1989 under EPRI sponsorship and the scoping test Mo was performed in August of that year. This was followed by the test M1, performed in November 1991. The results of these tests are described in an accompanying paper. Briefly, the test Mo was conducted as specified, except for power input, which was much greater than specified. The test Mo did not cool since a crust was formed and supported by the electrodes, which unfortunately bent due to the excessive thermal loading. The test M1 design corrected for the deficiencies of test Mo, however, in the operation of the test, the specified initial condition that the corium powder be completely molten to the top surface was not attained. The top surface remained as a sintered powder layer and did not allow water-melt contact. Post-test examination of test M1 confirmed these findings. Test M1 will be repeated as test M1B in April 1992 with the heatup procedure found to be successful in the ACE Phase C tests.

References

1. B.W. Spencer, J.J. Sienicki and L.M. McCumber, "Hydrodynamics and Heat Transfer Aspects of Corium/Water Interactions", EPRI NP-5127, Electric Power Research Institute, Palo Alto, California (1987); and B.W. Spencer, J.J. Sienicki, B.R. Sehgal and M. Merilo, "Results of EPRI/ANL DCH Investigations and Model Development", Proc. of the ANS/ENS Conference on Thermal Reactor Safety, Avignon, France (October 2-7, 1988).

2. T.G. Theofanous, W.H. Amarasooriya, H. Yan and V. Ratnam, "The Probability of Liner Failure in a Mark I Containment", NUREG/CR-5423 (1990).

3. W.W. Tarbell, D.R. Bradley, R.E. Blose, J.W. Ross and D.W. Gilbert", Sustained Concrete Attack by Low-Temperature, Fragmented Core Debris", NUREG/CR-3024, SAND82-2476 R3, R 4 (July 1987).

4. R.E. Blose, J.E. Gronager, A.J. Suo-Antilla and J.E. Brockman", Sustained Heated Metallic Melt/Concrete Interactions With Overlying Water Pools", NUREG/CR-4747, SAND85-1546 R3, R4, R7 (July 1987).

5. T.G. Theofanous and M. Saito, "An Assessment of Class 9 (Core-Melt) Accidents for PWR Dry Containment Systems", Nucl. Eng. & Design 66, 301-332 (1981).

6. G.A. Greene, C. Finfrock and S.B. Burson", Phenomenological Studies on Molten Core-Concrete Interactions", Nucl. Eng. & Design 108, 167-177 (1988).

7. P.J. Berenson, "Film Boiling Heat Transfer From a Horizontal Surface", J. Heat Transfer 83, 351-358 (1961).

8. L.S. Kao and M.S. Kazimi, "Thermal-Hydraulics of Core/Concrete Interaction in Severe LWR Accidents", Report MIT NE-276, Massachusetts Institute of Technology (June 1987).

RESULTS OF MACE TESTS M0 AND M1

B. W. Spencer[1], M. T. Farmer[1], D. R. Armstrong[1], D. J. Kilsdonk[1], R. W. Aeschlimann[1], and M. Fischer[2]

[1]Argonne National Laboratory
Argonne, IL 60439 USA

[2]Siemens AG
UB KWU FRG

ABSTRACT

The Melt Attack and Coolability Experiment (MACE) Program underway at Argonne National Laboratory under ACE/EPRI sponsorship is addressing the efficacy of water to terminate an accident situation if melt progression were to result in a molten core/concrete interaction (MCCI) in a reactor containment. Large-scale experiments are being conducted, in parallel with related modeling efforts, involving the addition of water to an MCCI already underway. The experiments utilize $UO_2/ZrO_2/Zr$ corium mixtures, direct electrical heating for simulation of decay heating, and various types of concrete basemats. Currently the tests involve 430 kg corium mass, 25 cm depth, in a 50 cm square test section. Test M0 was a successful scoping test, but the first full size test, M1, failed to achieve melt-water contact owing to existence of a preexisting bridge crust of corium charge. A heat flux of 3.5 MW/m^2 was measured in M0 which removed energy from the corium pool equivalent to its entire heat of solidification prior to abatement by formation of an interfacial crust. The crust subsequently limited heat extraction to 600 kW/m^2 and less. Both tests M0 and M1 revealed physical evidence of large pool swelling events which resulted in extrusion (and ejection) of melt into water above the crust, significantly increasing the overall quench and reducing the remaining melt in contact with the concrete. Furthermore, test M1 provided evidence of occasional "burst mode" ablation events and one additional important benefit of overlying water--aerosol capture.

INTRODUCTION

Programs are currently underway addressing the possible role of water to abate and eventually stabilize a molten core-concrete interaction (MCCI). These programs are WETCOR at Sandia National Laboratories, sponsored by the USNRC, and the Melt Attack and Coolability Experiments (MACE) underway at Argonne National

Laboratory under sponsorship of the international Advanced Containment Experiments (ACE) Consortium. The ACE/MCCI and ACE/MACE programs are described in Refs. 1 and 2. This paper describes the findings from early MACE tests.

OBJECTIVES/APPROACH

The general objective of the MACE program is to explore the possible benefits of massive addition of water to an MCCI already in progress insofar as:

- quenching and stabilizing the heat-generating core melt,
- arresting or even terminating basemat ablation, and
- scrubbing released aerosols.

The approach used in the MACE tests is to utilize selected PWR and BWR core melt compositions comprising UO_2, ZrO_2, Zr and possible control rod materials. Direct electrical heating (DEH) is used to produce bulk internal heat generation, and the power level is controlled to nominally depict the volumetric decay heat power level for the particular reactor type at some length of time into the accident. The ACE and MACE tests have typically used full decay heat at 2 hrs (i.e., ~350 watts/kg UO_2 for a PWR); heretofore, no account has been taken for reduction in this heating owing to release of volatiles from the fuel in the reactor accident.

MACE EXPERIMENT DESCRIPTION

The major elements of the MACE apparatus are shown in Fig. 1. The apparatus consists of a test section about 3 m tall. At the bottom of the test section is the concrete basemat, instrumented with Type K TC's to measure downward heatup and erosion rate and W-Rh TC's in tungsten thermowells to measure MCCI-zone temperatures. The corium charge is placed atop the concrete. This charge is in the form of crushed UO_2 pellets (unirradiated, natural or depleted) plus particles of ZrO_2 and typically a small amount of concrete decomposition product oxides CaO, SiO_2. Their presence is to create a lower, more prototypic melting temperature than a pure UO_2, ZrO_2 system, and furthermore can be rationalized from consideration of concrete erosion when the melt flows from the breached vessel onto the basemat floor [3]. A region of UO_2 crushed pellets is initially heated by tungsten heater elements until its temperature is such that oxide phase

conductance begins. The zone experiences first localized melting, and the melted zone grows to encompass eventually nearly all the loaded powders as the DEH power is gradually increased accordingly.

At a specified depth of concrete erosion, the water addition is initiated. Water is delivered by two wiers at the top of the test section in the walls adjacent to those having the electrodes. Initially, water is added steadily until a 50 cm head is established above the melt layer as recorded by redundant head measuring devices in the test section. Thereafter, the water is added intermittently to maintain a $50\ ^{+5}_{-10}$ cm level as boiloff progresses. Thermocouples in the test section measure the water and cover gas temperatures. The vertical dimension of the test section was sized such that roughly the upper one meter would be available for water droplet settling even if the corium and water pools were churn-turbulent owing to the vigorousness of gas sparging.

A large gas line is present in the top cover to duct dilution gas, noncondensable offgas, and steam to the adjacent quench tank. The quench tank provides a mass of water to condense transported steam and to cool other gases. Condensate spills over and is collected in the overflow tank. The quench tank has a cooling coil to maintain its water inventory in a subcooled state. The cooling coil, quench tank, and overflow tank are instrumented with flowmeters, thermocouples, level sensors, and pressure transducers in order to monitor the transient state of the system and extract the necessary heat balance information. Downstream from the quench tank is a spray tank which performs a redundant quench/gas cooldown function. While adding redundancy, the use of two quench tanks in series is designed to enhance resolution of the energy transport measurement. This overcomes the practical difficulty of attempting to make energy transport measurements equivalent to melt-to-water heat fluxes ranging from as high as 5 MW/m^2 during a postulated early bulk cooldown stage to as low as a few hundred or less kW/m^2 depending upon possible crust behavior. Both low and high energy transport rates can be reliably measured with the approach described here.

The argon dilution gas and noncondensable offgas species (CO_2, CO, H_2) are cooled to room temperature by transport through the quench tank and spray tank, and exit the system through an exhaust line at the top of the spray tank. The line includes a demister, filter, gas flowmeters, and a gas mass spectrometer to give

the time-varying composition of the gas. This gas is released into the exhaust line of the containment cell ventilation system where it flows, further diluted, through a final cleanup system before being released from the building stack. The MACE apparatus is housed within a containment building formerly used for a (dismantled) research reactor at ANL. This containment building provides convenient radiological control as well as protection from postulated end-of-spectrum steam explosion and hydrogen behavior effects.

Greater detail on equipment, instrumentation, data acquisition, and procedures is available in Project documentation.

MACE SCOPING TEST (M0)

The MACE scoping test was conducted to get an early indication of the mode and extent of corium quenching and as an aid to both model development and future experimentation. The scale was selected to be 30 cm x 30 cm test section with a corium mass of ~130 kg, equivalent to ~15 cm collapsed pool depth. This size and mass reflected an upper operational limit of the available 300 kW power supply (not from the power standpoint, but from the available voltage/current ranges). The size was slightly larger than the 21.6 cm dia vessel used in previous SWISS tests at SNL in which water was added atop molten stainless steel interacting with concrete in a MgO crucible [4]. In both those tests an upper bridge crust formed at the melt-water interface which prevented any significant abatement of the melt-concrete interaction. For the MACE M0 test it was decided to use concrete not only for the basemat but also for the sidewalls. The rationale was that any crust material formed in M0 would be unlikely to anchor to the sidewall if the sidewall were a readily decomposing material.

Conditions for the M0 test are listed in Table 1. These conditions were closely patterned after the ACE L1 test involving PWR corium composition with about 30% of the zirconium in unoxidized, metallic form, interacting with a limestone/common sand concrete basemat. The M0 test was conducted August 24, 1989. Water addition began when the basemat centerline thermocouple array indicated ablation had proceeded 1.2 cm into the concrete. When this depth was attained, it was evident in the video that the melt pool was highly agitated and that there was no significant floating crust on the pool, but also that there was a partial crust (remnants of the original charge powders) which had not collapsed

into the pool. This crust appeared to be cantilevered from the electrodes and extended outward about one-quarter of the test section width in the visible quadrant. Although not visible in the video, this cantilevered partial crust probably existed along the opposite electrode side as well. If so, it is estimated that the test section area was about one-half occluded by the sintered powders, albeit the surface of the melt itself was probably several centimeters below the elevation of this partial crust. Other test data revealed that the melt was attacking the basemat in an asymmetric profile; it had started in the southwest quadrant, proceeded to the central quadrant, and would later progress to the northeast quadrant. The experimenters did not observe the extremely intense interaction which accompanied the Zr ingression stage of the L1 MCCI test, and so left the power at the heatup level of about 100 kW rather than reduce it to 26 kW as planned.

Water was added to the test section at an initial rate of 10 l/s until the desired pool depth of 50 cm was attained. Makeup flow was added to maintain this level during boiloff. Figure 2 shows the cumulative energy transported from the test section to the quench tank via the steam and gas flow. This data has been corrected for heat transfer from apparatus structures other than heat flux from the melt pool itself. The data indicates that during the first three minutes of contact, there was an intense extraction of heat from the melt amounting to 3.5 MW/m^2, related to the planar cross-sectional area of 0.090 m^2. The energy extracted from the corium during this initial contact stage amounted to 44 MJ. Using a heat of fusion for the corium melt of about 0.3 MJ/kg and a corium mass of 130 kg, it can be seen that the measured energy extraction could have largely, if not completely, solidified the corium mass, albeit leaving it at very high temperature. Even if uniform bulk cooling were not achieved in an ideal sense during this early interaction stage, it is clear that a significant cooling transient occurred which would have resulted in slurry formation and thereby increased melt viscosity. Regrettably, the thermocouples in M0 did not capture this event owing to the asymmetric corium attack on the basemat.

While the first three minutes of contact were characterized by intense energy extraction, this stage was followed by a quite quiescent period for the next three minutes. The most plausible explanation for this has been put forth by Farmer et. al. [5] who relate the stability of an interfacial crust to the gas

sparging rate attributable to the concrete decomposition. That is, the large energy extraction during the initial interaction period so stabilized the corium that basemat attack, and thereby gas sparging rate, were greatly reduced. The Farmer model would predict a stable interfacial crust to form under such conditions. Indeed, we know from posttest examination that a bridge crust did form in this scoping test, and it is suggested that this first happened during the quiescent period from 3-6 min after water addition.

There is further indication of this from interpretation of the ablation data. Figure 3 shows basemat ablation as indicated by the centerline array of TC's attaining the concrete liquidus temperature of 1568 K [6]. The TC junctions are at discrete depths into the concrete; the straight line segments drawn through the actual data in Fig. 3 reflects the author's interpretation of a plausible trend. The initial ablation rate was 2.3 mm/min as recorded up to the time of water addition. After water addition (at 4.0 min) the ablation rate measures ~1.8 mm/min, but with an offset equivalent to ~6 min. It is interpreted that the cooling transient could in fact have stabilized the MCCI during this time, but with continued internal heat generation (~4x decay heat at this time during M0), a reheating occurred and the MCCI resumed.

It is important to note that in this small scale experiment, the bridge crust was well anchored by the tungsten electrode rods. The crust remained at the elevation where it formed as the resumed MCCI caused continued downward erosion of the melt into the concrete. At reactor scale, analyses suggest that the crust would break up and remain in contact with the melt [7]. Moreover, it is worthwhile to note in this test that the crust was also firmly attached to the concrete sidewalls. The use of an ablative wall material as an attempt to preclude that attachment was not successful owing to the cooling effect of the overlying water at the boundary.

The quench data in Fig. 2 shows that following the quiescent period the energy extraction from the melt pool resumed. While several perturbations are present, the general trend shows 600 kW/m^2 up to ~35 min and then a gradual diminishing to as low as 150 kW/m^2 by the end of the test. For comparison, the upward heat extraction to remove all the decay heat in a 15 cm deep corium pool is ~290 kW/m^2. The M0 test was run with diminishing power which was ~4x decay heat early

in the test and reduced to ~2x by the end of the test. Hence early in the test at the 600 kW/m^2 upward heat extraction rate the upward/downward heat transfer was about 50/50; by the end of the test it had reduced to about 30/70. The crust thickness may be estimated from

$$\delta = \frac{k \Delta T_c}{q''}$$

where $k \simeq 1 \frac{W}{m \cdot K}$ and ΔT_c = temperature drop across the crust ≃1600 K based on the underside temperature equal to the corium liquidus of ~2000 K and the top surface at T_{sat} = 373 K (nucleate boiling). This thickness is ~3 mm at the 600 kW/m^2 flux, and increases to an equivalent thickness of ~11 mm by the end of the test. The actual crust which was examined after the test (Fig. 4) was ~2 cm thickness in the central region and up to ~5 cm thickness where it was anchored to the electrodes.

Nature displayed a very remarkable phenomenon in this test which was also observed in the later WETCOR and M1 tests. Periodically, there was ejection of molten corium through the bridge crust into the overlying water. In M0 these ejections were driven by release of MCCI decomposition gas such that melt entered the water in a dispersed droplet mode. These droplets were quenched during their flight through the overlying water. They fell back onto the bridge crust and formed a deepening particle bed atop the crust (Fig. 4). By the end of the test this ejected debris had formed a bed about 10 cm in depth of which the top half was loosely packed particles and the lower half was sintered agglomerate approaching the character of the fully dense crust itself. The masses of debris in these two zones amounted to 10.1 and 12.5 kg, respectively. Hence, a corium mass amounting to nearly 20% of the original amount became quenched and coolable by a dispersive mechanism completely separate from the quasi-steady conduction limited heat transfer through the crust.

The times of the discrete eruptions are shown in relation to the quench data in Fig. 2. The events numbered 1 through 5 are visible in the test section video. Events 3 and 4 caused a jump in the quench data amounting to about 22 MJ each. Other events had considerably smaller effects on the quench rate. Events 1b and 1c are not visible on the video but are known to have occurred from correlation with other test data. The power supply current was sensitive to these events,

showing a sharp decrease at the onset of each dispersal; this is interpreted as a loss of conductor (melt) from the electrical path, although other factors may also have played a role. The melt pool temperature appeared to decrease at Events 2, 3, and 4, although this interpretation is not completely consistent for all events.

Each of the dispersive events 1b through 4 correlates perfectly with peaks in the measured gas flowrate data. The flowrate data indicated that up to t = 18 minutes, very little other than the argon dilution gas (82 slpm) passed through the system. There was no indication of the observed Event #1 at t = 15 min. However, events 1b through 4 are clearly evident as peaks in the flowrate curve at t = 20, 29, 38, 53, and 65 min. respectively. The flowmeter data shows that decomposition gas continually flowed through the crust from t = 18 min until termination at t = 84 min, with an exception that the crust appears to have been essentially plugged from Event 1c to Event 2. The data indicates large integrated gas releases attributable to Events 1b, 1c, and 2, but relatively little for Events 3 and 4, and essentially no spike-type release at all for Event 5. To understand the absence of a spike at Event 1 it must be postulated that essentially all the released noncondensable decomposition gas was in the form CO_2 (rather than H_2 and CO). Then a straightforward calculation reveals that the limit of solubility of CO_2 in the available water mass was not reached until about 18 min in the test as the data indicates. After that time the CO_2 passed through the system and was measured by the exit gas flowmeter.

The available quench water was exhausted in this test before the target ablation depth of 12 cm was attained. As a result, the test section experienced dryout at t = 75 min, but the corium internal heat generation continued until t = 85 min. Hence, the final 10 minutes of the test was conducted without water atop the crust/debris layer. Event #5 occurred during this period at t = 81 min. The melt ejection took place through a volcanic-type vent hole in the central region of the test section visible in the quadrant viewed by the video camera. The camera captured visual evidence of melt droplets being ejected through the vent hole as gas was being released. Although the gas release effects were visible, overall, this gas release was trivial compared to earlier events which coincided with large gas flowrate spikes; this event caused no detectable spike. Of particular interest was that the video also showed a single-phase extrusion of

melt; the melt emerged from the hole, ran down the particle bed surface in the field of view, and froze in a manner reminiscent of a lava tube.

Upon M0 disassembly, it was found that the concrete sidewalls had been eroded up to ~5 cm in the region of the original powders and as much as 10 cm in the MCCI zone below (Fig. 4). Thermocouple data indicated that sidewall concrete was being ablated into the corium charge as early t = -48 min and in some places had ablated to 1 cm depth at -35 min. It is estimated that at the onset of basemat ablation, the total corium mass amounted to ~130 kg of which 23% was concrete decomposition products and 4% was metallic Zr. The first available melt temperature data indicated ~2000 K, decreasing to ~1700 K by the end of the test. It is thought that the large influx of concrete from the sidewalls during the preheat stage depressed the melt temperature in this test to the extent that the zirconium (T_m = 2125 K) was not significantly melted. Unmelted rod segments were recovered after the test. Hence Zr oxidation would not have played an important role in this test which explains both the lack of expected agitation during Zr addition (based on L1 experience) as well as gas flowmeter behavior (since H_2 and CO which have very small solubility in water were not produced to any appreciable extent). Hence the actual M0 test conditions actually reflect a fully oxidized PWR corium composition ~30% diluted by concrete decomposition products run at ~2x to 4x prototypic decay heat power level (at 2 hrs into an accident).

To recap, this test showed very large initial heat extraction from the melt pool which may, in fact, have stabilized the pool. Data suggests that basemat erosion may have been temporarily halted and that the bridge crust probably formed during this interval. Data showed the crust was porous to release of offgas, but there is no indication of water ingression into the MCCI zone through the crust in this small scale test. The crust firmly anchored itself to a decomposing sidewall material (concrete) owing to the quenching effect of the water. The test revealed for the first time a heretofore unobserved phenomenon which augmented the heat extraction from the corium; i.e., melt eruption through the crust and particle bed formation atop the crust. The test gave evidence of large swelling of the corium pool into contact with the underside of the crust and associated extrusion of melt out the available passage. In general, however, the MCCI zone ablated away from the anchored crust, and the percentage of heat transferred upward through the crust diminished during the course of the test. At the end

of the test the cavity between the underside of the crust and the collapsed melt surface measured 15 cm. The remaining melt pool was ~12 cm deep. Hence, the void fraction in the melt layer must have increased to 56% to cause contact with the crust and the observed melt extrusion through the crust passage. Examination of the underside of the crust indicated a smooth, frozen surface with a semi-regular wave contour of ~3 cm wavelength and 1-2 cm amplitude.

MACE TEST M1

Following the Scoping Test, the MACE facility was revised to allow larger scale tests of 50 x 50 and 75 x 75 cm size. The test section was constructed of MgO sidewalls rather than concrete to prevent the early concrete dilution of the corium and to avoid the undue suppression of melt temperature experienced in M0. The tungsten electrodes were recessed into the MgO walls. Instrumentation was considerably enhanced, including lance probes to detect the formation of a crust. A 500 kw power supply was installed. For test M1 the test section size was 50 x 50 cm and the corium depth was 25 cm (collapsed pool depth); the corium mass was 430 kg. A mixture of Fe_2O_3 and Zr was blended with the corium charge in order that the chemical reaction would speed the corium preheat stage.

The M1 test was conducted November 25, 1991. Owing to three significant defects, this test did not meet its objectives and is being rerun as M1b. The first difficulty was the presence of an initial overlying crust of corium charge which prevented M1 from achieving its melt-water interaction objectives. Loss of data from one of the 100-channel MUX's as well as anomalous behavior of the high temperature thermocouples prevented satisfactory diagnostics of the L1-type MCCI that did take place. These problems are being addressed for M1b. However, the test does provide information which is worthy of note, and hence some preliminary aspects of the test results are described here. Test conditions are summarized in Table 1; conditions were very similar to the preceding M0 test except for the larger size. The conditions are also very analogous to the ACE L1 MCCI test.

The M1 test ran for 3.0 hours from the onset of basemat ablation until the test was terminated at an ablation depth of 25 cm. The preheat stage temperatures measured between 2200 and 2300 K. The test power ranged from 1x to 2x the desired heat generation rate. The overall average ablation rate was 1.4 mm/min. Figure 5 shows the individual data points which comprise the centerline ablation

history. The data has a peculiar "burst-type" ablation pattern, separated by periods of slower ablation. The "burst-type" ablation behavior depicted in Fig. 5 is not unique but is somewhat more pronounced than observed previously in ACE tests. It had been intended to add water to the test section when the ablation reached 2.5 cm. However, at that time the operators were preoccupied with instrumentation and crust-related issues. When the decision was made to continue the test and to add water, the average ablation depth over the entire basemat was ~8 cm (t = 169 cm). Figure 6 shows the measured heat flux data and integrated energy transport from the test section to the quench tank. The peak heat flux measured about 1.0 MW/m^2 when the water was first added to the test section, referenced to the test section area of 0.25 m^2. However, the heat flux from the corium would have been significantly less since this data has not been corrected for the transient quenching of the sidewalls and structures in the test section. This low heat flux, compared to the corrected values of 3.5 MW/m^2 measured in M0, confirms that water merely contacted the bridge crust of sintered corium powders rather than the corium melt pool beneath it.

Consistent with the M0 results, there were melt eruption events which also occurred during this test. These events are shown in relation to the quench data in Fig. 6. Event 1 occurred at t = 161 min, prior to water addition. Periodic bursts of sparks were visible through the dense aerosol for about 30 seconds. Events 2 and 3 produced visible bursts of sparks in the overlying water lasting for 5 and 1 1/2 minutes, respectively. According to other data, it is probable that unobserved extrusion events also occurred at events labeled 1b and 1c in Fig. 6.

The gas mass spectrometer indicated steady flow of noncondensable concrete decomposition gasses through the system. Prior to water addition the flowrate was ~200 slpm, about 95% H_2 + CO and 5% CO_2. By the end of the test this flow was ~120 slpm, about 80% CO_2 and 20% H_2+ CO. The data clearly shows the progressive oxidation of the metal constituent of the corium. With one exception there were no gas flowrate spikes attributable to the melt eruption events during M1. The preexisting crust of sintered charge material was sufficiently porous to the offgas flow that the melt eruptions could not be said to be blowdown events as was observed in M0. This data indicates that the eruption events cannot be attributed to gas pressurization in the cavity and subsequent breach

of the crust. This is further indication of the inferred periodic volumetric swelling of the corium pool.

The exception alluded to above occurred at Event #1, prior to addition of water. At that time the offgas flowrate peaked at 700 slpm. Note in Fig. 5 that this time coincides with a burst of basemat ablation. According to other data, this occurred globally over a large part of the basemat area. It is interpreted that a burst of concrete erosion occurred rather abruptly at this time, and as a consequence a corresponding burst of decomposition gas was released. The pool level swelled, and melt was ejected above the sintered crust, visible through the dense aerosol.

Figure 7 shows an illustration of the debris configuration remaining after M1. The hatched region contains both the remnants of the original charge which formed the sintered bridge crust plus debris and particles atop the charge from the various eruption events. It was difficult to clearly distinguish these regions during dissection because the entire top region was "cemented" in sediment. The sediment had been left following water boiloff and consisted of released aerosol retained by the overlying water. About 20 kg of such sediment was collected based on preliminary estimate. No water nor sediment were found in the void, indicating that no water penetrated the crust layer after the test. The bottom of the sintered crust had a layer of resolidified melt. Of particular note is that the melt had breached the crust along one wall and left an extruded mass exposed high up along the wall which solidified in place, depicted in Fig. 7. This suggests that the corium pool experienced volumetric swell with sufficient force that it was able to breach the overlying crust and extrude a large mass beyond the crust. Presently, it is not clear when this occurred. It is convenient to imagine that it may have occurred during the Event #1 ablation burst, in which case this mass would have contributed to the initial quench peak in Fig. 6. However, event 1c is also a candidate since this event precipitated a large integrated heat removal which is otherwise difficult to explain.

SUMMARY OF FINDINGS

Both MACE tests M0 and M1 contributed important information to the MCCI and melt coolability data base. Melt-water contact was achieved in M0, but after a period of intense energy removal a bridge crust formed which thereafter separated the

water from the melt zone. Melt-water contact was not achieved in M1 owing to presence of a bridge crust as an initial condition. Key findings are summarized as follows:

1) The melt-water interaction stage of M0 was very vigorous, removed heat from the melt pool at 3.5 MW/m^2 for about three minutes, and extracted an amount of energy greater than the heat of solidification of the entire melt mass. There was no steam explosion.

2) M0 data suggests that basemat erosion was temporarily halted following the initial aggressive quench period.

3) A bridge crust was formed which anchored to the test section sidewalls and prevented water ingression into the corium zone. This would not be expected at reactor scale. The crust was sufficiently porous to permit upward passage of concrete decomposition gasses.

4) Both tests M0 and M1 showed evidence of periodic occurrence of large pool swelling. The pool swelled to contact the underside of the crust and additionally caused extrusion of melt above the crust (eruption when accompanied by gas release/blowdown effects). This significantly augmented the corium quench process and depleted the remaining corium mass interacting with the concrete. The dispersed debris ranged from particles (which formed a particle bed atop the crust) to a large extruded mass. The corium pool void fraction increased to as high as 56% in M0 to account for this extrusion.

5) The upward heat flux after crust formation in M0 amounted to 600 kW/m^2 which gradually diminished to ~150 kW/m^2 as the extruded/dispersed mass grew in depth atop the crust.

6) Test M1 showed evidence of "ablation bursts" early in the test while appreciable metal remained in the corium composition.

7) Test M1 demonstrated the effectiveness of the overlying water to trap released aerosol.

It is premature to attempt to draw conclusions on melt coolability pertaining to the reactor system from the M0 and M1 tests. Their value lies first in guiding model development as regards the stages of cooling, crust formation, and pool swell effects. Secondly, these tests are stepping stones to improved tests addressing melt cooling phenomena.

ACKNOWLEDGEMENT

This work is performed under sponsorship of the Advanced Containment Experiments (ACE) international consortium organized by Electric Power Research Institute. The ERPI program manager is B. R. Seghal. The data is the property of the ACE Consortium, and the authors acknowledge their permission to release the information contained herein. The authors acknowledge the important contributions to the experiments by D. Bromberek, A. Kras, E. Pozzie, and J. Weber. The manuscript was prepared for publication by Ms. L. Ondracek.

REFERENCES

1. B. R. Seghal and B. W. Spencer, "ACE Program Phase C: Fission Product Release from Molten Corium-Concrete Interactions (MCCI)," submitted to OECD CSNI Specialist Meeting on Core Debris Concrete Interactions, Karlsruhe, Germany, April 1-3, 1992.

2. B. R. Seghal and B. W. Spencer, "ACE Program Phase D: Melt Attack and Coolability Experiment (MACE) Program," submitted to OECD CSNI Specialist Meeting on Core Debris Concrete Interactions, Karlsruhe, Germany, April 1-3, 1992.

3. J. J. Sienicki and B. W. Spencer, "The Jet Impingement Stage of Molten Core-Concrete Interactions," OECD CSNI Specialist Meeting on Core Debris/Concrete Interactions, Palo Alto, CA, September 3-5, 1986.

4. R. E. Blose, et. al., "Sustained Heated Metallic Melt/Concrete Interactions with Overlying Water Pools," NUREG/CR-4727, July 1987.

5. M. T. Farmer, et. al., "Modeling and Database for Melt-Water Interfacial Heat Transfer," submitted to OECD CSNI Specialist Meeting on Core Debris Concrete Interactions, Karlsruhe, Germany, April 1-3, 1992.

6. M. F. Roche, Argonne National Laboratory, private communication, November 1990.

7. M. L. Corradini and R. L. Engelstad, University of Wisconsin/Madison, private communication, January 1992.

Table 1. Specifications for MACE Test M1b

		M0	M1
Test Section Dimensions		30 x 30 cm	50 x 50 cm
Pressure, MPa absolute		0.1 (nominal)	0.1 (nominal)
Corium Mass, Kg		130	430
Collapsed Pool Depth, cm		15	25
Corium Type		PWR; Zr 70% oxidized	PWR; Zr 70% oxidized
Corium Composition at Onset of Ablation (Mass %)	UO_2	73 (56)	292 (68)
	ZrO_2	14 (11)	58 (13)
	Zr	5 (4)	19 (4)
	Fe	0	21 (50
	SiO_2	4 (3)	0
	CaO	4 (3)	31 (7)
	Conc	30 (23)	10 (3)
Initial Melt Temperature, K		2000 (est)	2300 (est)
Specific Power, Watts/kg UO_2 (actual)		350 (2x - 4x actual)	350 (1x - 2x actual)
Basemat Type		Limestone/Common Sand	Limestone/Common Sand
Basemat Height, cm		35	50
Ablation Depth at Water Addition, cm		1.2 cm	2.5 cm (8.0 cm actual)
Water Addition Rate, liter/second		10	2 (equivalent to 18 MW/m^2)
Water Collapsed Depth, cm		50	50
Water Makeup Rate, liter/second		10	2
Temperature of Added Water, K		296	296
DEH Power Operating Mode		Constant voltage	Constant voltage

Figure 1. Illustration of MACE Experiment Apparatus

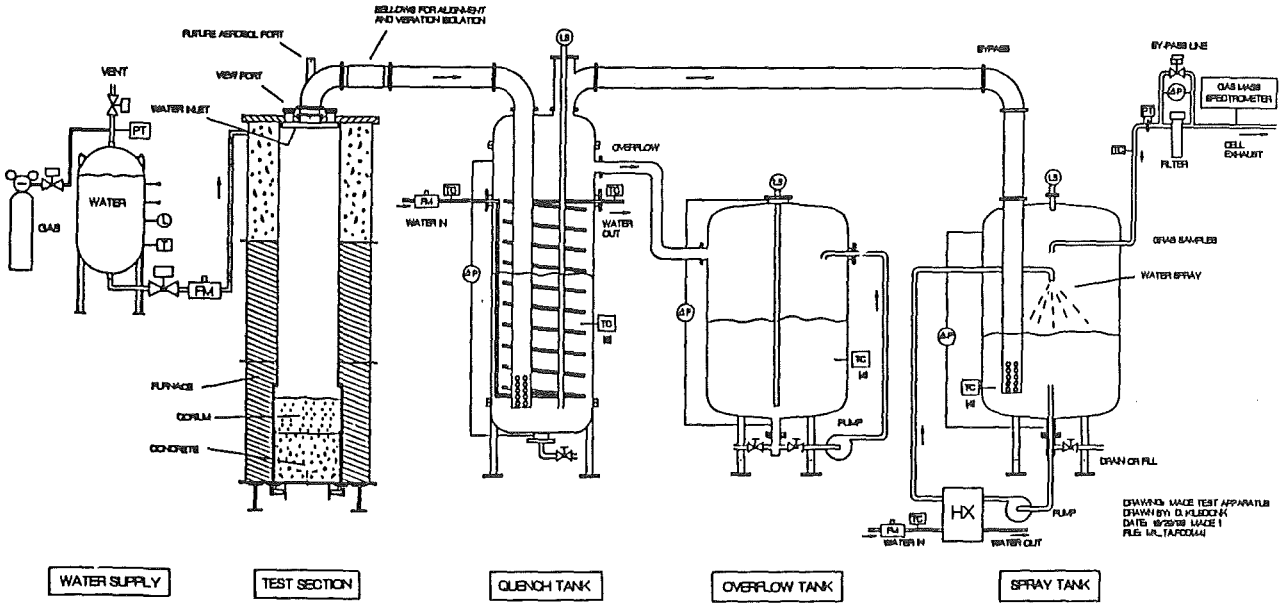

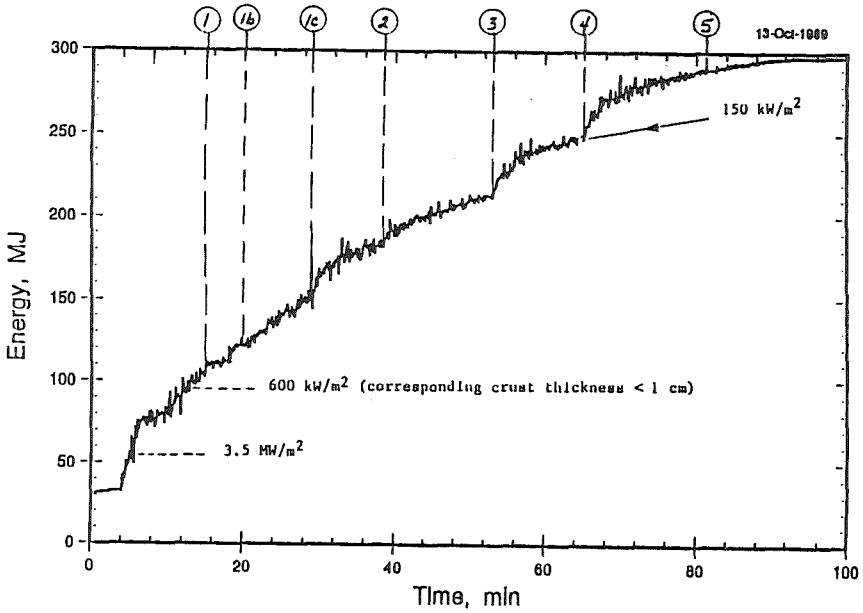

Figure 2. M0 Upward Heat Removal from Melt Pool

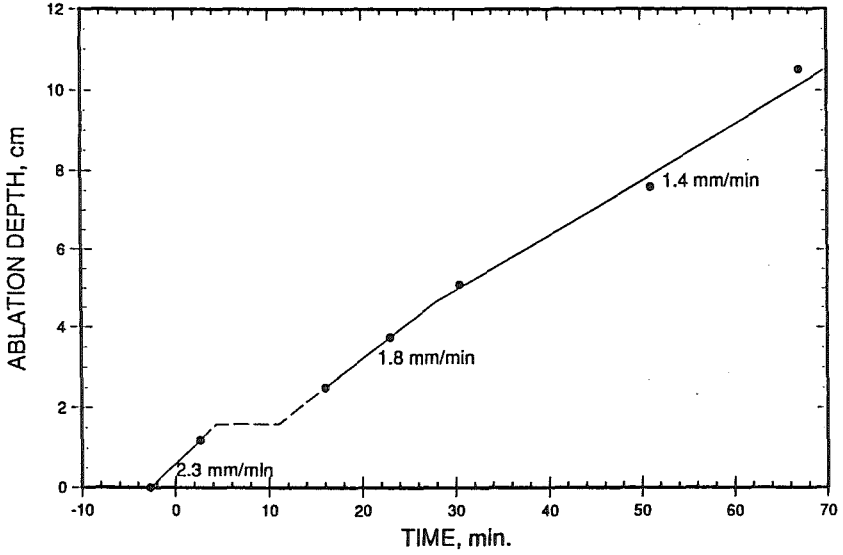

Figure 3. M0 Centerline Ablation Data

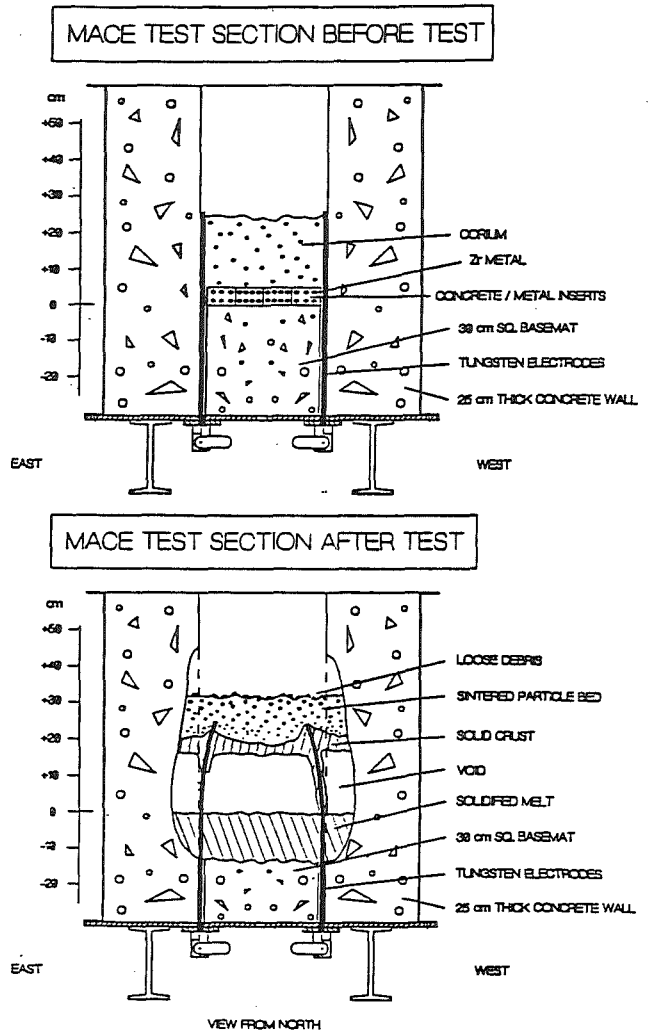

Figure 4. Illustration of M0 Test Section

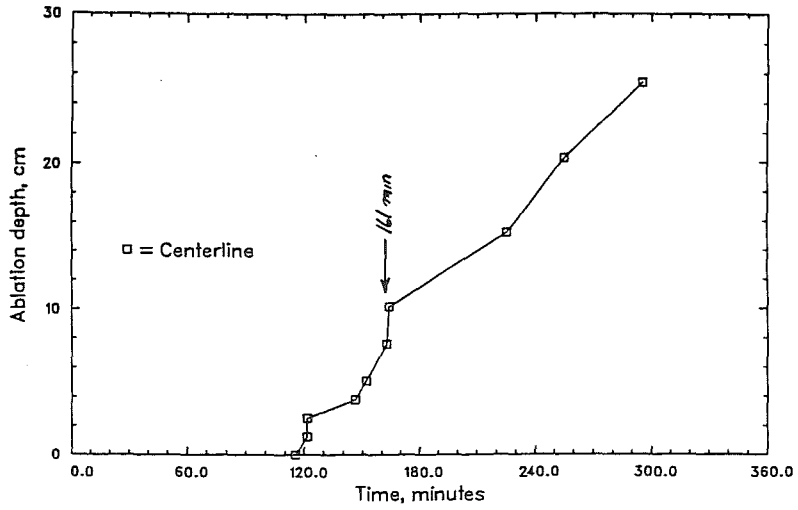

Figure 5. M1 Centerline Ablation Data

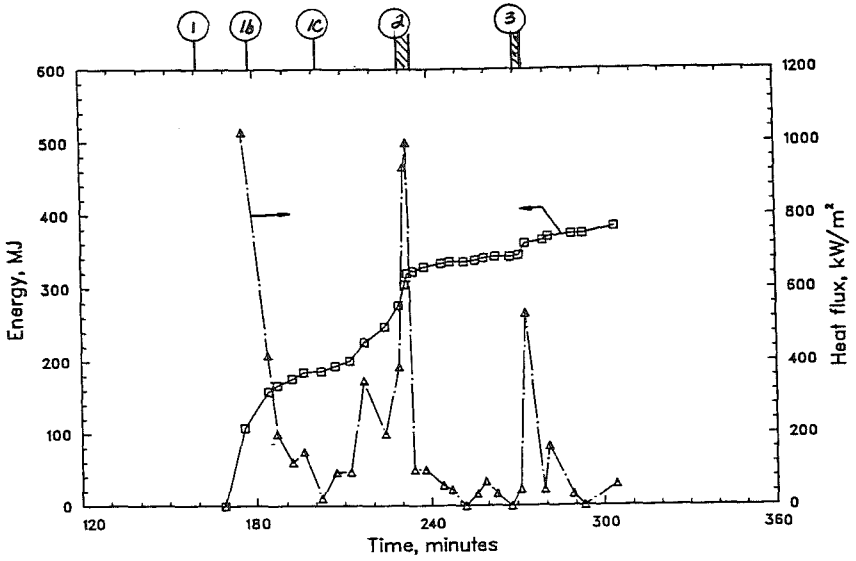

Figure 6. M1 Uncorrected Quench Rate Data

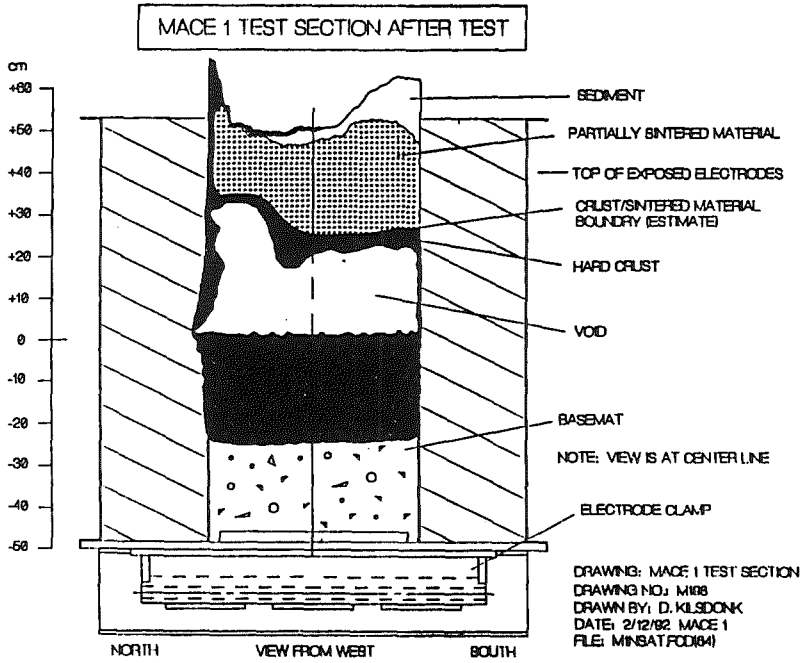

Figure 7. Illustration of M1 Posttest Debris Configuration

CORE-CONCRETE INTERACTIONS WITH OVERLYING WATER POOLS

E. R. Copus
Sandia National Laboratories
Albuquerque, New Mexico

ABSTRACT

An inductively heated experiment, WETCOR-1, was executed as part of the NRC research program to study and evaluate core debris coolability by overlying water pools. A 34 kg charge material of Al_2O_3 - CaO was heated to melting at 1850K within a 32 cm diameter tungsten annulus heated to 2100K. Ablation of a limestone/common sand concrete basemat was allowed to begin and water at 293K was then added continuously at 60 liters per minute. Both power and water flow were terminated after a 30 minute test period. The main observations from the WETCOR-1 test were that there was an initial period of vigorous melt-water interaction which lasted for 1-2 minutes and was replaced by a relatively stable crust-water geometry with substantially reduced rates of energy transfer to the overlying water. These rates of energy transfer were insufficient to either quench the melt or to discontinue the pre-established meltpool-concrete ablation process.

INTRODUCTION

One of the most important phenomenological issues in the progression of severe accidents after the reactor vessel has failed is whether or not the plant can be brought to a stable condition which avoids the threat to containment integrity, whether by basemat penetration or by containment pressurization. The most commonly available mechanism for removing heat from discharged melt in LWR containments is water addition. The DOE, industry, and the NRC are all now working to develop and evaluate design criteria to address core debris coolability by water pools (Fauske, 1990). The WETCOR experimental program being performed at Sandia National Laboratories is part of the NRC effort to address this issue which is identified as issue L5 under the revised Severe Accident Research Plan. These tests are intended to compliment and augment the ACE/MACE program sponsored by EPRI. Technically, the NRC approach will differ from the

basic approach in the MACE tests (Spencer, 1991) by including heating of the experiment perimeter to reduce crust attachment and support and thus promote conditions which might lead to bulk freezing. This is accomplished by inductively heating a 32 cm diameter tungsten annulus which is filled with molten oxide mixtures of Al_2O_3, ZrO_2, CaO, and SiO_2 at temperatures of 1800-2400K and then pumping subcooled water onto the melt.

The WETCOR tests are designed to answer two additional questions: These are (1) Is oxidic debris more or less coolable than the metallic debris studied in the SWISS test series? (Blose, 1987) (2) What are the limits of coolability in terms of the debris depth, the debris power, and the debris composition? (Tarbell, 1987) WETCOR-1 was performed using a different oxidic debris type and under different boundary conditions than either the SWISS tests or the MACE tests in order to focus on the first question. The remaining WETCOR tests will focus on conditions which will address the second question.

WETCOR-1 TEST

The test goals were to observe and record the initial simultaneous interactions among molten oxide debris, a concrete basemat, and an overlying water pool. The charge materials for the test were 34 kg of an oxide powder mixture composed of 80 w/o Al_2O_3 - 15 w/o CaO - 4 w/o SiO_2 - 1 w/o Fe_2O_3 with a density of 2.54 g/cm^3 (75% dense). The concrete material for the test was limestone/common sand with a density of 2.34 g/cm^3 and a composition of 36 w/o SiO_2 - 32 w/o CaO - 22 w/o CO_2 (as $CaCO_3$) - 5 w/o H_2O. The test procedure was to heat and melt the charge at 1850K, hold a tungsten wall temperature of 2100K, allow 2 cm of ablation to establish the concrete interaction, and then add water at 60 lpm. The water addition was continued for thirty minutes before the experiment was terminated by turning off the input power.

A schematic diagram for the WETCOR test apparatus is shown in Figure 1. Overall crucible dimensions were 60 cm in diameter and 100 cm in height. The inner tungsten sleeves contained the charge material and had an inside diameter of 32 cm, a height of 18 cm, and a thickness of two centimeters. The concrete basemat was 40 cm in diameter and 40 cm deep. This entire apparatus was contained in a stainless steel vessel which was continuously

purged with air at a rate of 1500 liters per minute and vented through a gravel filter so as to dilute and contain all of the aerosol effluents. Instrumentation for the test was designed to measure the debris temperature, the crucible sidewall temperatures, the heat flux to the overlying water pool, the concrete ablation rate, the approximate gas release rates and composition, and the approximate aerosol release rates and compositions. In addition, there was video coverage of the meltpool surface so that the initial debris-water interactions could be observed.

OBSERVATIONS

The main purpose for performing the WETCOR-1 test was to ascertain whether or not melt-coolant interactions were unstable for extended times during the initial interaction period. Long-lived instabilities might allow for extended periods of very high rates of heat transfer which would result in relatively rapid bulk freezing with very little interaction with the concrete basemat. Effort was made in the design and execution of the WETCOR-1 experiment to extend the time for unstable melt-coolant interaction and thus promote a bulk quenching process. This included the use of heated tungsten sidewalls to reduce heat flux-limiting crusts, the use of oxide materials with relatively high specific heats to maximize melt surface temperatures, and the use of a concrete basemat with an established high gas production rate to increase gas sparging, melt mixing, and crust breakup. In addition, the power input to the melt was held to relatively low levels and the meltpool height was relatively shallow.

The main observations from the WETCOR-1 test were that prior to water addition there were floating crust islands on top of the melt which slowly joined to form a bridging structure. Increased power to the melt removed these crusts and established a sparged meltpool. Water was then added to the interaction. Immediately after water addition there was an initial period of vigorous melt-water instability but this period only lasted for 1-2 minutes. This was replaced with a relatively stable crust-water geometry with substantially reduced rates of energy transferred to the overlying water.

Preliminary results for the major measured parameters are shown in the attached figures and table. These parameters are:

Net Induction Power and Water Flow (Figure 2)
Concrete Response and Ablation (Figures 3-6)
Meltpool Temperature (Figure 7)
Water Pool Temperatures (Figure 8)
Tungsten and MgO Thermal Response (Figures 9 & 10)
Aerosol Mass Concentrations (Table 1)

Net Induction Power and Water Flow (Figure 2)

At 522 minutes into the test the power was increased to extend the melt zone and remove any overlying crusts. The net power to the tungsten sleeves is calculated at 8-10% of the gross power or 16-20 kW. This power level was below our initial target level of 30 kW. Pretest predictions would estimate that only one-half to one-third of the net power would be absorbed by the meltpool with the remainder being absorbed by the MgO sidewalls and concrete basemat. Hence, a net power of 30 kW would yield 10-15 kW to the 30-40 kg meltpool or roughly .33 W/g. This relative distribution of input power is changed when the melt slumps and again when water is added. For the actual WETCOR-1 conditions, the net power to the melt was not a constant value since the geometry and temperature were not fixed. We estimate the range of effective power to the melt at 7-12 kW or roughly 0.2-0.3 W/g.

Water was added to the crucible at 528 minutes and was sustained for over an hour. The power was maintained at 200 kW with a 30-second pause at 538 minutes and then turned off at 556 minutes, essentially terminating the test. There was a brief period (556-562) where water flow was temporarily halted so that the water heatup rate for a fixed volume could be observed. Flow rates for the principal period of interest, (528-556) were 60 lpm.

Concrete Response and Ablation (Figures 3-6)

The concrete began to heat early in the test but did not reach ablation temperature until after 400 minutes. At the start of the principal period of interest (528-556) there was approximately 3 cm of existing ablation at the centerline of the concrete basemat, zero erosion at the mid-radius of the concrete basemat, and 2 cm at the far radius of the concrete basemat.

At the end of the water-power period (556), the erosion front was very uniform at a depth of 5-6 cm in all locations. [Thermocouple failures indicate the position of the erosion front and temperature in excess of 1380°C, these are indicated by vertical off-scale lines on Figures 2-5]. All ablation stops when power is removed at 556 minutes. The ablation rate appears fairly constant during the interaction period at a rate of 6-10 cm/hr.

Meltpool Temperatures (Figure 7)

Five thermocouple plots are overlaid to establish the meltpool temperature history. All five confirm the initial pool temperature of 1550-1580°C at 528 minutes and two confirm the final pool temperature of 1580 at 556 minutes when power is removed. The best measure of pool temperature in the interaction interval is at the 4 cm elevation. This is in the approximate center of the pool which extends from -5 cm to +15 cm. [-5 cm corresponds to 5 cm below the original concrete interface]. Pool temperatures hold constant and may even increase slightly during the interaction period (528-556) at the +4 cm elevation. After the power is removed at 556 minutes, uniform pool cooling is indicated by the +4, -4, and +8 cm thermocouples at a rate of 15°C/min.

Waterpool Temperatures (Figure 8)

Water is added to the crucible at 528 minutes and fills the crucible in approximately 30 seconds. The initial water exit temperature is 92°C. This falls to 40°C after 8 minutes and to 36°C after 28 minutes. There are no appreciable temperature spikes or other indications of high magnitude, short-term energy transfer periods. The water flow is halted at 556 minutes resulting in a pool temperature increase of 60°C between 556-563 minutes, flow is then restored and the exit temperature drops to 25°C in 8 minutes. The energy transfer rates to the water are 300 kJ/sec at 528 minutes and 60 kJ/sec at 556 minutes. These rates must be split among three principal energy sources -- the meltpool which has an approximate heat transfer surface area of 750 cm^2 and a mass of 40 kg; the tungsten sleeves with a heat transfer surface area of 500 cm^2 and a mass of 70 kg; and the MgO crucible walls with a surface area of 1800 cm^2 and a mass of 150 kg. Our current estimate is that 1/3 to 1/2 of the energy loss can be attributed to the meltpool surface resulting in heat transfer rates of 1.5 MW/m^2 initially which fall to 0.4 MW/m^2 after 10-15 minutes.

Tungsten and MgO Thermal Response (Figures 9 & 10)

The tungsten thermocouples fail due to high temperature overload at times after 300 minutes. There are, however, thermocouples located in the MgO at 1.5 and 3.0 cm which can be used to reasonably estimate the tungsten thermal response. The estimated tungsten temperatures at 528 minutes when water was added are 1800 ±50°C. MgO wall temperatures at 528 minutes are 900-400°C. Both the MgO and the tungsten cool quickly when water is added, starting at the top of the crucible and proceeding downward in an axial direction. The +35 elevation in the MgO cools rapidly after 530 minutes and is cooled to 25°C at 540 minutes. The MgO +20 cm location begins to cool rapidly after 535 minutes but at a slower rate. The MgO/tungsten at the +10 cm location begins to cool rapidly after 540 minutes again at a slower rate. The MgO at the concrete interface continues to heat during the interaction period and does not begin to cool until after power is terminated at 560 minutes. The MgO/tungsten materials in the upper crucible are a significant energy source throughout the interaction period due to their mass and temperature and are estimated to contribute at least half of the total energy released to the flowing water pool. The MgO materials below the concrete interface are unaffected by water addition and are sources for energy losses along with the concrete basemat materials.

Aerosol Mass Concentrations (Table 1)

A total of twenty-two aerosol filter samples were taken in WETCOR-1. The five samples taken before water addition at 528 minutes have an average concentration of 1.0 g/m^3. Samples taken after water was added are progressively less dense and the last samples taken just before power was shut down at 556 minutes have an average concentration of 0.2 g/m^3. This would indicate a decontamination factor of at least 5. No fission product simulants were included in the charge material so that the chemical composition of these aerosols should be limited to concrete decomposition products.

CONCLUSIONS AND FUTURE WORK

The main purpose for performing the WETCOR-1 Test was to ascertain whether or not melt-coolant interactions were unstable for extended periods during the initial interaction period. Extended instabilities might allow for

extended periods of very high rates of heat transfer which would result in relatively rapid bulk freezing with very little interaction with the concrete basemat. Extra effort was made in the design and execution of the WETCOR-1 experiment to extend the time for unstable melt-coolant interaction. This included the use of tungsten sidewalls which were heated to temperatures well in excess of the freezing point for the molten pool, the use of slowly freezing oxide materials with relatively high specific heats of 1.3 J/g-K as compared to 0.4 J/g-K for UO_2, and the use of a concrete basemat with an established high gas production rate. In addition, the power input to the melt was held to relatively low levels and the meltpool height was relatively shallow. The main observations from the WETCOR-1 Test were that there was indeed an initial period of vigorous melt-water instability but that this period only lasted for 1-2 minutes and was replaced with a relatively stable crust-water geometry with substantially reduced rates of energy transfer to the overlying water. These rates of energy transfer were insufficient to either quench the melt or to discontinue the pre-established meltpool-concrete ablation process.

The total energy to the overlying water pool was quantified by measuring the temperature rise in a water supply which was flowing constantly at 60 liters per minute. Initial energy removal rates were 300 kJ/s. These rates steadily dropped to 60 kJ/s after a few minutes and then were relatively constant for the remainder of the test. This total energy must be partitioned among the crucible wall surface area, the tungsten surface area and the meltpool surface area to obtain heat flux information. A quantitative estimate of the energy transfer rates from the debris surface to the water pool is 1.5 MW/m^2 initially with an exponential drop to .4 MW/m^2 at 8-10 minutes and times thereafter.

A comparison of the WETCOR-1 result to previous experiments and analysis indicates that no new dominant phenomena have been identified and that these results are comparable to those for the FRAG, SWISS, and MACE tests. In each of these previous tests there have been only short periods of high energy release, the concrete ablation process has continued, and stable crusts have formed which limited the upward heat flux to .3-.8 MW/m^2. None of these tests have defined the regime of coolability where the debris is solidified, all ablation is stopped, and the water pool is able to remove the decay heat power.

Our next goal is to analyze the extensive data return from the WETCOR-1 test and to compare these results to the data return from the MACE program sponsored by EPRI. Future WETCOR tests will be designed to focus on defining and bounding the limit of debris coolability by varying the debris depth, the debris power, and the debris composition.

REFERENCES:

R.E. Blose, J.E. Gronager, A.J. Su-Antilla, and J.E. Brockmann, "SWISS: Sustained Heated Metallic Melt/Concrete Interactions with Overlying Water Pools", NUREG/CR-4727, SAND85-1546, Sandia National Laboratories, Albuquerque, N.M., 1987

W.W. Tarbell, D.R. Bradley, R.E. Blose, et al., "Sustained Concrete Attack by Low Temperature, Fragmented Core Debris", NUREG/CR-3024, SAND82-2476, Sandia National Laboratories, Albuquerque, N.M., 1987

B.W. Spencer, M. Fischer, M.T. Farmer, and D.R. Armstrong, "MACE Scoping Test Data Report", MACE-TR-D03, Argonne National Laboratory, Argonne, IL., 1991

Fauske and Associates, "Technical Support for the Debris Coolability Requirements for Advanced Light Water Reactors in the Utility/EPRI Light Water Reactor Requirements Document", DOE/ID-10278, June 1990

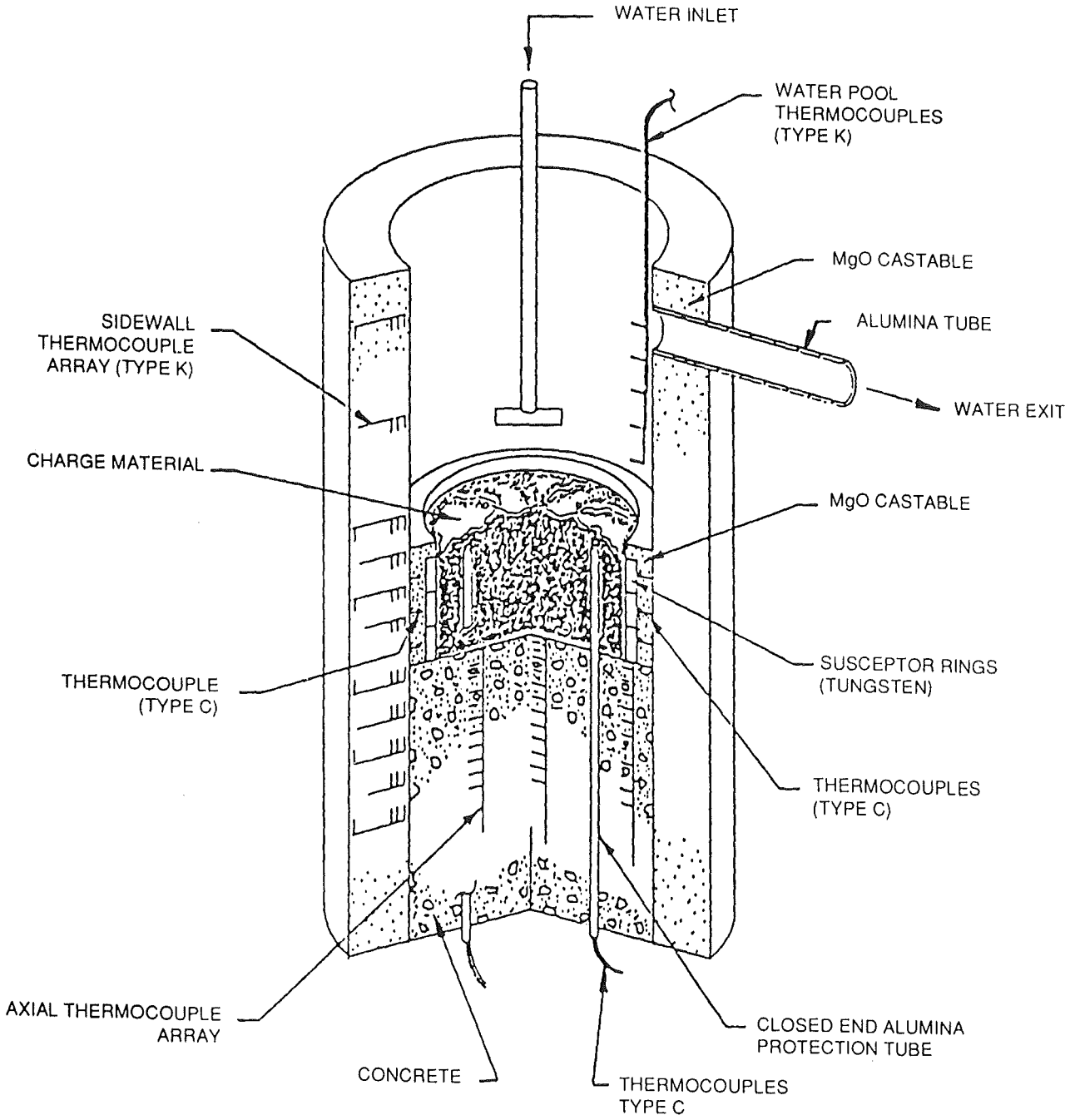

Figure 1. Interaction Crucible with Imbedded Instrumentation and Charge Installed

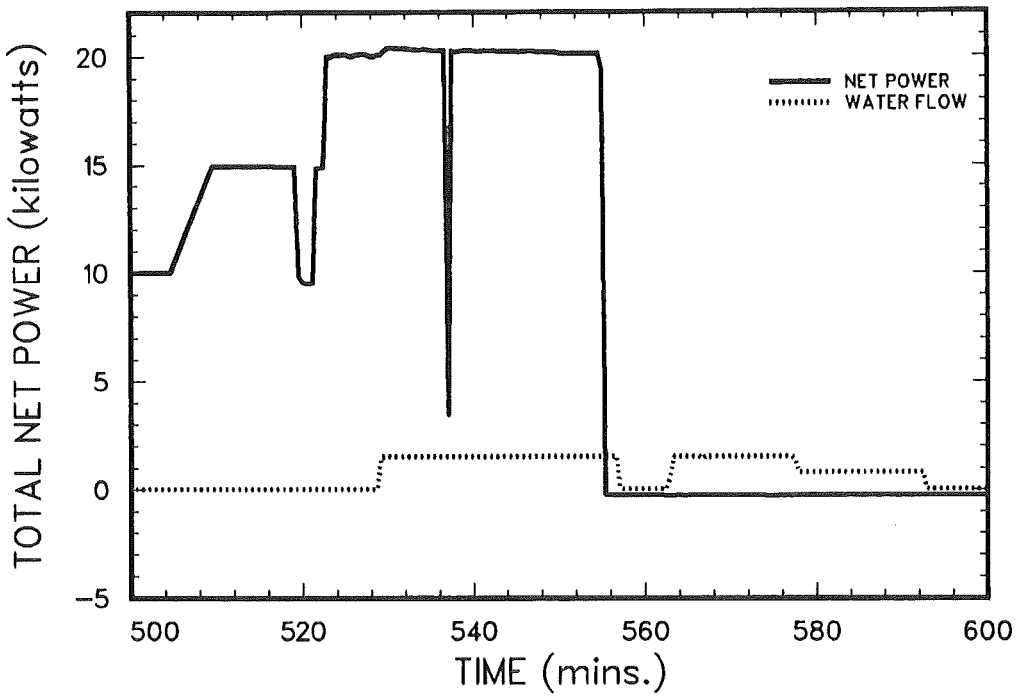

Figure 2. Net Power and Water Input Rates

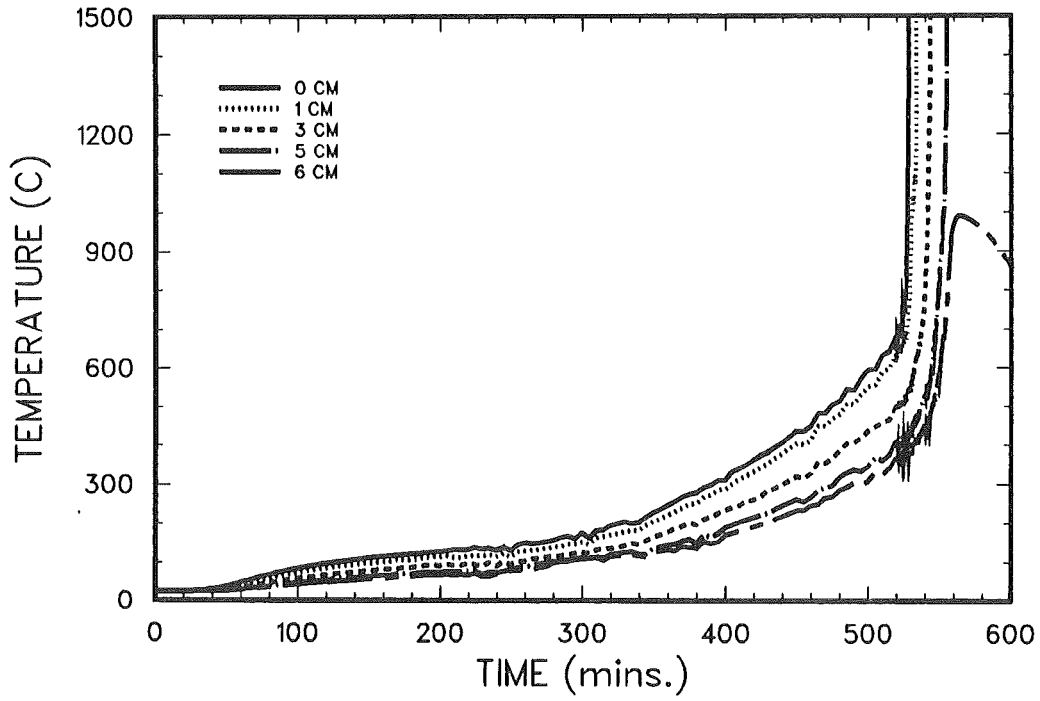

Figure 3. Overall Midradius Concrete Response at 5 Concrete Depths (0-6 cm)

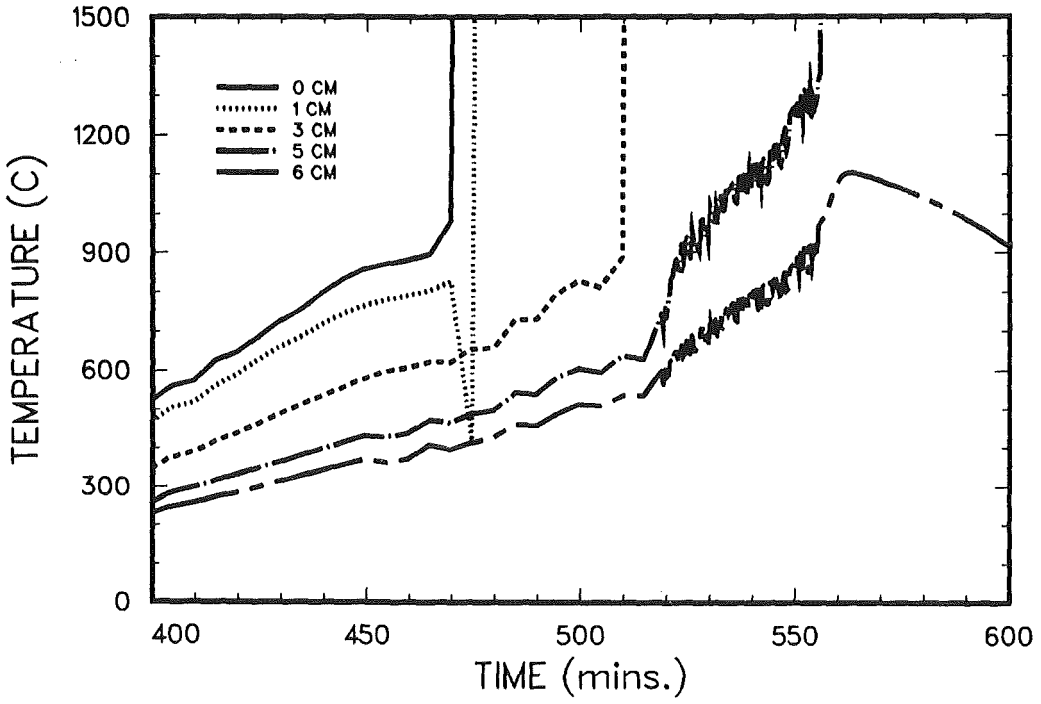

Figure 4. Centerline Concrete Response at 5 Concrete Depths (0-6 cm)

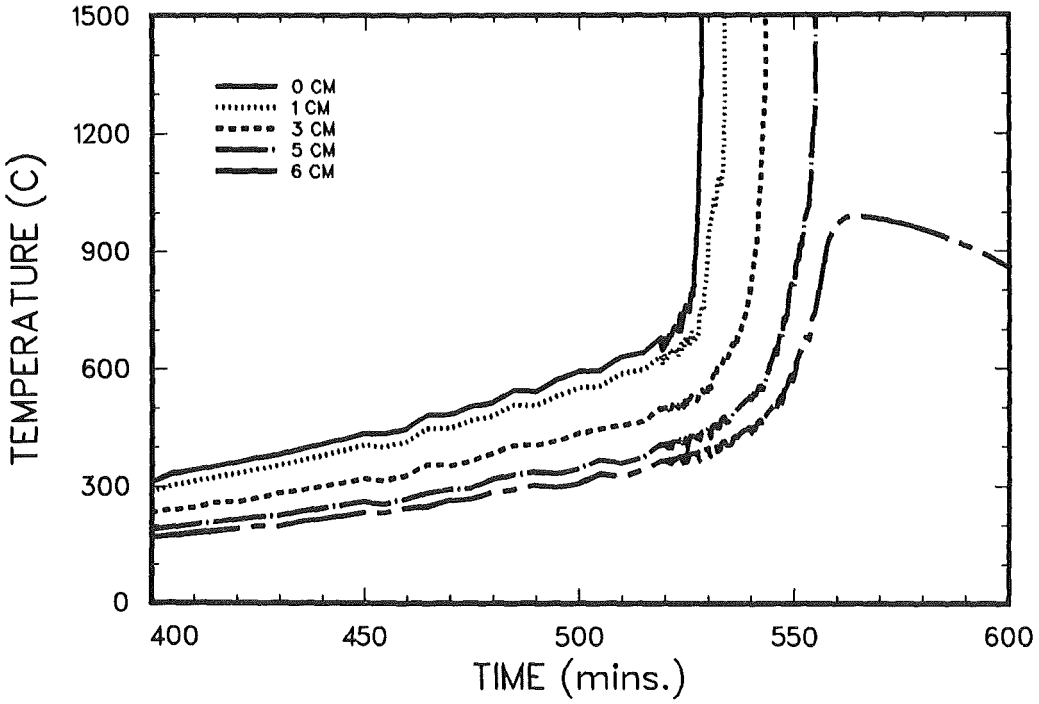

Figure 5. Midradius Concrete Response at 5 Concrete Depths (0-6 cm)

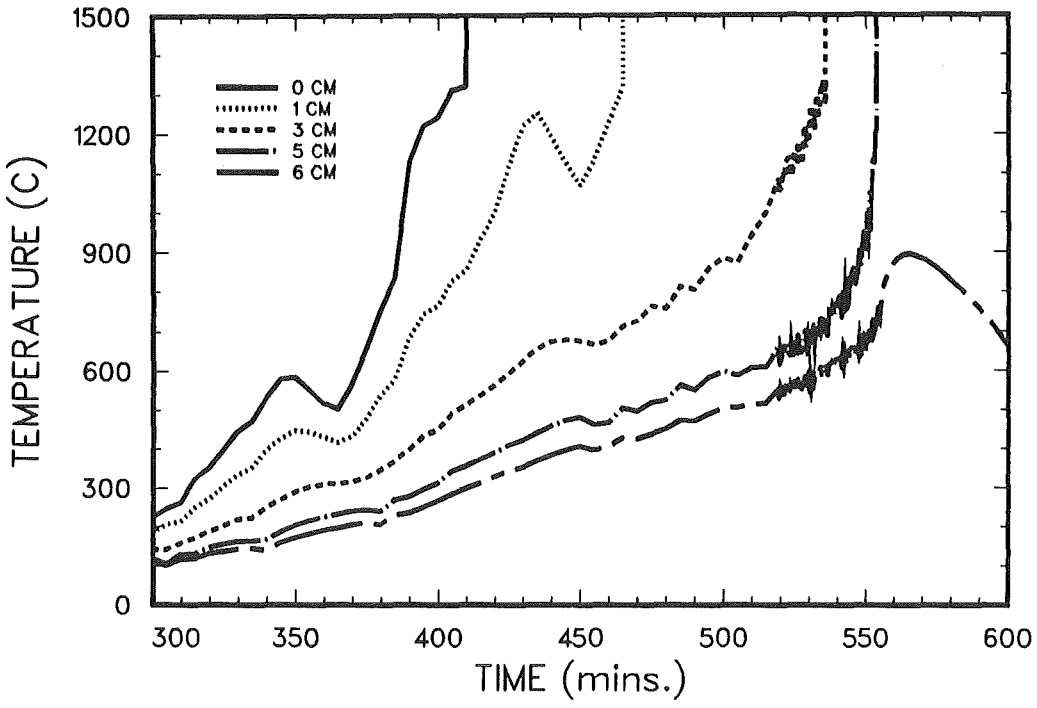

Figure 6. Outer Radius Concrete Response for 5 Concrete Depths (0-6 cm)

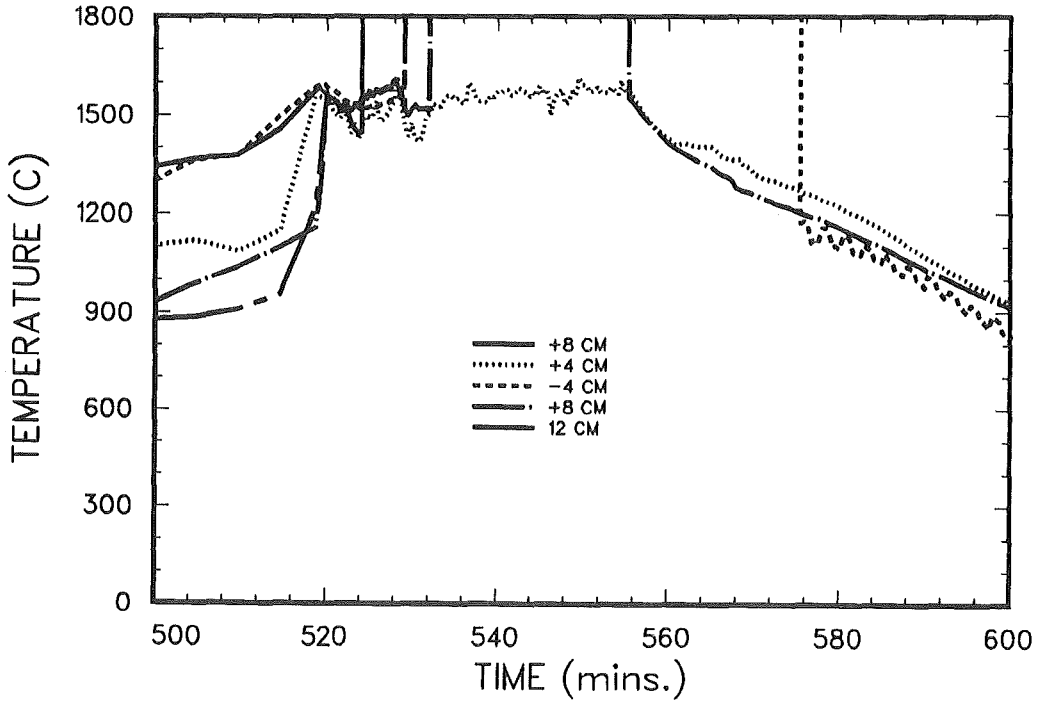

Figure 7. Meltpool Temperatures at 5 Axial Locations (-4 to 12 cm). There are Two Radial Locations for the +8 cm Depth. Total Pool Depth was from -5 to +15 cm.

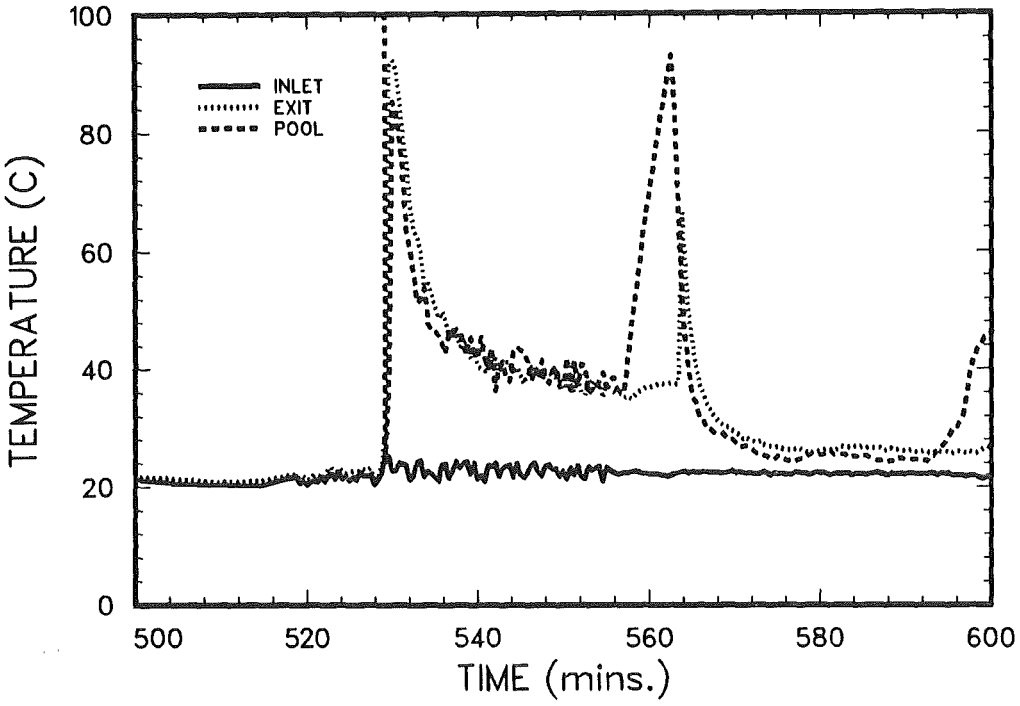

Figure 8. Water Pool Temperature

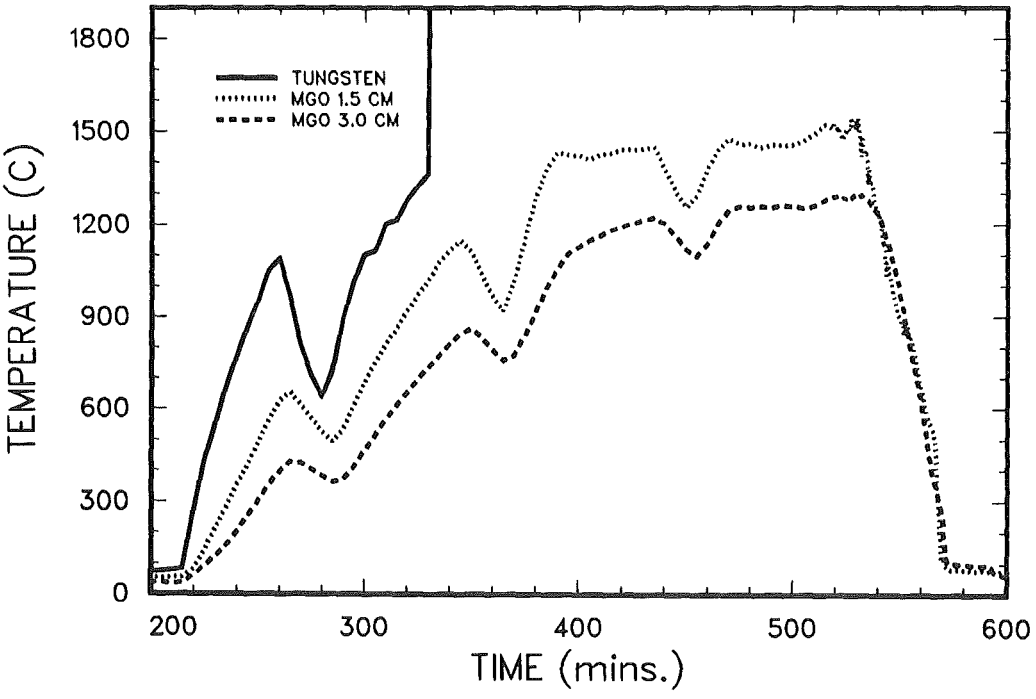

Figure 9. Tungsten and MgO Wall Temperature. MgO Profiles are at 1.5 cm and 3.0 cm Radial Distance from the Tungsten Sleeves.

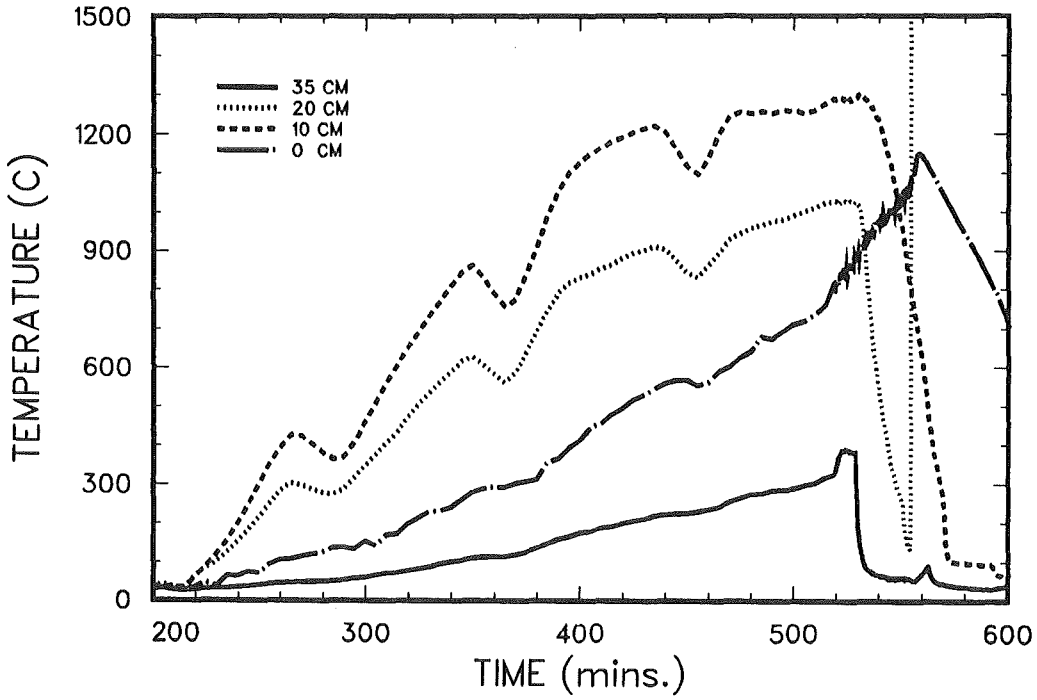

Figure 10: MgO Wall Temperature at Axial Locations (0-35 cm).

TABLE 1 - WETCOR-1 Aerosol Data

Filter Sample	On Time (min)	Duration (min)	Total Mass(g)	Mass Concentration(g/m^3)
1	520.7	1.0	0.00278	1.74
2	522.7	1.0	0.00137	0.86
3	524.7	1.0	0.00126	0.79
4	526.7	1.0	0.00536	0.50
5	528.7	1.0	0.01156	1.08
6	530.7	1.0	0.00339	0.32
7	532.7	1.0	0.00356	0.33
8	534.7	1.0	0.00306	0.29
9	536.7	1.0	0.00262	0.24
10	538.7	1.0	0.00353	0.33
11	547.3	1.0	0.00156	0.15
12	549.4	2.0	0.00389	0.36
A	552.4	2.0	0.00291	0.27
B	555.7	2.0	0.00213	0.20
C	557.7	2.0	0.00131	0.12
D	560.1	2.0	0.00063	0.06
E	562.4	2.0	0.00214	0.20
F	565.6	2.0	0.00401	0.37
G	567.9	2.0	0.00119	0.11
H	570.1	2.0	0.00108	0.10
I	572.4	2.0	0.00159	0.15

A Core Catcher Concept Based on Fragmentation of Melts

W. Tromm, H. Alsmeyer, H. Schneider
Kernforschungszentrum Karlsruhe GmbH
W - 7500 Karlsruhe 1, Germany

Abstract

A core catcher concept is proposed to be integrated into a new PWR design. The core catcher is designed to cope with high pressure and low pressure core melt scenarios and achieves coolability by spreading and fragmentation of the ex-vessel core melt. Direct water contact converts the decay heat to steam where the reflux of the steam condensate from the containment establishes a self-circulating steam/water flow. Prototypic transient experiments demonstrated the feasibility of the coolant concept which achieved early quenching and coolability by flooding the melt with water from the bottom. Further experiments are presently on the way to visualize the fragmentation process.

Introduction

An advanced containment design for a PWR concept has been proposed by KfK and Uni KA based on the standard German PWR design. One important feature of this new containment is the integration of a core catcher to cope with core material after penetration of the lower pressure vessel head under all conceivable severe accident conditions:

- Energetic failure as a consequence of an in-vessel steam explosion or a high pressure core melt down sequence with thermal melt attack of the lower pressure vessel head.
- Melt formation in the RPV during low pressure accidents causing drop of the lower RPV head or formation of smaller penetrations in the head with fast or prolonged release of melt.

The requirements for the core-catcher are:

- Safe enclosure of the ex-vessel corium in a predefined location in order to exclude penetration of the basemat and attack of important structures.
- Removal of decay heat which corresponds to a decay heat level of initially 25 MW and 10 MW in the long term for a 1300 MW_{el} reactor.

In this context it is important to consider the behaviour of the less volatile fission products which are still dissolved in the melt at time of the accident. They only will remain in the core material if the long-term temperature of the corium is low enough; i.e. considerably below 2000 K, to exclude vaporization release over a long period of time. This imposes a more specific cooling condition on heat extraction from the core material:

Heat removal from the corium can only be considered successfully when besides the necessary decay heat removal the highest temperatures in the bulk of the material are below the vaporization temperatures of fission products.

Complete solidification of the core material is therefore a goal we want to achieve. Consequently, heat extraction from the surfaces of large continuous melt volumes is not sufficient, because the central temperature could easily exceed several thousand Kelvin due to the poor conductive and convective heat transfer processes in the melt under natural convective internal flow.

Simple heat conduction calculations with internal heat sources show that the characteristic size of the corium layer or fragments should be on the order of 10 to 20 cm, if the oxidic melt is not diluted by sacrificial material. Then, complete freezing of the melt can occur with a long-term inclusion of the fission products. Therefore, the formation of a flat layer and/or fragmentation of the corium is one of the design principles of the proposed core catcher.

The core catcher must be able to handle 200 tons of melt from the pressure vessel, typically 120 tons of oxides and 80 tons of metal including 20 tons of metallic zircaloy. Special attention must be given to the behaviour of metallic zirconium because of its high chemical affinity to oxygen and its potential of dissolving steel by formation of low temperature eutectics. The initial temperature of the melt may be up to 2800 K.

Description of the Core Catcher

The most demanding RPV failure mode is the steam explosion sequence which may result in downward directed mechanical energies of the lower head of 1 GJ. To absorb this energy, a massive grid of heavily reinforced concrete is placed under the RPV which protects the lower core catcher surface from extreme mechanical loads (Fig. 1). The grid allows penetration of melts and smaller structures, but shall retain big and heavy fragments. The height of the grid can be designed according to the energy to be absorbed.

Depressurization of the RPV after lower head failure could result in transient pressure built-up in the cavity which is designed for static pressures of up to 30 bars. The pressure release ducts are situated in the upper part of the RPV shield to retain fragmented core material predominantly in the central part and to avoid the direct containment heating scenario. Inner high temperature isolation will exclude thermal attack of the concrete structures in the upper part.

The height of the lower cavity is mainly determined from the mechanical loads which are acting on the RPV support structures during energetic RPV failure and must finally be sustained by the lower plant foundation. It turns out, that also under the aspects of cavity volume and supply of coolant to the core catcher the double layered basement is a favorable design.

For the coolant of the core catcher the water inventory of the primary circuit and the accumulators is used, which is some 600 tons. This water is present on the upper containment floor in all accident scenarios where molten corium penetrates the RPV. The steam evaporating from the core catcher will pass into the containment transporting the decay heat, and condenses e.g. at the inner surface of the containment steel shell. Final decay heat removal is by natural convection heat transfer from the containment shell to the atmosphere. The vapor condensate will reflow to the containment sump and the catcher area. Thus, the self-cirulating steam/water flow establishes a totally passive decay heat removal system with no interference with normal operation or LOCA's.

The experience at KfK gained from melt-concrete investigations has been used to design the lower catcher area (Fig. 1).

The main part of the design is the flat perforated steel plate which form the lower catcher shell and is connected with the lower basement by a massive supporting structure. In case of an accident with large volumes of sumpwater as occur in melt-down accidents, the interfacial gap under the bottom plate is filled with sumpwater by passive overflow of a buffer tank. It is the role of the buffer tank to collect small volumes of sumpwater as they may occur during normal plant operation or minor incidents. Only large water volumes lead to buffer overflow and hence to totally passive flooding of the gap. In this case, the water supply pressure under the bottom plate is the geometrical height of the upper basement level which is typically 8 m. The upper surface of the catcher plate is initially free of water.

The bottom plate is covered with a sacrificial layer of concrete like material with special additions for safe inclusion of fission products. This layer protects the steel structure from the initial high temperature melt and lowers the corium temperature by fast melting and admixture to the melt. Use of concrete-like material is considered favorable because the release of gases during concrete decomposition helps to spread the melt over the large catcher surface so that a thin layer of corium is formed. Viscosity and solidification behaviour of the diluted melt may be influenced by the proper choice of the sacrificial concrete material.

The layer to be ablated during early dry interaction is some 10 cm. In the lower part of the concrete layer melt plugs are inserted which are the extension of the holes in the bottom steel plate. These plugs fail by melting when they are contacted by the melt and allow penetration of water into the melt from the bottom side. The onset of water/steam flow through the melt combined with fragmentation of the melt and the continuous cooling from the lower side of the bottom plate stabilizes the melt and finally allows flooding of the upper surface.

Neglecting any fragmentation of core material the minimum diameter of the catcher area would be 16 m. Then, all decay heat could be extracted only by heat conduction from the top and bottom water layer.

However, when the water penetrates into the melt, the formation of large volume fluxes of steam are expected to break up the corium layer and to establish a porous bed of corium, finally flooded and covered by evaporating water. The porous corium layer would be more easily coolable. If this is taken into account a substantial reduction of the catcher area would be possible.

A limited release of hydrogen and aerosols from the corium melt has to be expected during early contact phase with the catcher surface. This release, however, is terminated when the stable cooling condition is established.

Thermite Experiments

As described above, the key phenomenon for the safe operation of the core catcher is the process of flooding the melt from the bottom through the melt plugs. Additionally, the question has to be clarified if during the flooding process a substantial fragmentation of the melt may occur which would enhance coolability.

In order to identify the dominant processes during flooding from the bottom, prototypic experiments in small scale have been carried out. The experiments use two-component oxidic and metallic melts generated by a thermite reaction. In these transient tests the sensible heat of the initially very hot melt is sufficient to erode some 2 cm of the lower concrete slab during 5 minutes typically if no cooling by water would occur.

Figure 2 shows the experimental set-up, which is a 1-dimensional representation of the central part of the core catcher area. The test vessel consists of a 25 cm inner diameter cylinder of 60 cm height with radial MgO-isolation to minimize heat losses. The bottom of the cylinder is formed of steel plate with 13 holes of 10 mm diameter. 13 melt plugs in the concrete layer covering the steel plate are the extension of the holes. The melt plugs are fabricated from plastic for early melting at elevated temperatures. The overall thickness of the concrete layer is about 50 mm, 5 to 10 mm of which are covering the tip of the melt plugs. The water pool below the bottom plate is connected to a water reservoir in 5 m height via a flowmeter.

The experiment starts with the in situ ignition of the thermite powder which has been mixed with calcium-oxide mainly to reduce the solidification temperature and the viscosity of the oxidic melt. This produces 38 kg of oxidic (Al_2O_3 plus CaO) and iron melt with an initial temperature of about 1900°C within half a minute. The melt erodes the lower concrete layer causing vigorous gas release and agitation of the melt. About 1 minute after ignition the plugs were molten and melt/water contact did occur. A very fast steam release leads to a foamed melt and flooding of the melt starts with some ejection of melt fragments. This initially

vehement process of water penetration, evaporation and at the same time fragmentation of the melt leads to a solidificated melt permanently flooded and covered with water only 3 minutes after ignition.

The continuous upward water flow through the frozen melt indicates the persistence of open flow channels. During the experiment the flowmeter showed a water penetration rate of some 100 ml/s, which was verified by measurements of pressure loss after the test. This measured water supply rate exceeds the rate necessary to remove the decay heat by more than an order of magnitude, so that long-term coolability is assured.

The fast quenching and cool-down process of the melt accompanied by the intense steam-release indicates a very effective heat removal process which is mainly controlled by coarse mixing and direct water contact.

Post test inspection of ejected melt which has been collected around the vessel shows coarse fragments of 5 mm size and larger. This indicates, that a steam-explosion did not occur although for this situation a steam explosion of minor masses cannot be completely ruled out. However, the amount of water which might be involved is controlled by the water inlet through the plugs and therefore relatively small. This limits the mechanical energy release to a level which would not endanger the core catcher. Post test examination of the solidified melt and the bottom plate show that the metal, which has been produced from the thermite reaction, has solidified in a 4 cm thick layer above the concrete with well defined flow channels over the plugs and some smaller cavities near the plugs.

The frozen oxide forms a layer of high porosity, where in the lower part the porosity is finely distributed and the upper part is coarsely fragmented with cavities of several centimeters. The mean oxide void is about 50%. The results of the prototypic experiments may be summarized as follows: Flooding and early coolability of the melt by water addition from the bottom has been demonstrated. The oxidic and metallic melt solidify in form of a porous and permeable structure so that continuous supply and evaporation cooling by water is established within a few minutes only.

The investigations in small scale experiments with thermite melts will be continued with better instrumentation. Future planning aims to thermite melts with sustained heating.

Experiments with transparent plastic melts

The fragmentation of melts by flooding from the bottom is governed by the coupled process of water inlet, evaporation, fragmentation and therewith formation of new surfaces, which interact with the process of evaporation. Experiments with plastic melts as simulants are being conducted in laboratory scale to visualize these processes.

The plastic melt has a similar amorphous solidification and viscosity behaviour as the oxidic melt. Because of the elevated plastic-temperature of some 250 °C evaporation of water can occur while solidification of the melt takes place.

The experimental set up consists of a rectangular box of 10x4 cm with a height of 20 cm containing the high temperature plastic melt (s. Fig. 3). The water tank under the bottom plate is connected with a water reservoir of a certain elevation above the melt via a flowmeter. A sealed glass tube of 40 mm height and an inner diameter of 10 mm is inserted in the bottom plate representing one of the melt plugs of the coolant device with the possibility to allow water flow into the melt. The experiment starts with cutting the tip of the glass tube at a predefined time.

The use of a transparent plastic melt, an acrylic glass, and 2 glass windows in the box allows to visualize the process of water penetration into the melt and the resulting freezing and fragmentation phenomena and can be photographically registered by a high speed camera. The varied parameters are water pressure, melt height and melt temperature mainly influencing the viscosity of the melt. During the experiment pressure history, water flow rate and temperature in the melt and the water are measured.

To describe the solidified melt after the test a loss of pressure measurement was conducted and the apparent relative increase of melt volume was determined.

The results for simulated oxidic melts can be summarized as follows:

- In all the experiments the water inlet from the bottom causes flooding of the melt with simultaneous fragmentation.
- The melt is flooded in less than 10 seconds.
- Fragmentation of the melt is a result of the formation of channels and/or bubbles in the melt by the evaporation of water.

- Upward flow in the cross-section of the water-inlet is high enough to prevent penetration of melt into the plug.
- Depending on the viscosity of the melt a complete freezing of the melt in form of a porous, water permeable layer occurs between 10 seconds and some 3 minutes.
- High temperature of the melt and therefore low viscosity increases the fragmentation velocity.
- The melt is fragmented and flooded with water, also if the water pressure is equal to the pressure of the melt.

These experiments in laboratory scale are presently continued with 2 component melts, simulating a separated metallic and oxidic layer or an oxidic layer with dispersed metal, respectively.

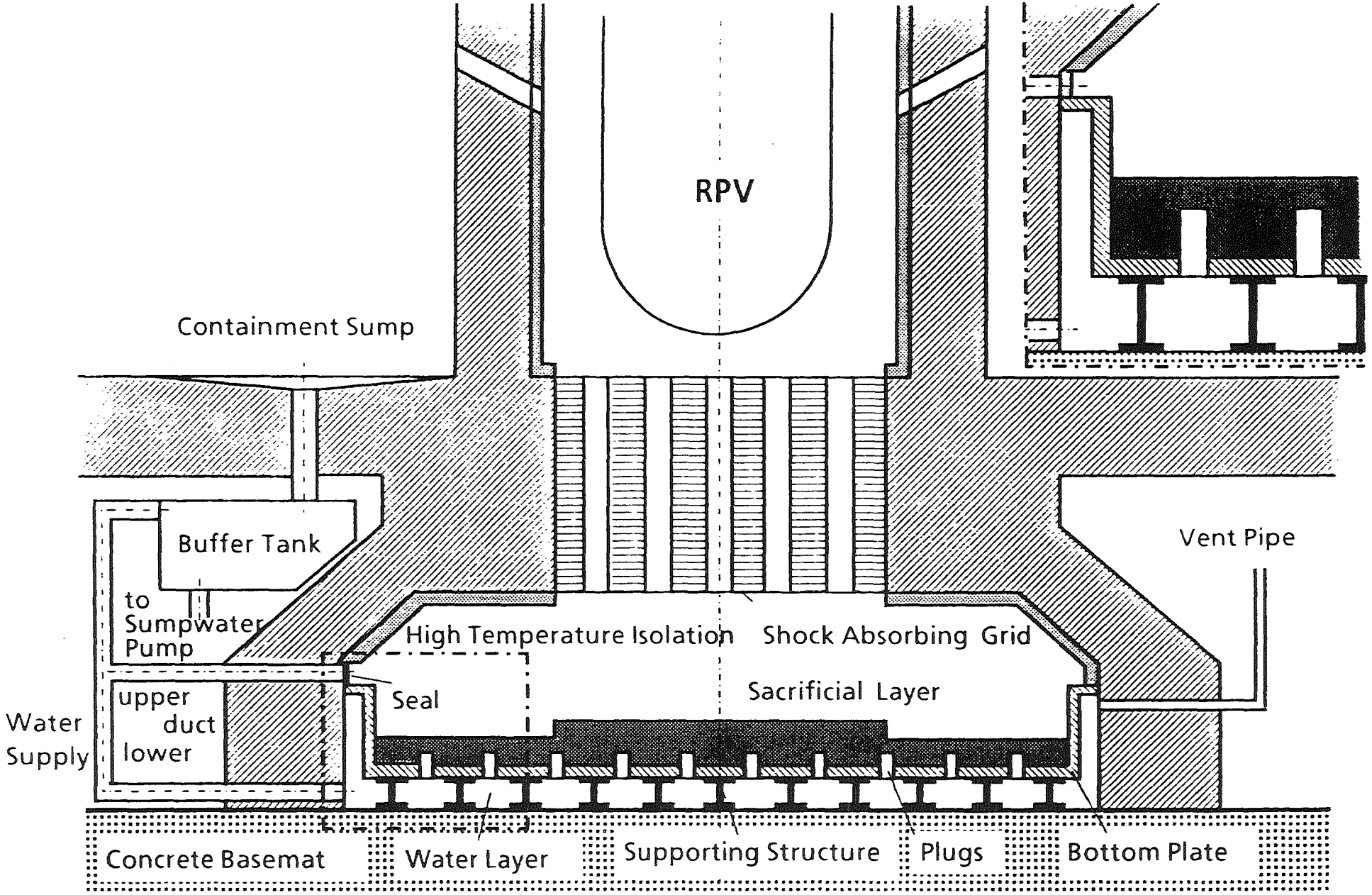

Fig. 1: Core Retention Device for a Modified PWR-Concept

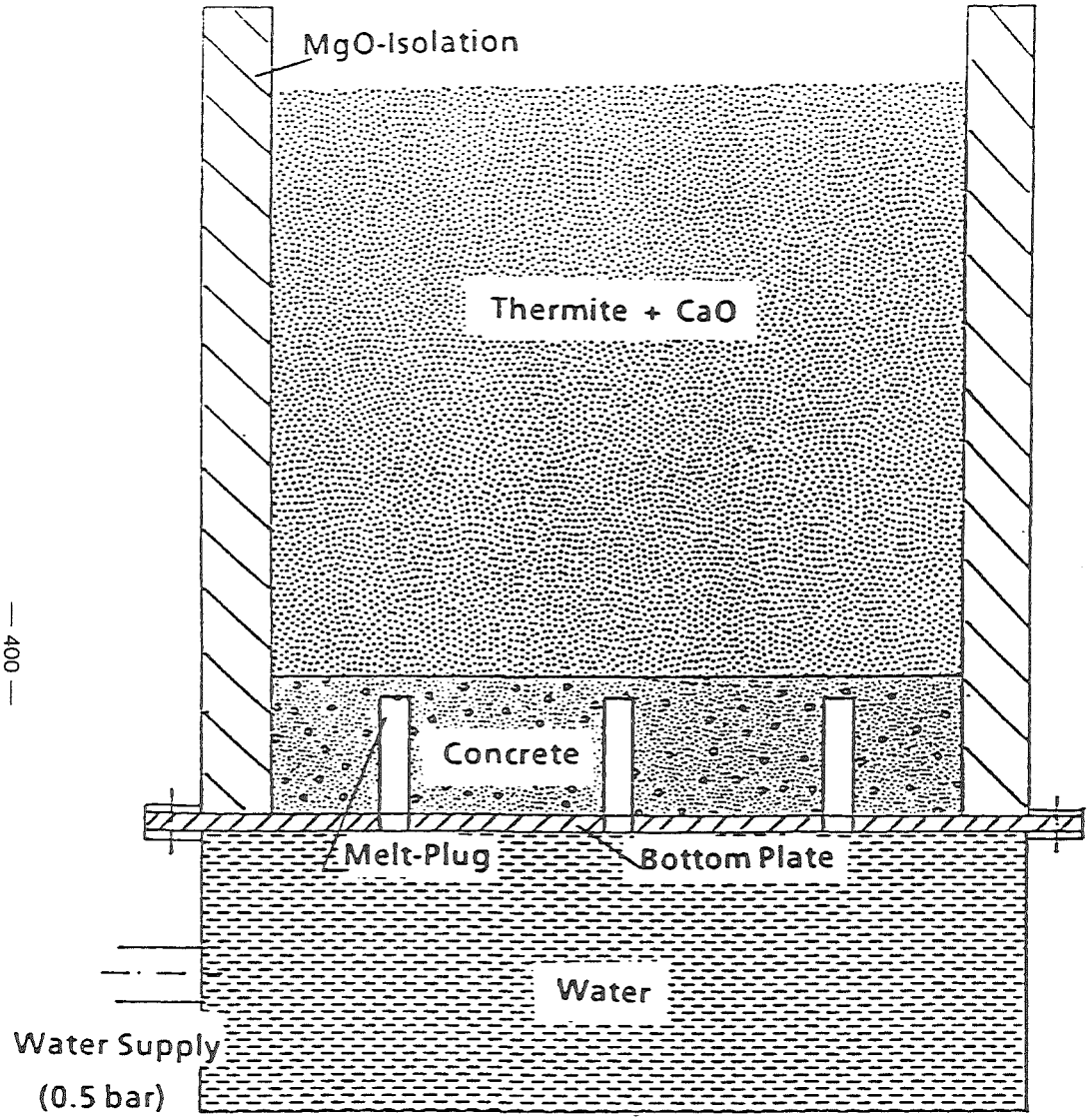

Diameter of Vessel: 30 cm

Fig. 2: Thermite Experiments

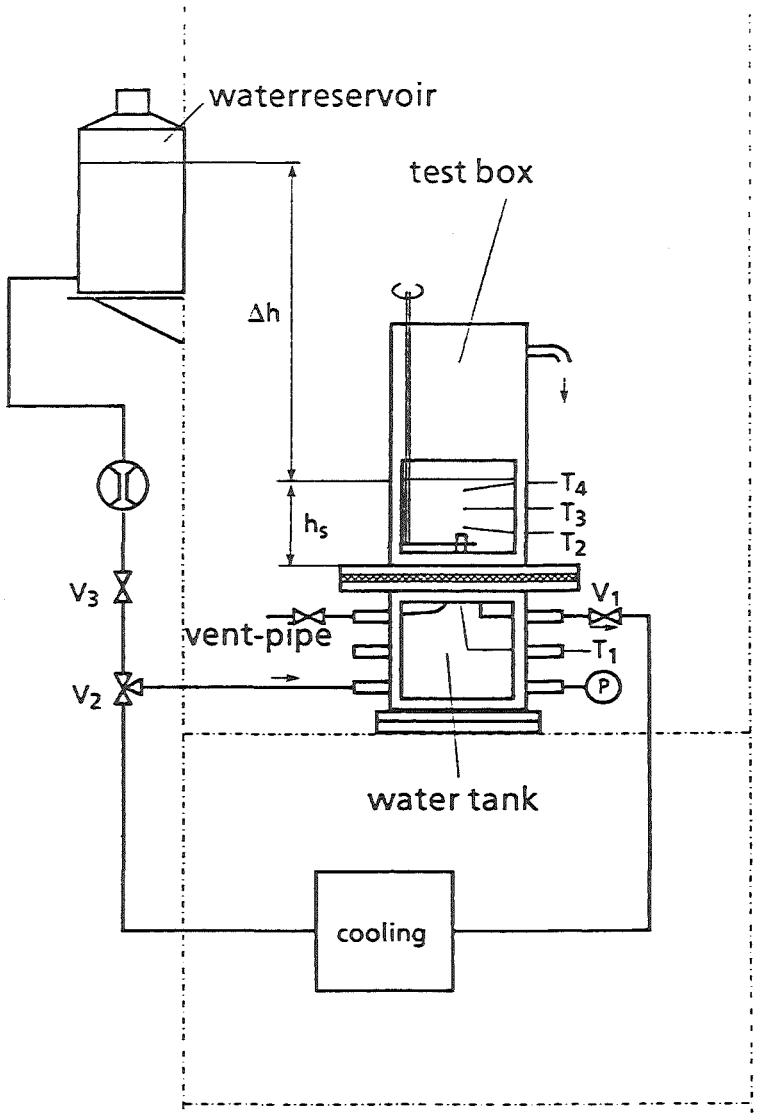

Fig. 3: Experiments with Plastic Melts

SECTION IV

MELT SPREADING AND COOLABILITY - PART B: MODELLING AND CODES

Separate Effects

Integral Codes

MODELING AND DATABASE FOR MELT-WATER INTERFACIAL HEAT TRANSFER

M. T. Farmer[1], J. P. Schneider[2], B. Bonomo[3], G. Theofanous[4], and B. W. Spencer[1]

[1]Argonne National Laboratory
Argonne, Illinois 60439 USA

[2]University of Illinois at Urbana-Champaign
Urbana, Illinois 61801 USA

[3]Northwestern University
Evanston, Illinois 60201 USA

[4]University of California at Berkley
Berkley, California 94704 USA

ABSTRACT

A mechanistic model is developed to predict the transition superficial gas velocity between bulk cooldown and crust-limited heat transfer regimes in a sparged molten pool with a coolant overlayer. The model has direct applications in the analysis of ex-vessel severe accidents, where molten corium interacts with concrete, thereby producing sparging concrete decomposition gases. The analysis approach embodies thermal, mechanical, and hydrodynamic aspects associated with incipient crust formation at the melt/coolant interface. The model is validated against experiment data obtained with water (melt) and liquid nitrogen (coolant) simulants. Predictions are then made for the critical gas velocity at which crust formation will occur for core material interacting with concrete in the presence of water.

INTRODUCTION

An important question in the assessment of ex-vessel severe accidents in light water nuclear reactors is the ability of water to quench molten core material. A case of particular interest is that in which molten core materials are postulated to be released from the reactor pressure vessel (RPV) and accumulate on the concrete basemat below. The heatup and decomposition of concrete is accompanied by the release of gases, principally water vapor and carbon dioxide. As the gases rise up through the melt, they may undergo further heating, or react with metallic melt constituents. In addition, the gases will cause agitation of the molten core materials. Ultimately, the gases pass through the melt upper

surface.

Should water be present atop the MCCI, then sparging gases may significantly influence the corium quenching process. Specifically, depending upon the MCCI initial conditions, several melt cooling regimes may be envisioned. If initial melt agitation forces due to gas sparging are insufficient to preclude incipient crust formation, then sustained crust growth may occur at the melt/water interface, which would then inhibit heat transfer from the MCCI zone to the water. However, if melt agitation forces are sufficiently high to preclude stable crust formation, then a bulk freezing regime may be observed in which crust segments intermittently formed at the melt/water interface are continuously broken up and mixed into the melt. In this regime, film boiling will be the dominant melt/water heat transfer mode owing to periodic introduction of high temperature melt at the interface. Efficient heat transfer may thus be anticipated owing to conduction and, predominately, radiation across the highly agitated melt/water interface.

As part of the Melt Attack and Coolability Experiment (MACE) program, both simulant and prototypic material experiments are underway to gain physical insight into melt coolability phenomena. An important part of this program has been the development of phenomenological models which describe the corium quenching process. The initial version of the Corium Quenching (CORQUENCH) model (1) considered the bulk freezing heat transfer regime described above, and is thus limited to the early quench phase prior to the formation of a stable interfacial crust. This paper describes (i) the development of a model for the MCCI conditions at which stable interfacial crust formation will occur, and (ii) validation of this model against simulant experiment data. The crust formation criterion developed herein is used as a basis to extend the initial version of the CORQUENCH model (1) to treat both the bulk freezing and crust-limited heat transfer regimes; the extension of this model is described elsewhere (2).

The modeling approach is to extend the periodic mixing concept underlying Szekely's interfacial heat transfer model (3). Specifically, an expression is developed for the critical superficial gas velocity at which intermittent crust segments formed at the melt-water interface become mechanically stable with respect to local hydrodynamic loads imposed by sparging concrete decomposition

gas bubbles. The model is validated against experiment data obtained with water (melt) and liquid nitrogen (coolant) simulants. Predictions for the critical melt superficial gas velocity to preclude stable crust formation for prototypic reactor materials are then made.

MODEL DEVELOPMENT

The objective is to develop an expression for the conditions at which sustained crust growth will occur at the interface between a sparged molten pool and a coolant overlayer. One possible criterion is the superficial gas velocity at which transition from bubbly to churn turbulent flow occurs. At the transition point, the two-phase flow pattern changes from one in which isolated bubbles rise in a relatively quiescent pool, to one in which gas slugs rise in a highly agitated, recirculating flow pattern. In the churn-turbulent flow regime, the highly agitated flow characteristics may be sufficient to preclude formation of a mechanically stable crust at the melt/water interface. Correlations for the transition superficial velocity are of the form (4, 5),

$$j_{b\text{-}ct} = C \left[g \frac{(\rho_m - \rho_g)}{\rho_m^2} \sigma_m \right]^{1/4} \tag{1}$$

where g = gravitational acceleration, ρ = density, σ = surface tension, C = empirical constant, and subscripts m and g denote the melt and sparging gas phases, respectively. The empirical constant, C, has been reported as 0.46 by Taitel et. al., (4), and 0.50 by Kataoka and Ishii (5). Examination of Eq. 1 indicates that, based on the flow regime transition concept, the critical gas velocity, j_c, scales roughly with the ratio of melt surface tension and density. This approach is deemed to be at least partially inadequate, however, as it does not embody other physical properties which may influence incipient crust formation, such as crust thermal conductivity, heat of fusion, and mechanical strength, among others. The model developed below constitutes a simplified analysis which attempts to link the hydrodynamic, thermal, and mechanical aspects of incipient crust formation at the interface between a sparged molten pool and coolant layer.

An illustration of the process under consideration is shown in Figure 1. The a priori assumption is made that the crust mechanical stability threshold lies

within the bubbly flow regime. Thus, to first order, the analysis may be restricted to isolated bubbles passing through the melt/coolant interface. Given j_c based on the current analysis, the assumption of bubbly flow may then be checked against correlations for j_{b-ct}, such as Eq. 1.

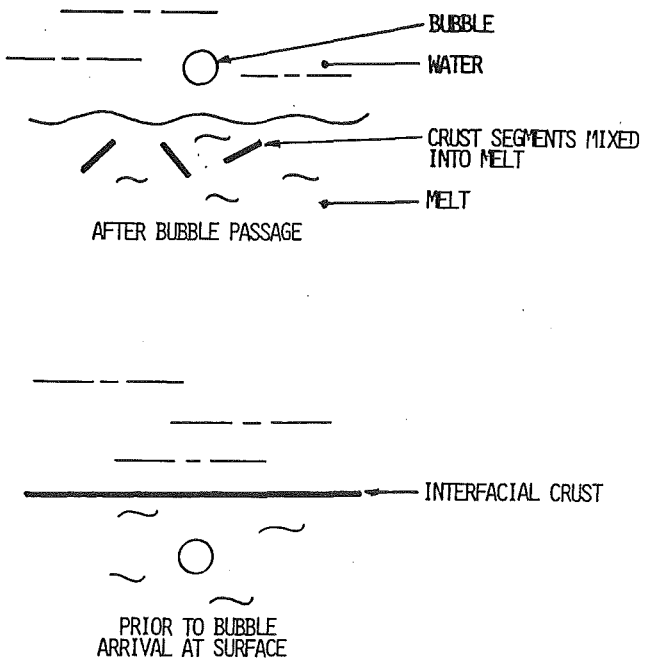

Figure 1. Illustration of Periodic Crust Breakup at Melt Surface Due to Bubble Passage.

As illustrated in Figure 1, above the critical point, bubbles arriving at the melt/coolant interface are assumed to perforate the crust which formed over the previous bubble cycle. As a result, hot melt is replenished at the surface, and crust growth begins anew. Neglecting decay heat in the crust, the crust growth rate equation is of the form,

$$\rho_{cr}\,\Delta e_{cr}\,\frac{d\delta}{dt} = k_{cr}\,\frac{(T_f - T_I)}{\delta} - h_m\,(T - T_f), \qquad (2)$$

where Δe = latent heat of fusion, k = thermal conductivity, h_m = convective heat transfer coefficient from melt to crust, T = melt temperature, T_f = melt freezing

temperature, T_I = crust/coolant interface temperature, and subscript cr denotes properties of the crust material. The crust/coolant interface temperature is found from an energy balance of the form,

$$k_{cr} \frac{(T_f - T_I)}{\delta} = h_w (T_I - T_{sat}), \tag{3}$$

where h_w = heat transfer coefficient from the coolant to the crust, and T_{sat} = coolant saturation temperature. Eliminating T_I from Eq. 2 with Eq. 3 and integrating the resultant expression subject to $\delta(t = o)$ yields,

$$\beta h_w \delta + \alpha \ln \left[1 - \frac{\beta h_w \delta}{\alpha - \beta k_{cr}}\right] + \beta^2 t = 0 \tag{4}$$

where

$$\alpha \equiv \frac{k_{cr} h_w^2}{\rho_{cr} \Delta e_{cr}} (T_f - T_{sat}) \tag{5}$$

$$\beta \equiv \frac{h_m h_w}{\rho_{cr} \Delta e_{cr}} (T - T_f) \tag{6}$$

Equation 4 provides the local crust depth at the time of arrival of the next bubble at the melt/water interface, t_a.

Whether or not the crust fails (i.e., breaks up) under the load imposed by subsequently arriving bubbles will depend upon the mechanical strength of the crust. Assuming that the crust can be modeled as a circular flat plate, then the required uniform load to produce collapse is given as (6),

$$F_f = C\pi \sigma_y \delta^2 \tag{7}$$

where σ_y = crust fracture stress, C = 3/2 for simply supported crust, and C = 2.814 for clamped edge crust. For the purposes of this analysis, dynamic affects associated with the bubble impacting the crust are neglected, and it is assumed that the load imposed by the bubble is solely due to buoyancy,

$$F_b = \frac{4}{3}\pi R^3 g(\rho_m - \rho_g) \tag{8}$$

where R = radius of sparging gas bubbles. The critical crust thickness at which collapse under the applied bubble buoyancy load will occur is found by equating Eqs. 7 and 8,

$$\delta_c = \left[\frac{4R^3(\rho_m - \rho_g)g}{3C\sigma_y}\right]^{1/2} \tag{9}$$

When Eq. 9 is substituted into Eq. 4, a relationship is obtained for the local bubble arrival time, t_a, at which mechanical failure of the incipient crust occurs under the applied buoyancy force of the bubble. What is required at this point is an expression which relates t_a to the overall melt superficial gas velocity. Blottner (7) developed the following correlation for the local bubble arrival time in terms of the superficial gas velocity and sparging gas bubble radius,

$$t_a = 0.445\,\frac{R}{j} \tag{10}$$

Substitution of Eqs. 5-6 and 9-10 into Eq. 4 yields the following expression for the critical superficial gas velocity to preclude sustained crust growth at the melt/water interface,

$$j_c = \frac{0.445\,Rh_m(T - T_f)}{\delta_c\,\rho_{cr}\,\Delta e_{cr}\left\{\frac{k_{cr}(T_f - T_{sat})}{\delta_c\,h_m\,(T - T_f)}\ln\left[\frac{1}{1-\xi}\right] - 1\right\}} \tag{11}$$

where

$$\xi = \frac{h_m\,h_w\,(T - T_f)\,\delta_c}{k_{cr}\left\{h_w(T_f - T_{sat}) - h_m(T - T_f)\right\}} \tag{12}$$

Equation 11 provides a relationship for the MCCI hydraulic conditions at which

stable crust formation will be precluded in terms of the melt thermal/mechanical properties and thermal properties of the coolant overlayer. From the denominator of Eq. 12, it is evident that the condition $h_w (T_f - T_{sat}) - h_m (T - T_f) > 0$ must be satisfied for realistic solutions to be obtained from this model. This condition is equivalent to requiring that the melt/water interface temperature in the absence of a crust falls below the melt freezing temperature, which is the basic thermal requirement for incipient crust growth.

A limiting case which may be of interest is that in which $h_m (T - T_f) \sim 0$, i.e., convective heat transfer to the underside of the crust is negligible. This situation may reflect a drop in melt temperature to near the freezing temperature, and/or a substantial reduction in the melt convective heat transfer coefficient. Due to the logarithmic nature of the solution, the critical gas velocity under the conditions in which $h_m (T - T_f) \to 0$ is difficult to infer from Eqs. 11 and 12. In this case, j_c may be obtained from a series expansion of Eq. 11 and then taking the limit as $h_m (T - T_f) \to 0$, or by integrating Eq. 2 with $h_m (T - T_f) \equiv 0$ and repeating the steps leading to Eq. 11. In either case, the solution is found as,

$$j_c = \frac{0.89\, k_{cr}\, Rh_w^2\, (T_f - T_{sat})}{\rho_{cr}\, \Delta e_{cr} \left\{ [h_w\, \delta_c + k_{cr}]^2 - k_{cr}^2 \right\}} \qquad (13)$$

As is evident from Eq. 2, convective heat transfer from the melt acts to reduce the crust growth rate, and therefore a lower superficial velocity is required to preclude crust formation. Thus, Eq. 13 is conservative from the viewpoint that it provides an upper bound prediction.

In the development of Eqs. 11-13, several simplifying assumptions were made; namely: (i) bubbly flow regime with isolated bubble passage through melt/water interface, (ii) bubble impact load equal to buoyancy force, and (iii) simple flat plate mechanical model for crust. Thus, the constants in front of Eqs. 11-13 need to be checked against experiment data. The validation experiment for this model is described in the next section.

EXPERIMENT VALIDATION

A series of simulant material coolability experiments were conducted to: (i) observe the affect of superficial gas velocity on the melt cooldown

characteristics (e.g., bulk freezing versus crust formation), and (ii) determine cooling regime transition point(s) for validation of Eqs. 11 and 13. In these experiments, distilled water was used to simulate the melt, liquid nitrogen (LN_2) was used to simulate the coolant, and argon was used to simulate concrete decomposition gases. Water and LN_2 were chosen as simulants since LN_2 film boils on water. (Using the reference properties shown in Table 1, a minimum film boiling temperature of 104 K is calculated from Berenson's correlation (8), which may be compared to the water freezing temperature of 273 K). The same behavior is anticipated when water is introduced over corium. (With properties shown in Table 1, a minimum film boiling temperature of 463 K is calculated from Berenson's correlation (8)).

Table 1. Reference Properties

Property	State	LN_2	Water	Oxidic Corium
Thermal Conductivity (W/m•k)	Vapor Liquid Solid	.031		 2.0 1.0
Density (kg/m^3)	Vapor Liquid Solid	4.6 807	 1000 917	 8000 7000
Specific Heat (J/kg•K)	Liquid			500
Surface Tension (N/m)		0.03	0.06	0.6
Viscosity (Kg/m•s)	Vapor Liquid	$2 \cdot 16 \cdot 10^{-5}$	$1 \cdot 28 \cdot 10^{-5}$	 0.01
Latent Heat (KJ/kg)	Fusion Vaporization	 197	334	250
Saturation Temperature (K)		77	373	
Freezing Temperature (K)			273	2200
Emissivity (-)				0.8
Fracture Stress (MPa)			3	20

The experiment apparatus is shown in Figure 2. The test section consisted of a 15.2 cm ID, 45.7 cm long Pyrex tube. A 2 cm ID standoff T was located at the

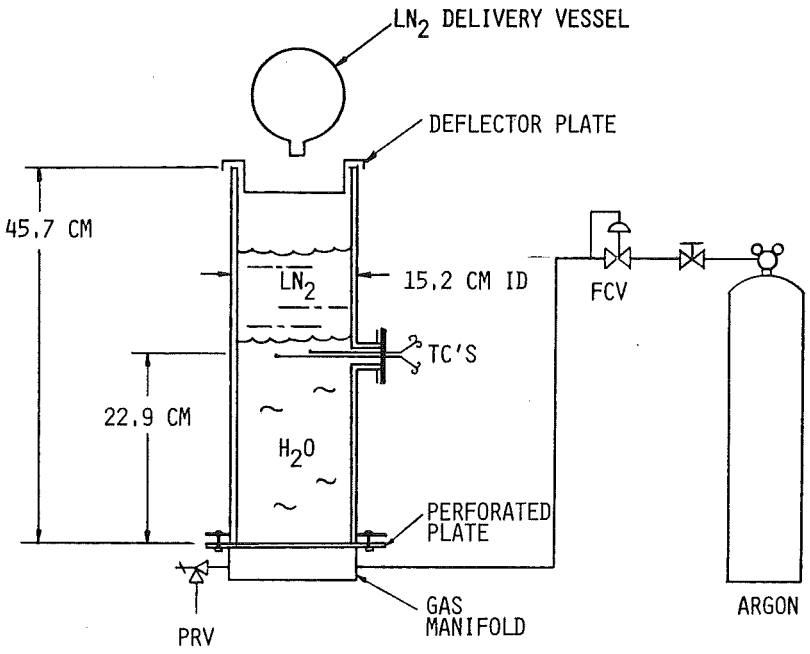

Figure 2. Illustration of Experiment Apparatus.

test section axial midplane, which provided access for two thermocouples. These were mounted at the same axial elevation; the TC's were wired as a thermopile to provide an average temperature reading at the midplane of the apparatus. Argon gas was bubbled through a perforated aluminum plate located at the base of the vessel; the flowrate was regulated by a Hastings flow controller. LN_2 was introduced from a delivery chamber located atop the test section. To prevent direct impingement of the LN_2 into the water, a deflector plate was installed near the top, which channeled the LN_2 down the apparatus sidewalls.

For all experiments, the test section was initially filled with ~4.2 ℓ of distilled water, which corresponded to a water height of ~1 cm above the axial midplane of the apparatus. To simplify data analysis (i.e., remove uncertainties regarding the melt convective heat transfer coefficient, h_m, in Eqs. 11-14), the initial water temperature was held within 2°C of the freezing temperature. To help visualize flow patterns, the water was laced with 3.2 mm diameter polypropylene spheres (0.9 specific gravity), which were painted flat black to aid visibility. At the start of each test, the initial LN_2 inventory of ~3 ℓ was poured from the delivery vessel over ~2 second time interval. Due to the possibility of minor fuel-coolant interactions (FCI's) for the water/LN_2 system (9), the experiments were conducted remotely. A visual record of the experiments was made using standard video recording equipment.

Before tests with LN_2 were initiated, void fraction and flow regime observations were made to serve as a basis for comparison with test results obtained when freezing behavior was involved. The void fraction measurements are shown in Figure 3. Visual observations indicated that a bubbly flow regime existed throughout the gas velocity range in which data were taken. Given the reference water properties in Table 1, a bubbly/churn turbulent transition gas velocity of 4.7 cm/s is calculated from Eq. 1 ($C = 0.46$ (4)) for this system.

A summary of the test results is provided in Table 2. For the case in which $j = 0$, a fully dense, very smooth crust formed immediately upon introduction of LN_2. The crust slowly propagated downward as LN_2 was boiled off. At low gas velocities $\left(j \lesssim 2 \text{ cm/s}\right)$, a dense interstitial crust also formed, but the surface of the crust was rough in comparison and was also characterized by several discrete vent holes which allowed passage of the sparging gas. In the gas velocity range $2 \lesssim j \lesssim 4$ cm/s, a gradual transition in freezing behavior was observed in which an annular crust formed on the sidewalls of the apparatus near the original water/LN_2 interface, while the balance of the water underwent bulk cooldown resulting in the eventual formation of a dense "slush". At j= 4.9 cm/s, the heat transfer mechanism was dominated by bulk cooling, with crust formation limited to a thin annular ring (< 1 cm radial thickness) near the original water/LN_2 interface.

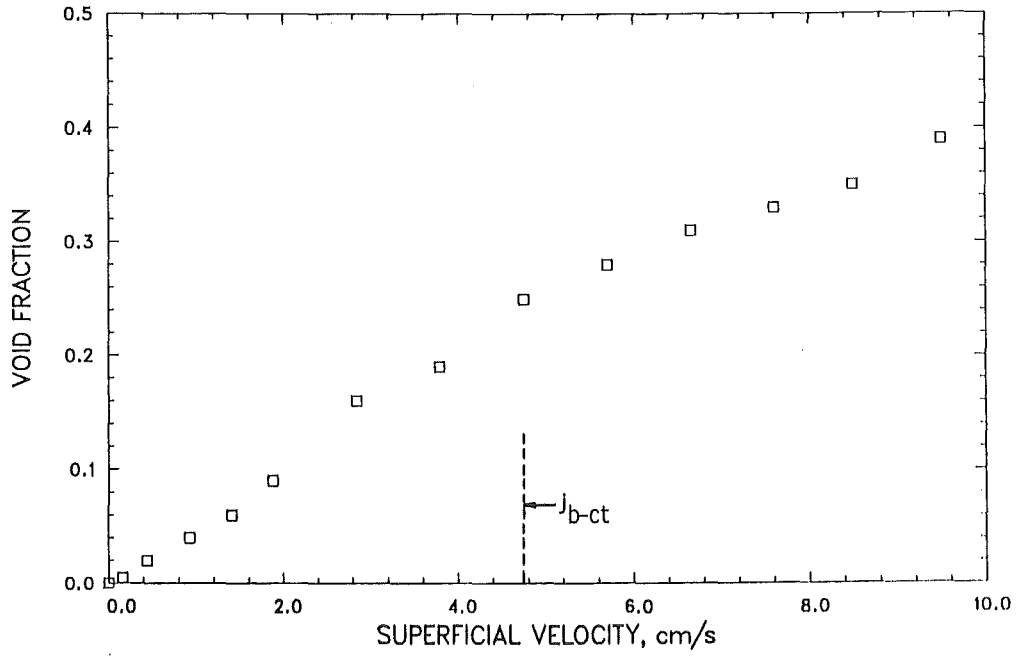

Figure 3. Measure void Fraction Versus Argon Superficial Gas Velocity.

Table 2. Summary of Simulant Material Tests

Test No.	j (cm/s)	Observations
1	0	Fully dense interstitial crust; smooth surface.
2	0.9	Dense interstitial crust with small discrete vent holes; surface roughened.
3	1.9	"
4	2.9	Annular crust occluding ~1/2 vessel diameter, slush in center.
5	3.9	Annular crust occluding ~1/4 vessel diameter, slush in center.
6	4.9	Slush with thin annular crust ($\lesssim$ 1 cm radial thickness).

In summary, the results of the simulant experiments illustrate a transformation in freezing behavior from crust limited to slurry (i.e., slush) formation as the superficial gas velocity is increased. For the water/LN_2 simulants used in this study, the transformation occurred between j = 2 to 4 cm/s. Within this range, the predominant freezing mode was slurry formation with concurrent generation of an annular crust which adhered to the sidewalls. Thus, crust formation in this range may be attributable to the vessel sidewalls, which acted as an anchor for frozen material to attach.

Due to the fact that the experiments were conducted with near freezing water (i.e., no superheat with respect to the freezing temperature), Eq. 13 may be compared directly with the experiment data. The local melt/water heat transfer coefficient in Eq. 13 is evaluated using Berenson's film boiling correlation (8),

$$h_w = 0.425 \left[\frac{k_v^3 \rho_v g (\rho_l - \rho_v) \Delta e_{lv}}{\mu_v \Delta T_{sat} \sqrt{\sigma_l / g (\rho_l - \rho_v)}} \right]^{1/4} \qquad (14)$$

where $\Delta T_{sat} = T - T_{sat}$ and subscripts l and v denote liquid and vapor states of the coolant, respectively. (Note that due to interfacial area enhancement, the actual heat flux off the melt surface is expected to be much higher than that predicted through direct application of Eq. 14 (1). However, the local heat

transfer behavior is still expected to be dominated by film boiling, and therefore Eq. 14 should provide a reasonable estimate of the local heat transfer coefficient during crust growth.) Evaluation of Eq. 14 using the reference properties in Table 1 and assuming $\Delta T_{sat} = 27$ K (i.e., LN_2 minimum film boiling superheat according to Berenson's correlation (8)) yields $h_w = 280$ W/m^2•K. The sparging gas bubble radius in Eq. 13 is assumed to equal one fourth the Taylor wavelength,

$$R = \frac{\lambda}{4} = \frac{\pi}{2}\sqrt{\frac{3\sigma_m}{g\,(\rho_m - \rho_g)}} \qquad (15)$$

Evaluation of Eq. 15 with the water properties in Table 1 yields $R \simeq 6.7$ mm. The compressive strength of ice has been reported to range from 2.5 to 3.4 MPa (10). For the purposes of this work, an average value of 3.0 MPa is assumed. Evaluation of Eq. 13 given the LN_2/water properties in Table 1 and the above assumptions yields, $j_c = 1.8$ cm/s for a simply supported crust, and $j_c = 2.5$ cm/s for a clamped edge crust. Both of these predictions lie near the lower end of the superficial velocity range where bulk freezing was initially observed (>2 cm/s), with the clamped edge crust case showing slightly better agreement. Thus, the constant C in Eqs. 7-9 is set equal to the value corresponding to the clamped edge case (2.814) for the balance of this work.

For water/LN_2 simulants, Eq. 13 has been shown to provide a reasonable prediction of the transition gas velocity between crust limited and slurry formation heat transfer regimes for the limiting case of no melt superheat. Validation of the more general expression, Eq. 11, will require additional experiments in which the melt superheat is parametrically varied.

APPLICATION TO REACTOR CASE

For the case of an MCCI, the melt sparging rate is proportional to the melt temperature. Thus, according to the present model, both the bulk cooldown and crust-limited heat transfer regimes may be encountered, depending upon the MCCI initial conditions. Specifically, if the initial superficial velocity lies above the critical value, then an aggressive melt/water heat transfer phase will be observed in which the predominant freezing mode is slurry formation. During this phase, the melt temperature will rapidly decline, which will cause the sparging

rate to decrease. The slurry formation phase will continue until the gas velocity decreases to the critical value. At this point, the surface of the melt is envisioned to crust over, and the crust-limited heat transfer phase is initiated. Although the slurry formation phase may prove to be short in duration relative to the entire course of an MCCI, it is perceived to be important since the melt thermal energy will rapidly decline (predominately via upward heat transfer) to the end point state at which crust formation occurs. This endpoint state may not be unique (i.e., it may be achievable over a protracted timescale with the crust in place due to the cooling affect of slag entrainment into the melt). However, the cumulative concrete ablation up to this point will certainly be less when the initial heat transfer occurs by slurry formation.

For the case of water over oxidic corium in the absence of a sustained crust, heat transfer will occur by radiation-dominated film boiling. In this case, the local melt/water heat transfer coefficient is assumed to be given by the radiant heat transfer solution,

$$h_w \sim \eta \, \epsilon \left(T_f^2 + T_{sat}^2\right)\left(T_f + T_{sat}\right) \tag{16}$$

where η = Stefan-Boltzmann constant, and ϵ = melt emissivity. Given the property data in Table 1, h_w is evaluated as 580 $W/m^2 \cdot K$.

In order to investigate the affects of melt superheat on the critical gas velocity (Eq. 11), two models for the melt/crust convective heat transfer coefficient, h_m, are considered. Both models are based on the concept of bubble-driven convection. Kutateladze's (11) correlation is of the form,

$$h_m = \begin{cases} 1.5 \cdot 10^{-3} \left(\dfrac{k_m}{L}\right)\left(\dfrac{C_m \, Pj}{k_m \, g}\right)^{2/3} \\ 1.5 \cdot 10^{-3} \left(\dfrac{k_m}{L}\right)\left(\dfrac{C_m \, Pj}{k_m \, g}\right)^{2/3} \left(\dfrac{j_{tr}}{J}\right)^{1/2} ; \; j \geq j_{tr} \end{cases} \tag{17}$$

where

$$L = \sqrt{\frac{\sigma_m}{g\left(\rho_m - \rho_g\right)}}, \tag{18}$$

$$j_{tr} = 4.3 \cdot 10^{-4} \, \frac{\sigma_m}{\mu_m}, \tag{19}$$

and P = system pressure which is assumed equal to 0.1 MPa for the purposes of

this study. Szekely's (3) correlation is given as,

$$h_m = \frac{2}{\sqrt{\pi t_a}} \sqrt{(k\rho c)_m}, \tag{20}$$

where the local bubble arrival time, t_a, is assumed to be given by Eq. 10. Both Eqs. 17 and 20 are functions of the superficial gas velocity, and therefore an iterative solution to Eq. 11 is required. The results of these calculations are shown in Figure 4, which illustrates the dependence j_c on melt superheat for oxidic corium. For the case of zero superheat, j_c is predicted to be ~6 cm/s. (Note that Eq. 1 predicts a bubble/churn turbulent transition velocity of 8.4

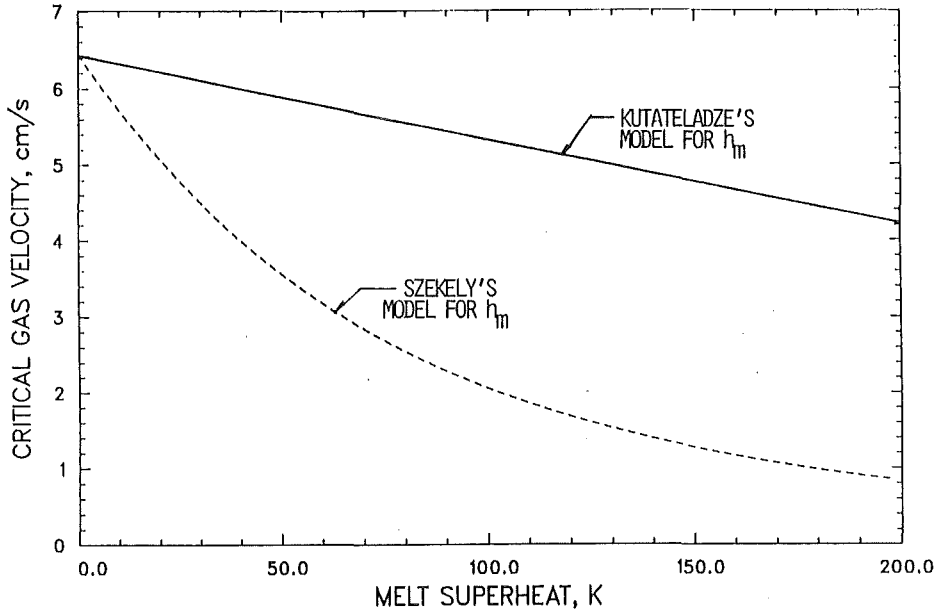

Figure 4. Calculated Critical Gas Velocity to Preclude Crust Formation for Molten Oxidic Core Material.

cm/s, and therefore the a priori modeling assumption of bubble flow appears to be valid for this case). The critical velocity is predicted to be a weak function of superheat when Katateladze's correlation (11) is used to evaluate h_m; the dependency is more pronounced when Szekely's correlation (3) is used.

Note that the analysis provided herein may readily be adapted to predict the final melt thermal state (i.e., temperature) at which crust formation will occur at the melt upper surface. Assuming quasi-steady concrete ablation, the melt temperature may be evaluated through the expression,

$$h_b (T_c - T_I) = \frac{\rho_g}{X_{dc}} e_{dc} j_c \qquad (21)$$

where T_c = critical melt temperature for crust formation at melt upper surface, h_b = downward heat transfer coefficient, ρ_g = concrete decomposition gas density, T_I = bottom temperature boundary condition, e_{dc} = concrete decomposition enthalpy, X_{dc} = weight fraction gas in concrete, and j_c is evaluated through Eq. 11 or Eq. 13. To make firm predictions regarding T_c requires the specification of concrete properties (note that T_c decreased with increasing X_{dc}), downward heat transfer coefficient, and bottom temperature boundary condition, which will depend upon the assumed presence/absence of a bottom crust. Presentation and evaluation of the requisite input models and property data to evaluate T_c is beyond the scope of this work.

SUMMARY AND CONCLUSIONS

A mechanistic model has been developed to predict the transition superficial gas velocity between bulk cooldown and crust-limited heat transfer regimes in a sparged molten pool with a coolant overlayer. The model has direct applications in the analysis of ex-vessel severe accidents, where molten corium interacts with concrete, thereby producing sparging concrete decomposition gases. The analysis approach embodies thermal, mechanical, and hydrodynamic aspects associated with incipient crust formation at the melt/coolant interface. To validate the model, benchtop experiments were performed which employed water (melt) and liquid nitrogen (coolant) simulants; decomposition gases were simulated using argon gas. The results of the experiments confirm the existence of distinct crust limited and bulk cooldown heat transfer regimes. The transition between the two regimes occurred gradually between j = 2 to 4 cm/s, with onset of bulk cooling occurring at j = 2 cm/s. The model predicts a transition gas velocity of j = 2.5 cm/s without empirical adjustment.

Application of the model to the case of oxidic corium over concrete indicates that efficient bulk cooling of melt will occur as long as the concrete decomposition gas velocity lies above 6 cm/s. When the gas velocity falls below this value, an interstitial crust is predicted to form. Thereafter, heat transfer from the MCCI zone to the coolant will be crust-limited.

ACKNOWLEDGEMENTS

This work is sponsored by the Advanced Containment Experiments (ACE) International Consortium through the Electric Power Research Institute, Contract No. RP 3047-08. The EPRI Program coordinator is B. R. Sehgal. The manuscript was typed by L. J. Ondracek.

REFERENCES

1. M. T. Farmer, J. J. Sienicki, and B. W. Spencer, "CORQUENCH: A Model for Gas Sparging Enhanced, Melt-Water, Film Boiling, Heat Transfer," ANS Winter Meeting on the Thermal Hydraulics of Severe Accidents, Washington, D.C., November 11-15, 1990.

2. M. T. Farmer, J. J. Sienicki, and B. W. Spencer, "Melt Coolability Modeling and Comparison to MACE Test Results," 2nd CSNI Specialist Meeting on Core-Debris Interactions, Karlsruhe, FRG, April 1-3, 1992.

3. J. Szekely, "Mathematical Model for Heat and Mass Transfer at the Bubble-Stirred Interface of Two Immiscible Liquids," Intl. J. Heat Mass Transfer, 6, pp. 307-311, 1963.

4. Y. Taitel and A. E. Dukler, "Flow Regime Transitions for vertical Upward Gas-Liquid Flow: A Preliminary Approach Through Physical Modeling," AIChE 70th Annual Meeting, N.Y., 1977.

5. I. Kataoka and M. Ishii, "Mechanistic Modeling and Correlations for Pool Entrainment Phenomenon," Int. J. Heat Mass Transfer, Vol. 27, pp. 1999-2014, 1984.

6. R. J. Roark and W. C. Young, Formulas for Stress and Strain, 5th Ed., McGraw-Hill Book Co., 1975.

7. F. G. Blottner, "Hydrodynamics and Heat Transfer Characteristic of Liquid Pool with Bubble Agitation," Sandia National Laboratory, SAND79-1132, NUREG/CR-0844, November 1979.

8. P. J, Berenson, "Film Boiling Heat Transfer from a Horizontal Surface," J. Heat Transfer, Vol. 83, pp. 351-357 (1961).

9. K. H. Bang and M. L. Corradini, " Stratified Vapor Explosion Experiments," Proc. 1988 National Heat Transf. Conf., Houston, TX, July 24-27, pp. 228-235, 1988.

10. R. L. Coble and W. D. Kingery, "Ice Reinforcement," Chapter 12, Ice & Snow, W. D. Kingery, Ed., The MIT Press, 1963.

11. S. S. Kutateladze and I. G. Malenkov, "Boiling and Bubbling Heat Transfer Under the Conditions of Free and Forced Convection," 6th Int. Heat Transfer Conf., Toronto, 1978.

STRESS ANALYSIS AND SCALING STUDIES OF CORIUM CRUSTS

Z. Feng*
R. L. Engelstad
E. G. Lovell
M. L. Corradini

Mechanical and Nuclear Engineering Departments
University of Wisconsin, Madison, WI 53706

*Also Jilin University of Technology
Changchun, China

ABSTRACT

In the event of a severe accident in a light water reactor, water may be input to cool the molten mixture of fuel and concrete. A number of structural models are developed and used to predict whether a crust will be formed and remain stable between the melt and water. Bending stresses and membrane stresses due to pressure loadings and the temperature differential are considered in the analyses to investigate the stability of the crust as a function of the time, thickness and span. The results from parametric studies show the conditions under which a crust could develop, and how such structural models could be used to determine scaling effects and provide correlations to prototypic accident situations.

INTRODUCTION

In a severe accident in a light water reactor, a molten mixture of fuel and metals could be deposited onto the concrete floor below the vessel. The termination of the subsequent molten core-concrete interaction (MCCI) by the addition of water is of major concern. This core coolability question is the primary focus of the tests being conducted by Argonne National Labs, i.e., those designated as MACE. The experiments to date have resulted in relatively thick solidified crusts that act as thermal barriers, limiting the heat transferred upward into the water pool. A number of technical issues need to be addressed to fully investigate the coolability issue when there is the possibility of crust formation, e.g., (a) under what conditions or circumstances will a crust develop (and be stable), (b) if such a crust does form, to what extent will it reduce the upward heat loss and retard core materials quench and (c) what are the scaling implications of such a crust as one extrapolates from test conditions to full scale accident conditions. This paper focuses on a methodology to answer the structurally related

questions of (a) and (c) above. A companion paper discusses additional details on (a) and provides supporting calculations for (b) and (c) [1].

If a crust does form between the molten pool and the water layer being added, the two primary loadings (considering the crust as a structural component) consist of a uniform pressure over the entire surface and a temperature gradient through the thickness. The absolute pressure acting on the crust can be found by taking into account the pressure from the overlying water and from the gases released from the molten fuel. For the analysis which follows, the worst case is often assumed, where the pressure loading is shown on the top surface and is equated with a water depth of 0.5 m. The bending stresses associated with this particular loading can be superimposed with the thermal stresses produced by the temperature loading, in effect decoupling the problem. A number of structural models of the crust have been developed to evaluate the stability of the crust under these external loads. In addition, the models were used to determine the effect of geometric features on the quasi-static state of stress present in the crust. Consequently, these analyses provide a predictive tool to study the effects of scaling.

STEPPED PLANAR BEAM MODEL

In the interest of determining the methodology involved in the scaling process, a planar beam-like model was first developed. Figure 1 shows the parameters of the stepped beam with "fixed-fixed" boundary conditions. In effect this assumes the supports do not allow any displacements or rotations. This one-dimensional model includes the possibility of having an increase in thickness at the wall (due to any preferential solidification the crust may exhibit), which are referred to as anchors. The loading condition includes a net uniform pressure load over the entire span of the beam. The magnitude of the pressure is given by p, with the load per unit length given by the pressure times the width of the beam, B.

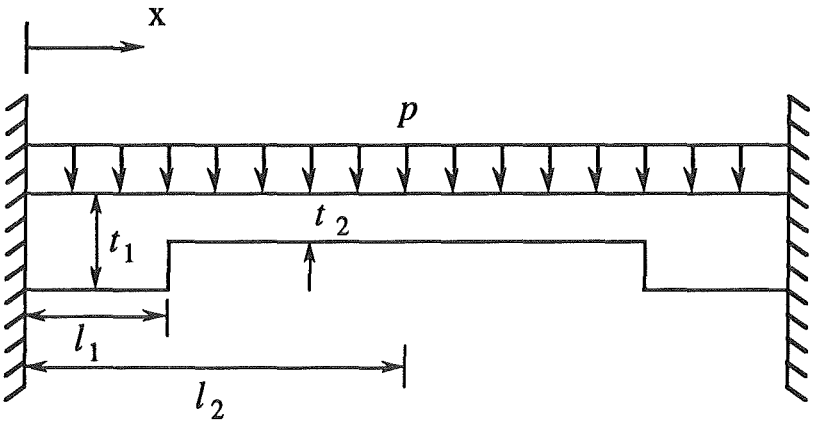

Fig. 1. Geometry and boundary conditions of the stepped beam model.

Considering the model as a statically indeterminate beam, the maximum bending stress at the wall (σ_w) is given by

$$\sigma w = p\frac{l_1^2}{t_1^2}\frac{l_2^2}{l_1^2}\left[\frac{2+(3l_1^2/l_2^2 - l_1^3/l_2^3)(t_2^3/t_1^3-1)}{1+(l_1/l_2)(t_2^3/t_1^3-1)}\right] \tag{1}$$

At the center of the span the stress σ_c can be found by using

$$\sigma c = p\frac{l_2^2}{t_2^2}\left\{3-\frac{\left[2+(l_1^2/l_2^2)(t_2^3/t_1^3-1)(3-l_1/l_2)\right]}{\left[1+(l_1/l_2)(t_2^3/t_1^3-1)\right]}\right\} \tag{2}$$

As shown in Eqs. (1) and (2), the stresses are dependent on the geometric ratios l_1/l_2, t_1/t_2, l_2/t_2 and l_1/t_1, but are independent of the elastic modulus of the material and the width of the beam (B). Thermal stresses have not been included here since they will depend solely on the material properties and will therefore not enter into the basic scaling methodology. At any point, however, the thermal stresses can be superimposed with the bending stresses to find the total state of stress in the crust.

The stresses σ_w and σ_c can be used to predict the survivability of a crust in terms of the geometric scaling parameters. If either stress (σ_w or σ_c) is larger than the fracture strength of the crust material (σ_f) the crust will fail. If they are both less than the fracture strength the crust will survive. By using this model, a number of parametric studies have been performed. The details can be found in reference [2]. Figure 2 illustrates an example. For a particular fracture strength, the critical crust thickness depends on the midspan length l_2. In this case the net pressure loading (p) was assumed to be 5 kPa, and the anchor size was taken to be $t_1 = l_1 =$ 5.0 cm. Consequently, the crust must grow to a particular thickness before it can bond together with the anchor and structurally survive as a mechanical barrier between the water and the melt pool.

AXISYMMETRIC FINITE ELEMENT MODELS

The beam model provides basic information on the flexural response of the crust. Although it is very simplistic in nature, it can be used for qualitatively displaying the effects of scaling the system parameters. However, finite element models can be used to effectively model the two-dimensional case. For this reason, a number of axisymmetric finite element models have been developed to simulate the response of the crust to the pressure and thermal loadings described above [3]. Obviously, these models represent a circular geometry, but an equivalent radius can

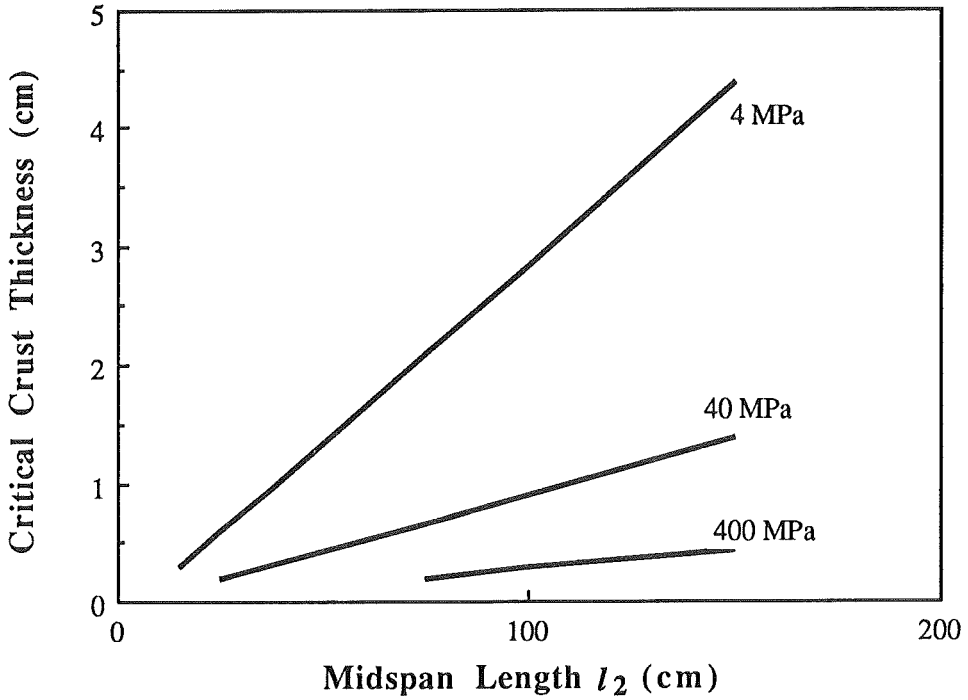

Fig. 2. Critical crust thickness versus midspan length at three critical stress levels for fixed-sized, square anchors ($l_1 = t_1 = 0.05$ m , $p = 5$ kPa).

be used to represent square containment vessels. Figure 3 shows one of the finite element meshes generated with eight-node axisymmetric solid elements. By using solid elements, the model can be used to analyze a thick crust whose material properties varies throughout the thickness.

The geometry and results for a particular example are shown in Figs. 3 - 7. A radius of 0.1922 m was used for the crust. (This is analytically equivalent to a 30 cm x 30 cm square size.) In the center region the crust thickness was assumed to be 2.0 cm, then gradually increased to 3.5 cm at the wall. The top surface was subjected to the pressure from 0.5 m of water, and the curved bottom surface was loaded by a gas pressure of 0.5 MPa (see Fig. 3). The reference (initial) temperature was assumed to be 2000 ^{o}K. The instantaneous temperature varied linearly across the thickness, with the top surface at 1300 ^{o}K and the bottom surface at 2000 ^{o}K (see Fig. 4). The modulus of elasticity for the crust material was taken to be 110.6 MPa, with Poisson's ratio set to 0.3. The coefficient of linear thermal expansion was assumed to be 5.3 x 10^{-6} /^{o}K. The material properties and the temperature distribution given here were used in all test cases throughout the paper, except where otherwise noted. Figure 5 shows the exaggerated deflected shape of the crust as a result of both loadings. The corresponding radial and circumferential stresses are shown in Figs. 6 and 7, respectively.

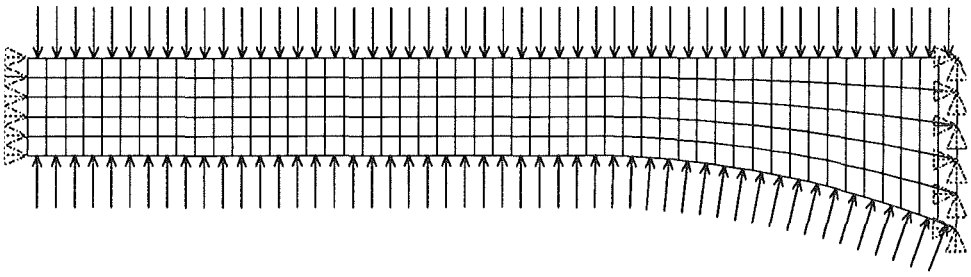

Fig. 3. Axisymmetric finite element model with pressure loadings.

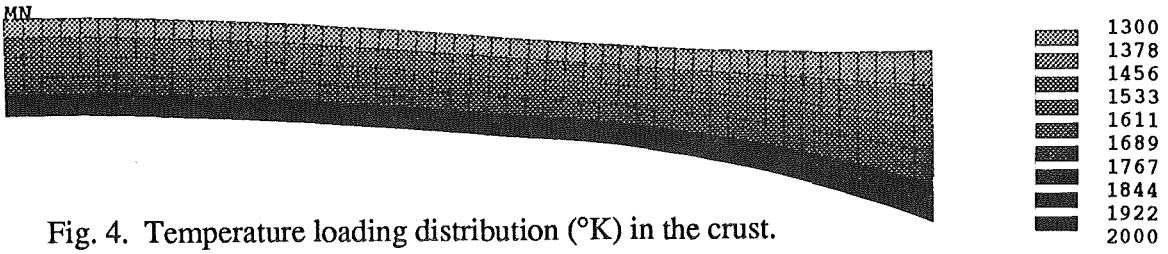

Fig. 4. Temperature loading distribution (°K) in the crust.

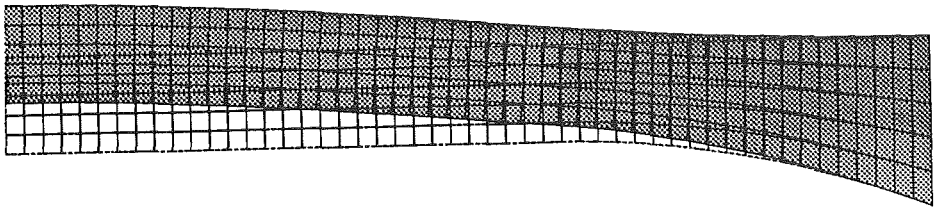

Fig. 5. Exaggerated deflection of the crust with the loadings assumed.

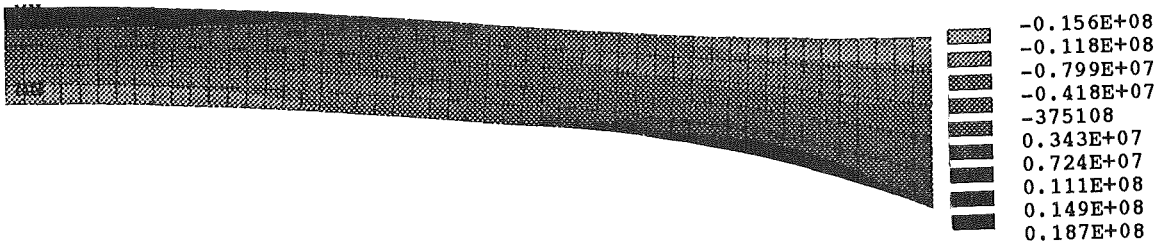

Fig. 6. Radial stresses (Pa) caused by the loadings assumed.

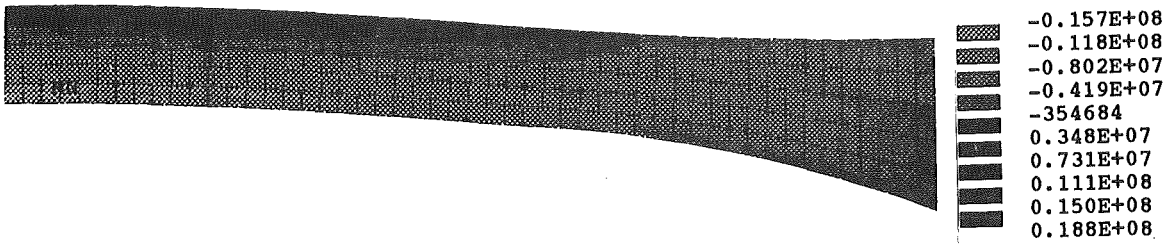

Fig. 7. Circumferential stresses (Pa) caused by the loadings assumed.

ANALYTICAL MODEL OF A CRUST WITH A CIRCULAR GEOMETRY

The finite element models are very versatile for determining the thermomechanical behavior of the crust. However, they are not practical for parametric studies involving changes in geometry. To overcome these drawbacks, theoretical solutions for both bending stresses and membrane stresses in a plate-like crust were developed.

The crust can be represented by a circular plate with a linearly thickened periphery as shown in Fig. 8. In the inner region ($0 \leq r \leq b$) the plate thickness is uniform, and in the annular outer region ($b \leq r \leq a$) the thickness varies linearly to the wall. There is a restriction in the formulation of the plate equations that requires the surface defining the tapered anchor to pass through the center of the plate, as shown by the dashed lines in Fig. 8. The maximum thickness of the anchor is denoted by H, whereas h_o defines the thickness of the crust in the center region. This automatically establishes the ratio h_o/H as being equal to b/a. Fixed boundary conditions are again used with a net uniform pressure loading given by q. The stresses caused by q have been reported by several investigators [4,5]. The thermal stresses resulting from a temperature differential across the thickness have been derived by the authors [6]. The details of theoretical solutions for both can be found in references [2,4,5,6], and a brief review is presented here.

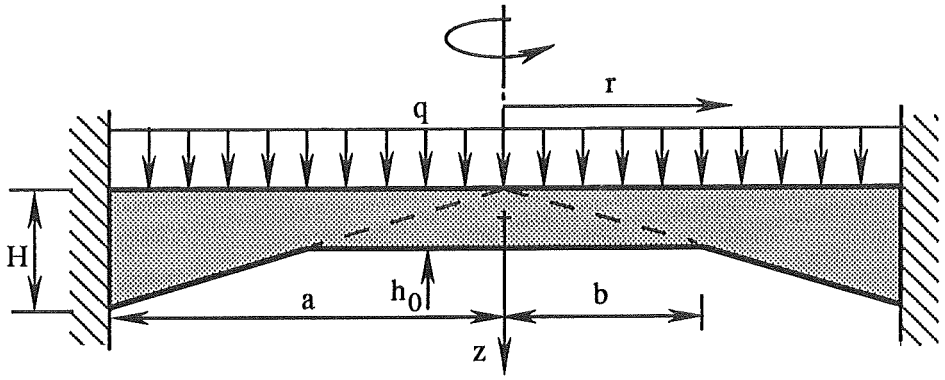

Fig. 8. Geometry and boundary conditions of the nonuniform plate model.

For the plate shown in Fig. 8, the reference (initial) temperature is uniform and denoted as T_{ref}. The instantaneous temperature is T_i, which varies linearly across the thickness, but does not vary over the two surfaces. On the top surface $T_i = T_{top}$, and on the bottom $T_i = T_{bot}$. Consequently, the thermal stresses caused by the temperature change $T = T_i - T_{ref}$ can be separated into two parts, i.e., membrane stresses and bending stresses. The membrane stresses are caused by the average temperature T_a, where

$$T_a=[(T_{top} - T_{ref}) + (T_{bot} - T_{ref})]/2 \qquad (3)$$

Bending stresses result from the linearly varying temperature function T(z), through the thickness of the plate. The function values on the top and bottom surfaces used to determine these stresses are given by

$$T_t = -(T_{bot} - T_{top})/2 \tag{4}$$

$$T_b = (T_{bot} - T_{top})/2 \tag{5}$$

The differential equations governing the the slope (θ) of the midsurface are

$$\frac{d^2\theta}{dr^2} + \frac{1}{r}\frac{d\theta}{dr} - \frac{\theta}{r^2} = -\frac{Q}{D_0} \qquad (0 \le r \le b) \tag{6}$$

$$r^2\frac{d^2\theta}{dr^2} + 4r\frac{d\theta}{dr} + (3\nu - 1)\theta = (1+\nu)\, r^2 \alpha \frac{dM_T}{dr} + 3r(1+\nu)\alpha M_T - \frac{Qb^3}{D_0 r} \qquad (b \le r \le a) \tag{7}$$

where

$$M_T = \frac{12}{h^3}\int_{-h/2}^{+h/2} T(z)\, z\, dz \tag{8}$$

$$D_0 = \frac{E\, h_0^3}{12(1-\nu^2)} \tag{9}$$

and r is the radial coordinate, z is the coordinate through the axis of symmetry of the plate (see Fig. 8), ν is Poisson's ratio, Q is the shear force per unit length, α is the coefficient of linear thermal expansion and h is the thickness at a generic position. Solving the two equations and considering the boundary conditions as well as the compatibility conditions between the inner and outer regions, the slope θ can be found. Then, the bending moment per unit length in circumferential direction (M_ϕ) and in radial direction (M_r) can be calculated from θ.

The solution and computation processes for determining θ, M_ϕ and M_r are complicated, but for engineering practice, simplified expressions for M_ϕ and M_r are available [2,6]. The possible locations for the maximum stress include the midspan of the crust (r = 0), at the start of the anchor (r = b) and at the wall (r = a). To simplify the calculations, the equations for the bending moments can be expressed as

$$M_r = \beta q a^2 + \pi\alpha E h_0^2 (T_b - T_t) \tag{10}$$

$$M_\phi = \beta_1 q a^2 + \pi_1 \alpha E h_0^2 (T_b - T_t) \tag{11}$$

where β, β_1, π and π_1 are dimensionless coefficients as a function of b/a for particular values of r. Equations 12 - 20 give the functions used for the coefficients over the range $0.2 < \lambda = b/a < 1.0$. Since the effects of Poisson's ratio are small, ν was set equal to 0.25.

(at r = 0)

$$\beta = \beta_1 = -4.40\text{x}10^{-3} + 6.521\text{x}10^{-2}\lambda + 0.105\lambda^2 - 8.021\text{x}10^{-2}\lambda^3 - 7.813\text{x}10^{-3}\lambda^4 \quad (12)$$

$$\pi = \pi_1 = -0.274 + 0.526\lambda - 0.771\lambda^2 + 0.618\lambda^3 - 0.211\lambda^4 \quad (13)$$

(at r = b)

$$\beta = -4.500\text{x}10^{-3} + 6.492\text{x}10^{-2}\lambda - 9.479\text{x}10^{-2}\lambda^2 - 8.542\text{x}10^{-2}\lambda^3 - 5.208\text{x}10^{-3}\lambda^4 \quad (14)$$

$$\beta_1 = -4.500\text{x}10^{-3} + 6.558\text{x}10^{-2}\lambda - 3.542\text{x}10^{-3}\lambda^2 - 8.333\text{x}10^{-2}\lambda^3 - 5.208\text{x}10^{-3}\lambda^4 \quad (15)$$

$$\pi = \pi_1 = -0.274 + 0.526\lambda - 0.771\lambda^2 + 0.618\lambda^3 - 0.211\lambda^4 \quad (16)$$

(at r = a)

$$\beta = -0.160 - 3.167\text{x}10^{-2}\lambda + 0.171\lambda^2 - 0.208\lambda^3 + 0.104\lambda^4 \quad (17)$$

$$\beta_1 = -3.600\text{x}10^{-2} - 4.292\text{x}10^{-2}\lambda - 0.147\lambda^2 - 0.177\lambda^3 + 7.813\text{x}10^{-2}\lambda^4 \quad (18)$$

$$\pi = -19.192 + 199.699\lambda - 956.496\lambda^2 + 2594.762\lambda^3 - 4214.479\,\lambda^4 + 4057.856\lambda^5 - 2134.543\lambda^6 + 472.282\lambda^7 \quad (19)$$

$$\pi_1 = -8.042 + 83.559\lambda - 400.736\lambda^2 + 1087.571\lambda^3 - 1766.924\lambda^4 + 1701.589\lambda^5 - 895.226\lambda^6 + 198.098\lambda^7 \quad (20)$$

The corresponding radial and circumferential stresses (σ_r and σ_ϕ) on the bottom surface at each location can be determined by using the following equations (at the top surface negative signs should be added to the right side of the stress equations):

$$\sigma_r = 6M_r / h_0^2 \qquad \sigma_\phi = 6M_\phi / h_0^2 \qquad (r = 0 \text{ and } r = b) \quad (21)$$

$$\sigma_r = 6M_r / H^2 \qquad \sigma_\phi = 6M_\phi / H^2 \qquad (r = a) \quad (22)$$

The thermal membrane stress depends on the average temperature T_a and does not vary across the thickness. The governing differential equations for the radial stress are

$$r\frac{d^2\sigma_r}{dr^2} + 3\frac{d\sigma_r}{dr} = 0 \qquad (0 \le r \le b) \quad (23)$$

$$r^2\frac{d^2\sigma_r}{dr^2} + 4r\frac{d\sigma_r}{dr} + (1+\nu)\sigma_r = 0 \qquad (b \le r \le a) \quad (24)$$

Solving the two equations and considering the boundary conditions as well as the compatibility conditions between the outer and inner region, the stress σ_r is determined. Then the circumferential stress (σ_ϕ) is found from considering equilibrium of an element [6,7], i.e.,

$$\frac{d}{dr}(r\,h\,\sigma_r) - h\,\sigma_\phi = 0 \tag{25}$$

At specific locations the stresses can also be expressed in more compact form, e.g.,

$$\sigma_r = \eta\alpha E T_a \qquad\qquad \sigma_\phi = \eta_1\alpha E T_a \tag{26}$$

where the coefficients are defined as (for $0.2 < \lambda = b/a < 1.0$ and $\nu = 0.25$):

$$\eta = \eta_1 = -3.981 + 11.303\lambda - 20.312\lambda^2 + 17.534\lambda^3 - 5.881\lambda^4 \qquad (0 \le r \le b) \tag{27}$$

$$\eta = -1.197 - 0.030\lambda - 0.026\lambda^2 - 0.081\lambda^3 \qquad (r = a) \tag{28}$$

$$\eta_1 = -0.786 - 0.118\lambda - 0.106\lambda^2 - 0.323\lambda^3 \qquad (r = a) \tag{29}$$

ANALYTICAL RESULTS USING THE PLATE MODEL

Thermal bending stresses, thermal membrane stresses and the flexural stresses caused by pressure loadings can all be calculated separately. Superimposing the results yield the total stress in the crust. For example, consider a crust with an outer radius of a = 0.5 m, a center thickness of h_0 = 2 cm and an anchor ratio of b/a = 0.4. It is loaded hydrostatically by 0.5 m of water on the top and a gas pressure of 10 kPa on the bottom. The temperature differential is again assumed to be 2000 °K - 1300 °K. Figures 9 and 10 show the radial and circumferential stress distribution across the crust's top surface. In this test case the thermal bending and membrane stress throughout the top surface are tensile, but the stresses caused by pressure change sign. It should be noted that the maximum total stress for both σ_r and σ_ϕ are equal to approximately 1.5 MPa, and this occurs at the center of the crust.

To illustrate the effects of scaling, pressure and temperature loadings are considered individually. Figures 11 and 12 show the results of a net pressure acting on the crust with no temperature differential. The bending stress contours of $\sigma_r = \sigma_\phi$ at the center are plotted in Fig. 11 by fixing the pressure at q = 5 kPa and the thickness at h_0 = 1.0 cm. It shows, for example, that as the radius a or the ratio b/a becomes larger, σ_r and σ_ϕ increase rapidly. Figure 12 illustrates the effects of h_0 when the ratio b/a is fixed at 0.5. Additional results can be found in reference [2]. It is important to note that bending stresses caused by pressure are independent of the material properties of the crust. Figures 13 and 14 identify the effects of scaling on the thermal stresses. In Fig. 13, the thermal stress σ_r on the top surface is plotted as a function of αE for various radial locations, fixing the anchor ratio at b/a = 0.5. The stress σ_ϕ is also proportional to the same product, but is not illustrated here. Figure 14 shows as the

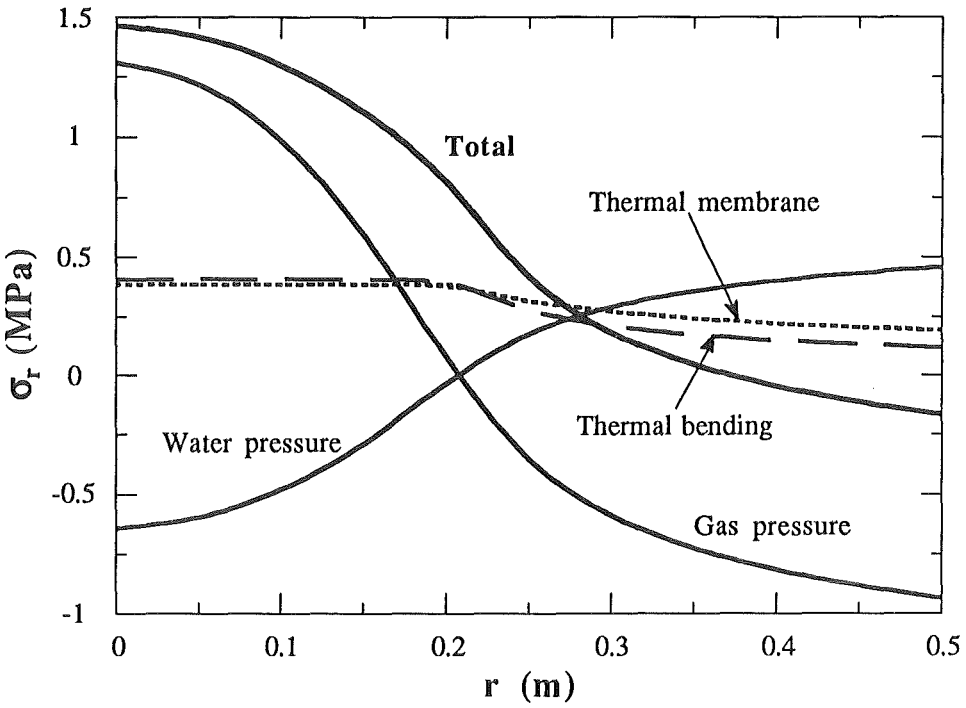

Fig. 9. Radial stress distribution across the top surface of the crust.
(a = 0.5 m, h_0 = 2.0 cm, b/a = 0.4)

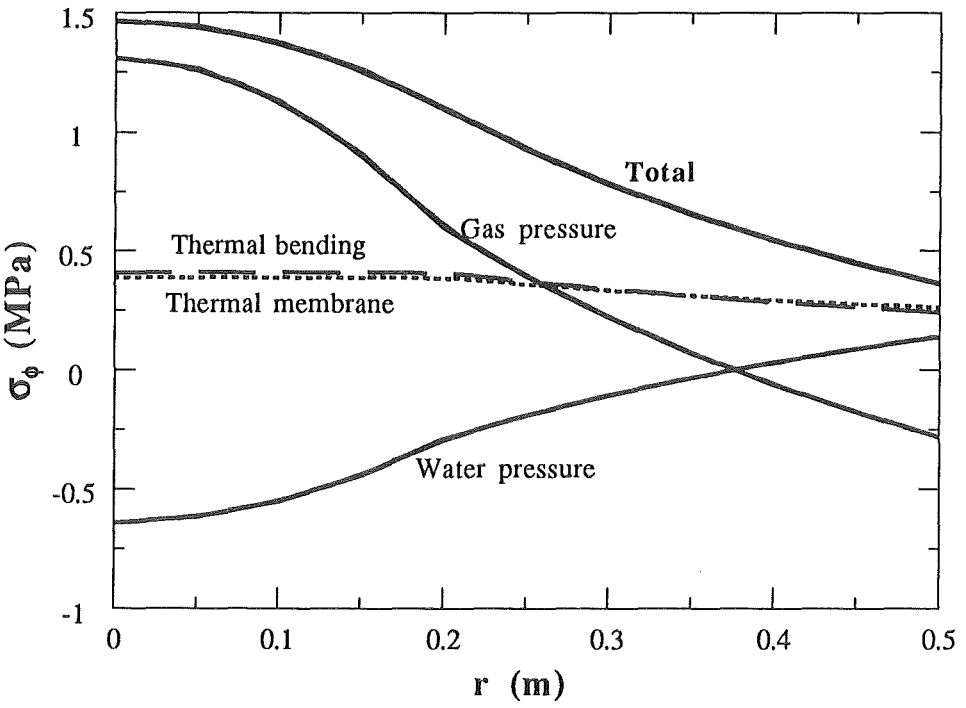

Fig. 10. Circumferential stress distribution across the top surface of the crust.
(a = 0.5 m, h_0 = 2.0 cm, b/a = 0.4)

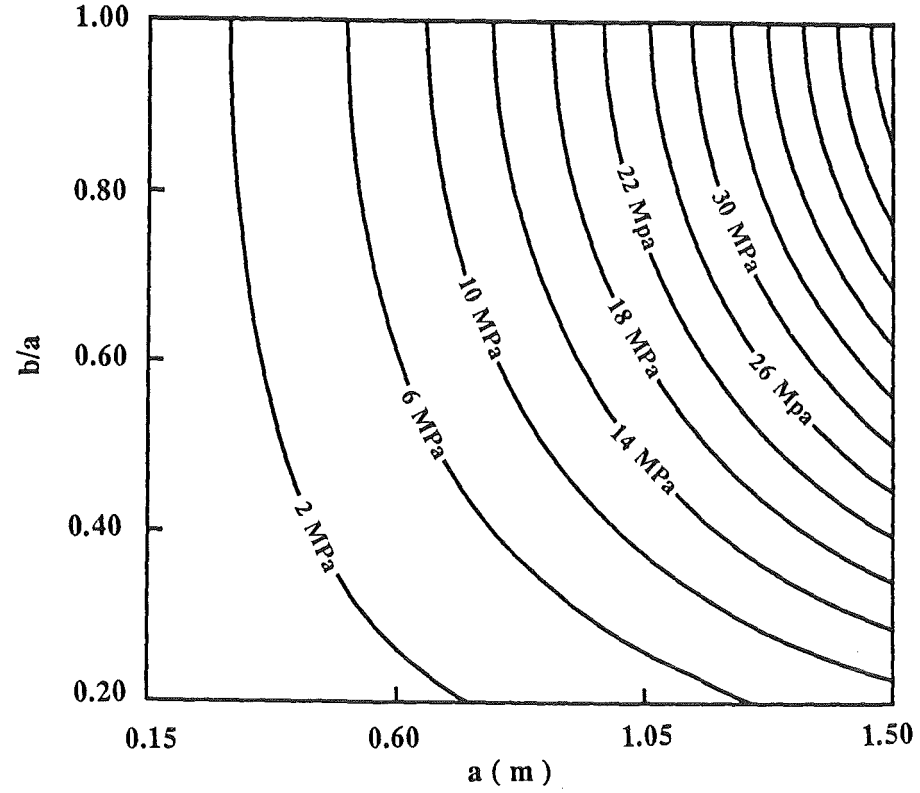

Fig. 11. Contours of bending stress $\sigma_r = \sigma_\phi$ at the center of the crust caused by pressure only. (h_0 = 1.0 cm, q = 5 kPa)

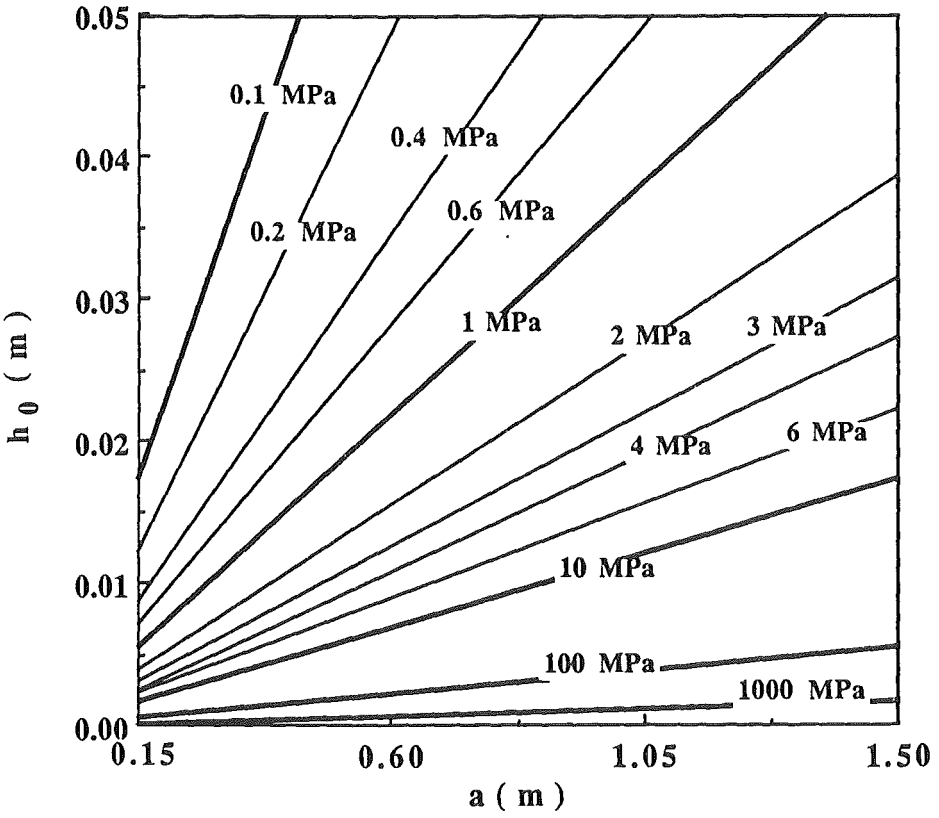

Fig. 12. Contours of bending stress $\sigma_r = \sigma_\phi$ at the center of the crust caused by pressure only. (b/a = 0.5, q = 5 kPa)

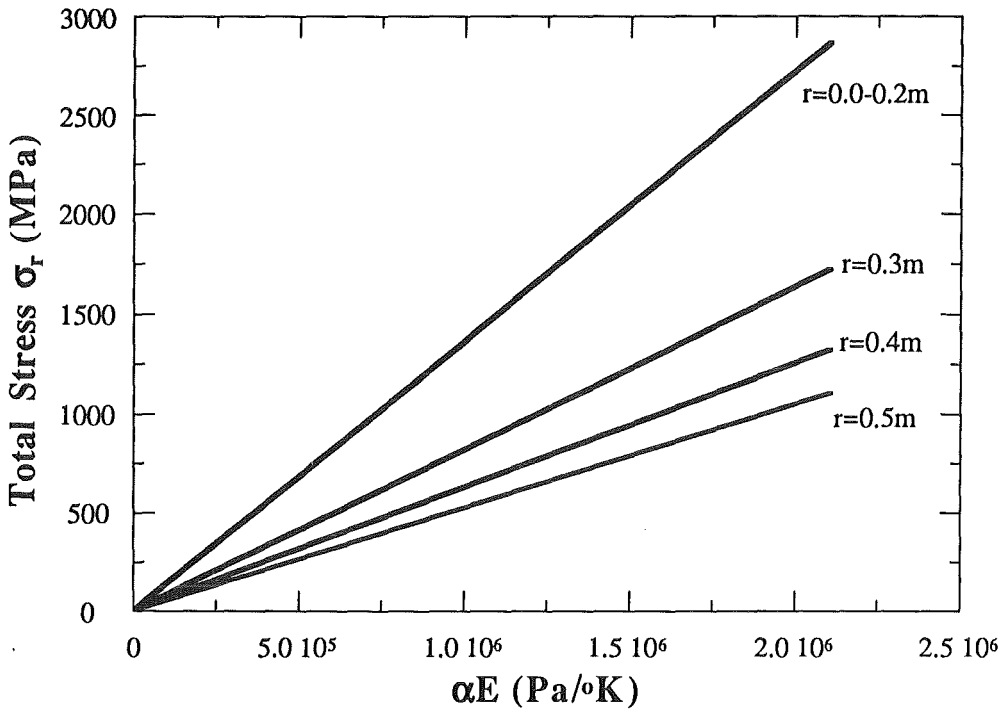

Fig. 13. Total thermal stress σ_r at various radial locations for b/a = 0.4.

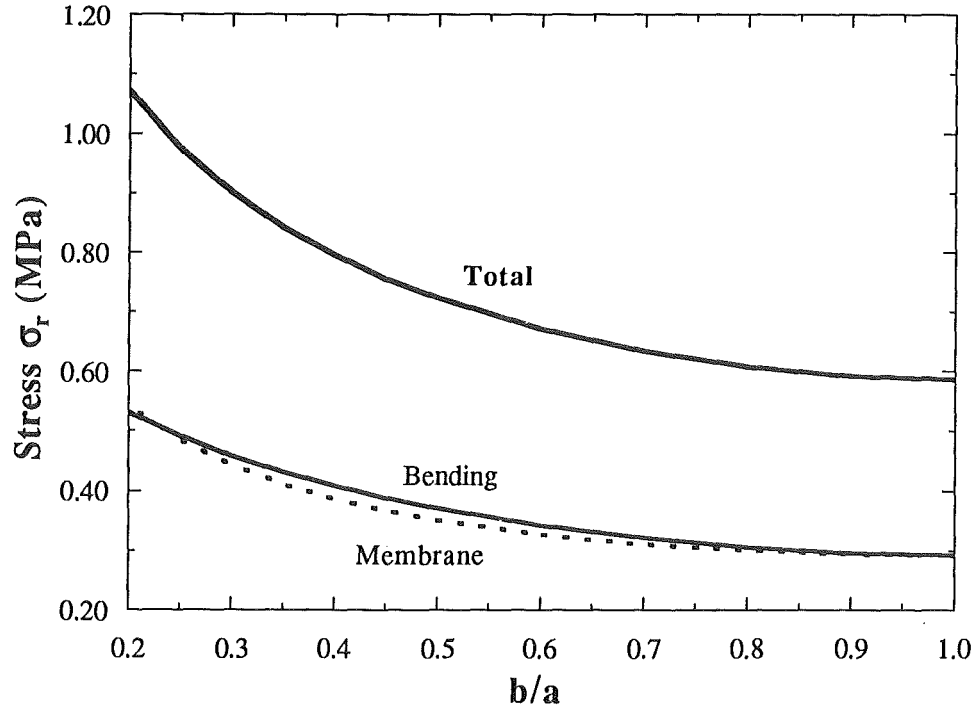

Fig. 14. Thermal stress σ_r for αE = 585.7 Pa/°K.

ratio of b/a decreases, the maximum stresses increase. It can be seen from Eqs. 11 - 29, that the thermal stresses are independent of the thickness h_0 and the radius a, but depend on b/a.

As an example case to illustrate how the analytical model can predict the stability of the crust, assume a thickness and temperature differential (ΔT) as shown in Figs. 15 and 16. If the thermal membrane stress is neglected, the thermal bending stress depends only on ΔT. If it is assumed that the water pressure is 5 kPa, the maximum stress will be σ_r located at the top surface at the wall. Figure 17 shows the maximum stress σ_r as a function of time for different crust radii a, and illustrates when the crust survives and becomes stable. For example, consider the radius a to be 1.28 m. Before a time of 590 sec, the maximum stress σ_r is larger than the expected fracture strength σ_f = 23.4 MPa, and the crust cannot bond over. After 590 sec the maximum stress is less than σ_f and the crust could anchor to the wall. In Fig. 18 the cavity size is fixed at a = 0.32 m, but the top surface pressure is allowed to vary. The maximum stress occurs at the center of the bottom surface for which $\sigma_r = \sigma_\phi$. It can be seen that the added pressure could inhibit the formation of an integral crust. If the pressure was kept at 5 kPa, the crust would become stable after 130 sec. For a pressure of 100 kPa, the corresponding time is 775 sec.

SUMMARY

A number of structural models have been presented that can be used to simulate the response of the crust to pressure and thermal loadings. Parametric studies can easily be performed to illustrate scaling effects and provide predictive analyses. In order to provide more quantitative data (rather than qualitative) the material properties of the crust as a function of temperature and porosity must be identified.

REFERENCES

[1] J. H. Ptacek, Z. Feng, R. L. Engelstad, E. G. Lovell, M. L. Corradini and B. R. Sehgal, "Modelling of the MCCI Phenomena with the Presence of a Water Layer," these proceedings.

[2] R. Engelstad, Z. Feng, E. Lovell and M. Corradini, "Uniaxial and Biaxial Models of an Oxide Crust in MACE: Scaling Effects of Bending Stresses," UWRSR Report No. 65, Department of Nuclear Engineering and Engineering Physics, University of Wisconsin-Madison, February 1991.

[3] R. D. Cook, D. S. Malkus and M. E. Plesha, *Concepts and Applications of Finite Element Analysis*, 3rd ed., John Wiley & Sons, New York, 1989.

[4] H. Favre, "Sur Un Type De Plaque Circulaire Encastree D'Epaisseur Lineairement Variable," *Bulletin Technique De La Suisse Romande*, Vol. 75, 1949, pp. 225 - 230.

[5] S. Timoshenko and S. Woinowsky-Krieger, *Theory of Plates and Shells*, McGraw-Hill, New York, 1959.

[6] R. Engelstad and Z. Feng, "Thermal Stresses in Circular Plates with Linearly Thickened Peripheries," to be published.

[7] S. Timoshenko and J. N. Goodier, *Theory of Elasticity*, 2nd ed., McGraw-Hill, New York, 1951.

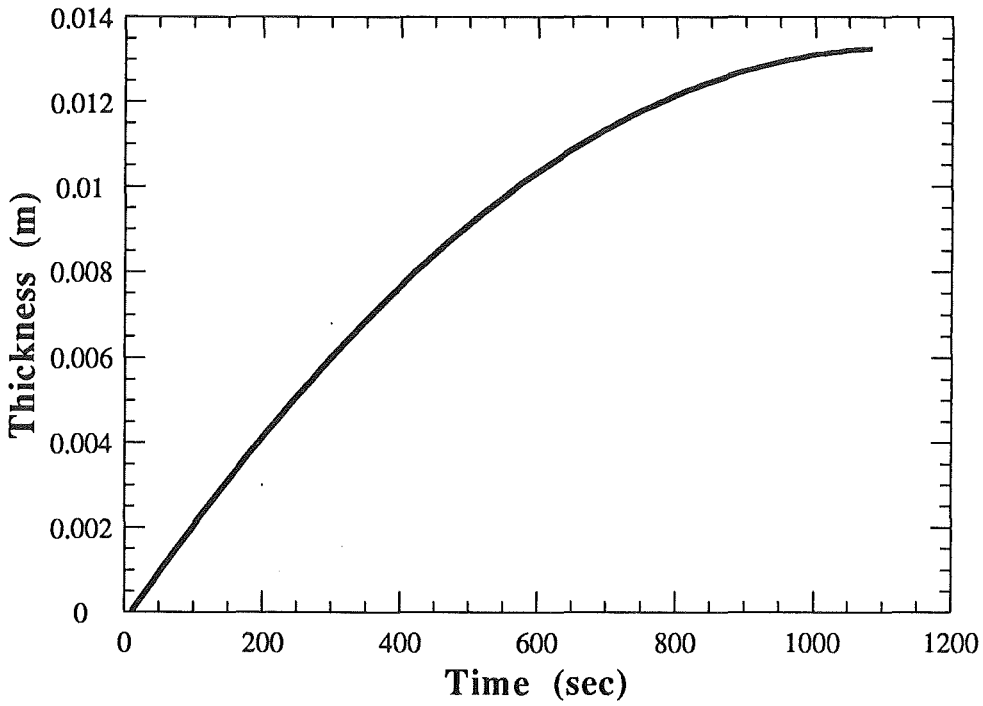

Fig. 15. Thickness as a function of time for an example case.

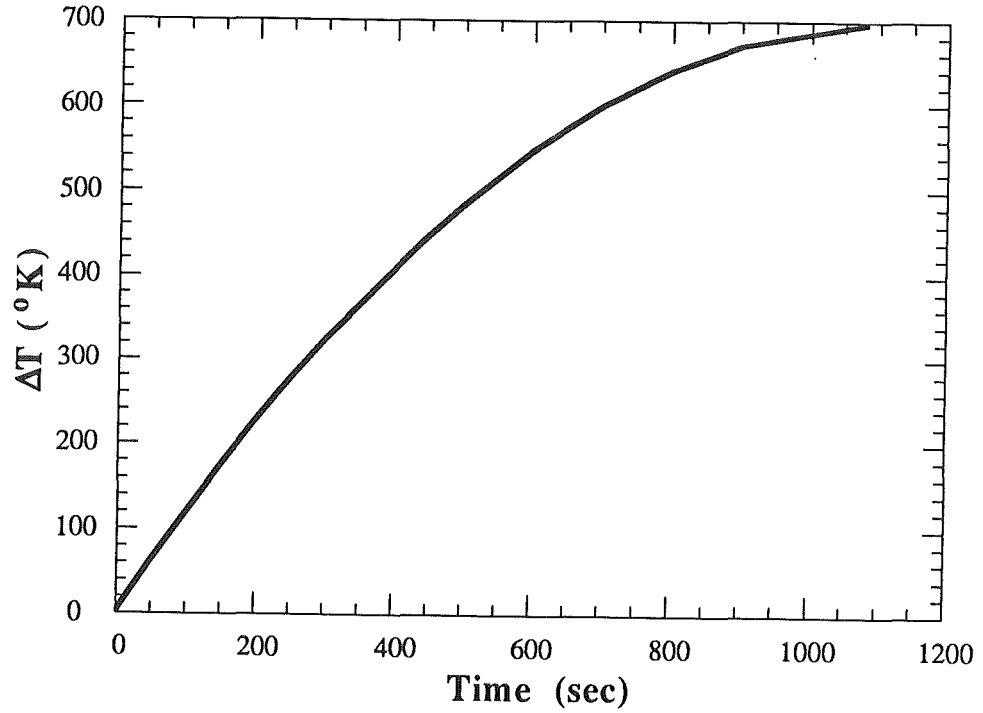

Fig. 16. Temperature as a function of time for an example case.

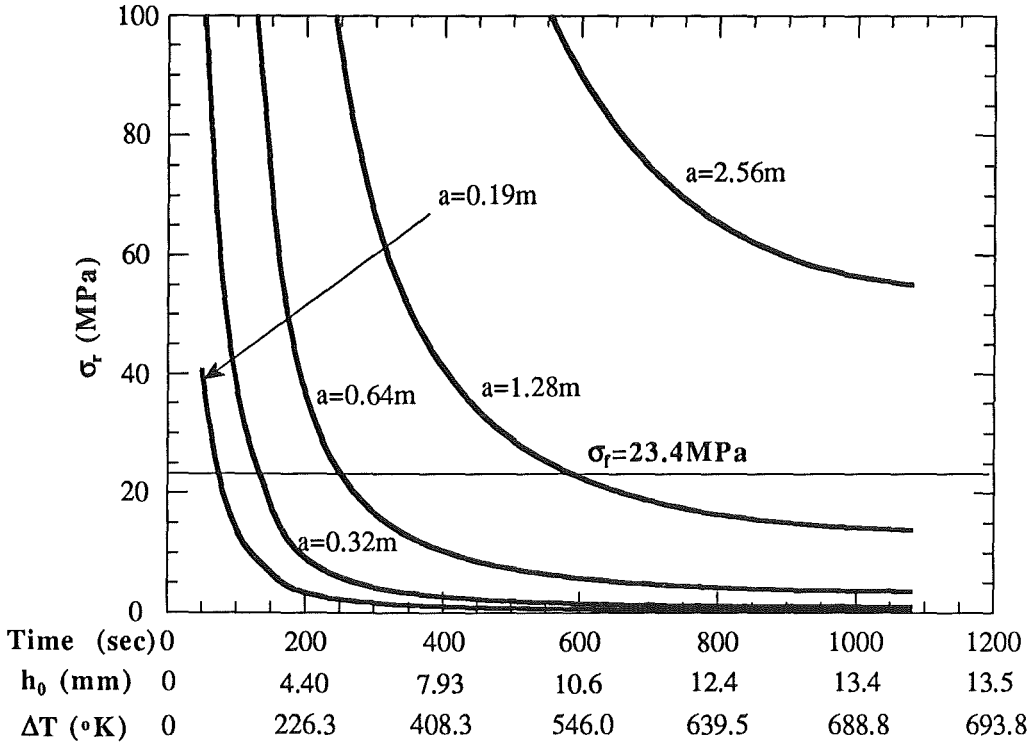

Fig. 17. Maximum stress σ_r at the boundary for an example case.

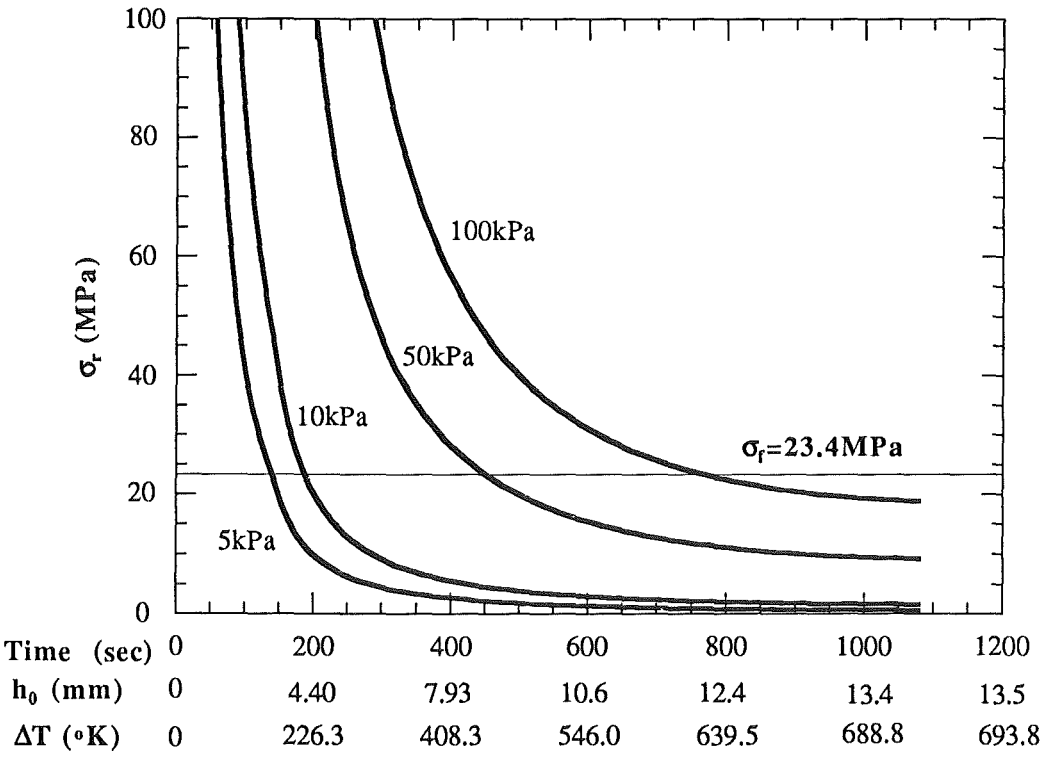

Fig. 18. Maximum stress σ_r at the center of the crust for an example case.

MODELLING OF THE MCCI PHENOMENA WITH THE PRESENCE OF A WATER LAYER

J.H. Ptacek+
Z. Feng+
R.L. Engelstad+
E.G. Lovell+
M.L. Corradini+
B.R. Sehgal*

+Mechanical and Nuclear Engineering Departments
University of Wisconsin, Madison WI 53706
*Nuclear Division, Electric Power Research Institute
3412 Hillview Avenue, Palo Alto CA 94306

ABSTRACT

If a severe reactor accident progresses to the point that the core melt breaches the reactor pressure vessel, the core is deposited onto the containment concrete basemat. Termination of the accident and attainment of a stable state where core cooling is assured requires the presence of a water layer which carries away nuclear decay heat. This paper discusses the possible set of conditions necessary for the attainment of this state and presents a simple thermal-structural model that predicts the transition of the molten core-concrete interaction from one state to the other. Such a model provides a semi-quantitative picture of how the interaction may proceed and how it scales from tests to prototypic reactor scale. All quantitative predictions are tentative pending more exact core-concrete properties.

INTRODUCTION

A severe reactor accident occurs when core cooling is lost or impaired for a significant length of time. Under this condition the core melt progression could proceed, without some intervention and cooling, to the point where a significant core melt mass pours onto the reactor pressure vessel lower plenum walls, causing a failure. Subsequently, the core melt would be deposited on the containment concrete floor and, if not quenched by residual water, it would begin to attack the concrete. In this situation termination of the accident and attainment of a coolable state for the core debris requires the presence of a water pool of significant size or with a means of replenishment to assure a heat removal path for decay heat to the ultimate heat sink. Even though this set of conditions is necessary to attain a stable coolable state it is not sufficient. One must consider further the local set of conditions at the melt-water interface that assure core debris coolability.

To do this we first must consider what coolability means. Next, we consider the various geometrical configurations in which coolability might be achieved. Finally, we try to identify

the key events or junctures in the path of this physical process that would determine if coolability is achievable and how the phenomena would scale from tests to the actual prototypic dimensions.

Criteria for Coolability

Core debris coolability in a stable state should be defined in terms of the ability of the containment system to reject the core decay heat to the environment without threatening its integrity. Since the containment is currently designed as a closed system with no mass transfer, this implies that not only should the decay heat be transferred out of the containment, but also the molten core-concrete interaction (MCCI) should be eventually halted to prevent the pressurization of containment by concrete decomposition gases, precluding eventual overpressurization. This general criterion implies that the water pool added to the core debris on the containment floor is effective in keeping the debris-concrete surface temperature below the concrete ablation temperature (<1500K) and also below a temperature at which the concrete degases and releases noncondensible gases (<1000K).

Now this criterion also has an element of time associated with it. The consideration of containment failure in the Zion/Indian-Point study [1-3] suggested that the water may be able to rapidly cool the debris ("quench" it) in a time which is short compared to the time for significant ablation (< 1 hr). This "quenched" debris configuration is one possible end-state to achieve debris coolability with a time scale of less than an hour. A second time period for achieving coolability may be within the first day of the accident where the final debris configuration may not necessarily be similar to that following a rapid quench. The major feature of this time interval is that the total amount of concrete attack during a MCCI is limited so that the concrete basemat is not penetrated by a core debris "melt-through". In past studies [4,5] this melt-through failure was estimated to occur in about one day. The third and final time period for achieving coolability would be within a time of a few days to weeks. In this case the MCCI could proceed within the containment, but at a very limited rate (< 1 cm/hr). In this situation operator intervention could be successful in allowing for containment filtered venting during this extended period and one could still successfully achieve stable debris coolability with possibly an even wider variety of possible geometric configurations; e.g., core debris with some of remaining molten mass surrounded by solidified debris.

One should consider the possible debris configurations that would be associated with these time intervals and the criterion for debris coolability.

Coolability Geometric Configurations

If the presence of water can cause the core melt to "quench", as depicted in References 1-3, then the core debris would solidify as individual discrete pieces, almost like a coarse debris bed (Figure 1). Such an arrangement would be enhanced by the vapor generation and decomposition gases mixing the melt and water together to promote quenching. Such a possible configuration was noted by Theofanous et al. [6] in simulant tests with water and liquid nitrogen as simulants for the core melt and coolant. The upward heat loss to the coolant pool was greater than 1 MW/m^2. However, this geometry has not been observed in the more prototypic material tests in the past [7,8]. This does not mean it would not occur, simply that for the limited tests performed to date this geometrical configuration has not evolved.

If the presence of water causes the core melt to solidify, not as discrete particles but as a solid layer, then the "quench" becomes a longer cooldown process. In the limit if the solid material that has solidified does not exhibit cracking or the development of fissures to allow water into the solid for cooling, the decay heat must be locally transferred to the water layer by conduction heat transfer through the solid "crust" as the dominant resistance (Figure 2). Under this situation the mass of core debris that can exist in a stable quenched state is determined by the containment cavity floor area and the thickness of this solid core "crust". (This assumes that the core debris can actually spread out over the whole cavity floor.) This thickness, L_f, is given by

$$L_f = \left(\frac{2k_f \Delta T}{q''} \right)^{1/2} \qquad (1)$$

where k_f is the fuel thermal conductivity, ΔT is the temperature difference between the crust maximum temperature and its surface temperature, and q" is the volumetric decay heat rate. The maximum temperature difference that could exist in the debris would be the maximum at the ablation temperature of the concrete (1500 K) and the surface at the water temperature above (400K). The decay heat nominally is about one percent of the core thermal power (~350 w/kg) about an hour after shutdown. A simple calculation indicates that this length scale is less than 100 mm and even under the most optimistic uniform spreading conditions could not accommodate all the reactor core debris in a stable configuration. The power transferred from the crust to water would be coolable if the heat flux is less than 0.2 MW/m^2. The time needed to achieve this condition could be longer than an hour, and would probably be relatively independent of dilution by concrete decomposition products, i.e., ΔT and q" would decrease proportionately. This geometry has also not been observed in prototypic material tests, although in theory it could evolve under certain reactor conditions.

The last geometrical configuration to consider is one in which the core debris does not "quench" nor does it form an impermeable solid crustal layer. [We have neglected the situation in which the core debris quenches as it pours through a water pool already present; this could be discussed separately, but does not seem to be a relevant mechanism for all the debris to be quenched.] Rather, the core melt is deposited as a molten pool on the concrete basemat and the water pool, if present, is atop this layer in a stratified geometry and an MCCI begins (Figure 3). In this situation the presence of the water layer will eventually cause a crust to form on the surface of the melt pool. In this case a discussion of coolability is more problematic and one must consider past data.

In past experiments [7,8], particularly the SWISS test, this was observed. More recently under the ACE Phase D experimental program the first scoping test was conducted to examine core melt coolability, MACE0 [9]. In this experiment about 100 kg of core melt simulant pool (UO_2, ZrO2, Zr, concrete decomposition products) was formed in a 300 x 300 mm square concrete crucible by electrical resistance heating. The Joule heating was supplied by tungsten electrodes on two sides of the pool. The molten pool was formed (temperature ~2000 K) in a manner similar to that used in other ACE tests and once concrete ablation began (as determined by thermocouples) and the pool was molten on top, water was added from above, and maintained at a depth of about 500 mm (Figure 4 and 5). Based on visual observation of the surface of the interaction, measurement of upward heat loss, downward ablation and melt temperature, four important observations were made:

(1) Early in the interaction a large upward heat flux was measured (Figure 6; >1 MW/m^2) and was attributed to a time when no crust was present.
(2) A crust formed on the surface of the melt (floating crust) after a few minutes and limited the upward heat flux to a value of about 0.2 MW/m^2.
(3) The crust bonded together, spanned the cross-section of the crucible and became structurally supported by the walls (actually partially supported by the tungsten electrodes).
(4) An instability developed in the MCCI whereby intermittment eruptions were usually observed and measured in the power input (Figure 5) and the upward heat loss (Figure 6). This caused a noticeable fraction of the melt to be ejected through the crust with gases; this was a cyclic phenomena over the course of the test.

These results are considered to be qualitatively similar to what might occur at larger reactor scales, although the specific behavior is this test was probably influenced by the presence of the ablating concrete walls at this scale (300 x 300 mm). It is our view that this geometric configuration is the most probable, and to determine the core coolability limit requires us to

examine the evolutionary path for the MCCI in such a geometry to attain a coolable state (Figure 7).

Key Events During Stratified Melt-Water Interactions

The first observation of the MACE0 scoping test indicated a large upward heat flux. This could be interpreted as a time regime when no crust was present between the melt pool and the water layer. Farmer, et al., [10] have considered this geometry in their analysis and propose a model, CORQUENCH, that predicts a large heat flux, similar in magnitude to that measured. In our view this time regime occurs when the melt is superheated and the MCCI is quite aggressively ablating concrete and generating a large amount of decomposition gases with a large superficial gas velocity in the pool (perhaps a churn-turbulent flow regime). Under this situation if a solid is formed at the melt-water layer interface it would be difficult for it to exist for a long period due to the gas agitation of the interface, which would cause it be submerged and remixed with the superheated bulk melt pool. Farmer has proposed a mechanistic criterion for this [11], and this may also correspond to the high gas velocity at these higher temperatures. As the bulk melt pool temperature falls below the liquidus then a solid fraction of one phase will be formed and the superficial gas velocity would decrease. Both of these effects together may allow a crust to form. A crust would form in a quiescent state when the interfacial temperature falls below the liquidus temperature. In the agitated state of an MCCI it seems likely that some combination of further cooling below the liquidus and/or a decrease in decomposition gas agitation would promote crust formation. The CORCON model [12] assumes crust formation when the interface temperature falls below the solidus regardless of gas agitation. This may be a useful limit to consider under MCCI conditions. This crust though would probably float on the interface of the two layers because of the gas flow suspending it from below and its own density and porosity.

Once the floating crust has formed it would act as a thermal resistance to further heat transfer upward into the water pool. The melt pool may probably be in a state where the bulk temperature has fallen below the liquidus and some solid fraction exists in the bulk as a slurry. Once again the CORCON conceptual model of this process considers this picture and may again be appropriate. In the model, gas generated by the MCCI agitates the pool, causes a level swell and can escape through the crust due to fissures or cracks within it, but water is assumed not to penetrate downward. Theofanous [13] has proposed that a necessary condition for coolability is that, if a crust is present, it should be "floating" (i.e., in direct contact with the melt pool) and that cracks or fissures be present to allow gas out and water to migrate into the crust for additional cooling. A key question is if the prototypic crust material possesses these features.

The final two observations from the MACE0 scoping test are more complex and involve structural as well as thermal considerations. The first consideration is under what set of conditions does the floating crust bond together to span the chamber cross-section and become structurally supported by the walls (Figure 7). An important corollary to this question is how this transition scales with geometry and material properties. Once the crust is "bonded", the possibility exists that the thermal and mechanical loads imposed upon it may cause it to rupture at a later time. This type of event was observed to regularly occur in the MACE0 test where eruptions caused core melt to be expelled from the pool and through the crust, then quenched as debris above in the water pool. This process proved to be quite efficient for the MACE0 test, however, scale effects must be considered to examine if this is possible at reactor scales. Both of these events are now under consideration [14].

Scaling of Crust Growth and Stability

To examine the key events between the melt layer and a water layer during an MCCI, particularly the effect of scale, we have developed a one-dimensional model for an MCCI including the structural modelling of the crust. This model is not intended to be a precise predictor of the MACE experiments, rather it is intended for use to describe the qualitative and quantitative trend of the MCCI as observed in the MACE tests and as expected at larger scales. A more detailed thermal and structural analysis is now underway for experimental interpretation using our modified CORCON model and structural analyses [14].

This model makes a number of simplifying assumptions:

(1) The MCCI process is one-dimensional, i.e., sidewall heat loss is either small compared to upward and downward losses at large scale (based on area) or can be included as a power decrement in the test analysis.

(2) The MCCI has proceeded to a stage where the majority of the melt is oxidic, i.e., more detailed CORCON calculations indicate rapid oxidation of the metal in the MACE scoping test (and in future tests), before significant crust formation.

(3) The melt pool thermophysical properties are not dependent on temperature and composition; this is a known simplification that can be corrected in later more sophisticated MCCI calculations (i.e., CORCON phase diagrams and temperature dependent properties).

(4) The structural model also uses temperature independent properties, although compositional effects are treated in a parametric fashion.

The basic energy balance considers the melt pool to be homogeneous and well-mixed with a single bulk temperature. The heat loss from the pool can occur due to ablation of the concrete from below, with evolution of decomposition gases to stir the pool and condensed phase

oxides added to the pool, and due to heat transfer to the water pool above. The gases added cause the pool to swell due to gas holdup and this agitation affects heat transfer. The heat transfer correlation used for energy transfer within the pool to its upper and lower boundary is that developed originally by Kutateladze and modified by Bradley [15]. The ablation process is assumed to be quasi steady-state, so that all energy transferred to the concrete interface from the pool goes into ablating the concrete. The energy transferred up into the water pool must pass through a crust (if one is predicted to form) and then be transferred to the water pool, by subcooled film boiling into a subcooled water pool or by vaporization of a saturated pool in a film boiling mode. In the model we have attempted to correct the convective film boiling coefficient for augmentation in agitation caused by the decomposition gases, based on the data of Duignan [16].

The determination of crust formation follows the qualitative observations of the MACE scoping test, i.e., the crust would not be formed when the melt pool is at a temperature above its liquidus and the flow regime is churn turbulent. Also we use the same crust formation criterion as CORCON [12], i.e., a solid is formed at the interface if the melt-water interface temperature is below the melt solidus temperature. If the melt pool bulk temperature decreases below the liquidus a solid fraction is considered to exist in the bulk as a slurry.

One crucial decision (Figure 7) involves a determination if the crust is floating or if it is structurally capable of bonding together and spanning the chamber, i.e. becoming self-supporting and separating from the melt pool. The second possible event of interest is whether the crust would break due to altered thermal/structural conditions that occur later in the MCCI, e.g., gas pressure. Let us consider each of these separately.

If a crust were to form at the melt-water interface during an MCCI, the primary loading (considering the crust as a structural component) would consist of a net uniform pressure over its entire surface (due to water above it and/or gases below) and a temperature gradient through its thickness. For a "floating" crust to bond together and span the chamber to become a "supported" crust, it would require that the combined mechanical bending stresses from pressure and thermal stresses from a temperature gradient in the "supported" crust be less than the fracture strength of the material. The one-dimensional model determines the conditions under which this would occur. The "supported" crust is pictured in Figure 8 with anchors which can exist at the chamber walls because of preferential solidification near the colder surface. In this one-dimensional "beam" geometry one can calculate the mechanical bending stresses. The thermal stresses can be superimposed on the bending stresses, in effect decoupling the problem. The maximum bending stress in this geometry would occur at the center, if the anchor is more than 50% thicker than the rest of the crust [14]. In our analysis

we arbitrarily consider the anchor to be of a square shape for simplicity. Parametric calculations indicate this assumption is not important to the results. The maximum bending stress, σ_c, is given by

$$\frac{\sigma_C}{p} = \sigma_C^* = \frac{l_2^2 / l_1^2}{t_2^2 / t_1^2}\left\{3 - \frac{\left[2 - \left(1 - t_2^3 / t_1^3\right)\left(3 - l_1 / l_2\right)\left(l_1^2 / l_2^2\right)\right]}{\left[1 - \left(1 - t_2^3 / t_1^3\right)\left(l_1 / l_2\right)\right]}\right\} \qquad (2)$$

where p is the net pressure on the crust and all the dimensions are defined in the figure. Notice that the maximum bending stress is independent of the crust material properties and depends only on geometry and the pressure loading. The thermal stress, σ_t, is known to be proportional to the expression

$$\sigma_t \sim \frac{Ea\Delta T}{(1-\nu)} \qquad (3)$$

where E is the elastic modulus, "a" is the thermal expansion coefficient, ν is Poisson's ratio and ΔT is the temperature drop through the crust (assuming a linear profile). In actuality the exact thermal stress expression is more complex and we use this to indicate the order of magnitude of the thermal stress. Note that the thermal stress is totally determined by material properties and the predicted temperature difference across the crust, derived from the MCCI model calculation.

The fracture strength, σ_f, for the crust depends on the type of material solidifying and herein lies the greatest uncertainty for experimental analysis and predictions of prototypic reactor behavior. The initial core melt composition upon deposition on the containment floor would be primarily urania, zirconia, and zirconium metal with some stainless steel. However, rapid oxidation of the metals and addition of concrete species (e.g., CaO, SiO_2, Al_2O_3) due to the MCCI would progressively change the composition and can radically affect the properties (Table I). As the Table indicates the fracture strength and elastic modulus is large for pure urania, but much lower for a mixture of urania, zirconia, and concrete products as measured from the MACE scoping test. In one case this implies thermal stresses are important and the other relatively unimportant. For our analyses in this paper we use the measured properties from the MACE scoping test as being representative of the prototypical situation. However, one must be aware of the importance of determining the appropriate material properties.

TABLE 1

Mechanical Properties for Core Materials

Material	UO2	MACEO Crust
Elastic Modulus	160 MPa	110 MPa
Density	8000 kg/m3	2700 kg/m2
Poisson's Ratio	0.32	0.3
Thermal Coef. (mullite)	1.35 (10^{-5}) K^{-1}	5.3$(10^{-6})K^{-1}$
Fracture Stren.	128 MPa	23.5 MPa
Thermal Stress ($\Delta T = 1000$)	3176 MPa	0.8 MPa

A series of calculations were performed to determine when the crust would bond together and form a "supported" crust. The initial conditions taken for the calculations were similar to the pretest conditions for the planned MACE tests, i.e., Joule heating of 350 watts/kg, a water layer of 500 mm, urania, zirconia, zirconium, calcia melt above a limestone-common sand basemat, initially at a temperature of 2300K. Under such a condition the MCCI would rapidly oxidize the zirconium metal while the heat transfer upward to the water is quite large (Figure 9). However, after a short time the heat flux rapidly decreases as the melt pool cools down by upward and downward heat loss. The discontinuity in the upward heat flux curve (~150 sec) indicates the point where the interface falls below the melt solidus temperature and a floating crust is formed. Notice that after this point the upward heat flux decreases even more rapidly so that after about ten minutes the upward heat flux has reached an asymptotic value of about 250 KW/m^2. If one now plots the maximum stress in the crust if it were self-supported (Figure 10), the point where the crust could actually exist as a structural member, supporting its weight and that of the water above it, occurs when this stress falls below the fracture strength, which is the horizontal line (~210 sec). Before this time the stress falls rapidly as it grows in thickness. For this example calculation we used the chamber dimensions to be 500 x 500 mm, which corresponds to the first MACE test dimensions.

An important point to note is that an uncertainty in the fracture strength of the crust material has a large effect (Figure 11) on when the floating crust would bond together and be self-supported. In this figure the fracture strength has been normalized to the experimentally measured value in the MACE scoping test. Also note that the crust thickness at this bonding time can vary. In both cases an increase in the fracture strength (all other properties remaining

unchanged) allows the crust to be thinner at the given time when it can bond and be self-supporting.

One can use such a model to predict the effect of experimental scale on the transition between a floating crust and a bonded self-supported crust (Figure 12). This is important because it indicates how the reactor scale (lateral dimensions greater than a few meters) might differ from the test sale (lateral dimensions less than a meter). The model results indicate that the time needed for the crust to bond increases dramatically for a lateral span greater than one meter. In fact the model predicts that the floating crust would not become self-supporting (physically and thermally isolating the melt pool from the water) until many hours after the MCCI begins for reactor scales. Actually no bonding is predicted for over ten hours if the lateral span exceeds four meters. The reason for this lies in the fact that the floating crust is predicted to asymptotically come to a quasi-steady thickness (15 mm) to balance decay heat losses. Thus a floating crust may be the most realistic condition at reactor scales, while test conditions may still exhibit a self-supported crust.

Once the crust has bonded and become self-supporting it can isolate the melt pool from the water layer. In the MACE scoping test, eruptions were observed at regular intervals throughout the test as evidenced by the input power history and upward heat loss (Figures 5 and 6). The reason for these eruptions is not clear, although we believe they could be explained by a pressure build-up of decomposition gases below the supported crust due to the continuing MCCI. The input power history would change in this scenario due to the change in resistivity as affected by the increase in melt temperature as the melt pool becomes thermally isolated. The pressure builds because the rate at which gas can escape through the porous crust is limited and decreases as the crust thickness grows in comparison to the rate it is generated by the MCCI. The crust growth reduces upward heat loss allowing the melt temperature to rise, thereby causing a faster pressure increase in the gases within than above the pool and the crust. At some point the bending stress within the crust would again exceed the fracture strength of the crustal material and it would break allowing gases to be rapidly vented, most likely with ejection of the melt debris due to a pool level swell as the gas escape. This picture qualitatively agrees with the observed MACE scoping test behavior. To quantitatively predict this we perform a simple mass balance on the gas mass that is trapped below the crust and solve for the rate of change of pressure, P_g, within this fixed volume given by

$$\frac{dP_g}{dt} = \frac{P_g}{m_g}\frac{dm_g}{dt} + \frac{P_g}{T_g}\frac{dT_g}{dt} \qquad (4)$$

where m_g is the trapped gas mass and T_g is its temperature and is assumed to correspond to the pool temperature. The rate of change of the gas mass is equal to that produced by the MCCI from decomposition gases, m_{abl}, and that flowing through the crust, m_c

$$\frac{dmg}{dt} = m_{abl} - m_c \tag{5}$$

where m_c is determined by flow through this porous crust by Darcy's law to be

$$m_c = \frac{\kappa_c(P_g - Po)}{\delta_c \mu_g} \tag{6}$$

where κ_c is the crust permeability (a function of the unknown porosity and microscopic length scale of flow passages), δ_c is crust thickness which increases with time, μ_g is the gas viscosity and P_o is the ambient pressure above the crust. Figure 13 indicates how the time to crust failure and eruption is affected by the crust permeability (sand has a permeability of about $10^{-10} m^2$). This indicates that the eruption time is on the order of a few to ten minutes after crust bonding and is consistent with experimental observations. The pressure necessary to induce this failure is also shown to be small; less than a tenth of a bar.

Current Observations and Future Work

Core debris coolability is a complex problem that requires further study and experimentation. At this juncture we have presented a complete picture of the conditions necessary for coolability, the possible melt-water geometrical configurations possible for ultimate coolability, and detailed analysis of the geometrical configuration observed in the MACE tests. This analysis suggests that structural as well as thermal effects must be considered to predict conditions for coolability. Specifically, the scaling analysis indicates a floating crust is the most likely configuration at large scales for the melt-water interface as coolability is reached. Test scales may be prone to producing self-supported crusts unless measures are taken to assure a floating crust geometry. Also the eruptions observed at test scales may be interpreted to be caused by gas buildup from below the crust. Finally, ultimate debris coolability may only occur if the floating crust allows water to filter downward toward the melt pool as decomposition for increased cooling gases pass out of the cooling melt pool. These effects must be verified in the MACE experiments where the upward heat flux is measured, given a floating crust configuration, and the ability of water to filter downward is assessed.

REFERENCES

(1) "Zion Probabilistic Safety Study," Commonwealth Edison Co, 1981.

(2) W.B. Murfin, Report of the Zion/Indian-Point Study, Sandia National Laboratories, NUREG/CR-1410, SAND 80-0617 (August 1980).

(3) J. Meyer, Preliminary Assessment of Core Melt Accidents at the Zion and Indian Point Nuclear Power Plants and Strategies for Mitigating Their Effects.

(4) USNRC, WASH 1400, "Reactor Safety Study--An Assessment of Accident Risks in U.S. Commercial Nuclear Power Plants," NUREG-75/014 (October 1975).

(5) USNRC, NUREG-1150, "Severe Accident Risks: An Assessment of Five US Nuclear Power Plants," NUREG-1150 (June 1989).

(6) T. Theofanous, M. Saito, "An Assessment of Class-9 (Core-Melt) Accident for PWR Large Dry Containment Systems," Nuclear Engr and Design, V66, p 301 (1981)

(7) F.R. Copus, D.R. Bradley, Interaction of Hot Solid Debris with Concrete, NUREG/CR-4558, SAND 85-1739 (1986).

(8) R.E. Blose, J.E. Gronager, A.J. Luo-Antilla, J.E. Brodeman, Sustained Heated Metallic/Melt Concrete Interactions with Overlaying Water Pools, NUREG/CR-4727, SAND 85-1546 (July 1987).

(9) B.W. Spencer, M. Fischer, M.T. Farmer, D.R. Armstrong, MACE Scoping Test, Argonne National Laboratory, MACE-TR-DO3 (June 1991).

(10) M.T. Farmer, "CORQUENCH: A Model for Gas Sparging-Enhanced Melt-Water Film Boiling Heat Transfer," ANS Winter Meeting (Nov 1990).

(11) MACE Technical Review Committee Meeting, Argonne National Laboratory (July and December 1991).

(12) R.K. Cole, D.P. Kelly, M.A. Ellis, CORCON-MOD2: A Computer Program for Analysis of Molten-Core Concrete Interactions, NUREG/CR-3920, SAND 84-1246 (August 1984).

(13) T.G. Theofanous, Presentation to MACE Technical Review Comm. Mtg. (January 1992).

(14) R. Engelstad, Z. Feng, E. Lovell, Uniaxial and Biaxial Models of an Oxide Crust in MACE: Scaling Effects of Bending Stresses, University of Wisconsin Report, UWRSR-65 (February 1991).

(15) D.R. Bradley, "Modelling of Heat Transfer Between Core Debris and Concrete," ANS Proc 1988 Nat'l Heat Transfer Conf., Houston TX (July 1988).

(16) M.R. Duignan, Enhanced Convective and Film Boiling Heat Transfer by Surface Gas Injection, PhD Thesis, SUNY, Stonybrook (1989).

FIGURE 1 : CONCEPTUAL PICTURE OF QUENCHED DEBRIS

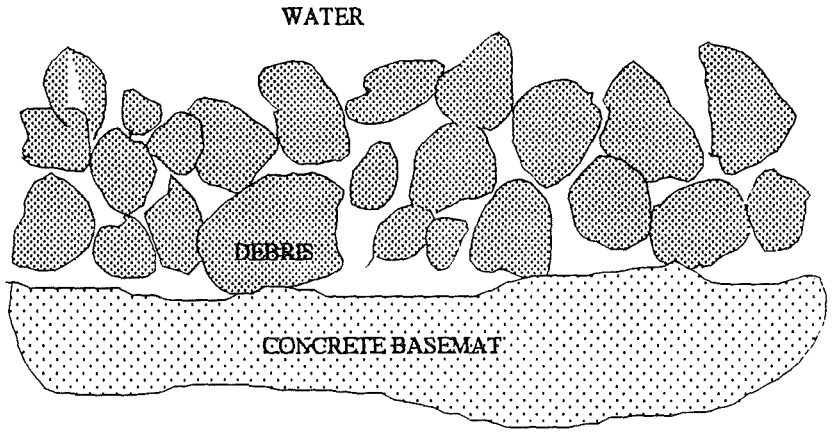

FIGURE 2: CONCEPTUAL PICTURE OF SOLIDIFIED FUEL

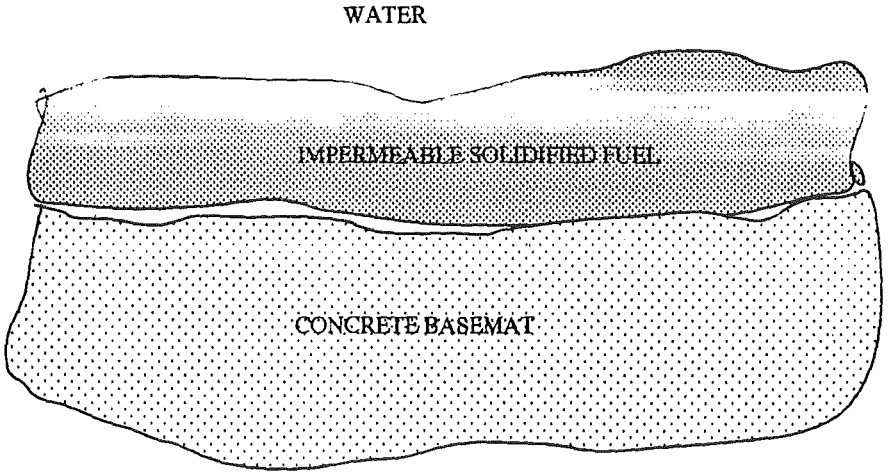

FIGURE 3: CONCEPTUAL PICTURE OF MCCI

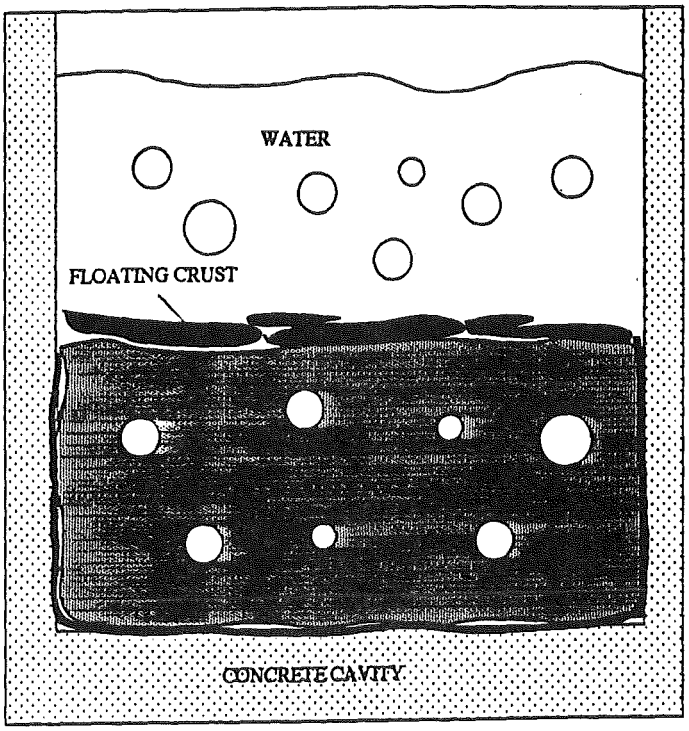

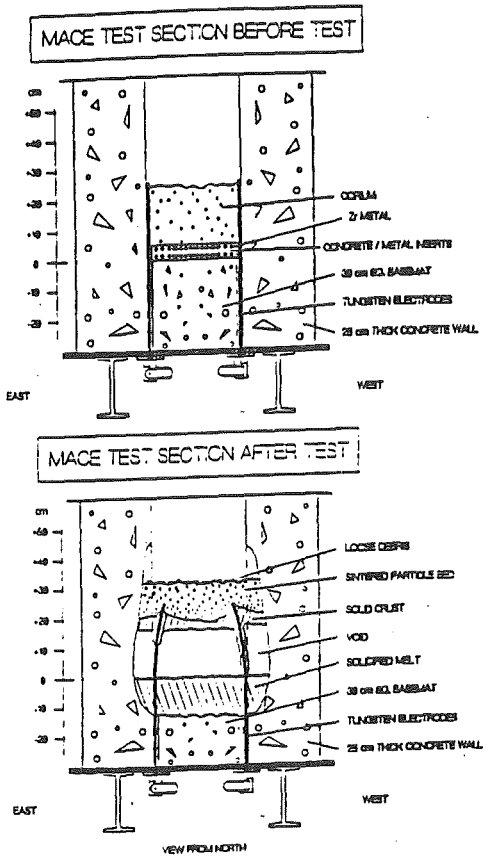

FIGURE 4. Cross-Sectional Illustration of the Test Section as Viewed From the West Before and After the Experiment.

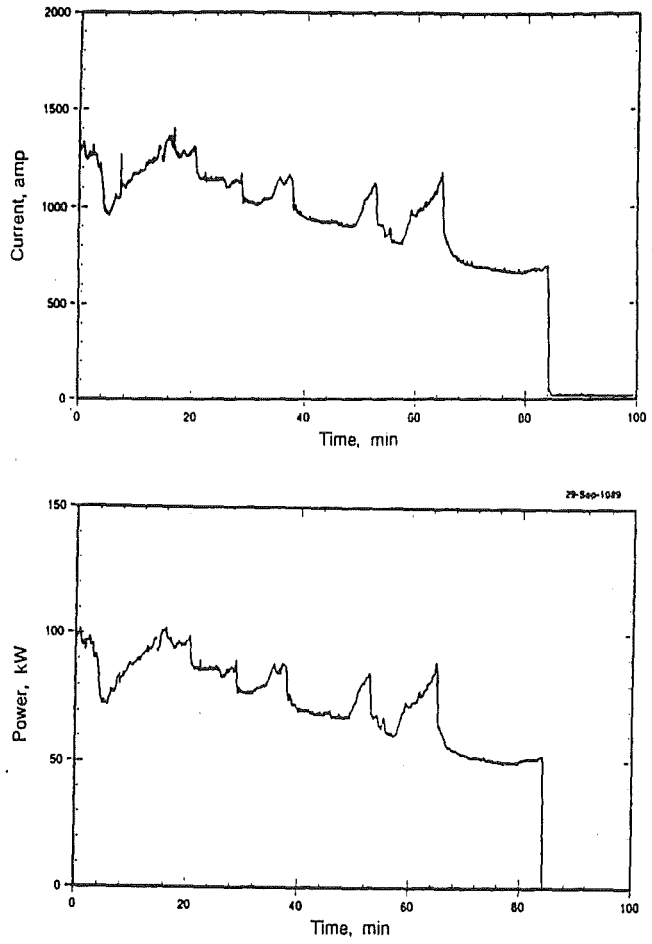

FIGURE 5. **Current and Total Electric Power Input for the Scoping Test.**

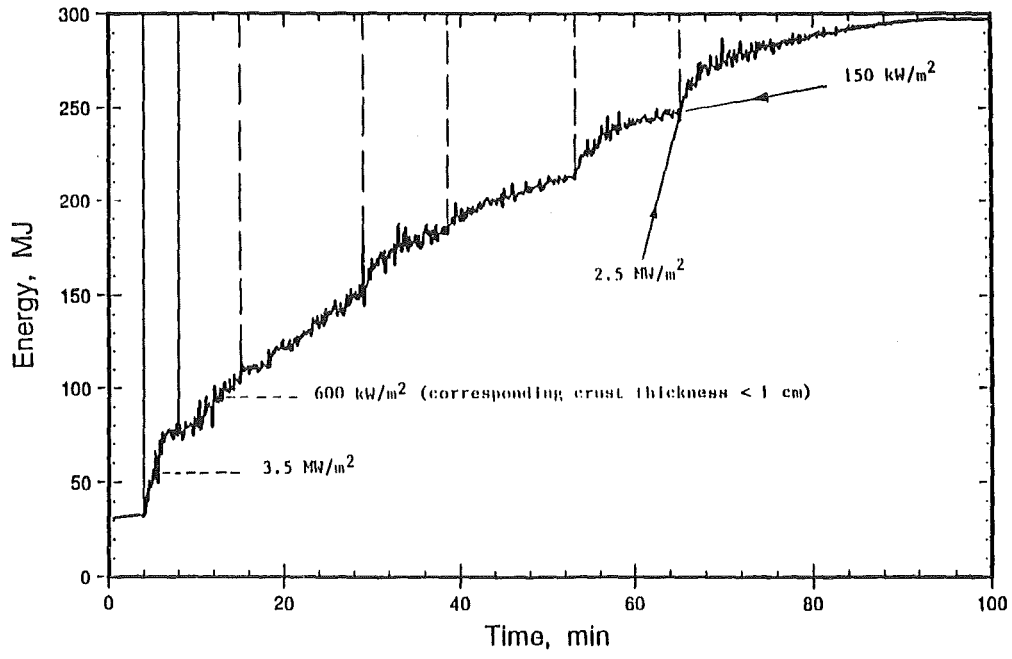

FIGURE 6. **Integrated Flow of Enthalpy Into the Quench System**

FIGURE 7: EVOLUTION OF MELT-WATER INTERACTION

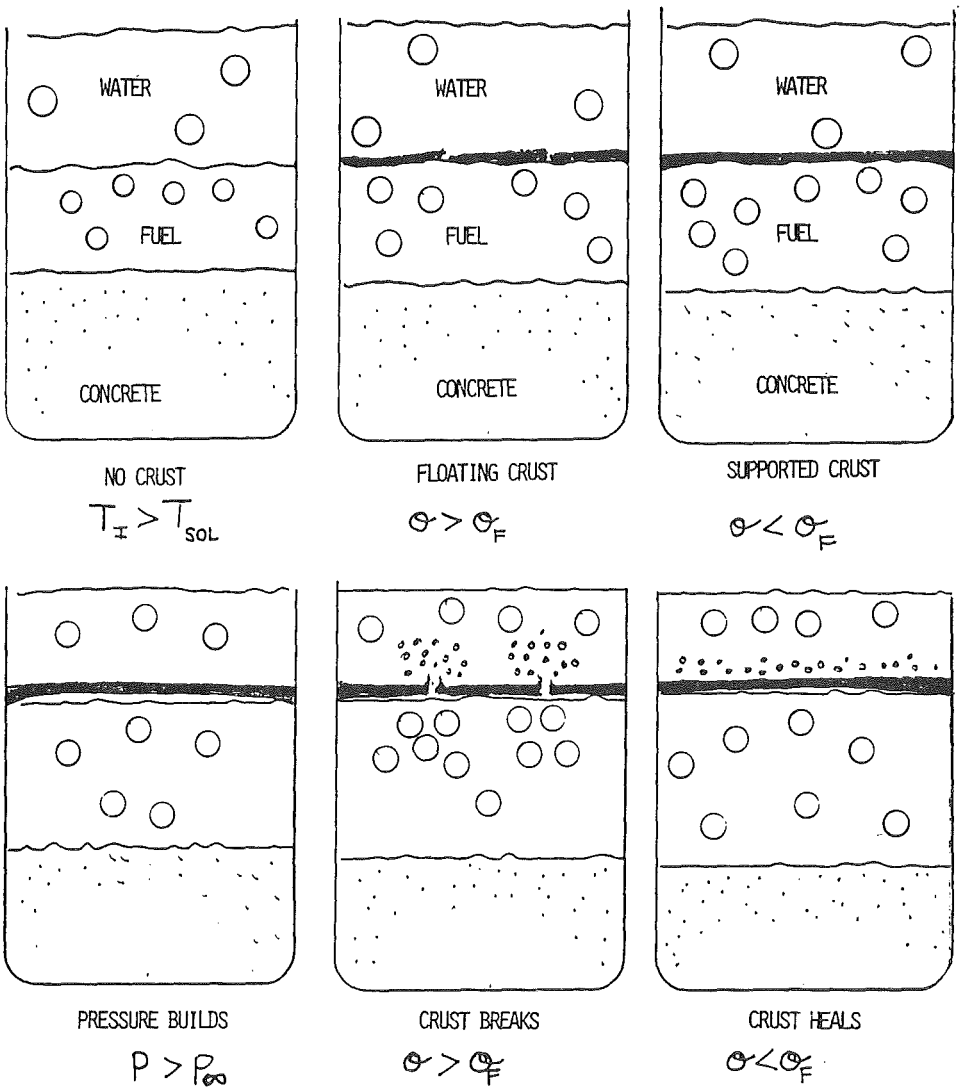

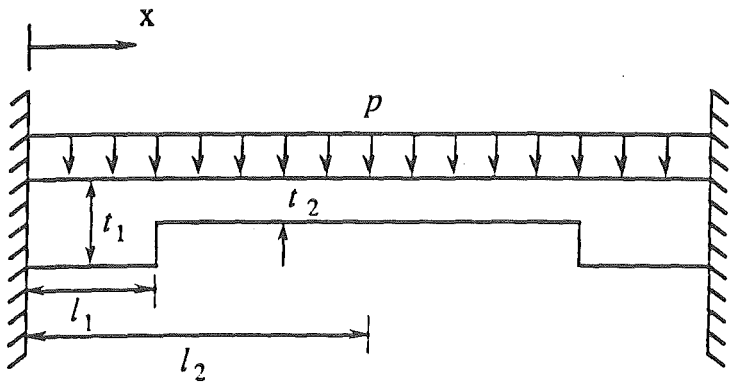

FIGURE 8. Geometry and boundary conditions of the beam model.

FIGURE 9

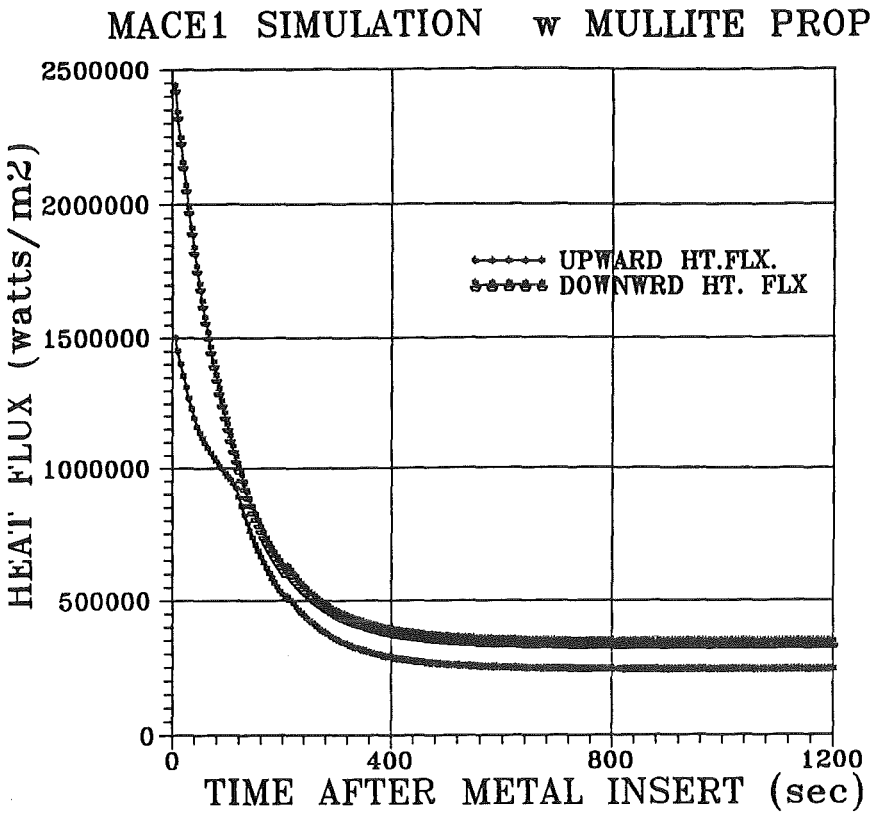

FIGURE 10

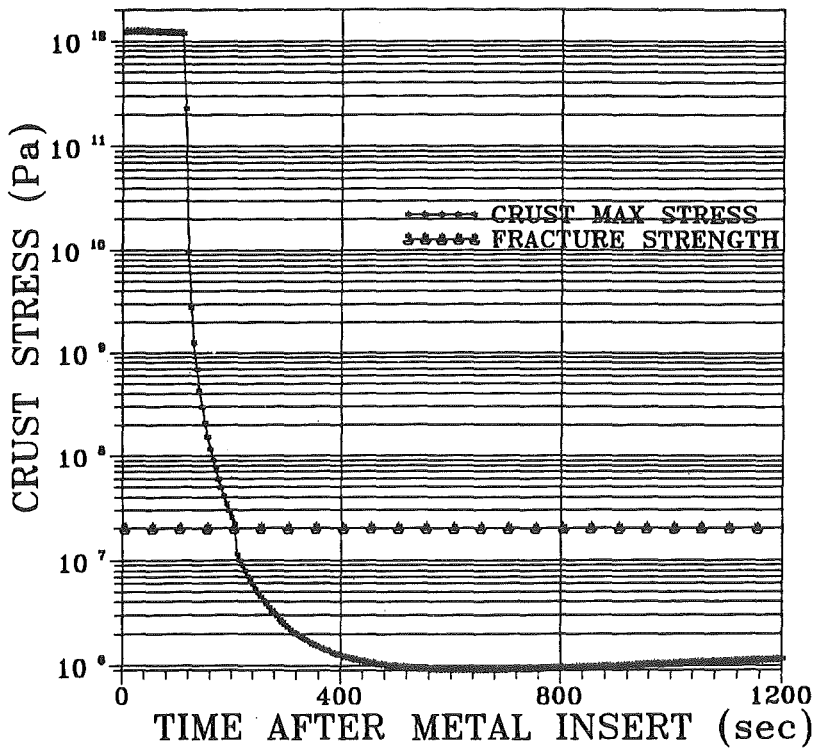

FIGURE 11a

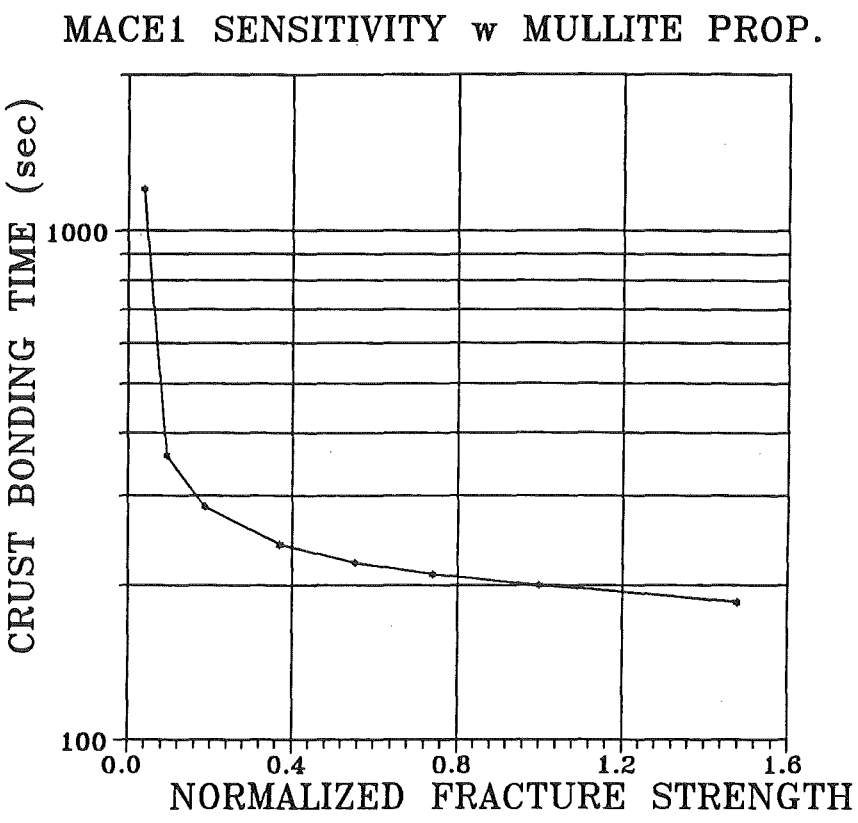

FIGURE 11b

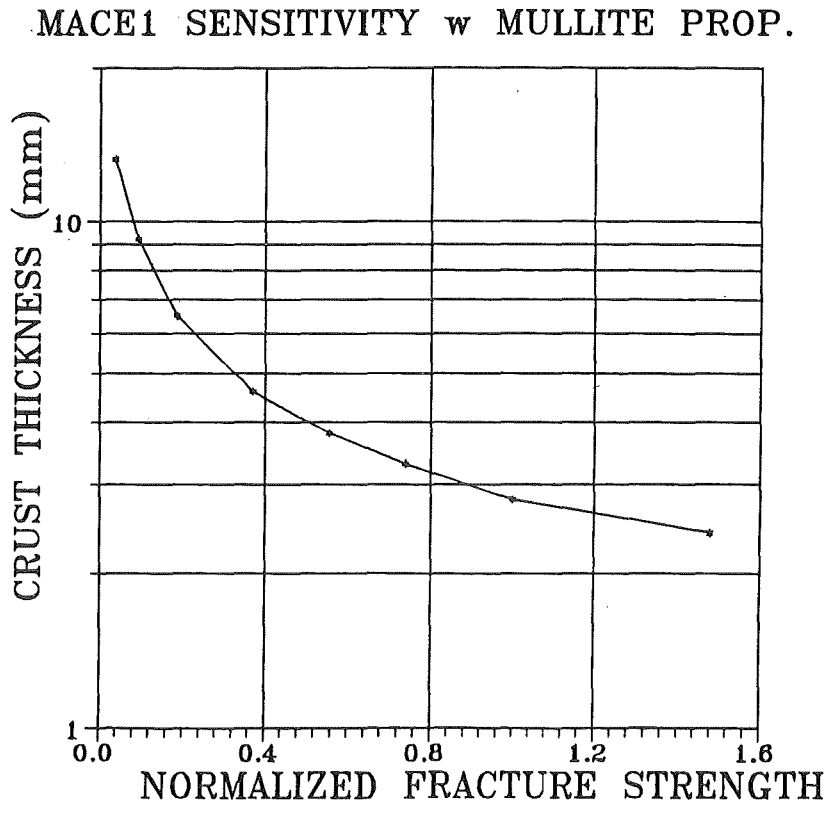

FIGURE 12a

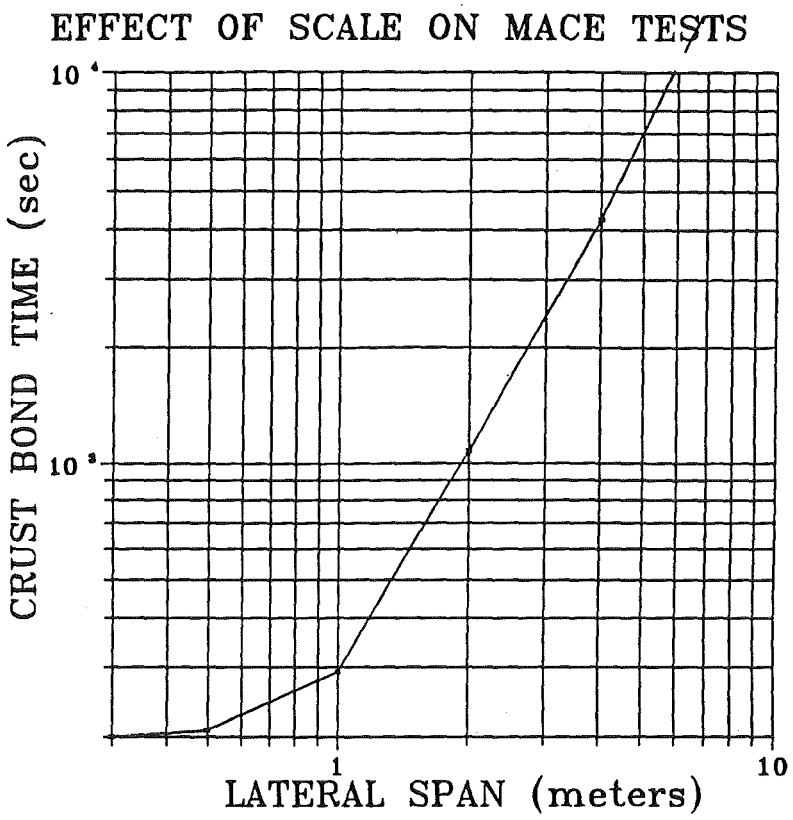

FIGURE 12b

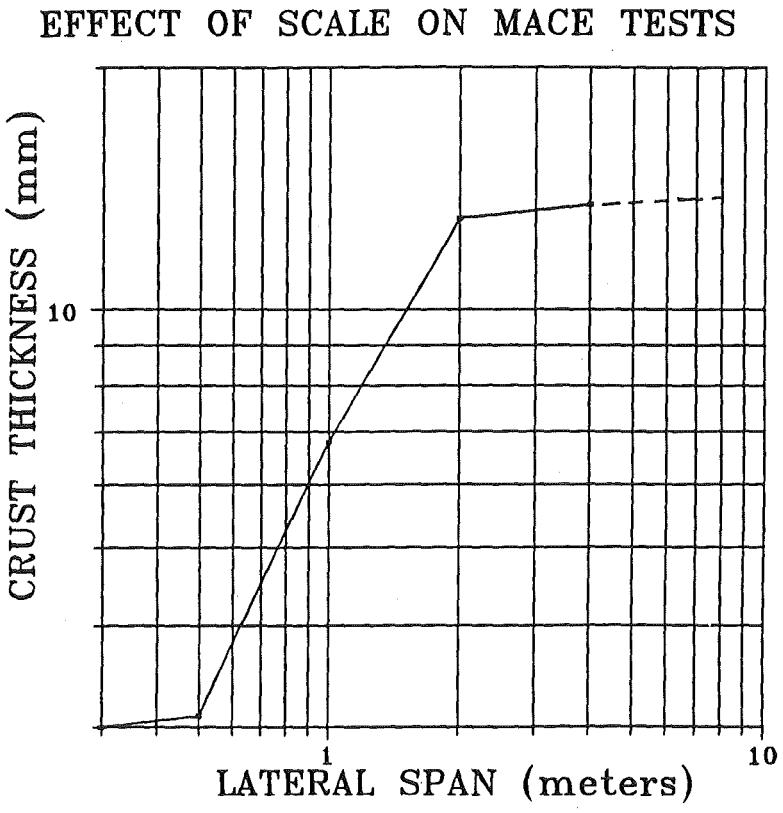

FIGURE 13a

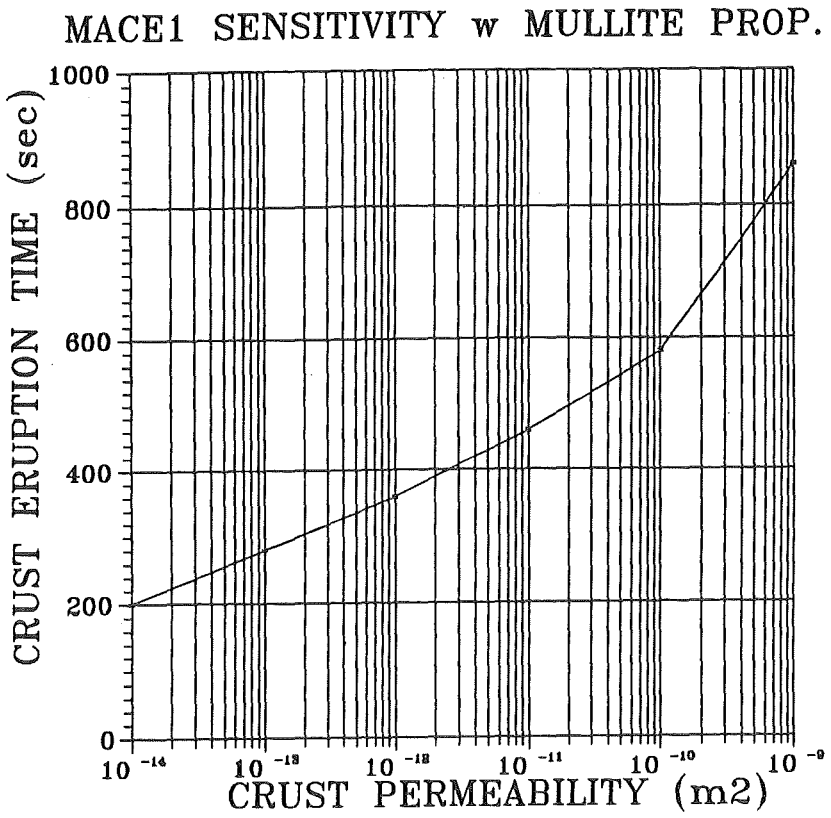

FIGURE 13b

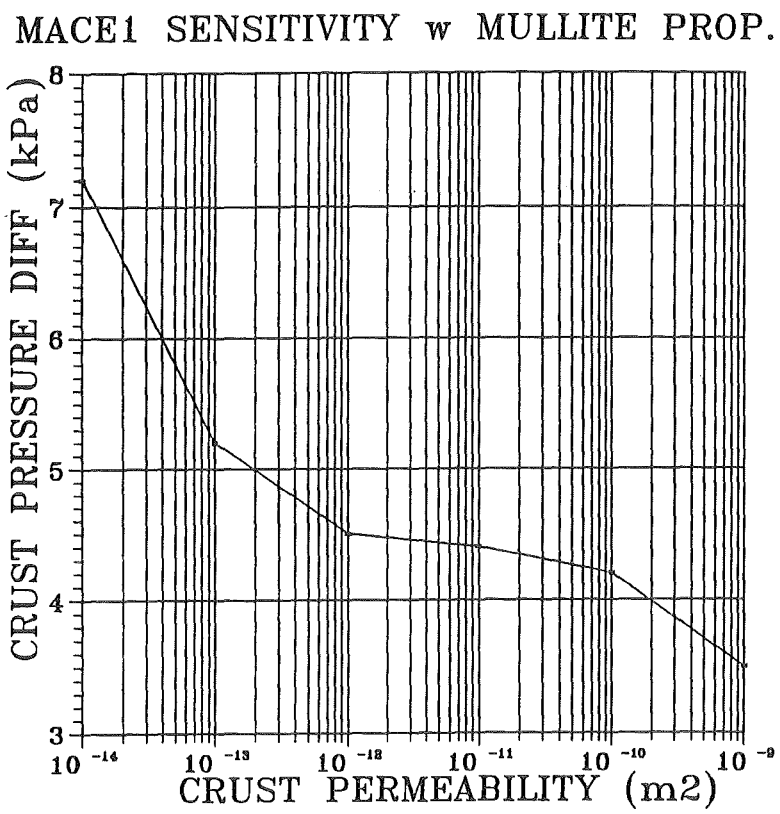

MELT COOLABILITY MODELING AND COMPARISON TO MACE TEST RESULTS

M. T. Farmer, J. J. Sienicki, and B. W. Spencer

Argonne National Laboratory
Argonne, Illinois 60439 USA

ABSTRACT

An important question in the assessment of severe accidents in light water nuclear reactors is the ability of water to quench a molten corium-concrete interaction and thereby terminate the accident progression. As part of the Melt Attack and Coolability Experiment (MACE) Program, phenomenological models of the corium quenching process are under development. The modeling approach considers both bulk cooldown and crust-limited heat transfer regimes, as well as criteria for the pool thermal hydraulic conditions which separate the two regimes. The model is then compared with results of the MACE experiments.

INTRODUCTION

Under certain severe accident sequences in current light water nuclear reactors, molten core material (corium) is postulated to breach the lower head of the reactor pressure vessel and relocate downward onto the concrete basemat of the containment building. In the absence of water, the subsequent molten corium-concrete interaction (MCCI) will lead to gas, aerosol, and fission product release into the containment atmosphere. A critical question to be addressed in these ex-vessel accident sequences is the ability of water introduced atop the MCCI to quench the corium and thereby terminate the accident progression.

When water is introduced atop an MCCI, several coolability sequences may be envisioned, depending upon the MCCI initial conditions. An illustration of a potential melt coolabilty flow diagram is shown in Figure 1. In the short term following water addition, the question of whether or not a significant amount of the melt thermal energy is removed may depend upon whether or not a stable crust is able to form which would then inhibit heat transfer from the MCCI region to the water layer. For a stable crust to form over an MCCI, it is envisioned that

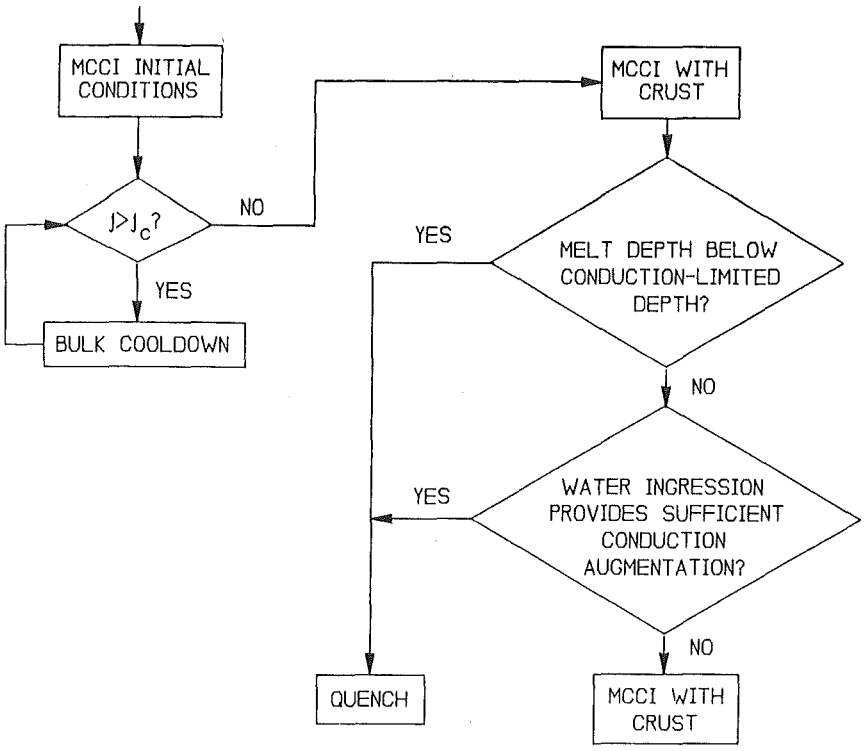

Figure 1. Illustration of a potential melt coolability flow diagram.

two necessary conditions must be met: (i) a thermal condition, viz., the melt/water interfacial temperature must fall below the corium freezing temperature, and (ii) a mechanical condition, viz., the incipient crust must be stable with respect to local mechanical loads imposed by the agitated melt. If either of these two conditions is violated, then stable crust formation at the interface between the MCCI zone and water layer may be precluded. In this regime, film boiling is expected to be the dominant heat transfer mode due to periodic introduction of high temperature melt at the interface as the crust segments are broken up. Efficient melt/water heat transfer may thus be anticipated owing to conduction and, predominately, radiation heat transfer across the agitated (i.e., area enhanced) melt/water interface, in addition to the possible entrainment of melt droplets into the water overlayer. In a purely bulk freezing heat transfer mode, frozen material formed at the interface will be mixed back into the melt causing an overall decline in the bulk melt temperature, and eventually lead to the development of a slurry mixture.

As the bulk cooling heat transfer mode continues, the melt temperature will gradually decline. If the downward heat transfer rate, which drives concrete ablation with concurrent noncondensable gas release, is proportional to melt temperature, then the melt sparging rate will also decrease. Thus, a point may be reached at which the thermal and mechanical thresholds for interfacial crust formation are both satisfied and an insulating crust forms between the coherent melt zone and water layer. The physical configuration at this point would consist of an ongoing MCCI zone at reduced temperature with a crust atop the melt. Cooling of the melt zone would then be limited by conduction through the crust. The crust will be characterized by some degree of porosity, or cracks, owing to the necessity of venting concrete decomposition gases. Thus, the possibility exists for enhanced cooling of the MCCI zone via water ingression through the crust perforations. After the crust is formed, quench will eventually be achieved if one of the following two conditions is met: (i) melt depth lies below the minimum depth at which decay heat can be removed via conduction alone, or (ii) water ingression through cracks/crevices within the crust provides sufficient conduction augmentation to remove the decay heat source.

As part of the Melt Attack and Coolability Experiment (MACE) program at ANL, phenomenological models are being developed to study the melt/water/concrete interaction process. A first order Corium Quenching (CORQUENCH) film boiling heat transfer model has been developed (1), which considers the affects of conduction and radiation heat transfer across the vapor film, bulk coolant subcooling, and interfacial area enhancement due to sparging concrete decomposition gases. This model is currently limited to the bulk cooling regime in which mixing associated with sparging gases is sufficient to preclude stable interfacial crust formation (1). The current paper describes the extension of the CORQUENCH model to treat both the bulk cooling and crust-limited heat transfer regimes. The approach is to define appropriate thermal/mechanical thresholds for incipient crust growth at the melt/water interface. Below these thresholds, the original CORQUENCH film boiling model (1) is embodied in a full boiling curve to treat quenching behavior of the crust upper surface. The current work focuses on the case in which heat transfer from the MCCI zone is limited by conduction through the crust; i.e., no treatment of water ingression phenomena is provided here. The modified version of the CORQUENCH model is then compared

to the results of MACE scoping test (2).

MODEL DEVELOPMENT

To assess the potential for crust formation over an MCCI with water present, expressions are required for the thermal and mechanical crust stability limits. The thermal condition for inception of crust growth at the melt/water interface is that the interfacial temperature, in the absence of a crust, must fall below the melt freezing temperature. The energy balance at the interface is of the form,

$$h_w (T_I - T_{sat}) = h_m (T_m - T_I), \tag{1}$$

where T_m = melt temperature, T_I = melt/water interfacial temperature, T_{sat} = water saturation temperature, h_w = heat transfer coefficient to water, and h_m = melt convective heat transfer coefficient to the underside of the crust. The thermal criterion for inception of crust growth is that the interface temperature, as determined from Eq. 1, must satisfy the condition,

$$T_I < T_f \tag{2}$$

where T_f = melt freezing temperature. The melt convective heat transfer coefficient is evaluated using Kutateladze's bubble agitation heat transfer coefficient (3), which is given through the equation

$$h_m = \begin{cases} 1.5 \cdot 10^{-3} \left(\frac{k_m}{L}\right) \left(\frac{Pc_m j_g}{k_m g}\right)^{2/3} & ; \; j_g < j_{tr} \\ 1.5 \cdot 10^{-3} \left(\frac{k_m}{L}\right) \left(\frac{Pc_m j_g}{k_m g}\right)^{2/3} \left(\frac{j_{tr}}{j_g}\right)^{1/2} & ; \; j_g \geq j_{tr} \end{cases} \tag{3}$$

where

$$j_{tr} = 4.3 \cdot 10^{-4} \frac{\sigma_m}{\mu_m}, \tag{4}$$

$$L = \sqrt{\frac{\sigma_m}{g\left(\rho_m - \rho_g\right)}}, \tag{5}$$

and j_g = superficial gas velocity, P = system pressure, μ = kinematic viscosity, σ = surface tension, c = specific heat, k = thermal conductivity, ρ = density, and g = gravitational acceleration. Subscripts m and g denote the melt and noncondensable gas phases, respectively. On the water side of the melt/water interface, film boiling heat transfer is assumed. The heat transfer coefficient is evaluated using the equation of Farmer et. al., (1),

$$h_w = A_* \left\{\frac{k_e}{\delta_g} + h_{rad}\right\} + h_{entr} \tag{6}$$

where

$$h_{rad} = \eta\, \epsilon_m \left(T_m^2 + T_{sat}^2\right)\left(T_m + T_{sat}\right), \tag{7}$$

$$A_* = 1 + 4.5\, \frac{j_g}{U_\infty}, \tag{8}$$

and h_{entr} = heat transfer coefficient due to melt entrainment into water, η = Stefan-Boltzman constant, ϵ = radiation emissivity, δ_g = gas film thickness, U_∞ = sparging gas bubble terminal rise velocity (4), and subscript e denotes properties of the vapor/noncondensable gas film mixture. The expressions for δ_g, h_{entr}, and k_e are lengthy and are omitted here for the purposes of brevity; these expressions are provided in Reference (1). Note that the entrainment heat transfer coefficient, h_{entr}, is set equal to zero when Eq. 6 is used to evaluate Eq. 1. Although this term acts to augment the overall heat transfer coefficient (<1% for oxide melts (1)), it is not included in the local energy balance from which the interfacial temperature is evaluated, due to the fact that the local heat transfer characteristics across the gas film leading to incipient crust growth are governed by conduction and radiation. Based on the same reasoning, the dimensionless interfacial area enhancement, A_*, is set equal to 1 when Eq. 6 is used to evaluate Eq. 1.

The mechanical stability of an incipient crust formed at the melt/water interface will depend upon a variety of factors which may include fracture strength of the core/concrete mixture, thermal conductivity of the crust material, and degree of melt agitation induced by sparging concrete decomposition gases. Farmer et. al., (5) presented a model for the critical superficial gas velocity to preclude stable crust formation at the interface between a molten pool and water overlayer when the interfacial heat transfer occurs by film boiling. The model development and validation against experiment data is described in Reference (5). The solution for the critical gas velocity is given as,

$$j_c = \frac{.445\, R\, h_m\, (T_m - T_f)}{\delta_c\, \rho_{cr}\, \Delta e_{cr} \left\{ \frac{k_{cr}\, (T_f - T_{sat})}{\delta_c\, h_m (T_m - T_f)}\, \ln \left[\frac{1}{1 - \xi} \right] - 1 \right\}}, \tag{9}$$

where

$$\xi = \frac{h_m\, h_w\, (T_m - T_f)\, \delta_c}{k_{cr} \left(h_w\, (T_f - T_{sat}) - h_m\, (T_m - T_f) \right)}, \tag{10}$$

$$\delta_c = .69 \left[\frac{R^3\, (\rho_m - \rho_g)\, g}{\sigma_y} \right]^{1/2}, \tag{11}$$

and R = gas bubble radius sparging melt, σ_y = crust fracture stress, and Δe_{cr} = crust latent heat of fusion. Subscript cr denotes properties of the crust material. Note from denominator of Eqs. 9-10 that the condition $h_w\, (T_f - T_{sat}) > h_m\, (T_m - T_f)$ must be satisfied to obtain a physically realistic solution from this model. This requirement is identical to the thermal stability criterion, viz. Eq. 2. Thus, in addition to Eq. 2, the condition

$$j_g < j_c, \tag{12}$$

must be satisfied for sustained crust growth to occur at the melt/water interface. Above these two limits, the melt is envisioned to undergo bulk cooldown, with the melt/water heat transfer coefficient given through Eqs. 6-8. The appropriate temperature difference driving the upward heat transfer for this

case is T_I - T_{sat}, where T_I is evaluated through Eq. 1. When the thermal condition for incipient crust formation is satisfied (Eq. 2), two potential melt freezing modes may be observed, depending upon the pool sparging rate: (i) $j_g \geq j_c$, where crust segments are periodically broken up and mixed into the bulk melt, or (ii) $j_g < j_c$, where sustained crust growth occurs at the melt surface. These two cases are treated sequentially.

For situations in which $j_g \geq j_c$, periodic crust formation occurs at the melt surface, but pool agitation forces are sufficient to preclude sustained growth. Neglecting the decay heat source over these intermittent growth cycles, then the crust growth rate equation is of the form,

$$\rho_{cr} \Delta e_{cr} \frac{d\delta}{dt} = k_{cr} \frac{(T_f - T_I)}{\delta} - h_m (T - T_f), \tag{13}$$

where the crust upper surface temperature T_I, is given through the following energy balance at the crust/water interface,

$$k_{cr} \frac{(T_f - T_I)}{\delta} = h_w (T_I - T_{sat}). \tag{14}$$

Using Eq. 14 to eliminate T_I from Eq. 13 and integrating the resultant expression subject to $\delta\ (t = 0) = 0$ yields

$$\delta + \frac{k_{cr}}{h_m} \frac{(T_f - T_{sat})}{(T_m - T_f)} \ln \left[1 - \frac{\xi \delta}{\delta_c}\right] + \frac{h_m (T_m - T_f)}{\rho_{cr} \Delta e_{cr}} t_b = 0. \tag{15}$$

Equation 15 provides the local crust depth at the time at which the crust is broken up due to pool agitation forces, t_b. Consistent with the development of Eq. 9 (5), t_b is assumed to correspond to the local bubble arrival time as given by Blottner's correlation (6), $t_b = .445\ R/j_g$. Given the intermittent crust depth from Eq. 15, the crust upper surface temperature, T_I, is evaluated from Eq. 14. The melt/water heat flux is then evaluated as $h_w(T_I - T_{sat})$, where h_w is evaluated through Eqs. 6-8.

For situations in which $j_g < j_c$, sustained crust growth at the melt/water interface will occur. Assuming (i) heat transfer through the crust is conduction limited (i.e., no heat transfer augmentation via water ingression is considered), and (ii) the heat transfer process is quasi-steady, then the conservation of

energy equation in the crust is of the form,

$$k_{cr}\frac{\partial^2 T}{\partial x^2} + \rho_{cr}\dot{q} = 0 \tag{16}$$

where $\dot{q}$ = crust decay heat level (W/kg). The boundary conditions on Eq. 16 at x = 0 (i.e., melt side of crust) are of the form

$$T(x = 0) = T_f \tag{17}$$

$$- k_{cr} \frac{\partial T}{\partial x}\Big|_{x = 0} = h_m \left[T_m - T(x = 0)\right]. \tag{18}$$

Integration of Eq. 16 subject to Eqs. 17-18 yields the following solution for the crust temperature profile,

$$T(x) = - \frac{\rho_{cr}\dot{q}\, x^2}{2k_{cr}} - \frac{h_m (T_m - T_f)}{k_{cr}}\, x + T_f. \tag{19}$$

The crust thickness is then determined from an energy balance at $x = \delta$ (i.e., water side of crust),

$$- k_{cr} \frac{\partial T}{\partial x}\Big|_{x = \delta} = h_w \left[T\ (x=\delta) - T_{sat}\right], \tag{20}$$

which yields,

$$h_w \left[T\ (x=\delta) - T_{sat}\right] = h_m (T_m - T_f) + \rho_{cr}\dot{q}\delta. \tag{21}$$

Substitution for T (x=δ) from Eq. 19 into the above expression produces a quadratic equation for δ, the solution of which is

$$\delta = - \frac{h_m (T_m - T_f)}{\rho_{cr} q} + \sqrt{\left[h_m \frac{(T_m - T_f)}{\rho_{cr} q}\right]^2 + 2\, k_{cr}\, \frac{\left[T_f - T\ (x=\delta)\right]}{\rho_{cr} q}}\ . \tag{22}$$

Eqs. 21-22 constitute two equations in two unknowns for T(x=δ) and δ. The top heat flux from the coherent MCCI zone is then given by h_m (T_m -T_f), whereas the cumulative heat flux from the MCCI zone plus crust is given by the left or right hand sides of Eq. 21.

For cases in which sustained crust formation occurs, the appropriate form of h_m

will most likely depend on the lateral distribution of "vent holes", or "fissures", through which concrete decomposition gases pass to the atmosphere. If the fissure spacing is fairly small (say on the order of the Laplace constant, L, defined in Eq. 5, which is ~5 mm for oxidic corium), then venting of decomposition gases will occur locally. In this situation, the heat transfer mechanism will be dominated by bubble agitation, for which Eq. 3 applicable. It is worth nothing, however, that if the fissure spacing is fairly large (>> L), then local voided regions may periodically form between the coherent melt zone and crust as the decomposition gases accumulate and flow to the vent sites. In this case, radiation heat transfer will play a significant role in determining the thermal loading on the crust lower surface. For the purposes of this work, this affect is neglected, and h_m is assumed to be given by Eq. 3.

According to Eq. 21, the cumulative heat flux to be extracted at the crust upper surface consists of decay heat within the crust plus heat convected to the crust underside from the melt. Thus, nucleate, transition, or film boiling heat transfer regimes may be encountered, depending upon where the cumulative heat flux lies with respect to the minimum film boiling and critical heat fluxes. Heat transfer in the nucleate boiling regime is calculated with Rohsenow's correlation (7). The crust upper surface is expected to be characterized by some degree of surface roughness. The associated surface area enhancement is expected to augment the boiling heat transfer over that which would be observed on a smooth surface. This tendency has been observed in the CWTI reactor material experiments (8, 9), as well as other experiments (10, 11). For definiteness, it is assumed that Rohsenow's heat transfer correlation (7) is augmented by a factor of 3 to characterize the surface roughness. The critical heat flux (CHF) is evaluated using the correlation of Ivey and Morris (12), which accounts for bulk coolant subcooling. The crust upper surface temperature at which CHF occurs is determined by setting the CHF expression equal to h_w ($T(x = \delta)$ - T_{sat}), where h_w is given by the modified version of Rohsenow's correlation, and solving for $T(x = \delta)$. The minimum film boiling temperature is evaluated using Henry's correlation (13), which accounts for coolant subcooling and properties of the surface material. The heat transfer coefficient in the film boiling regime is calculated using Eq. 6 with h_{entr} set equal to zero (i.e., no melt entrainment into overlying water when crust is present), and the dimensionless surface area enhancement, A_*, fixed at a value of three to characterize surface roughness as

described above. The minimum film boiling heat flux is then evaluated as $h_w \Delta T_{min}$, with ΔT_{min} given by Henry's correlation (13), and h_w is evaluated through Eq. 6 with the above assumptions incorporated.

As discussed previously, heat transfer from the crust upper surface is heat flux-controlled from the melt side, and therefore between CHF and the minimum film boiling heat flux the film, transition, or nucleate boiling regimes may be encountered. Transition boiling is not considered to be a plausible long-term heat transfer mechanism, owing to the highly unstable nature of this boiling process. Film boiling is assumed to be the initial heat transfer mechanism in this analysis, due to initially high melt temperatures. This boiling regime is assumed to persist as long as the heat flux is above the minimum film boiling heat flux; below this value, nucleate boiling is assumed. However, it is important to note the unstable nature of film boiling over irregular oxide surfaces (14), and the possibility exists for transition to nucleate boiling at heat fluxes significantly above that predicted by the current modeling approach. If water ingression through the crust is not significant, then from an overall energy extraction viewpoint, the assumption of film versus nucleate boiling is insignificant since the heat transfer from the MCCI zone will be determined by conditions on the melt side of the crust. However, a crust which is in nucleate boiling at its upper surface will thermally equilibrate at a greater thickness in comparison to the film boiling case due to lower surface temperature. Thus, if crust mechanical stability over large lateral length scales (e.g., reactor cavity) plays a significant role in coolability, then the actual boiling regime which is encountered becomes an important consideration.

MODEL APPLICATIONS

Based on the current model, the heat transfer behavior at the melt upper surface is closely linked to the melt pool thermalhydraulic conditions. Thus, to make predictions regarding the melt cooling regime and corresponding melt/water heat flux, both the melt temperature and gas sparging rate must be specified, in addition to material properties. To evaluate the sparging rate for a given melt temperature, quasi-steady downward heat transfer is assumed, for which the basemat ablation rate is given by the expression,

$$\rho_{cn}\, e_{dc,cn}\, \frac{d\delta_b}{dt} = h_b (T_m - T_b) \qquad (23)$$

where ρ_{cn} = concrete density, $e_{dc,cn}$ = concrete decomposition enthalpy, h_b = melt/concrete heat transfer coefficient, and T_b = bottom temperature boundary condition. The gas sparging rate is related to the basemat ablation rate through the equation

$$j_g = \frac{\chi_{up}\, \chi_g\, \rho_{cn}}{\rho_g} \frac{d\delta_b}{dt} \tag{24}$$

where ρ_g = sparging gas density, χ_g = weight fraction of decomposition gases in concrete, and χ_{up} = fraction of decomposition gases released upwards during concrete ablation. Results of the ACE MCCI reactor material experiments (15, 16) indicate that a significant fraction (~50%) of decomposition gases migrate downwards into concrete during the ablation process. Thus, for the purposes of this analysis, χ_{up} is set equal to 0.5.

The bottom heat transfer coefficient is evaluated with Bradley's model (17), which is a modified version of Kutateladze's correlation (3) (i. e., Eq. 3 is multiplied by 0.29 to account for the thermal resistance of the slag layer formed at the melt/concrete interface). The sparging gas is assumed to consist of H_2O and CO_2 (i.e., reduction of these gases by metals present in the melt is not considered). The gas densities are calculated using the ideal gas law evaluated at the particular melt temperature. Note that this assumption will influence the predictions since incomplete heating of gas bubbles as the bubbles ascend through the melt will lower the sparging rate for a given ablation rate, and therefore increase the melt temperature range over which crust formation occurs.

For the purposes of this study, the following melt thermal properties are assumed: k_m = 3.0 W/m•K, ρ_m = 7000 kg/m^3, C_m = 500 J/kg•K, μ_m = .01 kg/m•s, ϵ_m = 0.8, and σ_m = 0.6 N/m. Properties of the crust material are specified as: k_{cr} = 1.0 W/m•k, ρ_{cr} = 8000 kg/m^3, Δe_{ls} = 250 kJ/kg, and σ_y = 20 MPa. The concrete type is assumed to be limestone/common sand, for which ρ_{cn} = 2400 kg/m^3, $e_{dc,cn}$ = 2.5 MJ/kg, and χ_g = 0.27 (0.06 H_2O and 0.21 CO_2). The concrete decomposition temperature, T_{dc}, is taken equal to 1500 K. The calculations are performed at atmospheric pressure for which T_{sat} = 373 K. A representative coolant subcooling of 40 K is assumed. The surface/coolant constant, C_{sf}, in Rohsenow's correlation (7) is taken equal to 0.02, which is the reported value for water over stainless steel (note that the top crust surface temperature in the nucleate boiling regime

is insensitive to this parameter).

The melt/water heat flux, melt/concrete heat flux, critical gas velocity, concrete decomposition gas velocity, crust depth, and crust/melt surface temperature predictions are shown in Figures 2-3 for assumed melt freezing temperature of 1700 K and the bottom temperature boundary condition taken equal to T_{dc}. The low freezing temperature assumption is consistent with scenarios in which water is added atop the MCCI after significant concrete erosion has taken place, thereby causing a reduction in T_f due to entrainment of concrete decomposition products into the melt. This assumption is consistent with the experiment conditions of the MACE Scoping Test (2). Consistent with the experiment technique, the calculation was performed assuming no decay heat in the crust.

The upward heat flux during the scoping test decreased gradually from ~600 kW/m^2 at 20 minutes past water addition, down to ~150 kW/m^2 at 70 minutes after water was added. During this period, the average melt temperature decreased gradually from ~1900-2000 K down to ~1800 K. (Note that the initial melt/water heat flux was ~3.5 MW/m^2 over the first four minutes, but due to asymmetry in the ablation front, melt temperature data is not available until 20 minutes after water addition). From Figure 2, the predicted upward heat fluxes for T_m = 1900-2000 K

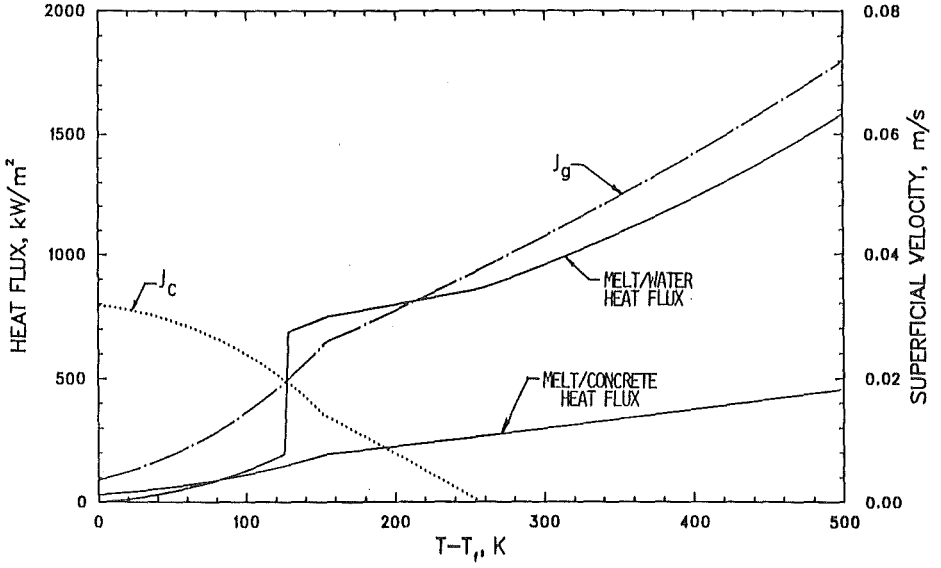

Figure 2. Predicted Melt/Water Heat Flux and Critical Gas Velocity Versus Melt Superheat for the Case T_f = 1700 K, T_b = 1500 K, and $\dot{q}$ = 0.

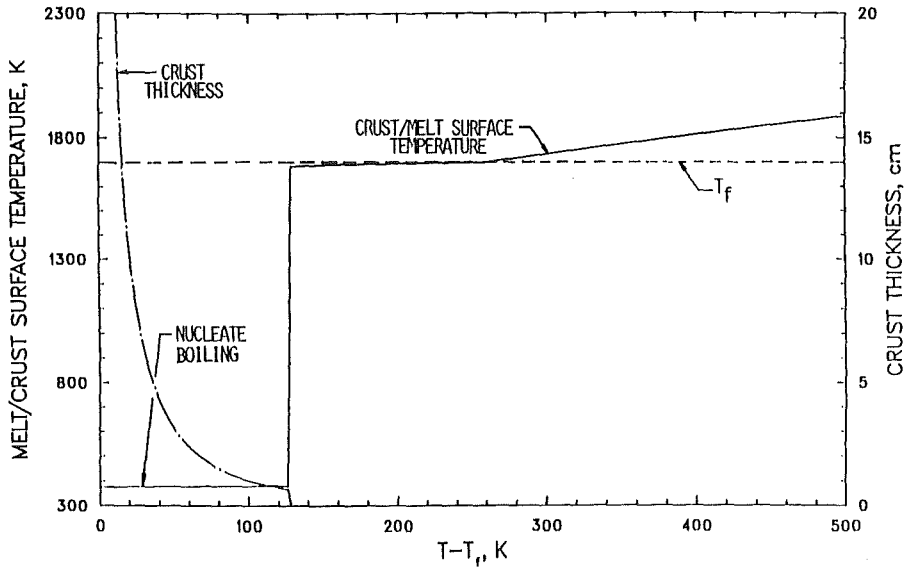

Figure 3. Predicted Crust Thickness and Melt/Crust Surface Temperature for the Case T_f = 1700 K, T_b = 1500 K, and $\dot{q}$ = 0.

are 700-950 kW/m^2, and the predicted flux for T_m = 1800 K is 120 kW/m^2. Thus, the predicted heat fluxes bracket those observed during the scoping test. Note from Figs. 2-3 that the heat transfer behavior is predicted to change from purely bulk cooldown to bulk cooling with periodic crust formation at T_m = 1960 K, at which point $T_I = T_f$, but $j_g > j_c$. Additionally, the heat transfer characteristics change from bulk cooldown with periodic crust formation to a stable crust configuration at T_m = 1830 K, at which point $j_g = j_c$. The heat flux at the bifurcation point in the latter case is predicted to drop from 680 kW/m^2 to 200 kW/m^2, reflecting the formation of a stable interfacial crust. A similar transformation was observed in the scoping test at t = 25 minutes, where the heat flux dropped from ~600 kW/m^2 to ~350 kW/m^2. The melt temperature measurements at this time ranged from 1800-2000 K. However, the change in heat flux was coincidental with an observed melt eruption from the surface (2). It is not clear whether the reduction in heat flux at this point is representative of a change in melt cooling regimes or an artifact of the eruptive event. As shown in Fig. 3, heat transfer from the crust upper surface is predicted to occur by nucleate boiling (i.e., $T_I \sim T_{sat}$ = 373 K). This is due to the fact that the crust thermal loading, $h_m(T_m - T_f)$, does not exceed the minimum film boiling heat flux over the melt temperature range where a stable crust configuration is

predicted. There is no experiment evidence to either confirm or deny this prediction. Also from Fig. 3, the crust depth at the end of the scoping test (T_m ~1800 K) is predicted to be 1.3 cm. Posttest examinations indicated crust depths ranging form 1.9-2.5 cm.

To assess the affects of decay heat in the crust on the scoping test predictions, the above calculation was repeated with $\dot{q}$ = 350 W/kg (i.e., PWR decay heat level at ~2 hrs into the accident progression). The results are shown in Figs. 4-5. In the range $j_g > j_c$, the predictions are identical. For $j_g < j_c$, the upwards heat flux increases from 90 kW/m^2 at T_m = 1700 K (reflecting decay heat in the crust) up to 210 kW/m^2 at $j = j_c$ (T_m = 1830 K). These heat fluxes may be compared with the predicted values of 0-200 kW/m^2 over the same temperature range for the experiment (see Fig. 2). The predicted crust depth for the reactor case varies from 3.1 cm at $T_m = T_f$ (again, reflecting decay heat in the crust) down to 0.0 cm at $j_g = j_c$. At T_m =1800 K (i.e., melt temperature at end of scoping test), the crust depth is found to be 0.9 cm, which may be compared with the previously cited prediction of 1.3 cm for the scoping test.

SUMMARY AND CONCLUSIONS

Modeling improvements have been incorporated into the CORQUENCH mechanistic melt/water heat transfer model such that the model is now capable of treating both the bulk cooldown and crust-limited heat transfer phases of the quench process. The approach is to define thermal and mechanical thresholds for incipient crust formation at the melt upper surface. Above these thresholds, the melt undergoes bulk cooling due to radiation dominated film boiling heat transfer across the agitated (i.e., area enhanced) melt/water interface. Below these thresholds, heat transfer from the MCCI zone is limited by conduction across an interstitial crust. The revised model is compared with the results of the MACE scoping test; the predicted melt/water heat flux and crust depth show reasonable agreement with the experiment data.

ACKNOWLEDGEMENTS

This work is sponsored by the Advanced Containment Experiments (ACE) International Consortium through the Electric Power Research Institute, Contract

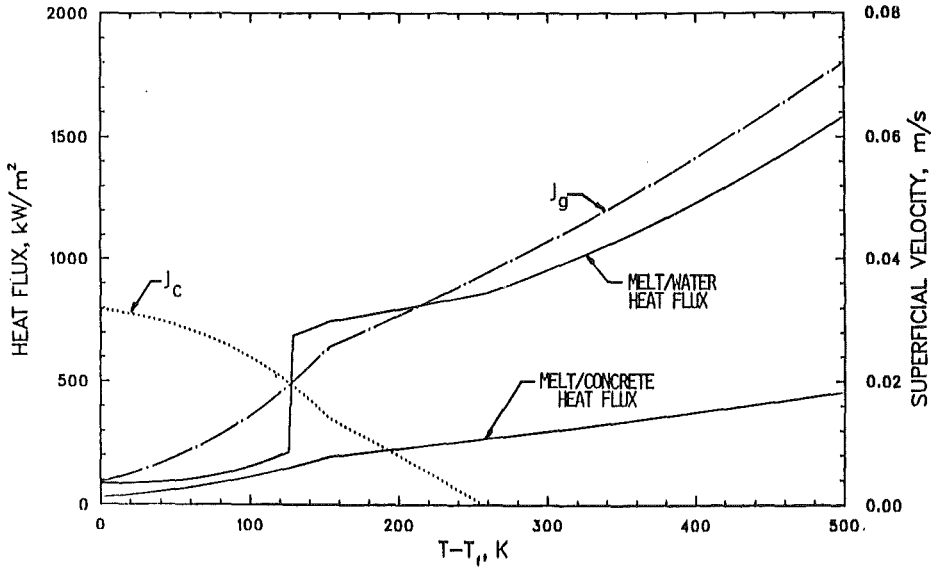

Figure 4. Predicted Melt/Water Heat Flux and Critical Gas Velocity Versus Melt Superheat for the Case T_f = 1700 K, T_b = 1500 K, and $\dot{q}$ = 350 W/kg.

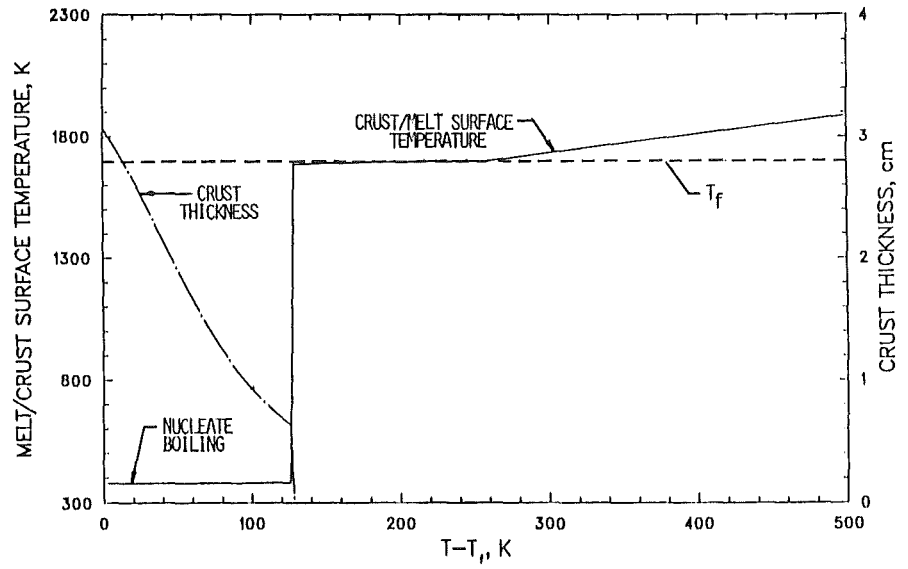

Figure 5. Predicted Crust Thickness and Melt/Crust Surface Temperature for the Case T_f = 1700 K, T_b = 1500 K, and $\dot{q}$ = 350 W/kg.

No. RP 3047-08. The EPRI Program coordinator is B. R. Sehgal. The manuscript was patiently typed by L. J. Ondracek.

REFERENCES

1. M. T. Farmer, J. J. Sienicki, and B. W. Spencer, "CORQUENCH: A Model for Gas Sparging Enhanced, Melt-Water, Film Boiling, Heat Transfer," ANS Winter Meeting on the Thermal Hydraulics of Severe Accidents, Washington, D.C., November 11-15, 1990.

2. B. W. Spencer, et. al., "MACE Scoping Test," MACE-TR-D03, June 1991.

3. S. S. Kutateladze and I. G. Malenkov, "Boiling and Bubbling Heat Transfer Under the Conditions of Free and Forced Convection," 6th Int. Heat Transfer Conf., Toronto, 1978.

4. F. N. Peebles and H. J. Garber, "Study on the Motion of Gas Bubbles in Liquids," Chem. Engr. Progr., Vol., 49, pp. 88-97, 1953.

5. M. T. Farmer, et. al., "Modeling and Database for Melt-Water Interfacial Heat Transfer," 2nd CSNI Specialist Meeting on Core-Debris Interactions, Karlsruhe, FRG, April 1-3, 1992.

6. F. G. Blottner, "Hydrodynamics and Heat Transfer Characteristic of Liquid Pool with Bubble Agitation," Sandia National Laboratory, SAND79-1132, NUREG/CR-0844, November 1979.

7. W. H. Rohsenow, "A Method of Correlating Heat Transfer Data for Surface Boiling of Liquids," Trans. ASME, Vol. 74, pp. 969-976, 1952.

8. J. J. Sienicki and B. W. Spencer, "Analysis of Reactor Material Experiments on Corium-Water Thermal Interactions in Ex-Vessel Geometry," Proc. International Meeting on Light Water Reactor Severe Accident Evaluation, Vol. 2, pp. 12.1-1 - 12.1-8, 1983.

9. B. W. Spencer, L. M. McUmber, and J. J. Sienicki, "Results and Analysis of Reactor-Material Experiments on Ex-Vessel Corium Quench and Dispersal," Proc. 5th International Meeting on thermal Nuclear Reactor Safety, Vol. 2, pp. 1079-1089, 1984.

10. D. S. Jung, J. E. S. Venart, and A. C. M. Sousa, "Effects of Enhanced Surfaces and Surface Orientation on Nucleate and Film Boiling Heat Transfer in R-11," International J. Heat Mass Transfer, Vol. 30, pp. 2627-2639, 1987.

11. S. K. R. Chowdhury and R. H. S. Winterton, "Surface Effects on Pool Boiling," International J. Heat Mass Transfer, Vol. 28, pp. 1881-1889, 1985.

12. H. J. Ivey and D. J. Morris, "On the Relevance of the Vapor-Liquid Exchange Mechanisms for Subcooled Boiling Heat Transfer at High Pressure," AEEW-R127, 1962.

13. R. E. Henry, "A Correlation for the Minimum Film Boiling Temperature," AIChE Symp. Ser., Vol. 70, pp. 81-90, 1974.

14. F. Moreaux, J. C. Chevrier, and G. Beck, "Destabilization of Film Boiling by Means of a Thermal Resistance," Int. J. Multiphase Flow, Vol. 2, pp. 183-190, 1975.

15. D. H. Thompson, et. al.., "Thermal Hydraulic Aspects of the Large-Scale Integral MCCI Lists in the ACE Program," 2nd CSNI Specialist Meeting on Core-Debris Interactions," Karlsruhe, FRG, April 1-3, 1992.

16. J. K. Fink, et. al., "Aerosol Released During Large-Scale Integral MCCI Tests in the ACE Program," 2nd CSNI Specialist Meeting on Core-Debris Interactions," Karlsruhe, FRG, April 1-3, 1992.

17. D. R. Bradley, "Modeling of Heat Transfer Between Core Debris and Concrete, "ANS Proceedings 1988 National Heat Transfer Conference, Houston, TX, July 24-27, 1988.

Coolability of Corium Spread Onto Concrete Under Water, the PERCOLA model

BONNET J.M., SEILER, J.M. (Commissariat à l'Energie Atomique)
Centre d'Etudes Nucléaires de Grenoble
Service de Thermohydraulique des Réacteurs
85X - 38041 Grenoble Cedex (FRANCE)
(F) 76.88.30.23

ABSTRACT

The paper presents a theoretical simplified model called PERCOLA whose objective is to estimate the time required to percolate the melt (interacting with concrete) into a debris bed (under water) such that the resulting upper and lower crusts can be cooled by conduction. It is supposed that the concrete decomposition gases sparging through the melt entrain part of the liquid through openings (cracks) in the upper crust. The entrainment coefficient is the main parameter of the model. The entrained melt solidifies in the water layer and is supposed to deposit to form a debris bed, which is cooled by the water. The interest of this model is to perform parametric calculations in order to state if the hypothesized scenario seems credible or not and if further development along this line makes sense or not. The results indicate that the transformation of the liquid melt into a debris bed is obtained for not unrealistic sets of parameters and low entrainment coefficients. The MACE scoping test also reveals the existence of a debris bed, despite the fact that the upper crust is separated from the liquid melt. It is concluded that further realistic experiments are needed.

Corium coolability after a severe PWR accident involving core meltdown and RPV failure is currently one of the main research items. The case considered here is a situation in which the corium is supposed to spread over a concrete floor and is flooded by water. The general question which should be answered is to determine what should be the maximum allowable corium thickness for which the coolability is assured without significative concrete ablation. This thickness is directly linked to the extension of the necessary spreading surface which may be a key factor in the design of future reactors.

If the only considered heat transfer mechanism in the corium is conduction, this would lead to very low allowable corium thicknesses, and consequently to large spreading surfaces (up to and even more than 400 m^2).

This situation has been analysed by FAUSKE et al. [6]. These authors concluded that "for ALWR materials, film boiling is unstable. As a result, high heat fluxed, rapid surface quenching, and debris cracking would occur allowing ingression of water". Their analysis is based on the observation that lava layers are

cooled by water ingression following crack development. In opposition to lava, the corium melt is submitted to internal heat dissipation (decay heat and exothermic chemical reactions) which may result in a limitation of the growth of the solid crust thickness and even re-melting of these crusts. SWISS experiment [3] showed that a metallic melt submitted to internal heat generation could not be cooled by an overlaying water pool. This was also the case for the MACE scoping test performed with oxidic material. In the later experiment, the existence of an overlaying crust anchored at the lateral walls of the test device impeded the contact between the melt and the water pool.

Further MACE (ANL) and WETCOR (SANDIA) tests are planned to investigate the cooling possibilities of a melt layer by an overlying water pool.

OBJECTIVES OF THE PRESENT WORK:

One of the main problems is to try to identify physical mechanisms which may enhance the heat transfer between the corium layer and the overlaying water pool.

The post mortem examinations of the MACE scoping test showed that a debris bed formed on the upper crust. This debris bed resulted from melt entrainment through cracks or little volcanoes. A significative part of the melt was entrained despite the fact that the crust separated from the melt due to side anchoring. The gas production due to the melt-concrete interaction is doubtless the motor of this melt entrainment. This suggests a physical process which may transform the melt into a particle bed as depicted in fig 1.

Other out-of-pile experiments performed at KfK [1] with simulant materials (melt was simulated by paraffin or by a water-glycerin mixture and water was simulated by liquid Nitrogen) also made it possible to observe melt entrainment phenomena (through a crust) due to gas sparging. The characteristics of the debris bed (particle size, porosity, etc.) formed on the crust and the height of these debris depended on the characteristics of the melt material. With paraffin a particle bed was obtained whereas with glycerin it was concluded that the entrained material was dense and homogeneous. This was due to the fact that paraffin is very brittle at low temperature, whereas solid glycerin stays coherent. As corium-concrete melts seem also to be very coherent at low temperature, the authors concluded that corium-concrete melts would not easily be transformed into a particle bed, and would thus not be easily coolable.

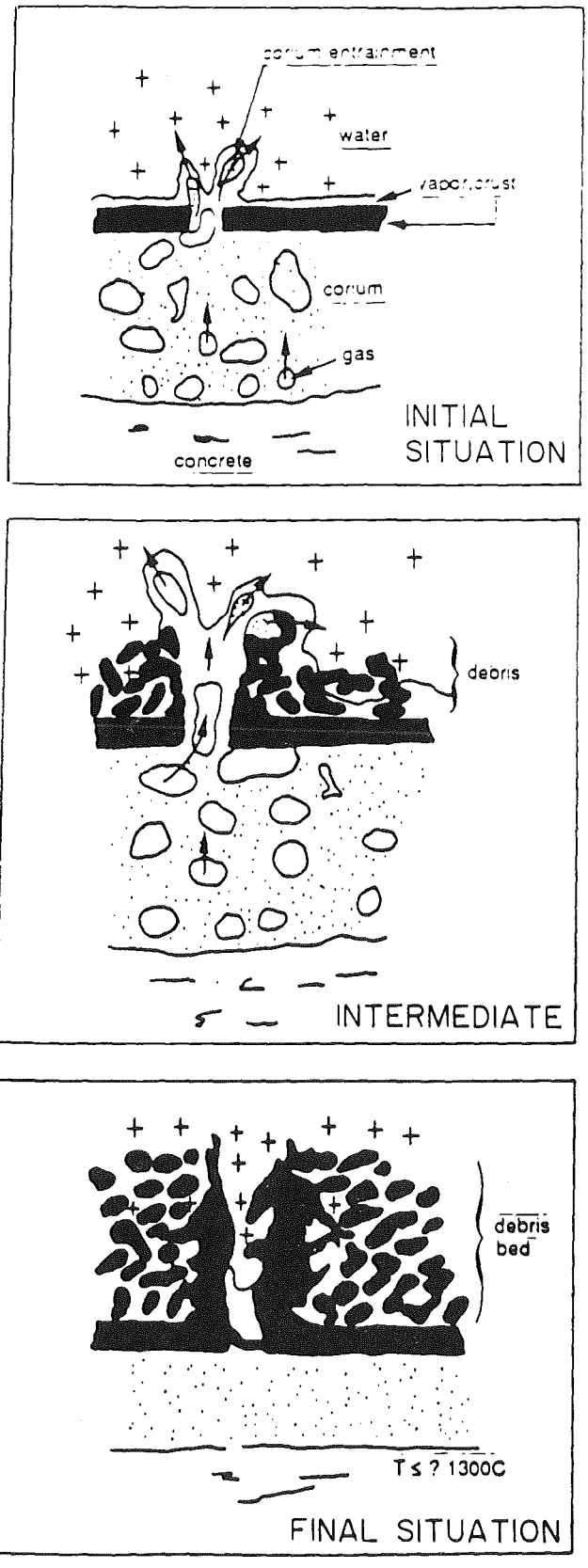

Fig. 1: Melt transformation; hypothesized scenario

The detailed characteristics of the debris bed obtained in MACE scoping test are not well known (it seems however that debris of more than 1 mm characteristic size are formed); further analyses are necessary.

On the other hand the cooling of a particle bed, with particles of a diameter larger than, say, 1 mm, is very efficient. Many studies have been performed, in the past, on particle bed cooling, mainly in the frame of fast reactor safety studies.

If one makes the assumption that the entrained corium-concrete melt transforms into a particle bed, this should result in a great increase of the cooling efficiency.

However, even if this entrainment phenomenon exists and melt transforms into a particle bed, one of the main problems is to know if the whole melt volume may be transformed. This question arises because the hypothesized phenomenon is self limited: in the initial phase of the corium-concrete interaction there is important ablation of the concrete, resulting in considerable gas release and melt entrainment; later, when the melt temperature and volume decrease, the concrete ablation and gas release also

diminish, the melt viscosity increases, and the entrainment phenomenon should be much less efficient.

The PERCOLA model was written in order to try to clarify this particular aspect of the problem

THE PERCOLA MODEL:

The model describes, in a simplified way, the interaction between a corium layer and concrete, the gas production, the growth of upper and lower crusts, the melt entrainment, the growth and cooling of a particle bed.

The considered geometry is depicted on figure 2.

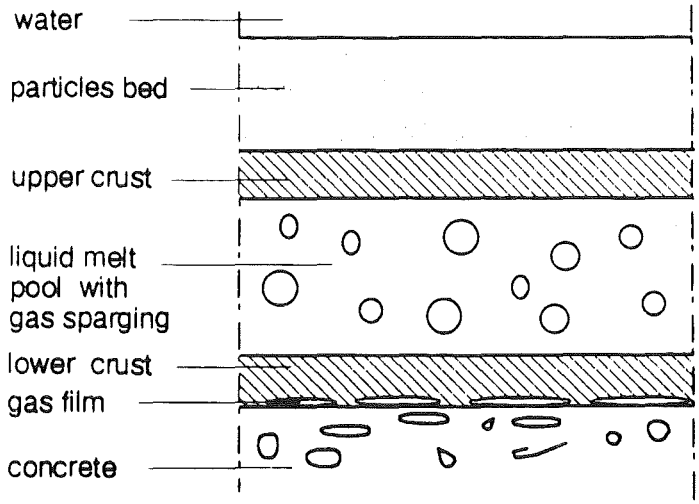

Fig. 2: PERCOLA model: considered geometry

The liquid melt is assumed to stay homogeneous (no separation between oxydic and metallic materials).

Mass exchanges between the different zones:

The concrete: The ablated concrete releases gases (CO_2, H_2O) and liquid phases (CaO, SiO_2, etc.) depending on its composition. The liquid phases are mixed with the liquid melt whose density diminishes with increasing concentration of concrete decomposition products. The parameter 'x' designates the mass of gases contained in one unit mass of concrete.

The lower and upper crusts: The crusts built up by solidification of the melt. The crust is assumed to be homogeneous (no stratification), the crust mean density is recalculated at each time step.

The liquid melt: The mass fluxes affecting the liquid melt are:

- The flux of concrete decomposition liquid products,
- The mass exchanges with the upper and lower crusts,
- The entrained mass flux. This mass flux is simply expressed, in a first step by:

$$Q_{vme} = Q_{vg} Ke \tag{1}$$

This expression supposes that the entrained mass flux is proportional to the gas volumetric flow rate. No effect of crack surface nor particle bed height is taken into account.

A void fraction is calculated in the melt. This void fraction is only needed for the calculation of the heat fluxes leaving the melt and has no effect on the melt entrainment modeling. The method of determination of the void fraction is based on the WALLIS approach [2] the rising velocity of a gas bubble in an infinite medium is given by the following formula [7]:

$$U_{\infty} = 1.53 \left(\frac{g(\rho_m - \rho_g)\sigma}{\rho_m^2} \right)^{1/4} . \tag{2}$$

The mean superficial velocity of the liquid is zero.

Supposing that the flow is churn turbulent, we come to following simple relation:

$$\alpha = \left(1 + \frac{U_{\infty}}{J_g} \right)^{-1} . \tag{3}$$

The particle bed: The entrained melt flow gathers on the upper crust and forms a particle bed of specified porosity and particle diameter.

Heat exchanges between the different zones:

The concrete: Transient heat conduction through the concrete is not taken into account. The heat coming from the melt serves to ablate the concrete following:

$$\Phi_c = L_c' \frac{dM_c}{dt} \tag{4}$$

The melting enthalpy takes into account the sensible heat needed to heat up the concrete to melting conditions.

Concrete-lower crust interface: A heat transfer resistance due to the accumulation of a gas film is taken into account. The model is taken from the WECHSL code [10].

Lower crust and upper crust: The model assumes steady state heat conduction through the crusts. For simplification, the heat flow due to decay power production in the crust thickness is supposed to be applied at the liquid melt-solid crust interface; thus the temperature profile through the crust is linear. The deposition rate of the solid melt is controlled by the difference between the heat flux evacuated by conduction through the crust and the heat flux delivered by the liquid melt to which is added the heat flux due to decay power production in the crust. The sensible heat related to the temperature variations of the crust is taken into account. The decay heat produced in the crust is calculated from the density of the crust. The assumption that the decay power produced in the crust is applied to the solid - liquid interface leads to an under-estimation of the crust thickness. The effect is negligible at the onset of the calculation (when the crust thicknesses are very low) but may be significative at the end of the calculation.

At the upper surface, the crust is only allowed to form if the interface temperature between the melt and the water is lower than the solidus temperature. The heat transfer between melt at high temperature and the water is calculated with the method used in CORQUENCH [5].

The liquid melt: The upward and downward heat transfers are calculated with the heat exchange correlations proposed by BLOTTNER [4]:

$$h_p = \lambda_\ell \left(\frac{Pr \cdot g}{\left(\frac{\mu_\ell}{\rho_\ell}\right)^2} \right)^{1/3} (C_1 \beta (T_{pool} - T_{sol}) + C_2 \alpha) \quad . \tag{5}$$

Coefficients	Lower Crust	Upper Crust
C_1	0.0003	0.00274
C_2	0.4	50

The temperature of the liquid melt is obtained from the following energy balance:

$$q''' Conc Hp = \Phi_{ac} + \Phi_{\ell c} + M_m C_m \frac{d Tm}{dt} + \frac{d M_C}{dt} C_c (T_m - T_{mc}) + \frac{d M_g}{dt} C_g (T_m - T_{mc}) \tag{6}$$

The concrete ablation products are supposed to enter the melt with the concrete melting temperature.

The solidus temperature of the melt is given by following arbitrary formula:

$$T_{sol} = C_{ocon} * T_{mcon} + C_{onuc} * T_{mnuc}$$

with:

C_{ocon}: Mass concentration of concrete ablation products
C_{onuc}: Mass concentration of Core melt products
T_{mcon}: Melting temperature of concrete
T_{mnuc}: Melting temperature of Core melt products.

The melt dynamic viscosity is calculated as a function of the melt temperature and melt composition following:

$$Visc = Exp\,(Avi/(T - Tvi) + Bvi)$$

T is the actual melt temperature

Avi, Bvi, and Tvi are parameters specified by the user to best approximate the slag viscosity.

The reference values for these parameters are:

Avi = 30000 ; Bvi = −15.4 ; Tvi = 0

These parameters lead to a viscosity of 0.004 $kg{\cdot}m^{-1}s^{-1}$ at 3000 K and 100 $kg{\cdot}m^{-1}s^{-1}$ at 1600 K.

Chemical reactions between concrete decomposition gases and melt are not taken into account (this should be taken into account in further developments).

The particle bed: The porosity of the bed and particle size are parameters which are specified by the user.

It is supposed that particle diameter is greater than 1 mm (this hypothesis is based on the preliminary observation from the debris obtained in MACE scoping test).

The particle bed is divided into two layers: a dry bed in contact with the upper crust and a wet bed above.

An equivalent conductivity is calculated for the dry layer.

The model supposes steady state heat conduction through the dry bed. As was done for the crusts, the heat flux due to decay power production in the dry bed is supposed to be applied at the solid crust-dry bed interface. This heat flux is added to the heat flux coming from the upper crust. These hypotheses lead to a linear temperature profile in the dry bed.

A dry-out heat flux is also calculated afterwards (surface tension effects are ignored) [9]:

$$\Phi_{D.O.} = 0.6\, L_w \rho_v \left(g\, \chi \frac{\mu_\ell}{\rho_v} \right)^{1/2} \left(1 + \left(\frac{\rho_v}{\rho_\ell} \right)^{1/4} \right)^{-2} \quad ; \quad \chi = \frac{\varepsilon}{1-\varepsilon} \frac{d}{6} \tag{7}$$

Knowing the dry-out heat flux, the thickness of the wet zone is calculated from the heat flux coming from the dry zone and the internal decay heat production in the wet zone.

The interface temperature between the upper crust and the bed is calculated by using an energy balance over the dry bed.

If the heat flux leaving the upper crust is lower than the dry out heat flux, the bed is quenched and the interface temperature between the upper crust and the bed is the saturation temperature of water.

CALCULATION RESULTS

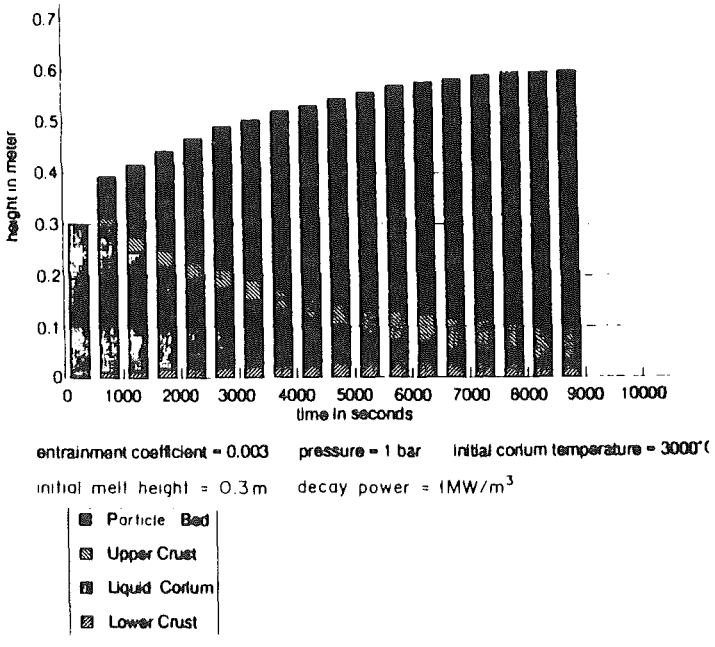

Fig. 3: PERCOLA model: Evolution of the corium layer geometry

An example of calculation result is presented on Fig. 3 for $x = 0.05$, $Ke = 0.03$, and a 10 bars ambient pressure. Figure 3 shows the calculated variations of the thicknesses of the lower crust, the thicknesses of the liquid melt, of the upper crust and of the particle bed. Level zero represents the interface bet-

ween the lower crust and the concrete. The thickness of the ablated concrete is not directly represented.

Parametric studies

Effect of concrete composition: The rate of gas release is different for various types of concrete (x ranges from, about, 0.05 to 0.25). If the gas content in the concrete is higher, the entrainment is also calculated to be more efficient. Table 1 presents transformation delays for various gas contents but for other similar common conditions: K = 0.03, pressure = 10 bars, particle diameter > 1 mm, initial melt temperature = 3000 K, initial melt height = 0.3 m; decay power = 1 MW/m^3.

Table 1: Effect of concrete gas content x on transformation time

gas content x	0.05	0.07	0.09	0.11	0.13
transformation time	8350 s	3900 s	2400 s	1650 s	1200 s

It is observed that under these conditions, transformation is obtained after about 20 min for x = 0.13 and 2 and a half hour for x = 0.05. The calculated heights of the particle bed are respectively about 35 cm for x = 0.25 and 0.4 m for x = 0.05.

Effect of pressure: The pressure affects the gas density. As the melt entrainment has been supposed to be proportional to the gas volumetric flow rate, it appears that the decrease of the pressure will have a sensitive effect on the kinetic of the transformation. A decrease of the pressure by a given factor has the same effect as an increase of the entrainment coefficient by the same factor.

Effect of entrainment coefficient: The entrainment coefficient has a very sensitive effect on the transformation kinetics. Table 2 below shows the transformation delays calculated for different values of the entrainment coefficient and for following constant parameters: initial melt temperature = 3000 K; pressure = 1 bar; x = 0.05; initial melt height = 0.3 m; decay power = 1 MW/m^3.

Effect of initial melt temperature: The initial melt temperature has been varied between 2700 K and 3000 K. In this range, the initial temperature does not have a significant effect. The effect is important during the beginning of the cooling transient. Table 3 gives an example of the effect of the initial temperature for

Table 2: Effect of entrainment coefficient

Entrainment coefficient	0.001	0.003	0.005	0.007
Melt transformation	for t = 100000 s 86% liquid	all solid at 8350 s	all solid at 3050 s	all solid at 1800 s

the following, common parameters: Pressure = 10 bars; x = 0.05; decay power = 1 MW/m^3; entrainment coefficient = 0.02.

Table 3: Effect of initial melt temperature

Melt transformation	Crusts formed after	Concrete erosion after 500 s
3000 K	200 s	6.7 cm
2700 K	80 s	3.5 cm

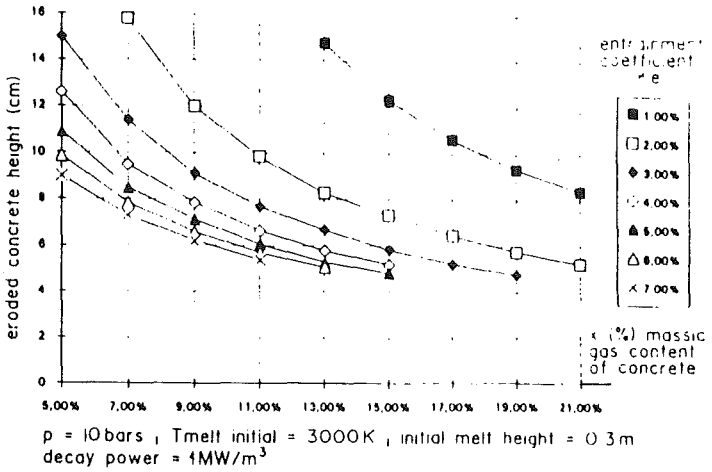

Fig. 4: Heights of eroded concrete

Heights of eroded concrete: An example of calculated heights of eroded concrete is presented in Fig. 4 as a function of the main parameters: x and Ke. The ablated height ranges from a few cm to about 16 cm.

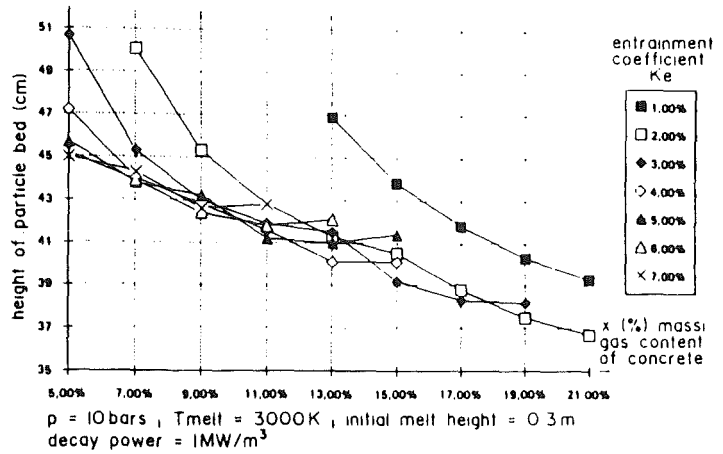

Fig. 5: Particle bed thickness after transformation

Heights of particle bed: Example of calculated heights of particle bed after transformation are presented in fig. 5 for an initial melt height of 0.3 m. The particle bed height variies from about 37 cm to 50 cm.

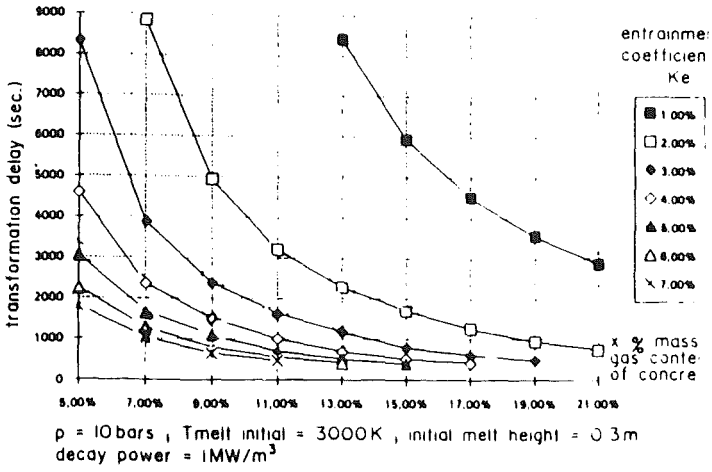

Fig. 6: Transformation chart

Transformation charts: For given initial conditions: melt temperature, pressure, melt height, decay power, etc., the transformation delay may be represented on a chart as a function of the main parameters: the concrete gas content (concrete type) and the entrainment coefficient. Figure 6 presents such a transformation chart.

ABOUT THE ENTRAINMENT COEFFICIENT AND MODELING ACCURACY

The entrainment coefficient is clearly the main parameter of the modeling.

The entrainment coefficient does not remain constant during the transformation as it is assumed in the actual model. It should depend, at least, on the height of the particle bed, on the surface of the cracks in the upper crust, on the viscosity of the melt, etc.

Determining the entrainment coefficient is not a simple task, which cannot be solved with our current level of knowledge; realistic experiments are required.

The efficiency of this type of entrainment depends to a large extent on the nature of the contact between the upper crust and the liquid melt.

If the crust and the debris bed "floate" on the melt surface, the entrainment may be much more efficient than in the case of a separation between the crust and liquid melt. If the load of the solid crust and debris is entirely supported by the liquid melt (and not by the side walls of the test device), the liquid melt may fill the channels penetrating into the solid material to a certain height, and the liquid melt expulsion from such channels may still remain significant even for rather high debris beds.

Therefore, it seems fundamental to avoid anchoring of the upper crust in the experiments.

The degree of detail for the different parts of the modeling is dictated by the part which is poorest depicted. This part is clearly the description of the entrainment phenomenon.

The different parts of the model may be improved if a more precise description of the entrainment phenomenon is available.

Determining the entrainment coefficient is not a simple task, which cannot be solved with our current level of knowledge; realistic experiments are required. The efficiency of this type of entrainment depends to a large extent on the nature of the contact between the upper crust and the liquid melt.

CONCLUSION

The objective of the PERCOLA model was to establish whether the long term cooling of a corium layer after transformation into a debris bed is something credible or not. Credible means that the complete transformation is obtained for not unrealistic sets of parameters. The self limitation of the hypothesized melt entrainment phenomenon by the gas flow coming from the concrete ablation was one of the main sources of uncertainty.

The calculations show that the theoretical transformation may be obtained for entrainment coefficients as low as 0.001 or 0.0001 at a pressure of 1 bar. These are not unrealistic entrainment coefficients.

So it is concluded that it seems worth continuing more detailed analysis along this line. Therefore further experimental results are needed.

The experiments should bring information concerning the relative importance of different potential phenomena which may enhance melt cooling (water ingression due to crack propagation, melt entrainment, etc.). If it is confirmed that melt entrainment is an important effect, the experiments should provide more insight into this phenomenon: evaluation of the variation of the entrainment efficiency, structures and properties of debris layers (compositions, particle diameters, if any, porosity, permeability, mechanical properties, etc.).

This study confirmed that it seems essential to avoid upper crust anchoring on the test device side walls in the experiments. Furthermore the load of the crust and the debris bed (if any) should rest entirely on the liquid melt, as would be the case in a reactor situation.

NOTATION

C	Heat capacity (J/Kg K)
C_{onc}	Concentration of nuclear materials in the melt
g	Gravity acceleration (m/s^2)
h	Heat exchange coefficient
H	Height (m)
J	Superficial velocity (m/s)
Ke	Entrainment coefficient
L'	Melting Enthalpy (J/Kg)
M	Mass per unit surface (Kg/m^2)
Pr	PRANDTL number
T	Temperature (K)
t	Time (sec)
U	Velocity (m/s)
Q	Volumetric Flow rate (m^3/sec)
L_w	Water latent heat of vaporization (J/kg)

Greek letters:

α	Void fraction
β	Volumetric expansion coefficient (1/K)
λ	Thermal conductivity (W/m K)
ρ	Density (Kg/m^3)
μ	Dynamic Viscosity (Kg/m·s)
ϕ	Heat Flux (W/m^2)
σ	Surface tension (N/m)

Subscripts:

c	Concrete
g	Gas
ℓ	Liquid
ℓ_c	Lower Crust
m	Melt
m_c	Melting of Concrete
s	Solid
sol	Solidus
uc	Upper crust
v_{me}	Volumetric Melt Entrained
vg	Volumetric Gas
v	Vapor
w	Water

LITERATURE CITED

1. ALSMEYER H., DRES K., REIMANN M., STIEFEL S., "Modellentwicklung zur analytischen Beschreibung von Kernschmelzunfällen", Sicherheitsorientierte LWR-Forschung, Jahresbericht 1987, KfK 4450, pp. 113-128 (1987)

2. BERGLES A.E., COLLIER J.G., DELHAYE J.M., HEWITT G.F., MAYINGER F., "Two Phase Flow and Heat Transfer in the Power and Process Industries", Hemisphere publishing corporation (1981)

3. BLOSE R.E. et al., "SWISS: Sustained Heated Metallic Melt/Concrete Interactions with Overlying Water Pool"; NUREG/CR-4727, SAND 85-1546 (July 1987)

4. BLOTTNER F.G., "Hydrodynamics and Heat Transfer Characteristics of Liquid Pools with Bubble Agitation"; NUREG/CR-0944 (November 1979)

5. FARMER M.T., SIENICKI J.J., SPENCER B.W., "CORQUENCH: A Model for Gas Sparging-Enhanced, Melt-Water, Film Boiling Heat Transfer"; ANS Winter Meeting on Thermal Hydraulics of Severe Accidents, Washington, D.C., (November 11-15, 1990)

6. FAUSKE & Ass., "Technical support for the EPRI debris coolability requirement for advanced light water reactors"; DOE/ID-10279 (March 1990)

7. HESTRONI G., "Handbook of Multiphase Systems", Hemisphere publishing company (1982)

8. MACE: to be published

9. OSTENSEN R.W., "Advanced reactor safety research program - quarterly report", SANDIA (October -December 1979)

10. REIMANN M., STIEFEL S., "The WECHSL-Mod 2 Code: A computer program for the interaction of a Core melt with concrete including the long term behaviour", KfK 4477 (June 1989)

11. WETCOR: to be published

STATUS OF THE MELTSPREAD-1 COMPUTER CODE FOR THE ANALYSIS OF TRANSIENT SPREADING OF CORE DEBRIS MELTS

M. T. Farmer, J. J. Sienicki, B. W. Spencer, and C. C. Chu

Argonne National Laboratory
Argonne, Illinois 60439 USA

ABSTRACT

A transient, one dimensional, finite difference computer code (MELTSPREAD-1) has been developed to predict spreading behavior of high temperature melts flowing over concrete and/or steel surfaces submerged in water, or without the effects of water if the surface is initially dry. This paper provides a summary overview of (i) models and correlations currently implemented in the code, (ii) code validation activities completed thus far, (iii) LWR spreading-related safety issues for which the code has been applied, and (iv) the status of documentation for the code.

INTRODUCTION

In certain severe accident sequences in light water nuclear reactors, molten core material (corium) is postulated to relocate into the lower regions of the reactor pressure vessel (RPV). The associated thermal loading may eventually lead to failure of the vessel lower head, causing discharge of melt onto the containment floor where it spreads laterally under the influence of gravity. From a coolability standpoint, a knowledge of the spreading behavior is important since the average melt depth decreases with increasing floor coverage, and therefore the debris configuration is more amendable to quenching and thermal stabilization the farther the melt spreads. However, if critical safety system(s) lie in the pathway of the melt, then excessive spreading is a concern. For example, a current significant question relates to the potential for corium to spread over the drywell floor and cause early failure of the Mark I containment shell (1).

Several research efforts on corium spreading potential and Mark I shell thermal attack have been reported in the literature. Predictions of shell meltthrough were first performed by Greene et. al. (1) using corium conditions obtained from CORCON calculations of the molten core concrete interaction (MCCI) following the

assumed uniform spreading of a large corium mass over the pedestal and drywell regions. Estimates of corium lateral migration associated with long-term MCCI were performed by Corradini (2) for the case of gradual corium addition to the MCCI zone. For this case, lateral relocation of corium occurs as a result of sidewards and downwards concrete ablation as calculated with a modified version of the CORCON code. Kazimi (3) estimated the corium spreading potential assuming that spreading takes place in a semi-circular region and that the heat transfer coefficient is characteristic of non-spreading, natural convective MCCI's. Henry (4) conducted simulant experiments in which iron-alumina thermite was injected into a steel walled linear flow channel containing two rectilinear compartments and a concrete base to investigate quenching of debris which has spread over concrete and come to rest against a vertical steel wall. Theofanous et. al. (5) conducted simulant spreading experiments using water in a 1/10 linear scale model of the Mk I containment. Water heights as a function of time at various locations in the pedestal and drywell regions were measured. Based on the results of their scaled experiments, Theofanous et. al. concluded that the flow characteristics in the drywell are controlled by the driving gravity head across the pedestal doorway.

The development of a computational capability to provide an analysis framework for the assessment of spreading potential and structural boundary heatup in containments was undertaken at Argonne National Laboratory. The initial version of a transient spreading model was the MELTSPREAD-0 code developed by Sienicki, et. al. (6). This code assumed quasi-steady concrete ablation and did not account for melt freezing, immobilization, and subsequent flow over the solidified leading edge. MELTSPREAD-0 was applied to analyze the iron-alumina thermite spreading experiments of Henry, (4) and was also used to perform scoping calculations of the flow out of the pedestal doorway in the full-scale Mk I system.

Development of a transient spreading model is continuing in the form of the MELTSPREAD-1 code (7, 8). MELTSPREAD-1 contains more detailed models for the processes treated in MELTSPREAD-0 as well as many new models for phenomena that were ignored in the earlier code. This paper provides a summary overview of the developmental status of MELTSPREAD-1, including (i) models currently implemented in the code, (ii) validation exercises completed thus far, (iii) code

applications, and (iv) code documentation.

SUMMARY MODEL DESCRIPTION

MELTSPREAD-1 has been developed to predict the spreading behavior of high temperature melts flowing across horizontal surfaces submerged in a depth of water, or without the effects of water if the surface is initially dry. For the current applications in nuclear reactor safety, the substrates specifically treated included steel and concrete, and the high temperature melts encompass a wide range of compositions of reactor core materials (corium) including distinct oxide phase (predominantly UO_2, ZrO_2, steel oxides) and metallic phase (predominantly Zr, steel). The code requires input pertaining to the conditions of the melt "pour" onto the surface; the code calculates transient hydrodynamics and heat transfer which determine the spreading and freezing behavior of the melt including heat transfer to overlying water and to the substrate, heatup/ablation of the substrate, concrete decomposition, heat transfer enhancement owing to gas sparging, internal heat generation owing to both decay heat and to chemical reactions between concrete decomposition products and melt constituents, leading edge immobilization owing to crust growth or bulk (slurry) freezing, spreading of melt over previously spread/solidified material, and impingement heat flux where vertical structures are contacted by the flowing melt. The code is used to establish conditions at the end of the spreading stage, including melt relocation distance, depth profile, substrate and wall ablation. The code output provides input to other codes such as CORCON (9) for molten core-concrete interaction (MCCI) or structure response codes to evaluate long term behavior following the transient spreading stage. Alternatively, MELTSPREAD-1 contains simplified modules for quasi-steady MCCI and melt coolability calculations that may be used for long term, quasi-steady solutions.

The relocation model incorporated into MELTSPREAD-1 performs a fluid dynamics calculation of the gravity driven motions of a molten mass spreading in a one-dimensional flow channel of varying cross-sectional area. The fluid velocity is assumed to satisfy the equation,

$$\frac{\partial U}{\partial t} + \frac{1}{2}\frac{\partial U^2}{\partial z} = -\frac{1}{2} g \frac{\partial}{\partial z}\left[\frac{h}{1-\alpha} + E\right] - \frac{4\tau}{\rho D}, \qquad (1)$$

where

$$D = \frac{4h}{1-\alpha}, \tag{2}$$

$$\tau = \frac{1}{2} \rho U|U| f_{fric}, \tag{3}$$

and U = local, h = collapsed melt depth, g = gravitational acceleration, and α = void fraction. The nonconservative form of the momentum equation is employed because it reduces to Bernoulli's law in the limit of frictionless flow. The friction factor is calculated using the correlation of Colebrook and White (10). The hydrostatic pressure gradient is based on the melt height plus the basemat elevation. The local melt void fraction due to concrete decomposition gases sparging through the melt is calculated based on the correlation of Kataoka and Ishii (11). The elevation gradient is included to account for the presence of previously solidified debris, in addition to any initial irregularities in the spreading surface, such as the presence of a sump pit. Spreading is restricted to occur such that the leading edge melt depth does not fall below the minimum depth at which surface tension balances gravity.

The collapsed depth, h, in Eq. (1) is written as a sum of the local melt constituents, h^i. MELTSPREAD-1 tracks a total of 16 melt constituents, which include Zr, Cr, Fe, Ni, B_4C, U, B, FeO, Fe_2O_3, Fe_3O_4, ZrO_2, Cr_2O_3, NiO, UO_2, B_2O_3, and slag. The metals are treated as a distinct phase from the oxides. The conservation of mass equation of the i^{th} melt constituent is of the form,

$$S \frac{\partial}{\partial t}\left(\rho^i h^i\right) + \frac{\partial}{\partial z}\left(S \rho^i h^i U\right) = \beta^i S \left[F_{H_2O} \gamma^i_{H_2O} \dot{m}''_{H_2O} + F_{CO_2} \gamma^i_{CO_2} \dot{m}''_{CO_2}\right]$$

$$+ S \frac{\rho^i_s}{\rho^i_l}\left[x^i_{surface} \frac{d\eta}{dt} - x^i_{melt} \frac{d\delta}{dt}\right] + S\, x^i_{vessel}\, \dot{m}''_{vessel}, \tag{4}$$

where

$$\beta^i = \begin{cases} +1, \text{ oxidizable melt constituents,} \\ -1, \text{ oxidized melt constituents,} \\ 0, \text{ non-oxidizable melt constituents,} \end{cases} \quad (5)$$

and S = spreading perimeter normal to flow, ρ = melt density, δ = crust depth, η = substrate ablation depth, and $x^i_{surface}$, x^i_{melt}, and x^i_{vessel} denote the weight fraction of the ith constituent in the basemat, flowing melt, and pouring melt, respectively. The functions F_{H_2O} and F_{CO_2} account for incomplete reaction of the sparging gases as the gas bubbles rise through the melt layer; these functions are calculated using standard transient diffusion theory models (12). The terms $\gamma^i_{H_2O}$ and $\gamma^i_{CO_2}$ are well known stoichiometric constants. Depending on the melt-substrate interfacial boundary condition, the fourth term in Eq. (4) accounts for mass transfer due to substrate ablation and/or crust formation.

The fifth term in Eq. (4) accounts for local, time-dependent mass addition to the melt layer due to drainage from the reactor pressure vessel. For BWR's, a significant amount of below vessel structure exists in the form of control rod drive and instrument tube housings, in addition to personnel access structure (e.g., cat walk). Corium draining from a localized breach in the reactor pressure vessel may thus undergo significant splashing as it passes through this structure, causing the corium to "rain" down on the pedestal floor. To account for this behavior, MELTSPREAD-1 permits melt addition to the spreading layer over a distributed area as well as a localized area.

The spreading melt constituents are assumed to be in local thermodynamic equilibrium at a single, local layer specific enthalpy. The enthalpy is obtained from the solution of the energy conservation equation,

$$\begin{aligned} & S\frac{\partial}{\partial t}(\rho he) + \frac{\partial}{\partial z}(S\rho heU) = -Sh_{bot}(T - T_{bot}) - Sh_{top}(T - T_{top}) \\ & + S\rho h\dot{q}_{decay} + S\dot{m}''_{vessel}\, e_{vessel} + S\rho\left[e_{ablation}\frac{d\eta}{dt} - e_{crust}\frac{d\delta}{dt}\right] \\ & + SF_{H_2O}\,\dot{m}''_{H_2O}\sum_i \gamma^i_{H_2O}\, q^i_{ox,H_2O} + SF_{CO_2}\,\dot{m}''_{CO_2}\sum \gamma^i_{CO_2}\, q^i_{ox,CO_2} \end{aligned} \quad (6)$$

and e/T = melt enthalpy/temperature, $\dot{q}_{dec}$ = decay heat level, q_{ox}^{i} = oxidation energy release for the reaction of i^{th} melt constituent with concrete decomposition gases, and subscripts top and bot denote conditions at the top and bottom of the melt layer, respectively.

The local enthalpy in the melt layer is checked to determine if the enthalpy has fallen below the solidus value. If so, the melt is immobilized and added to previously solidified melt, concrete, and steel in the calculation. If the enthalpy lies between the liquidus and solidus, the melt is modeled as a slurry with enhanced effective viscosity as given by the correlation of Ishii and Zuber (13).

At the melt lower surface, a variety of boundary conditions are treated to encompass a range of melt-substrate interaction conditions. These boundary conditions include: (1) a growing stable crust upon solid substrate, (2) thin crust segments upon a solid substrate, (3) substrate ablation with a growing stable crust, (4) substrate ablation without a crust, (5) substrate melting without removal of melt beneath a growing crust, and (6) solid substrate without crust formation.

A current source of uncertainty is the applicable heat transfer coefficients at the melt upper and lower surfaces during corium spreading. A the lower surface, the heat transfer coefficient options include: (1) forced convection, (2) bubble agitation, or (3) sum of forced convection and bubble agitation models. The bubble-agitation heat transfer coefficient is calculated using Bradley's model (14). Forced convection heat transfer is calculated using the Dittus-Bolter correlation (15).

At the melt upper surface, MELTSPREAD-1 treats heat transfer to either an overlying water layer or heat transfer to a dry atmosphere. Additionally, crusting may be assumed to be absent at the upper surface, or the heat transfer may be assumed to be limited by thin crust segments which move with the melt layer. If water is absent, the heat transfer coefficient is calculated assuming radiation off the top of the melt. If water is present, the heat transfer is calculated along a full boiling curve. Heat transfer in the nucleate boiling regime is calculated using Rohsenow's correlation (16). The critical heat flux

is calculated using Zuber's model (17) with a correction for subcooling due to Ivey-Morris (18). In the film boiling regime, the melt-to-water heat transfer is calculated using the CORQUENCH model (19), which accounts for radiant heat transfer across the film, noncondensable gases, bulk liquid subcooling, melt-water interfacial area enhancement due to sparging gas, and melt entrainment into the overlying water layer. The minimum film boiling temperature is calculated using Henry's correlation (20). In the transition boiling regime, a linear variation between the critical heat flux and the minimum film boiling heat flux is assumed. A local check on the height of the melt layer relative to a user-specified maximum water height (e.g., downcomer height in Mark I containments) is performed. If the melt height exceeds the user-specified maximum height, a radiation boundary condition is applied at the melt upper surface.

In the underlying substrate, MELTSPREAD-1 solves a one-dimensional transient heat conduction equation to obtain the local substrate enthalpy,

$$\rho \frac{\partial e}{\partial t} = \frac{\partial}{\partial y}\left[k \frac{\partial T}{\partial y}\right] + \rho \dot{q}_{decay}. \tag{7}$$

Equation (7) is applied to both concrete and steel substrates, as well as solidified debris. The concrete property routines incorporated into MELTSPREAD-1 implicitly account for the decomposition enthalpies associated with the generation of water vapor (evaporable H_2O and decomposition of $Ca(OH)_2$), and the generation of carbon dioxide (decomposition of $CaCO_3$ and $MgCa(CO_3)_2$). The front location for each of the decomposition processes is obtained by tracking the decomposition isotherm in the basemat (i.e., a dryout calculation is performed). This approach is motivated by the requirement of calculating the appropriate concrete degassing behavior during sequential pours in which previously heated concrete is reheated by subsequently arriving melt.

If the melt propagates to the containment structural boundary (the user has complete flexibility on the specification of the location of boundary), MELTSPREAD-1 invokes a two-dimensional transient heatup calculation. The boundary material is currently assumed to consist of carbon steel. The governing equation for the heatup calculation is of the form,

$$\rho \frac{\partial e}{\partial t} = \frac{\partial}{\partial x}\left[k \frac{\partial T}{\partial x}\right] + \frac{\partial}{\partial y}\left[k \frac{\partial T}{\partial y}\right]. \tag{8}$$

If the boundary surface temperature lies below the melt freezing temperature, stable crust growth is calculated. The user currently has the option of specifying forced convection, bubble recirculation, or a sum of forced convection and recirculation heat transfer coefficients between the melt and boundary. The convective heat transfer coefficient is currently modeled using a jet impingement heat transfer coefficient (21). The bubble recirculation heat transfer coefficient is calculated using the correlation of Theofanous et. al. (5).

If water is absent, the heat transfer from the boundary surface above the melt layer is calculated using a radiation heat transfer coefficient. Heating of the structure above the melt due to radiation from the melt adjacent to the structure is currently not modeled. If water is present, the heat transfer is calculated along a full boiling curve. Heat transfer in the nucleate boiling regime is again calculated using Rohsenow's equation (16) with a correction for inclination according to the correlation of Jung et. al. (22). The critical heat flux is assumed to be given by Zuber's model (17). The minimum film boiling temperature is calculated using Henry's correlation (20). The film boiling heat transfer coefficient is calculated using Berenson's model (23) with a correction for inclination according to the experimental results of Sauer et. al. (24).

CODE VALIDATION

An important part of MELTSPREAD development has been the comparison of model predictions with analytical solutions and experiment data. There is currently a lack of experiment data using prototypic materials in a scaled apparatus. Thus, validation efforts so far have focused on separate affects and simulant material experiments.

In order to test the hydrodynamics modeling in MELTSPREAD-1, the code has been compared to the analytical solution for a one-dimensional "dam break" problem (7). Since this problem contains no heat transfer effects, the heat transfer models in the code were bypassed. Of principal interest is whether correct spreading depths and velocities are calculated. According to gravity current theory (25), after the "dam" has been removed and short term transient effects have died away, the advancing front will obtain a depth equal to one half the initial fluid depth, and (in an Eulerian coordinate system) the advancing and receding wave fronts will achieve a velocity equal to $\frac{1}{2}\sqrt{dg}$, where d = the

initial water depth in the channel. For the particular example which was considered (7), the calculated advancing and receding front depths and velocities agree to within 6% of the analytical solution.

Given that MELTSPREAD-1 predicts spreading depths and front velocities for the dam break problem to within suitable tolerances, the model was applied (7) to predict the relocation behavior of water simulant in the more complex, scaled Mark I geometry employed by Theofanous et. al., (5). The apparatus was an approximate 1/10 linear scale model of the Peach Bottom pedestal and drywell. In this experiment, transient depth profiles were measured at five locations ranging from inside the pedestal to outside the pedestal in the drywell annulus 180° from the pedestal doorway. Transient height profiles for two runs were reported (5). Run No. 1 was a 1/10 scale simulation of 10 m^3 pour volume at a pour rate of 6.5 m^3/min. The corresponding pour rate in the scaled experiment was 19.5 liters/min. Run No. 2 considered the same pour volume at reactor scale, but the pour rate was reduced to 3.25 m^3/min. The corresponding pour rate in the scaled experiment was 9.75 liters/min. Calculations were performed for both of the reported tests. Comparison of model predictions (7) with the simulant data indicates that the model reasonably predicts the arrival times and transient depths within the pedestal and annular regions in the absence of freezing phenomena.

The CORQUENCH melt/water film boiling heat transfer module (19) embodied in MELTSPREAD has been compared with the experiment data obtained by Greene et. al., (26) using molten lead/saturated Freon 11 simulants. The model shows favorable agreement with this limited set of experiment data. Modeling enhancements to the CORQUENCH model have been made to extend the capability of this routine to treat both bulk cooldown and crust-limited heat transfer regimes (27, 28). These modeling enhancements will eventually be embodied in the MELTSPREAD-1 CORQUENCH module to improve the code's ability to treat long term, quasi-steady melt/water heat transfer behavior.

In terms of simulant spreading experiments involving freezing behavior, MELTSPREAD-0 was applied to analyze the iron-alumina thermite spreading experiments of Henry (4). In these experiments, the thermite injection time was short in comparison to the time for the melt to spread the length of the channel

(6). Therefore, in the analysis it was assumed that the thermite was instantaneously deposited in the injection compartment and, thereafter, relocated in a 1-D spreading trough under the influence of gravity. Model predictions indicated that the thermite would spread the full length of the channel without freezing at the leading edge, which is in agreement with the experiment observations. Since the ultimate spreading penetration in those experiments was predicted to be limited by the short length of the test section channel, the results of that comparison are also valid for MELTSPREAD-1 which would provide similar predictions.

While models in MELTSPREAD have been tested against available data, the validation database is meager. The SMELTR program of reactor material, integral effects tests is under development for this purpose (29). MELTSPREAD is being used to support the development of the SMELTR program insofar as evaluating experiment approaches to resolve key modeling uncertainties and plan an optimum test matrix.

CODE APPLICATIONS

The principal application that prompted development of MELTSPREAD was assessment of Mark I containment vulnerability in the event of a core melt accident. MELTSPREAD was specifically developed to address the accumulation of corium on the pedestal floor (from postulated core melt accident resulting in melt penetration of the vessel lower head). The accumulating corium spreads across the pedestal and drywell concrete floors to contact the steel liner of the containment shell where heating of the liner raises the question of its long term integrity.

Scoping calculations of the spreading behavior in the Mark I containment have also been carried out with MELTSPREAD-1 (7). The pour conditions in these calculations were based on the considerations of Theofanous et. al. (5) for a station blackout sequence[1]. The results indicate that with water present in the drywell, significant freezing of corium will occur between the pedestal doorway

[1]Pour volume of 10 m^3 discharged at a constant flowrate of 3.25 m^3/min. The first calculation assumed 30% oxidation of the zirconium inventory (corresponding composition: 81 wt% UO_2, 8 wt% ZrO_2, 11 wt% Zr); solidus/liquidus temperatures were estimated as 2170/2670 K, respectively (7). The second calculation assumed 100% oxidation of the Zr inventory; solidus/liquidus temperatures were estimated as 2910/2980 K, respectively (7). A 37 K melt superheat with respect to the liquidus was assumed for both calculations.

and the shell. Based on the conservative assumption that the corium is immobilized when the temperature reaches the solidus, the melt reaches the shell in the form of a slurry at 62 seconds past the start of the pour when the freezing temperature range for a UO_2-ZrO_2-Zr corium mixture is assumed. For a UO_2-ZrO_2 system, the corium reaches the shell as a slurry at 140 seconds.

In addition to these initial scoping calculations (7), MELTSPREAD-1 has been used to perform an extensive examination of spreading behavior in the Mark I containment. MELTSPREAD-1 has also been used to calculate transient spreading depth and basemat ablation profiles in U.S. advanced light water reactor cavity designs (both ALWR and SBWR).

CODE DOCUMENTATION

In addition to open literature publications describing MELTSPREAD model development and code applications (6, 7), a Code Manual has been prepared (8). The manual provides (i) descriptions of the models and correlations implemented in the code, (ii) descriptions of the implicit, finite difference numerical scheme, and (iii) a users guide for setting up input decks for the code. The manual has been peer reviewed and is in the final stages of the revision process. Verification and validation documentation will be provided in the future.

SUMMARY AND CONCLUSIONS

A transient, one-dimensional, finite difference computer code (MELTSPREAD-1) has been developed to predict the spreading behavior of high temperature melts flowing across horizontal surfaces submerged in water, or without the effects of water if the surface is initially dry. This paper has provided: (i) a summary overview of the models and correlations currently implemented in the code, (ii) a status report on the code validation activities that have been completed thus far, (iii) a summary of current LWR spreading-related safety issues for which the code has been applied, and (iv) a description of the status of documentation for the code.

ACKNOWLEDGEMENTS

The development work for MELTSPREAD-1 has been supported by the Electric Power Research Institute (EPRI) under contract No. 3047-2. The EPRI Program Manager is Dr. B. R. Sehgal. The manuscript was prepared for publication by L. J. Ondracek.

REFERENCES

1. G. A. Greene, K. R. Perkins, and S. A. Hodge, "Mark I Containment Drywell-Impact of Core/Concrete Interactions on Containment Integrity and Failure of the Drywell Liner," Source Term Evaluations for Accident Conditions-Proceedings of an International Symposium on Source Term Evaluation for Accident Conditions, Columbus, OH, October 28-November 1, 1985, pp. 429, International Atomic Energy Agency, Vienna, (1986).

2. M. L. Corradini, "Current Status of LWR Containment Loads Due to Severe Reactor Accidents," Third International Topical Meeting on Nuclear Power Plant Thermal Hydraulics and Operations, Seoul, Korea, November 14-18, 1988.

3. M. S. Kazimi, "Recent Development in Thermohydraulics of Severe Accidents," Third International Meeting on Nuclear Power Plant Thermal Hydraulics and Operations, Seoul, Korea, November 14-18 (1988).

4. R. E. Henry, "Mk I Containment Experiments," U.S. NRC Mk I Containment Workshop, Baltimore, MD, February 24-26 (1988).

5. T. G. Theofanous, W. H. Amarasooriya, H. Yan, and U. Ratnam, "The Probability of Liner Failure in a Mark-I Containment," NUREG/CR-5423, August 1991.

6. J. J. Sienicki, M. T. Farmer, and B. W. Spencer, "Spreading of Molten Corium in Mk I Geometry Following Vessel Meltthrough," Fourth Proceedings Nuclear Thermal Hydraulics, Washington, D.C., October 30-November 4, 1988.

7. M. T. Farmer, J. J. Siencki, and B. W. Spencer, "Spreading of Molten Corium in Mk I Geometry Following Vessel Meltthrough," Fourth Proceedings Nuclear Thermal Hydraulics, Washington, D.C., October 30-November 4, 1988.

8. M. T. Farmer, J. J. Siencki, and B. W. Spencer, "The MELTSPREAD-1 Code for the Analysis of Transient Spreading and Cooling of Molten Core Materials," Draft EPRI Report, March 31, 1991.

9. R. K. Cole, D. P. Kelley, and M. A. Ellis, "CORCON-mod2: A Computer Program for Analysis of Molten-Core/Concrete Interactions," U.S. Nuclear Regulatory Report NUREG/CR-3920, SAND84-1246, 1984.

10. H. Schlichting, Boundary Layer Theory, Fourth Edition, New York; McGraw-Hill, Inc., p. 525, 1960.

11. I. Kataoka and M. Ishii, "Prediction of Pool Void Fraction by New Drift Flux Correlation," NUREG/CR-4657, ANL-86-29, Argonne National Laboratory, June 1986.

12. J. K. Sherwood, R. L. Pigford, and C. R. Wilke, Mass Transfer, McGraw Hill, pp. 227, 1975.

13. M. Ishii and N. Zuber, "Drag Coefficient and Relative Velocity in Bubble, Droplet, or Particulate Flows," AIChE Journal, Vol. 25, pp. 854-855, 1975.

14. D. R. Bradley, "Modeling of Heat Transfer Between Core Debris and Concrete," ANS Proceedings 1988 National Heat Transfer Conference, Houston, TX, July 24-27, 1988, American Nuclear Society, La Grange Park, 1988.

15. H. Martin, "Heat and Mass Transfer between Impinging Gas Jets and Solid Surfaces," Advances in Heat Transfer, Vol. 13, p. 1, Academic Press, Inc., New York, 1977.

16. W. H. Rohsenow, "A Method of Correlating Heat Transfer Data for Surface Boiling of Liquids," Trans. ASME, Vol. 74, pp. 969-976, 1952.

17. N. Zuber, On the Stability of Boiling Heat Transfer," Trans. ASME, Vol. 80, pp. 711-720, 1958.

18. H. J. Ivey and D. J. Morris, "On the Relevance of the Vapor-Liquid Exchange Mechanisms for Subcooled Boiling Heat Transfer at High Pressure," AEEW-R127, 1962.

19. M. T. Farmer, J. J. Sienicki, and B. W. Spencer, "CORQUENCH: A Model for Gas Sparing-Enhanced, Melt-Water, Film Boiling Heat Transfer," ANS Winter Meeting on the Thermal Hydraulics of Severe Accidents, Washington, D.C., November 11-15, 1990.

20. R. E. Henry, "A Correlation for the Minimum Film Boiling Temperature," AIChE Symp. Ser., Vol. 70, pp. 81-90, 1974.

21. J. J. Sienicki and B. W. Spencer, "Analysis of Reactor Material Experiments Investigating Corium Crust Stability and Heat Transfer in Jet Impingement Flow," ANS Proceedings 1985 National Heat Transfer Conference, Denver, CO, August 4-7, 1985, pp. 255, American Nuclear Society, La Grange Park, IL, 1985.

22. D. S. Jung, J. E. Venart, and A. C. Sousa, "Effects of Enhanced Surfaces and Surface Orientation on Nucleate and Film Boiling Heat Transfer in R-11," Int. J. Heat Mass Transfer, Vol. 30, pp. 2627-2639, 1987.

23. P. J. Berenson, "Film Boiling Heat Transfer from a Horizontal Surface," J. Heat Transfer, Vol. 83, pp. 351-357, 1961.

24. H. J. Sauer and S. C. Lin, "Effect of Inclination on Film Boiling," Proc. 5th Int. Heat Transfer Conf., Vol. 4, pp. 110-114, 1974.

25. T. B. Benjamin, "Gravity Currents and Related Phenomena," J. Fluid Mechanics, Vol. 31, Part 2, pp. 209-248, 1968.

26. G. A. Greene, "Gas Bubbling-Enhanced Film Boiling of Freon-11 on Liquid-Metal Pools, Trans. Am. Nucl. Soc., Vol. 49, pp. 249-251, 1985.

27. M. T. Farmer, et. al., "Modeling and Database for Melt-Water Interfacial Heat Transfer," 2nd CSNI Specialist Meeting on Core-Debris Interactions, Karlsruhe, FRG, April 1-3, 1992.

28. M. T. Farmer, J. J. Sienicki, and B. W. Spencer, "Melt Coolability Modeling and Comparison to MACE Test Results," 2nd CSNI Specialist Meeting on Core-Debris Interactions, Karlsruhe, FRG, April 1-3, 1992.

29. B. R. Sehgal and B. W. Spencer, "Spreading of Melt in Reactor Containment (SMELTR)," 2nd CSNI Specialist Meeting on Core Debris-Concrete Interactions, Karlsruhe, FRG, April 1-3, 1992.

HOW TO AVOID MOLTEN CORE/CONCRETE INTERACTION (AND STEAM EXPLOSIONS)

A. Turricchia

ENEL-DCO, Via G.B Martini 3, I-00198 Rome

ABSTRACT

To safeguard the integrity of the containment basemat of future nuclear power plants, in case of severe accidents, it is proposed to locate, inside the reactor cavity (dry), a stack of staggered graphite beams with the aim of obtaining a three-dimensional corium redistribution after pressure vessel melt-through. The thin layers of the corium, on one side, and the large heat capacity and thermal conductivity of the stack of graphite beams, on the other, permit to achieve an initial quick solidification and cooldown of the melt. The final cooldown is achieved by gradually flooding the cavity. The flooding of solidified and relatively cold corium prevents steam explosions.
The results of preliminary calculations demonstrating the merits and the feasibility of the proposed design are given.

0. INTRODUCTION

In Ref. 1 a containment system, named L.I.R.A. and characterized by superior radioactivity retention capabilities also in case of severe accident, was described and proposed for future nuclear power plants. An important feature of the L.I.R.A. system is the reactor cavity design which is conceived in such a way as to avoid the molten core-concrete interaction. This report describes in more details the proposed safeguard of the containment basemat and gives the results of the first preliminary calculations performed to demonstrate its design feasibility and merits.

1.0 GENERAL

To avoid the erosion of the containment basemat by a molten core it is necessary to develop a design of the reactor cavity which permits the spreading of the melt over a large surface area, so that the thickness of the layer is thin enough (few centimetre) to permit a quick resolidification and cooldown of the melt. It is also important that the **large S/V ratio** of the melt be maintained untill a definitive cooldown is achieved, e.g. by flooding. To this end, a cavity design such as that (single-layer) proposed by the Karlsruhe Research Centre (Ref.2) or that (multiple-layers) proposed by the author (Ref.1 and 3) would serve the purpose.

In particular, the solution here proposed by the author (Fig. 1, 2, 3) consists in locating in the reactor cavity, below the pressure vessel, a stack of staggered graphite beams of square cross section, each with an upper channel for corium collection and distribution. This structure permits to have a **three-dimensional redistribution** of the molten core, after the pressure vessel melt-through, and prevents the direct contact of the corium with the containment basemat.

It is important to note the **large surface-to-volume (S/V) ratio** which can be achieved with this concept and the degree of freedom that the designer has in the choice of this parameter, without increasing the lateral dimensions of the reactor cavity beyond those of present containment systems.

It is useful to remember that the core of a 1000 MWe PWR has a volume of about 10 m^3 and a S/V ratio of 400 m^2/m^3. If this core melts down and falls into a cavity of limited cross section (40-50 m^3), such as that of many present containment buildings, the S/V ratio is reduced by 2 orders of magnitude: this is the main reason why many of the various core catchers so far proposed have failed to give a satisfactory solution to the heat removal problem.

With the solution proposed in this report, the thin molten core layers resting on the graphite beams become easily amenable to solidification and cooling, in the first phase thanks to the **heat capacity of the stack** itself and, later on, by **flooding** the cavity with water.

The heat capacity of the stack should be large enough to absorb all the latent heat of the melt (120-140 GJ) and at least one hour of decay heat (100-120 GJ) and yet remain at a relatively low temperature (to minimize chemical reactions both in the dry phase and in the flooding phase). In other words the heat capacity of the stack should be at least an order of magnitude higher than that of the corium.

If **graphite** is chosen for the beam material (Section 2), about 240 t of graphite (150 m^3) would be sufficient: with a uniform distribution of all the sensible heat of the corium and of 1 hour of decay heat into the graphite, the equilibrium temperature would be around **700-800 °C.**

The uniform and timely distribution of the sensible and decay heat of the corium into the heat sink is the main issue. If one considers a typical cavity of 50 m^2 cross section, putting a graphite slab (3 m thick) on the bottom of the cavity would not permit the corium solidification because the rate of heat transfer to the graphite is intrinsecally limited by:

- the small heat transfer area;
- the large thickness of the corium layer (20 cm);
- the low thermal diffusivity of the corium itself.

In other words, with such a geometry, the graphite slab cannot provide its full **heat sink potential.**
On the contrary, a large cavity cross section (e.g. 250 m^2) or a stack of staggered graphite beams in a cavity of unchanged cross section, would be able to give, with the same graphite volume, the S/V ratio necessary to solidify and cool the molten core. In the following chapters especially the option based on the stack of beams is investigated.

2.0 MATERIAL FOR THE BEAMS

The material of the beams must have, to the maximum extent possible, the following characteristics:

- a high thermal conductivity, to allow a quick corium cooldown and to facilitate the distribution of the heat removed from the corium into the mass of the beams;
- a high melting point and chemical stability, to preserve the initial geometry and limit the undesirable chemical reactions at high temperature;
- low cost.

At the moment, the preferred material for the beams of the structure is **graphite**, but other materials can be taken into consideration (and also composite materials).

3.0 REFERENCE DESIGN GEOMETRY

Stacks of graphite beams characterized by different geometries and different S/V ratios can be taken into consideration for the dispersing structure to be located in the bottom of the reactor cavity.

To demonstrate the feasibility of the proposed concept, the design shown in Fig. 4 has been chosen as a reference. Of course it shall have to be optimized on the basis of experimental tests.

This design consists of 7 layers of staggered graphite beams of square cross section , 60 cm side and 90 cm pitch. The overall length of the beams is 416 m. The cross section of the cavity (50 m^2) has the poligonal shape shown in Fig. 4b, but, of course it can have also other shapes without compromising the validity of the proposed concept.

A channel, 30 cm wide and 5 cm deep, is made on the top side of each beam for corium collection and distribution. In the bottom side of the beams, transversal grooves are made to avoid obstructions to the free flow of molten corium along the channels.

The sides of the reactor cavity, up to the level of the vessel, are lined with graphite bricks (also 60 cm thick) backed by refractory bricks (15 cm thick). In this way, also the concrete of the vertical cavity walls is isolated from the molten corium and a useful heat sink is provided for heat transfer by radiation from the corium deposited on the uppermost layers of the stack.

For a molten core spread uniformly on the reference stack of beams, the S/V ratio would be at least 5 times that related to a single slab, even if one considers only the area associated to the upper side of the beams; it is actually much larger if one considers that a fraction of the corium is bound to stick on the vertical sides of the beams.

With the uniform distribution of the molten core on the beams, a corium cross section of 240 cm^2 would be associated to the 3600 cm^2 graphite cross section of each beam. In addition to the filling up of the top channel (150 cm^2), there would be an equivalent layer of 1.5 cm thickness (90 cm^2) resting over the top. The equivalent uniform corium thickness resting over the graphite beam would then be 4 cm. In this way the volume ratio between corium and graphite on each beam is about 1/15, practically equal to the global ratio (10 m^3 of corium on 150 m^3 of graphite).

4.0 OPTIMIZATION OF SIZE, SHAPE AND PITCH OF THE BEAMS

The optimization of the geometric parameters of the beams and of the stack can come only after a series of experimental tests.

It is difficult to estimate, theoretically, the thickness of corium remaining on the shoulders and on the vertical sides of the beams after the fall of the melt. If the experimental tests shall demonstrate, for the corium thickness on the top and on the sides of the beams, values different from those of the present reference design, the optimum geometry could be different.

In particular, the fraction of corium sticking on the vertical sides could be increased by slanting the vertical sides outwards, giving the beam a trapezoidal cross section, with a large lower base. If, on the contrary, it were desired to reduce the mass of corium sticking on the vertical sides, it would be better to slant the vertical sides inwards, giving the beams an inverted trapeze cross section.

5.0 MECHANICAL IMPACT OF THE MELT

The impact of 100 tons of molten material falling from a height of 4 meter on the underlying structure could produce the displacement or overturning of the beams of the upper layer(s). This, however, is not a serious challenge to the structure as a whole and to the underlying layers which could still perform their function. At any rate, to better preserve the whole geometry of the stack, it is advisable to modify somewhat the two upper layers of beams by giving them also lateral stability.

6.0 UNIFORMITY OF THE MELT REDISTRIBUTION

This is a very important issue and should be carefully investigated.

In effect, it is difficult to precisely predict the degree of uniformity of corium distribution without some experimental tests. However, the following considerations can be made.

- Upon falling from a height of 4 meters (even with the primary circuit depressurized), the horizontal spread of the melt on the stack is inevitable upon impact, because of the conversion of a substantial fraction of its potential energy into kinetic energy. The corium spreading is enhanced if, at the time of pressure vessel melt-through, there is a slight overpressure inside the primary circuit.
- The heat capacity of the air present in the cavity is so small compared to the internal energy of the molten core that it can absorb only less than 1% of it. So its cooling effect can be neglected, even if there were an instantaneous transfer of heat to the surrounding atmosphere. Therefore, heat would be removed from the melt mainly by conduction and radiation to the graphite beams and to the cavity walls.
- Corium is a molten material with a high latent heat of fusion (280 kJ/kg) and internal heat generation (0.2-0.3 kW/kg): both these characteristics tend to maintain it in the liquid phase and to favor the uniformity of its spreading.

The uniformity of the melt distribution, even if desirable, needs not be rigorous, because there are margins for a certain degree of non-uniformity in the distribution. At any rate, a series of experimental tests to investigate the conditions for a uniform distribution of the melt are recommended. These experiments do not involve investigations into unknown scientific domains (no chemical problems): they can be considered a mere extrapolation of foundry experience. Therefore, if the decision to proceed is taken, they are expected to be completed in a short time .

In the meantime, to assess the degree of disuniformity which can be tolerated without adverse effects, heat transfer calculations have been performed both for uniform and non-uniform corium distribution (Section 8).

7.0 INTERFACE TEMPERATURE

The initial interface temperature between corium and the stack material depends on the thermal properties of the material themselves.

Figure 5 shows the dependence of the interface temperature on the ratio $(d_o c_o k_o / d_1 c_1 k_1)$, between the thermal properties of the beam material and those of corium, which is the most important parameter [d, c and k are the density, the specific heat and the thermal conductivity, respectively]. The convenience of using, for the beams, materials of high thermal conductivity is self-evident.

In particular, the graphite-corium interface temperature would span from 600 °C, in case of pure UO_2, to 1100 °C for a corium with a large metallic fraction.

If the corium ingot is **thin** enough to be quickly solidified, the interface temperature remains basically constant untill the solidification is completed. After that, the interface temperature starts decreasing untill a quasi-equilibrium temperature is reached in the beam. The decay heat would then start raising the temperature of the graphite beam and of the corium ingot, but at a rate reduced in proportion to the large heat capacity of the graphite beam with respect to that of the corium resting on it.

8.0 TEMPERATURE TRANSIENTS

8.1 Mono-dimensional model

With a three-dimensional distribution of the melt on the stack of beams, three-dimensional or at least two-dimensional heat transfer calculations should be made.

However, to prove the soundness of the proposed solution these complex calculations are not strictly necessary. In this preliminary phase only a simplified one-dimensional heat transfer model has been considered. Therefore a uniform thickness of corium on top of the graphite beam has been considered.

8.2 Heat transfer processes

For what concerns the heat transfer phenomena, two situations have been considered:

- Heat removal by **conduction** (only) from the bottom of the corium layer to the graphite;
- Heat removal by **conduction** from the bottom **and** by **radiation** (emissivity 0.75, view factor 1) from the top of the corium layer. In this case, the heat loss by radiation from the top of the beam has been fed back as a heat input to the bottom of the beam. (Only in the case of a single graphite slab the heat removed by thermal radiation has ben considered absorbed by the graphite wall surrounding the reactor cavity).

8.3 Decay heat distribution

Decay heat has been considered partly uniformely distributed in the corium and partly uniformely distributed in the graphite. The ratio between the two components of decay heat varies with the thickness of corium layer. In the reference case (4 cm of corium) the decay heat released directly into the graphite has been estimated at 15% of the total.

Decay power at 3 h after shutdown, reduced 20% for the loss of volatile fission products, has been taken as a reference.

8.4 Thermal properties

For what concern **corium properties**, in view of their uncertainties, calculations have been performed for:

- pure UO_2;
- corium with a high metallic fraction.

For graphite, the average values of commercially available types have been assumed in the calculations. In case of procurement, the graphite with the highest thermal conductivity should be preferred.

The initial corium temperature has been assume equal to 2370°C and that of graphite 100 °C.

8.5 Temperature Profiles

Figure 6 shows the temperature profiles in the corium and in the graphite in the case of a single graphite slab, 3 m thick and 50 m^2 cross section, over which a corium layer of 20 cm is distributed. As expected in this geometry, the corium cannot be solidified: its internal temperatures rises to extremely high values because the heat transfer area is too limited and cannot dissipate the internally generated decay power.

Figure 7 through 10 show the temperature profiles in the corium and in the graphite, at various times after the fall of the melt, for the reference case (corium layer 4 cm thick on graphite beam 60 cm thick) with and without radiation heat transfer and for the two corium types taken into consideration.

It can be seen that:

- the corium is always solidified and cooled down in a relatively short time. This conclusion holds irrespective of the thermal conductivity of the corium and of the heat removal scenario;
- in case of pure UO_2, whatever the heat removal scenario, the graphite temperature remains everywhere below 800 °C for at least one hour after the fall of the melt;
- in the case of corium of high thermal conductivity, and combined heat removal scenario, the corium-graphite interface temperature exceeds the 800 °C for the first 10-15 min; thereafter it drops below 800 °C, as in the bulk of the graphite, and remains below that temperature for at least one hour;
- in case of corium of high thermal conductivity and heat removal by conduction only, the corium graphite interface temperature remains between 900 and 1200 °C for the first hour; the bulk of the graphite however, stays below 800 °C also in this case.

The computer runs related to corium of high thermal conductivity shall be repeated when updated (and more realistic) corium data shall become available; in that circumstance, also the stratification of the oxidic and metallic fractions shall be taken into account.

Figures 11 and 12 show the temperature profiles in case the equivalent corium thickness on the top of the graphite beam is 7 cm (with combined conduction and radiation heat transfer, which is the worst heat removal scenario from the point of view of graphite temperature). This case corresponds to the situation in which the extra thickness of corium on the top and on the sides of the graphite beam is three times that of the reference case. It is representative of a non uniform corium distribution on the stack of beams. The main result is the following:

- the corium solidifies but the graphite temperature, after one hour, approaches 1000 °C. So, in this case, it would be wise to flood the cavity whithin half an hour.

In case of a 7 cm UO_2 layer cooled by conduction only (Fig. 13), the UO_2 would not fully solidify and its upper part would remain molten. The temperatures in the graphite, however, would remain everywhere below 800 °C for at least one hour.

For an equivalent corium thickness of 2 cm on 60 cm graphite beams, the temperatures would remain everywhere below 500 °C up to 1 h after corium fall.

Figure 14 shows the temperature profiles in case graphite is substituted by **copper**. As expected, the interface temperature is about 300 °C above that of graphite and the quasi-equilibrium temperature, after 1 h, is still below 500°C.

8.6 The cavity flooding

In the L.I.R.A. containment, the reactor cavity is in communication with the suppression pool through pipes (Fig. 1); these pipes are normally closed either by isolating valves or by melting plugs. The opening of the valves or the melting of the plugs causes the flooding of the cavity and the gradual quenching, starting from the bottom, of the molten corium distributed in the dispersing structure. In this manner **damaging steam explosions are avoided.**

The temperature transients in the corium-graphite complex after flooding, are strongly dependent on the heat transfer coefficient from graphite and from corium to water.

In the preliminary calculations performed, the heat transfer coefficient (film boiling) has been assumed conservatively equal to 100 $W/m^2°C$. The reference case, however, is not of great interest, because the temperature of the graphite is already low enough to rule out important chemical effects upon flooding (if this is performed within one hour). It is more interesting to see the transient in the graphite in case of a non uniform corium distribution, such as that represented by the transients of Figures 11 and 12: in fact, in these cases, the graphite temperature may approach 1000 °C after one hour. The time it takes to reduce the graphite temperature from 1000 °C to 700-800 °C is rather short (about 15 min) so that the graphite-water reaction is very limited. In fact in the range from 700 to 1000 °C the reaction rate R is estimated about 0.01 g/cm^2 min and the reaction is endothermic. In conclusion, the consequences of the

graphite-water reaction would be tolerable provided that the cavity flooding takes place before the graphite temperature goes above 1000 °C.

9.0 CONCLUSIONS

A design solution for the safeguard of the containment basemat against the attack of a molten core, based on the adoption of a stack of staggered graphite beams located in the bottom of the reactor cavity (initially dry and subsequently flooded), has been examined and found feasible and convenient. With the proposed solution, in addition to the complete protection of the basemat, no risk of steam explosion exists and no worsening of the hydrogen problem is introduced.

For the detailed design it shall be necessary, on one side, to perform a few experimental tests to verify the conditions for a distribution of the molten material as uniform as possible on the stack of beams and, on the other side, to perform more sophisticated heat transfer calculations (two or three-dimensional models, more accurate corium property data, stratification, etc.).

Flooding within half an hour from the fall of the melt is sufficient to avoid graphite-water reaction problems.

10.0 REFERENCES

1. A. Turricchia, "No Evacuation and no Land Contamination: A Possible Goal for Future Reactor Containment Systems", ENEL Report 9N0 2110 TNIU 0003, September 1991. A paper with the same title, which summarizes this report, has been presented at the ANS Winter Meeting Embedded Topical- The Next Generation of Nuclear Power Plants- San Francisco- November 10-14, 1991.

2. KfK, "Investigations for New Containment Concepts at KfK", 3rd SAC Meeting, OECD, Paris, 12-13 April 1991.

3. A. Turricchia, "Containment Design for Severe Accidents: Defense of Containment Basemat Integrity against Corium Attack", International Workshop on the safety of Nuclear Installations, Chicago, August 28-31, 1989.

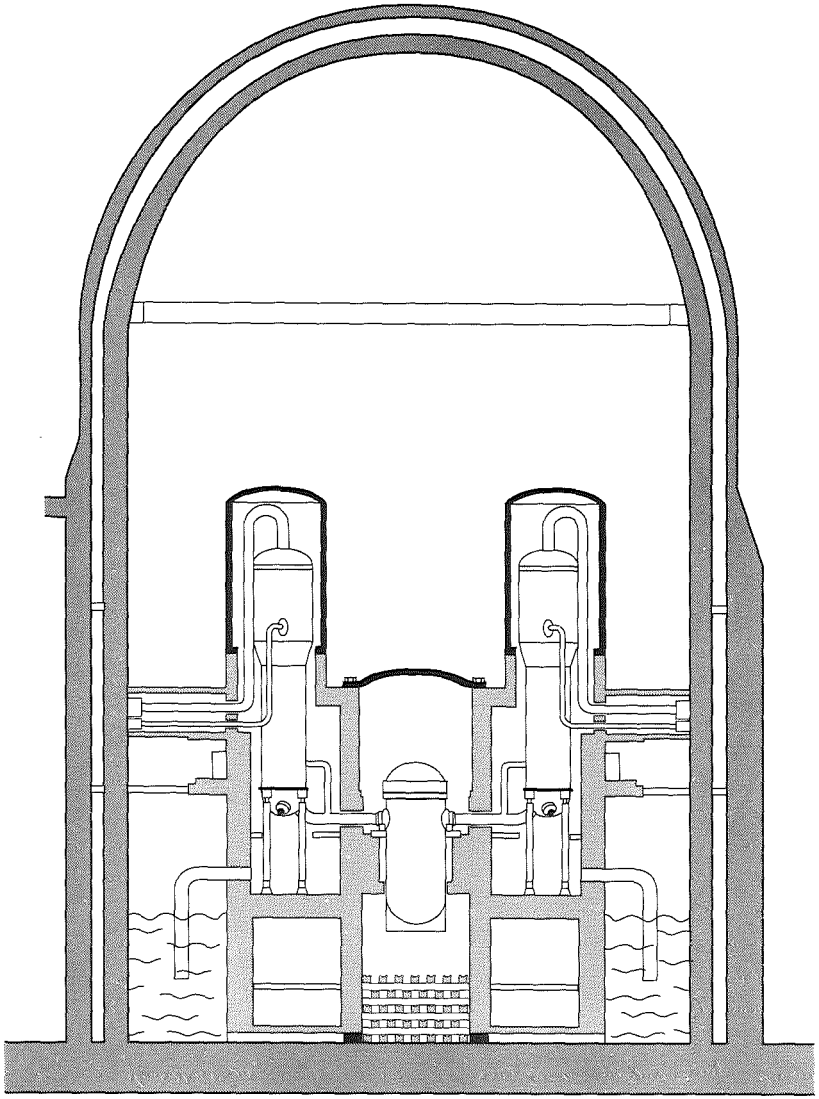

FIG. 1 - L.I.R.A. CONTAINMENT SYSTEM GENERAL LAYOUT

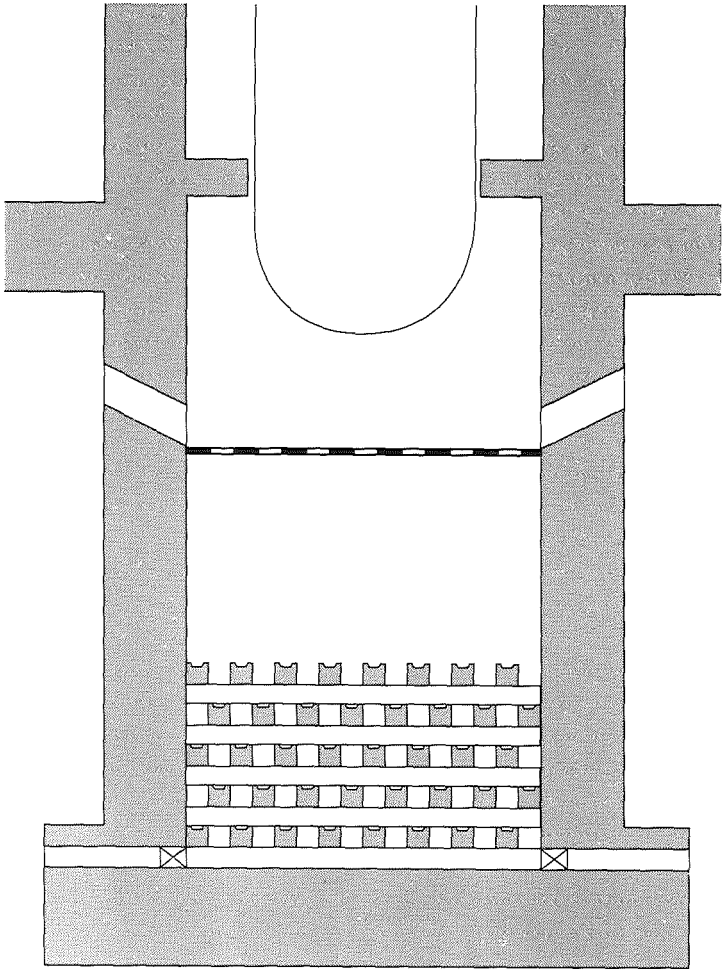

FIG. 2 - FLOODABLE REACTOR CAVITY FILLED WITH A STACK OF STAGGERED GRAPHITE BEAMS FOR CORE DISPERSION AND COOLING

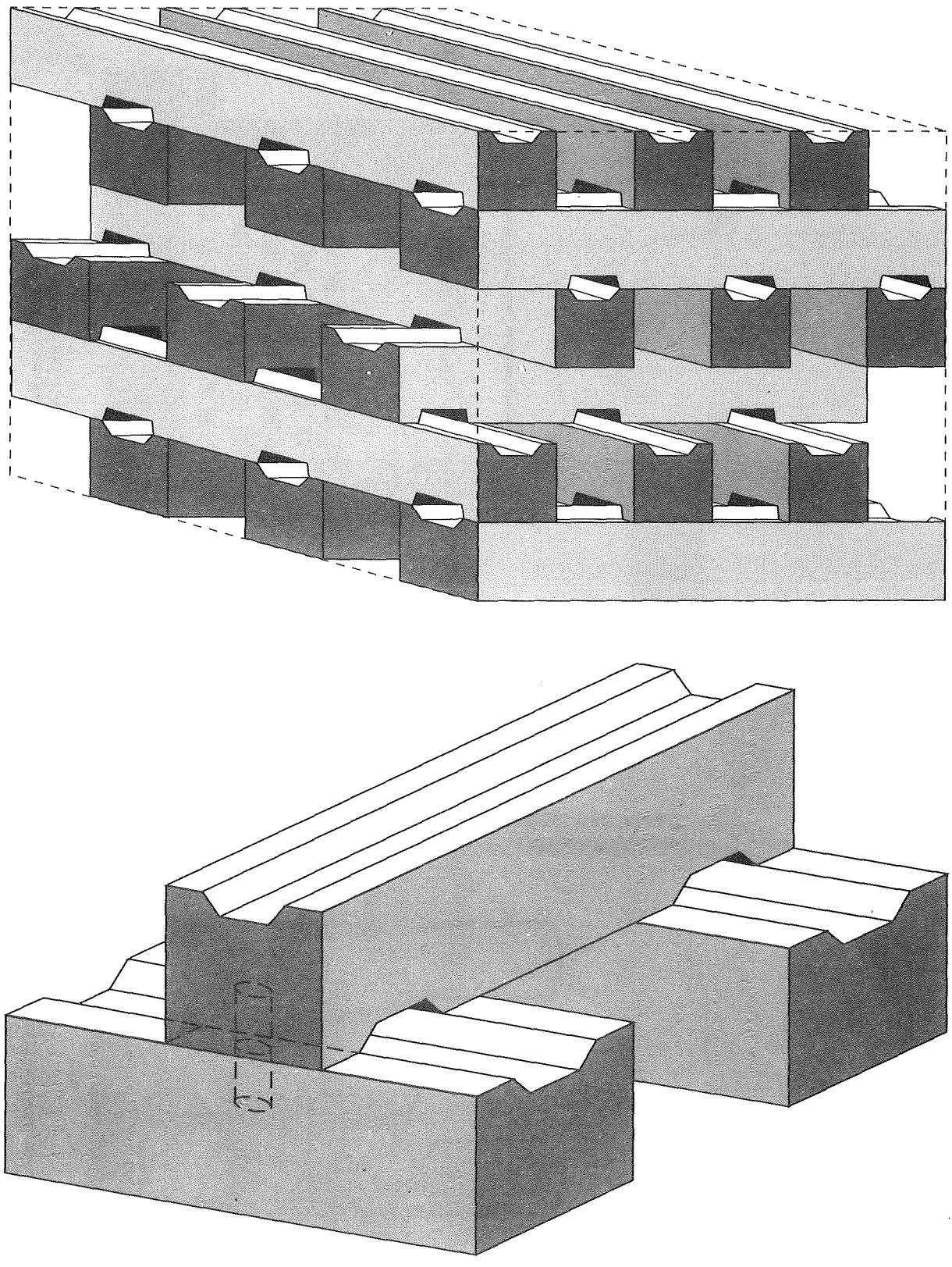

FIG. 3 - ASSONOMETRIC VIEW OF THE STACK OF GRAPHITE BEAMS TO BE LOCATED INSIDE THE REACTOR CAVITY

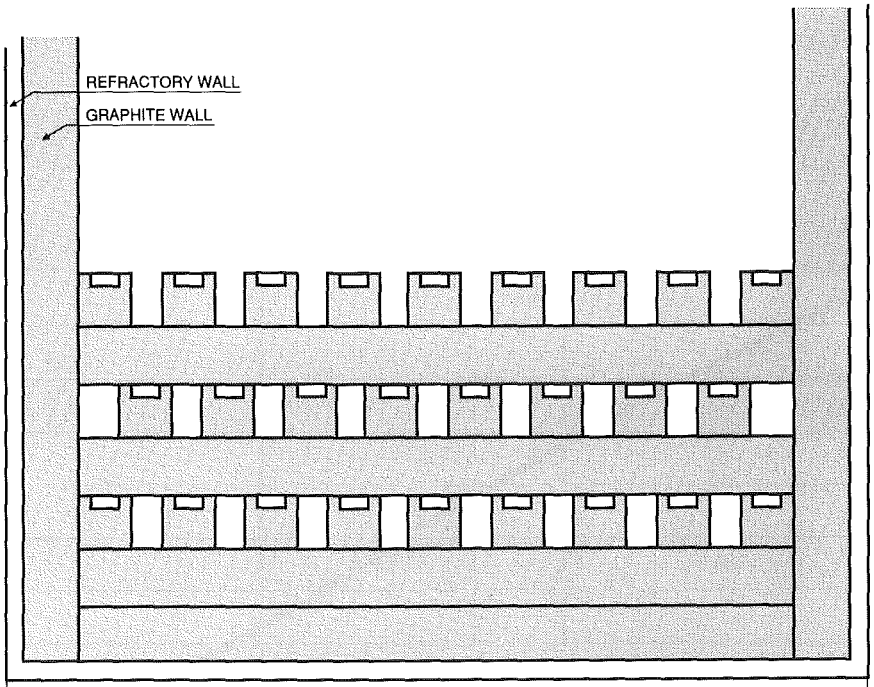

(b) VERTICAL CROSS SECTION OF THE REACTOR CAVITY

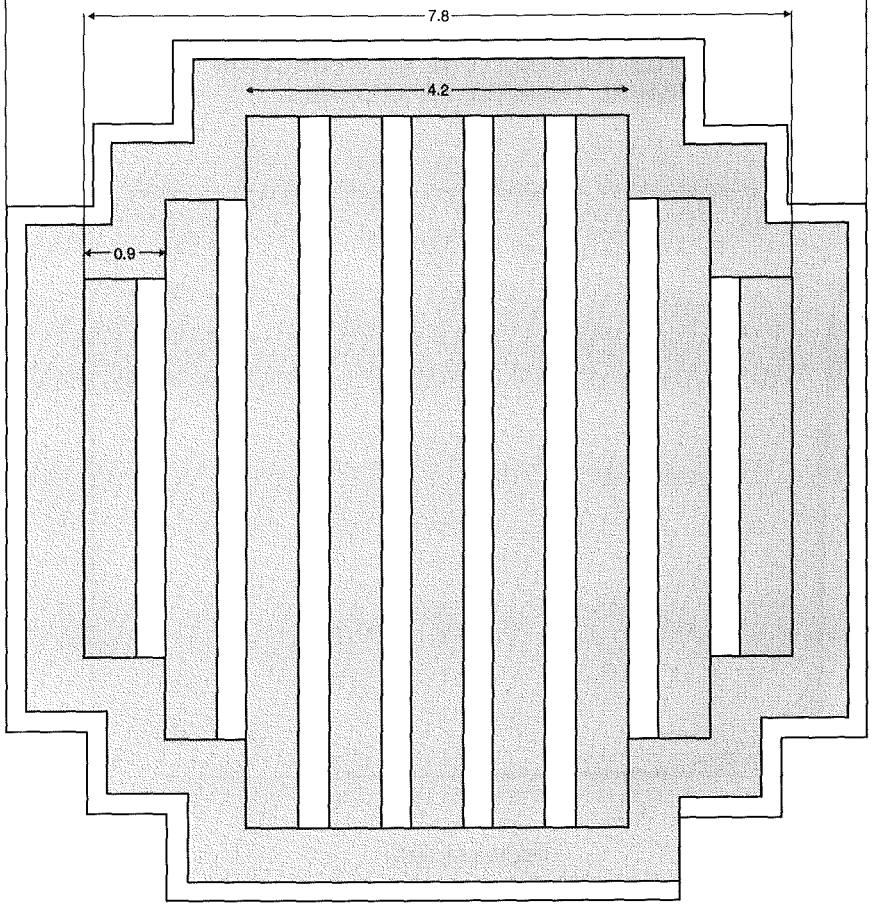

(a) HORIZONTAL CROSS SECTION OF THE REACTOR CAVITY

FIG 4 - STACK OF BEAMS TAKEN AS A REFERENCE

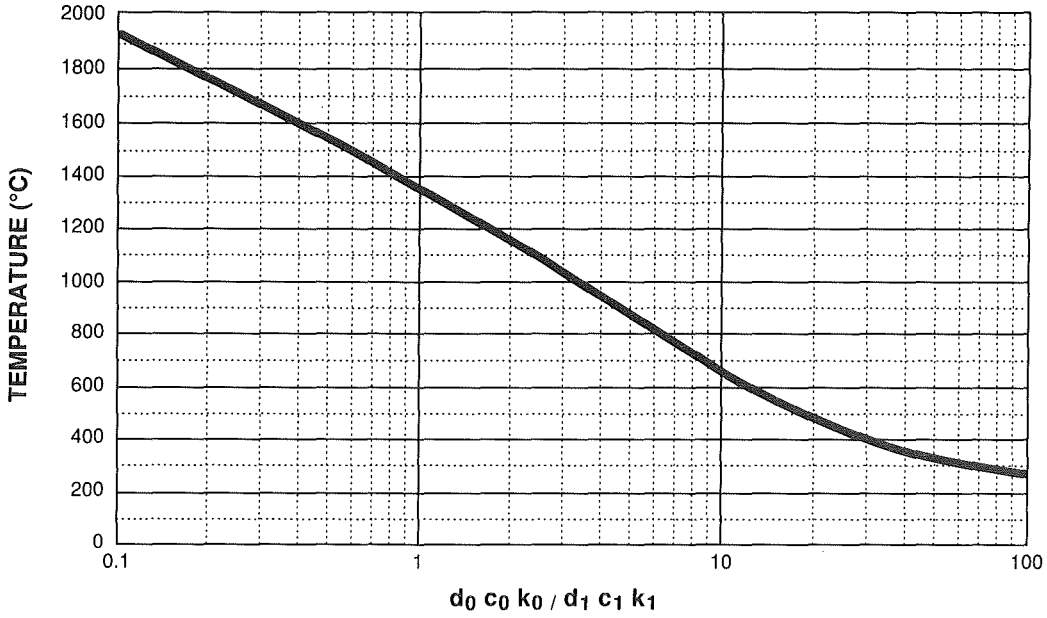

Fig. 5 - INTERFACE TEMPERATURE AS A FUNCTION OF MATERIAL THERMAL PROPERTIES

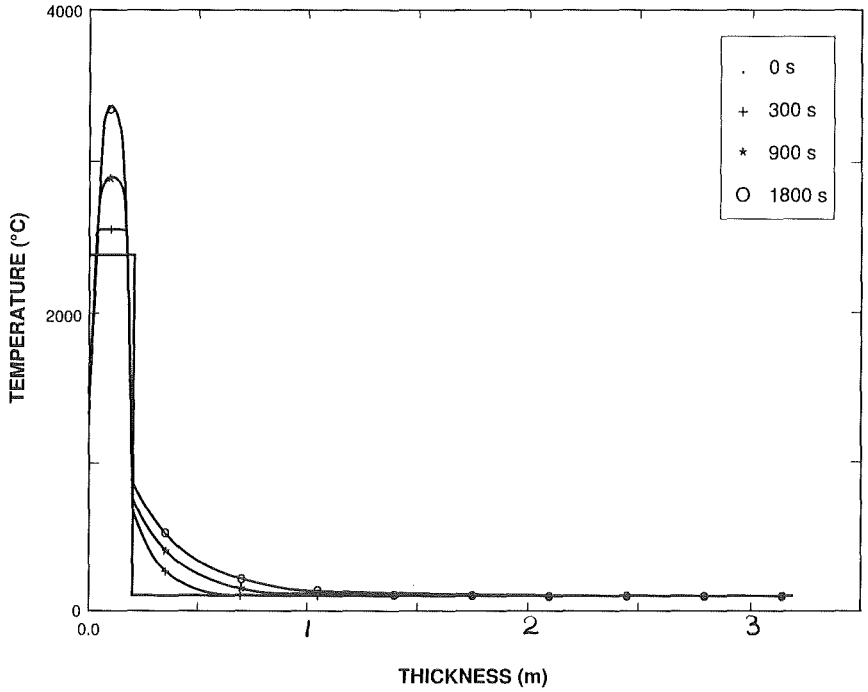

FIG. 6 - TEMPERATURE PROFILES IN CORIUM AND GRAPHITE (Corium layer 20 cm thick on single graphite slab 3 m thick - Heat removal by conduction and radiation)

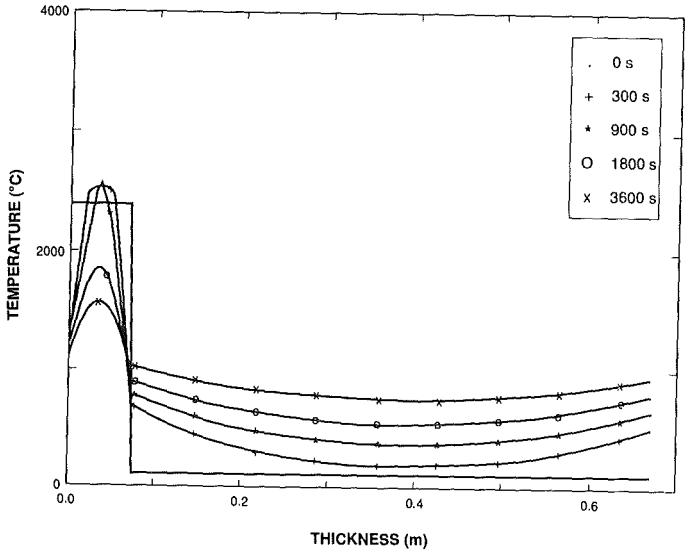

FIG. 11 - TEMPERATURE PROFILES IN CORIUM AND GRAPHITE
(UO_2 layer 7 cm thick on graphite beam of 60 cm side -
Heat removal by conduction and radiation)

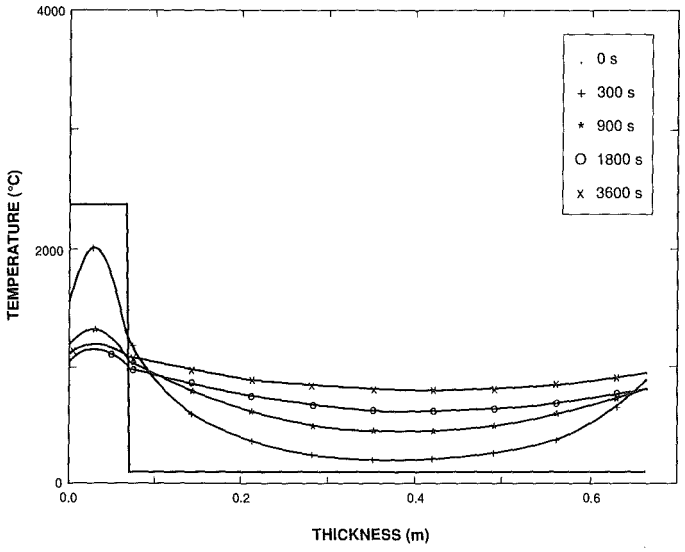

FIG. 12- TEMPERATURE PROFILES IN CORIUM AND GRAPHITE
(Metallic corium layer 7 cm thick on graphite beam of
60 cm side - Heat removal by conduction and radiation)

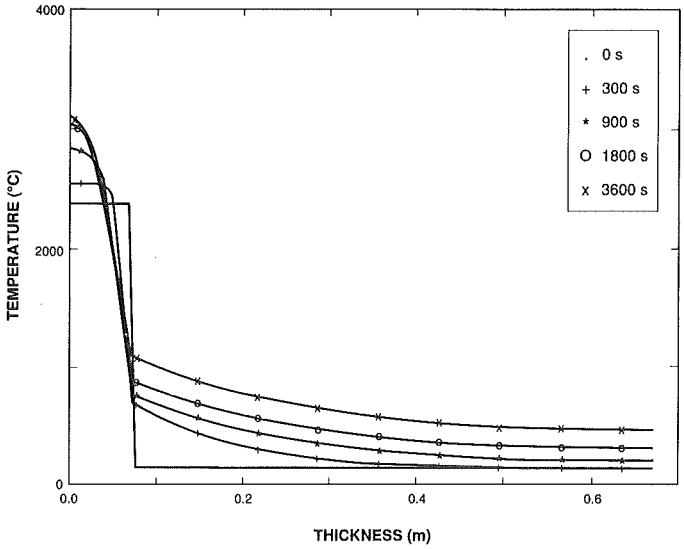

FIG. 13 - TEMPERATURE PROFILES IN CORIUM AND GRAPHITE
(UO_2 layer 7 cm thick on graphite beam of 60 cm side -
Heat removal by conduction)

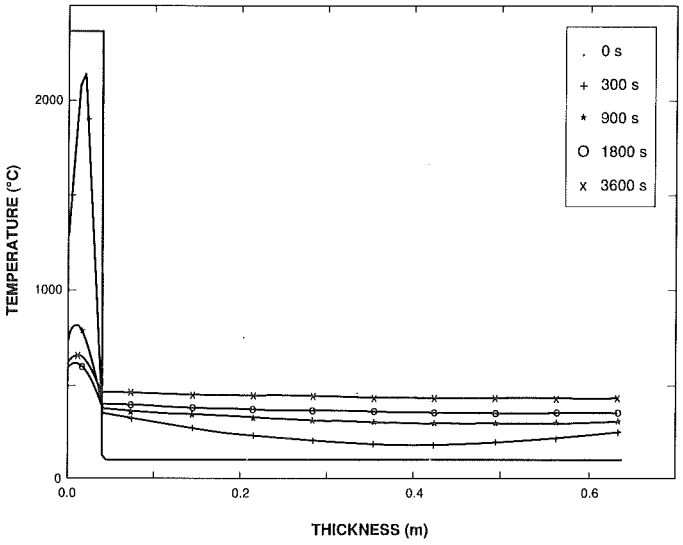

FIG. 14 - TEMPERATURE PROFILES IN CORIUM AND COPPER
(UO_2 layer 4 cm thick on copper beam of 60 cm side -
Heat removal by conduction and radiation)

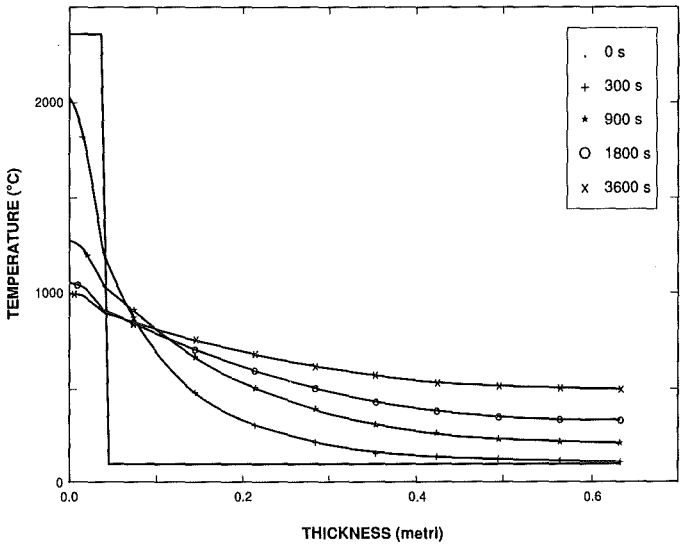

FIG. 7 - TEMPERATURE PROFILES IN CORIUM AND GRAPHITE
(Metallic corium layer 4 cm thick on graphite beam of
60 cm side - Heat removal by conduction)

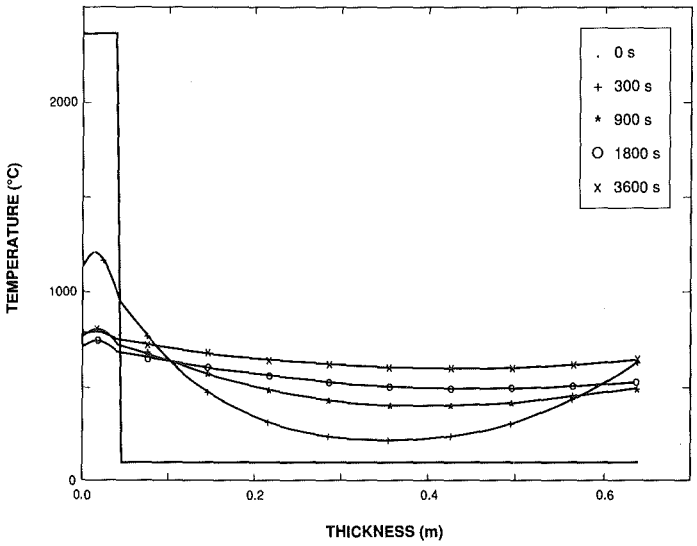

FIG. 8 - TEMPERATURE PROFILES IN CORIUM AND GRAPHITE
(Metallic corium layer 4 cm thick on graphite beam of
60 cm side - Heat removal by conduction and radiation)

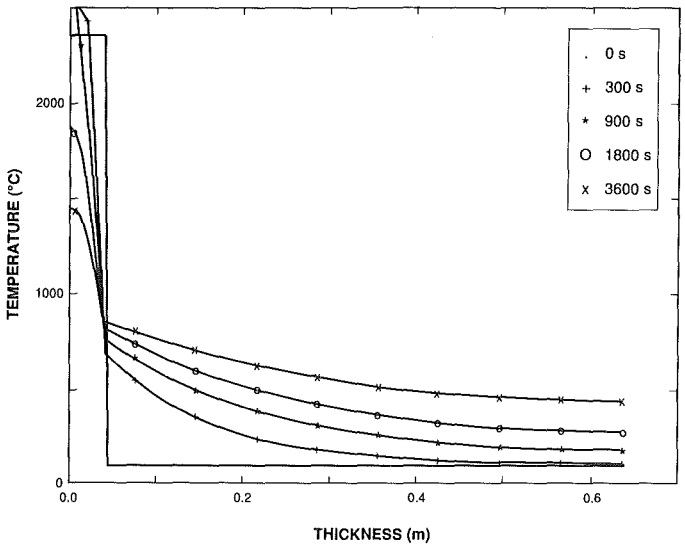

FIG. 9 - TEMPERATURE PROFILES IN CORIUM AND GRAPHITE
(UO_2 layer 4 cm thick on graphite beam of 60 cm side -
Heat removal by conduction)

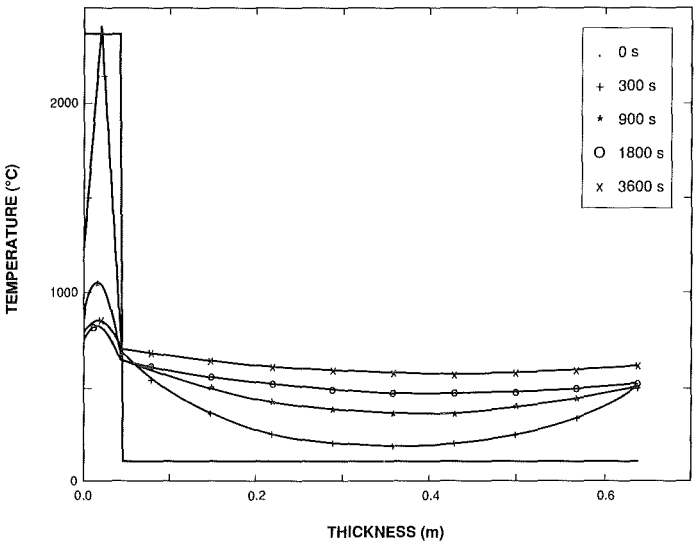

FIG.10 - TEMPERATURE PROFILES IN CORIUM AND GRAPHITE
(UO_2 layer 4 cm thick on graphite beam of 60 cm side -
Heat removal by conduction and radiation)

SECTION V

CODE COMPARISONS AND PLANT APPLICATIONS

Code Comparisons

Plant Applications

Gesellschaft für Reaktorsicherheit (GRS) mbH

INTERNATIONAL STANDARD PROBLEM NO 30
BETA TEST V5.1 ON CORE CONCRETE INTERACTION

M. Firnhaber

Gesellschaft für Reaktorsicherheit

5000 Köln 1

SECOND OECD (NEA) CSNI SPECIALIST MEETING ON MOLTEN

CORE DEBRIS-CONCRETE INTERACTIONS

Karlsruhe, Germany, 1-3 April 1992

Schwertnergasse 1 · 5000 Köln 1 · Telefon (0221) 2068–0 · Teletex 2214123 grs d

INTRODUCTION

The definition of International Standard Problem (ISP) Exercises organized by OECD-CSNI is the systematic comparison between experimental and analytical results for a given physical problem, especially in the field of nuclear safety /1/. For the analytical simulation, only computer code should be considered which are used or planned to use in designing an licensing of nuclear plants. The calculations for a standard problem are generally performed best estimate with or without previous kowledge of the experimental results.

The detailed comparison of the results permits the determination of the reliability and precision of analytical models as well as guidance for the selection of code options and input parameters. Moreover it contributes to an intensive international know how exchange between the parties involved.

Suggested by OECD-CSNI and sponsored by the German Ministery for Research and Technology the open International Standard Problem No. 30 was carried out on the basis of the molten core-concrete interaction experiment BETA V 5.1 /2/. The special objective of this experiment is to investigate the influence of high Zr metal content in a steel melt interacting with a siliceous concrete crucible.

Seven organization from five countries submitted their results for ISP30. They used the codes CORCON and WECHSL for the thermal-hydraulic calculation and VANESA for the aerosol release.

ISP30 is the second ISP on molten core-concrete aspects. The first one was ISP24 performed in 1988, which dealt with the SURC (Sustained Urania-Concrete) - 4 test conducted at Sandia National Laboratory /3/.

DESCRIPTION OF THE PHYSICAL PROBLEM AND OBJECTIVES OF ISP30

Molten core-concrete interaction (MCCI) can occur during a core meltdown accident in light water reactors if the core debris penetrates the reactor vessel lower head and is deposited onto the concrete basement. This results in four major consequences which are essential for risk evaluation:

- Pressure increase of containment atmosphere due to gas release,
- accumulation of burnable gases in the containment, especially H_2 and CO,
- release of aerosol and fission products from the melt,
- melting and erosion of the basement and other important internal containment structures.

In test BETA V 5.1 particular interest is given to the oxidation process of Zr. While earlier chemical modelling considers Zr oxidation by gases (H_2O, CO_2) only the SURC-4 experiment identified the existence of a so-called condensed phase chemistry that is the Zr oxidation by reduction of SiO_2.

This situation leads to the following objectives of ISP30:

- Contribution to the development, improvement and assessment of computer codes for MCCI and aerosol release.
- Improvement of the understanding of the physical and chemical phenomena involved
  - thermal-hydraulic behavior of metallic melt with high zirconium content
  - zirconium chemistry esp. in the condensed phase
  - two dimensional concrete erosion
  - aerosol release.

EXPERIMENT BETA V5.1

The experiment, which serves as a data base for the comparison, was chosen out of the BETA test series performed at Kernforschungszentrum Karlsruhe. The test BETA V5.1 was designed as a special experiment to investigate the influence of high Zr metal content in a steel melt interacting with a siliceous concrete crucible. The experimental data should give information mainly on the temperature of the melt, oxidation behavior of Zr, erosion of concrete, release and composition of gases, and release of aerosol.

Fig. 1 shows a schematic view of the BETA experimental setup used in this experiment. The melt is poured from the thermite reaction tank into the siliceous concrete crucible at the beginning of the experiment. The Zr addition was accomplished by dropping of 80 kg of solid Zircaloy rubble into the crucible before the experiment. The metallic part of the melt is heated electrically by the induction coil enclosing the concrete crucible. Gases and aerosols produced during the experiment are fed through the off-gas system and a fiber filter into the environment.

During the experiment, substantial erosion of the concrete crucible took place. Fig 2 shows the cross section of the crucible with the initial and final cavity shape.

COMPARISON OF ANALYTICAL AND EXPERIMENTAL RESULTS

Since the first step in evaluation the results of an ISP is the comparison of the analytical and experimental results, all data are grouped in overlay plots and discussed regarding their difference from the experiment and between each other. To distinguish

in the thermal-hydraulic case the two codes, the CORCON calculations are labeled with CUL, INR and NUP and the WECHSL calculation with CEA, GRS, IRS and UPM. A further difference is the consideration of condensed phase reaction (s. Tab. 1).

Tab. 1: Computer codes used

Legend	Code	Condensed Phase Reaction
CEA	WECHSL	yes
GRS	WECHSL	no
IRB	WECHSL	yes
UPM	WECHSL	no
CUL	CORCON	yes
INR	CORCON	no
NUP	CORCON	no

The most important variables compared are discussed below.

Melt Temperature

Starting at 2200 K the measured temperature of the metallic melt drops rapidly during the first 200 s to 1690 K, where it remains constant (Fig.3). This temperature level obviously correspondents to the "freezing" temperature of the metallic melt. The WECHSL calculations show a sharp decline to a constant plateau, but miss the "freezing" temperature by about 100 K. The gradient of the decline was captured only in the WECHSL calculation by IRB, while in the remaining three the gradient is to steep.

The results obtained with CORCON show initially a decline, followed by an increase until 200 s, and then decrease fairly smooth to a plateau at 1800 K. Here again the freezing temperature was missed by ~100 K.

Though all calculations do not match the measured data, the shape of the WECHSL results agree more with the experiment than the CORCON data. The fairly smooth gradient in the CORCON calculation may be due to the fact that the heat transfer models do not properly account for the heat transfer from the melt to the concrete.

The shape of the calculated temperatures for the oxidic melt are similar to those discussed above. But while in the CORCON calculations the temperatures of both layers are nearly identical in the WECHSL calculations the temperature of the oxidic melt is about 100 K lower.

Concrete Erosion

The measured axial concrete erosion, which increases with a nearly linear gradient up to 55 cm at t = 2100 s, is plotted together with the calculated data in Fig. 4. While the

two CORCON calculation without condensed Zr oxidation underestimate the axial erosion significantly, all WECHSL calculations, at least during the first half of the experiment, and the CORCON calculation with condensed Zr oxidation (CUL) overestimate the measured data. At about 200 s at the end of the experimental Zr oxidation, the gradient of the WECHSL calculations has a more or less sharp bend which can not be seen in the experimental data.

The calculated shape of the cavity compared with the experiment at the end of the test is qualitatively given in Fig 5. It can be seen that in the experiment the cavity is more slender than in the calculations. It is believed that the slender cavity which is specific for this test is mainly caused by the "loss of metal" to the upper structures early in the test which tends to reduce the cavity diameter during further erosion.

Gas Release Rate

The gases released from the melt are H_2O, H_2, CO_2, CO and minor quantities of CH_4. The calculated integrated total gas release (Fig. 6) is mostly in good agreement but with the tendency of under estimating the measurements. For the release of water vapor, however, the release rate with the exception of the initial peak is underpredicted by more than a factor 2 (Fig. 7). The main reason for this systematic deviation is that in the codes steam release is considered as a consequence of concrete erosion only. However, in the BETA experiment the transient heatup of the upper concrete structures without melting contributes significantly to steam release which is not modelled in the codes.

The release rates of CO_2 and CO agree within the experimental error band, while the H_2 release is overpredicted by a factor of 2 in the later period of the experiment. The reason for this overprediction is still unclear.

Melt Composition

An important objective of the ISP is the role of zirconium, especially the question of the condensed phase reaction. The BETA experiments show, that a condensed phase reaction takes place during the first 200 s and afterwards no metallic zirconium is present in the melt while elemental Si was found in the metal phase.

As can be seen in Fig. 8 three participants (the CORCON calculations CUL and the WECHSL calculation CEA and IRB) considered the condensed phase reactions which result in an very early zirconium oxidation. The three other presented results display the much slower zirconium oxidation by gas reactions.

According to the sequence of chemical reactions in the codes the silicon and then the chromium starts to decrease after the consumption of zirconium and silicon respectively. The content of iron and nickel remains constant, of course.

Aerosol Release

Besides thermal-hydraulic results aerosol data have been compared. Fig. 9 shows the total aerosol release rate. The measured data decrease during the first 1000 s from 100 mg/s to 10 mg/s, while the calculated results remain constant at a high level but

approach the measured data when the codes calculate that Zr metal is depleted. Regarding the experimental and analytical difficulties in determining aerosol data, the agreement of long term aerosol release within one order of magnitude seems to be quite satisfactory.

CONCLUSIONS

The comparison of the analytical and experimental data yields to the observation that, in general, the calculations give the right tendency of the experimental results. Some important variables, however, show significant discrepancies between each other and from the experimental results. Since the experimental results were known to the participants prior to the calculation the reason for the discrepancies is mainly due to deficiencies in the physical models.

The calculated temperature of the metallic melt deviates from the measurement in some important aspects. While the early temperature drop of the WECHSL calculations agrees reasonably with the measured temperature shape, WECHSL overpredicts the long term freezing temperature of the metal by about 100 K. CORCON predicts a much slower temperature drop than measured. The calculated results for the melt composition differ considerably between the different calculations. The main reason is the Zr-reaction in the condensed phase, which only three participants took into account. VANESA overpredicts the early aerosol rates but gives satisfactory agreement after the depletion of Zr metal is calculated.

A detailed comparison of all experimental and analytical results leads to the following conclusions of ISP30.

- The inclusion of condensed phase chemical reactions of zirconium with silica is necessary to model the experiment adequately. All codes with this option calculated the rapid zirconium depletion.

- The CORCON temperature gradient ramps down too slowly, while the WECHSL calculations with condensed zirconium reactions meet the temperature drop adequately.

- The effect of zirconium and silicon content on the solidus temperature of the metallic melt has to be included in the codes, which presently overestimate the freezing temperature of the metal melt after Zr depletion.

- Regarding the experimental and analytical difficulties the calculational data of aerosol release and concentrations are in reasonable agreement with the experiment.

The above mentioned results of ISP30 reveal some phenomena in MCCI which are not sufficiently modeled yet and it appears that further analytical and experimental effort is needed.

REFERENCES

/1/ CSNI
Standard Problem Procedures
CSNI Report No. 17, January 1984

/2/ Sicherheitsorientierte LWR Forschung
KfK-Bericht Nr. 4700,
November 1989

/3/ Lee, M., G.A. Greene, R.A. Bari,
Surc-4 Experiment on Core-Concrete Interactions (ISP24)
CSNI Report No. 155, Volume 1 + 2
December 88 + 89

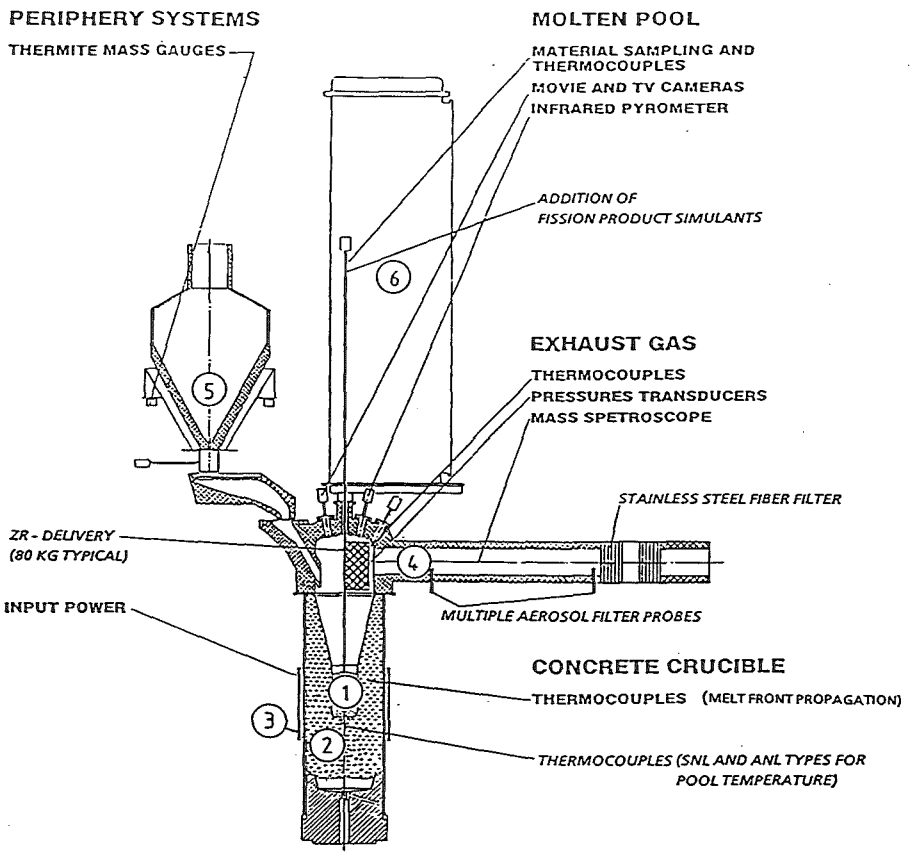

(1) Melt
(2) Concrete Crucible
(3) Induction Coil
(4) Offgas System
(5) Thermite Reaction Tank
(6) Tank for Measurement Probes

Figure 1 : Schematic View of BETA Facility in Experiment V5.1

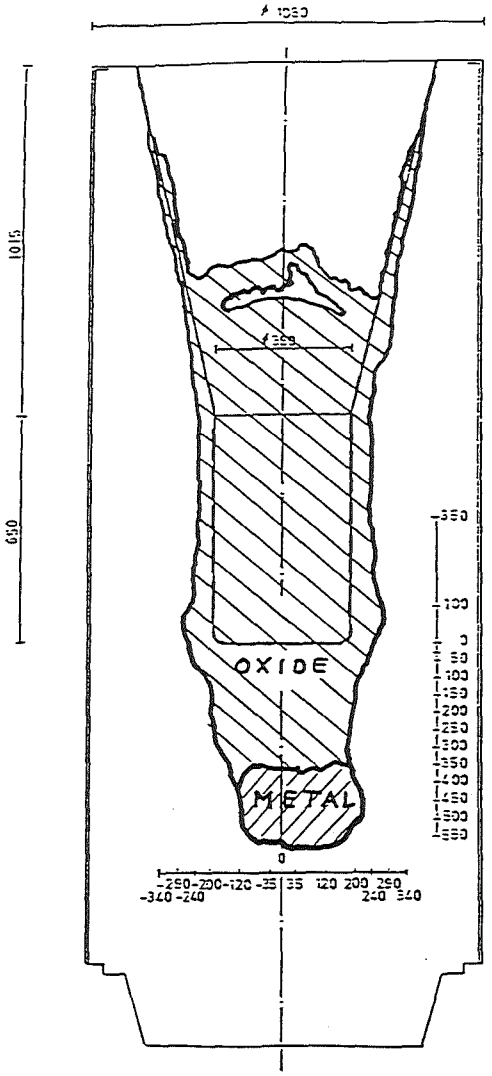

Figure 2 : Final Cavity Shape of BETA Crucible V 5.1

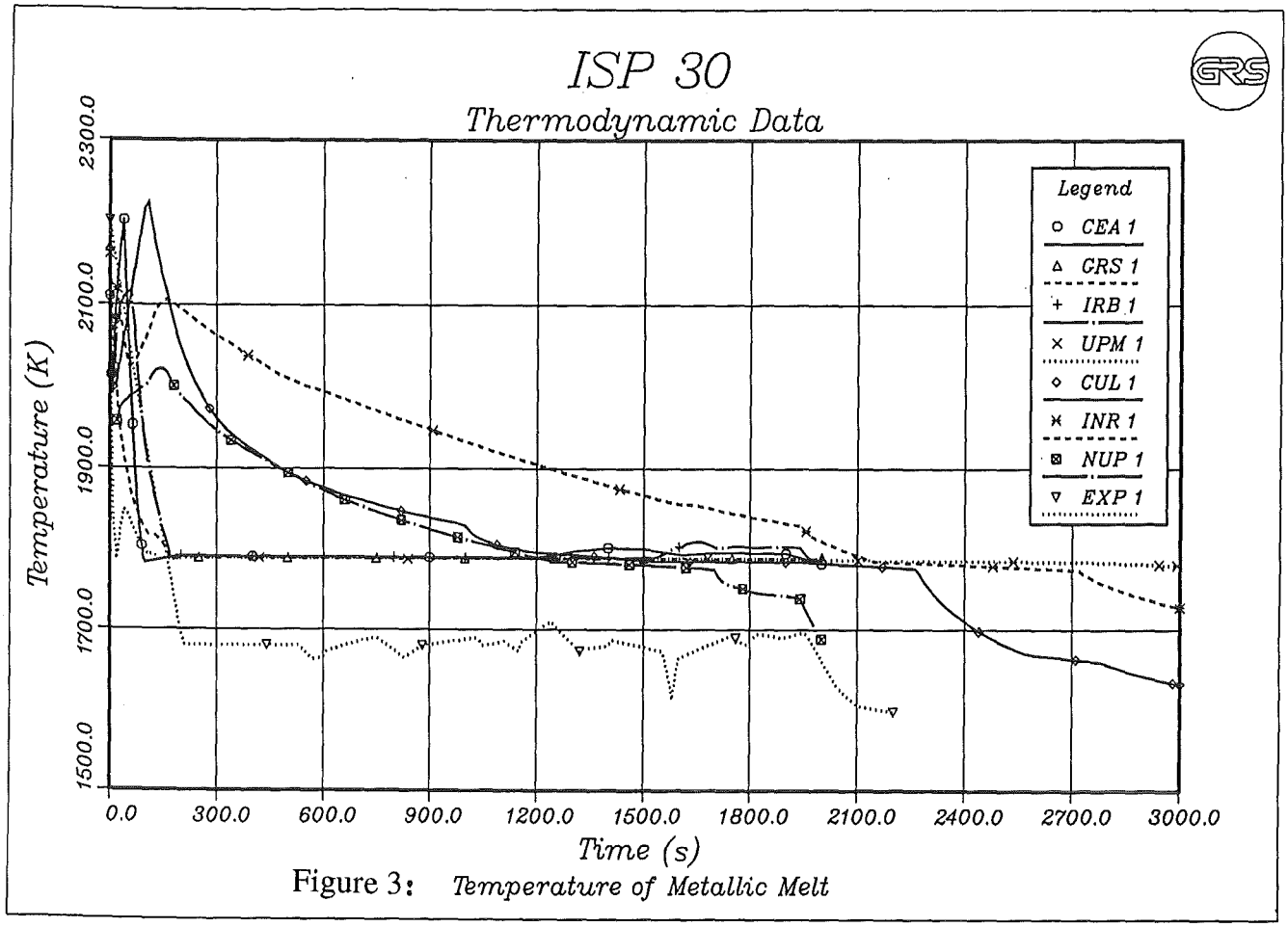

Figure 3: *Temperature of Metallic Melt*

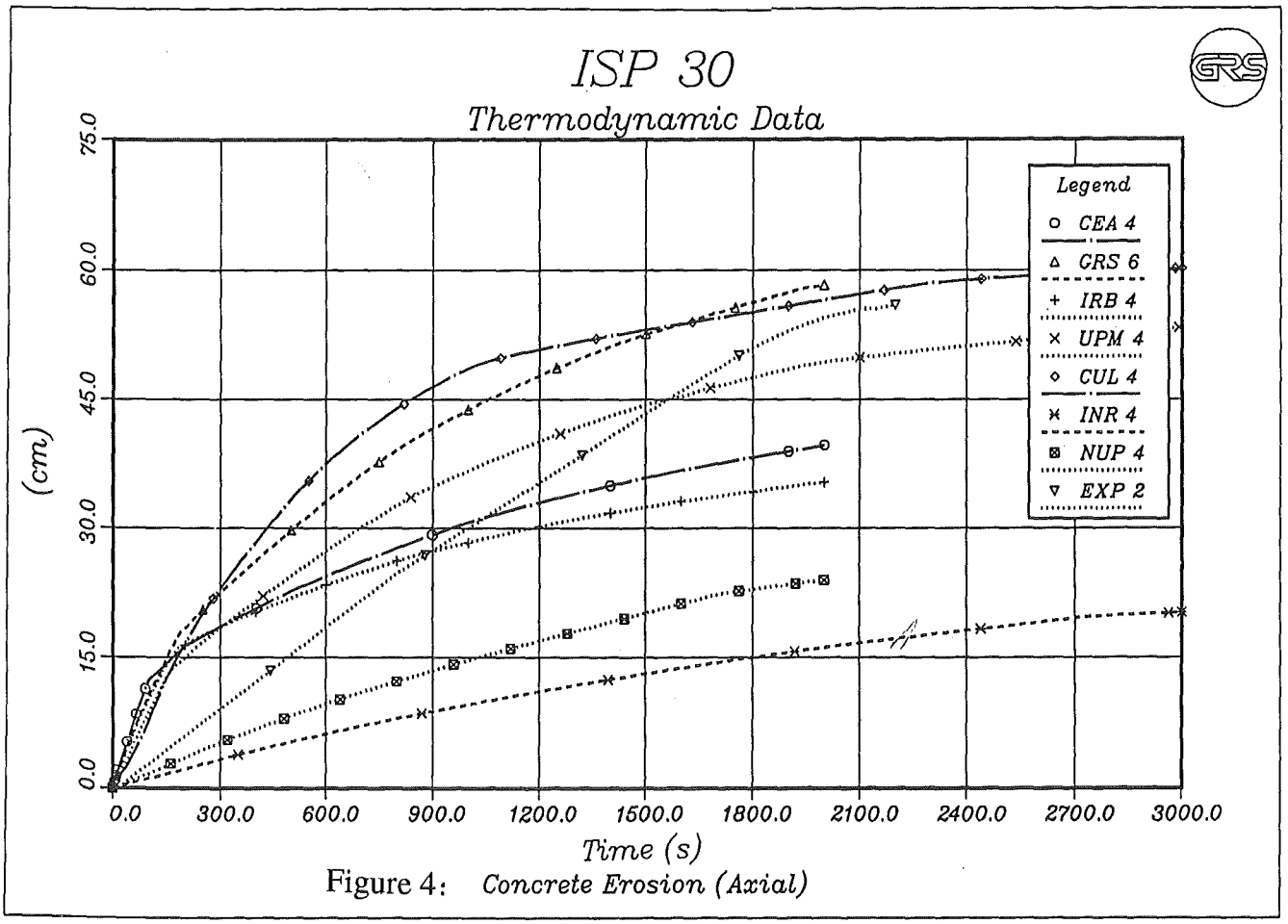

Figure 4: *Concrete Erosion (Axial)*

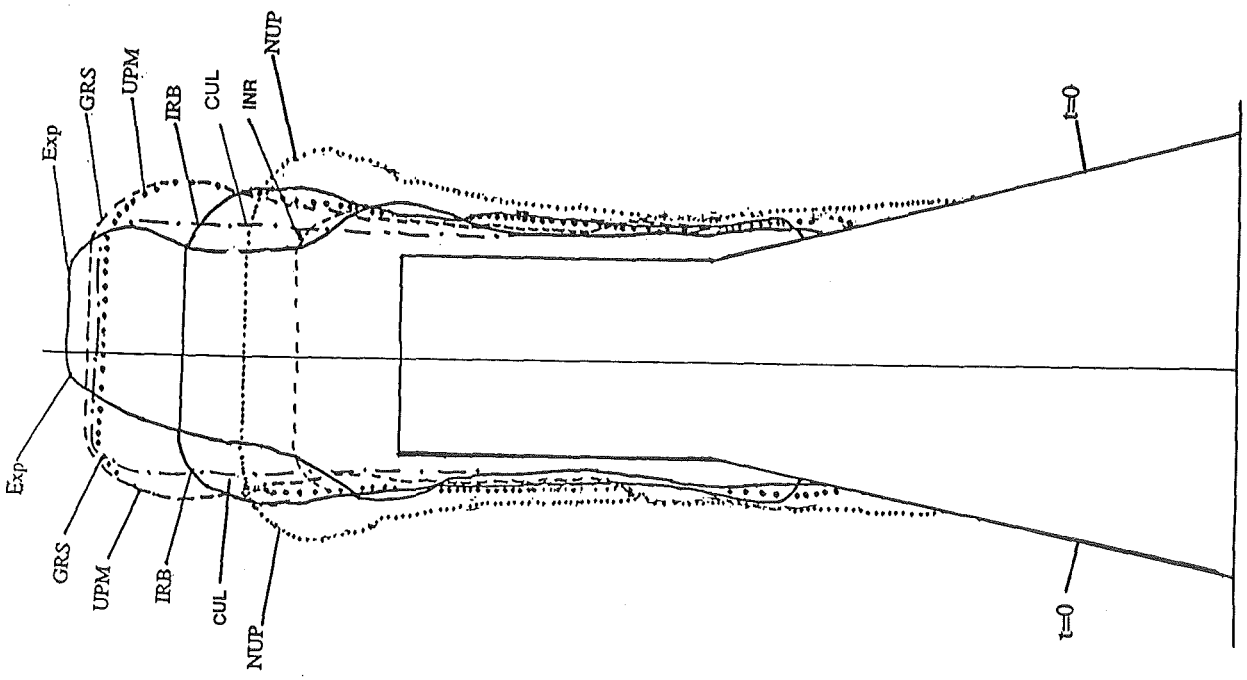

Figure 5 : Cavity Shape at the End of Experiment (t=2000s)

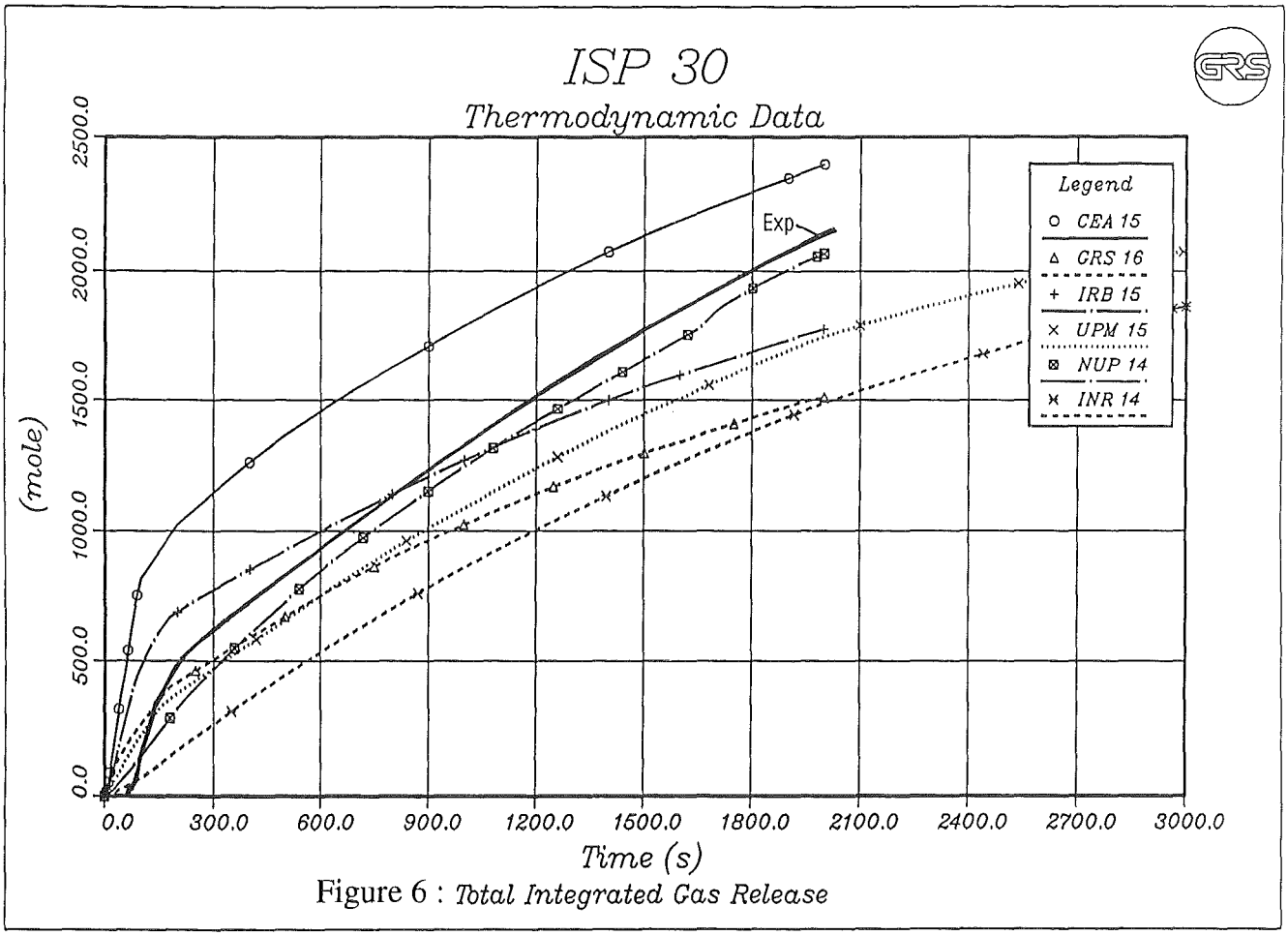

Figure 6 : *Total Integrated Gas Release*

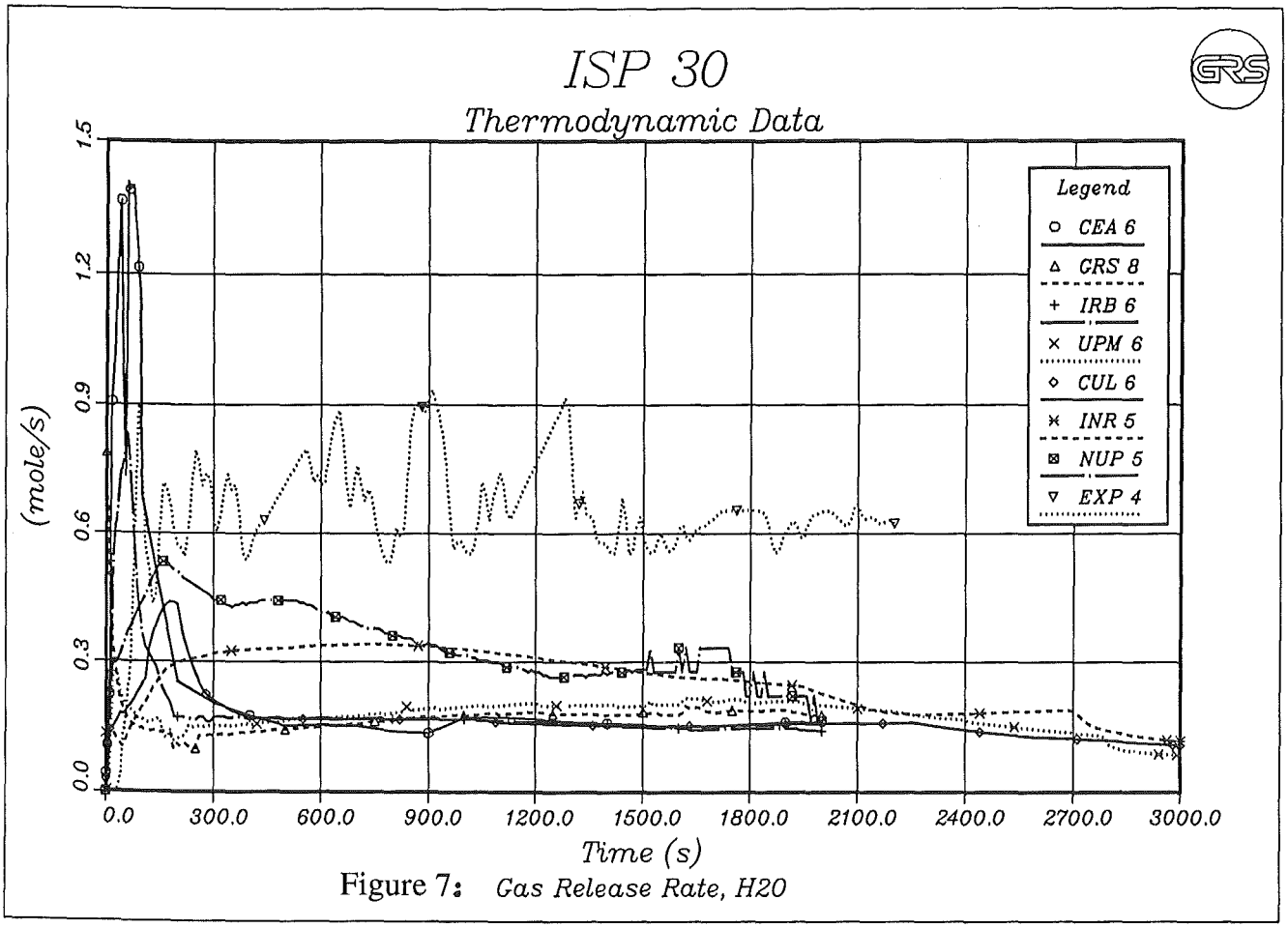

Figure 7: *Gas Release Rate, H20*

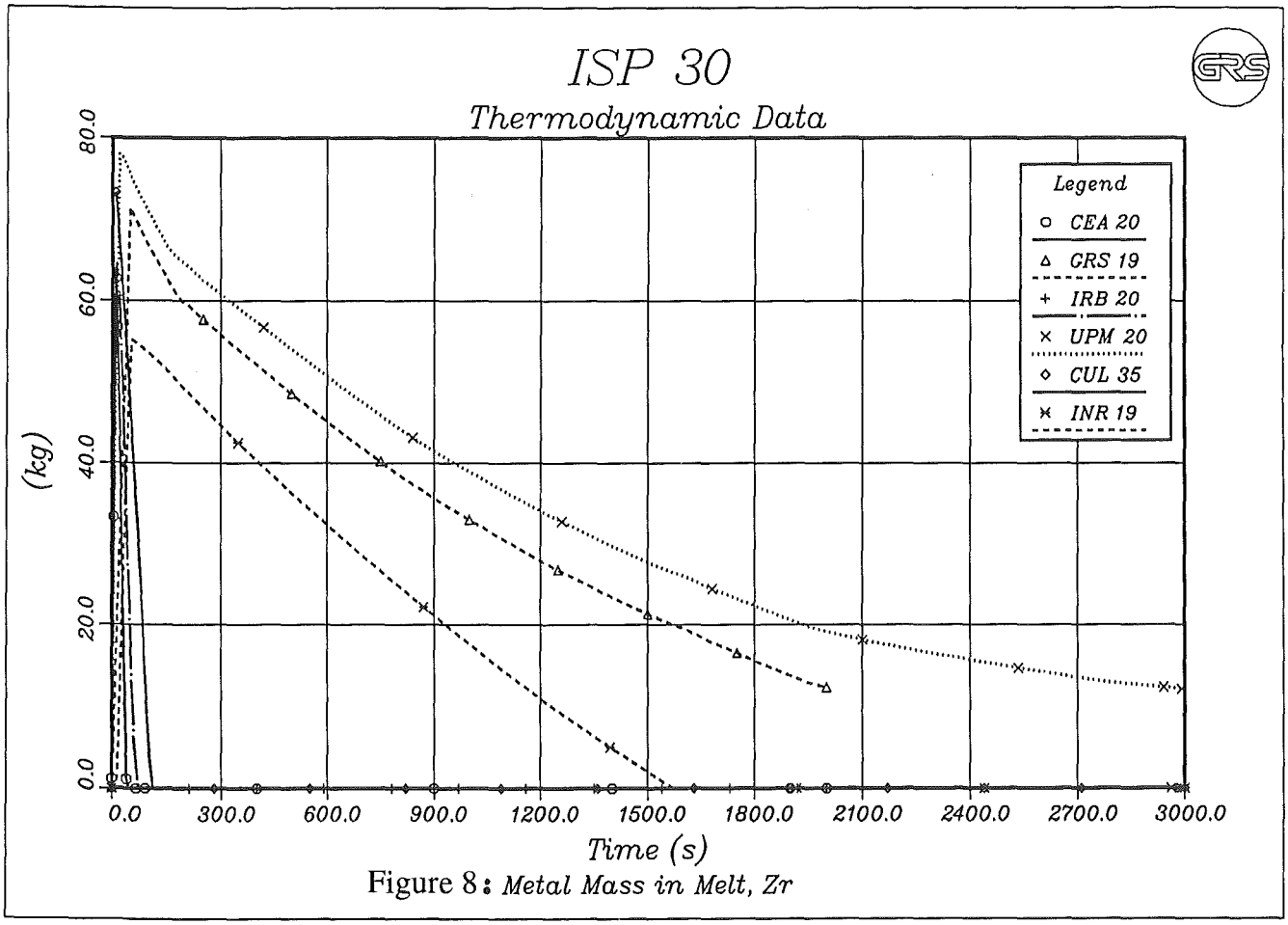

Figure 8: *Metal Mass in Melt, Zr*

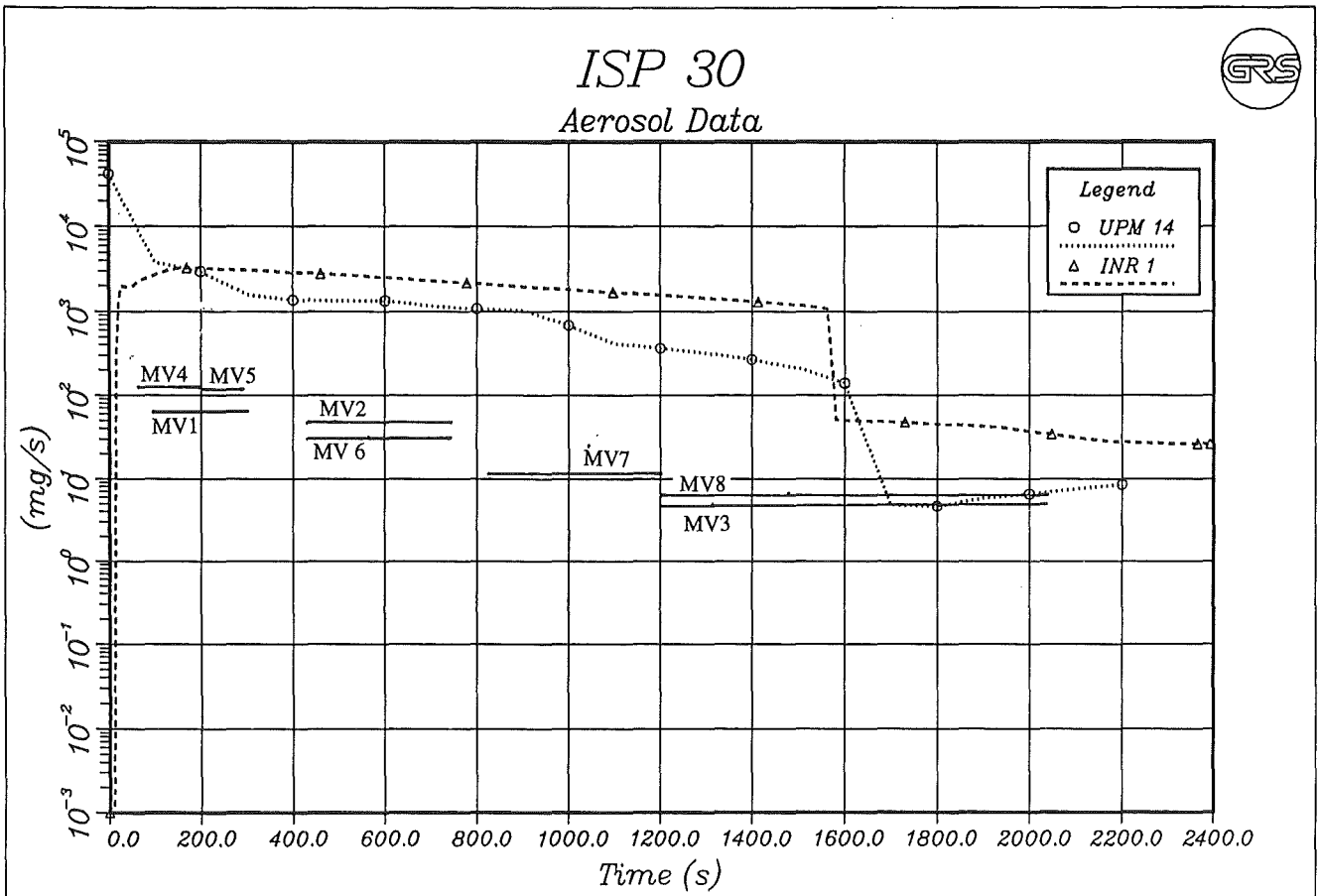

Figure 9: *Aerosol Release Rate, Total*

RESULTS OF AEROSOL CODE COMPARISONS WITH RELEASES FROM ACE MCCI TESTS

J. K. Fink
Argonne National Laboratory, Argonne, IL, USA

M. Corradini
University of Wisconsin, Madison, Wisconsin, USA

A. Hidaka
Japan Atomic Energy Research Institute,
Tokai-mura, Naka-gun, Ibaraki-ken, Japan

E. Hontañón
Polytechnical University of Madrid, Madrid, Spain

M. A. Mignanelli
AEA Technology, Harwell, UK

E. Schrödl
Gesellschaft für Reaktorsicherheit, Köln, Germany

V. Strizhov
Institute for Nuclear Safety, Moscow, Russia

ABSTRACT

Results of aerosol release calculations by six groups from six countries are compared with the releases from ACE MCCI Test L6. The codes used for these calculations included: SOLGASMIX-PV, SOLGASMIX Reactor 1986, CORCON.UW, VANESA 1.01, and CORCON mod2.04/VANESA 1.01. Calculations were performed with the standard VANESA 1.01 code and with modifications to the VANESA code such as the inclusion of various zirconium-silica chemical reactions. Comparisons of results from these calculations were made with Test L6 release fractions for U, Zr, Si, the fission-product elements Te, Ba, Sr, Ce, La, Mo, Ru and control materials Ag and In. Reasonable agreement was obtained between calculations and Test L6 results for the volatile elements Ag, In and Te. Calculated releases of the low volatility fission products ranged from within an order of magnitude to five orders of magnitude of Test L6 values. Releases were over and underestimated by calculations. Poorest agreements were obtained for Mo and Si.

INTRODUCTION

The CSNI benchmark exercise on the chemical modelling of the release of radionuclides due to core-concrete interactions [1,2] identified five reasons for different calculated releases by VANESA and other codes, namely: (1) absence of direct interaction between the condensed phases; (2) use of the metal phase alone to set the oxygen potential rather than the oxygen conservation equation and allowing the oxide phase to set its own oxygen potential; (3) failure to include important species in the gas composition; (4) neglect of vaporization from the metal phase; and (5) choice of an ionic versus molecular solution model for the condensed phase with failure to include certain condensed phase interactions such as Zr-SiO_2. The differences in releases due to different treatments of the solution phases, choice of thermodynamic functions, and uncertainties in thermodynamic data for a specific problem were also assessed in the benchmark exercise. The CSNI report [2] pointed out that uncertainties in the modelling of releases from core-concrete melts may be further reduced by comparison of calculations with releases from experiments. The Advanced Containments Experiments (ACE) molten core concrete interactions (MCCI) test program provides opportunities to compare calculations with experimental releases. Tests L6 and L8 have been selected for comparison with blind posttest calculated releases. Code comparisons for Test L6, a siliceous concrete test, have been completed. Comparisons with Test L8, which used limestone/limestone concrete, are underway.

The focus of this paper is the results of the Test L6 code comparison. Results of twenty-two aerosol release calculations by six groups from six countries were submitted for comparison with test data. Fourteen of these calculations were posttest blind calculations. Only results of these blind calculations have been included in this paper.

In the next section, Test L6 parameters required for the code calculations are given. The third section gives an overview of the codes used in the release calculations. The focus of the fourth section is a comparison of results of calculations with releases from the experiment and discussion of the results. Conclusions and recommendations are given in the last section.

TEST L6

Test L6 determined the releases from the interaction of a PWR corium with 30% Zr oxidation and a siliceous concrete basemat. The test apparatus and composition of the corium, concrete/metal inserts and concrete in the ACE MCCI experiments are described in other papers [3-5]. The corium contained UO_2, ZrO_2, CaO, SiO_2, and oxides of fission-product elements at twice the reactor inventory. The concrete/metal inserts contained stainless steel, Zr, Ru, Ag, In, and $ZrTe_2$. The siliceous concrete basemat was 50.2 cm by 49.2 cm in area. At the time aerosol collection was terminated, about 8.8 cm of the basemat had been ablated. Four reinforcing rods located at 5.2 cm in the basemat had been incorporated in the melt.

Test data provided for the aerosol code calculations included: moles of each species of off gas released upward as a function of time, ablation rate, and melt temperature as a function of time. Because off gas from the concrete migrated downward during the test, the off gas detected above the melt was only about half of the gas available from the ablated concrete. All times were given relative to the surface of the concrete basemat reaching 1673 K. The melt temperature during insert ablation was assumed to be 2500 K. Melt temperature during basemat ablation varied from 2425 K at 12.5 min to 2263 K at 30 min.

Aerosol and off gas release began at -52 min (52 min prior to the basemat surface reaching 1673 K) when the concrete/metal inserts reached 373 K. Concrete/metal insert ablation began at -44 min. At 31 min, the diluter in the off gas line plugged and collection of aerosols was terminated. Release calculations were to be done from -52 to 31 min.

PARTICIPANTS

The six participants and the codes used are given in Table 1. In order to minimize the number of comparisons shown in figures and tables, the calculation giving best agreement with experimental releases was chosen when more than one calculation was performed with one code or modifications of that code. Abbreviations for the calculations that are used in figures and tables in this

Table 1. Test L6 Aerosol Release Code Comparison Participants

Participant	Organization	Code	Total Release Calculations	Symbols
M. A. Mignanelli	AEA Technology Harwell, UK	SOLGASMIX REACTOR Version 1986	2	UK
E. Schrödl	GRS, Germany	SOLGASMIX - PV	3[a]	GRS
E. Hontañón	Polytechnical University of Madrid, Spain	SOLGASMIX	1	S-S
		VANESA 1.01	2	SV2
A. Hidaka	JAERI, Japan	VANESA 1.01	1	JPN
V. Strizhov	Nuclear Safety Institute, Moscow, Russia	VANESA Mod 7/15/1985 CORCON Mod2.04	4[b]	URC, URE
M. Corradini	University of Wisconsin, USA	CORCON.UW	1	WIS
			Σ 14	

[a]3 total releases were calculated. For one case, separate calculations gave the release for ablation of the concrete/metal insert and for the ablation of the basemat. The total release was the sum of the releases from these calculations.

[b]The release during the ablation of the concrete/metal inserts was determined in a separate calculation. Results of this calculation were used with 4 separate calculations of the ablation of the basemat to obtain 4 sets of total releases for Test L6.

paper are included in the last column of Table 1.

Data from various sources were used in these calculations. In some calculations, off gas was determined from concrete ablation. Others used the actual moles of upward off gas released (from Test L6 data). Melt temperatures were either held constant, obtained from the test data, or determined from thermal hydraulic code calculations. The sources of melt temperature, off gas released, and basemat ablation rate for each calculation are summarized in Table 2.

SOLGASMIX REACTOR is a version of the SOLGASMIX code developed by Eriksson [6] that performs sequential equilibrium calculations. In his calculation using the

Table 2. Data Used in Code Calculations

Calculation	Temperature, K		Gas Available		Basemat Ablation
	Inserts	Basemat	H_2O	CO_2	
SOLGASMIX					
UK	2500	Test L6	Concrete	Concrete	Test L6
GRS	2400	2400	Concrete	Concrete	-----[e]
S-S	2400	2400	Test L6	Test L6	-----[f]
VANESA					
SV2	CORCON[a]	CORCON[b]	Test L6	Test L6	Test L6
JPN	2500	Test L6	Test L6	Concrete	Test L6
URC	2500	Test L6	Test L6	Test L6	Test L6
URE	2500	CORCON	CORCON	CORCON	CORCON
CORCON.UW					
WIS	CORCON.UW[c]	CORCON.UW[d]	CORCON.UW	CORCON.UW	CORCON.UW

[a]Temperatures ranged from 2500 to 2239 K.

[b]Temperatures were 100 to 200 K below Test L6 measured values; Temperatures ranged from 2226 to 2172 K.

[c]Temperature fell from 2500 to 2350 K in first 25 min then stayed around 2350 K for rest of time.

[d]Temperature started at 2350 K vs 2425 K (Test L6); good agreement with Test L6 data at 20 and 25 min.

[e]Only 2 time steps: insert, basemat.

[f]Only 1 time interval for entire test (insert and basemat ablation).

SOLGASMIX REACTOR code, Mignanelli treated insert ablation in one time step and included 9 time steps for basemat ablation. SOLGASMIX-PV, the adaptation of SOLGASMIX by T. Besmann at ORNL [7], was used by Hontañón and Schrödl in their calculations. Only one time step at 2400 K was used in the calculation by Hontañón. Two calculations by E. Schrödl used single time steps at 2400 K. His third result, also at 2400 K, was comprised of two separate calculations. First the release from insert ablation was calculated. Then the residual mass from this calculation was included with the ablated basemat and rebar for the second calculation. The total release was the sum of the releases from the two

calculations. This combined calculation gave the best agreement with experimental releases.

The databases used by Mignanelli and Schrödl included zirconates and silicates. Mignanelli did calculations with and without lanthanum zirconate in the database. Agreement was best when lanthanum zirconate was included. The VANESA data base, which does not included silicates nor zirconates was used for the SOLGASMIX calculation by Hontañón.

VANESA 1.01 was used in all VANESA calculations. In response to the CSNI benchmark exercise which showed that failure to include condensed phase reactions of Zr with SiO_2 significantly effected releases[1,2], modifications of the VANESA chemistry to include additional condensed phase reactions were made in some calculations. The multiple calculations with the VANESA code by Hontañón and Strizhov included both calculations with the standard version and with modifications to include the chemical reactions of SiO_2 and Zr. Hontañón's calculation, SV2, included the reaction of SiO_2 and Zr to form SiO gas. The modified VANESA calculations (URC and URE) by Strizhov included the chemical reaction of SiO_2 and Zr to form Si. Results of calculations with either reaction gave better agreement than the unmodified VANESA 1.01 code. The four calculations by Strizhov included the four combinations of calculations with and without modifications to the VANESA chemistry and with either thermal hydraulic data from CORCON calculations or thermal hydraulic data from Test L6. Results of two calculations (URC and URE) were selected for comparison in order to compare completely blind posttest calculations and to evaluate the importance of test data versus CORCON output as input. The calculation by the JAERI analysts led by A. Hidaka used the standard VANESA code with a modification to limit the partial pressures of the releases. Details of the JAERI calculations are presented in a separate paper.[8]

CORCON.UW is a modified version of CORCON that includes complete melt chemistry.[9] It is a completely blind calculation in that both thermal hydraulic results and releases are calculated as a function of time in this code. The database for CORCON.UW does not include any silicates or zirconates in the condensed phase.

RESULTS

Release fractions were calculated from Test L6 for U, Zr, Si, Te, Ba, Sr, La, Ce, Mo, Ag, In, and Ru for comparison with the code calculations. In the ACE MCCI program, release fraction is defined as moles (gram-atoms) of element released as aerosol divided by moles (gram-atoms) of element in the melt. Si was included in the aerosol code comparison because of its dominance in the aerosols released from Test L6. For Ce, La and Ru, only maximum and minimum release estimates are currently available from the test data because these elements were below the level of detectability in most aerosol samples. Minimum values were calculated by assuming zero when the element was not detected. Maximum values were calculated assuming the limit of detectability when the element was not detected. Calculated releases for Ce and La will be reassessed when more sensitive neutron activation analysis for Ce and La are complete.

Calculated release fractions ranged from within an order of magnitude of Test L6 values to differences of 5 orders of magnitude. In Table 3, the differences between the release fractions obtained from the calculations and Test L6 are summarized. Results for each element are discussed below.

Ag, In, and Te

The best agreements between calculations and experimental data were obtained for the volatile elements: Ag, In, and Te. Results for Ag are shown in Figure 1. For these elements, releases from all calculations were within an order of magnitude of the Test L6 releases.

Ce and La

Calculated release fractions of Ce and La ranged over 3 orders of magnitude as shown in Figures 2 and 3. Releases from all VANESA calculations except for calculation SV2 were high for both Ce and La. Results of the SOLGASMIX calculation S-S, which used the VANESA database, were also high. Mignanelli found that inclusion of lanthanum zirconates significantly reduced the calculated La release. In his vaporization studies, Roche[10] found inclusion of silicates and zirconates in the melt chemistry was necessary to obtain good agreement between his experimental results and equilibrium calculation. Although preliminary results indicate that silicates and zirconates of Ce may also be

Table 3. Order of Magnitude Deviation of Calculated Releases from Test L6 Releases

	UK	GRS	S-S	SV2	JPN	URC	URE	WIS
Te	+0.5[a]	+0.5	-0.5	+0.5	-0.5	+0.5	+0.5	+0.5
Ag	+0.5	+0.5	-1	----	-0.5	-1	-0.5	+0.5
In	+0.5	+0.5	----	----	----	+1	+0.5	----
Ce	+0.5	0[b]	+0.5	0	+2	+2	+2	0
La	0	0	+0.5	0	+0.5	+1	+1	0
Ru	0	0	-0.5	-1	-1	-1	-1	0
Ba	-0.5	-1	+0.5	+0.5	+0.5	+2	+2	-0.5
Sr	-0.5	-0.5	+0.5	-1	+2	+2	+2	+1
U	-1	-1	-1	+0.5	-0.5	-3	-2	-2
Zr	-1	-2	-3	----	-2	----	----	-3
Mo	-3	-3	-5	+0.5	----	-2	-2	----
Si	+0.5	+0.5	+0.5	----	-2	-4	-5	----

[a]For orders of magnitude from 0.1 to 0.5, 0.5 is used.

[b]0 is used for calculated releases between maximum and minimum Test L6 releases.

important, no conclusion should be drawn until final Ce analyses for Test L6 have been completed. The lack of silicates and zirconates in the VANESA database could be a major factor in the high releases from VANESA calculations and the SOLGASMIX calculation, S-S. The good agreement of CORCON.UW, which does not include silicates and zirconates in the database, is surprising if these species are important. Examination of the CORCON.UW calculation shows that the calculated melt temperatures during insert and early basemat ablation are far

below Test L6 values (see Table 2). The good agreement of CORCON.UW results could be fortuitous, a result of these low temperatures. The VANESA SV2 calculation includes the silica-zirconium reaction to produce SiO(g). Inclusion of this interaction has a significant effect on the oxygen potential and this modification may compensate for not including additional species in the condensed phase.

Ru

Calculated Ru releases were either between the Test L6 maximum and minimum or low. All calculations that used the VANESA database were low.

Ba and Sr

Calculated releases for Ba and Sr ranged from one to three orders of magnitude of Test L6 values. Figures 4 and 5 indicate that releases are over- and underestimated. Roche [10] showed the importance of barium and strontium silicates and zirconates in the solidified melt and in his chemical equilibrium calculations for his vaporization release studies. Ba and Sr release calculations without silicates and zirconates in the database were high except for the VANESA calculation SV2 for Sr and CORCON.UW for Ba. The UK and GRS SOLGASMIX calculations, which included silicates and zirconates in their databases, were low. The GRS calculation for Ba was significantly worse than for Sr indicating that the low temperature used in this calculation had a greater effect on Ba release than on Sr release. A SOLGASMIX calculation by Schrödl with 2550 K for the insert temperature and 2400 K for the basemat temperature gave Ba and Sr releases within a factor of 2 of experimental values [11]. The better agreement for Ba compared to Sr in calculations without silicates and zirconates may be due to the sensitivity of Ba release to temperature and the low temperatures used in the calculations.

U and Zr

Calculated releases for U and Zr were low except for calculation SV2. Results for U are shown in Figure 6. In Test L6, higher fractions of U and Zr were detected in large particles, that may have been mechanically generated, than in small particles from vaporization. This effect was particularly great for Zr. A possible explanation for the deviations for U and Zr is that the mechanical contribution to the release of these elements is significant and is either not

calculated (SOLGASMIX and CORCON.UW) or is underestimated (VANESA). Other effects such as additional vapor species should also be considered.

Mo

For Mo, calculated releases ranged over 6 orders of magnitude. All calculations give low releases for Mo except for SV2. The reason for the large disagreement between calculations and experiment for Mo is not understood.

Si

For Si, deviations between calculated and experimental releases were as large as 5 orders of magnitude. The SOLGASMIX calculations gave significantly better agreement with Test L6 releases than the VANESA calculations. This may be due to the importance of the inclusion of all SiO_2-Zr reactions. In Test L6, the aerosol composition was dominated by aerosols formed from SiO gas.

Discussion of Results

The important differences in the calculations identified in the CSNI benchmark exercise were confirmed in the Test L6 code comparison. The five causes of differences in VANESA and other calculations identified in the CSNI study[1,2] are addressed with respect to the Test L6 code comparison below. The importance of inclusion of interactions between condensed phases is illustrated by the better agreement of results from the CORCON.UW code (WIS), which includes interaction between the condensed phases, compared with the standard VANESA calculations. Comparison of calculations with Test L6 releases confirm the importance of the oxygen potential and the assumptions used to set it. The oxygen potential from the JAERI VANESA calculation (JPN) was significantly lower than those from the UK and GRS SOLGASMIX calculations. In addition the JPN oxygen potential variation with time differed significantly from that obtained in the UK calculation. The lower oxygen potential in the JAERI VANESA calculation most likely is the result of the VANESA model setting the oxygen potential over both phases by the oxygen potential determined over the metal phase and the lack of the Zr-SiO_2 reactions in the VANESA code. Because Zr is oxidized in VANESA only by H_2O and CO_2, Zr remains in the metal layer for a longer time in the JAERI VANESA calculation (until the end of the calculation) compared to the UK calculation. As Zr is depleted from the metal phase, the oxygen potential in the chemical equilibrium calculation would increase.

Therefore, the oxygen potential determined by the UK calculation became larger than that in the JAERI calculation.

Failure to include all species in the gas composition and neglect of vaporization from the metal phase may contribute to the high releases for oxide species of Ce, La, Ba, and Sr and low releases of Ag and Zr in all VANESA calculations. The importance of inclusion of Zr-SiO_2 reactions was clearly illustrated by the differences in results of calculations: (1) SV2, which included the reaction to form SiO, (2) URC and URE, which included the reduction to Si, and (3) JPN, which did not include these reactions.

The CSNI study also found that the database used significantly effected the release calculations. Silicates and zirconates were included in the condensed phases in the databases used in the UK and GRS calculations. In general, agreements with Test L6 releases for Ba, Sr, and La were improved by inclusion of these species, as illustrated by comparison of the UK and GRS calculations with VANESA calculations JPN, URC, and URE. Although good agreement was obtained by the CORCON.UW calculation for some cases without inclusion of these species, the agreement is most likely fortuitous and due to the low temperature used in the calculations. Good agreement was not obtained for Sr which is not as temperature sensitive as Ba, Ce, and La. Inclusion of the reaction to form SiO(g) by Hontañón in calculation SV2 seemed to compensate in some way for failure to include condensed phase species in the VANESA database.

CONCLUSIONS AND RECOMMENDATIONS

Results of this code comparison effort are useful in assessing progress on fission-product release calculations and in providing guidance with respect to databases and further model development. Conclusions and recommendations are given below.

1. Significant progress has been made by the development of various SOLGASMIX chemical equilibrium codes with extensive databases and the development of the CORCON.UW code which gives better agreement with Test L6 than the CORCON mod2.04/VANESA 1.01 codes. The SOLGASMIX calculations on Test L6

and other ACE MCCI tests have provided valuable contributions on the importance of various species in the melt chemistry and the effects of various test parameters on the release.

2. Although some possible causes for discrepancies between calculated and measured releases have been proposed in this paper, the combined efforts of specialists are needed to identify the causes of discrepancies between the calculated and measured releases for each element.

3. International agreement on an assessed database that includes silicates and zirconates of Ba, Sr, La, and perhaps Ce is needed. Experiments required to provide the experimentally sound data required for this database should be identified.

4. The melt chemistry and physics, such as the representation of simple or complex phases for oxide and metal solutions, choice of solution model (ionic vs molecular), treatment of the melt as a mixture of immiscible liquids or separate layers and effect on oxygen potential, gas release and migration, and mechanical aerosol release should be examined to determine if more sophisticated models of thermochemical interactions and/or of the physical processes are necessary to obtain good agreement with experimental releases.

ACKNOWLEDGEMENTS

Work sponsored by the Electric Power Research Institute under Contract RP 2802-12.

REFERENCES

1. M. A. Mignanelli and P. N. Smith, "CSNI/PWG4/TGFPC Benchmark Exercise on the Chemical Modelling of the Release of Radionuclides due to Core-Concrete Interactions: Results of Part A," CSNI Report 164, Volume A, December 1989.

2. M. A. Mignanelli, "Benchmark Exercise on the Chemical Modelling of the Release of Radionuclides due to Core-Concrete Interactions: Results of Part B," CSNI Report 164, Volume B, October 1990.

3. B. R. Sehgal and B. W. Spencer, "ACE Program Phase C: Fission Product Release From Molten Corium Concrete Interactions (MCCI)," paper presented at the OECD CSNI Specialist Meeting on Core Debris Concrete Interactions, Karlsruhe, Germany, April 1-3, 1992.

4. D. H. Thompson, J. K. Fink, D. R. Armstrong, B. W. Spencer, and B. R. Sehgal, "Thermal-Hydraulic Aspects of the Large-Scale Integral MCCI Tests in the ACE Program," paper presented at the OECD CSNI Specialist Meeting on Core Debris Concrete Interactions, Karlsruhe, Germany, April 1-3, 1992.

5. J. K. Fink, D. H. Thompson, B. W. Spencer, and B. R. Sehgal, "Aerosols Released During Large-Scale Integral MCCI Tests in the ACE Program," paper presented at the OECD CSNI Specialist Meeting on Core Debris Concrete Interactions, Karlsruhe, Germany, April 1-3, 1992.

6. G. Eriksson, "SOLGASMIX, A Computer Program for Calculation of Equilibrium Compositions in Multiphase Systems," Chemica Scripta 8, 100-103, 1975.

7. T. M. Besmann, "SOLGASMIX-PV, A Computer Program to Calculate Equilibrium Relationships in Complex Chemical Systems," ORNL/TM-5775, April 1977.

8. A. Hidaka, K. Soda, J. Sugimoto, and N. Yamano, "Analyses of ACE MCCI Test L6 with the CORCON/VANESA Code," paper presented at the OECD CSNI Specialists Meeting on Core Debris Concrete Interactions, Karlsruhe, Germany, April 1-3, 1992.

9. J. K. Norkus and M. L. Corradini, "Modeling of Molten Core Concrete Interactions: Fission Product Release," Proceedings of the ANS/ENS Conference on Thermal Reactor Safety, Avignon, France, October 2-7 1988.

10. M. F. Roche, L. Leibowitz, J. L. Settle, C. E. Johnson, R. C. Vogel, and R. L. Ritzman, "Vaporization of the Strontium, Barium, Lanthanum, and Uranium from Mixtures of Urania, Zirconia, Steel, and Concretes at 2150 K and 2400 K," Nucl. Technol. 96, 96-116, 1991.

11. E. Schrödl, private communication, 1991.

Figure 1. Ag Release

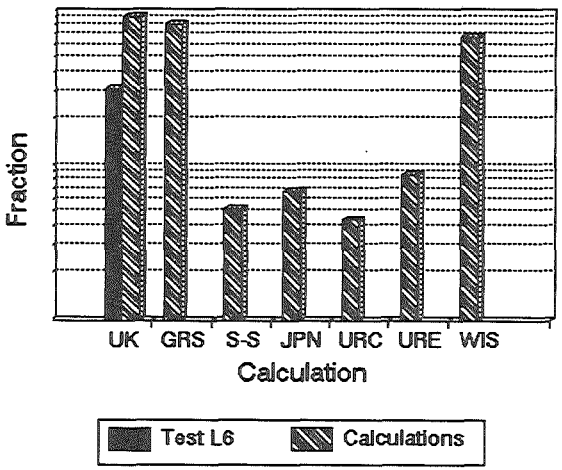

Figure 2. Ce Release

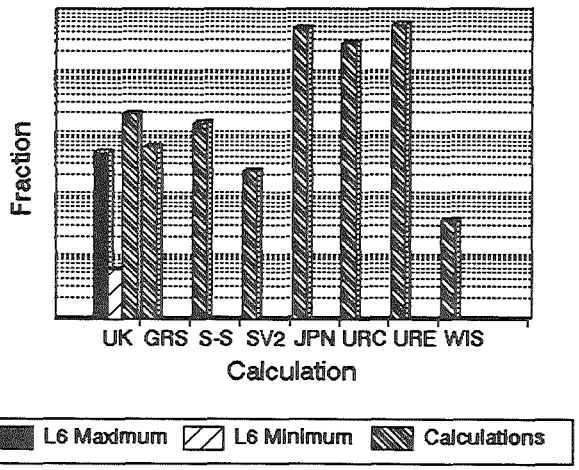

Figure 3. La Release

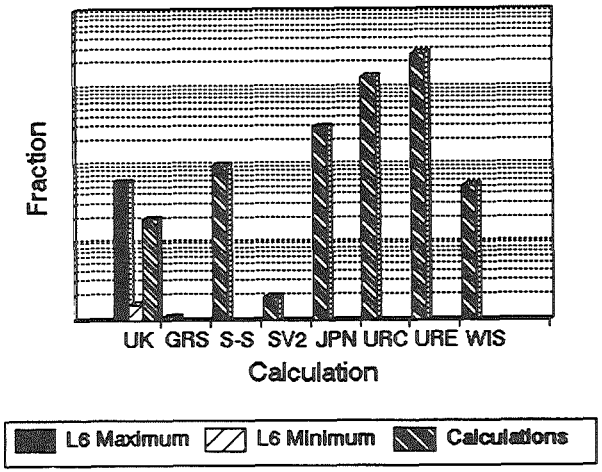

Figure 4. Ba Release

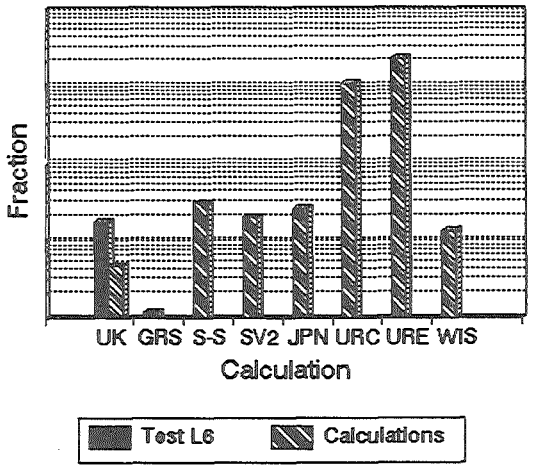

Figure 5. Sr Release

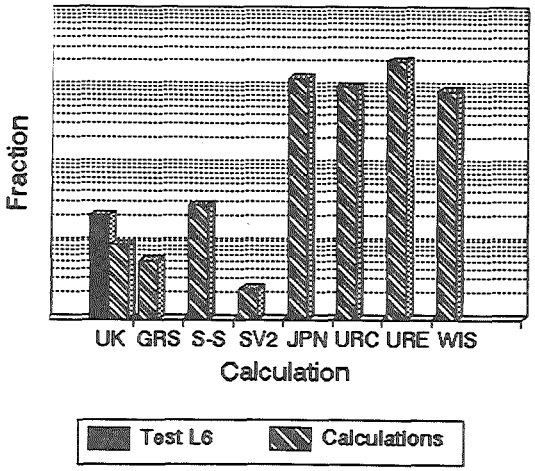

Figure 6. U Release

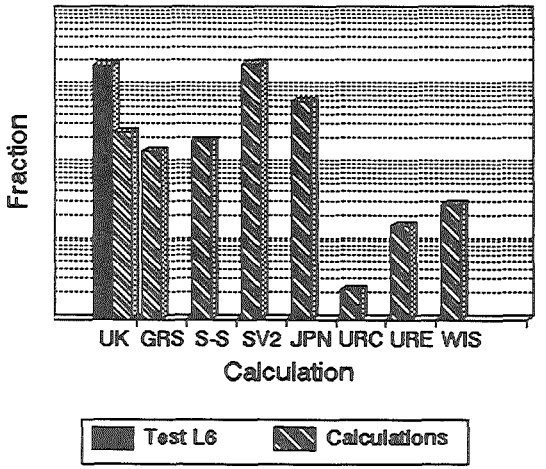

Contribution to the subject evaluating the core melt/ concrete interactions concerning the reactor type VVER-1000

C.J.Steinkopf, F.Müller

Technische Hochschule Zittau
Mechanical Engineering/Power Engineering Faculty
Theodor-Körner-Allee 16
O-8800 Zittau

Introduction

In Europe as well as the Asian part of the former USSR about 18 reactors of the VVER-1000 type have been put into operation and another 17 are under construction /1/. So far not any evaluations regarding the core melting behavior after a failure of the reactor pressure vessel have been available as a design-exceeding disturbance.
By order of the Federal Ministry for Research and Technology a sponsorship project concerning this VVER-1000 reactor type problem is being dealt with at the Technische Hochschule Zittau in order to obtain basic criteria for evaluating the safety characteristics of the nuclear power plants mentioned with respect to a hypothetical core melting accident. The investigations for this reactor type were performed at the nuclear power plant Stendal, with special emphasis to the transferability of the results obtained to all other VVER-1000 types.

1) Design characteristics

The design of VVER-1000 nuclear power plants greatly differs from that of Western European nuclear power plants with regard to

-the construction; due to the provision of a full-pressure containment, erected on a stationary basement,
-the overall design and arrangement of the installations including the safety regulations, and

-the core inventory.

The construction of the nuclear power plant Stendal differs from that of the Eastern European VVER-types due to the containment layout in form of a steel segment composite construction.
Figure 1 shows a cross-section of the reactor building of the nuclear power plant Stendal.

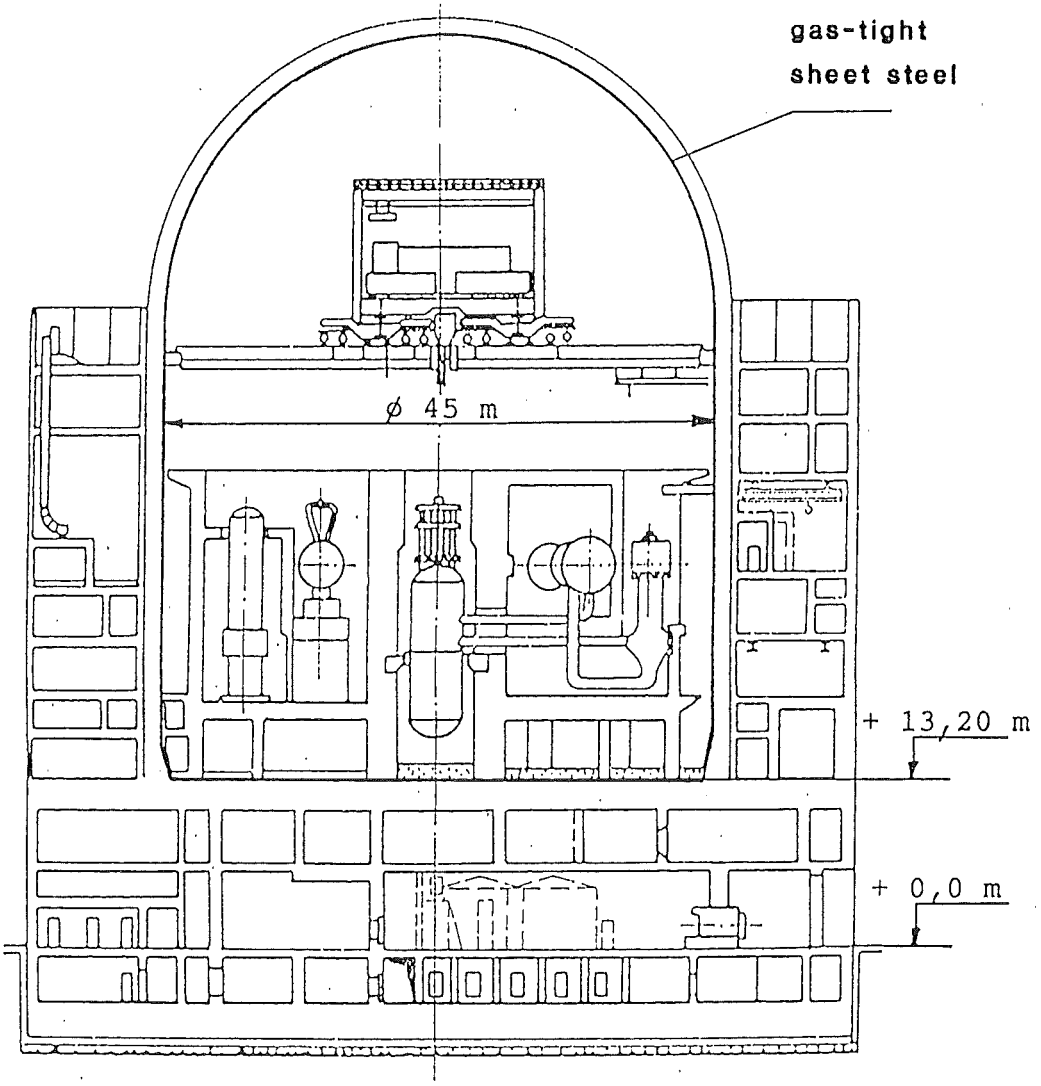

Figure 1: Cross-section of the reactor building of the nuclear power plant Stendal

Concerning geometry as well as arrangement of the reactor cavity, the Stendal nuclear power plant project is similar to that of other VVER-1000 types.

The reactor cavity is arranged on a ceiling construction (+13.20 m) forming the upper gas-tight sealing of the hermetical containment part. The ceiling provides for the statical carrying capacity and in case of a core melting accident it will be directly affected.

The installations below will be provided with air-conditioning, several emergency systems, measurement technology for reactor control as well as the emergency boron concentrate chamber. They are of great importance regarding the safe operation of the plant. The reactor cavity wall is provided with vertical measuring pipes in distances of 0.14 m and 0.52 m, respectively - so-called IK-pipes. They serve for the purpose of reactor control by moving the ionization test probes.

The reactor cavity design guarantees an entrance through the steel-made reactor cavity door. Thus inspection and test of the reactor pressure vessel can be done.

The reactor cavity bottom is made up of a layer of conrete with heat insulating properties. This layer has a thickness of about 0.50 m and consists of serpentinite-type concrete, which reinforces the ceiling construction (+13.20 m).

In the centre of the layer there is a circular hole (diam. = 0.75 m) provided for the ventilating system. From that hole four ventilating pipes extends radially in the cavity bottom in an outward direction up to an angular ventilating duct. Additionally the hole is equipped with an outward directed drainage duct having a diameter of about 82 mm.

The geometry is presented in Figure 2.

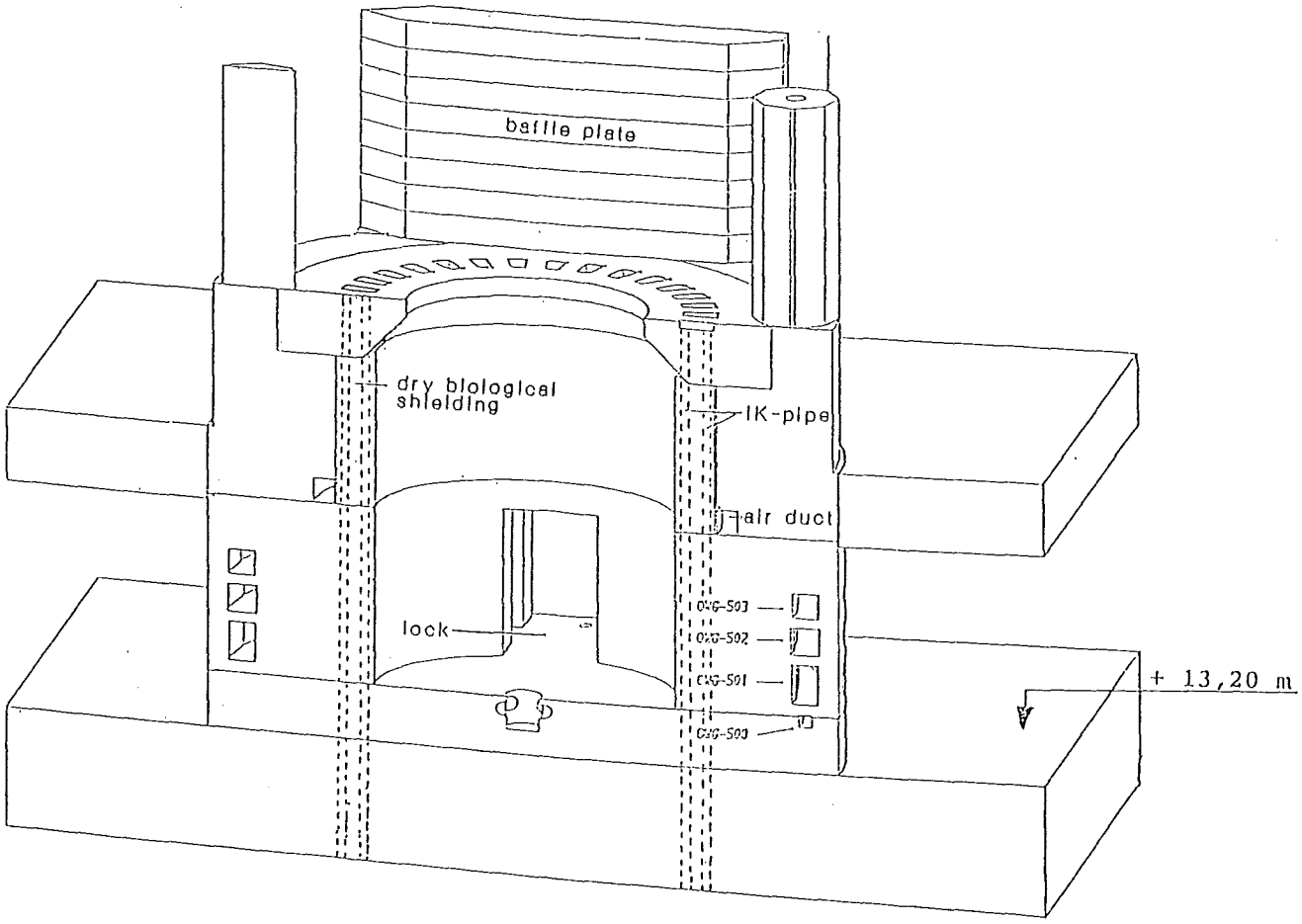

Figure 2: Cross-section of the VVER-1000 reactor cavity

2) Objective of the investigations

Starting points of all the investigations done was a loss-of-coolant accident initiated by a double-end rupture of the main coolant loop. After a time period of 24 sec the blowdown will be finished. It as assumed that immediately after finishing the blowdown the emergency cooling systems fail. After about 20 minutes the core melting begins and after 60 minutes the reactor pressure vessel fails.

The course of accident development was obtained by a MARCH3-M calculation and it served for the formulation of the starting

conditions necessary for calculating the melt/concrete interactions.
Based on the MARCH3-M calculations the zirconium content of the melt was determined, which is of special importance concerning the gas liberation rate in the initial stage of the melt/concrete interaction. The metallic zirconium content amounts to 46 per cent of the total reactor zirconium.
The project presented is meant to give an assessment of the core melt interactions by using the codes WECHSL and CORCON. In this connection the programmes available have to be adapted to the above-mentioned characteristics of design and installation.
In particular the IK-pipe arrangement should be considered in order to be able to get an understanding of the behaviour with regard to a hypothetical core melt accident.
Emphasis was placed on the transferability of the results obtained to other VVER-1000 plants.

3) Results of the hitherto investigations

3.1) Effects of varying the concrete steel content onto the erosion geometry

Statical-constructional reasons are responsible for a non-uniform distribution of the steel content across the ceiling cross-section (+13.20 m). This zone formation of the steel content gives almost no rise to an alteration of the temperature an energy behaviour of the core melt in relation to the particular horizons. Both the extremes "without steel content" as well as "double steel content" have been investigated.
However, differences can be observed on considering the metallic content of the melt. The calculation "without steel content" reveals a distinctly lower metal content of the melt compared with the calculations concerning a "double steel content". This fact also explains the differing erosion geometries based on the calculations with the codes CORCON-MOD2.00.00 and WECHSL-MOD3.
Increasing the steel content of the concrete results in an increase of the metal content of the melt. Since the energy content of the melt remains constant, the erosion rate will be delayed.

Figures 3 and 4 show the time steps 0, 1 hour, 24 hours and 72 hours.
The erosion will be insignificant enlarged in axial direction in case of a steel content reduction. Increasing the steel content of the concrete results in developing a marked delay of the axial erosion rate. The radial component is about equal for all calculations.

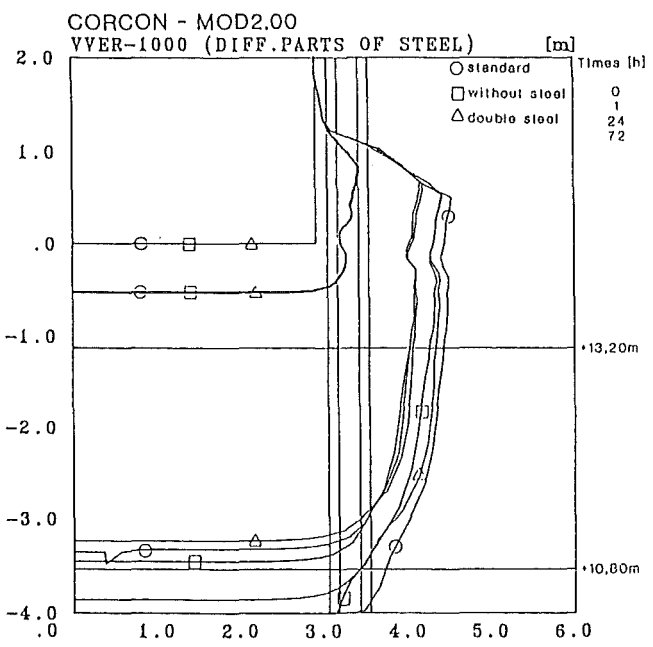

Figure 3: Erosion curves (CORCON)

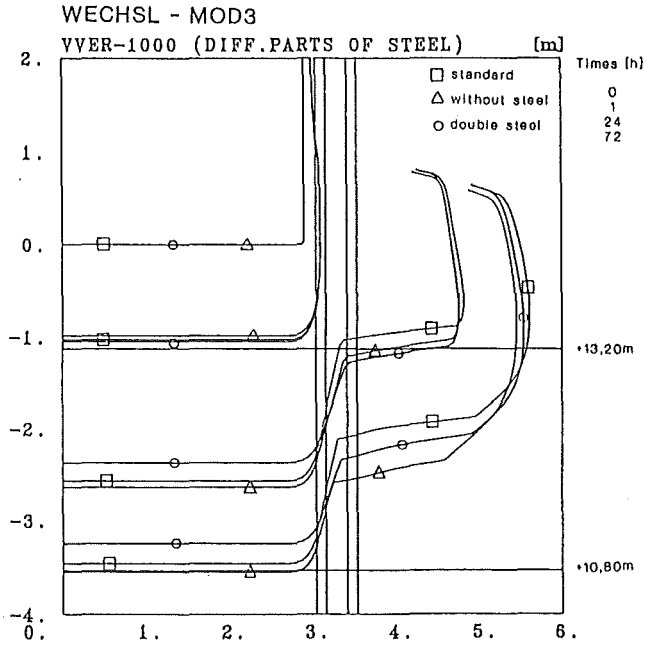

Figure 4: Erosion curves (WECHSL)

3.2) Serpentinite-type concrete influence on the melt/concrete interaction

The reactor cavity bottom of VVER-1000 reactors consists of an arrangement of serpentinite-type concrete and standard concrete layers. Serpentinite-type conrete differs to the standard concrete, which is applied in Germany, by the composition of the aggregate used. The following table comprises the composition of serpentinite-type concrete.

Composition

	Serpentinite-type concrete	Cement	Serpentinite coarse	Serpentinite fine
Net density g.cm^{-3}	2.54	3.11	2.65	2.66
SiO_2 mass - %	33.63	23.0	38.7	37.8
Al_2O_3 "	2.39	5.6	2.0	1.8
Fe_2O_3 "	6.37	4.0	6.4	8.4
CaO "	6.48	58.9	1.7	2.0
MgO "	30.54	2.6	39.1	37.1
SO_3 "	0.22	2.95	0.05	0.06
Mn_3O_4 "	0.10	0.09	0.12	0.11
Cr_2O_3 "	0.11	66 ppm	0.16	0.21
Na_2O "	0.05	0.06	0	0
K_2O "	0.05	0.4	0	0
TiO_2 ppm	460	560	275	390
Total loss % on ignition				
0 - 105 °C	6.31	-	0.09	0.18
105 - 500 °C	5.2	-	5.65	3.0
500 - 850 °C				
Loss on i. (total)	8.1	-	6.3	9.7
H_2O	6.49	-	5.43	8.8
CO_2	1.61	-	0.87	0.9
850 - 1000 °C	0.02	-	0.24	0.18

Table 1: Composition of serpentinite, serpentinite-type concrete and concrete used /2/

The analysis results reveal a distinctly enlarged proportion of physically and chemically bound water in serpentinite-type concrete in comparison to common standard concretes. In contrast to other standard concretes the crystal water will be liberated only at essentially higher temperatures. The mineral serpentinite is a magnesium silicate, thus a high MgO content of the concrete will be obtained.

The results calculated show that the higher melting point of the

serpentinite-type concrete reduces the axial erosion direction, the melt exhibits a slightly enlarged radial propagation. Due to the higher water content the gas liberation will be essentially enlarged.

The calculations were done by means of the code CORCON-MOD2.00.00. At present the WECHSL code fails to be used successfully for considering the MgO content. It is planned to improve the code in order to get results concerning the serpentinite-type concrete, too. Figures 5 and 6 illustrate the erosion characteristics and gas liberations of standard concrete as well as serpentinite-type concrete for the purpose of comparison.

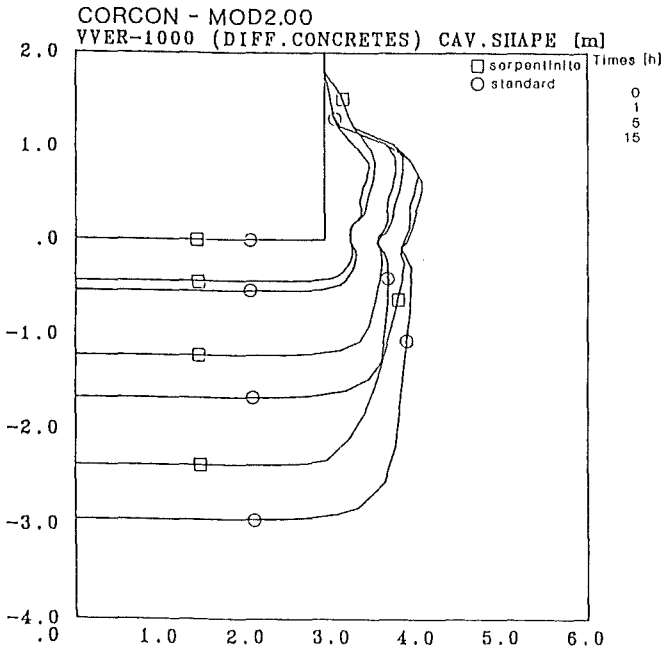

Figure 5: Erosion characteristics (CORCON)

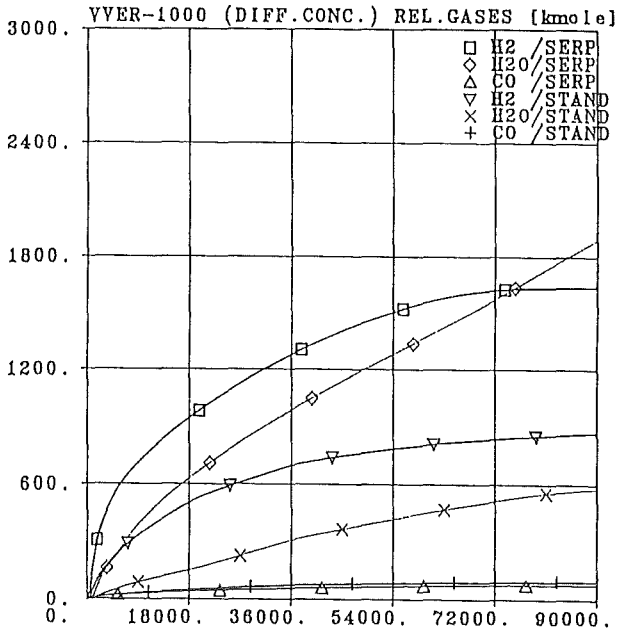

Figure 6: Gas liberation (CORCON)

3.3) Course of accident representation under consideration of the vertical test ducts in the cavity wall (IK-pipes)

Special attention has to given to the IK-pipes in the external cavity wall region. It is of special interest, whether the melt will drain-off into the lower, not hermetical part of the reactor

building after a pipe melting-on.
Results about the melt behaviour within the vertical test ducts, affected by radial erosion of the reactor cavity wall, were obtained by performing calculations with the code PLUGM. At the moment of an IK-pipe melting-on the melt in the reactor cavity is at a level of about 1.90 m in case of a WECHSL code calculation and at about 1.70 m by using a CORCON code calculation. A plug formation within the pipe owing to solidification processes can be excluded, owing to PLUGM code calculations, because the melt remains in a superheated condition at the pipe outlet. That is safe to assume that the whole melt being at the level of the outlet, produced by the melting-on process will drain-off into the area below.
This aspect would decisively affect the further course of the propagation and cooling of the melt.
In any case the results with the PLUGM code presented here have to be examined carefully, because they only have been obtained theoretically. An experimantal verification of the circumstances has still to be done.

3.4) Course of accident representation considering the original construction

Considering the observation corridor as well as the door in the course of accident representation, it can be assumed that the door will be molten nearly immediately and the melt will be spreading at the ceiling level +13.20 m. In this connection a drain-off into lower operational areas takes place. Taking into account these peculiarities a course of accident representation was established, considering the temporal as well as the spatial aspects.
Inserting finished parts, which can be dismantled, into the wall opening of the cavity door at that side facing the reactor, conditions can be established, which are similar to those of a monolithic design. Melting-on of the cavity door can be avoided.

4) Continuing the investigation

The results of the research work give the preconditions for developing the static-constructive testing method of the containment and the gas liberation as a pressure component of the hermetic rooms can be determined.

All the investigations were performed within the scope of a promotion project of the Federal Ministry for Research and Technology.

Reference

/1/ Atomwirtschaft/Atomtechnik, Handelsblatt GmbH, Verlag für Wirtschaftsinformation, Düsseldorf, November 1991

/2/ Chemisch-Physikalische Untersuchungen von Beton, Zement und Serpentinit grob und fein
Internes Material, Technische Hochschule Zittau, Fakultät Maschinenbau/Energietechnik, LS Bau-und Montagetechnologie, Betonanalyse vom 19.09.1991

Application of the WECHSL code to PWR and BWR specific accident scenarios

J. J. Foit

Kernforschungszentrum Karlsruhe
Institut für Angewandte Thermo- und Fluiddynamik
Postfach 36 40
W-7500 Karlsruhe 1, Germany

ABSTRACT

An accident analysis for a standard German PWR and a model BWR is performed with the WECHSL code. The cavity of the PWR is made of a siliceous type of concrete whereas the cavity of the BWR consists of a limestone concrete. An other important difference is the much higher content of metallic zirconium in the BWR melt. In the considered PWR there is a possibility of sump water ingression.

I. INTRODUCTION

The WECHSL Mod3 version is used to perform an accident analysis for a 1300 MW PWR and a BWR. The analysis starts after the melt has penetrated the reactor pressure vessel and is contained in the dry reactor cavity. The initial melt temperature is estimated to be 2673 K. In the initial phase of the melt/concrete interaction, the dominant energy source in the melt is the energy released in the zirconium oxidation reactions with the concrete decomposition products. Hence the concrete composition will determine the Zr-oxidation and the gas release rates as well as the composition of the released gases.

Recent experiments and analyses have shown that the solidus temperature of the oxidic melt decreases much more rapidly with addition of concrete oxide than modelled previously. The solidus temperature of the oxide phase drops rapidly as concrete oxides are incorporated into the melt, approaching the concrete solidus at only about 10 to 20 weight percent of concrete oxides [1]. The calculations are performed using the old estimate and the new solidus temperatures for both reactor types in order to study the influence of that oxide solidus temperature.

II. CALCULATIONAL MODELS

II.1 Concrete composition

The reactor cavity of the PWR consists of a siliceous type of concrete with SiO_2 as a main component (Tab. 1).

constituent	weight fraction
SiO_2	0.7655
$Ca(OH)_2$	0.0728
$CaCO_3$	0.0663
H_2O	0.0422
Al_2O_3	0.0532

Tab. 1: Composition of the idealized concrete of the PWR

The concrete of the BWR is a limestone concrete with a composition given in the following table, Tab. 2 [1].

constituent	weight fraction
SiO_2	0.04
$Ca(OH)_2$	0.082
$CaCO_3$	0.81
H_2O	0.04
Al_2O_3	0.028

Tab. 2: BWR-concrete composition

The decomposition temperature and the decomposition enthalpy for this limestone concrete are estimated to be $T_{dec} = 1800$ K and $H_{dec} = 4 \cdot 10^6$ J/kg, respectively.

For the siliceous concrete $T_{dec} = 1573$ K and $H_{dec} = 2.075 \cdot 10^6$ J/kg are used.

II.2 Melt composition

The melt consists of a metal phase consisting of Zr, Fe, Cr and Ni covered by an oxidic layer composed of UO_2 and ZrO_2. The most important difference in the melt composition for the reactor types considered is the much higher zirconium content

of the BWR. In case of the PWR there are 18000 kg of metallic Zr and in the BWR there are 41000 kg Zr in the metallic melt.

III. WECHSL RESULTS

III.1 Cavity shape

The initial radius of the reactor cavity is assumed to be r = 3.2 m for both reactor types. For the PWR sump water ingression is possible after the inner shield of a thickness of 0.9 m is eroded. The flooding of the melt surface by sump water causes a delay of the basemat penetration of about 48 min in WECHSL calculations. The penetration of the 6 m concrete basemat for the PWR using the new estimated oxide solidus temperature occurs at t = 4.9 days, the flooding by sump water at t = 7.2 hours (Fig. 1). The old solidus temperature leads to the almost identical results except for the radial erosion which is 0.2 m larger.

The thickness of the BWR concrete basemat is taken to be 3 m. The calculated cavity shape which differs significantly from that of the PWR is given in Fig. 2. The reason for that is that the high decomposition temperature of $T_{dec} = 1800$ K, which is higher than the solidus temperature of the metallic phase, will prevent a crust formation at the metal-concrete boundary. Hence there is a very efficient heat transfer to the concrete leading to the fast basemat penetration at t = 7.7 hours. For the old oxide solidus temperature the penetration occurs at t = 12 hours. Obviously there is a strong dependence of the results on the oxide solidus temperature in this case.

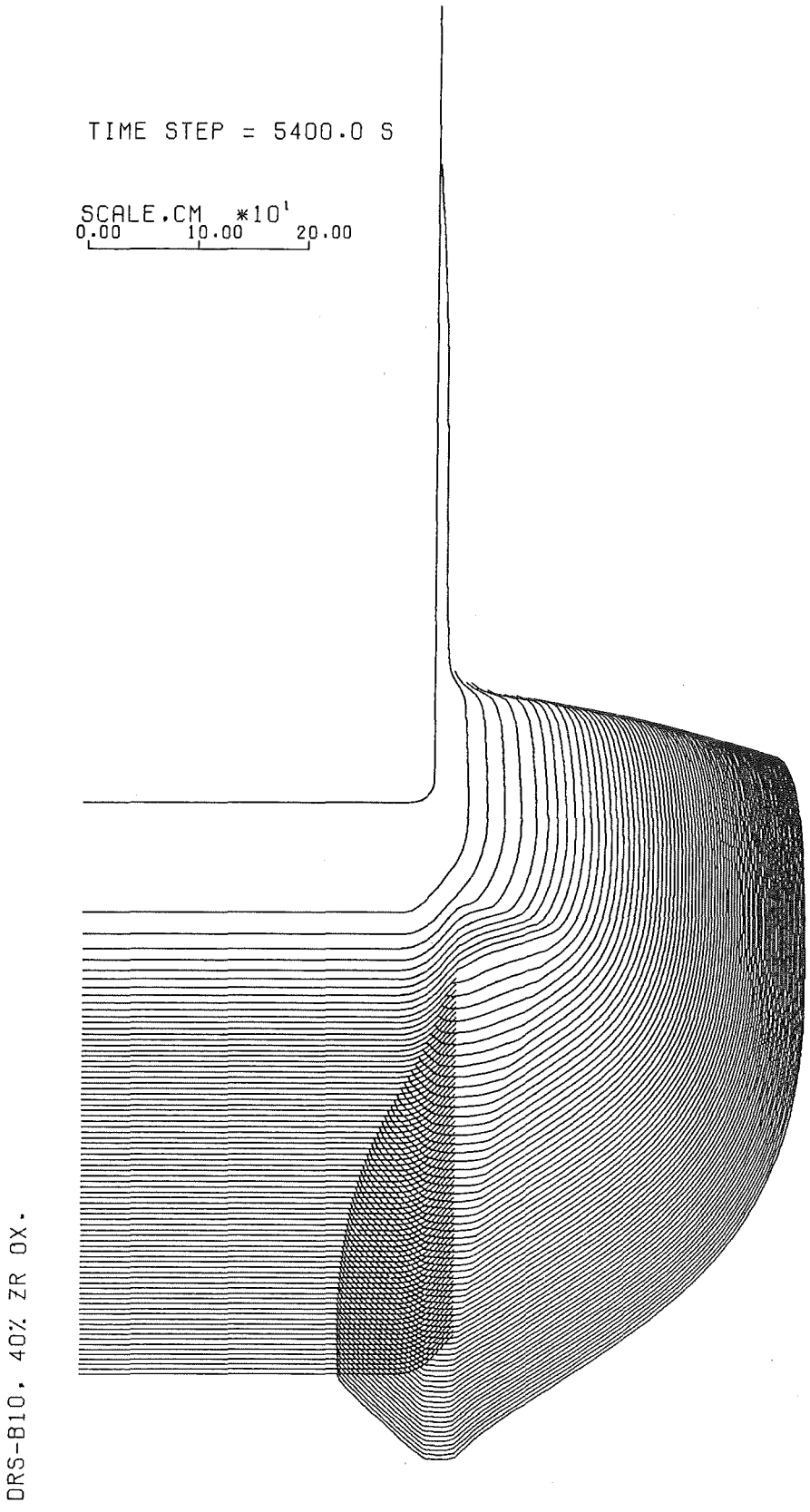

Fig. 1: PWR cavity shape

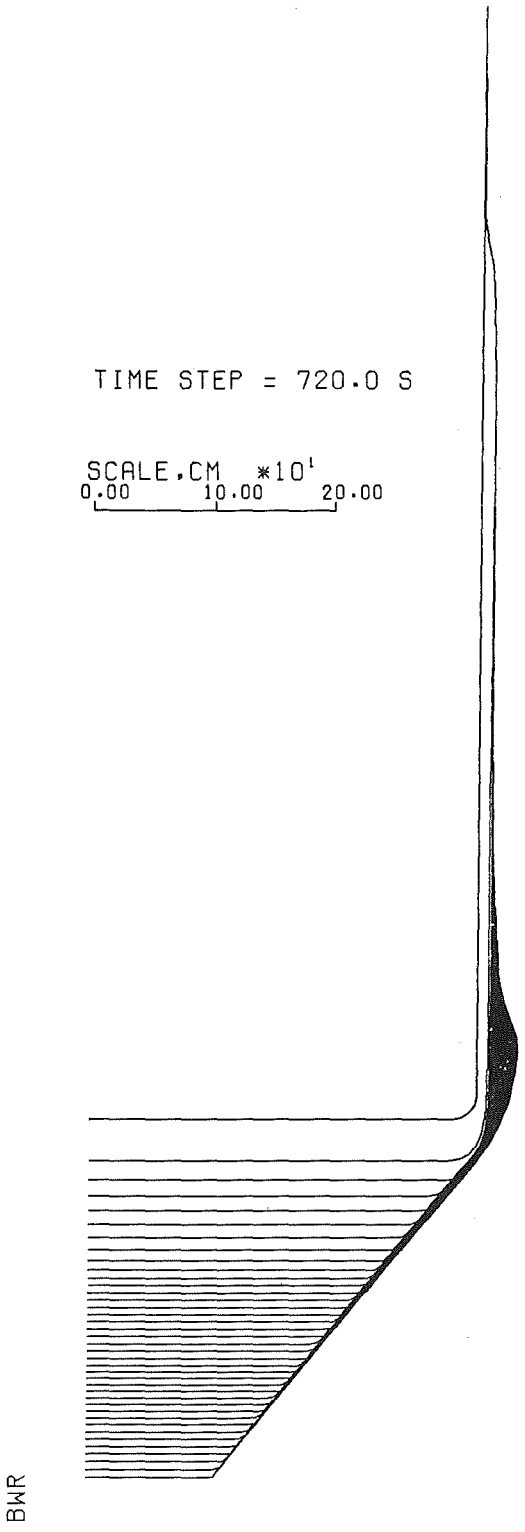

Fig. 2: BWR cavity shape

III.2 Temperature of the melt

The time history of melt temperatures is shown in the following Figure, Fig. 3.

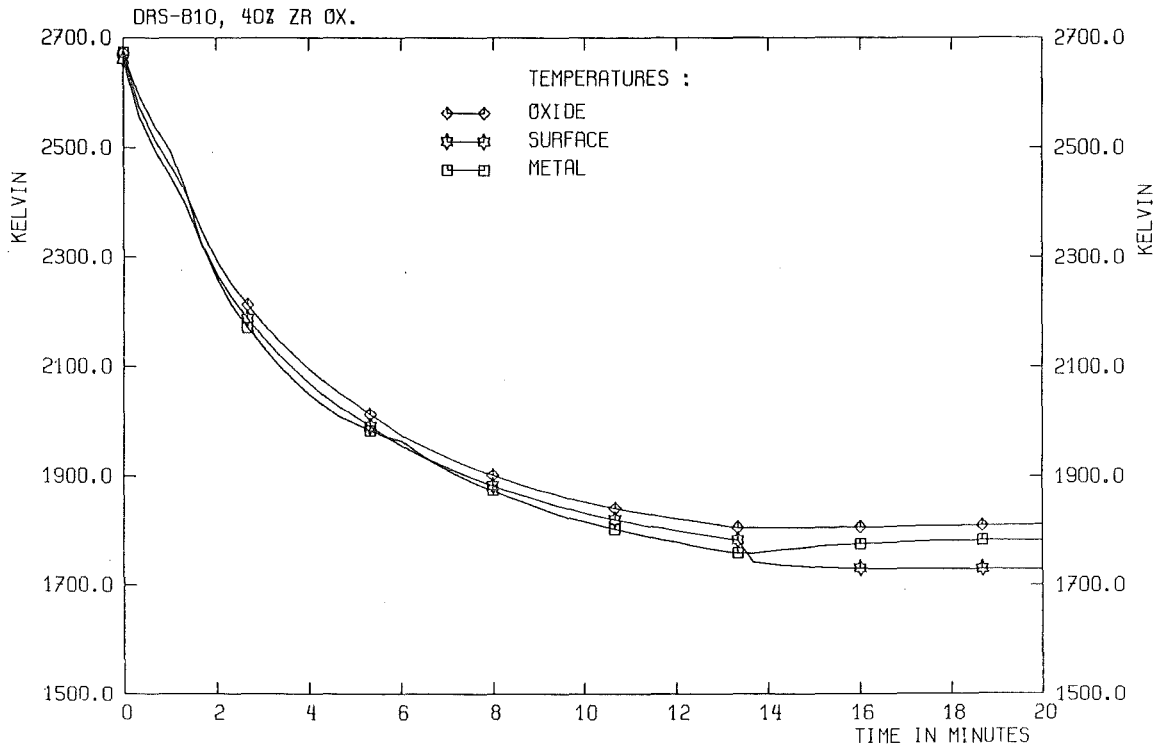

Fig. 3: Melt temperatures for PWR

In spite of the high amount of chemical energy released in the melt due to the exothermic Zr-oxidation reactions, which are completed only in 74 s, the temperature decreases very fast to a stationary level near to the freezing temperature of the metallic melt. During the Zr-oxidation, however, the temperature drop is not so fast as after the burn out of Zr. The following Si-oxidation lasts 166 minutes.

The crust formation starts at t=804 s. Similar results are obtained by using the old oxide solidus temperatures.

Because of a higher amount of Zr in the BWR melt and a very low content of SiO_2 in the limestone concrete considered, the Zr oxidations proceed much slower than in the PWR case. This reaction is completed after t=71 min. The calculated temperatures are given in the following figure.

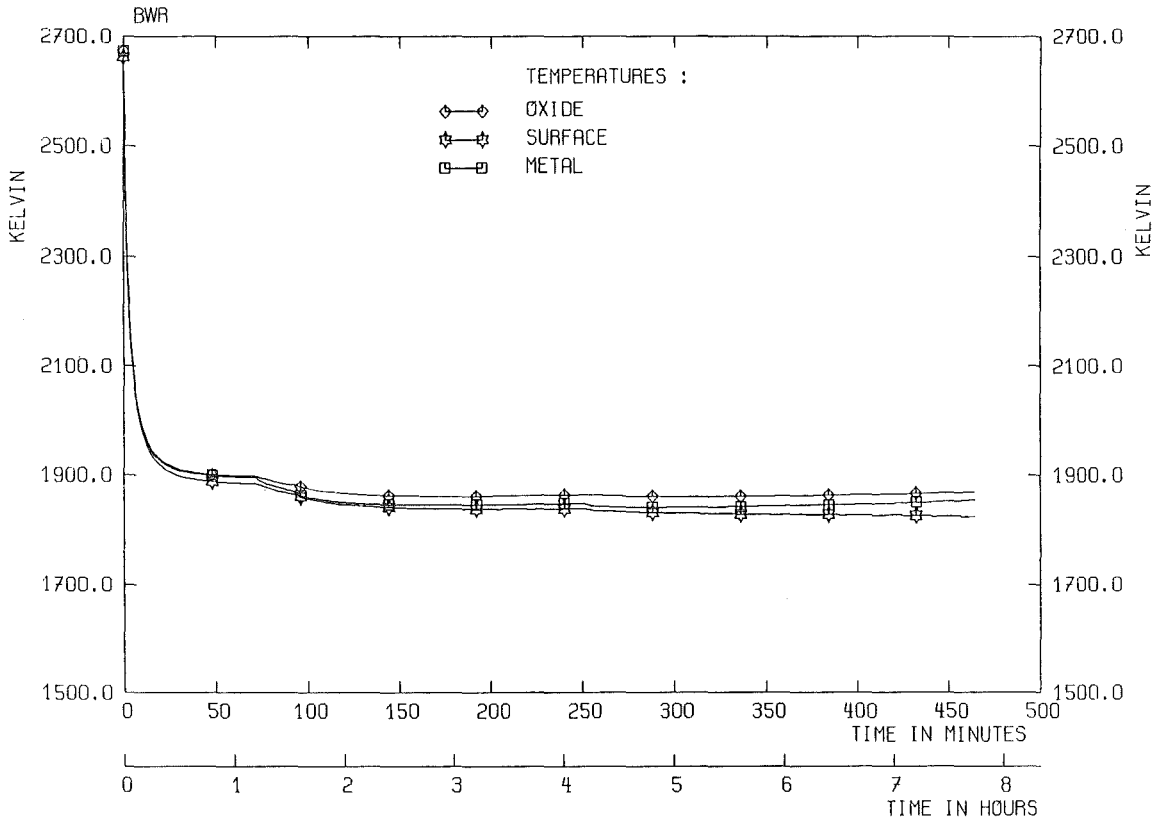

Fig. 4: BWR melt temperatures (new oxide solidus temperature)

In this case there is also a fast drop of the melt temperature to a stionary level above the decomposition temperature of the concrete which is higher than the solidus temperature of the metallic phase considered. Therefore there is no crust formation during the ablation time.

III.3 Gas release rates

As stated before, the concrete composition will determine the composition of the released gases during the melt/concrete interaction. The dominant component in case of the siliceous concrete of the PWR is hydrogen (Fig. 5).

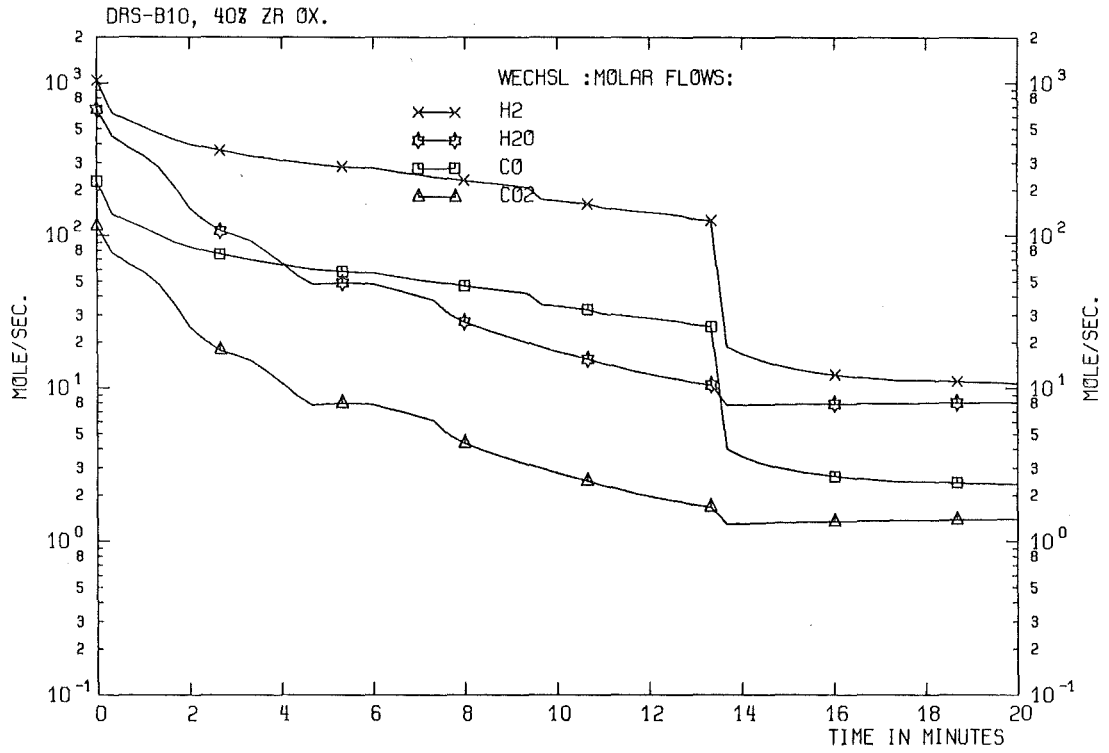

Fig. 5: Gas release rates for PWR

In the BWR case the highest long-term release rates are obtained for CO followed by H_2 (Fig. 6).

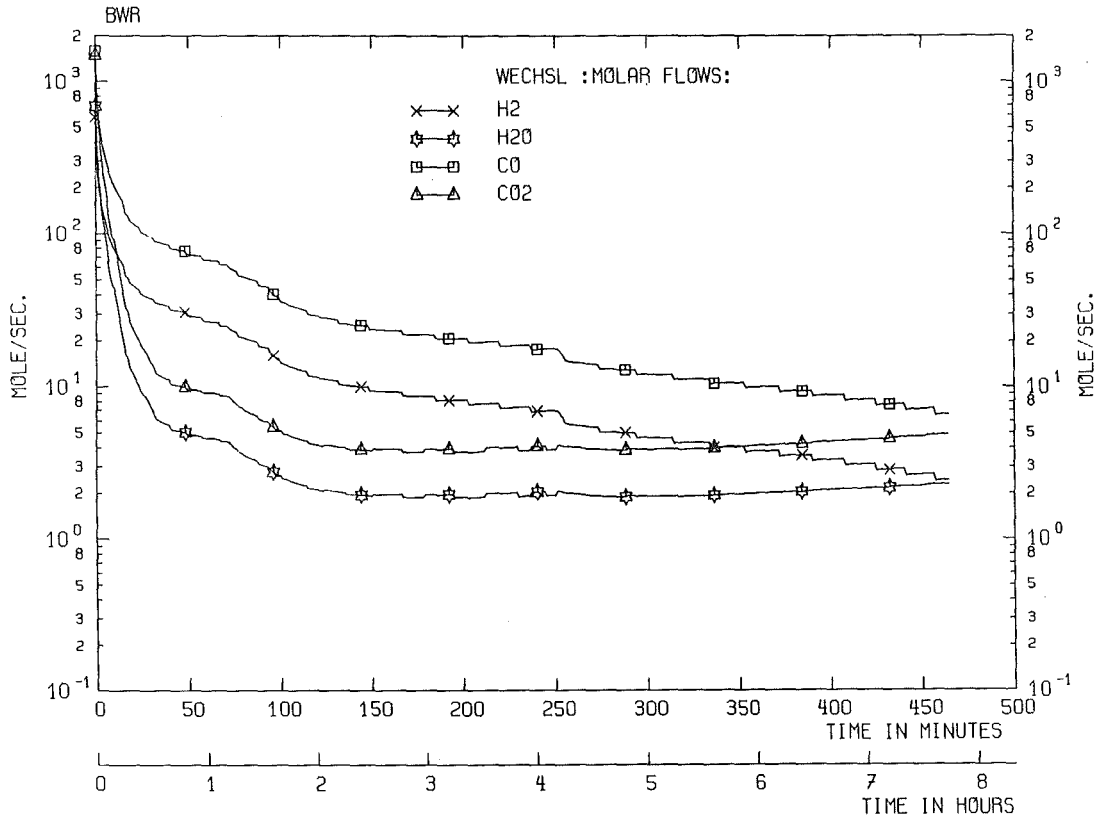

Fig. 6: Gas release rates for the BWR

IV. CONCLUSIONS

An accident analysis for a standard German PWR and a model BWR was performed using the condensed Zr/SiO_2 chemistry which is only relevant for the PWR because of the high content of SiO_2 in the siliceous conrete basemat. Compared to former analyses for the PWR the much faster zirconium oxidation leads to a higher temperature of about 100 K in the early phase of melt/concrete interaction and therefore the crust formation process starts later than in the former analyses leading to a longer duration of high gas release rates dominated by H_2 because of more effective heat transfer to the concrete in this period of time.

The concrete basemat of the BWR consists of pure limestone with a decomposition temperature which is higher than the solidus temperature of the metallic melt. This high concrete decomposition temperature prevents a crust formation at the metal-concrete boundary. Hence a very efficient heat transfer leads to fast base-

mat penetration. Because of the limestone concrete composition the metallic zirconium is oxidized mainly by gases. The highest release rates are obtained for CO followed by H_2. The H_2 release rates are lower than for the PWR. The results for the BWR show a strong dependence on the oxide solidus temperature.

REFERENCES

[1] David R. Bradley, private communication (1991)

APPENDIX A

MEETING PROGRAMME

SECOND OECD (NEA) CSNI SPECIALIST MEETING ON MOLTEN CORE DEBRIS-CONCRETE INTERACTIONS

KfK, Karlsruhe, Germany
1st - 3rd April, 1992

PROGRAMME

General Chairman: H. ALSMEYER (KfK, Germany)

Tuesday 31st March 1992

Pre-registration at hotel upon arrival

Wednesday 1st April 1992

08.15 – 8.25 Welcoming Remarks
by H.H. Hennies (KfK, Germany) and J. Royen (OECD/NEA)

08.25 – 09.00 Ex-Vessel Melt Behavior and Its Role in Safety Assessment of Light Water Reactors (Invited Paper)
by J. Rohde, (GRS, FRG) and G. Cenerino (CEA/IPSN, France)

09.00 – 14.30 SESSION I: MOLTEN CORE-CONCRETE INTERACTIONS UNDER PREDOMINANTLY DRY CONDITIONS -
PART A: EXPERIMENTS
Chairman: B. Kuczera (KfK, Germany)

(Thermal-Hydraulics and Aerosols)

09.00 – 09.30 Interaction Between a Superheated Uranium Dioxide Jet and Cold Concrete
by L.D. Howe, B.D. Turland, and R.J. Humphreys (AEA Technology/SRD, UK) and M.K. Denham and L.M.G. Dop (AEA Technology/WTC, UK)

09.30 – 10.00 Sustained Uranium Dioxide/Concrete Interaction Tests: the SURC Test Series
by E.R. Copus (SNL, USA)

10.00 – 10.30 BETA-Experiments on Zirconium Oxidation and Aerosol Release During Melt-Concrete Interaction
by H. Alsmeyer, C. Adelhelm, H.-G. Dillmann, M. Heinle, W. Ratajczak, G. Schumacher, A. Skokan, W. Tromm (KfK, Germany)

10.30 – 11.00 Break

11.00 – 11.30 ACE Program Phase C: Fission Product Release from Molten Corium - Concrete Interactions (MCCI)
by B.R. Sehgal (EPRI, USA) and B.W. Spencer (ANL, USA)

11.30 – 12.00 Thermal-Hydraulic Aspects of the Large-Scale Integral MCCI Tests in the ACE Program
by D.H. Thompson, J.K. Fink, D.R. Armstrong and B.W. Spencer (ANL, USA) and B.R. Sehgal (EPRI, USA)

12.00 – 12.30 Aerosols Released During Large-Scale Integral MCCI Tests in the ACE Program
by J.K. Fink, D.H. Thompson and B.W. Spencer (ANL, USA) and B.R. Sehgal (EPRI, USA)

12.30 – 14.00 Lunch

14.00 – 17.30 (first part) SESSION II: MOLTEN CORE-CONCRETE INTERACTIONS UNDER PREDOMINANTLY DRY CONDITIONS - PART B: MODELLING AND CODES
Co-Chairmen: P.N. Smith and B.D. Turland (AEA Technology, UK)

(Integral Codes)

14.00 – 14.30 Improved WECHSL Models Including Zirconium Oxidation and its Verification by New BETA Experiments
by J.J. Foit (KfK, Germany)

14.30 – 15.00 Assessment Status of the WECHSL-Mod 3 Code
by C. Renault (CEA/IPSN. France and, J.J. Foit (KfK, Germany)

15.00 – 15.30 Break

15.30 – 16.00 Development and Validation of CORCON-Mod 3
by D.R. Bradley (SNL, USA)

16.00 – 16.30 Energy Modelling of the ACE Molten Core-Concrete Interaction Experiment L6
by J.H. Ptacek and M.L. Corradini (U. of Wisconsin, USA)

16.30 – 17.00 Analyses of ACE MCCI Test L6 with the CORCON/VANESA Code
by A. Hidaka , K. Soda, J. Sugimoto, N. Yamano (JAERI, Japan)

17.00 Close of Day One - Bus transportation

20.00 Hospitality Dinner offered by KfK (H.H. Hennies and G. Heusener, KfK)

Thursday 2nd April 1992

08.15 – 11.45 (second part) SESSION II: MOLTEN CORE-CONCRETE INTERACTIONS UNDER PREDOMINANTLY DRY CONDITIONS - PART B: MODELLING AND CODES
Co-Chairmen: P.N. Smith and B.D. Turland (AEA Technology, UK)

(Thermal-Hydraulics)

08.15 – 08.45 Uncertainty of Corium-Concrete Heat Transfer Correlations due to Uncertainty of Melt Transport Properties
by F.J. Gonzalez (UPM, Spain)

(Materials Properties)

08.45 – 09.15 Non-Ideal Solution Modeling for Predicting Chemical Phenomena During Core Debris Interactions with Concrete
by D.A. Powers (SNL, USA)

09.15 – 09.35 The Calculation of Phase Equilibria of Oxide Core-Concrete Systems
by R.G.J. Ball and M.A. Mignanelli (AEA Technology/Harwell, UK)

09.35 – 09.55 Thermodynamic Calculation of Phase Equilibria in Oxide Complex Systems: Prediction of Some Selected Fission Products (BaO, SrO, La_2O_3) Release
by G. Cenerino (CEA/IPSN, France) and P.Y. Chevalier and E. Fischer (Thermodata, France)

09.55 – 10.15 Thermodynamic Data Bases and Calculation Code Adapted to the Molten Core Concrete Interaction Phenomena, Developed Jointly by THERMODATA and the IPSN
by P.Y. Chevalier (THERMODATA, France) and G. Cenerino (CEA/IPSN, France)

10.15 – 10.45 Break

10.45 – 11.15 A Study of the Parameters Influencing the Release of Species by Vaporization During Core-Concrete Interactions
by M.A. Mignanelli (AEA Technology/Harwell, UK)

11.15 – 11.45 Aerosol Removal from Gas Bubbles Resulting From Molten Core-Concrete Interactions
by G.J. Bamford and S.A. Ramsdale (AEA Technology/SRD, UK)

11.45 – 17.00 SESSION III: MELT SPREADING AND COOLABILITY
PART A: EXPERIMENTS
Chairman: B.R. Sehgal (EPRI, USA)

(Integral Tests)

11.45 – 12.10 Failure Mode of a Concrete Cylinder Due to Attack by an Eroding Melt While Cooled by Outside Water
by H. Alsmeyer, C. Adelhelm, H.-G. Dillmann, M. Heinle, W. Ratajczak, H. Schneider, G. Schumacher, S. Stiefel, A. Skokan and W. Tromm (KfK, Germany)

12.10 – 12.30 Spreading of Melt in Reactor Containment (SMELTR)
by B.R. Sehgal (EPRI, USA) and B.W. Spencer (ANL, USA)

12.30 – 13.03 Lunch

13.30 – 14.30 Visit of the BETA Facility

14.30 – 15.00 ACE Program Phase D: Melt Attack and Coolability Experiments (MACE) Program
by B.R. Sehgal (EPRI, USA) and B.W. Spencer (ANL, USA)

15.00 – 15.30 Results of MACE Tests M0 and M1
by B.W. Spencer, M.T. Farmer, D.R. Armstrong, D.J. Kilsdonk and R.W. Aeschlimann (ANL, USA) and M. Fischer (Siemens AG, UB KWU, Germany)

15.30 – 16.00 Core-Concrete Interactions with Overlying Water Pools
by E.R. Copus (SNL, USA)

16.00 – 16.30 Break

16.30 – 17.00 A Core Catcher Concept Based on Fragmentation of Melts
by W. Tromm, H. Alsmeyer and H. Schneider (KfK, Germany)

17.00 – 18.00 (first part) SESSION IV: MELT SPREADING AND COOLABILITY
PART B: MODELLING AND CODES
Chairman: C. Tinkler (USNRC)

(Separate Effects)

17.00 – 17.30 Modeling and Database for Melt-Water Interfacial Heat Transfer
by M.T. Farmer and B.W. Spencer (ANL, USA), J.P. Schneider (U. of Illinois, USA), B. Bonomo (Northwestern University, USA) and G. Theofanous (U. of California, USA)

17.30 – 18.00 Stress Analysis and Scaling Studies of Corium Crusts
by Z. Feng, R. Engelstad, E. Lovell and M. Corradini (U. of Wisconsin, USA)

Friday 3rd April 1992

08.15 – 11.45 (second part) SESSION IV: MELT SPREADING AND COOLABILITY
PART B: MODELLING AND CODES (continued)
Chairman: C. Tinkler (USNRC)

(Integral Codes)

08.15 – 08.45 Modelling of the MCCI Phenomena with the Presence of a Water Layer
by J.H. Ptacek, Z. Feng, R.L. Engelstad, E.G. Lovell and M.L. Corradini R. Sehgal (U. of Wisconsin, USA) and R. Sehgal (EPRI, USA)

08.45 – 09.15 Melt Coolability Modeling and Comparisons to MACE Test Results
by M.T. Farmer, J.J. Sienicki and B.W. Spencer (ANL, USA)

09.15 – 09.45 Coolability of Corium Spread onto Concrete Under Water: the PERCOLA Model
by J.M. Bonnet and J.M. Seiler (CEA/IPSN, France)

09.45 – 10.15 Status of the MELTSPREAD-1 Computer Code for the Analysis of Transient Spreading of Core Debris Melts
by M.T. Farmer, J.J. Sienicki, B.W. Spencer and C.C. Chu (ANL, USA)

10.15 – 10.45 Break

10.45 – 11.15 How to Avoid Molten Core/Concrete Interactions (and Steam Explosions)
by A. Turricchia (ENEL/DCO, Italy)

11.15 – 15.15 SESSION V: CODE COMPARISON AND PLANT APPLICATIONS
Chairman: C. Lecomte (CEA/IPSN, France)

(Code Comparisons)

11.15 – 11.45 Results of OECD International Standard Problem No. 30 on BETA Test V5.1 on Core-Concrete Interaction
by M. Firnhaber (GRS, Germany)

11.45 – 12.15 Results of Aerosol Code Comparisons with Releases from ACE MCCI Tests
by J.K. Fink (ANL, USA), M.L. Corradini (U. of Wisconsin, USA), A. Hidaka (JAERI, Japan), E. Hontañon (UPM, Spain), M.A. Mignanelli (AEA Technology/Harwell, UK), E. Schrödl (GRS. Germany) and V. Strizhov (INS, Russia)

12.15 – 13.45 Lunch

(Plant Applications)

13.45 – 14.15 Contribution to the Subject Evaluating the Core Melt/Concrete Interactions Concerning the Reactor Type VVER-1000
by C.-J. Steinkopf and F. Müller (T.H. Zittau, Germany)

14.15 – 14.45 Application of the WECHSL Code to PWR and BWR Specific Accident Scenarios
by J.J. Foit (KfK, Germany)

14.45 – 15.15 Break

15.15 – 17.15 SESSION VI: SUMMARY AND CONCLUSIONS
Chairman: H. Alsmeyer (KfK, Germany)

15.15 – 16.15 Session Chairmen Summaries

16.15 – 17.15 General Discussion

17.15 – 17.30 Closing Remarks (G. Heusener, KfK, Germany)

17.30 Close of Meeting - Bus transportation

19.30 Meeting of the Programme Committee/Session Chairmen:

H. Alsmeyer (KfK, Germany) - Chairman
B. Kuczera (KfK, Germany)
C. Lecomte (CEA/IPSN, France)
B.R. Sehgal (EPRI, USA)
P.N. Smith (AEA Technology/WTC, UK)
C. Tinkler (USNRC)
B.D. Turland (AEA Technology/SRD, UK)
J. Royen (OECD/NEA) - Secretary

Saturday 4th April 1992

09.00 – 13.00 Meeting of the Programme Committee:

H. Alsmeyer (KfK, Germany) - Chairman
B.R. Sehgal (EPRI, USA)
P.N. Smith (AEA Technology/WTC, UK)
C. Tinkler (USNRC)
B.D. Turland (AEA Technology/SRD, UK)
J. Royen (OECD/NEA) - Secretary

APPENDIX B

List of Participants

Belgium

Dr. Dries Gryffroy
AIB-Vinçotte Nuclear (AVN)
Avenue du Roi, 157
B-1060 Brussels
Telephone: + 32 (2) 536 8586
Telefax : + 32 (2) 537 4619
Telex : 22550 VINCOT B

Mr. Robert Prior
Safety, Training & Simulation Department
Westinghouse Energy Systems International S.A.
Rue de Stalle, 73
B-1180 Brussels
Telephone: + 32 (2) 370 2965
Telefax : + 32 (2) 370 2926
Telex : 24621 B

Dr. Jean Snoeck
Group Leader "Confinement Integrity"
Nuclear Generation Department
Tractebel Energy Engineering
Avenue Ariane, 7/5D
B-1200 Brussels
Telephone: + 32 (2) 773 8355
Telefax : + 32 (2) 773 8900
Telex : 21852 TRACT B

Czech & Slovak Federal Republic

Dr. Bohumir Kujal
Senior Scientist
Nuclear Research Institute
250 68 Rez near Prague
Telephone: + 42 (2) 6857831 ext. 3657
Telefax : + 42 (2) 6857567

Finland

Mr. Jari Ikänen
Imatran Voima OY (IVO)
Rajatorpantie 8
P.O. Box 112
SF-01601 Vantaa
Telephone: + 358 (0) 508 2466
Telefax : + 358 (0) 508 3403
Telex : 124608 VOIMA SF

Ms. Ilona Lindholm
Technical Research Centre of Finland (VTT)
Nuclear Engineering Laboratory (YDI)
P.O. Box 208 (Tekniikantie 4)
SF-02151 Espoo
Telephone: + 358 (0) 456 5031
Telefax : + 358 (0) 456 5000
Telex : 122972 VTTHA SF

France

Dr. Georges Berthoud
STR/LML
Commissariat à l'Energie Atomique
Centre d'Etudes Nucléaires de Grenoble
85X
F-38041 Grenoble CEDEX
Telephone: + 33 ( ) 7688 3244
Telefax : + 33 ( ) 7688 5177

Dr. Gérard Cenerino
Service d'Etudes des Accidents (SEAC)
Département de Protection de l'Environnement et des Installations (DPEI)
Institut de Protection et de Sûreté Nucléaire
Commissariat à l'Energie Atomique
Centre d'Etudes Nucléaires de Fontenay-aux-Roses
B.P. 6
F-92265 Fontenay-aux-Roses CEDEX
Telephone: + 33 (1) 4654 9098
Telefax : + 33 (1) 4654 3264
Telex : 270898 ENERGAT F

Dr. Pierre-Yves Chevalier
THERMODATA
Domaine Universitaire de Grenoble
B.P. 66
F-38402 Saint Martin d'Hères CEDEX
Telephone: + 33 ( ) 7642 7690
Telefax : + 33 ( ) 7682 6630 (specify: THERMODATA)

Mr. Jacques Duco
Adjoint au Chef du Département
Département de Protection de l'Environnement et des Installations (DPEI)
Institut de Protection et de Sûreté Nucléaire
Commissariat à l'Energie Atomique
Centre d'Etudes Nucléaires de Fontenay-aux-Roses
B.P. 6
F-92265 Fontenay-aux-Roses CEDEX
Telephone: + 33 (1) 4654 7068
Telefax : + 33 (1) 4654 4437
Telex : 270898 ENERGAT F

Mr. Alain Dumontet
Division "Thermohydraulique"
Service Etudes et Projets Thermiques et Nucléaires
(SEPTEN)
Direction de l'Equipement
Electricité de France
12-14 Avenue Dutriévoz
F-69628 Villeurbanne CEDEX
Telephone: + 33 ( ) 7894 4607
Telefax : + 33 ( ) 7894 4999
Telex : 305323 EDFEP F

Mrs. Catherine Lecomte
Chef du Service d'Etudes des Accidents (SEAC)
Département de Protection de l'Environnement et des
Installations (DPEI)
Institut de Protection et de Sûreté Nucléaire
Commissariat à l'Energie Atomique
Centre d'Etudes Nucléaires de Fontenay-aux-Roses
B.P. 6
F-92265 Fontenay-aux-Roses CEDEX
Telephone: + 33 (1) 4654 8183
Telefax : + 33 (1) 4654 3264
Telex : 270049 SURIN F

Dr. Claude Renault
Service d'Etudes et de Modélisation
d'Accidents de Réacteurs (SEMAR)
Département de Recherches en Sécurité (DRS)
Institut de Protection et de Sûreté Nucléaire
Commissariat à l'Energie Atomique
Centre d'Etudes Nucléaires de Cadarache
F-13108 Saint-Paul-Lez-Durance CEDEX
Telephone: + 33 ( ) 4225 4602
Telefax : + 33 ( ) 4225 6399
Telex : 440678 CEACA F

Mr. Jean-Marie Seiler
STR/LETC
Commissariat à l'Energie Atomique
Centre d'Etudes Nucléaires de Grenoble
85X
F-38041 Grenoble CEDEX
Telephone: + 33 ( ) 7688 3023
Telefax : + 33 ( ) 7688 5177

Mr. Jean-Michel Veteau
STR/LETC
Commissariat à l'Energie Atomique
Centre d'Etudes Nucléaires de Grenoble
85X
F-38041 Grenoble CEDEX
Telephone: + 33 ( ) 7688 4787
Telefax : + 33 ( ) 7688 5177

Germany

Dr. Hans-Josef Allelein
Gesellschaft für Anlagen- und Reaktorsicherheit (GRS) mbH
Schwertnergasse 1
Postfach 10 16 50
D-5000 Köln 1
Telephone: + 49 (221) 2068 305
Telefax : + 49 (221) 2068 442
Teletex : 17-2214123 GRS

Dr. Hans Alsmeyer
Institut für Angewandte Thermo- und Fluiddynamik
Kernforschungszentrum Karlsruhe GmbH
Postfach 3640
D-7500 Karlsruhe 1
Telephone: + 49 (7247) 82 3454
Telefax : + 49 (7247) 82 4837
Telefax : 17-724716 KFK

Mr. Volker Altus
Technische Hochschule Zittau
Fakultät Maschinenbau/Energietechnik
Lehrstuhl Bau- und Montagetechnologie
Schliebenstrasse 21
0-8800 Zittau
Telephone: + 37 (522) 61632
Telefax : + 37 (522) 61627
Telex : 25923 THZ DD

Dr. Werner Baukal
Energy and Process Technologies
Battelle - Institut e.V.
Am Römerhof 35
Postfach 90 01 60
D-6000 Frankfurt am Main 90
Telephone: + 49 (69) 7908 2293
Telefax : + 49 (69) 7908 80
Telex : 411966

Dr. Manfred Firnhaber
Gesellschaft für Anlagen- und Reaktorsicherheit (GRS) mbH
Schwertnergasse 1
Postfach 10 16 50
D-5000 Köln 1
Telephone: + 49 (221) 2068 315
Telefax : + 49 (221) 2068 442
Teletex : 17-2214123 GRS

Dr. Jerzy J. Foit
Institut für Angewandte Thermo- und Fluiddynamik
Kernforschungszentrum Karlsruhe GmbH
Postfach 3640
D-7500 Karlsruhe 1
Telephone: + 49 (7247) 82 3467
Telefax : + 49 (7247) 82 4837
Telefax : 17-724716 KFK

Dr. Sieghard Hellmann
Siemens AG
KWU 5531
Hammerbacherstrasse 12+14
D-8520 Erlangen
Telephone: + 49 (9131) 182428
Telefax : + 49 (9131) 185234

Mr. Günter Jacobs
Institut für Neutronenphysik und Reaktortechnik
Kernforschungszentrum Karlsruhe GmbH
Postfach 3640
D-7500 Karlsruhe 1
Telephone: + 49 (7247) 82 2435
Telefax : + 49 (7247) 82 4874
Telefax : 17-724716 KFK

Dr. Bernhard Kuczera
Deputy Head, Project Nuclear Safety Research (PSF)
Kernforschungszentrum Karlsruhe GmbH
Postfach 3640
D-7500 Karlsruhe 1
Telephone: + 49 (7247) 82 4000
Telefax : + 49 (7247) 82 5508
Teletex : 17-724716 KFK

Mr. Frank Müller
Technische Hochschule Zittau
Fakultät Maschinenbau/Energietechnik
Lehrstuhl Bau- und Montagetechnologie
Schliebenstrasse 21
0-8800 Zittau
Telephone: + 37 (522) 61632
Telefax : + 37 (522) 61627
Telex : 25923 THZ DD

Mr. J. Paulus
Lehrstuhl für Nukleare und Neue Energiesysteme
Fakultät für Maschinenbau
Ruhr-Universität Bochum
D-4630 Bochum
Telephone: + 49 (234) 700 6374
Telefax : + 49 (234) 700 6363
Teletex : 17-234356

Mr. Hermann Plank
Nuclear Power Generation Division
Siemens AG/UB KWU - R 212
Hammerbacherstrasse 12+14
D-8520 Erlangen
Telephone: + 49 (9131) 18-5634
Telefax : + 49 (9131) 18-4793
Teletex : 17-91314 SIKWUEH
Telex : 62929 SIK D

Dipl.-Ing. Willi Ratajczak
Abt. HVT/EA
Kernforschungszentrum Karlsruhe GmbH
Postfach 3640
D-7500 Karlsruhe 1
Telephone: + 49 (7247) 82 3013
Telefax : + 49 (7247) 82 3186
Telefax : 17-724716 KFK

Dr. Jürgen Rohde
Leiter, Abteilung Schwere Störfälle
Gesellschaft für Anlagen- und Reaktorsicherheit (GRS) mbH
Schwertnergasse 1
Postfach 10 16 50
D-5000 Köln 1
Telephone: + 49 (221) 2068 207
Telefax : + 49 (221) 2068 442
Teletex : 17-2214123 GRS

Mr. Edgar R. Schimetschka
Battelle - Institut e.V.
Am Römerhof 35
Postfach 90 01 60
D-6000 Frankfurt am Main 90
Telephone: + 49 (69) 7908 2380
Telefax : + 49 (69) 7908 86
Telex : 411966

Dr. Eugen Schrödl
Gesellschaft für Anlagen- und Reaktorsicherheit (GRS) mbH
Schwertnergasse 1
Postfach 10 16 50
D-5000 Köln 1
Telephone: + 49 (221) 2068 512
Telefax : + 49 (221) 2068 442
Teletex : 17-2214123 GRS

Mr. Walter Tromm
Institut für Angewandte Thermo- und Fluiddynamik
Kernforschungszentrum Karlsruhe GmbH
Postfach 3640
D-7500 Karlsruhe 1
Telephone: + 49 (7247) 82 3467
Telefax : + 49 (7247) 82 4837
Teletex : 17-724716 KFK

Italy

Mr. Leonardo Arru
Direzione Sicurezza Nucleare e Protezione Sanitaria (DISP)
ENEA
Via Vitaliano Brancati, 48
I-00144 Roma
Telephone: + 39 (6) 5007 2147
Telefax : + 39 (6) 5007 2044
Telex : 612167 ENEUR I

Mr. Gianfranco Capponi
Safety Studies Division
Direzione Sicurezza Nucleare e Protezione Sanitaria (DISP)
ENEA
Via Vitaliano Brancati, 48
I-00144 Roma
Telephone: + 39 (6) 5007 2146
Telefax : + 39 (6) 5007 2044
Telex : 612167 ENEUR I

Dr. Flavio Parozzi
Centro Ricerca Termica e Nucleare (DSR/CRTN)
Ente Nazionale per l'Energia Elettrica (ENEL)
Via Monfalcone, 15
I-20132 Milano
Telephone: + 39 (2) 7224 3420
Telefax : + 39 (2) 7224 3496
Telex : 310496 ENELMICRTNS

Mr. Massimo Pezzilli
Innovative Reactors Department
ENEA
C.R.E. Casaccia
Via Anguillarese 301
I-00060 Roma
Telephone: + 39 (6) 3048 4197
Telefax : + 39 (6) 3048 6308
Telex : 613296 ENEACA I

Mr. Ivo Tripputi
Manager, Safety Criteria and Licensing
DSR/VDN
Ente Nazionale per l'Energia Elettrica (ENEL)
Viale Regina Margherita, 137
I-00198 Roma
Telephone: + 39 (6) 8509 8308
Telefax : + 39 (6) 8509 8601

Mr. Arnaldo Turricchia
Head, Nuclear Systems Group
Direzione delle Costruzioni (DCO)
Ente Nazionale per l'Energia Elettrica (ENEL)
Via G.B. Martini, 3
I-00198 Roma
Telephone: + 39 (6) 8509 3703
Telefax : + 39 (6) 8509 3086
Telex : 610518 ENELDG I

Japan

Dr. Jun Sugimoto
Severe Accident Research Laboratory
Japan Atomic Energy Research Institute
Tokai Research Establishment
Tokai-mura
Naka-gun
Ibaraki-ken, 319-11
Telephone: + 81 (292) 82 5871
Telefax : + 81 (292) 82 5570 or 6199
Telex : 03632340 JTOKAI J

Russian Federation

Prof. A. Khrulev
I.V. Kurchatov Institute of Atomic Energy
Kurchatov Square
123182 Moscow
Telephone:
Telefax : + 7 (095) 196 1702 or 194 3259

Dr. Yuri Zvonarev
I.V. Kurchatov Institute of Atomic Energy
Kurchatov Square
123182 Moscow
Telephone:
Telefax : + 7 (095) 196 1702 or 194 3259

Spain

Mr. Fco Javier Gonzalez
Universidad Politécnica
Escuela Técnica Superior
de Ingenieros Industriales
Calle José Guttiérez Abascal, 2
E-28006 Madrid
Telephone: + 34 (1) 562 6200 ext. 301
Telefax : + 34 (1) 561 8618
Telex : 48495 ETSII E

Sweden

Mr. Gunnar Jung
PTR
Vattenfall AB (Swedish State Power Board)
S-162 87 Vällingby
Telephone: + 46 (8) 7395349
Telefax : + 46 (8) 877469
Telex : 11914 SVVSTH S

Switzerland

Mr. Bruno Covelli
TECOVA AG
Litzibuech 8
CH-5610 Wohlen
Telephone: + 41 (57) 227030
Telefax : + 41 (57) 229812

Mr. Karl Lieber
Paul Scherrer Institute
CH-5232 Villigen PSI
Telephone: + 41 (56) 992708
Telefax : + 41 (56) 982327
Telex : 827417 PSI CH

Dr. Ulrich Schmocker
Head, Reactor Technology Section
Swiss Federal Nuclear Safety Inspectorate
Hauptabteilung für die Sicherheit der Kernanlagen
CH-5232 Villigen-HSK
Telephone: + 41 (56) 993964
Telefax : + 41 (56) 993907
Telex : 827427 ASK CH

United Kingdom

Dr. G.J. Bamford
AEA Technology
SRD
Wigshaw Lane
Culcheth
Cheshire WA3 4NE
Telephone: + 44 (925) 232 000
Telefax : + 44 (925) 254570
Telex : 629301 ATOMRY G

Dr. Michael A. Mignanelli
Section Leader
Reactor Chemistry Department
Materials and Chemistry Division, B.540.1
AEA Reactor Services
AEA Technology
Harwell Laboratory
Oxfordshire OX11 ORA
Telephone: + 44 (235) 821111 ext. 4300
Telefax : + 44 (235) 436314
Telex : 83135 ATOMHA G

Dr. Paul. N. Smith
Thermal-Hydraulics and Degraded Core Section
Reactor Safety Department
Safety and Performance Division
215/A32
AEA Technology
Winfrith Technology Centre
Dorchester
Dorset DT2 8DH
Telephone: + 44 (305) 251 888 ext. 2977
Telefax : + 44 (305) 202 508
Telex : 41231 ATOMWH G

Dr. Brian D. Turland
Section Leader, Severe Accidents
SRD Culham Office, D5/45
AEA Technology
Culham Laboratory
Abingdon
Oxfordshire OX14 3DB
Telephone: + 44 (235) 463294
Telefax : + 44 (235) 464143

United States of America

Mr. Ervin R. Copus
Division 6422
Sandia National Laboratories
P.O. Box 5800
Albuquerque, New Mexico 87185-5800
Telephone: + 1 (505) 845-3220
Telefax : + 1 (506) 845-3435

Prof. Michael Corradini
Department of Nuclear Engineering
and Engineering Physics
College of Engineering
University of Wisconsin
153 Engineering Research Building
1500 Johnson Drive
Madison, Wisconsin 53706-1687
Telephone: + 1 (608) 263 2196
Telefax : + 1 (608) 262 6707

Dr. Farouk Eltawila
Chief, Accident Evaluation Branch
Division of Systems Research
U.S. Nuclear Regulatory Commission
Washington, D.C. 20555
Telephone: + 1 (301) 492-3525
Telefax : + 1 (301) 492-3585

Prof. Roxann L. Engelstad
Department of Mechanical Engineering
College of Engineering
University of Wisconsin-Madison
307 Mechanical Engineering Building
1513 University Avenue
Madison, Wisconsin 53706-1572
Telephone: + 1 (608) 262 5745
Telefax : + 1 (608) 265 2316

Dr. Mitchell T. Farmer
Assistant Nuclear Engineer
RE Building 206
Argonne National Laboratory
9700 South Cass Avenue
Argonne, Illinois 60439-4837
Telephone: + 1 (708) 252 4539
Telefax : + 1 (708) 252 6080

Dr. Joanne K. Fink
Building 206 - Room A107
Argonne National Laboratory
9700 South Cass Avenue
Argonne, Illinois 60439-4837
Telephone: + 1 (708) 252 6512
Telefax : + 1 (708) 252 6080

Mr. John Kudrick
Section Chief, Plant Systems Branch
U.S. Nuclear Regulatory Commission
Washington, D.C. 20555
Telephone: + 1 (301) 504-2871
Telefax : + 1 (301) 504-2260

Prof. Edward G. Lovell
Department of Mechanical Engineering
College of Engineering
University of Wisconsin-Madison
1415 Johnson Drive
Madison, Wisconsin 53706
Telephone: + 1 (608) 262 0944
Telefax : + 1 (608) 265 3735

Mr. Martin Plys
Manager, Nuclear Methods Development
Fauske and Associates, Inc.
16W070 West 83rd Street
Burr Ridge, Illinois 60521
Telephone: + 1 (708) 887 5207
Telefax : + 1 (708) 986 5481

Dr. Michael F. Roche
Chemical Technology Division, Building 205
Argonne National Laboratory
9700 South Cass Avenue
Argonne, Illinois 60439-4837
Telephone: + 1 (708) 252 5338
Telefax : + 1 (708) 252 4176

Dr. B. Raj Sehgal
Senior Scientific Advisor
Safety & Reliability Department
Nuclear Power Division
Electric Power Research Institute
3412 Hillview Avenue
P.O. Box 10412
Palo Alto, California 94303
Telephone: + 1 (415) 855 2719
Telefax : + 1 (415) 855 1026 or 2774
Telex : 82977 EPRI UF

Dr. Bruce W. Spencer
Manager, Engineering Development Laboratories
Reactor Engineering Division/Bldg 206
Argonne National Laboratory
9700 South Cass Avenue
Argonne, Illinois 60439-4837
Telephone: + 1 (708) 252 6564
Telefax : + 1 (708) 252 6080

Mr. Ashok Thadani
Director
Division of Systems Technology
U.S. Nuclear Regulatory Commission
Washington, D.C. 20555
Telephone: + 1 (301) 504 2884
Telefax : + 1 (301) 504 1137

Dr. David H. Thompson
Reactor Engineering Division
Building 206 - Room A107
Argonne National Laboratory
9700 South Cass Avenue
Argonne, Illinois 60439-4837
Telephone: + 1 (708) 252 6664
Telefax : + 1 (708) 252 6080

Mr. Charles Tinkler
Section Leader, Containment Challenges Section
Accident Evaluation Branch
Division of Systems Research
Office of Nuclear Regulatory Research
U.S. Nuclear Regulatory Commission
Washington, D.C. 20555
Telephone: + 1 (301) 492 3569
Telefax : + 1 (301) 492 3585

Commission of the European Communities

Mr. Enzo Della Loggia
Division of Safety of Nuclear Installations
Directorate-General for Science, Research and Development (DG XII/D/1)
Commission of the European Communities
Rue de la Loi, 200
B-1049 Bruxelles
Belgique
Telephone: + 32 (2) 235 7886
Telefax : + 32 (2) 236 2006 or 235 8046 or 235 0145
Telex : 21877 COMEU B

OECD Nuclear Energy Agency

Dr. Jacques Royen
Deputy Head, Nuclear Safety Division
OECD Nuclear Energy Agency
38 Boulevard Suchet
F-75016 Paris
France
Telephone: + 33 (1) 4524 9692
Telefax : + 33 (1) 4524 9624
Telex : 645668 AENENA F

APPENDIX C

ORIGIN AND PURPOSES OF THE OECD, NEA, AND CSNI

ORIGIN AND PURPOSES OF THE OECD, NEA, AND CSNI

OECD

The Convention establishing the Organisation for Economic Co-operation and Development (OECD) was signed on 14th December 1960.

Pursuant to article 1 of the Convention, the OECD shall promote policies designed:

- to achieve the highest sustainable economic growth and employment and a rising standard of living in Member countries, while maintaining financial stability, and this to contribute to the development of the world economy;
- to contribute to sound economic expansion in Member as well as non-member countries in the process of economic development; and
- to contribute to the expansion of world trade on a multilateral, non-discriminatory basis in accordance with international obligations.

The current Signatories of the Convection are Australia, Austria, Belgium, Canada, Denmark, Finland, France, the Federal Republic of Germany, Greece, Iceland, Ireland, Italy, Japan, Luxembourg, the Netherlands, New Zealand, Norway, Portugal, Spain, Sweden, Switzerland, Turkey, the United Kingdom, and the United States.

NEA

The OECD Nuclear Energy Agency (NEA) now groups all the European Member countries of OECD and Australia, Canada, Japan, and the United States. The Commission of the European Communities takes part in the work of the Agency.

The primary objectives of NEA are to promote co-operation between its Member governments on the safety and regulatory aspects of nuclear development and on assessing the future role of nuclear energy as a contributor to economic progress.

NEA works in close collaboration with the International Atomic Energy Agency, with which it has concluded a Co-operation Agreement, as well as with other international organisations in the nuclear field.

CSNI

The NEA Committee on the Safety of Nuclear Installations (CSNI) is an international committee made up of scientists and engineers. It was set up in 1973 to develop and coordinate the activities of the OECD Nuclear Energy Agency concerning the technical aspects of the design, construction and operation of nuclear installations insofar as they affect the safety of such installations. The Committee's purpose is to foster international co-operation in nuclear safety amongst the OECD Member countries.